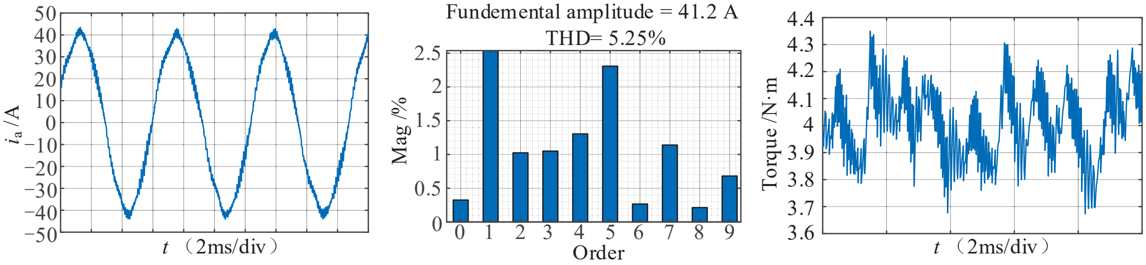

(**a**) (**b**) (**c**)

Figure 17. Simulation results under pulse time compensation. (**a**) i_{as}; (**b**) FFT; and (**c**) output torque.

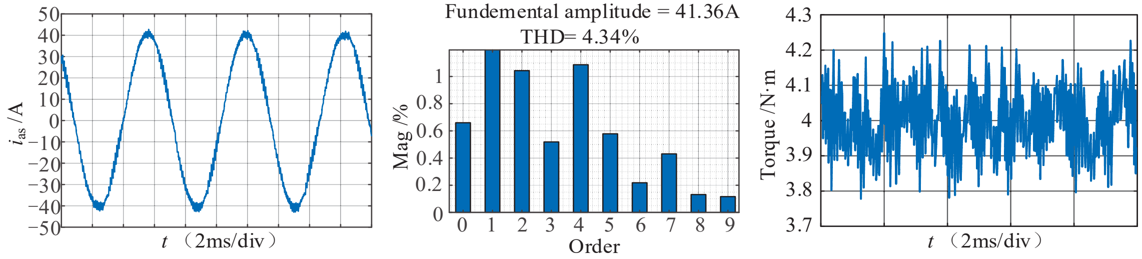

(**a**) (**b**) (**c**)

Figure 18. Simulation results under 6th harmonic controller. (**a**) i_{as}; (**b**) FFT; and (**c**) output torque.

Table 3. Comparison of the simulation results.

Compensation Method	THD	5th Harmonic	7th Harmonic	Torque Ripple (N·m)
No compensation	5.88%	2.9%	1.4%	3.6 to 4.3
Pulse time compensation	5.33%	2.3%	1.2%	3.7 to 4.3
6th harmonic controller	4.34%	0.58%	0.43%	3.8 to 4.2

To certify the effectiveness of the resonant controller shown in Formula (12) at low frequency, the fundamental frequency is set as 30 Hz, two simulations are carried out by the controller (11) and (12), respectively. The low-order harmonics distribution of the stator current is shown in Figure 19. It is obvious that the resonant controller of (11) cannot suppress the 5th and 7th harmonic components of the stator current. As opposed to this, the 5th and 7th harmonic components are significantly reduced when the resonant controller of (12) is adopted.

Next, the impact on the dynamic performance of the system from the resonant controller is verified. Firstly, the load torque is set to 4 N·m constantly, and the command value of speed changes from 3000 rpm to 4500 rpm, the dynamic simulation results with and without the resonant controller are shown in Figure 20. Then, the command value of speed is set to 4000 rpm, the load torque increases from 2 N·m to 4 N·m, and the dynamic simulation results with and without the resonant controller are shown in Figure 21. After the resonant controller is introduced, only a slight difference occurs in the dynamic waveforms of speed and torque, so the resonant controller has no impact on the dynamic performance.

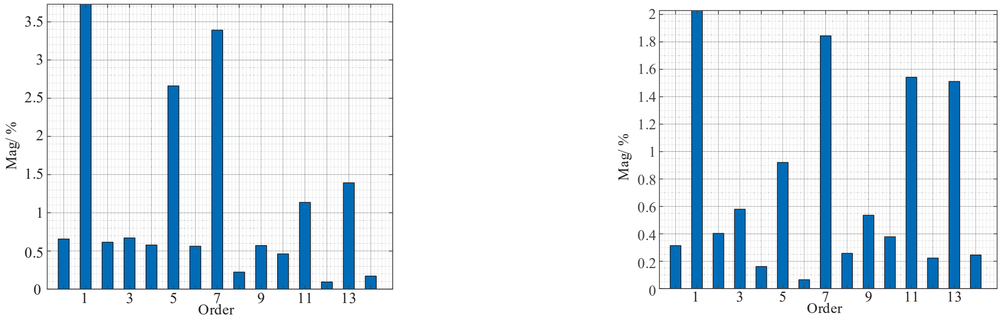

(**a**) (**b**)

Figure 19. The FFT analysis results of the stator current under different resonant controllers. (**a**) $G_R(s)$ of (11); (**b**) $G_R(s)$ of (12).

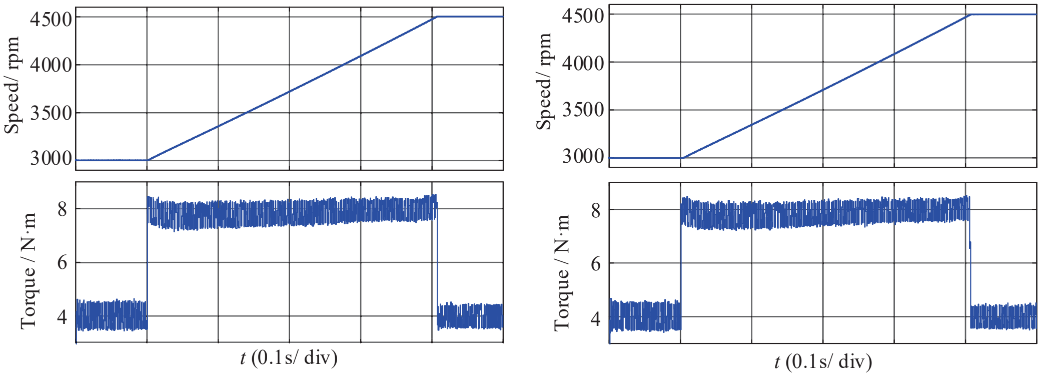

(**a**) (**b**)

Figure 20. The dynamic simulation waveforms when the speed changes from 3000 rpm to 4500 rpm. (**a**) Without resonant controller; (**b**) with resonant controller.

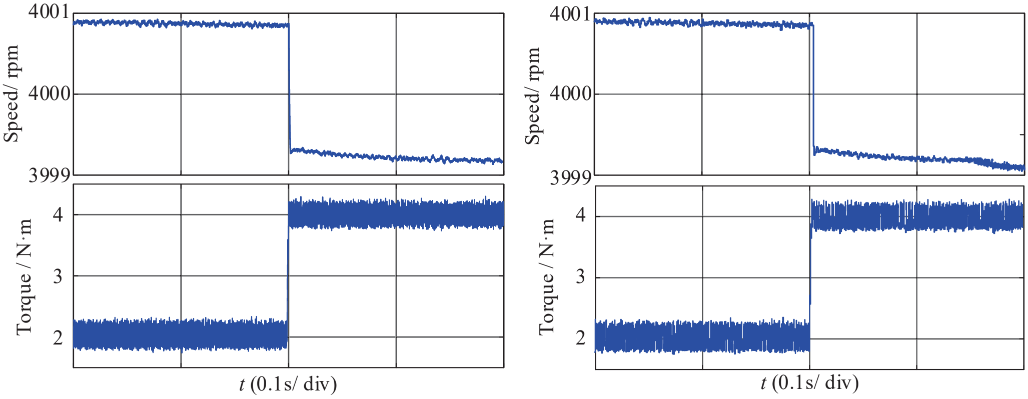

(**a**) (**b**)

Figure 21. The dynamic simulation waveforms when the load changes from 2 N·m to 4 N·m. (**a**) Without resonant controller; (**b**) with resonant controller.

6. Experimental Results

The experimental prototype, shown in Figure 22, is established to verify the suppression effect of the proposed method on the low-order harmonics in the stator current. TMS320F28069 is used to execute the control algorithm, and three non-contact sensors MLX91205 is used to sample the stator current. The inverter bridge is composed by the MOSFET, the type is IPB042N10N, the DC-link voltage is 72 V, and is supplied by the battery pack. The parameters of the IM are the same as in Table 1, and the experimental parameters and operation are the same as in Table 2. The experimental results under no compensation, pulse time compensation, and the 6th harmonic controller in d-q axis are shown in Figures 23–25, respectively. Under the influence of deadtime and conduction voltage drop, without compensation, the stator current has serious harmonic distortion, the 5th harmonic content is 3.2%, the 7th harmonic content is 2.3%, and there is a little DC component. After the pulse time compensation, the content of the 5th and 7th harmonics and THD are slightly reduced, and the power spectral density at the natural frequency drops below −10 dB/Hz. By adopting the 6th harmonic controller in d-q axis proposed in this paper, the 5th harmonic content is only 1%, the 7th harmonic content 0.6%, and the THD decreases to 4.62%. At the same time, the DC component of the current is eliminated, and the power spectral density at all frequencies is less than −20 dB/Hz. The experimental results are consistent with the simulation results, which show that the proposed resonant controller in d-q axis can reduce the low-order harmonics of the stator current.

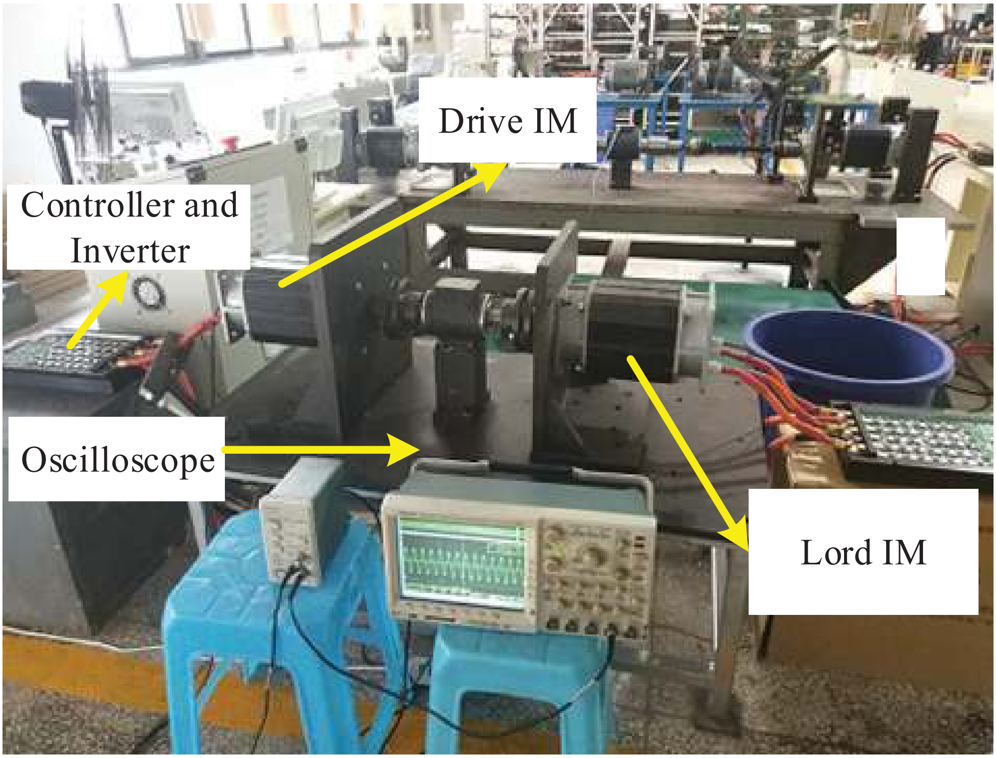

Figure 22. Experimental prototype.

To verify the effectiveness of the control algorithm in reducing vibration, a vibration measurement instrument is used to measure the vibration of the IM, and the measurement experiment platform is shown in Figure 26.

Figure 27 shows the power spectral density of the vibration within 1.8 kHz under no compensation, there are two peaks of vibration at the 1st and 2nd natural frequencies. Figure 28 shows the power spectral density of the vibration within 1.8 kHz under the 6th harmonic controller in d-q axis, the vibrations are significantly suppressed. The whole experimental results further prove that the 6th harmonic controller with its parameter design method in d-q axis has a good suppression effect on the 5th and 7th harmonics distortion of the stator current, which can not only reduce the torque ripple, but also weaken the vibration of the IM.

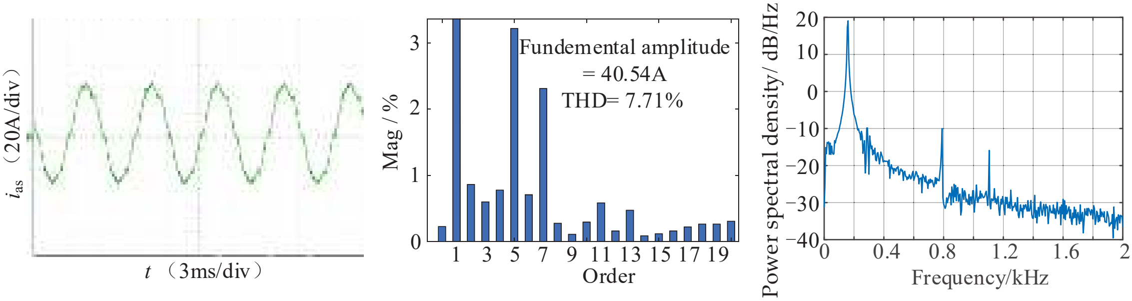

(**a**) (**b**) (**c**)

Figure 23. Experimental results under no compensation. (**a**) i_{as}; (**b**) FFT; and (**c**) power spectral density.

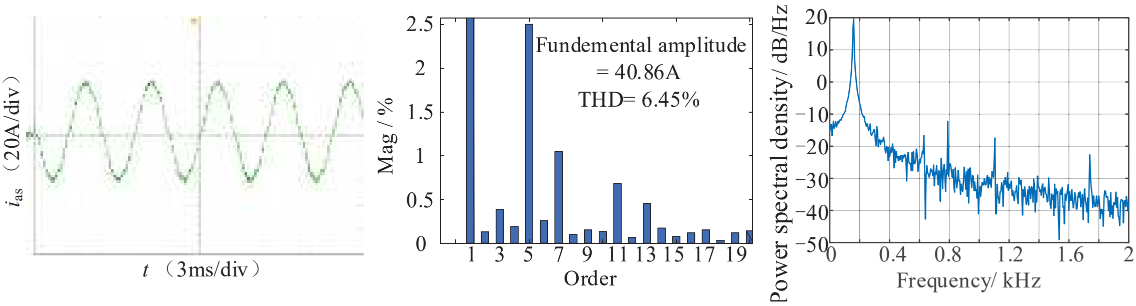

(**a**) (**b**) (**c**)

Figure 24. Experimental results under pulse time compensation. (**a**) i_{as}; (**b**) FFT; (**c**) Power spectral density.

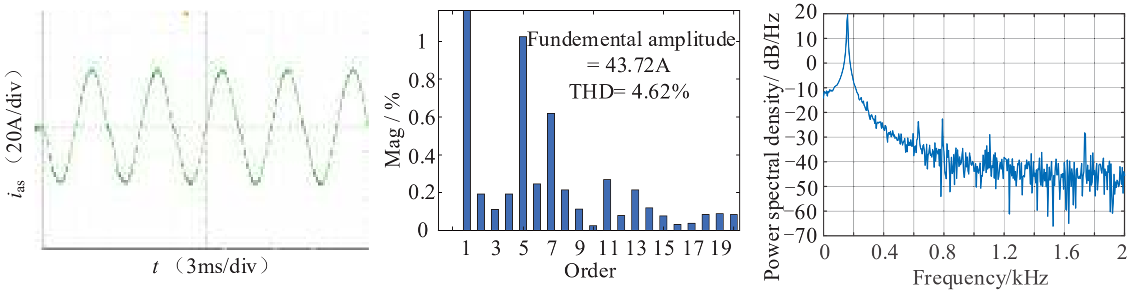

(**a**) (**b**) (**c**)

Figure 25. Experimental results under 6th harmonic controller. (**a**) i_{as}; (**b**) FFT; and (**c**) power spectral density.

Figure 26. The vibration measurement platform.

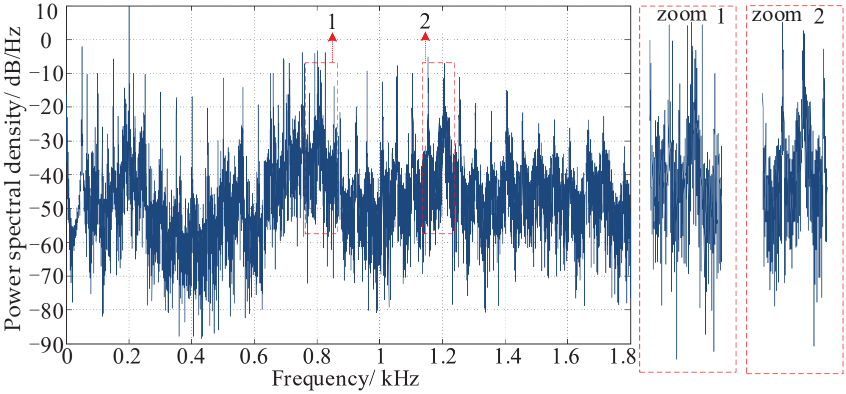

Figure 27. The power spectral density of vibration in IM without compensation.

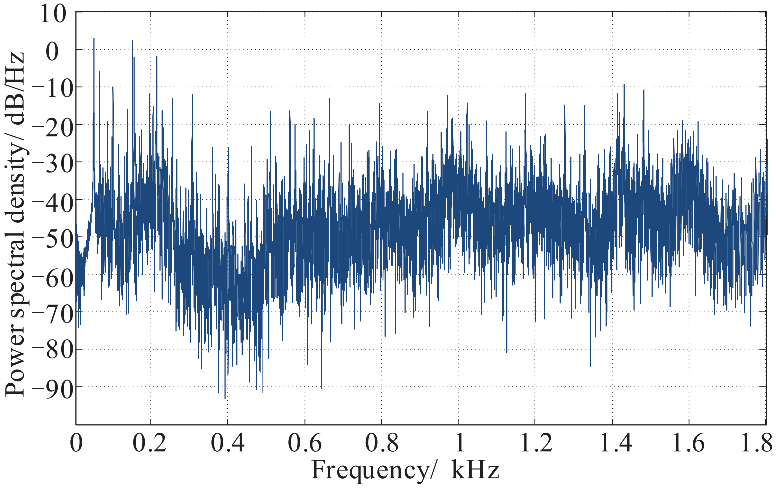

Figure 28. The power spectral density of vibration in IM 6th harmonic controller.

7. Conclusions

The simulation and experimental results prove that the proposed 6th harmonic controller with its parameter design method in d-q axis has good effects on reducing the 5th and 7th harmonic distortion of the stator current, weakening the low-frequency resonance of the motor, and improving the dynamic performance of the motor drive system. Finally, the following conclusions are formed:

(1) The dead time and the conduction voltage drop of the switching tube and body diode will produce nonlinear errors in the inverter output voltage. The current PI controller based on rotor flux orientation cannot suppress the 5th and 7th harmonic distortion of the stator current caused by the nonlinear voltage;
(2) Based on current loop stability and the harmonic suppression effect, according to the bode plot and the pole distribution diagram, the proposed 6th harmonic controller can effectively suppress the low-order harmonic distortion of the nonlinear voltage, without generating harmonic distortion of other frequencies, and does not affect the control performance of the current loop;
(3) Since another resonant controller for the low-speed range is introduced, low-order harmonic suppression at all operating frequencies can be achieved;
(4) Suppressing the 6th harmonic component of the stator current in d-q axis is an effective means to weaken the low-frequency resonance and vibration of the motor.

Author Contributions: Conceptualization and methodology, P.S.; simulation, Y.L.; validation and experiment, P.S. and T.L.; writing and supervision, L.W. and T.L.; review and editing, P.S.; funding acquisition, H.W. All authors have read and agreed to the published version of the manuscript.

Funding: This work was supported by "the Fundamental Research Funds for the Central Universities", Southwest Minzu University (Funder, Huazhang Wang; Funding number, 2021101).

Data Availability Statement: Not applicable.

Conflicts of Interest: The authors declare no conflict of interest.

References

1. Du, G.; Zou, Y.; Zhang, X.; Guo, L.; Guo, N. Heuristic Energy Management Strategy of Hybrid Electric Vehicle Based on Deep Reinforcement Learning with Accelerated Gradient Optimization. *IEEE Trans. Transp. Electrif.* **2021**, *7*, 2194–2208. [CrossRef]
2. Liang, J.; Howey, B.; Bilgin, B.; Emadi, A. Source of Acoustic Noise in a 12/16 External-Rotor Switched Reluctance Motor: Stator Tangential Vibration and Rotor Radial Vibration. *IEEE Open J. Ind. Appl.* **2020**, *1*, 63–73. [CrossRef]
3. Miao, Y.; Liu, H.; Zhang, W.; Liu, P. Optimal Control Strategy of Storage Inductor Current and Rotor Flux for Current Source Inverter Motor Drive System. *Proc. CSEE* **2019**, *39*, 2757–2767.
4. Song, P.; Liu, Y.; Liu, C. Research on Parameter Design and Control Method for Current Source Inverter–Fed IM Drive Systems. *Machines* **2022**, *10*, 922. [CrossRef]
5. Jiang, Z.; Ying, D.; Jian, S. Electromagnetic Noise Characteristics of Permanent Magnet Synchronous Motor Applied in Electric Vehicle. *Trans. China Electrotech. Soc.* **2016**, *31*, 53–59.
6. Dong, Z.; Liu, C.; Song, Z.; Liu, S. Suppression of Dual−Harmonic Components for Five−Phase Series−Winding PMSM. *IEEE Trans. Transp. Electrif.* **2022**, *8*, 121–134. [CrossRef]
7. Lai, Y.-S.; Chang, Y.-T.; Chen, B.-Y. Novel Random-Switching PWM Technique with Constant Sampling Frequency and Constant Inductor Average Current for Digitally Controlled Converter. *IEEE Trans. Ind. Electron.* **2013**, *60*, 3126–3135. [CrossRef]
8. Peng, H.; Heping, L.; Yiru, M.; You, X.; Guo, Q. Variable Switching Frequency Pulse Width Modulation for Induction Motors based on Current Ripple Peak Value. *Trans. China Electrotech. Soc.* **2020**, *35*, 4373–4383.
9. Liu, P.; Xu, J.; Sun, M.; Yuan, J.; Blaabjerg, F. New Discontinuous Space Vector Modulation Strategies for Impedance-Source Inverter with Superior Thermal and Harmonic Performance. *IEEE Trans. Ind. Electron.* **2022**, *69*, 13079–13089. [CrossRef]
10. Guo, Q.; Dong, Z.; Liu, H.; You, X. Nonlinear Characteristics Compensation of Inverter for Low-Voltage Delta-Connected Induction Motor. *Energies* **2020**, *13*, 590. [CrossRef]
11. Liu, P.; Xu, J.; Yang, Y.; Wang, H.; Blaabjerg, F. Impact of Modulation Strategies on the Reliability and Harmonics of Impedance-Source Inverters. *IEEE J. Emerg. Sel. Top. Power Electron.* **2020**, *8*, 3968–3981. [CrossRef]
12. Zhang, Z.; Xu, L. Dead-Time Compensation of Inverters Considering Snubber and Parasitic Capacitance. *IEEE Trans. Power Electron.* **2014**, *29*, 3179–3187. [CrossRef]
13. Liu, H.; Liu, Q.; Zhang, W.; Miao, Y.; Liu, P. Random PWM Technique for Acoustic Noise and Vibration Reduction in Induction Motors used by Electric Vehicles. *Trans. China Electrotech. Soc.* **2019**, *34*, 1488–1495.

14. Kobayashi, T.; Tajima, F.; Ito, M.; Shibukawa, S. Effects of Slot Combination on Acoustic Noise from Induction Motors. *IEEE Trans. Magn.* **1997**, *33*, 2101–2104. [CrossRef]
15. Gao, X.; Su, D. Suppression of a Certain Vehicle Electrical Field and Magnetic Field Radiation Resonance Point. *IEEE Trans. Veh. Technol.* **2018**, *67*, 226–234. [CrossRef]
16. Wu, Z.; Ding, K.; Yang, Z.; He, G. Analytical Prediction and Minimization of Deadtime-Related Harmonics in Permanent Magnet Synchronous Motor. *IEEE Trans. Ind. Electron.* **2021**, *68*, 7736–7746. [CrossRef]
17. Liu, H.; Lu, Y.; Wang, H.; Miao, Y. Dead-time Compensation Modulation Strategy of Subsection Integrated in Voltage Source Inverter. *Electr. Mach. Control* **2018**, *22*, 25–32.
18. Miao, Y.; Liu, H.; Wang, H.; Lu, Y. Average Current Feedforward Compensation Strategy of Overlap-Time Effect for Current Source Inverter. *Proc. CSEE* **2018**, *38*, 4183–4193.
19. Liao, Y.; Zhen, S.; Liu, R.; Yao, J. Torque Ripple Suppression of Permanent Magnet Synchronous Motor by the Harmonic Injection. *Proc. CSEE* **2011**, *21*, 119–127.
20. Yang, Y.; Zhou, K.; Wang, H.; Blaabjerg, F.; Wang, D.; Zhang, B. Frequency Adaptive Selective Harmonic Control for Grid-Connected Inverters. *IEEE Trans. Power Electron.* **2015**, *30*, 3912–3924. [CrossRef]
21. da Silveira, D.B.; Farias, J.V.M.; Pereira, H.A.; Luiz, A.-S.A.; Stopa, M.M.; Cupertino, A.F. Mitigation of torque oscillations caused by dc injection-based resistance estimation through resonant controllers. In Proceedings of the 2021 Brazilian Power Electronics Conference (COBEP), João Pessoa, Brazil, 7–10 November 2021; pp. 1–6.

machines

Article

Reinforcement Learning Control of Hydraulic Servo System Based on TD3 Algorithm

Xiaoming Yuan [1,*], Yu Wang [1], Ruicong Zhang [1], Qiang Gao [2], Zhuangding Zhou [1], Rulin Zhou [3] and Fengyuan Yin [1]

[1] Heavy Machinery Fluid Power Transmission and Control Laboratory of Hebei Province, Yanshan University, Qinhuangdao 066004, China
[2] National Research Center of Pumps, Jiangsu University, Zhenjiang 212013, China
[3] Beijing Tianma Intelligent Control Technology Co., Ltd., Beijing 100013, China
* Correspondence: yuanxiaoming@ysu.edu.cn; Tel.: +86-137-8056-0557

Abstract: This paper aims at the characteristics of nonlinear, time-varying and parameter coupling in a hydraulic servo system. An intelligent control method is designed that uses self-learning without a model or prior knowledge, in order to achieve certain control effects. The control quantity can be obtained at the current moment through the continuous iteration of a strategy–value network, and the online self-tuning of parameters can be realized. Taking the hydraulic servo system as the experimental object, a twin delayed deep deterministic (TD3) policy gradient was used to reinforce the learning of the system. Additionally, the parameter setting was compared using a deep deterministic policy gradient (DDPG) and a linear–quadratic–Gaussian (LQG) based on linear quadratic Gaussian objective function. To compile the reinforcement learning algorithm and deploy it to the test platform controller for testing, we used the Speedgoat prototype target machine as the controller to build the fast prototype control test platform. MATLAB/Coder and compute unified device architecture (CUDA) were used to generate an S-function. The results show that, compared with other parameter tuning methods, the proposed algorithm can effectively optimize the controller parameters and improve the dynamic response of the system when tracking signals.

Keywords: reinforcement learning; TD3; DDPG; hydraulic servo; Speedgoat

Citation: Yuan, X.; Wang, Y.; Zhang, R.; Gao, Q.; Zhou, Z.; Zhou, R.; Yin, F. Reinforcement Learning Control of Hydraulic Servo System Based on TD3 Algorithm. *Machines* **2022**, *10*, 1244. https://doi.org/10.3390/machines10121244

Academic Editors: Kan Liu and Wei Hu

Received: 28 November 2022
Accepted: 15 December 2022
Published: 19 December 2022

1. Introduction

As a high-precision closed-loop control system, a hydraulic servo system can make the output (displacement, velocity or force) of a system follow the changes of the input quickly and accurately. This offers the unique advantages of fast response speed, large load stiffness and large control power and is widely used in the aerospace, heavy industry, robotics and national defense fields. However, as a high-order nonlinear system, the inherent nonlinearity, time-variability and parameter coupling of a hydraulic servo system pose challenges to the design of control methods [1]. The determination of controller parameters and the deployment of a control strategy are the main difficulties. Thus, the question of how to control a hydraulic servo system with high precision is of great significance to its popularization and application.

The use of reinforcement learning algorithms to solve control problems such as nonlinear engineering problems has been widely studied by many researchers. For instance, Wu, M. et al. [2] used a safe deep reinforcement learning (DRL) control method based on a safe reward shaping method and applied it to the constrained control for an electro-hydraulic servo system (EHSS). Chen, P. et al. [3] proposed a novel control strategy of speed servo systems based on deep reinforcement learning, which can achieve proportional–integral–derivative automatic tuning and effectively overcome the effects of inertia mutation and torque disturbance. Wyrwał, D. et al. [4] proposed a novel control strategy for a hydraulic cylinder based on deep reinforcement learning, which can automatically control the hydraulic system online so that the system can consequently maintain a consistently good control performance. Zhang, T. et al. [5] proposed a strategy based on deep reinforcement learning for the optimization of gain parameters of a cross-coupled controller, allowing the effective convergence of the gain parameters with the optimal intervals. The optimal gain parameters obtained by the proposed strategy can significantly improve the contour control accuracy in biaxial contour tracking tasks. Zamfirache, I.A. et al. [6] proposed a new control approach based on reinforcement learning (RL) that used policy iteration (PI) and a metaheuristic grey wolf optimizer (GWO) algorithm to train neural networks (NNs). In so doing they demonstrated good results for NN training and the solving of complex optimization problems. Shuprajhaa, T. et al. [7] developed a generic-data-driven modified proximal policy optimization (m-PPO) for an adaptive PID controller (RL-PID) based on reinforcement learning for the control of open-loop unstable processes, which eliminated the need for process modeling and pre-requisite knowledge on process dynamics and controller tuning.

Some studies have also integrated multiple comprehensive methods to achieve optimal control. Vaerenbergh, K.V. et al. [8] presented a practical application of a hybrid approach where reinforcement learning is the global layer to tune the controllers of every subsystem for the problem. It was shown that developing a centralized global controller for systems with many subsystems or complex interactions is usually very hard or even unfeasible. Lv, Y. et al. [9] used an RL-based approximate dynamic programming (ADP) structure to learn the optimal tracking control input of a servo mechanism, where unknown system dynamics were approximated with a three-layer NN identifier. Radac, M.B, and Lala, T. [10] proposed a Q-learning-like data-driven model-free (with unknown process dynamics) algorithm. They used neural networks as generic function approximators and validation on an active suspension system and it was shown to be easily amenable to artificial road profile disturbance generation for the optimal and robust control of a data-driven learning solution. Oh, T.H. et al. [11] proposed a DDPG-based deep RL method to simultaneously design and tune several notch filters and used a real industrial servo system with multiple resonances to demonstrate the proposed method effectively. They found the optimal parameters for several notch filters and successfully suppressed multiple resonances to provide the desired performances. Chen, W. et al. [12] proposed a novel adaptive law for the critical network in an RL framework to address the problem of nonlinear system control, which is driven by historical estimation errors but uses an auxiliary matrix instead of a historical data set, thus reducing the computational effort of the controller.

Reinforcement learning mainly learns and optimizes its own behavioral strategies through the idea and mechanism of trial and error. The behavior acts on the environment and obtains a response from the environment. The response is the evaluation index of the behavior. In the process of constantly interacting with the environment, the agent constantly changes their actions according to the rewards they get from the environment. With enough training, the agent can accumulate experience and then interact with the environment in a way that maximizes reward.

Although many studies have been undertaken in the practice of RL design and have laid a great theoretical foundation, there still exist some challenges and shortcomings. For instance, the classic reinforcement learning methods such as Q-learning do not have good generalizability and are usually only useful for specific tasks. Methods of control that have been optimized by neural network algorithms or genetic algorithms are usually effective only for specific cycle periods, lack on-line learning capabilities and have limited generalizability. Additionally, the experimental research on pure hydraulic servo systems has rarely been concerned with RL, and the verification of tests is relatively simple. As a result, most studies fail to set comparison tests or compile reinforcement learning algorithms for testing and verification.

In this study, the application of a reinforcement learning algorithm as the optimal control is presented Ref. [13]. This algorithm learns the optimal control strategy through direct interaction with objects. A deep neural network based on TD3 reinforcement learning training is introduced to realize this complex control [14–16]. Firstly, the feasibility and effectiveness of the controller are verified by simulation, and rapid prototype control is then carried out based on a Speedgoat prototype target machine. A GPU coder and LCT packaging tool are then used to deploy the reinforcement learning control program after the reinforcement learning training is completed. Finally, we verify the rationality of the control scheme and the effectiveness of the control algorithm by experiments.

2. Reinforcement Learning

Reinforcement learning [17] is a type of learning method in machine learning. It aims to construct and train agents to complete corresponding tasks in an unknown environment and its basic framework is shown in Figure 1 Since the actions in the learning process can affect the environment and the environment will then affect the subsequent actions, reinforcement learning can be regarded as, in essence, a closed-loop control, and the strategies of the agent allow it to complete the task in an optimal way through iterative updates, which is similar to the controller in the system [18,19].

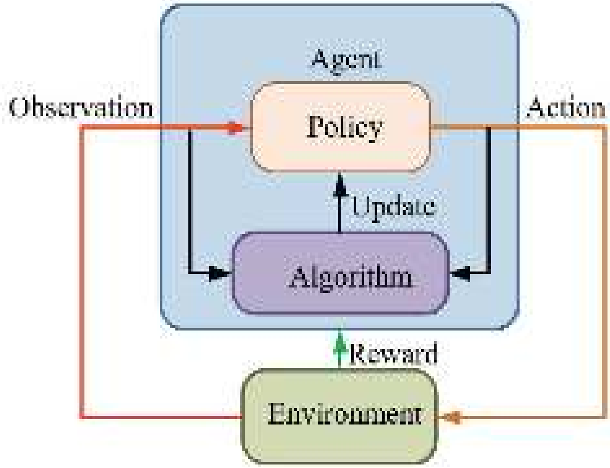

Figure 1. The basic framework of reinforcement learning.

Interactions between the agent and the environment in a period T are as follows:

(a) The *Agent* observes the system state after the previous action A;
(b) Under the current state of S and strategy P, agent undertakes action A by exploring the noise ϵ;
(c) The reward value R is obtained under the new environment state S, then the Agent updates the strategy P according to the reward value R;
(d) Repeat the above steps until the requirements are met.

Among these illustrated above, the reward value R is to evaluate the quality of the actions made by the agent in the environment. Since the reasonable setting of a reward function determines its convergence speed and stability, it is key for the agent to learn strategy effectively.

This paper takes a servo valve controlled asymmetric hydraulic cylinder system as the research object, builds a simulation environment based on a MATLAB/Simulink module, and carries out precise positional control of a hydraulic cylinder through a reinforcement learning algorithm. Additionally, the TD3 reinforcement learning algorithm was designed to interact with the environment so that ultimately the strategy of the control requirements can be satisfied. The servo valve controlled asymmetric hydraulic cylinder system is shown in Figure 2.

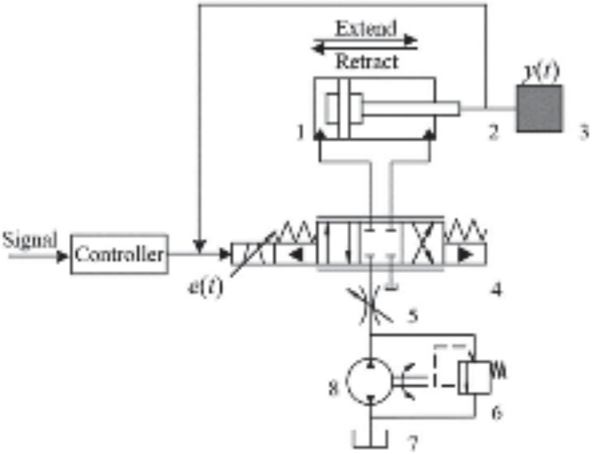

Figure 2. The schematic diagram of hydraulic servo system. 1. Asymmetric hydraulic cylinder 2. Sensor 3. Load 4. Servo hydraulic valve 5. Throttle hydraulic valve 6. Relief value 7. Hydraulic oil tank 8. Pump.

3. Design of the Algorithm

3.1. Actor–Critic Algorithm

The actor–critic [20] method combines the advantages of two methods: Actor and Critic. The method of Critic can be used to estimate a function of value that can lay a foundation to update the Actor function. As in Figure 3, there are two neural networks, one of these is the Actor network which determines the output in response to the environment, which can be either continuous or discrete. According to the combination of action and state on the output, the Critic network evaluates the value of the action of the Actor network. Meanwhile, the actual reward can be compared with the estimated value of the Critic to get the time difference error (TD-Error), which can judge how to adjust the parameters of the Critic network to obtain a more accurate estimate value. It can also judge the quality of the current action value [21,22], so as to achieve the purpose of updating the Actor parameters. In the process of the constant interaction between the agent and the environment, the weights of the Actor and Critic are updated and a relatively ideal control effect is achieved [23].

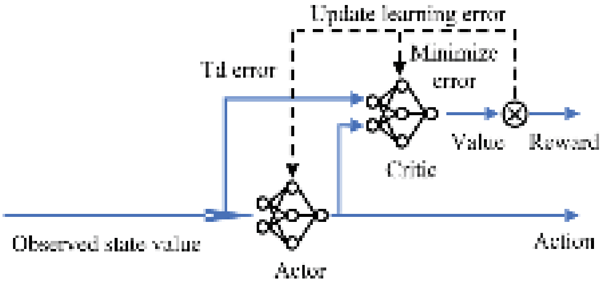

Figure 3. The Actor–Critic algorithm.

3.2. The Algorithm of DDPG and TD3

The depth deterministic policy gradient (DDPG) algorithm is a deep reinforcement learning algorithm based on Actor–Critic architecture for continuous action space [24]. The structure of a DDPG algorithm is shown in Figure 4.

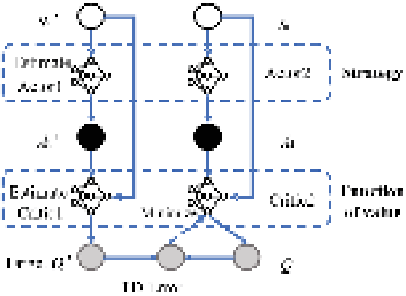

Figure 4. Structure of a DDPG algorithm.

The twin delayed deep deterministic policy gradient (TD3) algorithm (Figure 5) improves the network structure and update mode [25–27], which is based on DDPG algorithm.

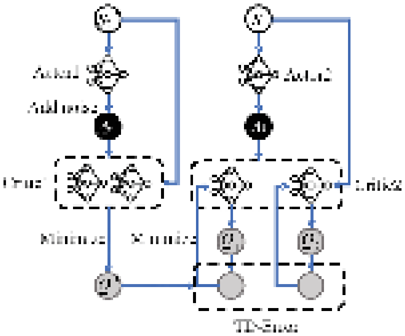

Figure 5. Structure of TD3 algorithm.

This uses the Actor–Critic framework and builds six neural networks to build the reinforcement learning body. The reward function is constructed based on the tracking error and error integral of the hydraulic position servo system, and the state set is composed of the output error of the position servo system. The TD3 algorithm has two advantages, which are as follows:

(i) A reduced overestimation of a dual Critic network.

Since noise θ appears in the sample value y, the target value E_θ of Q network in the real case of the learning process is:

$$y = r + \gamma \max_{a'} Q(s', a') \tag{1}$$

$$E_\theta[\max_{a'} Q(s', a') + \theta] \geq \max_{a'} Q(s', a') \tag{2}$$

After updating the Q function many times, errors will accumulate, leading to a number of bad states being assigned with higher value, and to a large deviation. A double Q-value network reduces estimation errors because it decouples the action and update operations [28]. The roles of the main and target networks and the update mode are shown in Table 1.

Table 1. Double Q-value network.

	Main Net	Target Net
Function	Approximation of action value function Q	Providing TD targets
Update	Updating the weights by minimum gradient method	Copy the Main weight

Using two independent Critics (sharing experience pool) in the TD3 algorithm, we can take the minimum value between the two Critics to eliminate the phenomenon of overestimation and to update the target value. However, although this may lead to an underestimated value for the strategy, this is preferable to overestimating it, as cumulative overestimation will make the strategy ineffective.

(ii) Smooth regularization of the target strategy.

Each step of the TD update produces a small error, which is more noticeable for approximate estimates. After many updates, a large number of errors will accumulate, eventually leading to an inaccurate Q value [29]. When the Actor and Critic are trained simultaneously, there may be a situation where training is unstable or divergent. In this paper, the target network is introduced by the delayed update of the policy. The method includes two aspects. First, a regularization of the parameters (add noise). Secondly, we update the target network every d times after updating Critic. The update objectives of Critic are calculated by the target network to improve the value function convergence, wherein the value function is updated at a higher frequency and the strategy is updated at a lower frequency.

3.3. Flow of Control

Reinforcement learning in this paper consists of *PI* parameters K_p and K_i to form an action set, and its learning process is shown in Figure 6 below.

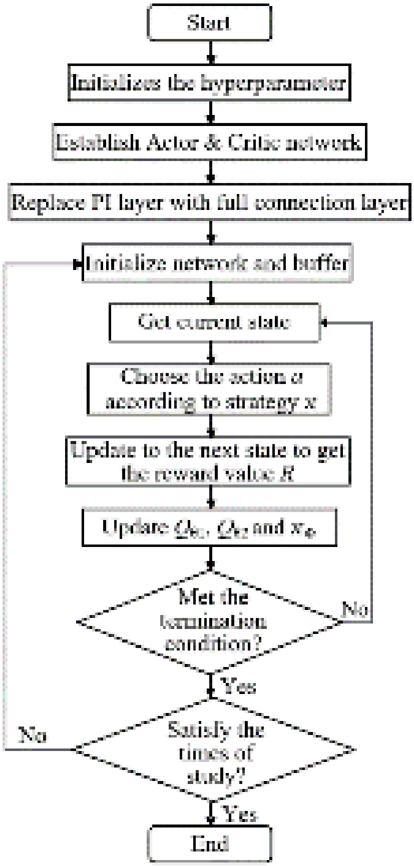

Figure 6. Flow chart of TD3 algorithm.

The TD3 servo control algorithm is shown in Figure 7. In the initial target network, we use a DQN mechanism and the initialization playback buffer B to eliminate the influence of catastrophic neural network forgetting [30,31]. By introducing a random noise with SARSA ideas ϵ (disturbance smooth value function in the action dimensions) to choose a actions and storage transition matrix to B, the memory pool can be formed. The process of updating the weights of Actor and Critic (π_{φ}, $Q_{\theta 1}$ and $Q_{\theta 2}$) is as follows:

$$\begin{cases} \tilde{a} \leftarrow \pi_{\phi'}(s') + \epsilon \\ y \leftarrow r + \gamma \min\limits_{i=1,2} Q_{\theta'_i}(s', \tilde{a}) \\ \epsilon \sim \text{clip}(\eta(0, \tilde{\sigma}), -c, c) \end{cases} \tag{3}$$

Updating the Critic network with minimized loss function:

$$L_{\theta_i} = \min_{\theta_i} \frac{1}{N} (y - Q_{\theta_i}(s, a))^2 \tag{4}$$

Updating Actor networks using policy gradients:

$$\nabla_{\phi} J(\phi) \approx \frac{1}{N} \sum_i \nabla_a Q_{\theta_1}(s, a)\big|_{a=\pi_{\phi}(s)} \nabla_{\theta} \pi_{\phi}(s) \tag{5}$$

Reducing the cumulative error by updating the target network smoothly:

$$\begin{cases} \theta'_i \leftarrow \tau\theta_i + (1-\tau)\theta'_i \\ \phi' \leftarrow \tau\phi + (1-\tau)\phi' \end{cases} \tag{6}$$

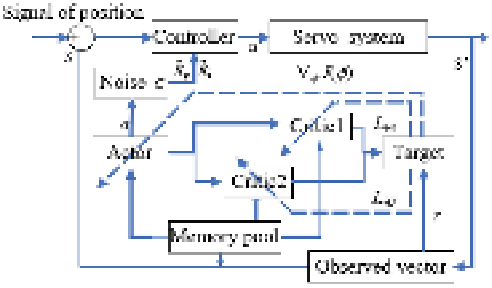

Figure 7. The servo control algorithm of TD3.

A neural network should be established before creating an Actor network, including an observation input and action output [32]. As a network, a *PI* controller can set error and error integral observation vectors on the fully connected layer.

$$u = K_p e(t) + K_i \int_0^t e(t)dt \tag{7}$$

$$w = [K_p, K_i] \tag{8}$$

Here, u is the output of the Actor network and w is the weight of the Actor network.

Since the gradient descent optimization may turn the weight negative, function Y should be executed to ensure that the weights are positive before setting the fully connected *PI* layer.

$$Y = \text{abs}(w) * [e(t), \int_0^t e(t)dt] \tag{9}$$

$$J = \lim_{T\to\infty} E\left(\frac{1}{T}\int_0^T [A(ref - y(t))^2 + Bu^2(t)]dt\right) \tag{10}$$

White noise ($E[n^2(t)] = 1$) is added to the model to simulate signal acquisition and external interference, so as to minimize the output control signal while ensuring minimal errors under the objective function standard.

4. The Establishment of the Environment

4.1. The Establishment of the Network

The reinforcement learning (RL) agent is used to replace the *PI* controller to keep the network structure of the two Critics in the same state (Figure 8), we then set the number of network neurons (Table 2).

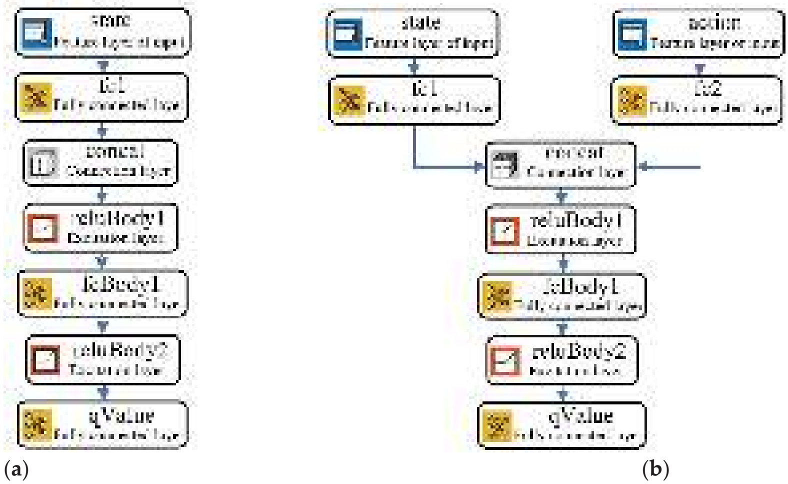

(**a**) (**b**)

Figure 8. The neural network structure layer defined by TD3. (**a**) The network layer of the Actor and (**b**) the network layer of the Critic.

Table 2. Number of network neurons.

The Name of Layer	Critic Network	Actor Network
Layer of state	3 × 2	3 × 2
Layer of action	4 × 1	-
Fully connected layer 1	50 × 1	50 × 1
Fully connected layer 2	50 × 1	-
Connection layer	32 × 1	32 × 1
Layer of activation 1	25 × 1	25 × 1
Fully connected layer 3	50 × 1	50 × 1
Layer of activation 2	25 × 1	25 × 1
Fully connected layer 4	4 ×1	4 × 1

4.2. Establishment of the Environment

The environment receives operations from agents in reinforcement learning scenarios, outputs observations generated by the dynamic behavior of the environment model and generates rewards to measure the contribution of actions to the completion of tasks [33]. The observer structure is shown in Figure 9.

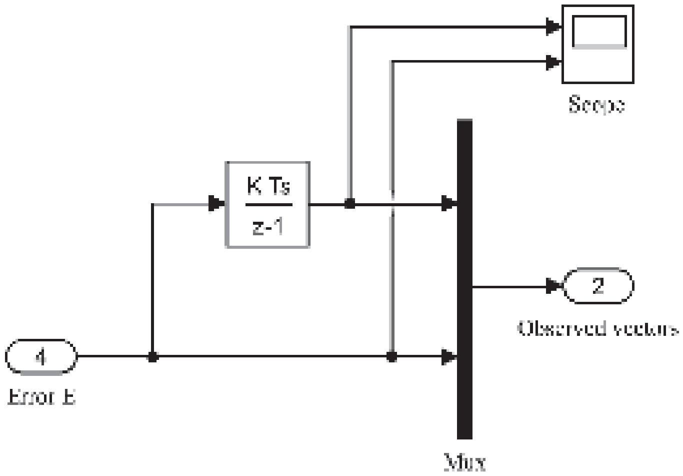

Figure 9. Observed vectors.

Mixed rewards are used for rewarding signals, which include continuous rewards and discrete rewards. Here, the discrete reward signals keep the system away from the bad state, while continuous reward signals improve the convergence by providing smooth rewards near the target state [34]. The following hybrid reward function R is designed for position control of the hydraulic servo system:

$$\begin{cases} r_1 = -10^a e_t^2 - u_t^2 \\ r_2 = -10^a (p \leq -125 || p \geq 125) \\ R = r_1 + r_2 \end{cases} \quad (11)$$

The larger a is, the better the network exploration is, but the longer the learning time and the higher the learning cost. When comprehensively considering the parameter $a \in (1,4)$, as the displacement is outside the range of activity, there will be a large reward and punishment ($P \in (125125)$). The program block diagram of the above Equation (11) is shown in Figure 10, and the Simulink reinforcement learning training program is shown in Figure 11 below.

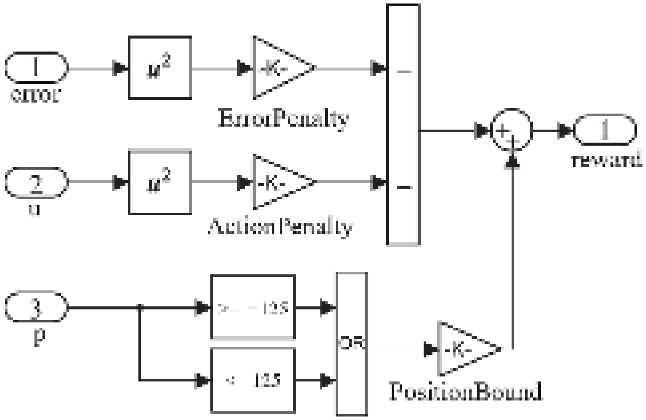

Figure 10. Calculation of the reward function.

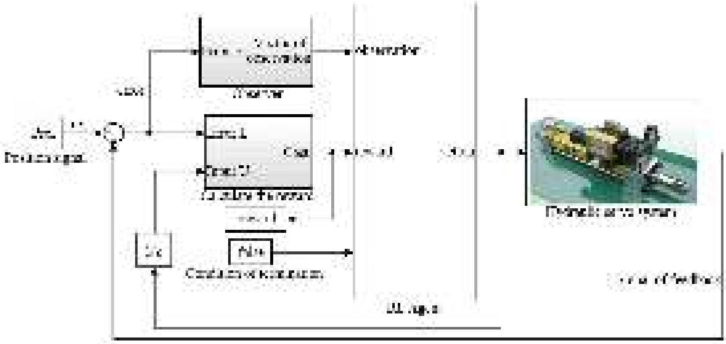

Figure 11. Block diagram of reinforcement learning.

4.3. Setting the Hyperparameter

Variables and expressions were used in MATLAB to parameterize the hydraulic model, and the control system of the hydraulic system was designed in Simulink. The super parameters can be set after setting up the environment (Table 3).

Table 3. Hyperparameter settings.

Hyperparameter	Symbol	Value
Random seed	α_r	1
Maximal set	M	2000
Maximum substep size per episode	T	100
Time of sampling	T_S	0.01
Time of simulation	T_f	3
Playback buffer	B	106
Quantity of batch	N	250
Threshold of gradient	ε	1
Learning rate of Actor network	r_a	0.0003
Learning rate of Critic network	r_c	0.0002
noise of exploration	e	0.1
Delayed updating	D	2
Factor of discount	γ	0.99
Rate of soft renewal	τ	0.01

Since training is the foundation of reinforcement learning, the coefficient of the reward function needs to be set several times in normal circumstances, so as to let the agent obtain a better training effect. By setting the error coefficient appropriately, the rates of change for the node reward and average node reward obtained by the agent in training can be shown in Figures 12 and 13 below, where the value of *a* is set to 1, 2, 3, and 4.

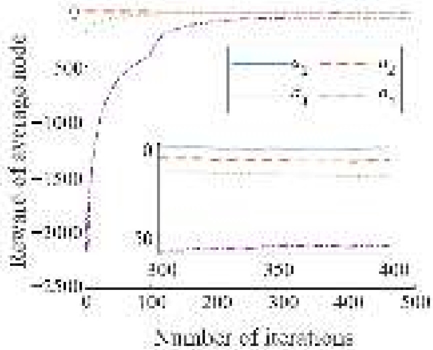

Figure 12. Reward of average node.

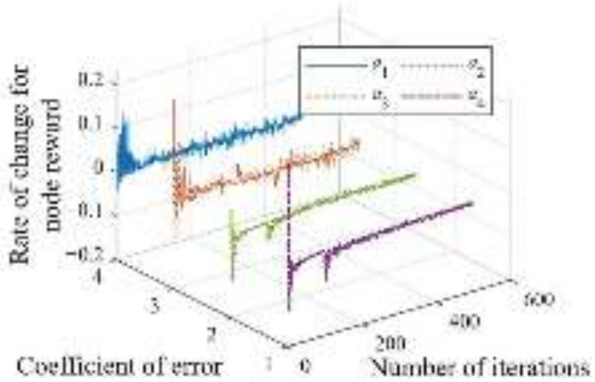

Figure 13. Average rate of change for node reward.

Figure 12 shows the average compensation of agents in training within 500 nodes. The node reward is the actual value of each training round (which fluctuates greatly), while the average reward is the smoothed effect of the actual training (the mean of node training), which eventually increases and becomes stable.

It can be seen from Figure 12 that the smaller the error coefficient is, the greater the final node reward will be, but this does not mean that the smaller the error coefficient is, the better. As can be seen from Figure 13, when the coefficient is 1 or 2, the growth rate of the point reward changes frequently, which means that it is still fluctuating in a small range at 500 steps; however, when the coefficient is 3 or 4, it changes dramatically at the beginning and becomes stable at about 100 steps, while the rate of change in the later period is basically 0. This proves that the first two groups have a higher final reward, though the training was not completed and so the average reward fluctuated wildly. The latter two groups completed the training and, although a higher coefficient of error was set, it ultimately converged to results that are similar to those of the first two groups.

The same reward function was set to compare the training effect of the DDPG and TD3 algorithms. As can be seen from the comparison graph of reinforcement learning curves, DDPG agents learn faster (about 400 sets) and reach the local minimum at the beginning. Compared with DDPG, TD3 has a slower start but a small bottom, and will end up with a higher reward as it avoids the overestimation of the value of *Q*. Compared with DDPG, TD3 has a steadily improved learning curve, indicating it has improved its stability and the curve graph comparison of learning is shown in Figure 14.

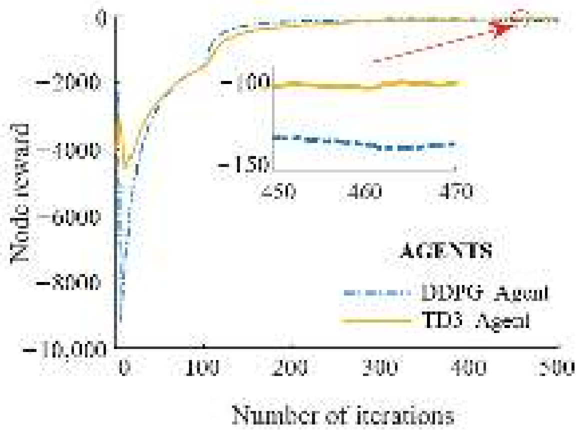

Figure 14. The curve graph comparison of learning.

The above reinforcement learning parameter optimization method was compared with the optimal controller (LQG) by simulation experiments, in order to test the actual control performance of the obtained parameters. Under the same input conditions, the response performance of controller parameters obtained by different methods was compared at the same time (the comparison data are shown in Figure 15). Figure 15a,d are sinusoidal signals and trapezoidal signals. It can be seen from the comparison data that TD3 has a better effect than DDPG and LQG as PID controls the errors of the TD3 algorithm. The comparison curves shown in Figure 15b,e are smaller than those of the other two algorithms. Figure 15c,f show the absolute error integral (Int-IAE) curves under the two respective signals. The error cumulative integral (Int-IAE) is taken as the evaluation index to compare the fixed-parameter PID control performance of the control strategy based on reinforcement learning with that of the servo system structure under different signal types and signal amplitude values and shows that, as the cumulative error integral gets smaller, the accuracy increases.

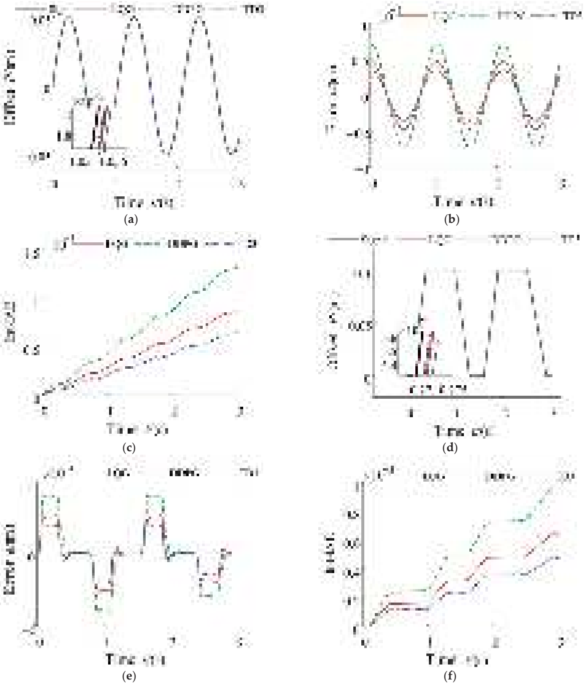

(a) (b) (c) (d) (e) (f)

Figure 15. Comparison diagram of control method effect. (**a**) Following the sinusoidal signal, (**b**) subsequent error of the of sinusoidal signal, (**c**) comparison graph of IAE index, (**d**) following the trapezoidal signal, (**e**) error of the subsequent of sinusoidal signal, and (**f**) comparison graph of IAE index.

The change of the *PI* layer parameters after TD3 training is shown in Figures 16 and 17. In the case of the sine and trapezoidal signals, the error and error cumulative integral of the TD3 algorithm are smaller than those of the other two algorithms. It can be seen from Table 4 that, compared with DDPG, the overshoot of the TD3 step signal is reduced by 24%, and the stabilization time reaches 0.056 s, which is half as long as that of the LQG, and the overshoot time reaches 7%. The TD3-based reinforcement learning control has relatively simple control tasks with a few adjustable parameters, allowing it to obtain better results. Therefore, the correctness of the agent model and the effectiveness of training can be verified by the above results in this study.

Table 4. System response under step signal.

Strategy	K_p	K_i	Time of Rise (s)	Time of Stability (s)	Overshoot (%)	Phase Margin
LQG	50.52	12.56	0.057	0.102	31	87.45
DDPG	43.41	8.99	0.067	0.114	32	87.85
TD3	54.81	9.11	0.052	0.056	7	87.62

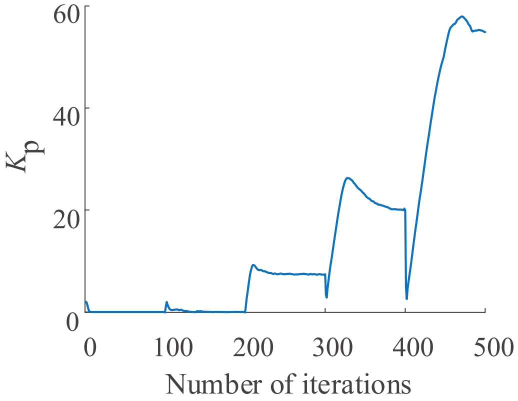

Figure 16. Variation curve of K_p.

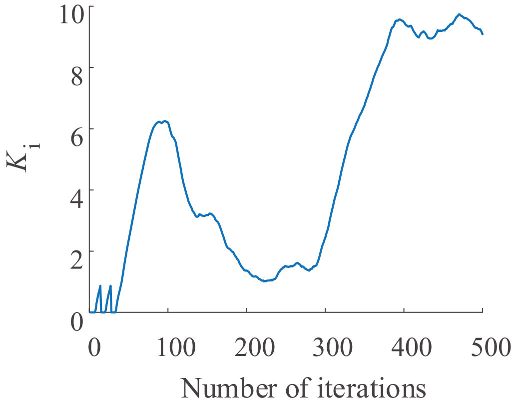

Figure 17. Variation curve of K_i.

5. Rapid Prototype Control Experiment

The fast prototype control (Figure 18) is a real-time system that can be created on the desktop, or in a laboratory or field environment. It can also test the automation system and verify its control algorithm, which greatly reduces the development and testing cycle [35].

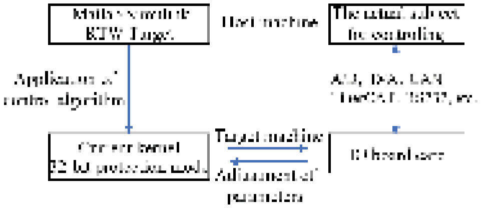

Figure 18. Fast prototype control.

A better reward function was designed and a greater control strategy was obtained in the simulation environment, both of which are based on the TD3 reinforcement learning environment described above.However, the work needs to be verified by experiment to prove the rationality of the previous work in this paper. The Speedgoat target machine based on a MATLAB kernel can be used for rapid prototype control and to verify the correctness of the simulation results and control strategy.

5.1. Test Equipment

The Speedgoat real-time target machine (Figure 19) in the experiment was used as the controller of the hydraulic servo system, and a rapid prototyping (RP) technology was used to deploy the pure software algorithm to the hardware for implementation, so that it could be tested in a real environment [36,37]. The board configuration of Speedgoat and the mainframe's technical specifications of Baseline-S are shown in Tables 5 and 6 respectively.

Table 5. Board configuration of Speedgoat.

Type	Name	Number of Interfaces
Master computer for controlling	Baseline-S Bus	Interfaces of ethernet and video
Input of simulation	IO191 Board card	Single-ended AI of No.24
Output of simulation	IO191 Board card	AO of No.12
CAN Bus	IO691 Board card	No.2
Input of digitization	IO191 Board card	DI of No.24
Output of digitization	IO191 Board card	DO of No.24

Table 6. Mainframe's technical specifications of Baseline-S.

Type	Technical Specifications
CPU	Intel Celeron 2 GHz 4 cores
Current operating system	Simulink Real-Time
memory space	4GB RAM & 32GB SSD
USB interface	1 × USB 3.0 & 2 × USB 2.0
Computer Interface	1 × ethernet interface
serial interface	2 × RS232(Support 120 kb/s)
power supply	9-36V
Protocol Support	TCP/IP, EtherCAT, XCP Master,

Figure 19. Fast prototype control of Speedgoat.

5.2. Using Reinforcement Learning for Control

To use reinforcement learning-based control, third-party software is required: a CUDA supported NVIDIA GPU; NVIDIA CUDA package and drivers; NVIDIA cuDNN library; Visual Studio compiler; Simulink Real-Time Target Support Package; and other extension packages and environment variables.

The policy used in this paper uses an extract function to extract the policy part of the agent and generates an "m type" interface function named evaluatePolicy, which is passed to the GPU coder for code generation which generates a series of class dynamic link library codes, whose type is shown in Table 7 below.

Table 7. Type of generated code.

Types of Configuring Object	Generated Code
'Mex'	MEX function
'Lib'	Static library
'Dll'	Dynamic library
'Exe'	Executable file

For the hydraulic servo system studied in this paper, a legacy code tool (LCT) was used to encapsulate the dynamic library code into an S-function module, where Figure 20 shows the flow chart of the reinforcement learning control strategy code generation. Figure 21 shows the actual control effect of the control program built on Simulink, which demonstrates that the curve of the experimental results corresponds to the curve of the simulation results and confirms the effectiveness of reinforcement learning control in practical engineering applications. Figure 22 shows the comparison diagram of control method effect.

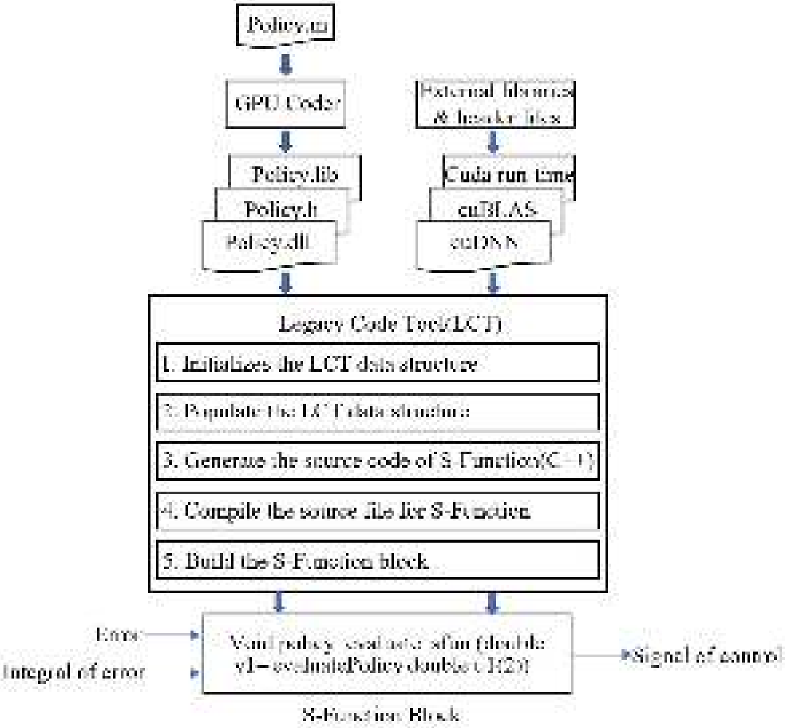

Figure 20. Process of code generation.

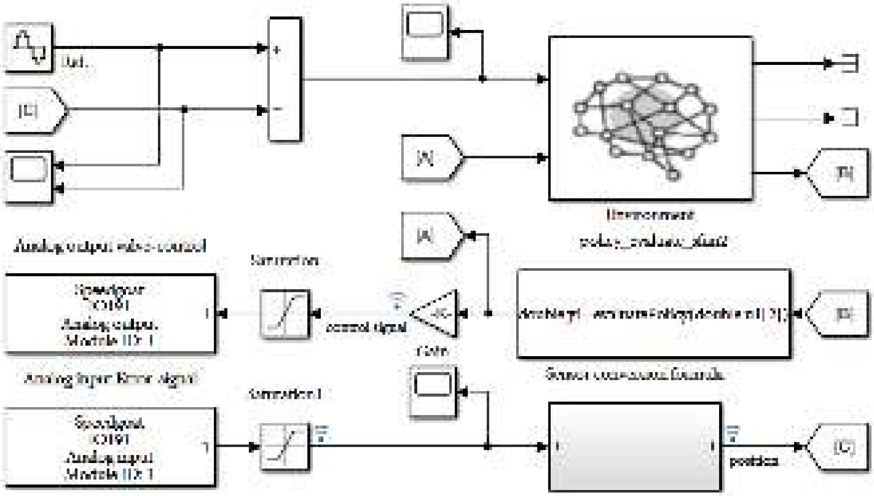

Figure 21. Rapid prototyping control program of Speedgoat.

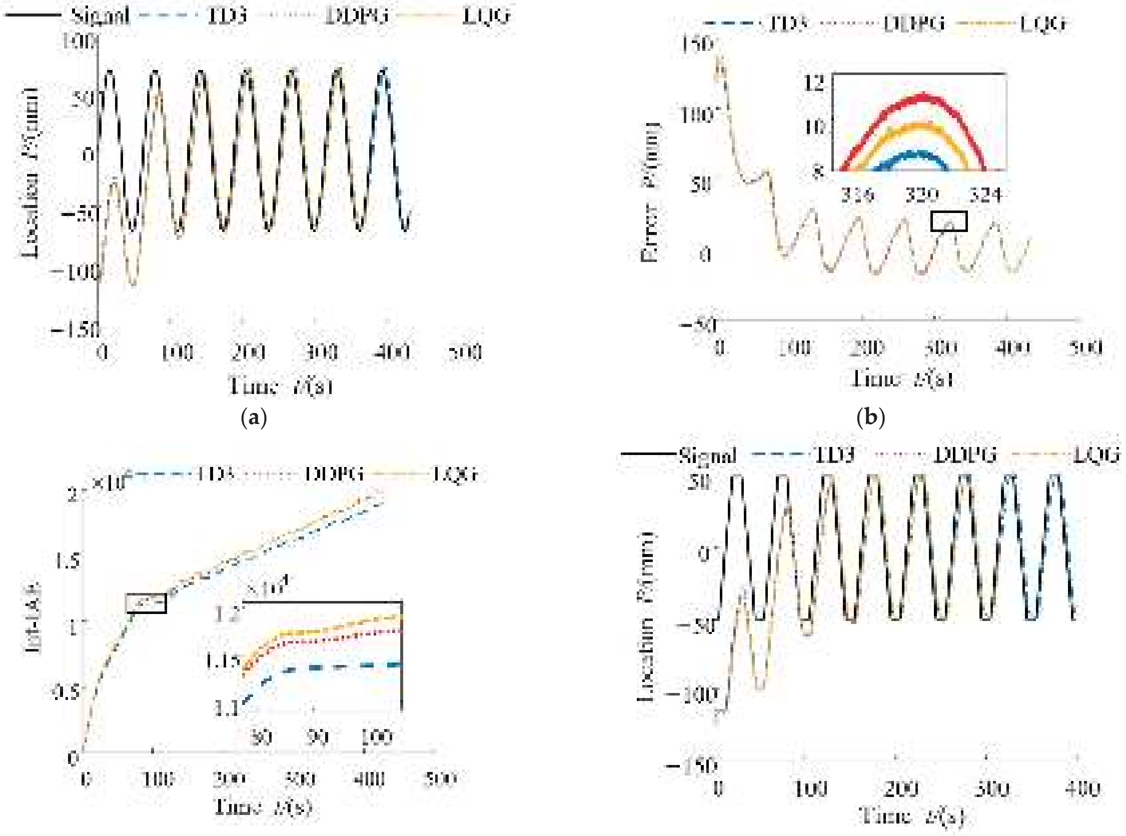

(**a**) (**b**)

(**c**) (**d**)

Figure 22. *Cont.*

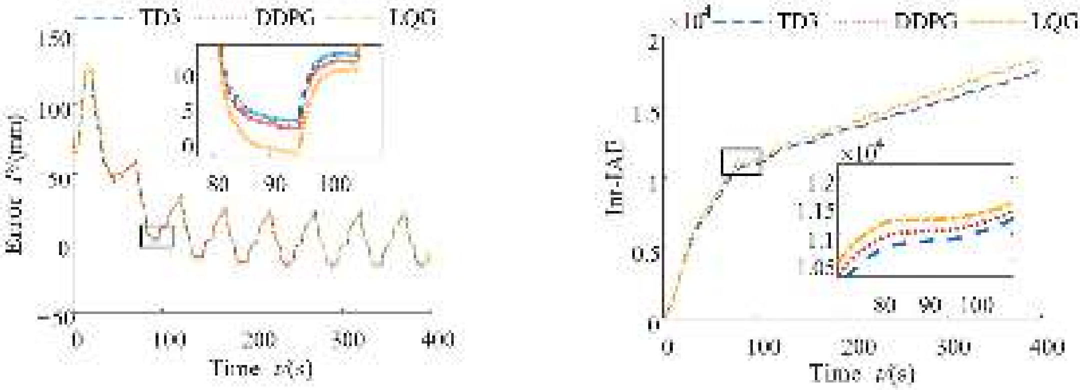

(**e**) (**f**)

Figure 22. Comparison diagram of control method effect. (**a**) Following the sinusoidal signal, (**b**) curve of error, (**c**) absolute error of the of sinusoidal signal, (**d**) Following the trapezoidal signal, (**e**) curve of error, and (**f**) absolute error of the trapezoidal signal.

6. Conclusions

(1) The reinforcement learning control model of the hydraulic servo system was built based on MATLAB/Simulink. The reinforcement learning model was trained by creating an Actor and Critic layer and defining the observation vector and hyperparameter. The DDPG and TD3 algorithms were trained under the same reward function and the simulation experiments were compared with the linear–quadratic–gaussian (LQG) controller.

(2) The mixed reward function FR was planned according to the training purpose. When the error coefficient a reaches 4, the average node reward reaches -50, and the average node reward change rate ultimately reaches approximately 0. Thus, it can be seen that the system achieves a higher reward value in the iteration and tends to converge.

(3) Using the Speedgoat as the reinforcement learning controller, MATLAB/Coder and CUDA were used to generate an S-function, and the reinforcement learning algorithm was compiled and deployed to the test-bed controller for testing by building a fast prototype control test bed for a hydraulic servo system, one which was based on reinforcement learning. The trajectory tracking performance of the proposed algorithm is about 30% higher than that of other algorithms, which verifies the rationality of the control scheme and the effectiveness of the control algorithm.

Author Contributions: Validation, X.Y.; software, Y.W.; writing—original draft preparation, R.Z. (Ruicong Zhang); investigation, Q.G.; writing—review, Z.Z.; resources, R.Z. (Rulin Zhou); writing—editing, F.Y.; All authors have read and agreed to the published version of the manuscript.

Funding: This research was supported in part by National Natural Science Foundation of China (Grant No. 52175066 and 51805468), the National Natural Science Foundation of Hebei Province of China (Grant No. E2020203090).

Institutional Review Board Statement: Not applicable.

Informed Consent Statement: Not applicable.

Data Availability Statement: The authors confirm that the data supporting the findings of this study are available within the article.

Conflicts of Interest: The authors declare no conflict of interest.

References

1. Liu, Y.; Wang, A.; Wang, Z.; Liu, C. Research on modeling and model-free control of hydraulic servo system. *Mach. Des. Manuf.* **2019**, *5*, 10–13.
2. Wu, M.; Liu, L.; Yu, Z.; Li, W. Safe reward-based deep reinforcement learning control for an electro-hydraulic servo system. *Int. J. Robust Nonlinear Control.* **2022**, *32*, 7646–7662. [CrossRef]
3. Chen, P.; He, Z.; Chen, C.; Xu, J. Control Strategy of Speed Servo Systems Based on Deep Reinforcement Learning. *Algorithms* **2018**, *11*, 65. [CrossRef]
4. Wyrwał, D.; Lindner, T.; Nowak, P.; Białek, M. Control strategy of hydraulic cylinder based on Deep Reinforcement Learning. In Proceedings of the 2020 International Conference Mechatronic Systems and Materials (MSM), Bialystok, Poland, 1–3 July 2020; pp. 1–5.
5. Zhang, T.; Wu, C.; He, Y.; Zou, Y.; Liao, C. Gain parameters optimization strategy of cross-coupled controller based on deep reinforcement learning. *Eng. Optim.* **2021**, *54*, 727–742. [CrossRef]
6. Zamfirache, I.A.; Precup, R.E.; Roman, R.C.; Roman, R.C.; Petriu, E.M. Policy Iteration Reinforcement Learning-based control using a Grey Wolf Optimizer algorithm. *Inf. Sci. Int. J.* **2022**, *585*, 162–175. [CrossRef]
7. Shuprajhaa, T.; Sujit, S.K.; Srinivasan, K. Reinforcement learning based adaptive PID controller design for control of linear/nonlinear unstable processes. *Appl. Soft Comput.* **2022**, *128*, 109450. [CrossRef]
8. Vaerenbergh, K.V.; Vrancx, P.; Hauwere, Y.D.; Nowé, A.; Hostens, E.; Lauwerys, C. Tuning hydrostatic two-output drive-train controllers using reinforcement learning. *Mechatronics* **2014**, *24*, 975–985. [CrossRef]
9. Lv, Y.; Ren, X.; Zeng, T.; Li, L.; Na, J. Neural Network Tracking Control of Unknown Servo System with Approximate Dynamic Programming. In Proceedings of the 38th Chinese Control Conference, Guangzhou, China, 27–30 July 2019.
10. Radac, M.B.; Lala, T. Learning nonlinear robust control as a data-driven zero-sum two-player game for an active suspension system-ScienceDirect. *IFAC-PapersOnLine* **2020**, *53*, 8057–8062. [CrossRef]
11. Oh, T.H.; Han, J.S.; Kim, Y.S.; Yang, D.Y.; Cho, D.D. Deep RL Based Notch Filter Design Method for Complex Industrial Servo Systems. *Int. J. Control. Autom. Syst.* **2020**, *18*, 2983–2992. [CrossRef]
12. Chen, W.; Hu, J.; Xu, C.; Zhou, H.; Yao, J.; Nie, W. Optimal tracking control of mechatronic servo system using integral reinforcement learning. *Int. J. Control. Autom. Syst.* **2022**, *16*, 1–11. [CrossRef]
13. Ding, X.F.; Xu, X.L. Nonlinear Optimal Control of Hydraulic Servo System. *Chin. Hydraul. Pneum.* **2004**, *4*, 32–35.
14. Yuan, X.; Wang, W.; Zhu, X.; Zhang, L. Theoretical Model of Dynamic Bulk Modulus for Aerated Hydraulic Fluid. *Chin. J. Mech.* **2022**, *35*, 121. [CrossRef]
15. Wiens, T. Engine speed reduction for hydraulic machinery using predictive algorithms. *Int. J. Hydromechatronics* **2019**, *2*, 1. [CrossRef]
16. Rehab, I.; Tian, X.; Gu, F.; Ball, A.D. The influence of rolling bearing clearances on diagnostic signatures based on a numerical simulation and experimental evaluation. *Int. J. Hydromechatronics* **2018**, *1*, 16–46. [CrossRef]
17. Liu, Q.; Zhai, J.; Zhang, Z. A review of deep reinforcement learning. *Chin. J. Comput.* **2018**, *41*, 1–27.
18. Sung, O.; Jin, K. The design of a real-time simulator on the hydraulic servo system. *Int. J. Precis. Eng. Manuf.* **2003**, *4*, 9–14.
19. Yang, X.; He, H.; Wei, Q.; Luo, B. Reinforcement learning for robust adaptive control of partially unknown nonlinear systems subject to unmatched uncertainties. *Inf. Sci.* **2018**, *463–464*, 307–322. [CrossRef]
20. Chen, X.; Yang, Y. Adaptive PID control based on Actor-Critic learning. *Control. Theory Appl.* **2011**, *28*, 1187–1192.
21. Gao, Q.; Zhu, Y.; Liu, J. Dynamics modelling and control of a novel fuel metering valve actuated by two binary-coded digital valve arrays. *Machines* **2022**, *10*, 55. [CrossRef]
22. Chao, Q.; Xu, Z.; Tao, J.; Liu, C. Capped piston: A promising design to reduce compressibility effects, pressure ripple and cavitation for high-speed and high-pressure axial piston pumps. *Alex. Eng. J.* **2023**, *62*, 509–521. [CrossRef]
23. Li, J.; Ji, L.; Li, J. Optimal consensus control for unknown second-order multi-agent systems: Using model-free reinforcement learning method-ScienceDirect. *Appl. Math. Comput.* **2021**, *410*, 126451. [CrossRef]
24. Wei, X.; Zhang, Q.; Jiang, T.; Liang, L. Fuzzy adaptive deep reinforcement learning method for transient optimization of servo systems. *J. Xi'an Jiaotong Univ.* **2021**, *55*, 68–77.
25. Lee, D.; Lee, S.J.; Yim, S.C. Reinforcement learning-based adaptive PID controller for DPS. *Ocean. Eng.* **2020**, *216*, 108053. [CrossRef]
26. Zhen, H.; Zhai, H.; Ma, W.; Zhao, L.; Weng, Y.; Xu, Y.; Shi, J.; He, X. Design and tests of reinforcement-learning-based optimal power flow solution generator. *Energy Rep.* **2022**, *8*, 43–50. [CrossRef]
27. Chu, Z.; Sun, B.; Zhu, D.; Zhang, M.; Luo, C. Motion Control of Unmanned Underwater Vehicles Via Deep Imitation Reinforcement Learning Algorithm. *IET Intell. Transp. Systems* **2020**, *14*, 764–774. [CrossRef]
28. Zeng, R.; Zhou, J.; Liu, M. Transfer reinforcement learning algorithm for double Q network learning. *Appl. Res. Comput.* **2021**, *38*, 1699–1703.
29. Liu, P.; Bai, C.; Zhao, Y.; Bai, C.; Zhao, W.; Tang, X. Generating attentive goals for prioritized hindsight reinforcement learning. *Knowl.-Based Syst.* **2020**, *203*, 106–140. [CrossRef]
30. Yang, Y.; Li, J.; Peng, L. Multi-robot path planning based on a deep reinforcement learning DQN algorithm. *CAAI Trans. Intell. Technol.* **2020**, *5*, 177–183. [CrossRef]

31. Chen, J.; Yang, Z.; Liu, Q.; Wu, H.; Xu, Y.; Fu, Q. Heuristic Sarsa algorithm based on value function transfer. *J. Commun.* **2018**, *39*, 37–47.
32. Chen, J.; Zheng, M. A review of robot operating behavior based on deep reinforcement learning. *Robot* **2022**, *44*, 236–256.
33. Self, R.; Coleman, K.; He, B.; Kamalapurkar, R. Online Observer-Based Inverse Reinforcement Learning. In Proceedings of the 2021 American Control Conference (ACC), New Orleans, LA, USA, 25–28 May 2021; Volume 5, pp. 1959–1964.
34. Zhao, Y.; Qin, J.; Yuan, L. Intrinsic rewards that combine novelty and risk assessment. *Comput. Eng. Appl.* **2022**, 1–9.
35. Wei, L.; Luo, L.; Wang, Y.; Wang, G. Rapid Control Prototype Design of Electro-hydraulic Position Control Servo System Based on xPC Target. *Chin. Hydraul. Pneum.* **2018**, *7*, 24–28.
36. Maghareh, A.; Silva, C.E.; Dyke, S.J. Servo-hydraulic actuator in controllable canonical form: Identification and experimental validation. *Mech. Syst. Signal Process.* **2018**, *100*, 398–414. [CrossRef]
37. Lyu, L.; Chen, Z.; Yao, B. Advanced Valves and Pump Coordinated Hydraulic Control Design to Simultaneously Achieve High Accuracy and High Efficiency. *IEEE Trans. Control. Syst. Technol.* **2021**, *29*, 236–248. [CrossRef]

machines

Article

Crowning Method on Bearing Supporting Large Wind Turbine Spindle Considering the Flexibility of Structure of Shaft System

Xiangyang Liu [1], Rongjun Niu [1,*], Bin Wang [2], Shuai Zhang [3], Yongcun Cui [1] and Zhanli Zhang [1]

[1] School of Mechatronics Engineering, Henan University of Science and Technology, Luoyang 471003, China
[2] China State Shipbuilding Corporation Haizhuang Wind Power Co., Ltd., Chongqing 401123, China
[3] School of Mechanical Engineering, Henan Institute of Technology, Xinxiang 453003, China
* Correspondence: niurj@haust.edu.cn

Abstract: To meet the precision design of bearings on large wind turbine spindles, a crowning method of bearing on wind turbine spindles considering the flexibility of the support structure is proposed. Firstly, a finite element (FE) model of the shaft system with a flexible structure is constructed by connecting the shaft and bearing through constraint equations (CE) and multi-point constraint (MPC) algorithms and replacing the bearing rollers with nonlinear spring elements and dampers. Then, the Newmark integration algorithm is used to solve the model and analyze the effect of the structure's rigidity on the load distribution of bearings. Then, perform convergence analysis of the sequences of the spring load distribution using a high-pass filter based on fast Fourier transform (FFT) and root mean square error (RMSE) to obtain a suitable number of replacement springs. Finally, a sub-model of the upwind bearing is constructed with structured mesh. With the maximum Von Mises stress of the roller profile as the design target, the optimal logarithmic crowning of the roller and its tolerance zone under the given working conditions are obtained. The results show that the FE model of the shaft system proposed has good convergence. The FE model of the shaft system considering the flexibility of the support structure can obtain more accurate load distributions of bearings and can make the accurate crowning design of the bearing rollers based on the actual working conditions. This provides support for the precision design of bearings in large shaft systems.

Keywords: tapered bearing; logarithmic crowning; FEM; nonlinear spring; damper; sub-model

Citation: Liu, X.; Niu, R.; Wang, B.; Zhang, S.; Cui, Y.; Zhang, Z. Crowning Method on Bearing Supporting Large Wind Turbine Spindle Considering the Flexibility of Structure of Shaft System. *Machines* **2023**, *11*, 28. https://doi.org/10.3390/machines11010028

Academic Editors: Kan Liu and Wei Hu

Received: 22 November 2022
Revised: 21 December 2022
Accepted: 22 December 2022
Published: 26 December 2022

1. Introduction

To solve the problem of energy shortage and environmental pollution, wind turbines are deployed in large numbers around the world. The bearings on the wind turbine spindle are the key rotary parts of wind power equipment, and their failure will cause great economic losses [1,2]. Because the bearings on wind turbine spindles are usually installed in pairs, the actual load of a single bearing is difficult to measure. At present, the traditional design theory of bearing is to use the design formula or experience to design a single bearing according to the given design load, but the structural flexibility of the shaft system cannot be considered in the design. In a shaft assembly, the contact stress distribution of bearing rollers designed by this method is not optimal and cannot meet the accuracy requirements. The finite element method (FEM) can consider the structural flexibility result by constructing the overall model of the shaft assembly, which can obtain a more accurate bearing load and stress distribution under the global load. It has higher calculation accuracy than the traditional design theory of bearing and can be used for the precision design of bearings in complex assembly. However, due to the large size, complex structure, and the large number of rollers of bearings on the wind turbine spindle, the FE analysis of it needs to include two sets of bearings and support structure at the same time, it is very difficult to carry out FE analysis. Therefore, the reliability design of large-size bearings, such as bearings on wind turbine spindles, has become increasingly prominent.

For the design and analysis of large-size bearings, the simplified FE method is now widely used by scholars. Smolnicki et al. [3] proposed a superelement-based FE model for large bearings, using superelements instead of the nonlinear contact actions between rollers and raceways, while the rings of the bearings are still modeled using solid elements. Chen et al. [4,5] used extension spring elements to replace the balls of a wind turbine pitch turntable bearing to analyze the effects of the rigidity of the support structure, the number of bolts, and the preload force on the bearing life. The effect of hub rigidity on the bearing load distribution was also analyzed. Plaza et al. [6] replaced the nonlinear contact actions between the balls and raceways of the pitch turntable bearing with extension spring elements and used superelements to model the rings of the bearing, thus significantly reducing the computational effort. Li et al. [7] proposed an equivalent FE modeling method to analyze the bearing and mounting structure by replacing the balls with nonlinear extension spring elements and using beam elements instead of solid mounting bolts. Aguirrebeitia et al. [8] developed a FE model of a four-point contact ball bearing based on nonlinear spring elements and calculated the static load-carrying capacity of the bearing, which was verified by comparing with the theoretical results, pointing out that the results of the FE model are more accurate than the theoretical results and the theoretical solution is more conservative. He et al. [9] used nonlinear springs instead of solid rollers to study the effect of raceway hardening on slewing bearing life. The use of nonlinear springs enabled the model to obtain results quickly. Śpiewak et al. [10] developed both a FE model and a theoretical analytical model of a double slewing bearing and verified them in comparison. It was suggested to replace each roller with one or more truss elements in the FE model of the bearing. To reduce the calculation scale of wire bearings in FEM, Martín et al. [11] proposed the method based on a custom matrix element and the replacement-element method for a roller based on a nonlinear spring element, among which the former has higher accuracy and the latter has a simpler operation process. The above studies have shown that the use of simplified elements instead of solid rollers in the analysis of bearings by the FEM can significantly reduce the calculation effort and has good accuracy, which is widely used in the analysis of large-size bearings.

The working load of bearings on large wind turbine spindles is extremely high. The profile of the roller or raceway has a direct impact on the stress distribution of the roller and the life of the bearing. The modification of the profile of the raceway or roller can optimize the load distribution. Kania [12] proposed a method for modification of the raceway profile of four-point contact rotary table bearings in a wind turbine, which improved the load-carrying capacity of bearings. However, compared with crowned rollers, this method increases the technical difficulty and production cost. Ju et al. [13] studied the effect of the power function profile and exponential profile on the stress concentration of bearing rollers and pointed out that the exponential profile can effectively reduce the stress concentration, but the unsmooth connection between the straight line of the roller and the exponential trim line is still prone to sudden stress changes. Fujiwara [14] and He [15] offered a method to study the optimal crowning amount of a logarithmic crowned roller, and the optimal crowning function was obtained by adjusting the control coefficient of load and control coefficient of contact. Based on the nonlinear equation of elastic contact, Li [16] established a numerical model of tapered roller bearings on wind turbine spindles and analyzed the load distribution of bearing with logarithmic crowned rollers, pointing out that the logarithmic crowning is widely accepted by bearing manufacturers. Zhang et al. [17] analyzed the effects of load, tilting angle, and the crowning curve of the roller on the stress distribution of rollers of three-row cylindrical roller turntable bearings in wind turbines, and proposed a crowning method using logarithmic curve and tangent arc for axial and radial rollers, respectively, based on the load characteristics of turntable bearings. Li et al. [18] constructed an overall model and a sub-model for a wind turbine with a large taper angle, respectively. The overall model analyzed the effect of axial bearing clearance on the load distribution of bearing, the sub-model analyzed the effect of different crowning shapes on the contact stress of the roller, and the use of simplified FEM greatly reduced the computational effort. The logarithmic crowning curve was found to enable the bearing to have a high load-carrying capacity under the studied working conditions. The above researches show that the logarithmic crowning makes the stress on the roller profile uniformly distributed under the non-extreme bias load condition, which is the optimal crowning method at present.

At present, the analysis of large-size bearings is widely focused on the analysis of individual bearings. For bearings on large wind turbine spindles, more accurate load distribution can be obtained by constructing a FE model of the shaft system, but the analysis type of the above traditional simplified method is still nonlinear, and the model is more difficult to converge after coupling the bearing further to the shaft system. The research of [17] considered the effect of mounting bolts on the load distribution of bearings but assumed that the design load of the bearing was known. The research of [4,5] established a FE model of a turntable bearing with a flexible support structure and investigated the effect of the rigidity of the support structure on the bearing life. However, the support structure is directly coupled to a single bearing and is not applicable to shaft systems of wind turbine spindles containing multiple sets of bearings. The research of [18] established a FE model of a flexible shaft system to analyze the bearings, but the coupling method of the FE model was not introduced in detail. To sum up, there is a lack of relevant literature on the design of spindle bearing considering the structure flexibility of complex shaft systems like large wind turbine spindles by using FEM.

In view of this, considering the flexibility of the support structure of the shaft system, a FE model of the shaft system of the wind turbine spindle is established based on CE, MPC algorithm, and nonlinear spring elements in ANSYS® 2020 R2 software. The critical damping technique is used to improve the convergence of the model. A FE modeling method with good convergence for the shaft system is proposed, which can obtain the accurate load distribution of the bearings by the external wind load of the shaft system and can optimize the bearing roller profile directly. Then the bearing sub-model with structured mesh is constructed. The design method of roller crowning's tolerance of large bearing is given with logarithmic crowning parameters as design variables and the maximum stress along the profile of the roller at the center of the contact area as the design target. The analysis flow of the work is shown in Figure 1.

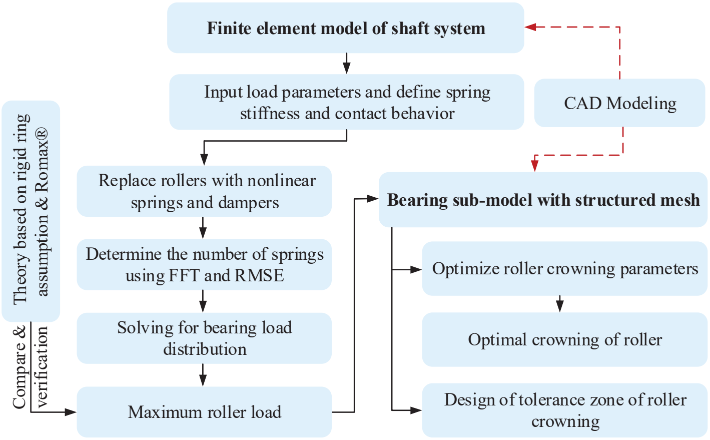

Figure 1. Design of logarithmic crowned roller for wind turbine spindle bearing.

2. FE Modeling Method of the Shaft Assembly

The main shaft assembly of a 6.25 MW wind turbine is used as the study object, and the installation structure consists of two sets of tapered roller bearings, a main shaft, and a bearing housing, as shown in Figure 2. The wind load is transmitted to the bearing through the hub and shaft, where L_1 = 2500 mm and L_2 = 2100 mm. Do not consider the effect of heat treatment and other effects on the material of the shaft, bearing, and housing in the analysis, using the same metal material parameters with a density of 7850 kg·m^{-3}, an elastic modulus of 2.1 × 10^{11} Pa, and a Poisson's ratio of 0.3. The structural parameters of the bearings are shown in Table 1. The wind load parameters are shown in Table 2.

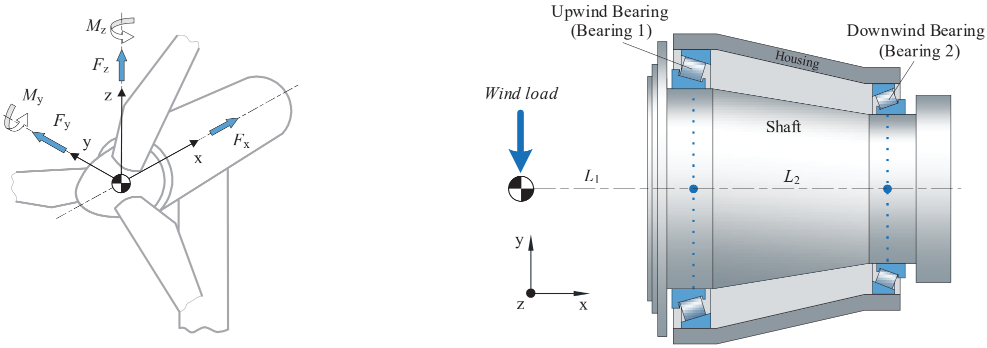

(**a**) (**b**)

Figure 2. Structure and load of wind turbine spindle. (**a**) Load direction coordinate system; (**b**) Structure and load.

Table 1. Geometrical parameters of bearings.

Parameter	**Value**	
	Bearing 1	**Bearing 2**
Inner diameter d (mm)	1850	1600
Number of rollers Z	62	65
The contact angle of inner raceway α_i (°)	15.58	19.5
The contact angle of outer raceway α_e (°)	17.1	21.17
The contact angle of roller end–ring flange α_f (°)	83.52	69.67
Length of rollers l (mm)	121	98
Roller diameter in the middle D_w (mm)	95.085	73.26
Roller half taper angle β (°)	0.75	0.833
pitch diameter d_m (mm)	2043	1750

Table 2. Load parameters of the shaft system.

F_x/N	F_y/N	F_z/N	M_y/Nm	M_z/Nm
7.5 × 10^5	1.1 × 10^6	3 × 10^4	1700	−2700

2.1. Bearings Modeling

Due to the large size of bearings on the wind turbine spindle and the large number of rollers, it will generate massive nonlinear contact calculations if the solid elements are used to model the rollers. Meanwhile, it will introduce extremely strong nonlinearity to the FE model, which results in difficulty in solving the model.

In FE analysis of large-size bearings, modeling the rings with three-dimensional solid elements and the rollers with one-dimensional nonlinear elements can significantly reduce the computational effort. The simplification methods widely used are [4–6,19,20].

1. Nonlinear spring elements with special nonlinear stress-strain characteristics.
2. Superelements with the reduction matrix of structural stiffness.

Replacing rollers with nonlinear spring elements can significantly reduce the number of elements, and speed up the discrimination calculation of the contact algorithm. Compared with the superelement, it is more convenient to operate, so the nonlinear spring elements are adopted to replace the bearing rollers. The connection method is shown in Figure 3.

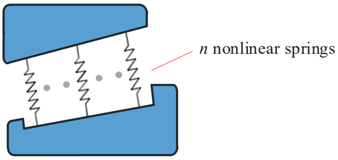

Figure 3. Replace rollers with nonlinear spring elements.

Nonlinear spring elements mainly consist of nonlinearity of state (Compressed Only) and nonlinearity of material (Load-deformation Curve). The nonlinearity of state allows the spring elements to better simulate the real physical contact process of rollers, and the nonlinearity of material allows the spring elements to accurately describe the stress-strain relationship of rollers. For ball bearings, each ball of the bearing can be replaced by one spring element, the length of which is equal to the diameter of the ball. For roller bearings, each roller should be replaced by two or more spring elements to simulate the bias load on the roller. The higher the number of spring elements replacing a roller, the closer the calculated result is to the actual one.

The larger the error of the FE model, the larger the fluctuation of the distribution curve of the spring reaction. To quantitatively determine the appropriate number of replacement springs, the root mean square error (RMSE) of the load distribution is used as an evaluation indicator to obtain the ideal number of replacement springs. The RMSE is the standard deviation, and the RMSE is very sensitive to the deviation of the data and can reflect the accuracy of the measured data. The smaller the value of the RMSE, the higher the accuracy of the measured value, so the RMSE can be used to evaluate the accuracy of the measured value.

For bearings on wind turbine spindles, the ideal load distribution has one peak value and is smooth. The sequence of spring reaction force distribution has the same low-frequency component, and the distribution of spring reaction force fluctuates irregularly along the ideal distribution due to the FE model error.

The sequence of the reaction force distribution X of a series of springs is

$$X = (x_1, x_2, \cdots, x_Z) \tag{1}$$

The high-frequency fluctuation characteristic sequence X_{F} of the data can be obtained by filtering sequence X with a high-pass filter based on FFT.

$$X_{\mathrm{F}} = (x_{\mathrm{F}1}, x_{\mathrm{F}2}, \cdots, x_{\mathrm{F}Z}) \tag{2}$$

Then the RMSE of sequence X is

$$\mathrm{RMSE} = \sqrt{\frac{\sum_{i=1}^{Z} \left(X_i - \overline{X}_{\mathrm{F}}\right)^2}{Z}} \tag{3}$$

where Z is the number of bearing rollers and $\overline{X}_{\mathrm{F}}$ is the mean value of the sequence X_{F}.

Figure 4 shows the stress-strain characteristics of the nonlinear truss elements in the FE analysis, where $\varepsilon_{S(\Delta)}$ is the strain under the action of clearance S and clamp Δ. The truss element has a defined length d_{r} and cross-section, while the special material properties $\sigma(\varepsilon)$ can be defined, and such an element can be used as a nonlinear spring element [9,16]. The clearance of the bearing in the FE analysis can be achieved directly by translating the material property curve of the truss element as shown in Figure 4 along the transverse axis.

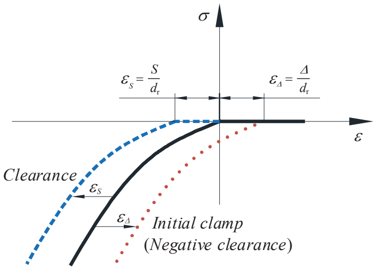

Figure 4. Stress-strain characteristics of the nonlinear spring element.

The mechanical properties of a roller can be simulated by assigning the stiffness curve of the roller to nonlinear spring elements. The contact type of tapered roller bearings is line contact. According to the Hertzian contact theory, the relationship between the contact load and the contact elastic deformation of the roller is [21]

$$Q = K_n \delta^{1.11} \tag{4}$$

where K_n is the total load-deformation constant between the roller and ring; δ is the total elastic deformation of the roller and two rings.

Palmgren gave a formula for calculating the elastic deformation of line contact [22].

$$Q = 0.71 \frac{l^{0.89}}{\eta} \delta^{1.11} \tag{5}$$

where l is the length of the roller, η is the combined elastic constant of two bodies in contact, and the formula is

$$\eta = \frac{1 - \mu_1^2}{E_1} + \frac{1 - \mu_2^2}{E_2} \tag{6}$$

where $\mu_{1(2)}$ is Poisson's ratio of the two bodies and $E_{1(2)}$ is the elastic modulus of the two bodies.

Comparing Equations (4) and (5), the load-deformation constant ($\mathrm{N/mm^{10/9}}$) between the roller and the rings is

$$K_\mathrm{n} = 0.71 \frac{l^{0.89}}{\eta} \tag{7}$$

The stiffness curve of the tapered roller can be approximated by Equations (4) and (7).

Assuming that each roller is replaced by n nonlinear spring elements, the load-deformation constant for each spring element is

$$K_\mathrm{spr} = \frac{K_\mathrm{n}}{n} \tag{8}$$

For the FE model of the whole shaft system, the nonlinear spring elements in the critical loading state perform rigid body movement, which may cause the singular stiffness matrix and make the FE model not converge. Such a simplified method is not very suitable for the FE analysis of large and complex structures. The use of critical damping technology based on nonlinear spring elements can realize the process of slow dynamic loading, i.e., a linear damper is established at the position of each nonlinear spring element, and the existence of the damper has no effect on the strain energy of the model and does not affect the solution accuracy. At the same time, the Newmark integration algorithm is used to solve the FE model by incremental integration method, and stable convergence results can be obtained quickly. The critical damping coefficient is determined by [23,24]

$$c = 2\sqrt{km} \tag{9}$$

where c is the critical damping constant, Ns/m; k is the stiffness of spring, N/m; m is the mass of roller, kg.

The method of replacing the rollers with nonlinear spring elements and linear dampers is shown in Figure 5.

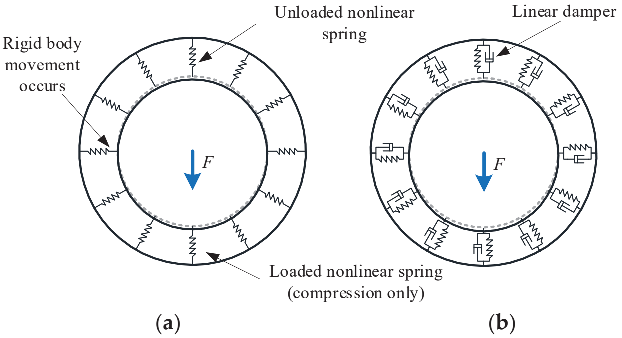

Figure 5. Replace rollers with nonlinear springs and dampers. (**a**) Replace rollers with springs; (**b**) Replace rollers with springs and dampers.

2.2. Main Shaft Modeling

The wind load is mainly distributed to the two support bearings through the main shaft, and the flexural deformation of the main shaft has a great influence on the load distribution of the bearings. Modeling of the main shaft with flexible beam elements. The bore surface of each bearing is coupled to a master node I at the center of the inner diameter surface through the CE. The MPC algorithm was used to constrain the degrees of freedom between the master node I and node J on the flexible beam, and the axial rotational degrees of freedom are simultaneously constrained to prevent shaft rotation. The wind load will be transferred to the bearing bore surface through the flexible beam. The shaft is connected to any of the bearings as shown in Figure 6, where q_I and q_J are the coordinate systems of degrees of freedom of the I and J nodes. The I and J nodes both have six degrees of freedom, and the I and J nodes spatially overlap.

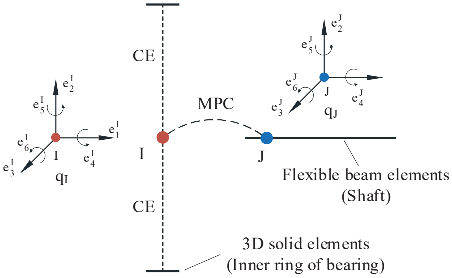

Figure 6. Shaft-bearing coupling diagram.

The degree of freedom constraint relationship of the two coupled nodes can be expressed as

$$C\left(q_I, q_J, t\right) = 0 \tag{10}$$

where q_I and q_J are the degrees of freedom corresponding to the coordinate system of degrees of freedom of the coupled nodes and t is the time.

2.3. Housing Modeling

In a wind turbine, the outer casing acts as the bearing housing for the bearings on the main shaft. The wind load is finally transferred to the outer casing through the shaft and bearings. The bearing housing holds the bearings on the spindle in place. Its elastic deformation under load affects the relative position of the outer rings of the bearings, and its flexibility directly affects the load distribution of the bearings just like that of the spindle. Ignoring its flexibility will result in too large spindle stiffness, which makes the calculation of the bearing load distribution inaccurate. Therefore, it is necessary to establish a flexible housing in the model. So the outer housing is modeled with 3D solid elements. To avoid the excessive introduction of nonlinearity in the system, the outer casing is coupled to the bearings' outer rings by sharing nodes.

The shaft, bearing rings, and rollers are assembled and the final FE connection method is shown in Figure 7.

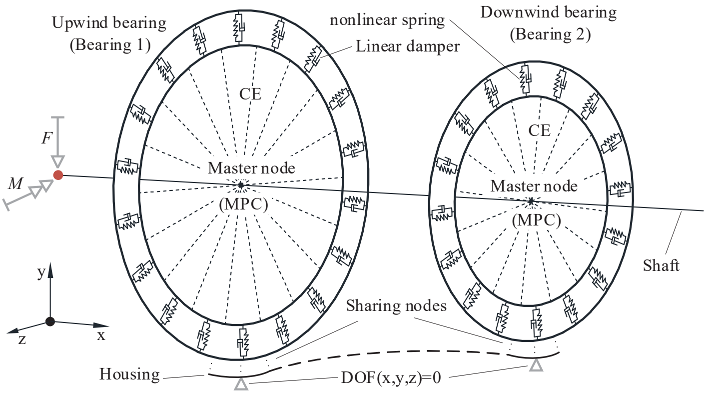

Figure 7. Coupling connection relationship of the shaft assembly.

For a roller, at least two springs are required to simulate tilt or offset load. To study the effect of the number of replacement springs on the load distribution of bearing rollers, each roller is replaced by 2, 3, and 5 nonlinear spring elements (denoted as 2 spr, 3 spr, and 5 spr), respectively, corresponding to the partial view of the model shown in Figure 8. It contains $n \times (Z_1 + Z_2)$ nonlinear spring elements, $n \times (Z_1 + Z_2)$ linear dampers, and 2 MPC elements.

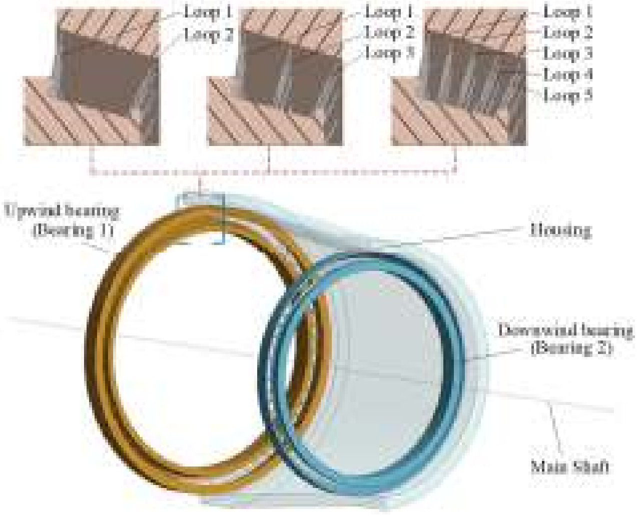

Figure 8. FE model of shaft system with different quantities of replacement springs.

3. Theoretical Calculation of Maximum Roller Load

Figure 9 shows the cross-section of bearings on the wind turbine spindle. Under the action of external load, the contact loads between the tapered roller and the inner raceway, outer raceway, and end-ring flange are Q_i, Q_e, and Q_f, respectively, and the contact angles are α_i, α_e, and α_f, respectively. The roller load satisfies the following equilibrium equation.

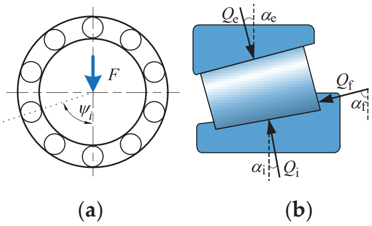

Figure 9. The positions and forces of the tapered rollers. (**a**) The angular positions of the rollers; (**b**) Forces of tapered rollers.

$$\begin{cases} Q_\mathrm{e}\sin\alpha_\mathrm{e} - Q_\mathrm{i}\sin\alpha_\mathrm{i} - Q_\mathrm{f}\sin\alpha_\mathrm{f} = 0 \\ Q_\mathrm{e}\cos\alpha_\mathrm{e} - Q_\mathrm{i}\cos\alpha_\mathrm{i} - Q_\mathrm{f}\cos\alpha_\mathrm{f} = 0 \end{cases} \tag{11}$$

It is further deduced that:

$$Q_\mathrm{i} = Q_\mathrm{e}\frac{\sin(\alpha_\mathrm{e}+\alpha_\mathrm{f})}{\sin(\alpha_\mathrm{i}+\alpha_\mathrm{f})} = c_\mathrm{i}Q_\mathrm{e} \tag{12}$$

$$Q_\mathrm{f} = Q_\mathrm{e}\frac{\sin(\alpha_\mathrm{e}-\alpha_\mathrm{f})}{\sin(\alpha_\mathrm{i}+\alpha_\mathrm{f})} = c_\mathrm{f}Q_\mathrm{e} \tag{13}$$

where

$$c_\mathrm{i} = \frac{\sin(\alpha_\mathrm{e}+\alpha_\mathrm{f})}{\sin(\alpha_\mathrm{i}+\alpha_\mathrm{f})},\ c_\mathrm{f} = \frac{\sin(\alpha_\mathrm{e}-\alpha_\mathrm{f})}{\sin(\alpha_\mathrm{i}+\alpha_\mathrm{f})}.$$

The tapered roller bearing installed on the wind turbine spindle is mainly affected by two forces, radial force F_r and axial force F_a, as shown in Figure 10. The radial displacement δ_r and axial displacement δ_a of the inner ring are generated relative to the outer ring under the action of the radial force F_r. Let the radial clearance of the bearing be zero, the radial displacement at the roller with position Angle ψ_i is

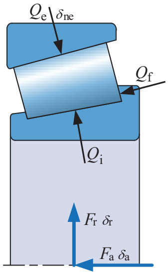

Figure 10. Tapered roller forces and bearing forces.

$$\delta_{\mathrm{r}i} = \delta_\mathrm{r}\cos\psi_i \tag{14}$$

The axial displacement components of all rollers are δ_a, then for the *i*th roller, the total displacement along the contact normal direction of the outer raceway is

$$\delta_{\mathrm{n}i} = \delta_{\mathrm{r}i}\cos\alpha_\mathrm{e} + \delta_{\mathrm{a}i}\sin\alpha_\mathrm{e} \tag{15}$$

The load-deformation relation of the *i*th roller is [21,25]

$$Q_{\mathrm{e}i} = K_{\mathrm{ne}} \delta_{\mathrm{n}i}^{1.11} \tag{16}$$

where K_{ne} is the total stiffness coefficient at the contact of the outer raceway, and the calculation formula is [25]

$$K_{\mathrm{ne}} = 8.06 \times 10^4 l^{0.89} \left[1 + {c_i}^{0.89} \cos(\alpha_{\mathrm{e}} - \alpha_i) \right]^{-1.11} \tag{17}$$

where l is the length of the roller.

As shown in Figure 11, the components of $Q_{\mathrm{e}i}$ in the direction of F_{r} and F_{a} are, respectively,

$$Q_{\mathrm{r}i} = Q_{\mathrm{e}i} \cos \alpha_{\mathrm{e}} \cos \psi_i \tag{18}$$

$$Q_{\mathrm{a}i} = Q_{\mathrm{e}i} \sin \alpha_{\mathrm{e}} \tag{19}$$

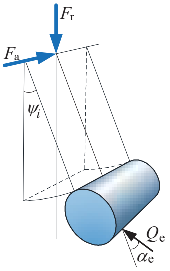

Figure 11. Spatial relationship between roller force and bearing forces.

Then the equilibrium equation of the bearing can be derived as

$$\begin{cases} F_{\mathrm{r}} - \sum\limits_{i=1}^{Z} Q_{\mathrm{r}i} = 0 \\ F_{\mathrm{a}} - \sum\limits_{i=1}^{Z} Q_{\mathrm{a}i} = 0 \end{cases} \tag{20}$$

Equation (20) is a nonlinear system of equations with δ_{r} and δ_{a} as unknown variables. The radial force F_{r} and axial force F_{a} of bearing 1 under wind load can be obtained by statics analysis and calculation of the shafting system. Combined with Equations (12) and (13), the theoretical values of the maximum load of the roller, such as Q_{emax}, Q_{imax}, and Q_{fmax} can be obtained by using iterative algorithms such as Newton's method. Since the general Q_{emax} is the largest, Q_{emax} is taken as the maximum roller load Q_{max}.

4. Sub-Model of Bearing

4.1. Logarithmic Crowning of Roller

The roller profile of bearings on the wind turbine spindle needs to be modified to reduce stress concentration and optimize load distribution. There is generally, power function crowning and logarithmic (exponential) crowning of the roller. Logarithmic crowning is not as good as power function crowning under extreme bias load conditions, but the stress distribution of the roller is more uniform under normal conditions [13,17], so the logarithmic crowning method is chosen for the study. The crowning zone of the tapered roller is shown in Figure 12.

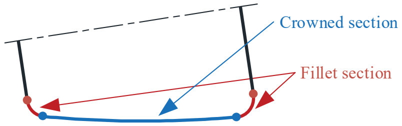

Figure 12. Crowned section and fillet section of tapered roller.

In practice, bearing rollers are often subjected to different and changing loads, yet the profile of the rollers in a set of bearing should remain consistent. Therefore, the maximum roller load is taken as the design load in the design of the roller's crowning.

In the FE model, n nonlinear spring elements are used to replace each roller, and the maximum value after superimposing the n loops spring reaction force is the maximum equivalent roller load $Q_{\max}$, and the expression is

$$Q_{\max} = (F_{\text{sum}i})_{\max} = \left(\sum_{j=1}^{n} F_{ji}\right)_{\max} \quad i = 1, 2, \ldots, Z \tag{21}$$

where $Q_{\max}$ is the maximum roller load, $F_{\text{sum}i}$ is the ith equivalent roller reaction force after superimposing n loops of spring reaction force, F_{ji} is the ith spring reaction force in loop j, and Z is the number of rollers.

The expression of the crowning function z of the tapered roller is

$$z = \frac{2Q}{\pi E' l_{we}} \times \ln\left[1 - \left(1 - 0.3033\frac{2b}{l_{we}}\right)(2x/l_{we})^2\right]^{-1} \tag{22}$$

where Q is the roller load, E' is the equivalent elastic modulus, b is the Hertzian contact half-width, and l_{we} is the crowning length.

The crowning profile of the roller is shown in Figure 13, where the maximum amount of crowning is denoted as $z_{\max}$.

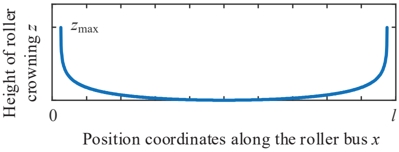

Figure 13. Logarithmic crowning profile of roller.

For line contact, according to Hertzian contact theory, the contact half-width b is

$$b = \left(\frac{4\eta Q}{\pi l \sum \rho}\right)^{1/2} \tag{23}$$

where $\Sigma\rho$ is the Curvature sum.

The formula for calculating $\Sigma\rho$ is as follows:

$$\sum \rho = \frac{2\cos\beta}{D_w} + \frac{2\gamma_i}{D_w(1-\gamma_i)} \tag{24}$$

where β is the tapered roller half-cone angle, D_{w} is the middle diameter of the roller, and $\gamma_i = D_w \cos\alpha_i / d_m$.

Defining $f_1 = 2Q/\pi E' l_{we}$ as the load parameter of logarithmic crowning and $f_2 = 1 - 0.3033 \times 2b/l_{we}$ as the width parameter of logarithmic crowning, the crowning function changes to

$$z = f_1 \times \ln\left[1 - f_2(2x/l_{we})^2\right]^{-1} \tag{25}$$

Equation (25) contains two crowning parameters f_1 and f_2. f_1 and f_2 are determined by the roller load Q and material parameters, and the roller load Q is the common influence variable. The research of [15] indicated that the effect of the parameter f_2 on the stress distribution of the roller is very small, while f_1 on the stress distribution of the roller is large. Only f_1 needs to be optimized and an adjustment-coefficient *cof* is added in front of Q in f_1 to make it variable, and the expression of the roller crowning function changes to

$$z = cof \times f_1 \times \ln\left[1 - f_2(2x/l_{we})^2\right]^{-1} \tag{26}$$

The reference values of the crowning parameters f_1, f_2, b, and z can be derived from theoretical calculations. Using the value of theoretically calculated z as a reference, the amount of crowning z can be adjusted by the adjustment-coefficient *cof*.

4.2. Mesh of Sub-Model

The profile of bearing roller crowning is an exact function curve and the sub-model needs to have a fine mesh to simulate the contact characteristics of the roller contact area. The mesh of the contact zone of the roller is refined, and the transition mesh is handled finely. The final mesh of the symmetric sub-model is shown in Figure 14, containing a total of 91,364 elements and 99,585 nodes.

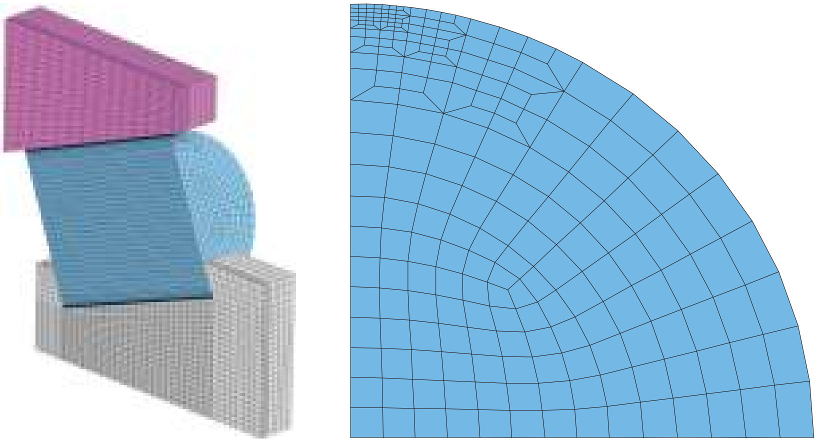
(**a**) (**b**)

Figure 14. Mesh of the symmetric sub-model. (**a**) The mesh of sub-model; (**b**) The mesh of roller cross-section.

For rollers without fillets, especially rollers with a straight profile, stress concentration is generated at the edge of the roller in the analysis with a very high calculated stress value, which neither does match the actual situation [13] nor is conducive to the stress assessment.

After meshing the geometry, the mesh of the roller edge needs to be shrunk in the radial direction by a certain amount, to meet the realistic fillet or chamfer features, the shrunk mesh of the roller edge is shown in Figure 15.

4.3. Boundary Conditions

Superimpose the n loops reaction forces of springs obtained from the FE model of the shaft system. The maximum value of the reaction force after superposition is used as the load boundary of the sub-model. Its direction is approximately the contact normal of the inner raceway. All degrees of freedom of the outer diameter surface of the outer ring of the bearing are fixed. The symmetry boundary is created on the symmetry surface of the rings and roller. Based on the direction of the force boundary vector, a coordinate system is established to constrain the other degrees of freedom of the inner ring bore surface except for the direction of the force. This is shown in Figure 16.

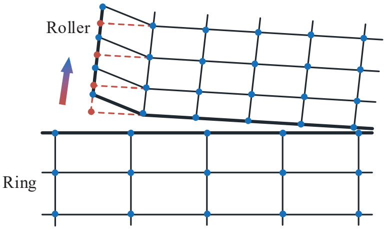

Figure 15. Radial shrinkage of mesh at roller edge.

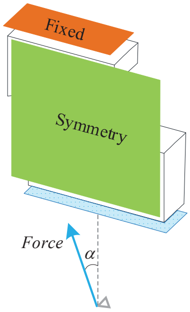

Figure 16. Boundary conditions of the sub-model.

On the symmetry plane, a path is created in the fillet and crowned section on the roller profile on the inner ring side, as shown in Figure 17, to extract the Von Mises stress of the nodes on the path.

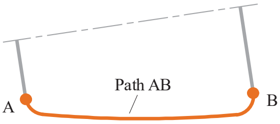

Figure 17. Path defined in post-processing.

5. Analysis and Discussion of Results

5.1. Effect of Damping on the Solution of the Shaft System

For the 5 spr case, the undamped model and the critically damped model of the FE model of the shaft system are solved, with the maximum displacement of the shaft system as the response index. The comparison of the response of the undamped and damped models is shown in Figure 18. It can be seen that the use of the critical damping technique can solve the FE model of the shaft system quickly and obtain a stable mechanical response.

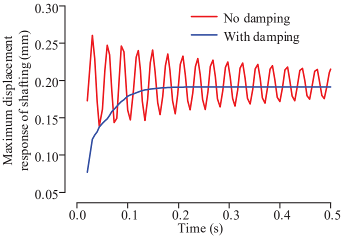

Figure 18. Mechanical response of FE model of the shaft system.

5.2. Influence of Structural Rigidity on the Shaft System

Figure 19 shows the deflection deformation of the shaft under load with a rigid/flexible structure (shaft and bearing housing). Figure 20 gives the relative position change of the profiles of the outer rings of two bearings.

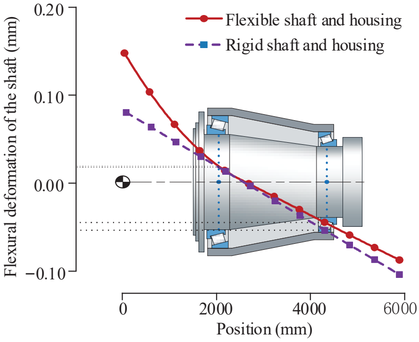

Figure 19. Comparison of shaft deformation under rigid and flexible structure.

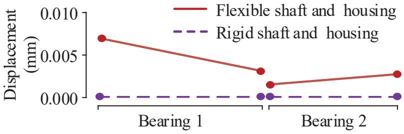

Figure 20. Relative position of the outer profiles of the outer rings of two bearings.

As can be seen in Figure 19, for a model with a rigid shaft and rigid housing, the shaft cannot deform flexibly and can only balance the load by deflecting an angle. In the model with a flexible shaft and a flexible bearing housing, the shaft can be bent and deformed flexibly and the deformation is greatest at the location of the loaded end of the shaft. This is also the location where the deflection is the largest compared to the rigid structure model.

As shown in Figure 20, the flexible housing allows the outer ring of the bearing to have a deflection deformation, which allows the bearing to better balance the load. The outer ring of bearing 1 has the largest deflection. However, combining the above factors, the displacement of the rigid shaft at the center position of bearing 1 has a smaller deviation compared to the flexible shaft, and the displacement of the rigid shaft at the center position of bearing 2 has a larger deviation compared to the flexible shaft. The large displacement of the rigid shaft will cause the load on the bearing to be larger, making the bearing life assessment biased, especially for bearing 2. Therefore, in the actual calculation for the bearing on the shaft system, the coupling effect of the flexibility of the structure on the bearing should be considered.

5.3. Effect of the Quantity of Replacement Springs on the Bearing Load Distribution

The n loops reaction forces of the springs for each case are extracted and shown in Figure 21. The equivalent roller load distribution is obtained after superimposing the n loops spring reaction force, and the equivalent roller load distribution under the three cases is shown in Figure 22. All the rollers of bearing 1 under the three cases are under load, and the trend was the same in all three cases, but the fluctuation of the equivalent roller load distribution is different in different cases.

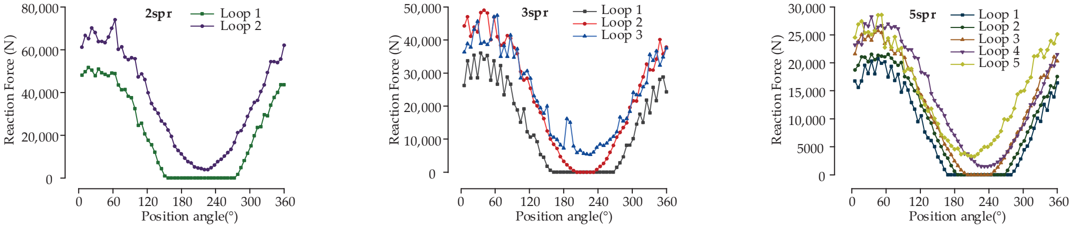

(**a**) (**b**) (**c**)

Figure 21. Spring reaction force in different cases. (**a**) Spring reaction force of 2 spr; (**b**) Spring reaction force of 3 spr; (**c**) Spring reaction force of 5 spr.

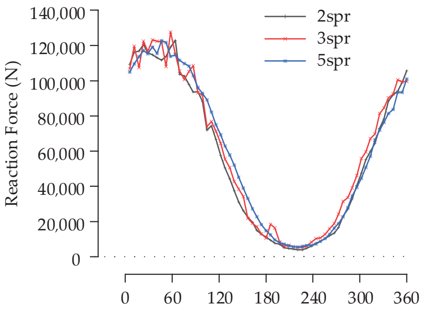

Figure 22. Equivalent roller load distribution of bearing 1 under different cases.

All the rollers of bearing 1 under the three cases are under load, and the trends of the equivalent roller load distribution in the three cases are the same, but the fluctuation of the equivalent roller load distribution is different in different cases. The smaller the data fluctuation, the more uniform the load distribution and the higher the precision. The X_{F} sequences corresponding to the different cases are shown in Figure 23.

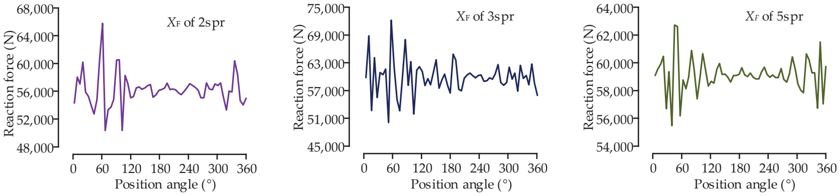

(**a**) (**b**) (**c**)

Figure 23. X_{F} sequences in different cases. (**a**) X_{F} sequences of 2 spr; (**b**) X_{F} sequences of 3 spr; (**c**) X_{F} sequences of 5 spr.

As Shown in Figure 24, when the number of replacement springs of a roller is two, three, and five, respectively, the maximum roller load varies irregularly, and the convergence and accuracy of the solution results cannot be evaluated effectively. The RMSE of the equivalent roller load distribution is 259.97, 7.54, and 4.75, respectively. The RMSE shows a significant convergence characteristic. When each roller is replaced by five springs, the RMSE of the equivalent roller load distribution is less than five, which is 98.46% lower than the maximum value of 259.97. At this time, the load distribution is uniform, indicating that the error of the FE model is small and the model has good calculation accuracy. Therefore, the calculation is more accurate when each roller is replaced by five or more springs.

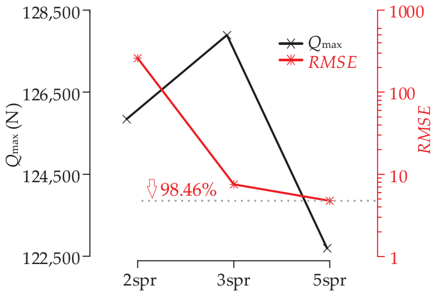

Figure 24. Maximum roller load vs. RMSE of maximum equivalent roller load.

Each roller is replaced by five springs. The FE model considering the flexibility of the structure is solved, and the maximum equivalent roller load is 122,731.03 N. The result of the FE model with a rigid structure is 125,830.48 N. Under the loading conditions in Table 2, the statics solution of the shaft system by ROMAX® 14.5 gives an axial reaction force of $F_a = 1.5 \times 10^6$ N and a radial reaction force of $F_r = 1.9 \times 10^6$ N for bearing 1. According to Equation (20), the theoretical result of the maximum roller load is 145,680 N. The FEM result with a rigid structure is 13.63% smaller than the theoretical solution, while the FEM result with a flexible structure is 15.75% smaller than the theoretical solution. The results are compared in Table 3. FEM and numerical theory were used to analyze the bearing capacity of large bearings in the literature [7], and it was pointed out that the numerical results were more conservative than the FEM results, and the FEM load results were generally about 30% smaller than the theoretical solution, with a maximum difference of 98.9%. In the research of [26], it is also pointed out that the theoretical result of the bearing load based on the flexible ring assumption is less than the results based on the rigid ring assumption. The results of the FE model with flexible structure in this paper are smaller than the theoretical solution, and the deviation is within 20%, so the FE model proposed in this paper is reasonable.

Table 3. Maximum roller load of FEM and theoretical results.

FEM with Flexible Structure/N	FEM with Rigid Structure/N	Theory Based on Rigid Ring Assumption/N
122,731.03 (−15.75%)	125,830.48 (−13.63%)	145,680 (—)

From Figure 22 and Table 3, it can be seen that all rollers of bearing 1 in the shaft system are loaded, which is the same as the actual. The maximum equivalent roller loads of the FE model with the flexible structure and the FE model with the rigid structure are lower than the theoretical results to some extent. The results of the FE model with a flexible structure are the smallest and within a reasonable range. This is because the FE model takes into account the flexibility of the structure, which optimized the load distribution of the bearing. The maximum roller load calculated is reduced and is more in line with reality. Compared with the FE model with a rigid structure, the FE model considering the flexibility of structure can better balance the load and calculate the load distribution more accurately.

5.4. Design of Optimum Crowning and Its Tolerance of the Roller

The maximum value of the superimposed spring reaction force of five loops is used as the boundary of the bearing sub-model, and the Von Mises stress distribution of the nodes along the profile at the inner ring side of the roller when the logarithmic crowning parameter *cof* takes different values are shown in Figure 25.

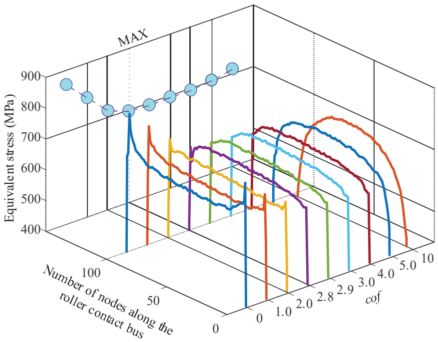

Figure 25. Stress distribution along the roller profile at different crowning parameter cof.

This can be seen in Figure 25. When the roller is not crowned, there is obvious stress concentration at both ends of the roller, and a slight sawtooth-like fluctuation of stress in the middle of the roller, which is caused by the FE mesh error. With the increase of crowning parameter cof of the roller, the stress concentration at the roller edge is effectively relieved or eliminated, and the maximum stress along the roller profile is obviously reduced. With the further increase of crowning parameter cof, the stress concentration appears in the middle of the roller, and the maximum stress along the roller profile rebounds slowly.

The effect of the crowning parameter cof on the maximum stress along the roller profile is shown in Figure 26.

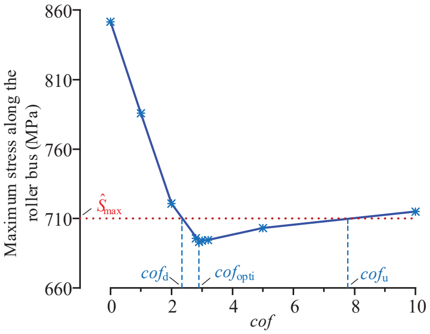

Figure 26. Maximum stress of the roller profile at different crowning parameter cof.

From Figure 26, it is clear that the maximum stress of the roller profile is a function of the logarithmical crowning parameter cof. With the increase of cof, there exists a unique value cof_{opti} which makes the maximum stress of the roller profile minimum. To meet the engineering application, the cof boundary values can be obtained when given the upper limit of the range of the maximum stress $\hat{S}_{\max}$, which are noted as cof_{d} and cof_{u}, and the tolerance range of the crowning parameters is $[cof_{\mathrm{d}}, cof_{\mathrm{u}}]$.

The value of $\hat{S}_{\max}$ affects the tolerance range of the profile of the bearing roller. Too large $\hat{S}_{\max}$ will lead to large roller contact stress, and too small $\hat{S}_{\max}$ will lead to a narrow tolerance band, which is not conducive to practical application. Note that the range of maximum contact stress of the bearing roller in Figure 26 is R_{S}. The variation range of the maximum equivalent stress is set as 0.1 R_{S}, that is, the $\hat{S}_{\max}$ is set as 710 MPa, and the tolerance range $[cof_{\mathrm{d}}, cof_{\mathrm{u}}]$ of the modification parameters is [2.3, 7.8].

The crowning profile of the roller and its tolerance zone corresponds to the optimum crowning parameter cof for bearing 1 as shown in Figure 27.

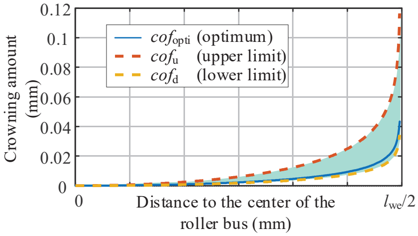

Figure 27. Optimal crowning profile and its tolerance zone of roller of bearing 1.

The stress distribution along the profile of the maximum loaded roller before and after being crowned is shown in Figure 28.

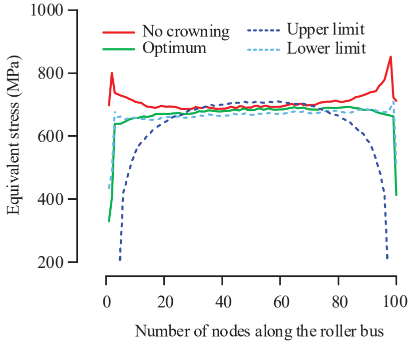

Figure 28. Stress distribution along the roller profile before and after being crowned.

When *cof* is equal to 0, i.e., when the roller is not crowned, the stress distribution along the roller profile appears as obvious edge stress concentration, and the maximum stress of the roller profile is 851.52 MPa. When *cof* is equal to cof_{opti}, that is when the roller is optimally crowned, the stress distribution along the roller profile is uniform without obvious stress concentration, the maximum stress is 693.07 MPa, and the maximum stress of the roller profile is reduced by 18.6% compared with the uncrowned. When *cof* is equal to cof_{d} or cof_{u}, the maximum stress of the roller profile is 710 MPa, and the maximum stress of the roller profile of the roller is reduced by 16.6% compared with the uncrowned.

6. Conclusions

1. CE and MPC algorithms were used to connect the shaft and bearing, and nonlinear spring elements and dampers with critical damping were used to replace the rollers to construct the FE model of the shaft assembly. The model has good convergence.
2. The high-pass filter based on FFT was used to filter the sequences of spring load distribution and then performed convergence analysis using RMSE, which can obtain the ideal number of replacement springs for each roller.
3. By analyzing the deformation of the shaft and the relative position of the outer profiles of the outer rings of two bearings, the FE model of the shaft system considering the structure's flexibility has higher calculation accuracy than the FE model with a rigid structure. The maximum roller load of the FE model with a flexible structure is 15.75% less than the theoretical solution, which is within a reasonable range.
4. The sub-model of the upwind bearing is constructed with structured mesh. With the crowning parameters of the logarithmically crowned roller as the design variables and the maximum Von Mises stress of the roller profile at the center of the contact area as the design target, the optimal logarithmic crowning of the roller and its tolerance zone under the given working conditions are obtained.

The FE model considering the flexibility of the support structure of the shaft system can obtain a more accurate load distribution of bearing, and can accurately design the bearing profile based on actual working conditions. The FE modeling method proposed can be further used to construct the calculation and analysis system of the shaft assembly of a large wind turbine and to provide support for the precision design of bearings in large shaft systems.

Author Contributions: Conceptualization, R.N. and X.L.; methodology, R.N.; software, X.L.; validation, S.Z., Y.C. and Z.Z.; formal analysis, X.L.; investigation, X.L.; resources, B.W.; data curation, X.L.; writing—original draft preparation, X.L.; writing—review and editing, R.N.; visualization, X.L.; supervision, R.N.; project administration, R.N.; funding acquisition, R.N. All authors have read and agreed to the published version of the manuscript.

Funding: This research was funded by the National Natural Science Foundation of China, grant number 52005158, and the Key Research and Development Project of Shandong Province, grant number 2020CXGC011003.

Data Availability Statement: Not applicable.

Conflicts of Interest: The authors declare that they have no conflict of interest.

References

1. Doll, M.N.K.; Gary, L. Tribological advancements for reliable wind turbine performance. *Philos. Trans.* **2010**, *368*, 4829–4850.
2. Hart, E.; Clarke, B.; Nicholas, G.; Amiri, A.K.; Stirling, J.; Carroll, J.; Dwyer-Joyce, R.; McDonald, A.; Long, H. A review of wind turbine main bearings: Design, operation, modelling, damage mechanisms and fault detection. *Wind. Energy Sci.* **2020**, *5*, 105–124. [CrossRef]
3. Smolnicki, T.; Rusiński, E. Superelement-based modeling of load distribution in large-size slewing bearings. *J. Mech. Des.* **2007**, *129*, 459–463. [CrossRef]
4. Chen, G.; Wang, C.; Xiao, Z. Effects of supporting structure and bolt connection on the fatigue life and carrying capacity of a slewing bearing. *J. Eng. Tribol.* **2016**, *231*, 766–782. [CrossRef]
5. Chen, G.; Wen, J. Load Performance of Large-Scale Rolling Bearings With Supporting Structure in Wind Turbines. *J. Tribol.* **2012**, *134*, 041105. [CrossRef]
6. Plaza, J.; Abasolo, M.; Coria, I.; Aguirrebeitia, J.; Igor, F.B. A new finite element approach for the analysis of slewing bearings in wind turbine generators using superelement techniques. *Meccanica* **2015**, *50*, 1623–1633. [CrossRef]
7. Li, Y.; Jiang, D.; Song, L. Finite Element Analysis of Pitch Bearing in Wind Turbine Considering Influence of Installation Structures. *Acta Energ. Sol. Sin.* **2019**, *40*, 2021–2027. (In Chinese)
8. Aguirrebeitia, J.; Abasolo, M.; Avilés, R.; Igor, F.B. General static load-carrying capacity for the design and selection of four contact point slewing bearings: Finite element calculations and theoretical model validation. *Finite Elem. Anal. Des.* **2012**, *55*, 23–30. [CrossRef]
9. He, P.; Liu, R.; Hong, R.; Wang, H.; Yang, G.; Lu, C. Hardened raceway calculation analysis of a three-row roller slewing bearing. *Int. J. Mech. Sci.* **2018**, *137*, 133–144. [CrossRef]
10. Śpiewak, S. Methodology for calculating the complete static carrying capacity of twin slewing bearing. *Mech. Mach.* **2016**, *101*, 181–194. [CrossRef]
11. Martín, I.; Aguirrebeitia, J.; Heras, I.; Abasolo, M. Efficient Finite Element modelling of crossed roller wire race slewing bearings. *Tribol. Int.* **2021**, *161*, 107098. [CrossRef]
12. Kania, L.; Pytlarz, R.; Śpiewak, S. Modification of the raceway profile of a single-row ball slewing bearing. *Mech. Mach. Theory* **2018**, *128*, 1–15. [CrossRef]
13. Ju, S.H.; Horng, T.L.; Cha, K.C. Comparisons of contact pressures of crowned rollers. *J. Eng. Tribol.* **2000**, *214*, 147–156. [CrossRef]
14. Fujiwara, H. Logarithmic profile of rollers in roller bearing and optimization of the profile. *Trans. Jpn. Soc. Mech. Eng.* **2006**, *72*, 338–345. (In Japanese) [CrossRef]
15. He, Z.; Shao, M.; Ye, G. Optimum Design Method for Logarithmic Crowned Tapered Rollers. *Mech. Eng. Technol.* **2016**, *5*, 38–46. [CrossRef]
16. Li, Y.; Gao, Y. Internal load distribution of single-row tapered roller bearings doubly supporting main shaft of wind turbine. *Adv. Mech. Eng.* **2022**, *14*, 16878132221098895. [CrossRef]
17. Zhang, T.; Yang, X.; He, L.; Bu, Z.J.; Nie, W.; Li, M. Research on the Design Method of Roller Modification Curve for Wind Turbine. *J. Mech. Strength* **2021**, *43*, 183–190. (In Chinese)
18. Li, Y.; Xu, Z.; Liu, Q.; Wang, H. Analysis on Contact Behavior for Extra Large Size Tapered Roller Bearings in Wind Turbines Based on PERMAS. *Bearing* **2014**, *5*, 1–4. (In Chinese)
19. Liu, J.; Dong, H.; Wang, H.; Wang, Y.Y. Finite Element Analysis of Slewing Bearing Based on Rolling Element Solid Model and Substructure Technology. *Bearing* **2018**, *12*, 9–13. (In Chinese)

20. Kania, L. Modelling of rollers in slewing bearing calculations with the use of finite elements. *Mech. Mach. Theory* **2006**, *41*, 1359–1376. [CrossRef]
21. Harris, T.A.; Kotzalas, M.N. *Advanced Concepts of Bearing Technology: Rolling Bearing Analysis*, 5th ed.; CRC Press: Boca Raton, FL, USA, 2006; pp. 3–7.
22. Palmgren, A. *Ball and Roller Bearing Engineering*, 3rd ed.; SKF Industries Inc.: Philadelphia, PA, USA, 1959.
23. Wang, P.; Wang, Q.; Xu, X.; Chen, N. Fractional Critical Damping Theory and Its Application in Active Suspension Control. *Shock. Vib.* **2017**, *2017*, 2738976. [CrossRef]
24. Zeng, P.; Lei, L.; Fang, G. *Finite Element Analysis Guide: Modeling and Analysis of Structure*; China Machine Press: Beijing, China, 2011; pp. 428–430.
25. Lundberg, G.; Palmgren, A. Dynamics capacity of rolling bearings. *Acta Polytech.* **1947**, *1*, 7. [CrossRef]
26. Zhang, H.; Chen, S.; Dou, Y.; Fan, H.; Wang, Y. Mechanical model and contact properties of double row slewing ball bearing for wind turbine. *Rev. Adv. Mater. Sci.* **2021**, *60*, 112–126. [CrossRef]

applied sciences

Article

Modified Design of Two-Switch Buck-Boost Converter to Improve Power Efficiency Using Fewer Conduction Components

Sunghwan Kim [1], Haiyoung Jung [2,*] and Seok-hyun Lee [1,*]

[1] Department of Electrical Engineering, Inha University, 100 Inha-ro, Michuhol-gu, Incheon 22212, Republic of Korea
[2] Department of Fire and Disaster Prevention, Semyung University, 65 Semyung-ro, Jecheon-si 27136, Republic of Korea
* Correspondence: hyjung@semyung.ac.kr (H.J.); plasma@inha.ac.kr (S.-h.L.)

Abstract: In this study, a modified design of a two-switch buck-boost (TSBB) converter is proposed to improve power efficiency using fewer conduction components, and the optimal power range is measured. The proposed TSBB converter operates in three topologies: buck, boost, and buck-boost, like the conventional TSBB converter. However, the proposed converter improves the power efficiency in the buck and buck-boost topologies by decreasing conduction loss using the diode in the switch-off section while maintaining the same number of semiconductors as that in the conventional TSBB converter. The power efficiency of the buck topology improves for the power range 10–80 W in the constant voltage (CV) and constant current (CC) modes; it increases on average by 0.75–1.36% and 0.83–2.27% in the CV and CC modes, respectively. The power efficiency of the buck-boost topology step-down improves for the 10–80 W in all modes. This increases the average by 0.73–0.99% and 3.33–4.75% in the CV and CC modes, respectively. The power efficiency of the buck-boost topology step-up increases on average by 1.65–2.00% for 10–80 W in the CV mode. In the CC mode, it increases by 2.17–2.77% on average for 10–50 W.

Keywords: converter; buck-boost converter; TSBB converter; conduction loss; switching loss; metal-oxide-semiconductor field effect transistor (MOSFET); switch; diode; voltage stress

Citation: Kim, S.; Jung, H.; Lee, S.-h. Modified Design of Two-Switch Buck-Boost Converter to Improve Power Efficiency Using Fewer Conduction Components. *Appl. Sci.* **2023**, *13*, 343. https://doi.org/10.3390/app13010343

Academic Editors: Kan Liu and Wei Hu

Received: 4 December 2022
Revised: 21 December 2022
Accepted: 22 December 2022
Published: 27 December 2022

1. Introduction

The DC–DC converter is a power conversion device that converts the received DC voltage to a DC voltage required by the system for transferring energy to the load [1]. It is used in several electronic devices for stabilizing the operation of systems; this can range from high-power applications such as solar photovoltaics, electric vehicles, and energy storage systems to low-power applications such as laptops, mobile phones, and portable batteries [2]. DC–DC converters are becoming miniaturized, and these parts are becoming denser because of the weight reduction and miniaturization of various application products [3]. DC–DC converters require high-power conversion efficiency for the reduction of energy consumption and long life [4]. Such high power-conversion efficiency is an important factor for a high-performance high-reliability DC–DC converter [5,6].

There are three topologies for non-isolated-type DC–DC converters: buck for step-down, boost for step-up, and buck-boost for both step-down and step-up. Figure 1 shows the circuit diagrams of each topology that consists of a switch, a diode, an inductor, and a capacitor. Step-down and step-up are determined by the duty ratio (d) and wiring of the semiconductors. Table 1 summarizes the current path and gain (G) of each topology based on switch operation; these topologies of the single switch type should be selected based on the input and output voltage specifications of the system; it is difficult to switch between topologies owing to the fixed element connection. Buck-boost topology with both step-down and step-up cannot be used in applications that require an output voltage of the same polarity as the input voltage because the polarity of the output voltage is opposite to that of the input voltage. Moreover, the power conversion efficiency decreases compared to that of other topologies because the voltage stress of the switch and diode equals the sum of the input voltage V_i and output voltage V_o. Therefore, the TSBB converter that can switch to a different topology based on system requirements is used frequently [7–10].

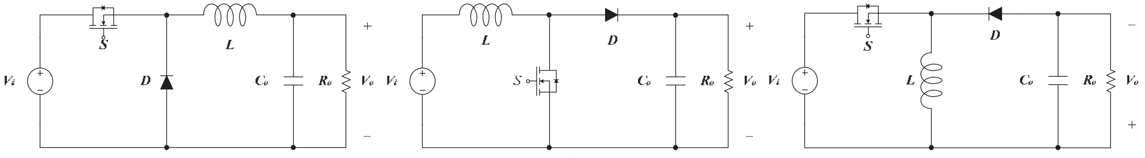

(**a**) (**b**) (**c**)

Figure 1. Circuit diagram: (**a**) buck; (**b**) boost; (**c**) buck-boost.

Table 1. Current path and gain in topologies.

Topology	**Current Path**		**Gain (G)**
	Switch ON	**Switch OFF**	
Buck	V_i-S-L-C_o	L-C_o-D	d
Boost	V_i-L-S	V_i-L-D-C_o	1/(1 − d)
Buck-Boost	V_i-S-L	L-C_o-D	d/(1 − d)

Figure 2 shows a circuit diagram of a conventional TSBB converter that comprises two switches, two diodes, an inductor, and a capacitor. This TSBB converter operates in the buck, boost, or buck-boost topology based on the operation of the switch [5–7]. Table 2 summarizes the switching operations of the conventional TSBB converter; it operates in the buck topology by the on/off switching of S_1 while S_2 is always off, and in boost topology by the on/off switching of S_2 while S_1 is always on. Further, the TSBB converter operates in the buck-boost topology by the on/off switching of both S_1 and S_2. It is easy to change the topology despite the increase in parts; the output voltage has the same polarity as the input in the buck-boost topology. Moreover, it is easy to select semiconductors because the voltage stress of the parts does not exceed the input voltage V_i and output voltage V_o [9–13].

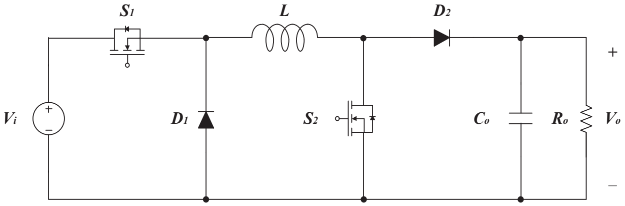

Figure 2. Circuit diagram of the conventional TSBB converter.

Table 3 presents the switching and conduction semiconductors in each topology of a single switch converter and a TSBB converter. The TSBB converter uses more parts than the single switch converter in each topology owing to the composition and wiring of the semiconductors; this increases the power loss and lowers the power efficiency. The loss of the TSBB converter increases because of the amount of the conduction loss of one diode than the single switch type in the buck topology and the amount of the conduction loss of one switch in the boost topology. Moreover, the power efficiency in the buck-boost topology decreases owing to the switching and conduction losses of one switch and one diode [5,6,10].

Table 2. Switch operation of the conventional TSBB converter.

Topology	Period	Component			
		S_1	S_2	D_1	D_2
Buck	Switch ON Switch OFF	ON OFF	Always OFF	OFF ON	Always ON
Boost	Switch ON Switch OFF	Always ON	ON OFF	Always OFF	OFF ON
Buck-Boost	Switch ON Switch OFF	ON OFF	ON OFF	OFF ON	OFF ON

Table 3. Switching and conduction semiconductors of single switch converters and the conventional TSBB converter.

Topology	Single Switch Type				Conventional TSBB			
	Switch ON		Switch OFF		Switch ON		Switch OFF	
	Switching	Conduction	Switching	Conduction	Switching	Conduction	Switching	Conduction
Buck	S	S	D	D	S_1	S_1, D_2	D_1	D_1, D_2
Boost	S	S	D	D	S_2	S_1, S_2	D_2	S_1, D_2
Buck-Boost	S	S	D	D	S_1, S_2	S_1, S_2	D_1, D_2	D_1, D_2

New circuits are suggested in [5,6] to prevent such a decrease in power efficiency. They demonstrated that power efficiency can be increased compared to those of the conventional TSBB converter by reducing the number of switching and conduction semiconductors in the current path. However, there is a trade-off between the number of semiconductors in the current path and the voltage stress. Therefore, in the new circuits of [5,6], the voltage stress of the semiconductors in the boost and buck-boost topologies increases, and it will lower power efficiency above a specific power range. The experimental results confirm the efficiency based on changes in the output current; however, it is difficult to find the optimal power range according to the changes in the input voltage and duty that influence the voltage stress of the semiconductors. To solve this problem, this study proposed a new type of TSBB converter for improving power efficiency and analyzing the optimal power range that can improve power efficiency. The proposed TSBB converter can increase power efficiency in buck and buck-boost topologies by reducing conduction loss caused by the diode in the switch-off section while using the same number of semiconductors as that of the conventional TSBB converter. Moreover, the optimal power range of each topology is analyzed by evaluating the effect of an increase in the voltage stress of semiconductors.

The contributions of this study are as follows:

- We investigated related research about the TSBB converter and proposed a modified design of the TSBB converter to improve power efficiency using fewer conduction components in the current path.
- We presented the optimal power range according to the buck, boost, and buck-boost topologies in CV and CC modes, and, in particular, divided into step-up/step-down sections in the buck-boost topology.
- We analyzed the power dissipation of the three topologies and explained why the CC mode of the buck-boost step-up is less efficient than conventional converters over a certain power range through analytic and experimental diode stress analysis.

The remainder of this paper is organized as follows. Section 2 describes the operation principle of the proposed TSBB converter. In Section 3, the power loss is compared between the proposed TSBB converter and the conventional TSBB converter in each topology by analyzing the switching and conduction losses. The experiment results are described in Section 4, and, finally, the conclusions are presented in Section 5.

2. Operation Principle

Figure 3 shows the circuit diagram of the proposed TSBB converter. Like the conventional TSBB converter, the proposed TSBB converter is composed of two switches, two diodes, an inductor, and a capacitor; further, it operates in three topologies based on the switching of S_1 and S_2, and it operates in the buck topology by the on/off switching of S_1, in the boost topology by the switching of S_2, and in the buck-boost topology by the simultaneous on/off switching of S_1 and S_2.

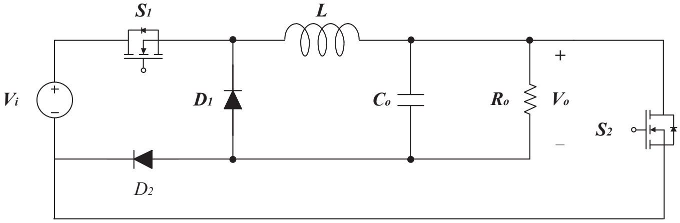

Figure 3. Circuit diagram of the proposed TSBB converter.

Table 4 summarizes the switching operations of the proposed TSBB converter. Table 4 indicates that the switching operations of S_1, S_2, and D_1 are the same as those of the conventional TSBB converter. However, D_2 performs on/off switching in the buck topology and is always off in the buck-boost topology.

Table 4. Switch operation of the proposed TSBB converter.

Topology	Period	Component			
		S_1	S_2	D_1	D_2
Buck	Switch ON Switch OFF	ON OFF	Always OFF	OFF ON	ON OFF
Boost	Switch ON Switch OFF	Always ON	ON OFF	Always OFF	OFF ON
Buck-Boost	Switch ON Switch OFF	ON OFF	ON OFF	OFF ON	Always OFF

Figure 4 presents the operation principle of the proposed TSBB converter in each topology. The switch-on/off sections are divided by the operation of the switch that transfers the energy to the inductor. The semiconductors located in the current path in each section are conduction semiconductors; the semiconductor that only operates in one of the switch-on/off sections is the switching semiconductor. Table 5 compares the switching and conduction semiconductors between the conventional and proposed TSBB converters. In comparison with the conventional TSBB converter, the proposed TSBB converter undergoes an increase in the switching loss of D_2 in the switch-on section and a decrease in the conduction loss of D_2 in the switch-off section. In the buck-boost topology, the switching and conduction losses of D_2 in the switch-off section decrease. Table 6 compares the stress between the conventional and proposed TSBB converters; they have the almost same voltage stress in buck and boost topologies, but in the buck-boost topology, the stress of D_1 increases to $V_i + V_o$.

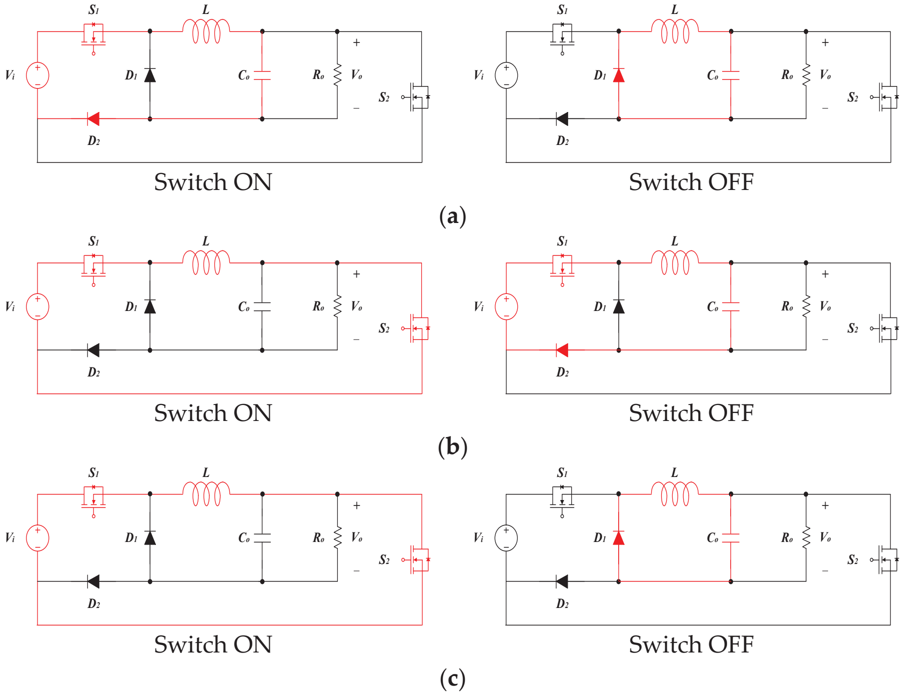

Figure 4. Operation principle of the proposed TSBB converter: (**a**) Buck; (**b**) Boost; (**c**) Buck-boost.

Table 5. Switching and conduction semiconductors of the conventional and proposed TSBB converters: (a) Switching semiconductors; (b) Conduction semiconductors.

Topology	**Gain**	**Conventional**		**Ref. [5]**		**Proposed**	
		Switch ON	**Switch OFF**	**Switch ON**	**Switch OFF**	**Switch ON**	**Switch OFF**
Buck	d	S_1	D_1	S_1, D_2	D_1	S_1, D_2	D_1
Boost	1/(1 − d)	S_2	D_2	S_2	D_2	S_2	D_2
Buck-Boost	d/(1 − d)	S_1, S_2	D_1, D_2	S_2	D_1	S_1, S_2	D_1

(a)

Topology	**Gain**	**Conventional**		**Ref. [5]**		**Proposed**	
		Switch ON	**Switch OFF**	**Switch ON**	**Switch OFF**	**Switch ON**	**Switch OFF**
Buck	d	S_1, D_2	D_1, D_2	S_1, D_2	D_1	S_1, D_2	D_1
Boost	1/(1 − d)	S_1, S_2	S_1, D_2	S_2	S_1, D_2	S_1, S_2	S_1, D_2
Buck-Boost	d/(1 − d)	S_1, S_2	D_1, D_2	S_2	D_1	S_1, S_2	D_1

(b)

Table 6. Comparison of stress in each TSBB converter: (a) Voltage stress; (b) Current stress.

Topology	**Conventional**			
	S_1	**S_2**	**D_1**	**D_2**
Buck	V_i	-	V_i	-
Boost	-	V_o	-	V_o
Buck-Boost	V_i	V_o	V_i	V_o

Table 6. *Cont.*

Topology	Ref. [5]			
	S_1	S_2	D_1	D_2
Buck	$\frac{C_{oss,D2}}{C_{oss,S1}+C_{oss,D2}}V_i$	-	V_i	$\frac{C_{oss,S1}}{C_{oss,S1}+C_{oss,D2}}V_i$
Boost	-	V_o	-	$\frac{C_{oss,S1}}{C_{oss,S1}+C_{oss,D2}}V_o$
Buck-Boost	$\frac{C_{oss,D2}}{C_{oss,S1}+C_{oss,D2}}V_i$ or $\frac{C_{oss,D2}}{C_{oss,S1}+C_{oss,D2}}V_o$	$V_i + V_o$	$V_i + V_o$	$\frac{C_{oss,S1}}{C_{oss,S1}+C_{oss,D2}}V_i$ or $\frac{C_{oss,S1}}{C_{oss,S1}+C_{oss,D2}}V_o$
Topology	**Proposed**			
	S_1	S_2	D_1	D_2
Buck	$\frac{C_{oss,D2}}{C_{oss,S1}+C_{oss,D2}}V_i(\cong V_i)$	-	V_i	$\frac{C_{oss,S1}}{C_{oss,S1}+C_{oss,D2}}V_i(\cong 0)$
Boost	-	V_o	-	V_o
Buck-Boost	$\frac{C_{oss,D2}}{C_{oss,S1}+C_{oss,D2}}V_i(\cong V_i)$	$\frac{C_{oss,D2}}{C_{oss,S2}+C_{oss,D2}}V_o(\cong V_o)$	$V_i + V_o$	-

(a)

Topology	Conventional/Proposed			
	S_1	S_2	D_1	D_2
Buck	$V_o\left(\frac{1}{R^{1}}+\frac{1-d}{2L\cdot f_{sw}}\right)$	-	$V_o\left(\frac{1}{R^{1}}+\frac{1-d}{2L\cdot f_{sw}}\right)$	$V_o\left(\frac{1}{R^{1}}+\frac{1-d}{2L\cdot f_{sw}}\right)$
Boost	-	$V_i\left[\frac{1}{(1-d)^2\cdot R^{1}}+\frac{d}{2L\cdot f_{sw}}\right]$	-	$V_i\left[\frac{1}{(1-d)^2\cdot R^{1}}+\frac{d}{2L\cdot f_{sw}}\right]$
Buck-Boost	$V_i\left[\frac{d}{(1-d)^2\cdot R^{1}}+\frac{d}{2L\cdot f_{sw}}\right]$	$V_i\left[\frac{d}{(1-d)^2\cdot R^{1}}+\frac{d}{2L\cdot f_{sw}}\right]$	$V_i\left[\frac{d}{(1-d)^2\cdot R^{1}}+\frac{d}{2L\cdot f_{sw}}\right]$	-

(b)

[1] Output resistance.

3. Analysis of Semiconductor Power Loss

The power loss of a TSBB converter includes the losses of the switch, diode, inductor, and capacitor when various parasitic components in the circuit are ignored. The power loss of the two converters is determined by the power loss of the semiconductors assuming that the losses of the inductor and capacitor are the same between the conventional and proposed TSBB converters. Therefore, the increase or decrease in power efficiency is determined by the operation of the switch and diode.

3.1. Switch and Diode Current

Figure 5 presents the switch and diode current of the proposed TSBB converter in each topology. In the buck topology, the inductor current flows through S_1 and D_2 during the switch-on section and through D_1 during the switch-off section. The inductor current I_L is the output current I_o and $\Delta I_L = \frac{V_o(1-d)}{L\cdot f_{sw}}$ by the volt-sec balance law at switching frequency f_{sw}, the inductor current I_{max}, I_{min} flowing through switch S_1 and diode D_1/D_2 can be expressed as:

$$I_{max} = I_o + \frac{\Delta I_L}{2} = V_o\left(\frac{1}{R} + \frac{1-d}{2L\cdot f_{sw}}\right) \tag{1}$$

$$I_{min} = I_o - \frac{\Delta I_L}{2} = V_o\left(\frac{1}{R} - \frac{1-d}{2L\cdot f_{sw}}\right) \tag{2}$$

The inductor current flows through S_1 and D_2 during the switch-on section and through D_1 during the switch-off section in the boost topology. Since the inductor current

I_L is $\frac{I_o}{1-d}$ and $\Delta I_L = \frac{d \cdot V_i}{L \cdot f_{sw}}$, the inductor current I_{max}, I_{min} flowing through switch S_1/S_2 and diode D_2 can be expressed as:

$$I_{max} = I_o + \frac{\Delta I_L}{2} = V_i\left[\frac{1}{(1-d)^2 \cdot R} + \frac{d}{2L \cdot f_{sw}}\right] \tag{3}$$

$$I_{min} = I_o - \frac{\Delta I_L}{2} = V_i\left[\frac{1}{(1-d)^2 \cdot R} - \frac{d}{2L \cdot f_{sw}}\right] \tag{4}$$

In buck-boost topology, the inductor current flows through S_1 and D_2 during the switch-on section and through D_1 during the switch-off section. Since the inductor current $I_L = \frac{I_o}{1-d}$ and $\Delta I_L = \frac{d \cdot V_i}{L \cdot f_{sw}}$ same as boost topology, the inductor current I_{max}, I_{min} flowing through switch S_1/S_2 and diode D_2 can be expressed as:

$$I_{max} = I_o + \frac{\Delta I_L}{2} = V_i\left[\frac{d}{(1-d)^2 \cdot R^1} + \frac{d}{2L \cdot f_{sw}}\right] \tag{5}$$

$$I_{min} = I_o - \frac{\Delta I_L}{2} = V_i\left[\frac{d}{(1-d)^2 \cdot R^1} + \frac{d}{2L \cdot f_{sw}}\right] \tag{6}$$

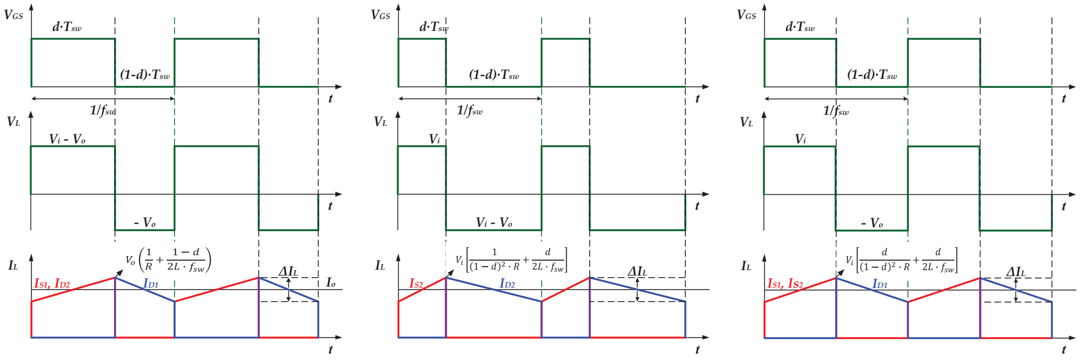

(**a**) (**b**) (**c**)

Figure 5. Switch and diode current of the proposed TSBB converter: (**a**) Buck; (**b**) Boost; (**c**) Buck-boost.

The power loss of a TSBB converter includes the losses of the switch, diode, inductor, and capacitor when various parasitic components in the circuit are ignored. The power loss of the two converters is determined by the power loss of the semiconductors assuming that the losses of the inductor and capacitor are the same between the conventional and proposed TSBB converters. Therefore, the increase or decrease in the power efficiency is determined by the operation of the switch and diode.

The losses of semiconductors are divided into switching and conduction losses. A switching loss occurs during the transient time of the switching operation. Although the switching loss is 0 in the ideal condition, it is caused by the time delay attributed to the parasitic resistance and parasitic capacitance at the time of turn-on or turn-off [14,15]. The conduction loss is caused by the current that flows by the turn-on of the semiconductor and on the resistance of the semiconductor [16–18].

3.2. Switching Loss

The switching loss of MOSFET, $P_{S,SW}$ is divided into switch turn-on loss, $P_{S,SW,ON}$ switch turn-off loss $P_{S,SW,OFF}$, and output capacitance loss $P_{S,SW,Coss}$ as [5,15,17]:

$$P_{S,SW} = P_{S,SW,ON} + P_{S,SW,OFF} + P_{S,SW,Coss} \tag{7}$$

The switch turn-on and turn-off losses are difficult to calculate because of the nonlinear characteristics of the drain-source voltage v_{DS} and drain current i_D. Therefore, they can be determined by applying linear approximation in the rising and falling sections of v_{DS} and i_D. The output capacitance loss of MOSFET can be determined by calculating the stored energy of the capacitor because the energy is charged in the output capacitance when the MOSFET turns off, and is discharged when the MOSFET turns on. The MOSFET switching loss can be represented by using the turn-on time t_{on}, turn-off time t_{off}, switching frequency f_{sw}, and output capacitance C_{oss} of the MOSFET as [5,17,18]:

$$\begin{aligned} P_{S,SW} &= \tfrac{1}{2}\cdot v_{DS}\cdot i_D\cdot t_{on}\cdot f_{sw} + \tfrac{1}{2}\cdot v_{DS}\cdot i_D\cdot t_{off}\cdot f_{sw} + \tfrac{1}{2}\cdot C_{oss}\cdot {v_{DS}}^2\cdot f_{sw} \\ &= \tfrac{1}{2}\cdot v_{DS}\cdot i_D\cdot (t_{on} + t_{off})\cdot f_{sw} + \tfrac{1}{2}\cdot C_{oss}\cdot {v_{DS}}^2\cdot f_{sw} \end{aligned} \tag{8}$$

The output capacitance of the MOSFET is several tens to hundreds of picofarads. Therefore, it is negligible compared to the switch turn-on and turn-off losses and can be represented as [5,6,17,18]:

$$P_{S,SW} = \frac{1}{2}\cdot v_{DS}\cdot i_D\cdot (t_{on} + t_{off})\cdot f_{sw} \tag{9}$$

The switching loss $P_{D,SW}$ of the diode can be divided into the switch turn-on loss $P_{D,SW,ON}$ and the switch turn-off loss $P_{D,SW,OFF}$ it is represented as:

$$P_{D,SW} = P_{D,SW,ON} + P_{D,SW,OFF} \cong P_{D,SW,OFF} \tag{10}$$

The switching loss of the diode can be approximated as the switch turn-off loss because the loss of the diode caused by the reverse recovery in the turn-off section is considerably larger than the turn-on loss [19,20].

Figure 6 shows the reverse recovery characteristic of the diode [6]. In an ideal diode, the current flows when the voltage is applied in the forward direction, and no current flows when the voltage is applied in the reverse direction. However, in an actual operation, the reverse current flows for a certain time before it reaches zero when the diode is turned off after a forward current flow. Here, the time during which the reverse current flows is referred to as the reverse recovery time (t_{rr}); the maximum value of the reverse current that flows in the diode is referred to as the repetitive peak reverse current (I_{RRM}). The turn-off loss $P_{D,SW,OFF}$ of the diode when the reverse voltage applied to the diode is V_R and the switching frequency is f_{sw} can be expressed as [21,22]:

$$P_{D,SW} = \frac{1}{2}\cdot V_R\cdot I_{RRM}\cdot t_{rr}\cdot f_{sw} \tag{11}$$

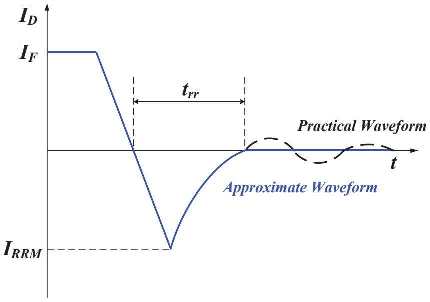

Figure 6. Diode reverse recovery characteristics.

3.3. Conduction Loss

The instantaneous value of the conduction loss of the MOSFET, $P_{S,CD}(t)$ can be expressed by $v_{DS}(t)$, $i_D(t)$, and the drain-source resistance $R_{DS(ON)}$ in the complete switch turn-off section as [6,15,16,19]:

$$P_{S,CD}(t) = v_{DS}(t) \cdot i_D(t) = {i_D}^2(t) \cdot R_{DS(ON)} \tag{12}$$

The average value can be determined by integrating Equation (6) over the switching period T_{sw} as:

$$P_{S,CD}(t) = \frac{1}{T_{sw}} \int_0^{T_{sw}} {i_D}^2(t) \cdot R_{DS(ON)}\, dt \tag{13}$$

$$P_{S,CD} = {I_{D(rms)}}^2 \cdot R_{DS(ON)} \tag{14}$$

The instantaneous value of the conduction loss of the diode $P_{D,CD}(t)$ can be expressed by the forward voltage drop $v_F(t)$, forward current $i_F(t)$, and diode resistance R_D as [5,6]:

$$P_{D,CD}(t) = v_F(t) \cdot i_F(t) + R_D \cdot {i_F}^2(t) \tag{15}$$

The average value can be determined by integrating Equation (8) over the switching period T_{sw} as [5,12,15]:

$$P_{D,CD}(t) = \frac{1}{T_{sw}} \int_0^{T_{SW}} \left\{ v_F(t) \cdot i_F(t) + R_D \cdot {i_F}^2(t) \right\} dt \tag{16}$$

$$P_{D,CD} = V_F \cdot I_{F(AVG)} + R_D \cdot {I_{F(RMS)}}^2 \tag{17}$$

4. Analysis of Power Loss in Topologies

Table 5 summarizes the switching and conduction semiconductors of the conventional and proposed TSBB converters in each topology. Table 6 presents the voltage and current stresses of the conventional and proposed TSBB converters in each topology. In each topology, the switching loss that has reflected the voltage stress and conduction loss based on the switch on/off time can be determined and compared.

4.1. Buck Topology

In Table 5, the switching semiconductors of the conventional TSBB converter are S_1/D_1, and the conducting semiconductors are $S_1/D_1/D_2$. Thus, the switching loss $P_{CON,SW}$ and conduction loss $P_{CON,CD}$ can be expressed, respectively, as:

$$P_{CON,SW} = P_{SW,S1} + P_{SW,D1} \tag{18}$$

$$P_{CON,CD} = P_{CD,S1,ON} + P_{CD,D2,ON} + P_{CD,D1,OFF} + P_{CD,D2,OFF} \tag{19}$$

The switching semiconductors of the proposed TSBB converter are $S_1/D_1/D_2$, and those of the conducting semiconductor are $S_1/D_1/D_2$. Therefore, the switching loss $P_{PRO,SW}$ and conduction loss $P_{PRO,CD}$ can be expressed as:

$$P_{PRO,SW} = P_{SW,S1}\left(\frac{C_{oss,D2}}{C_{oss,S1} + C_{oss,D2}} V_i\right) + P_{SW,D1}(V_i) + P_{SW,D2}\left(\frac{C_{oss,S1}}{C_{oss,S1} + C_{oss,D2}} V_i\right) \tag{20}$$

$$P_{PRO,CD} = P_{CD,S1,ON} + P_{CD,D2,ON} + P_{CD,D1,OFF} \tag{21}$$

The switching loss varies by the voltage stress; however, the internal voltage of semiconductors is V_i for both the conventional and proposed TSBB converters. Consequently, the switching losses of the semiconductors are the same. Therefore, the difference in power loss between the two converters can be expressed as:

$$P_{CON} - P_{PRO} = P_{CD,D2,OFF} - P_{SW,D2}\left(\frac{C_{oss,S1}}{C_{oss,S1} + C_{oss,D2}} V_i\right) \tag{22}$$

This difference can be determined by the conduction and switching losses in the switch-off section of D_2. Since the switch-off section is $(1 - d) \cdot T_{SW}$, the lower the duty ratio, the higher the efficiency of the proposed TSBB converter.

4.2. Boost Topology

In the boost topology, the switching semiconductors are S_2/D_2, and the conducting semiconductors are $S_1/S_2/D_2$. Thus, the switching loss $P_{CON,SW}$ $(= P_{PRO,SW})$ and the conduction loss $P_{CON,CD}$ $(= P_{PRO,CD})$ can be expressed as:

$$P_{CON,SW} = P_{PRO,SW} = P_{SW,S2} + P_{SW,D2} \tag{23}$$

$$P_{CON,CD} = P_{PRO,CD} = P_{CD,S1,ON} + P_{CD,S2,ON} + P_{CD,S1,OFF} + P_{CD,D2,OFF} \tag{24}$$

There is no difference in the efficiency between the conventional and proposed TSBB converters because there is no change in the operation of semiconductors.

4.3. Buck-Boost Topology

In Table 5, both the switching and conducting semiconductors of the conventional TSBB converter are $S_1/S_2/D_1/D_2$. Therefore, the switching loss $P_{CON,SW}$ and conduction loss $P_{CON,CD}$ can be expressed as:

$$P_{CON,SW} = P_{SW,S1}(V_i) + P_{SW,S2}\ (V_o) + P_{SW,D1}(V_i) + P_{SW,D2}(V_o) \tag{25}$$

$$P_{CON,CD} = P_{CD,S1,ON} + P_{CD,S2,ON} + P_{CD,D1,OFF} + P_{CD,D2,OFF} \tag{26}$$

Both the switching and conducting semiconductors of the proposed TSBB converter are $S_1/S_2/D_1$. Therefore, the switching loss $P_{PRO,SW}$ and conduction loss $P_{PRO,CD}$ can be, respectively, expressed as:

$$\begin{gathered} P_{PRO,SW} = P_{SW,S1}\left(\tfrac{C_{oss,D2}}{C_{oss,S1}+C_{oss,D2}} V_i\right) + P_{SW,S2}\left(\tfrac{C_{oss,D2}}{C_{oss,S2}+C_{oss,D2}} V_o\right) \\ +P_{SW,D1}(V_i + V_o) \end{gathered} \tag{27}$$

$$P_{PRO,CD} = P_{CD,S1,ON} + P_{CD,S2,ON} + P_{CD,D1,OFF} \tag{28}$$

The voltage stress of each semiconductor is indicated in parentheses since the switching loss varies by the voltage stress. The loss difference between the conventional and proposed TSBB converters is determined by the switching loss of D_1/D_2 and the conduction loss of D_2 in the switch-off section, and it can be expressed as:

$$P_{CON} - P_{PRO} = P_{SW,D1}(V_i) + P_{SW,D2}(V_o) + P_{CD,D2,OFF} - P_{SW,D1}(V_i + V_o) \tag{29}$$

There are no switching and conduction losses by D_2 because the proposed TSBB converter D_2 does not operate. However, the voltage stress of D_1 increases to $V_i + V_o$, the voltage stress and reverse current of the diode in a linear section are $P_{SW,D1}(V_i) + P_{SW,D2}(V_o) \cong P_{SW,D1}(V_i + V_o)$. Therefore, the loss is determined by the conduction loss of the switch-off section of D_2. The power efficiency of the proposed TSBB converter is higher than that of the conventional TSBB converter. In contrast, the switching loss by D_1, $P_{SW,D1}(V_i + V_o)$, increases in the section where the reverse current of the diode increases sharply owing to the voltage stress. Therefore, the power efficiency of the proposed TSBB converter is lower than that of the conventional TSBB converter.

5. Experimental Results

Figure 7 shows a prototype of a 100 W TSBB converter fabricated to verify the improved power efficiency. The Arduino controller generates a 5 V pulse width modulation (PWM) to control the MOSFET driver IC input; upon receiving this signal, the MOSFET driver IC converts it to an 18 V drive signal and transfers it to the gate of the MOSFET. The specifications of the components are 20% or more larger than the calculated maximum stress considering the various input/output conditions of the experiment. Table 7 summarizes the detailed specifications of the components; Table 8 presents the maximum values of the voltage stress measured in the CV/CC modes.

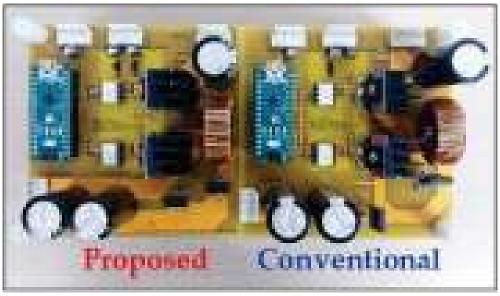

Figure 7. 100 W TSBB prototype.

Table 7. Components specifications.

Component	Part Name	Specification
PWM Generator	Arduino Nano	5 V, 16 MHz
MOSFET Driver	HCPL-J312	Output Peak Current = 2.5 A, Input Current = 7–16 mA Supply Voltage = 15–30 V, Input Capacitance = 60 pF Rise Time = 0.1 us, Fall Time = 0.1 us
MOSFET	RCX510N25	Drain-Source Voltage V_{DSS} = 250 V Gate-Source Voltage V_{GSS} = ±30 V Drain Current I_D = 51 A Static Drain-Source ON-State Resistance = 48 mΩ Output Capacitance = 350 pF Rise Time = 300 ns, Fall Time = 210 ns
Diode	RF2001T3D	Reverse voltage (DC) V_R = 300 V Forward voltage V_F = 1.3 V (at I_F = 10 A) Average Rectified Forward Current I_F = 20 A Reverse recovery time t_{rr} = 25 ns (at I_F = 0.5 A, I_R = 1 A, $I_{rr} = 0.25 \times I_R$)
Inductor	CH270125	Cross Section = 0.654 cm^2, Path Length = 6.35 cm Window Area = 1.56 cm^2, Volume = 4.154 cm^3 AL Value = 157 nH/Turn^2, Permeability μ = 125 Inductance = 250 uH
Electrolytic Capacitor	100YXG820MEFC18 × 40	Rated Voltage (V_{dc}) = 100 V Rated ripple current = 2330 mA (at 100 kHz) Leakage Current = 3 μA, Impedance = 20 °C, 100 kHz Dissipation Factor(MAX) tanδ = 0.08 Capacitance = 820 uF

The experiments are conducted in the CV/CC modes of the three topologies. The experiment for the buck-boost topology is conducted separately for the step-down and step-up sections. In the CV mode, the power efficiency is measured for the output power range of 10–80 W at the switching frequency f_{sw} = 100 kHz of the output current. The power efficiency was measured at three duty ratios to analyze the power efficiency based on the change in the duty ratio. If the input/output voltage variation ratio V_{var} is defined as the ratio of the difference between the input and output voltages to the input voltage, it can be expressed using the input voltage V_i and the output voltage V_o as:

$$V_{var}\ (\%) = \frac{|V_i - V_o|}{V_i} \times 100 \tag{30}$$

In each topology, the power efficiency was measured at the duty ratios where V_{var} was 25%, 33%, and 50%. Table 9 shows the duty ratio based on V_{var} in each topology. Figure 8a–d shows PWM waveforms of the conventional and the proposed TSBB converter in each topology implemented using Arduino Nano. Figure 8e–h presents waveforms of the inductor current, the gate-source voltage, and the output voltage of the conventional and proposed TSBB converters measured in CC mode at V_{var} = 33% (V_o ≅40 V).

Table 8. Measured maximum voltage stresses on components in CV and CC modes.

V_{var}	Device	CV								CC							
		Conventional (V_{max})				Proposed (V_{max})				Conventional (V_{max})				Proposed (V_{max})			
		Buck	Boost	Buck-Boost		Buck	Boost	Buck-Boost		Buck	Boost	Buck-Boost		Buck	Boost	Buck-Boost	
				Step-Down	Step-Up			Step-Down	Step-Up			Step-Down	Step-Up			Step-Down	Step-Up
25%	S_1	53.3	-	53.3	32.0	53.3	-	53.3	32.0	80.0	-	80.0	80.0	80.0	-	80.0	80.0
	S_2	-	41.3	46.0	45.5	-	41.6	47.5	46.8	-	104.5	67.2	114.8	-	105.2	68.9	116.9
	D_1	53.3	-	53.3	32.0	53.3	-	100.8	78.8	80.0	-	80.0	80.0	80.0	-	148.9	196.9
	D_2	-	41.3	46.0	45.5	-	41.6	-	-	-	104.5	67.2	114.8	-	105.2	-	-
33%	S_1	60.0	-	60.0	30.0	60.0	-	60.0	30.0	80.0	-	80.0	80.0	80.0	-	80.0	80.0
	S_2	-	41.3	45.9	44.9	-	41.7	47.5	46.3	-	111.9	59.0	121.0	-	112.0	60.5	123.0
	D_1	60.0	-	60.0	30.0	60.0	-	107.5	76.3	80.0	-	80.0	80.0	80.0	-	140.5	203.0
	D_2	-	41.3	45.9	44.9	-	41.7	-	-	-	111.9	59.0	121.0	-	112.0	-	-
50%	S_1	80.0	-	80.0	26.7	80.0	-	80.0	26.7	80.0	-	80.0	80.0	80.0	-	80.0	80.0
	S_2	-	41.8	46.3	45.5	-	41.7	47.9	46.9	-	126.5	43.2	138.5	-	127.3	44.6	141.2
	D_1	80.0	-	80.0	26.7	80.0	-	127.9	73.6	80.0	-	80.0	80.0	80.0	-	124.6	221.2
	D_2	-	41.8	46.3	45.5	-	41.7	-	-	-	126.5	43.2	138.5	-	127.3	-	-

Table 9. Duty ratio according to V_{var} in each topology.

V_{var}	Buck	Boost	Buck-Boost	
			Step-Down	Step-Up
25%	0.750	0.200	0.430	0.556
33%	0.667	0.250	0.400	0.571
50%	0.500	0.330	0.330	0.600

5.1. Buck Topology

Figure 9 shows the power efficiency of the buck topology in the CV and CC modes. If the power efficiency difference P_{Diff} is positive (+), it means efficiency improvement; if it is negative (-), it indicates an efficiency decline. The power efficiency improves in every condition from 10–80 W because of the removal of D_2 in the switch-off section in the CV and CC modes. P_{Diff} increases as the switch-off section becomes longer, i.e., when there is an increase in the duty ratio. In the same duty ratio condition, P_{Diff} decreases with an increase in the input voltage and output current. The improvement effect is large in the low-power region. The proposed converter can achieve a greater efficiency improvement effect in a region where the voltage conversion is large, and the output current is low.

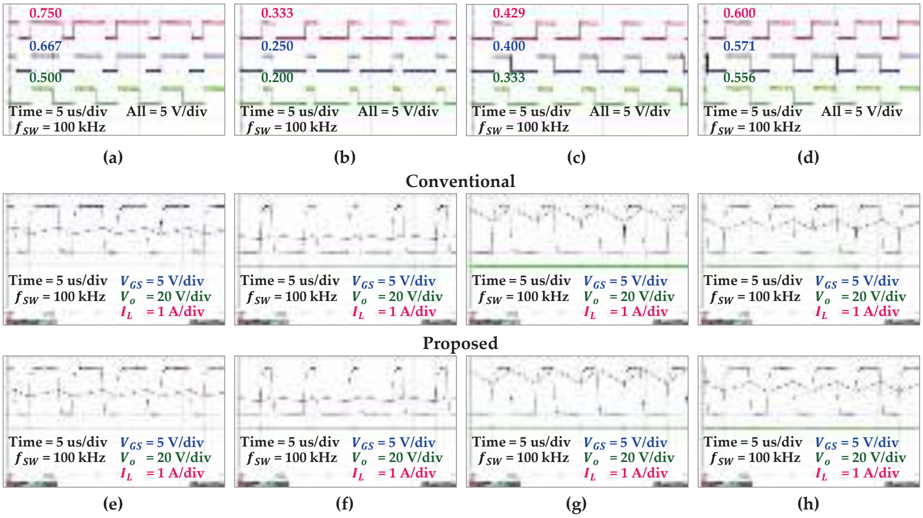

Figure 8. Waveforms of PWM, inductor current I_L, gate-source voltage V_{GS}, and output voltage V_o: PWM of (**a**) buck; (**b**) boost; (**c**) buck-boost step-down; (**d**) buck-boost step-up; I_L, V_{GS}, V_o of (**e**) buck (at d = 0.667; I_L = 1.5 A); (**f**) boost (at d = 0.250, I_L = 0.75 A); (**g**) buck-boost step-down (at d = 0.400, I_L = 1.5 A); and (**h**) buck-boost step-up (at d = 0.571, I_L = 0.75 A).

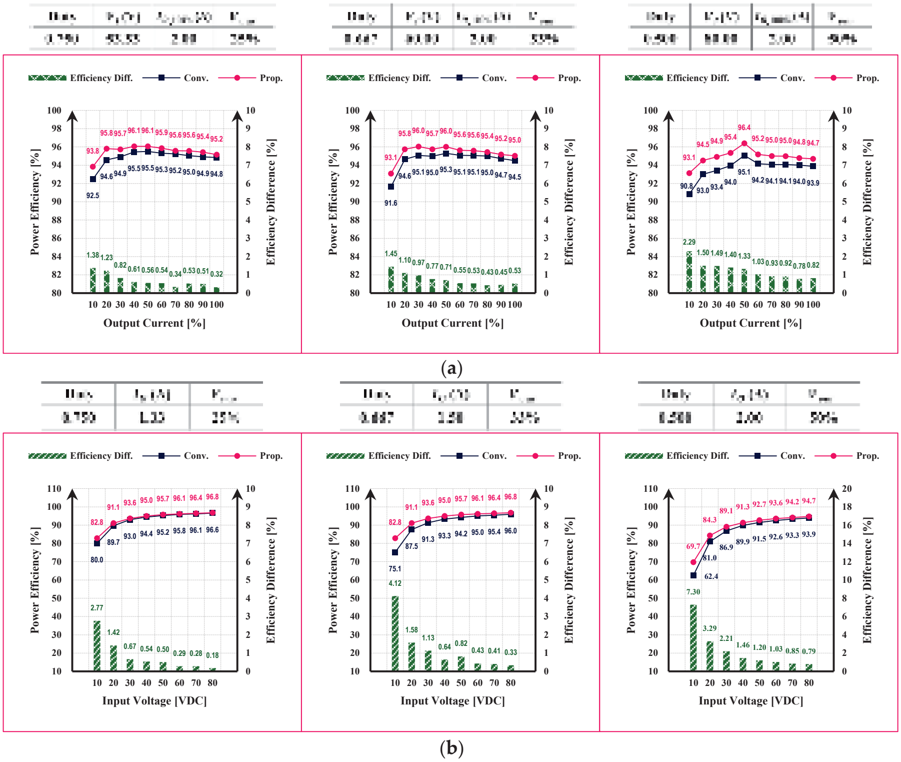

Figure 9. Power efficiency comparison of the buck topology: (**a**) CV mode; (**b**) CC mode.

5.2. Boost Topology

Figure 10 shows the power efficiency of the boost topology. The proposed converter shows the same power efficiency in the measured error range because it has the same number of semiconductors and the same stress as the conventional converter.

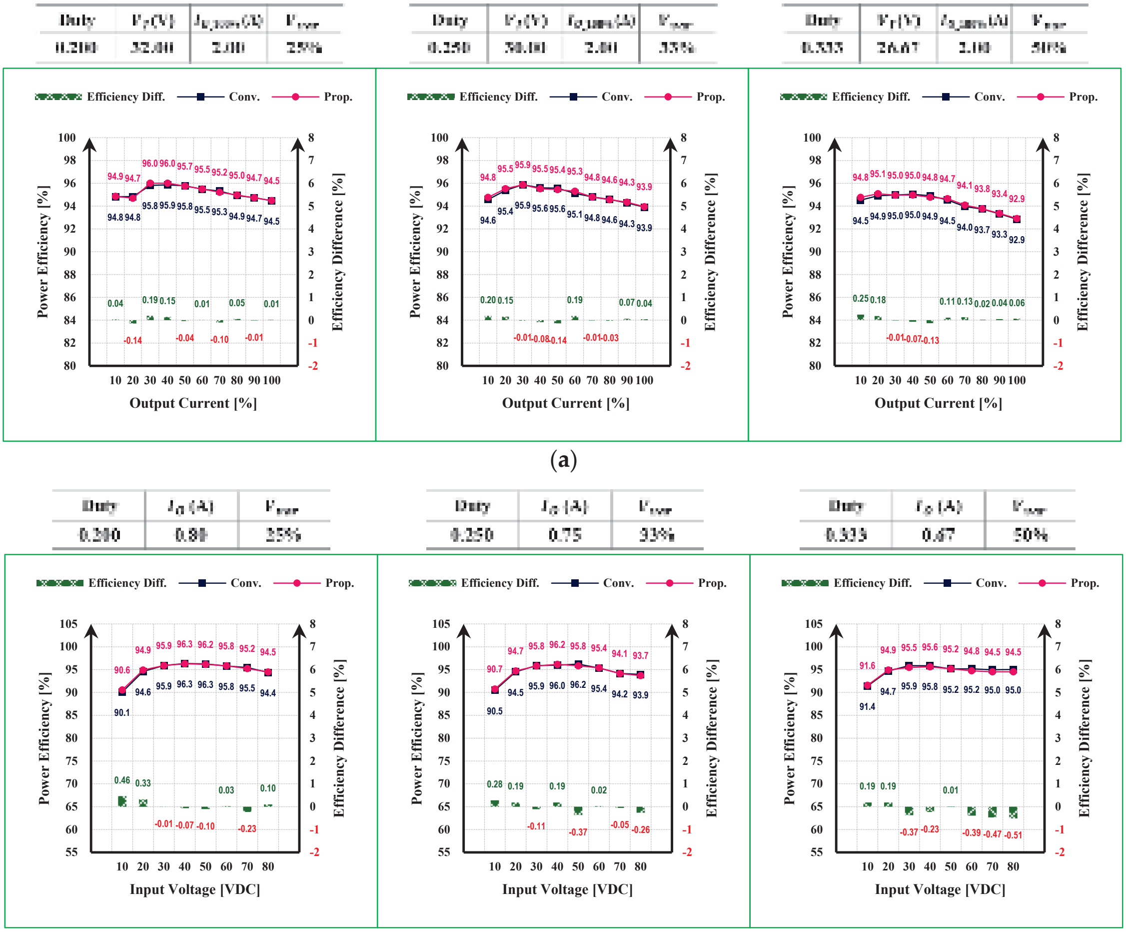

(**a**)

(**b**)

Figure 10. Power efficiency comparison of the boost topology: (**a**) CV mode; (**b**) CC mode.

5.3. Buck-Boost Topology

5.3.1. Step-Down

Figure 11 shows the power efficiency in the step-down section of the buck-boost topology in the CV and CC modes. The power efficiency is improved in every condition because of the removal of D_2 in the switch-off section. In the CV mode, the efficiency improvement becomes larger with an increase in the output current; P_{Diff} increases in the high-power region. In the CC mode, the power efficiency improves with a decrease in the input voltage, and P_{Diff} increases in the low-power region. In the same duty condition, the voltage stress of the diode D_1 increases with the input voltage; P_{Diff} decreases with an increase in loss.

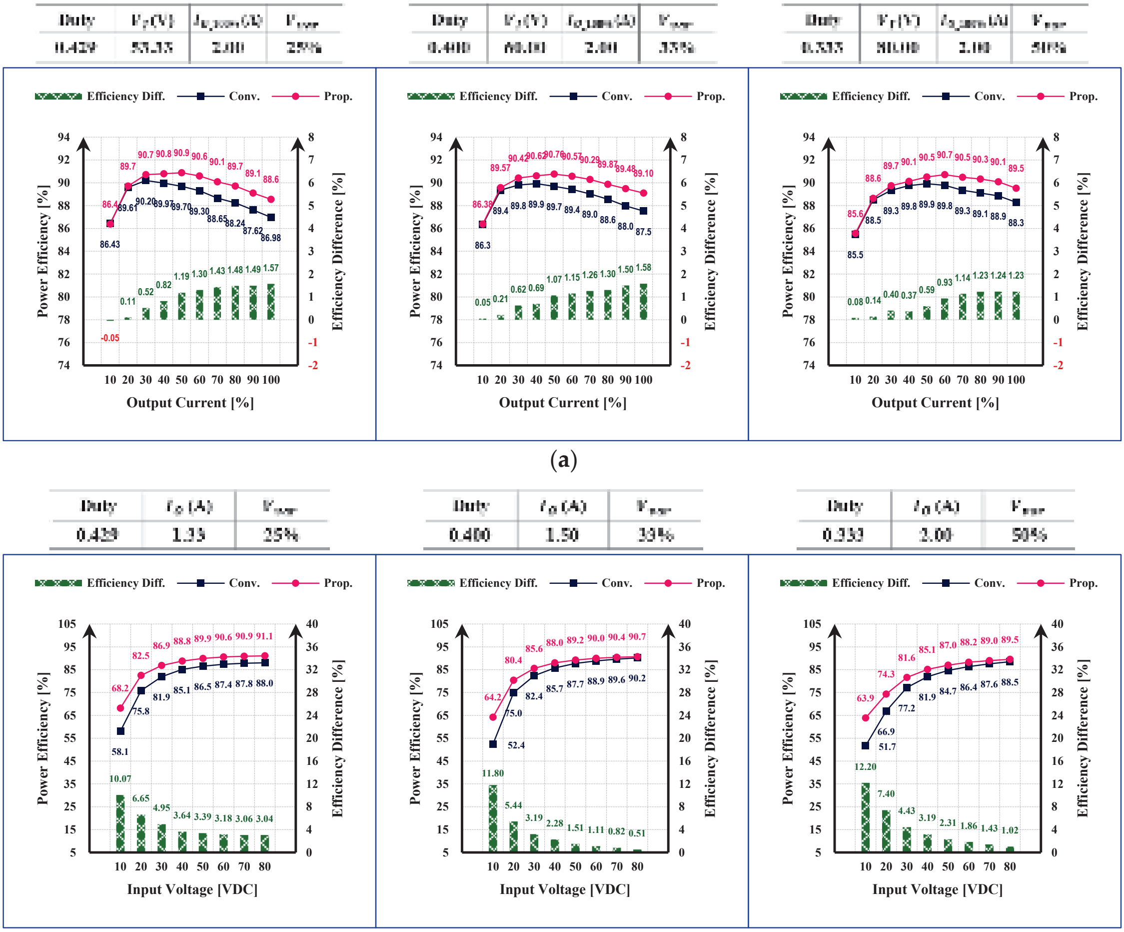

Figure 11. Power efficiency comparison of the buck-boost topology (step-down): (**a**) CV mode; (**b**) CC mode.

5.3.2. Step-Up

Figure 12 shows the power efficiency of the step-up buck-boost topology in the CV and CC modes. In the CV mode, the efficiency improves in general to 10–80 W and P_{Diff} increases in the high-power region where the output current increases. In the CC mode, P_{Diff} decreases with an increase in V_{var} and the input voltage. The power efficiency decreases more than the conventional converter at a power of 50 W or higher. In the step-up section, the output voltage increases with the input voltage, and the voltage stress of diode D_1 also increases. The efficiency decreases more than the conventional converter because the resulting diode loss exceeds the increase in the efficiency obtained by the removal of D_2 in the switch-off section. Therefore, the proposed converter is suitable for applications below 50 W in the step-up section of the buck-boost topology.

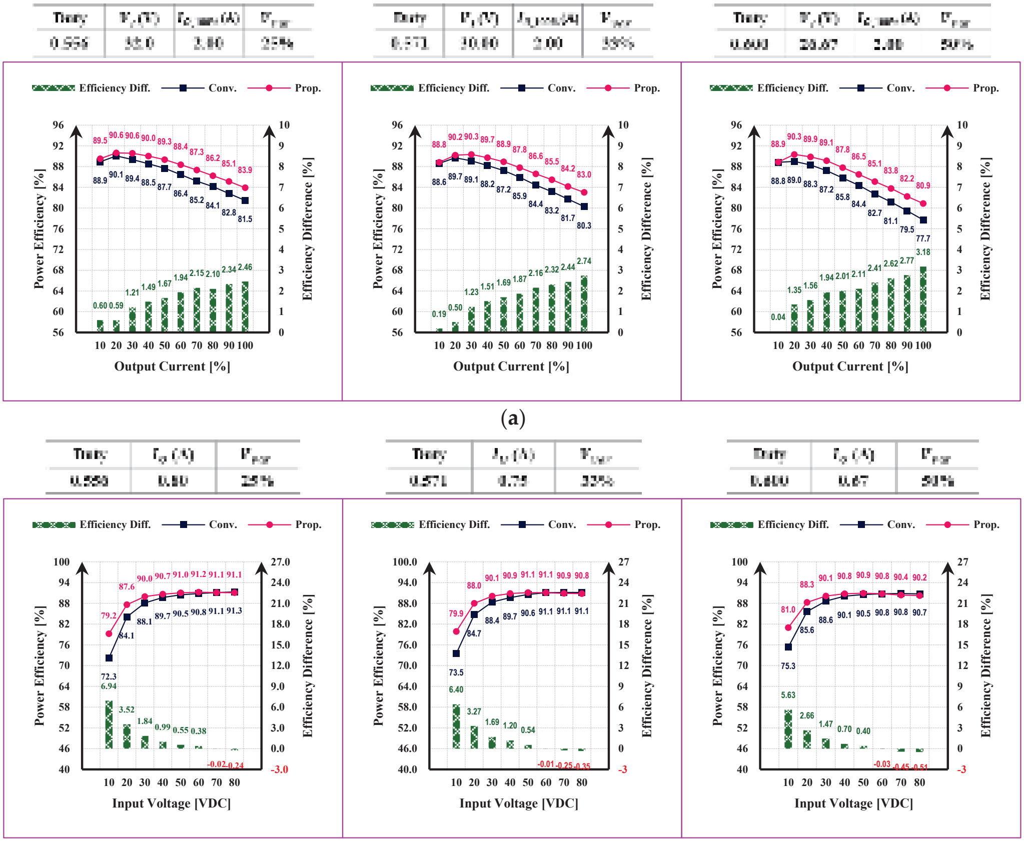

(**a**)

(**b**)

Figure 12. Power efficiency comparison of the buck-boost topology (step-up): (**a**) CV mode; (**b**) CC mode.

5.3.3. Diode Stress (Buck-Boost Step-Up, CC Mode)

Figure 13 shows the analytic and experimental diode power loss in the CC mode in the step-up section of the buck-boost topology. A positive power loss difference L_{Diff} implies that the diode loss of the proposed TSBB converter is large, whereas if it is negative, it implies a large diode loss of the conventional TSBB converter.

To calculate the diode loss, information on several parameters was referenced from the datasheet and all data are typical values at 25 degrees. Parameters not provided in the datasheet were used to calculate the diode loss with some assumptions.

- Forward voltage V_F: obtained from the V_F-I_F characteristic curve.
- Equivalent resistance R_D: obtained from the V_F-I_F characteristic curve by linear approximation under the current conditions used in the experiment.
- Reverse recovery time T_{rr} and peak reverse recovery current I_{rrm}: estimated and calculated using value 16 nsec at the forward current I_F = 1.0 A and the reverse current I_R = 0.5 A.
- Peak reverse recovery voltage V_{rrm}: assumed $\frac{dI_F}{dI_R} = 0.5$ at $V_R\left(1+\frac{dI_F}{dI_R}/\frac{dI_F}{dI_R}\right)$ and corrected coefficient by temperature with V_R characteristic curve.
- Ignored any other parasitic factors like internal inductance, capacitance, and so on.

Due to several assumptions and uncertain parameter values, the two results are slightly different. This is expected to be due to the reverse recovery characteristics that change exponentially with the increase in temperature and voltage stress, and also to be affected by parasitic components on the PCB and errors in measurement equipment.

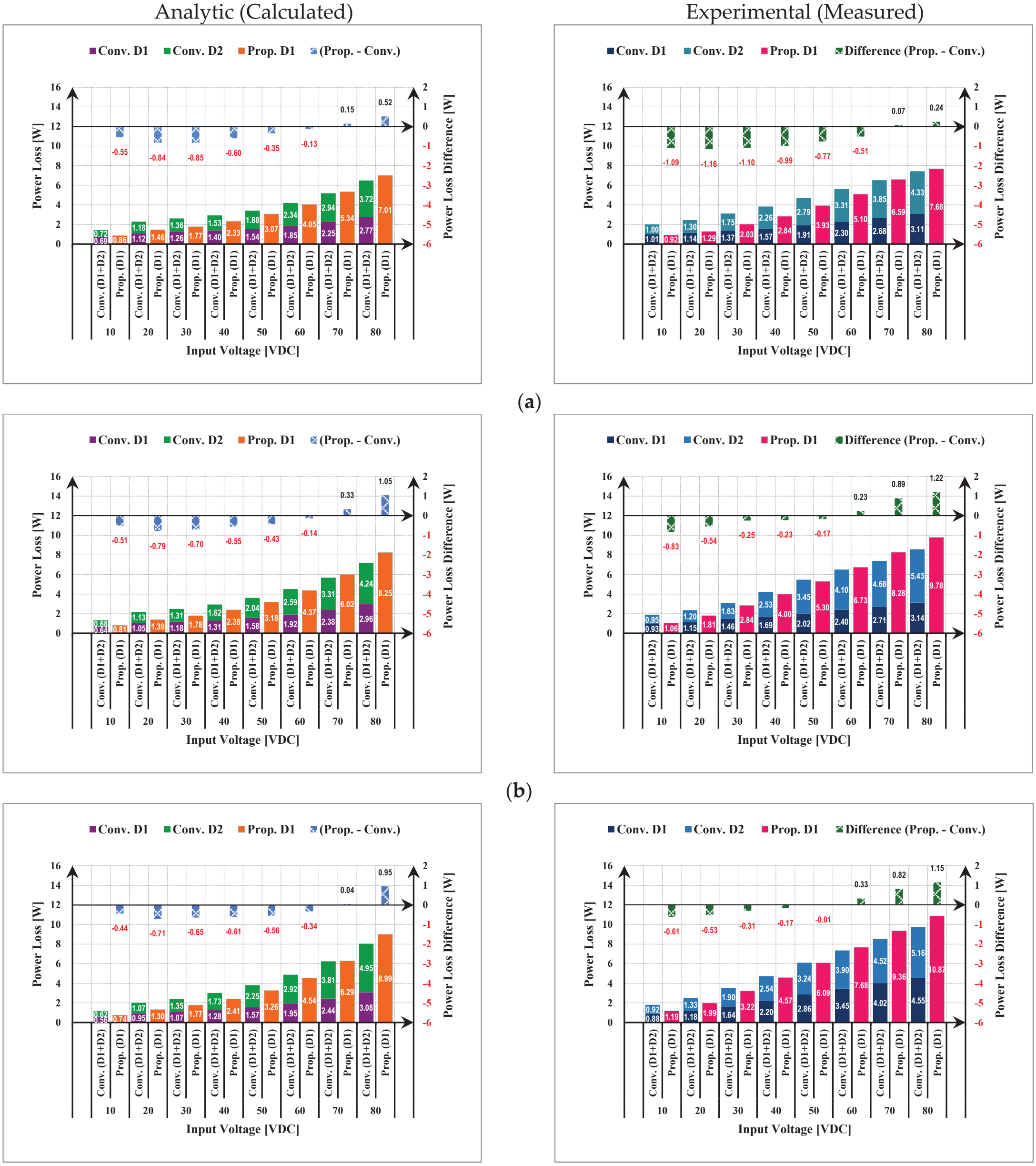

(**a**)

(**b**)

(**c**)

Figure 13. Analytic and experimental diode power loss of the buck-boost topology step-up period in the CC mode: (**a**) Duty = 0.556, I_O = 0.8 A; (**b**) Duty = 0.571, I_O = 0.75 A; and (**c**) Duty = 0.600, I_O = 0.667 A.

Despite these differences, both results show a similar trend in which diode losses rapidly increase with voltage stress over a certain region, thereby diode power loss of the proposed TSBB converter is bigger than the conventional converter over a certain input voltage. The increase in the D_1 loss of the proposed TSBB converter becomes larger than the power efficiency improvement by the removal of D_2. The power efficiency is reversed at the point where the difference in diode loss changes from negative to positive (+). For the proposed TSBB converter, the power efficiency increases at 60 W or lower at the duty ratio of 0.556; the power efficiency increases at 50 W or lower at the duty ratios of 0.571 and 0.600.

6. Conclusions

This study proposed a modified design of the TSBB converter to improve power efficiency using fewer conduction components and measured the optimal output power range. The proposed TSBB converter improved power efficiency in buck and buck-boost topologies by reducing the conduction loss caused by the diode in the switch-off section power efficiency. A 100 W prototype was designed and fabricated to verify the improvement. Experiments were conducted in the CV/CC modes of three topologies, and the power efficiency was measured for 10–80 W. In the buck topology, power efficiency improved in the entire power range of 10–80 W; it increased on average by 0.75–1.36% and 0.83–2.27% in the CV and CC modes, respectively. In the buck-boost topology step-down, the power efficiency improved in the entire power range of 10–80 W; it improved on average by 0.73–0.99% and 3.33–4.75% in the CV and CC modes, respectively. In the buck-boost topology step-up, the power efficiency increased on average by 1.65–2.00% in the entire power range of 10–80 W in the CV mode, and by 2.17–2.77% in the power range of the 10–50 W in the CC mode.

In future research, we will study how to reduce the conduction and switching losses by reducing the voltage and current stress of semiconductors for efficiency improvement. In addition, we will analyze the effect on output ripple under various conditions by using inductance, capacitance, and switching frequency as design variables, and study how these parameters affect converter efficiency.

Author Contributions: Conceptualization, S.K. and H.J.; methodology, S.K. and H.J.; software, S.K. and H.J.; validation, S.K. and H.J.; formal analysis, S.K. and H.J.; investigation, S.K. and H.J.; data curation, S.K. and H.J.; writing—original draft preparation, S.K. and H.J.; writing—review and editing, S.K. and H.J.; supervision, H.J. and S.-h.L.; project administration, H.J. and S.-h.L.; funding acquisition, H.J. All authors have read and agreed to the published version of the manuscript.

Funding: This work is supported by the Korea Agency for Infrastructure Technology Advancement (KAIA) grant funded by the Ministry of Land, Infrastructure and Transport (Grant RS-2021-KA164174).

Informed Consent Statement: Informed consent was obtained from all subjects involved in the study.

Data Availability Statement: Data sharing not applicable.

Conflicts of Interest: The authors declare no conflict of interest.

References

1. Zhou, X.; Sheng, B.; Liu, W.; Chen, Y.; Wang, L.; Liu, Y.F.; Sen, P.C. A high-efficiency high-power-density on-board low-voltage dc–dc converter for electric vehicles application. *IEEE Trans. Power Electron.* **2021**, *36*, 12781–12794. [CrossRef]
2. Jin, F.; Nabih, A.; Chen, C.; Chen, X.; Li, Q.; Lee, F.C. A high efficiency high density dc/dc converter for battery charger applications. In Proceedings of the 2021 IEEE Applied Power Electronics Conference and Exposition (APEC), Phoenix, AZ, USA, 14–17 June 2021.
3. Yang, C.; Xie, S.; Mao, L.; Zhang, Z. Efficiency improvement on two-switch buck-boost converter with coupled inductor for high-voltage applications. *IET Power Electron.* **2014**, *7*, 2846–2856. [CrossRef]
4. Sahu, B.; Rincón-Mora, G.A. A low voltage, dynamic, noninverting, synchronous buck-boost converter for portable applications. *IEEE Trans. Power Electron.* **2004**, *19*, 443–452. [CrossRef]
5. Moon, B.; Jung, H.Y.; Kim, S.H.; Lee, S.H. A modified topology of two-switch buck-boost converter. *IEEE Access* **2017**, *5*, 17772–17780. [CrossRef]

6. Jung, H.Y.; Kim, S.H.; Moon, B.; Lee, S.H. A new circuit design of two-switch buck-boost converter. *IEEE Access* **2018**, *6*, 47415–47423. [CrossRef]
7. Chandran, C.; Chandran, L.R. Two switch buck boost converter for power factor correction. In Proceedings of the 2015 International Conference on Technological Advancements in Power and Energy (TAP Energy), Kollam, India, 24–26 June 2015.
8. Veerachary, M.; Khuntia, M.R. Design and analysis of two-switch-based enhanced gain buck–boost converters. *IEEE Trans. Ind. Electron.* **2021**, *69*, 3577–3587. [CrossRef]
9. Ahmad, A.A.; Abrishamifar, A. A simple current mode controller for two switches buck-boost converter for fuel cells. In Proceedings of the 2007 IEEE Canada Electrical Power Conference, Montreal, QC, Canada, 25–26 October 2007.
10. Son, H.S.; Kim, J.K.; Lee, J.B.; Moon, S.S.; Park, J.H.; Lee, S.H. A new buck–boost converter with low-voltage stress and reduced conducting components. *IEEE Trans. Ind. Electron.* **2017**, *64*, 7030–7038. [CrossRef]
11. Fan, H. Design tips for an efficient non-inverting buck-boost converter. *Analog Appl. J.* **2014**, 20–25.
12. Chen, J.; Maksimovic, D.; Erickson, R.W. Analysis and design of a low-stress buck-boost converter in universal-input PFC applications. *IEEE Trans. Power Electron.* **2006**, *21*, 320–329. [CrossRef]
13. MOSFET Power Losses and How They Affect Power-Supply Efficiency. Available online: https://www.ti.com/lit/an/slyt664/slyt664.pdf (accessed on 5 November 2022).
14. Infineon Application Note. Available online: https://application-notes.digchip.com/070/70-41484.pdf (accessed on 5 November 2022).
15. Xiong, Y.; Sun, S.; Jia, H.; Shea, P.; Shen, Z.J. New physical insights on power MOSFET switching losses. *IEEE Trans. Power Electron.* **2009**, *24*, 525–531. [CrossRef]
16. Lirio, L.E.A.; Bellar, M.D.; Neto, J.A.M.; Dos Reis, M.S.; Aredes, M. Switching losses analysis in sic power mosfet. In Proceedings of the 2015 IEEE 13th Brazilian Power Electronics Conference and 1st Southern Power Electronics Conference (COBEP/SPEC), Fortaleza, Brazil, 29 February 2016.
17. Ren, Y.; Xu, M.; Zhou, J.; Lee, F.C. Analytical loss model of power MOSFET. *IEEE Trans. Power Electron.* **2006**, *21*, 310–319.
18. Power MOSFET Basics: Understanding MOSFET Characteristics Associated with the Figure of Merit. Available online: https://www.vishay.com/docs/71933/71933.pdf (accessed on 5 November 2022).
19. Shen, Z.J.; Xiong, Y.; Cheng, X.; Fu, Y.; Kumar, P. Power MOSFET switching loss analysis: A new insight. In Proceedings of the 2006 IEEE Industry Applications Conference and Forty-First IAS Annual Meeting, Tampa, FL, USA, 8–12 October 2006.
20. Rodríguez, M.; Rodríguez, A.; Miaja, P.F.; Lamar, D.G.; Zúniga, J.S. An insight into the switching process of power MOSFETs: An improved analytical losses model. *IEEE Trans. Power Electron.* **2010**, *25*, 1626–1640. [CrossRef]
21. Li, X.; Jiang, J.; Huang, A.Q.; Guo, S.; Deng, X.; Zhang, B.; She, X. A SiC power MOSFET loss model suitable for high-frequency applications. *IEEE Trans. Ind. Electron.* **2017**, *64*, 8268–8276. [CrossRef]
22. Ivanovic, Z.; Blanusa, B.; Knezic, M. Power loss model for efficiency improvement of boost converter. In Proceedings of the 2011 XXIII International Symposium on Information, Communication and Automation Technologies, Sarajevo, Bosnia and Herzegovina, 27–29 October 2011.

applied sciences

MDPI

Article

Adaptive Fractional-Order Anti-Saturation Synchronous Control for Dual-Motor Systems

Yongbin Zhong, Jian Gao * and Lanyu Zhang

State Key Laboratory of Precision Electronic Manufacturing Technology and Equipment,
Guangdong University of Technology, Guangzhou 510006, China
* Correspondence: gaojian@gdut.edu.cn; Tel.: +86-1356-0125-827

Featured Application: High-speed synchronous motion system for precision electronic packaging equipment.

Abstract: The synchronization error of a dual-motor system will seriously affect the motion profile accuracy. To solve this problem, an adaptive fractional-order anti-saturation synchronous control method based on fractional-order frequency-domain control theory is proposed in this paper. On the one hand, the proposed method performs a compensation on the closed-loop feedback control loop to unify the frequency-domain characteristics for a dual-motor system. With the frequency-domain characteristics' unification module, the dual-motor system will have the same response performance regarding the input signal. On the other hand, considering that the nonlinear problem of control voltage saturation will also cause the asynchronization problem of the dual-motor system, the proposed method involves an adaptive fractional-order anti-saturation module to prevent voltage saturation and eliminate the nonlinear effects. The experimental results verify that the proposed method can accurately avoid the saturation effect and effectively reduce the synchronization error of the dual-motor system, with a root-mean-square synchronization error reduction of 80.974%. Hence, the proposed method provides an effective solution for the high-precision synchronous motion of a dual-motor system.

Keywords: dual-motor system; synchronous motion; fractional-order frequency-domain control theory; saturation effect

Citation: Zhong, Y.; Gao, J.; Zhang, L. Adaptive Fractional-Order Anti-Saturation Synchronous Control for Dual-Motor Systems. *Appl. Sci.* **2023**, *13*, 2307. https://doi.org/10.3390/app13042307

Academic Editors: Kan Liu and Wei Hu

Received: 4 January 2023
Revised: 6 February 2023
Accepted: 8 February 2023
Published: 10 February 2023

1. Introduction

With the development of power electronics technology and high-performance permanent magnet materials, the permanent magnet linear synchronous motor (PMLSM) has gained significant attention. Because its structure has no mechanical friction problem, a large thrust force, and small volume, the PMLSM is widely used in transportation systems, machine tools, precision positioning platforms, and other fields [1,2]. In addition, the market demand for chip semiconductors has increased in recent years, leading to the rapid development of the semiconductor manufacturing industry; therefore, the high-speed and high-acceleration motion platform built by the PMLSM has gradually become an essential part of the equipment [3]. However, the performance requirements are becoming increasingly stringent, and the single-motor driving method can no longer meet the high-acceleration requirement. To overcome the thrust force limit of the PMLSM and further improve the efficiency of semiconductor manufacturing equipment, a dual-motor driving method has been designed and widely used [4,5]. A redundant direct-drive gantry platform is a common application of the dual-motor driving method. The Y-degree-of-motion freedom is driven by two PMLSMs simultaneously, and the rigid connection between the PMLSMs ensures that the thrust force can act on the beam together, realizing high speed, high acceleration, and a large stroke motion [6].

A dual-actuator system can usually achieve a higher acceleration motion, but it also introduces the asynchronous motion problem, which will cause tension in the connection structure and decrease the service life or even seriously damage the mechanical structure [7]. Scholars have proposed a variety of control methods for the synchronous motion of a dual-motor system, including the series synchronous control method [8], parallel synchro-nous control method [9], and cross-coupling synchronous control method [10]. Because the cross-coupling synchronous control method can adjust the control voltage of each motor in real time according to the synchronization error, it has certain advantages in ensuring the synchronous motion of the dual-motor system [11,12]. The control structure of the cross-coupling synchronous control method is simple; therefore, the accuracy of the control parameter selection is the key factor that determines the synchronous motion performance of the dual-motor system. Some scholars improved the synchronous control method by considering cross-coupling, such as the variable-gain cross-coupling synchronous control method [13], fuzzy neural network cross-coupling synchronous control method [14], and self-tuning cross-coupling synchro-nous control method [15]. These methods can improve the real-time adjustment ability of the parameters of the cross-coupling controller, thereby ensuring the adaptability of the control parameters under different synchronization errors. However, accurately establishing the parameter adjustment law of the cross-coupling synchronous control method requires long-term pre-learning, and the control parameter adjustment algorithm has a high degree of complexity, making it difficult for practical applications. Considering that the characteristics of the PMLSM system can be obtained through system identification, several methods were studied, for example, a model-based feed-back-feedforward decoupling control method [16], model-based adaptive synchronous control method [17], robust immersion and invariance adaptive coordinated control method [18], adaptive thrust-allocation based synchronous control method [19], and other related methods [20–22]. The introduction of model information can reduce the design complexity of the parameter adjustment method and provide a basis for control parameter selection, thus effectively suppressing the dual-motor system's synchronization error. However, these synchronous control methods adjust the control voltage of the PMLSM through position compensation or force compensation when synchronization error is observed. Since there is a time delay, the methods will have difficulty eliminating the synchronization error completely.

Through investigation, we found that the synchronization error is caused by the characteristic difference in the dynamic response of the dual-motor system, and, because the fractional-order deferential operator can accurately describe the control frequency-domain characteristics required by the controlled object, there are several control methods based on fractional-order control theory [23–25]. In literature [26], the authors developed a feedforward control method for PMLSM based on the fractional-order control theory. Through the accurate description of the system's control frequency-domain characteristics, the fractional-order feedforward control method improved the PMLSM tracking accuracy effectively for a single-motor system. However, for a dual-motor system, besides the tracking accuracy of each motor, the synchronization accuracy of the two motors is the key issue and needs to be further studied. Therefore, considering the advantage of the fractional-order control theory, this paper proposes an adaptive fractional-order anti-saturation synchronous control method to improve the synchronization accuracy of the dual-motor system. Through compensation, we unified the frequency-domain characteristics of the motors in a dual-motor system to ensure they have the same dynamic response characteristics. With the design of the frequency-domain characteristics' unification module (FDC-UM), the dynamic response characteristics of the two motors were adjusted to be consistent. Then, the adaptive fractional-order anti-saturation module (AFOAM) was designed to avoid the saturation effect of the control voltage. By calculating the theoretical peak voltage, the parameters of the AFOAM were determined by the relationship between the parameter selection and the FDC adjustment of the fractional-order lead-lag controller (FOLLC). Through the AFOAM, the dual-motor system can prevent the control voltage from reaching the voltage limitation and thus guarantee the suppression of the FDC-UM for the synchronization error. Therefore, the proposed adaptive fractional-order anti-saturation synchronous method can actively suppress the generation of the synchronization error and avoid the saturation effect, ensuring a dual-motor system with high-precision synchronous motion performance.

The remainder of this paper is organized as follows. Section 2 introduces the kinetic model of the dual-motor system and the proposed adaptive fractional-order anti-saturation synchronous control method in detail. In Section 3, based on the established relationship between the FDC and the dynamic response characteristics of the motor systems, the FDC-UM and the AFOAM are designed and finalized with the required parameters. In Section 4, the experimental setup is described, and experimental work is performed to verify the effectiveness and superiority of the proposed method. Section 5 presents the discussion, and Section 6 presents the conclusions.

2. The Proposed Synchronous Control Method for the Dual-Motor System

2.1. Kinetic Model of the Dual-Motor System

A schematic of the redundant direct-drive gantry platform is shown in Figure 1. A cross beam was installed on two linear guides arranged in parallel and jointly driven by two PMLSMs. Motors Y_1 and Y_2 were rigidly connected to the beam, and the stators were installed on the base where the two linear guides were located. For the sake of simplicity, this study only focused on the synchronous control of the *Y*-axis, and it is assumed that the motor X is rigidly connected to the cross-beam. Therefore, from Figure 1 and the dynamic analysis in literature [27], the kinetic model of the dual-motor system can be obtained as follows:

$$\begin{cases} M_1\ddot{y}_1 + c_1\dot{y}_1 + k_1\xi_1 = F_{m1} - F_{r1} - F_{c1} \\ M_2\ddot{y}_2 + c_2\dot{y}_2 + k_2\xi_2 = F_{m2} - F_{r2} + F_{c2} \end{cases}, \tag{1}$$

where $F_{ci} = f\ (y_1, y_2)$ is the coupling force, which is related to the displacements of motors Y_1 and Y_2, and i = 1, 2. F_{mi} is the thrust force, F_{ri} is the friction, M_i is the mass, c_i is the viscosity coefficient, k_i is the elasticity coefficient, y_i is the displacement of the motor, and ξ_i is the deformation between the mover and slider. The control method typically adopted by a dual-motor system is also shown in Figure 1. Each motor has an independent feedback controller (FBC); by designing the reasonable friction compensator (FC) and the synchronous control method, the synchronous motion performance of the dual-motor system is guaranteed.

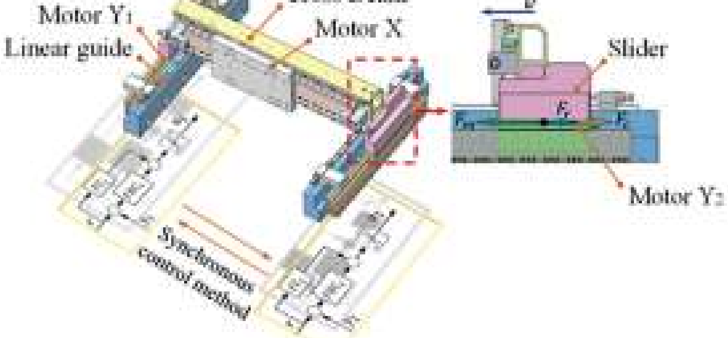

Figure 1. Schematic of the structure and control strategy of redundant direct-drive gantry platform.

The relationship between the motor thrust force and control system characteristics can be obtained as follows:

$$\begin{cases} F_{m1} = K_{u1}u_1 = K_{u1}sat\{u_{FC1} + u_{FBC1}\} \\ F_{m2} = K_{u2}u_2 = K_{u2}sat\{u_{FC2} + u_{FBC2}\} \end{cases}, \tag{2}$$

where K_{ui} is the thrust force constant of the motor, *sat* {} is the saturation function, and u_{FCi} and u_{FBCi} are the control voltages of FC and FBC, respectively. Because the coupling force is related to the displacements of motors Y_1 and Y_2, it appears with the generation of the synchronization error. When the synchronization error is eliminated, the influence of the coupling force on the motor movement will also be negligible, so the kinetic model can be re-expressed as follows:

$$\begin{cases} M_1\ddot{y}_1 + c_1\dot{y}_1 + k_1\xi_1 = F_{m1} \\ M_2\ddot{y}_2 + c_2\dot{y}_2 + k_2\xi_2 = F_{m2} \end{cases}. \tag{3}$$

We can establish the following transfer function of each motor system according to Equation (3):

$$g_{yi}(s) = \frac{b_{0i}s^{m_i} + b_{1i}s^{(m-1)_i} + \cdots + b_{mi}}{s^{n_i} + a_{1i}s^{(n-1)_i} + \cdots + a_{ni}}, \tag{4}$$

where a_{ni} and b_{mi} are the parameters of the denominator and numerator polynomials, respectively, and n_i and m_i are the orders of the denominator and numerator polynomials, respectively. By designing a proper feedback controller $c_i(s)$, the transfer function between the input signal r and output signal y_i is as follows:

$$G_i(s) = \frac{y_i(s)}{r(s)} = \frac{c_i(s)g_{yi}(s)}{1 + c_i(s)g_{yi}(s)}. \tag{5}$$

From Equation (5), we can calculate the amplitude and phase characteristics of each closed-loop feedback control loop in the dual-motor system, and these characteristics determine the dynamic response characteristics of the motor system. Therefore, we can know when the dual-motor system is in a synchronous-state, and the motion of the motor system is mainly affected by its electric characteristic, structure, and control system, leading to the differences in the dynamic response characteristics between the motor systems.

2.2. Description of the Proposed Method

To make the dual-motor system have consistent dynamic response characteristics and realize the two motors' synchronous motion, we proposed a frequency-domain characteristic compensation-based adaptive fractional-order anti-saturation synchronous control method, which contains two modules: the FDC unification module (FDC-UM), which can adjust the dynamic response characteristics of the two motors to be consistent, and the adaptive fractional-order anti-saturation module (AFOAM), which can avoid the saturation effect of the control voltage adaptively. Figure 2 illustrates the working principle of the proposed synchronous control method. The FDC-UM performs the FDC unification through compensation in the feedback control loops. With the FDC-UM, the FDC of the dual-motor system can be unified. We have

$$\begin{cases} A_1 = A_2 = A_f \\ \varphi_1 = \varphi_2 = \varphi_f \end{cases}, \tag{6}$$

where A_1, A_2 are the amplitude characteristics of the Equation (5), and φ_1, φ_2 are the phase characteristics. A_f, φ_f are the amplitude and phase characteristics unified by the FDC-UM. In addition to the FDC-UM, the AFOAM is designed to prevent the peak voltage of the motion from reaching the voltage limitation. With these modules, the amplitude and phase characteristics are determined to be A_a and φ_a according to the input signal spectrum and theoretical calculation of the peak voltage. With the FDC unification and the elimination of the nonlinear saturation effect, the dual-motor system will possess consistent dynamic response characteristics for the two motors and thus ensure their synchronous motion.

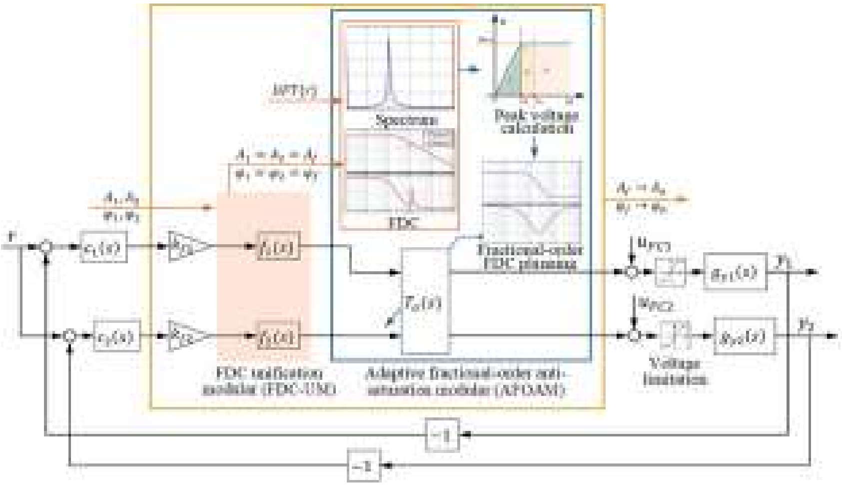

Figure 2. The transfer block diagram of the proposed adaptive fractional-order anti-saturation synchronous control method.

3. Adaptive Fractional-Order Anti-Saturation Synchronous Control Method

3.1. FDC Unification Module (FDC-UM)

According to the frequency-domain control theory, the dynamic response characteristics of the LTI system are determined by the FDC of the control system. In literature [28], the relationship between the input and output signals of the control system was analyzed in detail, and the output signal corresponding to the input signal $r = \sin(\omega_r t)$ was obtained as follows:

$$y = K\sin(\omega_r(t - \Delta t)). \tag{7}$$

The signals have the same frequency ($f = \omega_r/2\pi$), but there is a certain time delay Δt_i and an amplitude ratio K_i between them. Therefore, the synchronization error expression of the dual-motor system can be defined as follows:

$$e_{syn} = K_1\sin(\omega_r(t - \Delta t_1)) - K_2\sin(\omega_r(t - \Delta t_2)), \tag{8}$$

$$\Delta t_i = \varphi_i/\omega_r, \tag{9}$$

$$K_i = 10^{A_i/20}, \tag{10}$$

where $\varphi_i(\omega) = \arctan(\mathrm{Im}\,[G_i(\omega)]/\mathrm{Re}\,[G_i(\omega)])$ and $A_i(\omega) = 20\log_{10}|G_i(\omega)|$ are the phase and amplitude characteristics of the transfer function shown in Equation (5), respectively. According to Equations (8)–(10), to achieve high-synchronous motion performance of the dual-motor system, both feedback control systems must have consistent FDC. That is, the dual-motor system must satisfy the following condition:

$$C(s)F(s)G_Y(s)K_F = 0, \tag{11}$$

where $C(s) = [c_1(s), c_2(s)]$, $G_Y(s) = \mathrm{diag}(g_{y1}(s), g_{y2}(s))$. $F(s) = \mathrm{diag}(f_1(s), f_2(s))$, in which $f_i(s)$ is the transfer function of the FDC-UM. $K_F = [k_{f1}, -k_{f2}]^T$ is the gain matrix used to adjust the control performance of the system. According to Equations (5) and (11), we can derive the following when $\varphi_1 \geq \varphi_2$ in the main frequency domain.

$$\begin{cases} f_1(s) = \left(k_{f1}c_1(s)g_{y1}(s)\right)^{-1}k_{f2}c_2(s)g_{y2}(s) \\ f_2(s) = 1 \end{cases}, \tag{12}$$

When $\varphi_1 < \varphi_2$ in the main frequency domain,

$$\begin{cases} f_1(s) = 1 \\ f_2(s) = \left(k_{f2}c_2(s)g_{y2}(s)\right)^{-1}k_{f1}c_1(s)g_{y1}(s) \end{cases}. \tag{13}$$

After the compensation, the transfer function of the feedback control system is as follows:

$$G_{fi}(s) = \frac{y_i(s)}{r(s)} = \frac{k_{fi}f_i(s)c_i(s)g_{yi}(s)}{1 + k_{fi}f_i(s)c_i(s)g_{yi}(s)}. \tag{14}$$

Based on the analysis performed above, we know that the dynamic response characteristics of the control system are related to the frequency of the control signal. Through compensation, the dual-motor system meets the requirements of $A_{f1}(\omega) = A_{f2}(\omega)$ and $\varphi_{f1}(\omega) = \varphi_{f2}(\omega)$, so the two motor systems possess a unified dynamic response characteristic and thus can achieve a synchronous motion. To verify the effectiveness of the FDC-UM, we used the chirp signal for the experiments. Figure 3 shows the working principle of the FDC-UM and the synchronization error comparison by the control methods of the PID feedback control method (Method 1 in Figure 3a), the force compensation cross-coupling synchronous control method (Method 2 in Figure 3b), and the FDC-UM based synchronous control method (Method 3 in Figure 3c). Figure 3d shows that both Method 2 and Method 3 can ensure excellent synchronous-motion performance of the dual-motor system, and the FDC-UM-based synchronous control method achieves the best performance, which can avoid the effects of control signal variation in frequency.

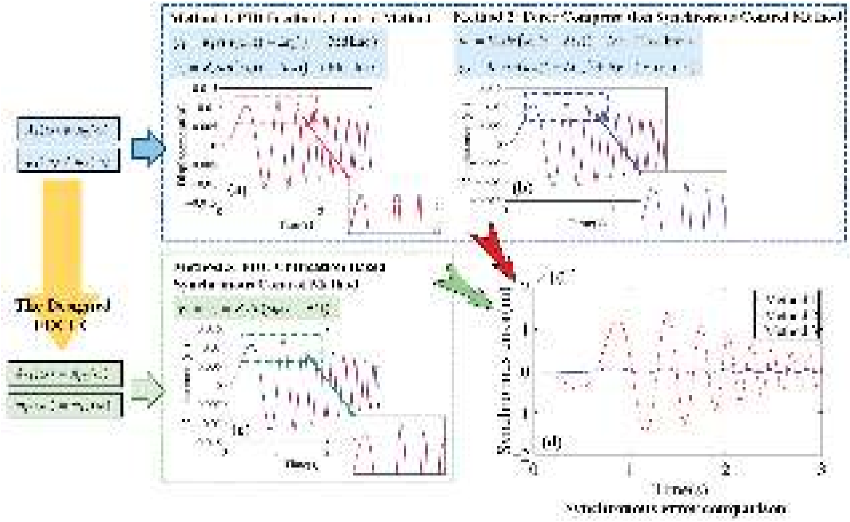

Figure 3. Working principle of the FDC-UM and comparison of synchronization errors with three different control methods: PID feedback method, force compensation method, and the proposed FDC-UM method.

Since the proposed FDC-UM is used for the LTI system, when the control voltage overpasses the voltage limitation, the control voltage will induce a nonlinear behavior and affect the dynamic response characteristics of the dual-motor system, as shown in Equation (15). When the total control voltage of the feedback control system u_{FBC} and the friction compensator u_{FC} are beyond the voltage limitation, the control voltage u is limited to the highest (lowest) voltage u_{max} ($-u_{max}$).

$$u = \begin{cases} -u_{\max},\ for\ (u_{FBC} + u_{FC}) \leq -u_{\max}, \\ u_{FBC} + u_{FC}, \\ u_{\max},\ for\ (u_{FBC} + u_{FC}) \geq u_{\max}. \end{cases}, \tag{15}$$

Figure 4 shows the influence of the saturation effect on the synchronization error of the dual-motor system. In Figure 4a, the synchronization errors of the dual-motor system are compared with the PID feedback control method and the FDC-UM-based synchronous control method. Figure 4b shows the control voltage of the motor system in the range of $[-u_{max}, u_{max}]$. We can see that the saturation effect influences the synchronization errors of the two control methods and deteriorates the performance of the FDC-UM. Therefore, to ensure the synchronous motion performance of the dual-motor system, the saturation effect needs to be eliminated.

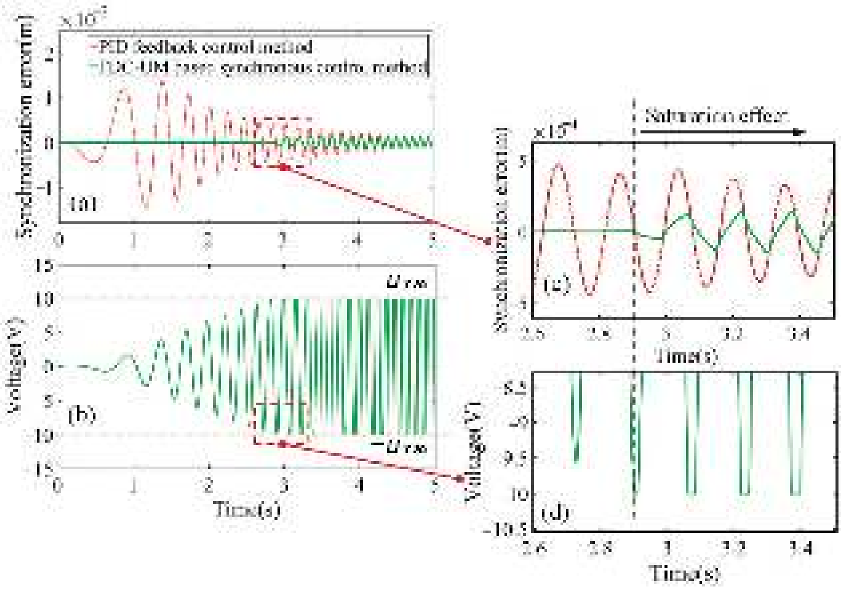

Figure 4. The saturation effect of the control voltage on the synchronization error of the dual-motor system: (**a**) under different control methods; (**b**) control voltage of the motor system in the range of $[-u_{max}, u_{max}]$; (**c**) partial enlarged view of (**a**); (**d**) partial enlarged view of (**b**).

3.2. Adaptive Fractional-Order Anti-Saturation Module (AFOAM)

3.2.1. Peak Voltage Calculation and Amplitude Characteristic Adjustment Value Determination

To avoid the nonlinear problem caused by the saturation effect, it is necessary to recognize the determinants of the control voltage in the feedback control loop and calculate the required suppression value of the control voltage. According to the dynamic response characteristics of the control system and Equations (4) and (14), the transfer function from the input signal r to the feedback control voltage u_{FBCi} is as follows:

$$G_{ui}(s) = \frac{u_{FBCi}(s)}{r(s)} = \frac{k_{fi}f_i(s)c_i(s)}{1 + k_{fi}f_i(s)c_i(s)g_{yi}(s)}. \tag{16}$$

In the frequency domain, $s = j\omega$, so the amplitude characteristic $A_{ui}(\omega)$ of Equation (16) is $20\log_{10}(|G_{ui}(\omega)|)$. Because the input signal amplitude in the frequency domain can be obtained by spectrum analysis, the calculation expression of the theoretical peak voltage of the control system can be expressed as

$$u_i^{\max} = |s_p(\omega_k)|10^{A_{ui}(\omega_k)/20} + u_{FCi}, \tag{17}$$

where $|s_p(\omega_k)|$ is the amplitude spectrum of the input signal when $\omega = \omega_k$, and u_{FCi} is the friction compensation voltage. Therefore, the amount by which the theoretical peak voltage exceeds the voltage limitation can be calculated as follows:

$$\widetilde{u}_i = \mathrm{sgn}_i(u)|u_i^{\max} - u_{\max}|, \tag{18}$$

in which the symbolic function for determining whether the theoretical peak voltage exceeds the voltage limitation is defined as follows:

$$\mathrm{sgn}_i(u) = \begin{cases} 1, \ for\ u_i^{\max} > u_{\max}, \\ 0, \ for\ u_i^{\max} \le u_{\max}. \end{cases} . \tag{19}$$

According to Equation (17), we know that the control voltage can be changed by adjusting the spectrum of the input signal or the amplitude characteristic of the control system. Since the main work of this paper is the design of the synchronous control system, the adjustment of the input signal will directly affect the trajectory of the dual-motor system. Therefore, in order to avoid the saturation effect, the amplitude characteristic $A_{ui}(\omega)$ at ω_k must be adjusted to be the value as shown in Equation (20).

$$\overline{A}_{ui}(\omega_k) = 20\log_{10}\left|10^{A_{ui}(\omega_k)/20} - \widetilde{u}_i/|s_p(\omega_k)|\right|. \tag{20}$$

The amplitude characteristic adjustment value of each motor system is

$$\Delta A_i = \overline{A}_{ui}(\omega_k) - A_{ui}(\omega_k). \tag{21}$$

To ensure that the adjustment of the amplitude characteristic does not affect the unification of the dynamic response characteristics of the dual-motor system, it is necessary to unify the adjustment value to a smaller value ΔA, so that the anti-saturation module can satisfy the adjustment requirements of both feedback control loops simultaneously. The amplitude characteristic adjustment value can be determined as follows:

$$\Delta A = -MAX\{|\Delta A_1|, |\Delta A_2|\}. \tag{22}$$

3.2.2. AFOAM Design and Implementation

A. AFOAM design

Combined with the above theoretical peak voltage calculation, we can obtain the saturation situation of the control voltage by analyzing the input signal when the frequency domain characteristics of the dual-motor system are determined. On this basis, we developed an AFOAM based on fractional-order frequency-domain control theory to realize the specific amplitude characteristic adjustment in which the saturation status of the control voltage is determined by analyzing the input signal when the frequency-domain characteristics of the dual-motor system are determined. The implementation block diagram of AFOAM is shown in Figure 5. When the input signal is determined, the controller calculates the peak voltage according to Equation (17) to adjust the control system to avoid the saturation effect, i.e., not adjust the control parameters in real time during motion.

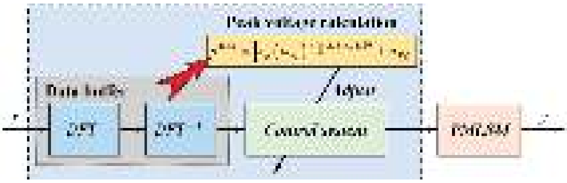

Figure 5. Implementation block diagram of AFOAM.

As shown in Equation (20), we only need to adjust the amplitude characteristic at ω_k. Since the adjustment at a specific frequency will affect the amplitude and phase characteristics of the surrounding frequency and will further influence the dynamic response performance of the feedback control system, we propose the AFOAM in this paper to adjust the specific FDC accurately and flexibly by introducing the fractional-order lead-lag controller (FOLLC) as the fractional-order FDC planning target. The expression for the FOLLC is described as follows:

$$C_f(s) = K_C\left(\frac{1+\lambda x s^{\alpha}}{1+\lambda s^{\alpha}}\right), \tag{23}$$

where K_C, λ, and x are coefficients. The order α can be any real number in the range (0, 2), which enables the FOLLC to accurately describe the specified FDC at the specified frequency through accurate parameter selection. The transfer function from the input signal r to the feedback control voltage u_{FBCi} with the AFOAM is as follows:

$$\overline{G}_{ui}(s) = \frac{k_{fi} f_i(s) c_i(s) T_a(s)}{1 + k_{fi} f_i(s) c_i(s) g_{yi}(s) T_a(s)}, \tag{24}$$

where $T_a(s)$ represents the transfer function of the AFOAM. With the AFOAM, the voltage amplitude characteristic of the feedback control system is changed as

$$\overline{A}_{ui}(\omega) = A_{ui}(\omega) + A_f(\omega), \tag{25}$$

where $A_f(\omega)$ is the amplitude characteristic of the FOLLC. According to the transfer block diagram of the proposed adaptive fractional-order anti-saturation synchronous control method, the transfer function of AFOAM can be expressed as follows:

$$T_a(s) = \frac{K_C(1+\lambda x s^{\alpha})}{(1+\lambda s^{\alpha} - K_C(1+\lambda x s^{\alpha}))k_{fi} f_i(s) c_i(s) g_{yi}(s) + \lambda s^{\alpha} + 1}. \tag{26}$$

B. Parameter determination

It can be seen from Equation (26) that the parameters of the AFOAM can be determined by selecting the parameters of the FOLLC. Therefore, we first need to establish the relationship between the parameters of the FOLLC and the FDC adjustment. Equation (23) can be rewritten as

$$C_f(j\omega) = K_C\left(\frac{1+x\lambda(j\omega)^{\alpha}}{1+\lambda(j\omega)^{\alpha}}\right). \tag{27}$$

The amplitude and phase characteristics of the FOLLC can be calculated as follows:

$$A_f(\omega) = 20\log_{10}\left(K_C\sqrt{\frac{1+x^2\lambda^2\omega^{2\alpha}+2x\lambda\omega^{\alpha}\cos(\alpha\pi/2)}{1+\lambda^2\omega^{2\alpha}+2\lambda\omega^{\alpha}\cos(\alpha\pi/2)}}\right), \tag{28}$$

$$\varphi_f(\omega) = \tan^{-1}\left[\frac{(x-1)\lambda\omega^{\alpha}\sin(\alpha\pi/2)}{1+(x+1)x\lambda^2\omega^{2\alpha}\cos(\alpha\pi/2)}\right], \tag{29}$$

Let

$$g(\omega) = K_C\sqrt{\frac{1+x^2\lambda^2\omega^{2\alpha}+2x\lambda\omega^{\alpha}\cos(\alpha\pi/2)}{1+\lambda^2\omega^{2\alpha}+2\lambda\omega^{\alpha}\cos(\alpha\pi/2)}}. \tag{30}$$

The logarithmic function is monotonic, and thus, $g(\omega)$ represents the trend of A_f (ω). Because the FOLLC has equal-order properties, that is, the orders of the differential operator in the numerator and denominator polynomials are the same, we can deduce that the FOLLC has the following properties: (1) $A_f\,(\omega)\,|_{\,\omega\to 0}$ = 20log$_{10}(K_C)$ and $A_f\,(\omega)\,|_{\,\omega\to+\infty}$ = 20log10($K_C x$); (2) $\varphi_f\,(\omega)\,|_{\,\omega\to 0}$ = $\varphi_f\,(\omega)\,|_{\,\omega\to+\infty}$ = 0; (3) when $\omega = \omega_m$, the FOLLC reaches its extreme phase characteristic value. By deriving Equation (29), we obtain

$$\omega_m = \left(\lambda\sqrt{x}\right)^{-1/\alpha}, \tag{31}$$

The parameter λ can be obtained by Equation (32).

$$\lambda = \left(\sqrt{x}\omega_m^{\alpha}\right)^{-1}, \tag{32}$$

Because the middle- and low-frequency domains are the main control-frequency domains of the motor system, the FDC adjustment should avoid excessive influence on the amplitude and phase characteristics in these areas. However, owing to the continuity of the FDC adjustment, this influence cannot be completely avoided. To minimize the influence of the FDC adjustment caused by the AFOAM on the outer area of the specified angular frequency, especially the middle- and low-frequency domains, we need to let K_C = 1. According to the above analysis, to minimize the influence range of the FDC adjustment, we determine $A_f\,(\omega)\,|_{\,\omega\to+\infty}$ = ΔA and $|\,A_f\,(\omega_k)$ + $\Delta A\,|\ \leq \varepsilon_1$. Because the logarithmic function is a monotonic function, $A_f\,(\omega_k)$ satisfies $\left|\dot{g}(\omega_k)\right| \leq \varepsilon_2$ simultaneously, where ε_1 and ε_2 represent the minimum values. Thus, parameter x can be calculated by Equation (33).

$$x = 10^{\Delta A/20}, \tag{33}$$

To simplify the calculation, we let $A_f\,(\omega_k) \approx \Delta A$ and substitute it into Equation (28), and then we can obtain the relationship between ω_j and α by the following expression:

$$\omega_j = \omega_k\left(-2\sqrt{x}\cos(\alpha\pi/2)/(x+1)\right)^{2/\alpha}, \tag{34}$$

where ω_j satisfies the condition ω_m = $(\omega_k\omega_j)^{1/2}$, and (ω_k–ω_j) is the range of the FDC adjustment. Since the variables x, ω_k, and ω_j are not less than zero, the order α should be in the range of [1, 2). We can see that when the order α = 1, ω_j = 0, which means that the FDC adjustment of the AFOAM will influence the amplitude and phase characteristics at all frequencies. Under this condition, because ω_m = $(\omega_k\omega_j)^{1/2}$, ω_m will be zero by calculation, so the parameters of the AFOAM cannot be determined uniquely and adaptively. Therefore, to reduce the influence of the FDC adjustment, the order must be in the range of (1, 2).

Through the derivation of Equation (30), we obtain

$$\dot{g}(\omega_k) = \frac{\left(1+\frac{\omega_k^{\alpha}}{\omega_j^{\alpha}}+2\frac{\omega_k^{\alpha/2}}{\sqrt{x}\omega_j^{\alpha/2}}\cos(\alpha\pi/2)\right)^{1/2}\left((x-1)\alpha\frac{\omega_k^{(\alpha/2-1)}}{\sqrt{x}\omega_j^{\alpha/2}}\cos(\alpha\pi/2)+\frac{\omega_k^{\alpha/2}}{\sqrt{x}\omega_j^{\alpha/2}}+\sqrt{x}\frac{\omega_k^{\alpha/2}}{\omega_j^{\alpha/2}}+\frac{\omega_k^{\alpha}}{\omega_j^{\alpha}}\cos(\alpha\pi/2)\right)}{\left(1+x\frac{\omega_k^{\alpha}}{\omega_j^{\alpha}}+2\sqrt{x}\frac{\omega_k^{\alpha/2}}{\omega_j^{\alpha/2}}\cos(\alpha\pi/2)\right)^{1/2}\left(1+\frac{\omega_k^{\alpha}}{x\omega_j^{\alpha}}+2\frac{\omega_k^{\alpha/2}}{\sqrt{x}\omega_j^{\alpha/2}}\cos(\alpha\pi/2)\right)^{2}}, \tag{35}$$

For Equation (35), $\left|\dot{g}(\omega_k)\right| \leq \varepsilon_2$, so there is a minimum value ε, making $\left|\dot{g}(\omega_k)-\varepsilon\right| = 0$. Combining Equations (34) and (35), and the above conditions, the optimal model for parameter α can be deduced as follows:

$$\begin{cases} \min Z(\alpha) = \omega_k - \omega_k\left(-2\sqrt{x}\cos(\alpha\pi/2)/(x+1)\right)^{2/\alpha} \\ s.t. \quad 1 < \alpha < 2. \\ \qquad \left|A_f(\omega_k) + \Delta A\right| \le \varepsilon_1. \\ \qquad \left|\dot{g}(\omega_k) - \varepsilon\right| = 0. \end{cases}, \tag{36}$$

Through Equation (36), parameter α can be solved and determined. Then, parameters λ and ω_m can be calculated by combining Equations (31)–(33), and $\omega_m = (\omega_k\omega_j)^{1/2}$. Therefore, through the establishment of the relationship between the FOLLC and FDC adjustment, the parameters K, x, λ, and α of the AFOAM can be determined properly.

4. Experiment

4.1. Experimental System

Based on the above theoretical analysis and derivation, we implemented the proposed adaptive anti-saturation synchronous control system using a dSPACE prototyping system and conducted experiments on the redundant direct-drive gantry platform to verify the improvement in the synchronous motion performance of the proposed method. Figure 6 shows the experimental setup. The Y-direction motion of the redundant direct-drive gantry platform was driven by AUM3 PMLSMs from Akribis. Each motor was equipped with RGS20-S grating from Renishaw, with a resolution of 0.1 μm.

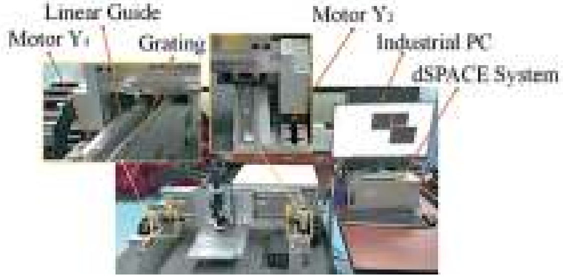

Figure 6. Experimental system.

The beam had a length of 836 mm, and its weight exceeded 25 kg, which caused the synchronous motion performance of the dual-motor system to be significantly affected by the synchronous control method. During the experiments, the dSPACE system controlled the PMLSMs in real time, and the feedback signals were provided by the gratings. By establishing the mathematical model of the motor system and using a frequency sweep experiment to identify the model parameters, the transfer functions of the motor systems were calculated as follows:

$$\begin{cases} g_{y1}(s) = \dfrac{0.9183s^3 + 5.994s^2 + 8959s + 8499}{s^5 + 16.92s^4 + 1.061e04s^3 + 7.916e04s^2 + 5.448e04s} \\ g_{y2}(s) = \dfrac{0.8818s^3 + 8.583s^2 + 8918s + 2.223e04}{s^5 + 12.51s^4 + 1.104e04s^3 + 3.237e04s^2 + 4.215e04s} \end{cases}, \tag{37}$$

The dual-motor system adopted a proportional–integral–derivative (PID) feedback control method. According to the controlled object models shown in Equation (37), the Ziegler–Nichols tuning rules were used to obtain a set of PID parameters that were more consistent with the synchronous-motion requirements of the dual-motor system. The PID controller and its parameters are as follows:

$$\begin{cases} c_1(s) = \left(27.41s^2 + 388.52s + 1.05\right)/s \\ c_2(s) = \left(28.12s^2 + 275.44s + 1.12\right)/s \end{cases}, \tag{38}$$

According to Equations (37) and (38), the FDC diagrams of the dual-motor system under the open-loop, closed-loop, and control methods in this study were obtained, as shown in Figure 7. As seen in the figure, even if the FDC values of the motor systems are significantly different, the closed-loop FDC of the motor systems can be guaranteed to be relatively consistent through the adjustment of the PID feedback controllers. However, there is still a large difference in the amplitude and phase characteristics around ω = 1 rad/s. Because the phase characteristic of Motor Y_2 is ahead of that of Motor Y_1, the FDC-UM can be calculated using Equation (13). When K_F = [1, $-1]^T$, the FDC-UM is given by Equation (39). With the FDC-UM, the FDC of the two motor systems can be made consistent, as shown in Figure 7c.

$$\begin{cases} f_{11}(s) = 1 \\ f_{22}(s) = \dfrac{\begin{array}{l} 25.17s^{11} + 836s^{10} + 5.323e05s^{9} + 1.33e07s^{8} + \\ 2.804e09s^{7} + 4.909e10s + 1.672e11s^{5} + 2.638e11s^{4} + \\ 1.399e11s^{3} + 3.761e08s^{2} \end{array}}{\begin{array}{l} 24.8s^{11} + 903.8s^{10} + 5.244e05s^{9} + 1.447e07s^{8} + \\ 2.784e09s^{7} + 5.286e10s^{6} + 3.228e11s^{5} + 6.536e11s^{4} + \\ 3.361e11s^{3} + 1.356e09s^{2} \end{array}} \end{cases}, \tag{39}$$

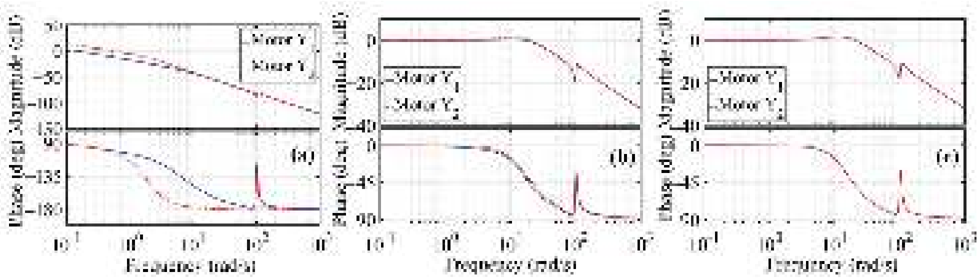

Figure 7. Comparison of the dual-motor system FDC: (**a**) open-loop control; (**b**) closed-loop control; (**c**) closed-loop control with the designed FDC-UM.

According to Equation (17), it is necessary to obtain the friction compensation voltage to accurately calculate the adaptive gain adjustment value. The Stribeck friction model is a commonly used friction model that can more comprehensively reflect the change in the friction of the guide when the PMLSM moves continuously [29]. Based on the Stribeck friction model, the functions of the friction compensation voltage are shown in Equations (40) and (41), and the curves are shown in Figure 8. From Figure 8, we can see the high nonlinearity and complexity of friction, and there is a sudden change in friction during the low-speed period, which seriously deteriorates the accuracy of the motor system. However, when the speed reaches a certain value, the friction remains within a certain range. At this time, the friction changes very little; therefore, the friction compensation voltage used in the calculation of Equation (17) can be clearly obtained.

$$u_{FC1} = \begin{cases} \left(11.13 + 0.00037v_1 + 5.51e^{-(v_1/0.0123)^2}\right)/72,\ for\ v_1 > 0, \\ \left(-13.15 + 0.00011v_1 - 5.33e^{-(v_1/0.0139)^2}\right)/72,\ for\ v_1 < 0. \end{cases}, \tag{40}$$

$$u_{FC2} = \begin{cases} \left(13.03 + 0.00047v_2 + 5.25e^{-(v_2/0.0103)^2}\right)/72,\ for\ v_2 > 0 \\ \left(-16.22 + 0.00018v_2 - 5.51e^{-(v_2/0.0156)^2}\right)/72,\ for\ v_2 < 0. \end{cases} \tag{41}$$

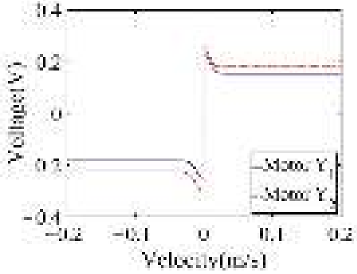

Figure 8. Diagram of the friction compensation voltage.

4.2. Synchronized Motion Experiments

4.2.1. Verification of Peak Voltage Calculation

The AFOAM calculates the theoretical peak voltage based on the spectrum of the input signal and designs the corresponding fractional-order FDC, aiming to avoid the saturation effect of the control voltage. Therefore, the correctness of the calculation expression for the theoretical peak voltage directly affects the effectiveness of the proposed method in improving the synchronization accuracy. The experiments verified the accuracy of the calculation under different accelerations and velocities.

To accurately analyze the spectrum of the input signal, we modified the short-term input signal into a long-period signal through periodic processing and calculated the spectrum according to the discrete Fourier transform shown in Equation (42).

$$s_p(\omega) = T_s^2 \sum_{n=-\infty}^{+\infty} \left(\sum_{k=-\infty}^{n} \left(\sum_{i=-\infty}^{k} a(i) \right) \right) e^{-j\omega n}, \tag{42}$$

where $s_p(\omega)$ is the spectrum of the input signal, T_s is the sampling time, $a(i)$ denotes the discrete acceleration sequence, k is the number of discrete acceleration sequences, and n is the number of discrete velocity sequences. The cubic curve shown in Equation (43) is a commonly used point-to-point motion planning that can realize the adjustment of acceleration, velocity, and displacement. Therefore, this curve was used for experimental analysis. Figure 9 shows the motion planning when the displacement is 0.05 m, maximum speed is 0.4 m/s, and maximum acceleration is 30 m/s^2.

$$r = \begin{cases} a_0 + a_1 t + a_2 t^2 + a_3 t^3, \ for\ t \le t_a, \\ a_0 + a_1 t_a + a_2 t_a t + a_3 t_a^3\ , for\ t_a\ < t \le (t_a + t_c), \\ a_0 + a_1(t - t_c) + a_2 t_a t_c + a_2 (t - t_c)^2 + a_3 (t - t_c)^3, \\ for\ (t_a + t_c)\ < t \le (2t_a + t_c). \end{cases}, \tag{43}$$

where a_i (i = 1, 2, . . . , k) is a parameter of the cubic curve, t_a is the acceleration time, t_c is the uniform motion time, and r is the displacement.

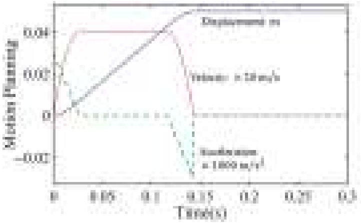

Figure 9. Motion planning of a cubic curve.

Figure 10 shows the calculated amplitude spectrum of the motion planning with different accelerations under the same acceleration time, and Figure 11 shows the calculated amplitude spectrum of the motion planning with different velocities under the same acceleration. It can be seen from Figure 10 that, as the acceleration increases, the amplitude spectrum at the non-zero frequency increases, but all accelerations are at a similar frequency. The results in Figure 11 show that, under the same acceleration, with an increase in velocity, the amplitude spectrum at the non-zero frequency increases, but the frequencies are all retained within a small range.

Based on the spectrum analysis of the input signal, the voltage amplitude characteristics of the motor system at the corresponding angular frequency were calculated. Table 1 shows the comparison results of the theoretical and experimental peak voltages under different motion planning conditions. The relative error δ in the table is calculated as follows:

$$\delta = |u_{cal} - u|/u \times 100\%, \tag{44}$$

where u is the experimental peak voltage, and u_{cal} is the calculated theoretical peak voltage. In the experimental results shown in Table 1, the maximum relative error between the experimental and the calculated theoretical peak voltages was 3.86%, which proves the accuracy of the calculation of the theoretical peak voltage; thus, Equation (17) can guarantee the accurate fractional-order FDC planning for the adaptive fractional-order anti-saturation synchronous control method.

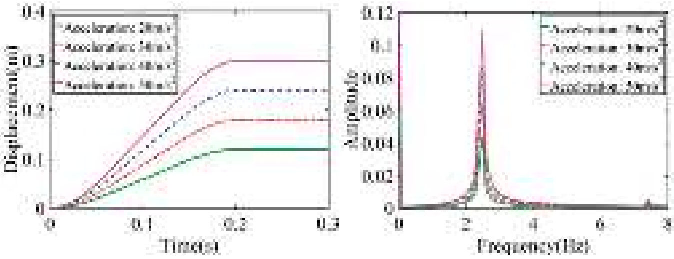

(**a**) (**b**)

Figure 10. Calculated amplitude spectrum of different accelerations under the same acceleration time (80 ms): (**a**) displacement comparison; (**b**) amplitude spectrum comparison.

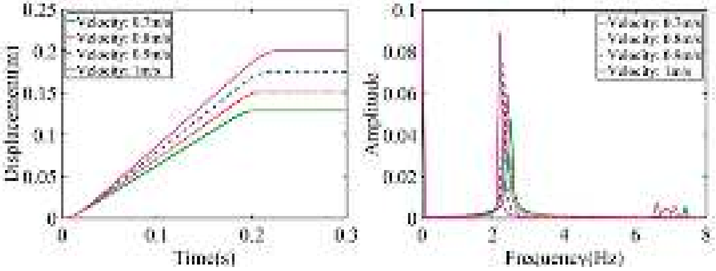

(**a**) (**b**)

Figure 11. Calculated amplitude spectrum of different velocities under the same acceleration ($50\ \mathrm{m/s^2}$): (**a**) displacement comparison; (**b**) amplitude spectrum comparison.

Table 1. Comparison of calculated theoretical and experimental peak voltages.

Motion Planning		Amplitude Spectrum		Voltage Amplitude Characteristic of the Motor Y_1 (dB)	Peak Voltage (V)		δ
Acceleration (m/s^2)	Velocity (m/s)	Frequency (Hz)	Peak Value		Experiment	Calculation	
20	0.8	2.5	0.0435	50.3265	14.8562	14.2828	3.86%
30	1.2	2.5	0.0653	50.3265	22.2843	21.4406	3.79%
40	1.6	2.5	0.0870	50.3265	29.7124	28.5655	3.86%
50	2.0	2.5	0.1088	50.3265	37.1405	35.7233	3.82%

4.2.2. Synchronization Accuracy Verification

To further verify the correctness of the calculation for the proposed adaptive fractional-order anti-saturation synchronous control method and its effectiveness in improving the synchronization accuracy of the dual-motor system, the cubic curve shown in Equation (43) was selected to perform the high-speed high-acceleration motion experiments. According to the above analysis and experiments of the FDC-UM, the parameters of the PID feedback controller selected in the experiments are shown in Equation (38), and those of the friction compensator are shown in Equations (40) and (41). When the dual-motor system was controlled by the proposed synchronous control method, the AFOAM analyzed the spectrum of the input signal and the FDC of the control system and then used Equation (36) to calculate the order of the FOLLC as 1.3190. According to Equations (31)–(33), $\omega_j = 7.1740$, $K_C = 1$, $x = 0.8055$, and $\lambda = 0.1381$. Therefore, using Equation (26), the transfer function of the AFOAM was calculated as Equation (45). According to Equation (45), we could draw the adjustment curve of the voltage amplitude characteristic realized by the AFO-AM, as shown in Figure 12a. An FDC comparison of the motor system with and without the designed AFO-AM is shown in Figure 12b.

The anti-saturation module can avoid synchronization errors owing to the voltage limitation; therefore, compared with the force compensation cross-coupling synchronous control method, the proposed synchronous control method can avoid the artificial secondary parameter adjustment of the control system to achieve high-synchronization accuracy under different motion plannings. Figure 13 shows the experimental results of the synchronous motion of the dual-motor system. Under force compensation cross-coupling synchronous control, both motor systems were affected by long-term saturation, which led to a large synchronization error. However, there was no control voltage saturation under the proposed synchronous control, as shown in Figure 13b, so the synchronization error was reduced obviously, as shown in Figure 13c. Table 2 shows the comparison results of experimental data under three different motion plannings, in which we use the commonly used indicators, such as absolute maximum value (|MAX|), mean absolute error (MAE), and root mean square error (RMSE) to compare the synchronization error under different control methods. Under the proposed adaptive fractional-order anti-saturation synchronous control, the root-mean-square synchronization error of the dual-motor system can be reduced by more than 77.580% compared with that under the force compensation synchronous control. The comparison results of the three sets of experimental data verify that the proposed adaptive fractional-order anti-saturation synchronous control method has obvious advantages in improving the synchronization accuracy of the dual-motor system.

$$T_a(s) = \frac{1 + 0.1112s^{1.3190}}{0.0269s^{1.3190}\left(\frac{25.17s^5 + 521.1s^4 + 2.479e05s^3 + 3.714e06s^2 + 3.311e06s + 8924}{s^6 + 16.92s^5 + 10610s^4 + 79160s^3 + 54480s^2}\right) + 0.1381s^{1.3190} + 1}. \tag{45}$$

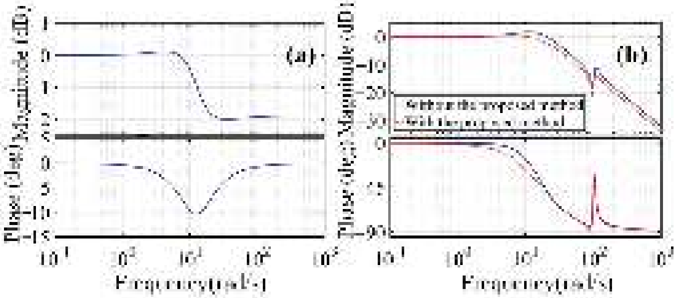

Figure 12. FDC adjustment of the proposed adaptive fractional-order anti-saturation method: (**a**) fractional-order FDC planning target for the voltage amplitude characteristic; (**b**) FDC comparison of the two motor systems with and without the proposed method.

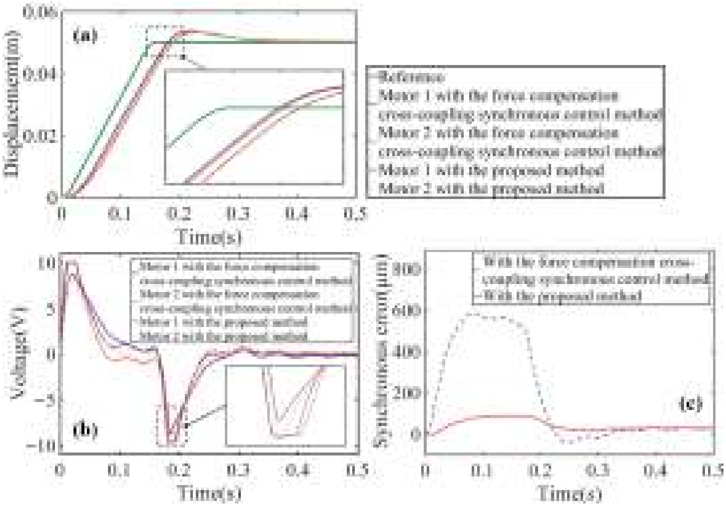

Figure 13. Synchronous motion experimental results of the dual-motor system under different synchronous control methods: (**a**) displacement comparison; (**b**) control voltage comparison ($|u_{max}| = 10$V); (**c**) synchronization error comparison.

Table 2. Experimental data comparison results of the synchronous motion experiments.

Experiment	Motion Planning			Control Method	Synchronization Error (μm)			RMSE Reduction (%)
	Displacement (m)	Velocity (m/s)	Acceleration (m/s^2)		|MAX|	MAE	RMSE	
1	0.05	0.35	30	Method 2	584.500	117.259	221.443	-
				Proposed method	89.800	36.987	42.132	80.974
2	0.05	0.5	30	Method 2	561.600	80.388	161.193	-
				Proposed method	52.900	31.436	32.338	79.938
3	0.05	0.5	50	Method 2	769.000	106.681	220.616	-
				Proposed method	141.400	40.019	49.454	77.580

Method 2: Force compensation cross-coupling synchronous control method.

5. Discussion

Synchronization error of a dual-motor system will usually lead to degradation of equipment performance. Several researchers focused on the cross-coupling synchronous control method, by reducing the synchronization error from the aspects of the compensation method and the control parameter tunning method, to improve the synchronous motion performance of a dual-motor system [19,30]. However, the cross-coupling synchronous control method is usually used to compensate the control voltage after the synchronization error occurred, so there is a time delay between the generation and the compensation of the synchronization error. As shown in Figure 3, under the control of the chirp signal, although the cross-coupling synchronous control method could greatly reduce the synchronization error of the dual-motor system, it was difficult to eliminate the synchronization error completely due to the constant changes in the amplitude and frequency of the input signal and the inconsistent response characteristics of the dual-motor system. The experimental results showed the relationship between the dynamic response characteristics and the FDC of the motor systems. With the proposed adaptive fractional-order anti-saturation synchronous control method, the FDC of the dual-motor system was adjusted to be consistent to guarantee the same dynamic response output of the dual-motor system. Compared with the cross-coupling synchronous control method, our method can suppress the generation of the synchronization errors of the dual-motor system and eliminate the influence of the saturation effect and thus can achieve a better synchronous-motion control performance, as shown in Table 2. It can be seen from the experimental results in Figure 13 that our method can effectively avoid the non-linear phenomenon of control voltage saturation and ensure the high-precision synchronization accuracy of the dual-motor system. Considering the problem of the hysteresis nonlinearity and gap nonlinearity of the dual-motor system, the synchronous control performance of the proposed method may be affected. Next, we will tackle this problem to further improve the synchronous control method for the dual-motor system.

6. Conclusions

In this study, we proposed an adaptive fractional-order anti-saturation synchronous control method to deal with the asynchronous problem of the dual-motor system. With the elimination of the differences in FDC by the designed FDC-UM, both motor systems possessed consistent dynamic response characteristics. Based on the theoretical peak voltage calculation, we further developed an adaptive fractional-order anti-saturation module (AFOAM) to eliminate the nonlinear saturation effect caused by the control voltage saturation and thus effectively improved the synchronization accuracy of the dual-motor system. The experimental results showed that the maximum relative error between the calculated and experimental peak voltage was only 3.86%, which confirmed the correctness of the theoretical calculation of the peak voltage in this paper. On this basis, the proposed adaptive fractional-order anti-saturation synchronous control method could prevent the control voltage from reaching the limitation and reduce the root-mean-square synchronization error from 221.443 μm to 42.132 μm, with a reduction of 80.974%. The experimental results demonstrated that the proposed method can effectively suppress the inconsistent characteristics of the dual-motor system and avoid the nonlinear saturation effect. Therefore, the proposed method can effectively improve the synchronization accuracy of the dual-motor system.

Author Contributions: Writing–original draft, Y.Z.; Writing—review & editing, J.G. and L.Z. All authors have read and agreed to the published version of the manuscript.

Funding: This work was supported by the National Natural Science Foundation of China under Grant No. 52075106, No. 51905108, and No. U20A6004.

Conflicts of Interest: The authors declare no conflict of interest.

References

1. Tan, L.; Gao, J.; Luo, Y. Super-twisting sliding mode control with defined boundary layer for chattering reduction of permanent magnet linear synchronous motor. *J. Mech. Sci. Technol.* **2021**, *35*, 1829–1840. [CrossRef]
2. Yu, W.; Yang, G.; Li, Z. A tubular linear motor structure suitable for large thrust. *J. Mech. Sci. Technol.* **2021**, *35*, 4987–4995. [CrossRef]
3. Liu, W.; Shu, F.; Xu, Y. Iterative learning based neural network sliding mode control for repetitive tasks: With application to a PMLSM with uncertainties and external disturbances. *Mech. Syst. Signal Process.* **2022**, *172*, 108950. [CrossRef]
4. Chung, S.-U.; Kim, J.-W.; Woo, B.-C. Design and experimental validation of doubly salient permanent magnet linear synchronous motor for precision position control. *Mechatronics* **2013**, *23*, 172–181. [CrossRef]
5. Chen, S.-Y.; Chen, C.-S.; Yang, Z.-W. Self-tuning cross-coupled two degree-of-freedom PID control for position synchronization of dual linear motors. *Appl. Math. Model.* **2018**, *64*, 214–234. [CrossRef]
6. Chen, R.; Yan, L.; Jiao, Z. Dynamic modeling and analysis of flexible H-type gantry stage. *J. Sound Vib.* **2019**, *439*, 144–155. [CrossRef]
7. Nguyen, V.H.; Kim, W.-J. Error analysis to minimize cross-axis couplings in 6-DOF motion systems with a single moving part. *Precis. Eng.* **2020**, *63*, 49–61. [CrossRef]
8. Sarachik, P.; Ragazzini, J.R. A 2-dimensional feedback control system. In *Transactions of the American Institute of Electrical Engineers, Part II: Applications and Industry*; IEEE: New York, NY, USA, 1957; Volume 76, pp. 55–61.
9. Koren, Y. Cross-Coupled Biaxial Computer Control for Manufacturing Systems. *J. Dyn. Syst. Meas. Control* **1980**, *102*, 265–272. [CrossRef]
10. Huo, F.; Poo, A.-N. improving contouring accuracy by using generalized cross-coupled control. *Int. J. Mach. Tools Manuf.* **2012**, *63*, 49–57. [CrossRef]
11. Chen, W.; Wang, D.; Geng, Q. Robust adaptive cross-coupling position control of biaxial motion system. *Sci. China Technol. Sci.* **2016**, *59*, 680–688. [CrossRef]
12. Zhu, X.; Yao, B.; Tao, G.; Wang, Q.; Cao, J. Adaptive robust synchronous control of a individual metering dual-cylinder pneumatic system with composite parallel method. In Proceedings of the 2014 IEEE/ASME International Conference on Advanced Intelligent Mechatronics (AIM), Besançon, France, 8–11 July 2014; pp. 304–309.
13. Koren, Y.; Lo, C.C. Variable-Gain Cross-Coupling Controller for Contouring. *CIRP Ann.* **1991**, *40*, 371–374. [CrossRef]
14. Chou, P.-H.; Chen, C.-S.; Lin, F.-J. DSP-based synchronous control of dual linear motors via Sugeno type fuzzy neural network compensator. *J. Frankl. Inst.* **2012**, *349*, 792–812. [CrossRef]
15. Huang, Z.; Song, G.; Li, Y. Synchronous control of two counter-rotating eccentric rotors in nonlinear coupling vibration system. *Mech. Syst. Signal Process.* **2019**, *114*, 68–83. [CrossRef]
16. García-Herreros, I.; Kestelyn, X.; Gomand, J. Model-based decoupling control method for dual-drive gantry stages: A case study with experimental validations. *Control Eng. Pract.* **2013**, *21*, 298–307. [CrossRef]
17. Teo, C.S.; Tan, K.K.; Lim, S.Y. Dynamic modeling and adaptive control of a H-type gantry stage. *Mechatronics* **2007**, *17*, 361–367. [CrossRef]
18. Wang, K.; Liu, X.; Su, H. Robust immersion and invariance adaptive coordinated control for a class of biaxial gantry systems. *J. Control Decis.* **2021**, *9*, 289–300. [CrossRef]
19. Li, C.; Li, C.; Chen, Z. Adaptive thrust allocation based synchronization control of a dual drive gantry stage. *Mechatronics* **2018**, *54*, 68–77. [CrossRef]
20. Gordon, D.J.; Erkorkmaz, K. Precision control of a T-type gantry using sensor/actuator averaging and active vibration damping. *Precis. Eng.* **2012**, *36*, 299–314. [CrossRef]
21. Wang, Z.; Hu, C.; Zhu, Y. Trajectory modification method based on frequency domain analysis for precision contouring motion control systems. *Mech. Syst. Signal Process.* **2021**, *158*, 107646. [CrossRef]
22. Zou, M.; Fang, P.; Peng, H. Study on synchronization characteristics for self-synchronous vibration system with dual-frequency and dual-motor excitation. *J. Mech. Sci. Technol.* **2019**, *33*, 1065–1078. [CrossRef]
23. Nirmala, R.J.; Balachandran, K.; Trujillo, J.J. Null controllability of fractional dynamical systems with constrained control. *Fract. Calc. Appl. Anal.* **2017**, *20*, 553–565. [CrossRef]
24. Yaghooti, B.; Hosseinzadeh, M.; Sinopoli, B. Constrained control of semilinear fractional-order systems: Application in drug delivery systems. In Proceedings of the 2020 IEEE Conference on Control Technology and Applications (CCTA), Montreal, QC, Canada, 24–26 August 2020; pp. 833–838.
25. Rhouma, A.; Bouani, F.; Bouzouita, B. Model predictive control of fractional order systems. *J. Comput. Nonlinear Dyn.* **2014**, *9*, 031011. [CrossRef] [PubMed]
26. Zhong, Y.; Gao, J.; Zhang, L. Fractional-order feedforward control method for permanent magnet linear synchronous motor based on frequency-domain adjustment theory. *Mech. Syst. Signal Process.* **2023**, *190*, 110115. [CrossRef]
27. Dai, L.; Li, X.; Zhu, Y. The Generation Mechanism of Tracking Error During Acceleration or Deceleration Phase in Ultraprecision Motion Systems. *IEEE Trans. Ind. Electron.* **2019**, *66*, 7109–7119. [CrossRef]
28. Tao, J.; Mercan, O. A study on a benchmark control problem for real-time hybrid simulation with a tracking error-based adaptive compensator combined with a supplementary proportional-integral-derivative controller. *Mech. Syst. Signal Process.* **2019**, *134*, 106346. [CrossRef]

29. Yoon, J.Y.; Trumper, D.L. Friction microdynamics in the time and frequency domains: Tutorial on frictional hysteresis and resonance in precision motion systems. *Precis. Eng.* **2019**, *55*, 101–109. [CrossRef]
30. Deng, Z.; Shang, J.; Nian, X. Synchronization controller design of two coupling permanent magnet synchronous motors system with nonlinear constraints. *ISA Trans.* **2015**, *59*, 243–255. [CrossRef]

applied sciences

MDPI

Article

Study on Stator-Rotor Misalignment in Modular Permanent Magnet Synchronous Machines with Different Slot/Pole Combinations

Danilo Riquelme [1,*], Carlos Madariaga [2], Werner Jara [1], Gerd Bramerdorfer [3], Juan A. Tapia [2] and Javier Riedemann [4]

[1] School of Electrical Engineering, Pontificia Universidad Católica de Valparaíso, Valparaíso 2362804, Chile
[2] Department of Electrical Engineering, University of Concepcion, Concepcion 4070386, Chile
[3] Department of Electrical Drives and Power Electronics, Johannes Kepler University Linz, 4040 Linz, Austria
[4] Department of Electronic and Electrical Engineering, University of Sheffield, Sheffield S1 3JD, UK
* Correspondence: danilo.riquelme.s@mail.pucv.cl

Featured Application: The results of this work can be included in the design stage of modular permanent magnet synchronous machines for fault-tolerant applications.

Abstract: Addressing stator-rotor misalignment, usually called eccentricity, is critical in permanent magnet (PM) machines since significantly high radial forces can be developed on the bearings, which can trigger a major fault and compromise the structural integrity of the machine. In this regard, this paper aims to provide insight into the unaddressed identification and analysis of the impact of eccentric tolerances on relevant performance indices of permanent magnet synchronous machines (PMSMs) with modular stator core. Static and dynamic eccentricity are assessed for different slot/pole combinations through the finite element method (FEM), and the results are compared with those of PMSMs with a conventional stator core. The unbalanced magnetic forces (UMF), cogging torque, back-emf, and mean torque variations are described and related to the eccentricity magnitude and classification. The main findings indicate that severe radial forces and significant additional cogging torque harmonics are generated because of eccentricity. Additionally, it is found that the main differences between modular PMSMs and conventional PMSMs rely on the value of slots per pole per phase.

Keywords: cogging torque; dynamic eccentricity; finite element analysis; modular stator; permanent magnet; static eccentricity; stator-rotor misalignment; tolerance analysis

Citation: Riquelme, D.; Madariaga, C.; Jara, W.; Bramerdorfer, G.; Tapia, J.A.; Riedemann, J. Study on Stator-Rotor Misalignment in Modular Permanent Magnet Synchronous Machines with Different Slot/Pole Combinations. *Appl. Sci.* **2023**, *13*, 2777. https://doi.org/10.3390/app13052777

Academic Editors: Kan Liu and Wei Hu

Received: 17 January 2023
Revised: 13 February 2023
Accepted: 17 February 2023
Published: 21 February 2023

1. Introduction

In safe-critical applications, the uninterrupted and reliable operation of the electrical machine is requisite, which is described by their fault-tolerance capability. This is the case, for instance, of aeronautical, aerospace, and electromobility applications [1–3]. As a concept, fault-tolerant machines should provide acceptable levels of electric, magnetic, physical, and thermal isolation of phase windings [3], and can also consider multiphase windings [4,5] or limiting short-circuit current capability [6,7].

In addition to the fault-tolerance capability, electrical machines must provide enough power density, efficiency, and electromagnetic performance to meet the application's requirements. In this regard, electrical machines based on permanent magnets (PMs) are well known as the most promising technology in terms of power density and efficiency [8–11], but they lack inherent fault-tolerance capability [12]. It is desirable that PMSMs resist winding open-circuit and short-circuit faults without compromising the integrity of magnets. Nevertheless, since their electromagnetic performance is unmatchable by other conventional topologies so far, considerable efforts have been carried out in the last few years to enhance the fault-tolerant capability of PM machines [2–5,7,12–14]. In the technical literature, adopting a modular stator core, as illustrated in Figure 1b, has been shown to be a feasible solution to enhance the fault-tolerant capability of PM machines [15–23]. This obeys mechanical and electromagnetic reasons, since PM synchronous machines with modular stator core (MPMSMs) offer several advantages in high-power density and fault-tolerance applications [15]: they can provide physical, thermal, and electromagnetic insulation between phases, lower material requirements (laminations) than conventional topologies and a high slot fill factor [16]. Notwithstanding, the cost of MPMSMs developing these features is the presence of manufacturing and assembly challenges, decrease in mean torque, and increase in torque ripple [15,18,19]. As can be seen from Figure 1b, the stator structure in MPMSM is segmented and, therefore, the attachment of the modules to the stator body can provide the design with additional manufacturing and assemblies tolerances (uncertainties) when compared with conventional PMSMs (Figure 1a).

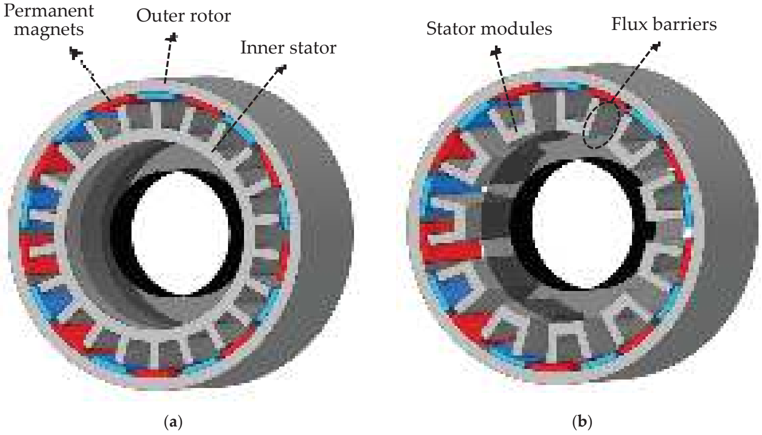

(**a**) (**b**)

Figure 1. Three-dimensional representation of stator/rotor structure of a 24-slot, 20-pole PMSM: (**a**) conventional PMSM with non-segmented stator (monolithic), (**b**) PMSM with modular stator core (MPMSM).

Recent studies have approached the analysis of some of these uncertainties, giving insight into the effect of design parameters and dimensional tolerances on the machine performance [15,17,18]. Although these studies are relevant for describing the impact of dimensional tolerances on the performance of MPMSMs and provide guidelines for devising more robust designs, there is a critical uncovered aspect that compromises the reliability and continuous operation of these machines: stator-rotor misalignment.

Stator-rotor misalignment, which can be classified into static eccentricity or dynamic eccentricity depending on the dynamics of the misalignment [24,25], wears down the bearings since it generates vibration and pulsing forces on their structure [26,27] and can truncate the fault-tolerance capability of electrical machines. In addition, eccentricity affects the performance of several topologies in terms of the generation of radial forces in the rotor structure [27–29], cogging and ripple torque increase [24,30], input current harmonic distortion when the machine is fed with inverters [31], and back-emf unbalance [30].

Studies on eccentricity effects are particularly relevant in PM machines, as the magnets on the rotor can generate significantly high radial forces on the stator structure and the bearings [24], which can trigger a major fault. The impact of eccentricity on PMSMs with non-segmented stators has been covered in [25–27,29–31], focusing on quantifying and analyzing the effects on the electromagnetic performance of the machine. Particularly, [29] disclosed a crucial design tendency that can be included in the early stages of the machine design: the electromagnetic performance penalization due to eccentricity strongly depends on the machine slot-pole combination, becoming especially relevant as the slot count and pole count get closer.

In turn, the impact of eccentricity on MPMSMs has been recently addressed in [24] for axial-even eccentricity in a single 24-slot, 28-pole machine: relevant radial forces appear as expected, but the cogging torque, back-emf, and electromagnetic torque seem to be insensitive. The authors concluded that the addressed slot/pole combination was mostly insensitive to eccentricity even when the slot count and pole count differed by four, but the study required to be expanded to more slot/pole combinations. The comparison between the results of [24,29] suggests that the effect of slot/pole combinations on PMSMs with eccentricity may be different from their modular counterpart. This could also be inferred from the analysis of [18], which states that, in presence of manufacturing tolerances, the periodicity of the stator core changes when adopting a modular structure, affecting the cogging torque main period and its sensitiveness to assembly tolerances for the same slot/pole combination.

All things considered, if the fault-tolerance capability of a MPMSM is to be assured, its electromagnetic performance and structure integrity should not be greatly affected by mild degrees of eccentricity. Nevertheless, and despite of its relevance, the effects of eccentricity on the performance of MPMSMs for different slot/pole combinations and their inclusion in the early design stages of the machine remains uncovered in the technical literature so far.

The aim of this work is, therefore, to identify and analyze the impact of eccentric tolerances on relevant performance indices of MPMSMs for different slot/pole combinations, comparing their response to that of PMSMs with conventional stators. Both static and dynamic eccentricity are analyzed by means of the finite element method (FEM) for five slot/pole combinations, evaluating the radial forces that the rotor structure is exposed to cogging torque, back-EMF, and rated torque. The relevance of this paper lies with providing a quick yet reliable comparison of the MPMSM performance between slot/pole combinations and the reasons behind the observed phenomena, critical in the design stage of a MPMSM, as well as disclosing relevant similarities and differences with respect to PMSMs with conventional stator core. This paper is organized as follows: in Section 2, the selected topology and its main data are presented; in Section 3, the methodology and details regarding the considered eccentricity types are described; in Section 4, the results of key performance indices when the machine has eccentricity tolerances are presented and discussed. The conclusions are drawn at the end of the paper.

2. Selected Topology and Slot/Pole Combinations

In order to compare the effect of eccentricity on different slot/pole combinations of both modular and non-modular PMSMs, tooth coil windings (TCW) were adopted since they allow a higher power/weight ratio due to the shorter end winding turns, lower cogging torque, and compactness when compared with the distributed windings [32]. The modular machine is considered to have U-Shaped stator segments and surface-mounted magnets as depicted in Figure 1b as they have been of interest in the last years for fault-tolerance applications [15,21]. The main data of the machines and their design parameters are presented in Table 1 and schematized in Figure 2. The machines assessed in this work aim to provide maximum mean torque within dimensional constraints, following the optimization criteria established in [17,21]. These machines represent low-power scaled protoypes with a rated power of 5 [kW], considering a current density of 10 A/mm^2 and a speed range of 0 to 6000 [RPM].

In turn, the slot/pole combinations were selected with the aim of covering different values of slots per phase per pole (q) given by:

$$q = \frac{Q_s}{2pm}, \tag{1}$$

where Q_s is the slot number, $2p$ is the pole number, and m is the number of phases. For the case of TCW-PMSM, it is recommended to adopt a value of q between 0.25 and 0.5 [32], which is the reason why the selected slot/pole combinations are within this range. The combinations evaluated in this work are summarized in Table 2, which also shows their winding layouts. For all considered designs, the coil pitch is equal to 1 slot, as documented in [32].

Table 1. Main data of the machines (MPMSM and PMSM).

Symbol	Quantity	Value
d	Effective core length	70.0 mm
r_{se}	Stator outer radius	133.0 mm
δ_g	Airgap length	2.0 mm
b_s	Slot width	24.8 mm *
h_s	Slot height	27.5 mm
b_t	Tooth width	10.0 mm *
h_{ys}	Height of the stator yoke	10.5 mm
h_{yr}	Height of the rotor yoke	10.0 mm
h_{pm}	PM height	5.0 mm
B_r	PM remanence	1.1 T
μ_r	Relative recoil permeability	1.04

* Reference tooth width and slot width values were considered for the 28-slot, 20-pole machines, as suggested in [17,18], and they were adjusted for another slot/pole combinations to develop similar saturation levels, based on [17,21].

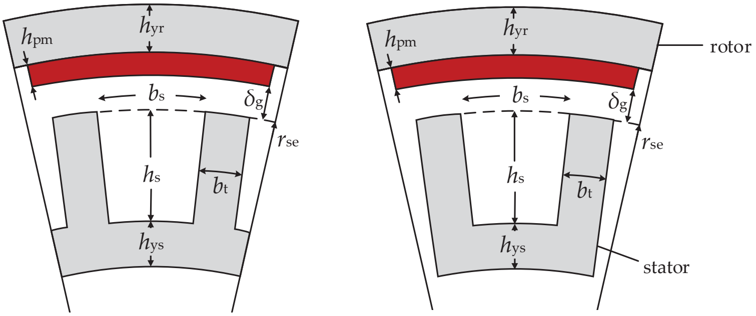

(**a**) (**b**)

Figure 2. Schematics of selected PMSMs: (**a**) conventional PMSM with non-segmented stator, (**b**) PMSM with modular stator core.

Table 2. Selected slot/pole combinations, including their winding layout considering TCW.

Slot Number	Pole Number	q	$\Delta(Q_s, 2p)$	Winding Layout
18	12	1/2	6	$\ldots\ \lvert A\ A'\lvert B\ B'\lvert C\ C'\lvert\ \ldots$
18	20	3/10	2	$\ldots\ \lvert C'\ A\lvert A'\ A'\lvert A\ A\lvert A'\ B\lvert B'\ B'\lvert B\ B\lvert B'\ C\lvert C'\ C'\lvert C\ C\lvert\ \ldots$
24	20	2/5	4	$\ldots\ \lvert C'\ A\lvert A'\ A'\lvert A\ B'\lvert B\ B\lvert B'\ C\lvert C'\ C'\lvert C\ A'\lvert A\ A\lvert A'\ B\lvert\ B'\ B'\lvert B\ C'\lvert C\ C\lvert\ \ldots$
24	22	4/11	2	$\underbrace{\ldots A\lvert A\ A'\ A\ldots A\lvert A\ A'}_{Q_s/3}\underbrace{B'\ B\ B\ B'\ldots B'\lvert B\ B'}_{Q_s/3}\underbrace{C'\ C\ C'\lvert C\ldots C\lvert C'\ C\ C\ldots}_{Q_s/3}$
24	28	2/7	4	$\ldots\ \lvert C'\ A\lvert A'\ A'\lvert A\ B'\lvert B\ B\lvert B'\ C\lvert C'\ C'\lvert C\ A'\lvert A\ A\lvert A'\ B\lvert\ B'\ B'\lvert B\ C'\lvert C\ C\lvert\ \ldots$

In addition, machines with dissimilar differences between the slot number (Q_s) and the pole number ($2p$) are considered in this work from 2 to 6, as addressed in [33].

3. Types of Eccentricities Evaluated and Assessed Performance Indicators

In this research, both static eccentricity (SE) and dynamic eccentricity (DE) are assessed by means of FEM. When SE is present, and as depicted in Figure 3a, the rotor and stator structures are not coaxial and a non-uniform airgap distribution that does not vary with the rotation of the rotor is generated. On the other hand, when DE is present, the rotor and stator are not coaxial and, additionally, the rotational axis and the rotor geometry axis do not match. As shown in Figure 3b, this creates a non-uniform airgap distribution that circulates with the rotor spinning.

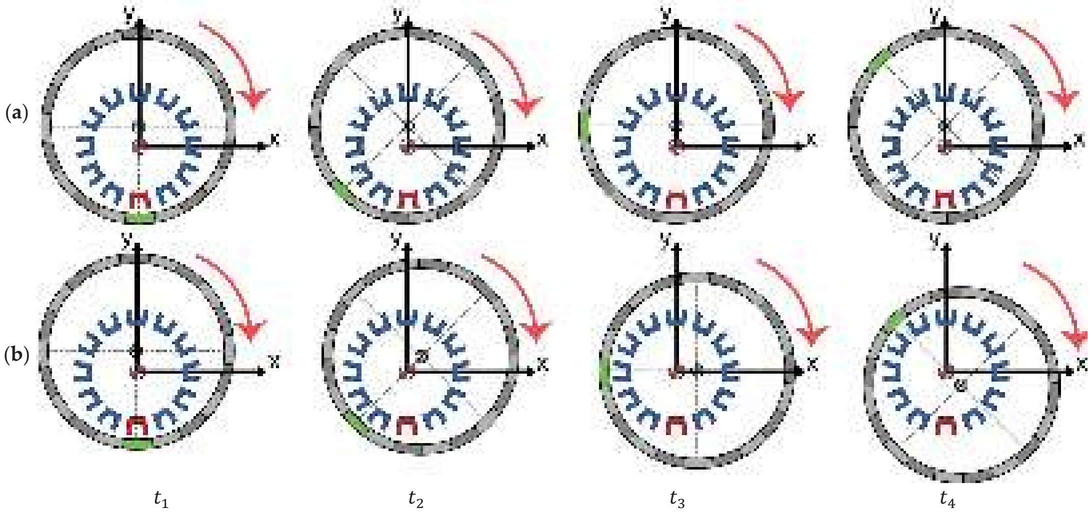

Figure 3. Representation of eccentricity types depending on its dynamics: (**a**) SE, in which the position of the minimum airgap is fixed, (**b**) DE, in which the position of the minimum airgap changes as the rotor structure rotates. Four arbitrary time instants are represented in the figure.

This work considers the difference between the nominal airgap length and the minimum airgap length generated by the stator/rotor misalignment as the magnitude of eccentricity as suggested in [24,30,33]. In addition, potential axis deflections and axial variations of the eccentricity magnitude are neglected. As a result, five eccentricity magnitudes are studied to cover from very low eccentricity (12.5% of the nominal airgap length) to high eccentricity (half the nominal airgap length), as presented in Table 3.

The effects of eccentricity on the performance of both PMSMs and MPMSMs are studied by means of: (i) the analysis of the generated radial forces, also called unbalanced magnetic force (UMF), (ii) cogging torque, (iii) back-emf, and (iv) mean torque, as these indicators have proven to be affected in conventional topologies for at least one slot/pole combination.

Table 3. Eccentricity magnitudes analyzed in the selected PMSMs.

Eccentricity Magnitude (% of Nominal Airgap Length)	Eccentricity Magnitude (mm)	Severity
12.5	0.25	Very low
25.0	0.50	Low
37.5	0.75	Medium
50.0	1.00	High

The following sections present the results organized so as to cover the impact of eccentricity on each performance indicator separately. In each case, the results are firstly presented in detail for one slot/pole combinations to show graphics of relevant curves and their harmonic spectrum. From these graphics, the main numerical indicators are extracted and summarized in tables for all the addressed slot/pole combinations, in order to allow an organized comparison and analysis of results. All results are obtained by means of 2D FEM simulations carried out with the commercial package Ansys Electronics.

4. Results and Discussion: Unbalanced Magnetic Forces

One of the most critical consequences of eccentricity is the generation of unbalanced magnetic forces between the rotor and stator structures. In the case of radial-flux topologies, this may translate into radial forces of considerable magnitude that affect the bearings of the machine and whose dynamics depend on the eccentricity type. In this section, net forces acting on the rotor are assessed considering that in $t = 0$ the minimum airgap position is in $\theta = \frac{3}{2}\pi$ rad, as indicated in time instant t_1 of Figure 3.

4.1. Evaluation on a 24-Slot, 22-Pole PMSM and MPMSM

As an example, in Figure 4 the outcomes of the FEM evaluation of a 24-slot, 22-pole PMSM and a 24-slot, 22-pole MPMSM are presented for both SE and DE. The results were extracted considering the rotor structure completes one full turn. In Figure 4a,b the x-axis and y-axis forces acting on the rotor structure are shown when DE is present for the modular and the conventional machine, respectively. The X represents the average radial forces generated in a full rotation, which is zero for the case of DE. It may be noted that a rotating force vector is generated in both cases, with an almost constant magnitude and low ripple (visualized as saw teeth in the force circumference periphery).

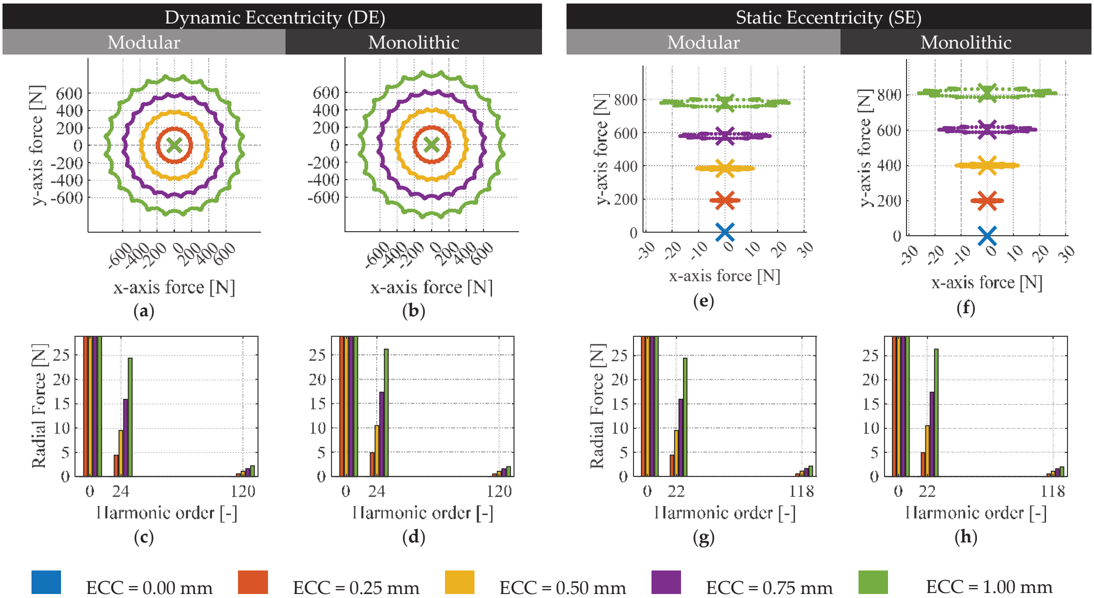

Figure 4. FE evaluation of radial forces acting on the rotor structure in the presence of DE (left column) and SE (right column) for a 24-slot, 22-pole PMSM and MPMSM: (**a**) x-axis and y-axis forces of DE on MPMSM, (**b**) x-axis and y-axis forces of DE on PMSM, (**c**) radial force spatial harmonic content of DE on MPMSM, (**d**) radial force spatial harmonic content of DE on PMSM, (**e**) x-axis and y-axis forces of SE on MPMSM, (**f**) x-axis and y-axis forces of SE on PMSM, (**g**) radial force spatial harmonic content of SE on MPMSM, (**h**) radial force spatial harmonic content of SE on PMSM.

From Figure 4c,d, which show the spatial harmonic content of the radial forces, it can be seen that the spatial frequency of the radial force ripple matches the slot pitch of the machine (HO = 24). This can be explained since for DE the relative position between the magnet symmetry axis and teeth symmetry axis is periodical and repeats each $360/Q_s$ mechanical degrees. Similar findings were described for the cogging torque in conventional PMSMs in [34]. In turn, in Figure 4e,f, the x-axis and y-axis forces acting on the rotor structure are shown when SE is acting in the modular and the conventional machine, respectively. The X represents the average radial forces generated in a full rotation, which points from the minimum airgap position towards the center of rotation for the case of SE. It may be noted that the x-axis forces are not zero and configure the radial force ripple. From Figure 4g,h, which show the spatial harmonic content of the radial forces, it can be seen that the spatial frequency of the radial force ripple matches the pole pitch of the machine (HO = 22). This is because in SE the relative position between the magnet symmetry axis and teeth symmetry axis is periodical and repeats each $360/2p$ mechanical degrees, as described in [24].

In summary, relevant features of the radial force results can be summarized by the following indicators, useful for evaluating and comparing the different slot/pole combinations in Table 2.

- Mean value of the radial force acting on the rotor structure, measured in N.
- Peak-to-peak value of the radial force, representing the radial force ripple and measured in N.

4.2. Comparison of Slot/Pole Combinations for PMSMs and MPMSMs

In Table 4, the average forces generated by different DE magnitudes are presented for both the modular and monolithic machines considering different slot/pole combinations. In the first place, it may be noted that not all selected slot/pole combinations exhibit unbalanced magnetic forces in the absence of eccentricity. Secondly, and according to the tendencies of Figure 4a,b, it can be seen that the generated radial forces are directly proportional to the eccentricity magnitude. This means that the radial force created by eccentricity can be quickly predicted from a single ECC value.

Table 4. Average UMF of different PMSM and MPMSM slot/pole combinations in the presence of DE.

ECC **Q/2p**	**0 mm (Faultless)**		**0.25 mm**		**0.50 mm**		**0.75 mm**		**1.00 mm**	
	Mod [N]	Mon [N]	Mod [N]	Mon [N]	Mod [N]	Mon [N]	Mod [N]	Mon [N]	Mod [N]	Mon [N]
18S 12P	0	0	92	116	184	231	277	348	370	466
18S 20P	0	0	148	151	296	304	446	458	599	614
24S 20P	0	0	181	194	362	390	546	588	733	790
24S 22P	0	0	192	200	385	401	580	604	780	813
24S 28P	0	0	203	209	408	419	617	634	833	856

From Table 4, it can be also noted that the unbalanced magnetic force increases as the slot number and pole number increase. The effect of the slot number can be noted from the comparison of the 18-slot, 20-pole machine to the 24-slot, 20-pole machine, which develops a consistent 20% force increase for all the evaluated ECC values. In consequence, it can be stated that the slot count has a medium impact on the radial forces generated by eccentricity and should not be neglected. In turn, the pole count effect can be deduced from the comparison of the 24-slot, 20-pole and the 24-slot, 28-pole machine, the latter having 12% more radial force. On the other hand, it is observed that in some slot/pole combinations, the radial force generated in the monolithic machine is significantly different from the modular machine. This can be explained by the flux density penalization of modular machines with a high value of q (See Equation (1)). To this end, Figure 5 shows the flux density lines for two slot/pole combinations that have different q values. Figure 5a,b show the flux lines when q is high, in which case the pole number is much smaller than the slot number. In this case, the flux lines require to travel through several teeth, crossing the stator yoke which is absent between the modules of MPMSMs. Therefore, in the modular machine, the flux lines will cross the gap between modules, circulating across a high-reluctance path that penalizes the airgap flux density and, subsequently, the radial forces. Instead, Figure 5c,d show the flux lines when q is lower, in which case the pole number is closer to the slot number. In this situation, flux lines need to use fewer teeth to close the path, which is the reason why in modular machines the lines can circulate using a single module and not penalize the airgap flux density to a high extend.

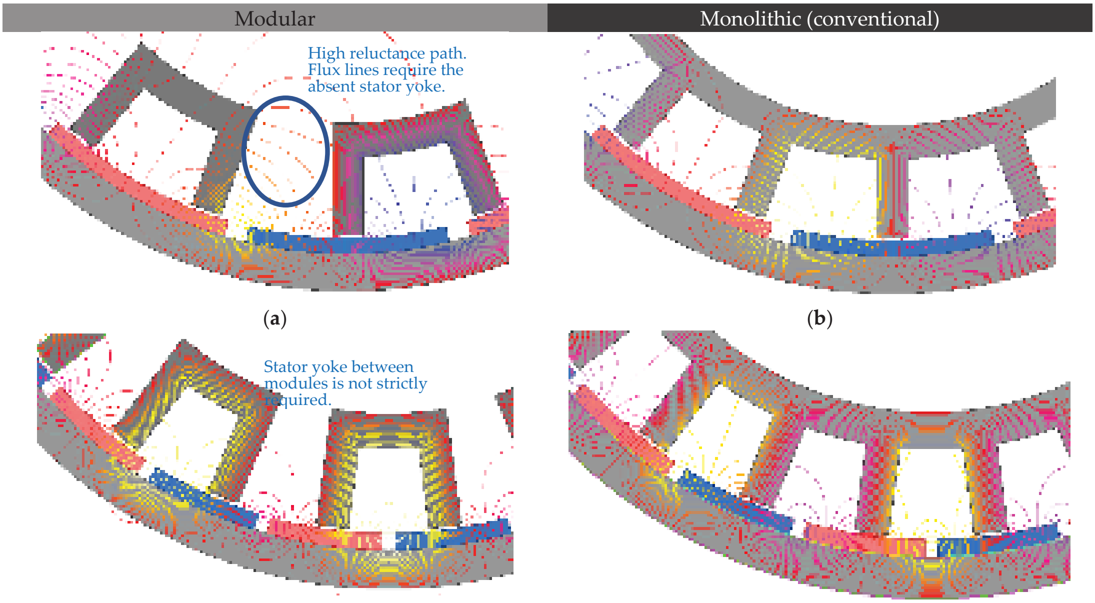

(**a**) (**b**)

(**c**) (**d**)

Figure 5. Close-up to flux density lines for different values of q: (**a**) Modular 18-slot, 12-pole, $q = 0.5$, (**b**) monolithic, 18-slot, 12-pole, $q = 0.5$, (**c**) modular, 24-slot, 22-pole, $q = 0.36$ (**d**) monolithic, 24-slot, 22-pole, $q = 0.36$.

In Table 5, the maximum radial force (ECC = 1 mm) for each slot/pole combination is presented and compared between modular and monolithic machines. It can be noted that, effectively, the difference between the radial forces generated on the modular machine vs. on the monolithic machine is higher as the value of q is greater.

Table 5. Difference between the radial force on modular and monolithic machines in terms of the number of slots per pole per phase.

Q/2p	q	F_{max} [N] **Mod**	F_{max} [N] **Mon**	ΔF_{max}
18S 12P	1/2	370	466	25.9%
18S 20P	3/10	599	614	2.5%
24S 20P	2/5	733	790	7.8%
24S 22P	4/11	780	813	4.2%
24S 28P	2/7	833	856	2.7%

In Table 6, the radial force ripple generated by different magnitudes of DE is presented for each slot/pole combination. It is worth noting that slot/pole combinations with a lower difference between the slot count and the pole count exhibit the highest force ripple. This is particularly relevant since it translates into higher-frequency vibration and force pulses that can reach the bearings. For instance, for the 18-slot, 20-pole machines, the force ripple is around 40% of the average radial force, which is already significant in magnitude, and it generates a force that pulses 18 times for each machine rotation. For all slot/pole combinations, the main harmonic order (HO) of the torque ripple matches the slot number, and there are no significant differences between the modular and the monolithic machines in this regard.

Table 6. Radial force ripple for different slot/pole combinations of PMSM and MPMSM in the presence of DE.

ECC / Q/2p	0 mm (Faultless)		0.25 mm		0.50 mm		0.75 mm		1.00 mm		Main HO	
	Mod [N]	Mon [N]	Mod [N]	Mon [N]	Mod [N]	Mon [N]	Mod [N]	Mon [N]	Mod [N]	Mon [N]	Mod [-]	Mon [-]
18S 12P	0	0	4	2	12	4	23	7	38	9	18	18
18S 20P	0	0	81	83	160	164	235	242	304	314	18	18
24S 20P	0	0	3	1	6	3	10	7	22	13	24	24
24S 22P	0	0	10	11	22	24	37	39	55	58	24	24
24S 28P	0	0	1	1	2	1	3	3	7	5	24	24

Table 7 summarizes the average value of the radial force generated by different SE magnitudes for both the modular and monolithic machines. In concordance with the tendencies of Figure 4e,f and similarly to DE, it can be seen that the generated radial forces are directly proportional to the eccentricity magnitude. Nevertheless, and as occurred in the case of DE, modular machines have significantly lower radial forces when the value of q is high, for the reasons explained in Figure 5. From Table 7, it can also be seen that the unbalanced magnetic force increases as the slot number and pole number increase. Finally, when comparing Table 4 with Table 7, it may be appreciated that the force magnitude generated by DE is similar to that of SE.

Table 7. Average UMF for different slot/pole combinations of PMSM and MPMSM in the presence of SE.

ECC / $Q_s/2p$	q	0 mm (Faultless)		0.25 mm		0.50 mm		0.75 mm		1.00 mm	
		Mod [N]	Mon [N]	Mod [N]	Mon [N]	Mod [N]	Mon [N]	Mod [N]	Mon [N]	Mod [N]	Mon [N]
18S 12P	1/2	0	0	92	115	183	231	276	348	370	466
18S 20P	3/10	0	0	148	151	296	303	446	457	599	614
24S 20P	2/5	0	0	180	194	362	389	546	587	733	790
24S 22P	4/11	0	0	192	200	384	400	580	604	779	812
24S 28P	2/7	0	0	203	208	408	419	617	634	833	855

In Table 8, the radial force ripple generated by different magnitudes of SE is presented for each slot/pole combination. Similar to DE, slot/pole combinations with a lower difference between the slot count and the pole count exhibit the highest force ripple. Again, the 18-slot, 20-pole machines provide the highest ripple of around 40% of the average radial forces. Different to what was observed for DE, in the case of SE, the main HO of the torque ripple matches the pole number, and there are no considerable differences between the modular and the monolithic machines.

Table 8. Radial force ripple for different slot/pole combinations of PMSM and MPMSM in the presence of SE.

ECC / $Q_s/2p$	0 mm (Faultless)		0.25 mm		0.50 mm		0.75 mm		1.00 mm		Main HO	
	Mod [N]	Mon [N]	Mod [N]	Mon [N]	Mod [N]	Mon [N]	Mod [N]	Mon [N]	Mod [N]	Mon [N]	Mod [-]	Mon [-]
18S 12P	0	0	4	2	12	4	23	6	36	8	12	12
18S 20P	0	0	81	83	160	165	236	244	307	318	20	20
24S 20P	0	0	2	1	5	3	10	6	20	12	20	20
24S 22P	0	0	11	12	22	24	37	40	55	60	22	22
24S 28P	0	0	1	0	2	1	3	2	7	5	28	28

4.3. Summary: DE and SE on the UMF of PMSMs and MPMSMs

In summary, it was found that radial forces on machines with SE and DE scale with the slot number and pole number, and that the severity of these forces is lower in the case of modular machines depending on the value of q. Moreover, a force ripple of significant magnitude appears in machines in which the slot number and pole number are close to each other.

5. Results and Discussion: Cogging Torque

5.1. DE: Evaluation of 24-Slot, 22-Pole PMSM and MPMSM

In Figure 6, the cogging torque outcomes of the FE evaluation of a 24-slot, 22-pole PMSM and a 24-slot, 22-pole MPMSM are presented for DE. The results were extracted considering the rotor structure completes 360 mechanical degrees to correctly obtain the harmonic content of the cogging torque signal. However, only the main period (when eccentricity is present) is shown in the figure in order to provide a clearer visualization. In Figure 6a,c, the cogging torque waveforms are shown for a 24-slot, 22-pole MPMSM and PMSM respectively. In turn, Figure 6b,d present the harmonic spectrum of the cogging torque waveform for both machines, modular and conventional, when dynamic eccentricity (DE) is present.

The main period of the cogging torque was found to be 1.36 mechanical degrees when no eccentricity is applied in both cases. This changes when DE is present: the main period changes to 15 degrees, which corresponds to the slot pitch. This can be explained since in conventional PMSMs, the cogging torque main period is defined by the periodicities of the stator and rotor structures when no eccentricity is present (native harmonic content) and is accounted by [34]:

$$T_{\mathrm{T\ NHC}} = \frac{360}{\mathrm{LCM}(\mathrm{Q_s}, 2p)}. \tag{2}$$

This results in 1.36° for the 24-slot, 22-pole machine. However, when dimensional tolerances are affecting the machine, the stator/rotor periodicity breaks. For the case of DE, the minimum airgap is rotating with the rotor and the modules are stationary, and hence, the relative position between magnet symmetry axis and teeth symmetry axis is periodical and repeats each $360/Q_\mathrm{s}$ mechanical degrees. Therefore, the main cogging torque period should change to the additional harmonic components generated, given by:

$$T_{T\ \mathrm{AHC\ DE}} = \frac{360}{Q_\mathrm{s}}, \tag{3}$$

which happens to occur for the 24-slot, 22-pole machine and generates a significant increase in the peak-to-peak value of the cogging torque. The cogging torque after eccentricity is therefore comprised of the native harmonic components (faultless) and the additional harmonic components (AHC) as per [34]:

$$T_{\mathrm{cogg}}(\alpha) = T_{\mathrm{NHC}}(\alpha) + T_{\mathrm{AHC}}(\alpha) \tag{4}$$

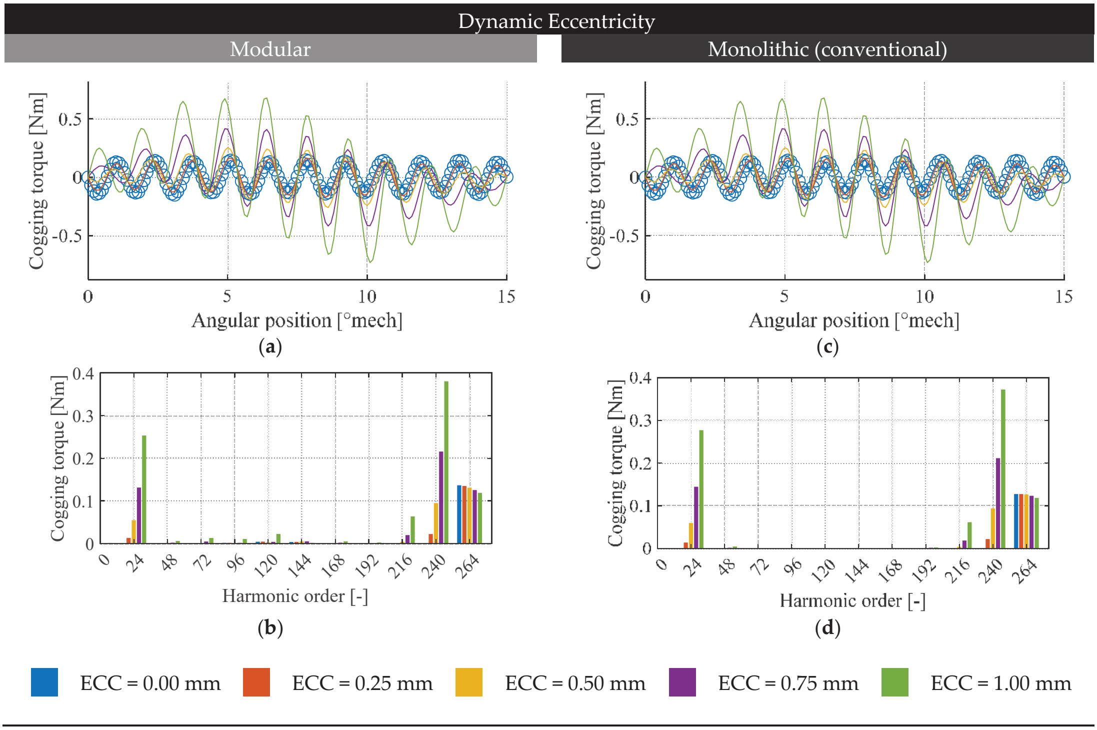

(**a**)

(**c**)

(**b**)

(**d**)

Figure 6. FE evaluation of cogging torque in the presence of DE for the 24-slot, 22-pole PMSM and MPMSM: (**a**) cogging torque waveform for the modular machine, (**b**) cogging torque spectrum for the modular machine, (**c**) cogging torque waveform for the monolithic machine, (**d**) cogging torque spectrum for the monolithic machine.

From Figure 6, it can be noted that significant cogging torque components with HO = 24 and their multiples are generated with DE, which results in a peak-to-peak value increase of up to 400%. Nevertheless, this does not hold true for all evaluated slot/pole combinations.

In summary, relevant features of the cogging torque results can be summarized by the following indicators, useful for evaluating and comparing the different slot/pole combinations of Table 2.

- NHC of the cogging torque, measured in Nm;
- AHC of the cogging torque, measured in Nm;
- AHC of the cogging torque, measured in percentage of the NHC.

5.2. DE: Comparison of Slot/Pole Combinations for PMSMs and MPMSMs

In Table 9, the natural harmonic component of cogging torque for different DE magnitudes is presented. Both the modular and monolithic machines are evaluated considering different slot/pole combinations. From Table 9, it may be noted that the cogging torque magnitude is very different depending on the slot/pole combination and it does not have a clear scalation with respect to the slot count or pole count separately. In this regard, it is commonly accepted in faultless machines to consider the cogging torque HO ($\mathrm{HO_{NHC}}$) as a comparative indicator for cogging torque magnitude ([35], see (2)). The higher the HO, the lower the main period of the cogging torque and the lower its magnitude should be. As can be seen from Table 9, the NHC of the cogging torque is barely affected by DE, and $\mathrm{HO_{NHC}}$ is able to compare slot/pole combinations regardless of the eccentricity magnitude. It may draw the attention that a significant difference in the NHC magnitude can be observed for the 24-slot, 20-pole and the 24-slot, 28-pole machines when comparing the modular and the monolithic machine. This is related to a stator/rotor periodicity break generated by the modular structure of U-shape MPMSMs. In those cases, $\mathrm{HO_{NHC}}$ should be corrected to include the periodicity provided by the modular stator core. As an example, in the case of the 24-slot, 28-pole machine, the main period of the cogging torque is 84 for the modular machine, which explains the difference regarding the monolithic machine.

Table 9. Cogging torque NHC of different PMSM and MPMSM-slot/pole combinations in the presence of DE.

ECC $Q_s/2p$	HO_{NHC}	**0 mm (Faultless)**		**0.25 mm**		**0.50 mm**		**0.75 mm**		**1.00 mm**	
		Mod [Nm]	Mon [Nm]	Mod [Nm]	Mon [Nm]	Mod [Nm]	Mon [Nm]	Mod [Nm]	Mon [Nm]	Mod [Nm]	Mon [Nm]
18S 12P	72	19.11	22.42	19.13	22.44	19.17	22.46	19.24	22.49	19.34	22.54
18S 20P	180	0.63	0.66	0.62	0.65	0.59	0.62	0.54	0.56	0.47	0.48
24S 20P	120	3.92	2.70	3.91	2.71	3.88	2.77	3.84	2.86	3.83	2.99
24S 22P	264	0.27	0.25	0.27	0.25	0.26	0.25	0.25	0.25	0.24	0.24
24S 28P	168	2.28	0.72	2.28	0.73	2.30	0.74	2.34	0.77	2.40	0.81

In Table 10, the peak-to-peak value of the additional harmonic components of cogging torque for different DE magnitudes is summarized. Both the modular and monolithic machines are evaluated considering different slot/pole combinations. From Table 10, it is clear that the generated AHC of cogging torque is very different from a one slot/pole combination to another. Nevertheless, and contrary to what was observed for NHC, the AHC does not scale with $\mathrm{HO_{NHC}}$. This can be explained by analyzing airgap flux density. As developed in [33], a simple analytical model of the additional airgap flux density radial and circumferential components accounting for the eccentricity can be expressed by:

$$B_{\mathrm{r_{ecc}}} = B_{\mathrm{sr}}\lambda_{\mathrm{ecc}} \tag{5}$$

$$B_{\alpha\_\mathrm{ecc}} = B_{\mathrm{s}\alpha}\lambda_{\mathrm{ecc}} \tag{6}$$

where B_{sr} and $B_{\mathrm{s}\alpha}$ are the radial and circumferential air flux densities (without the presence of eccentricity) with harmonic order n, and λ_{ecc} is the real component of the equivalent complex permeance that represent the influence of eccentricity given by:

$$\lambda_{\mathrm{ecc}} = 1 + \sum_{v} \lambda_v \cos(v\alpha - \chi v \omega t) \tag{7}$$

where λ_v is the magnitude of the v-th order component of equivalent permeance representing the eccentricity and χ allows to select between SE ($\chi = 0$) and DE ($\chi = 1$). Since the stator slotting effect generates field harmonics of order $n = mp \pm \mu Q_s$, then the additional field harmonics due to eccentricity are $n \pm v$. By virtue of this, there are two scenarios in which eccentricity have an impact on the cogging torque:

- If both the additional flux density due to eccentricity and the flux density without eccentricity share harmonic spatial orders, eccentricity has an influence on the cogging torque;

- If the additional flux density due to eccentricity has a component of spatial order l resulting from different values of n and v, then eccentricity can also contribute to the cogging torque (for instance, if $l = n_1 \pm v_1 = n_2 \pm v_2$);
- In the case of machines having $2p = Q_s \pm 2$ (18-slot, 20-pole and 22-slot, 24-pole), the interaction between spatial harmonics from n and $n \pm 2$ generate the AHC; in the case of machines that have $2p = Q_s \pm 4$ (24-slot, 20-pole and 28-slot, 24-pole), the interaction between spatial harmonics from n and $n \pm 4$ generate the AHC; in the case of machines that have $2p = Q_s \pm 6$ (18-slot, 12-pole), the interaction between spatial harmonics from n and $n \pm 6$ generate the AHC. It can be noted that several field harmonic components interact in machines with $2p = Q_s \pm 2$, and interacting harmonic components decrease as the difference between the slot number and the pole number is higher. The result of this analysis is that slot/pole combinations with the slot number being close to the pole number ($2p = Q_s \pm 2$) should have a more significant effect of eccentricity on cogging torque that machines with it slot number very different from its pole number ($2p = Q_s \pm 4$ and $2p = Q_s \pm 6$). This is verified from the results presented in Table 10.

Table 10. Peak-to-peak value of cogging torque AHC of different PMSM and MPMSM slot/pole combinations in the presence of DE.

ECC $Q_s/2p$	HO_{NHC}	$\Delta(Q_s, 2p)$	**0.25 mm**		**0.50 mm**		**0.75 mm**		**1.00 mm**	
			Mod [Nm]	Mon [Nm]	Mod [Nm]	Mon [Nm]	Mod [Nm]	Mon [Nm]	Mod [Nm]	Mon [Nm]
18S 12P	72	6	0.06	0.06	0.12	0.15	0.26	0.29	0.45	0.48
18S 20P	180	2	0.20	0.20	0.74	0.78	1.59	1.70	2.80	2.95
24S 20P	120	4	0.04	0.06	0.13	0.09	0.32	0.22	0.63	0.50
24S 22P	264	2	0.08	0.09	0.30	0.31	0.72	0.73	1.39	1.36
24S 28P	168	4	0.02	0.02	0.05	0.04	0.13	0.09	0.29	0.21

The results of the 18-slot, 12-pole machines versus that of the 24-slot, 28-pole machines may draw attention since they do not exactly follow this tendency: the 18-slot, 12-pole machine has higher absolute AHC than the 24-slot, 28-pole machine, but it has a higher difference between the slot count and the pole count. However, the analysis must consider the proportion between the AHC generated by eccentricity and the NHC. From Table 9, it can be recalled that the 18-slot, 12-pole machine has a significantly higher cogging torque NHC than the 24-slot, 28-pole machine, which translates into AHC being proportionally lower than that of the 24-slot, 28-pole machine.

Table 11 is created to account for this proportion and presents the relative cogging torque increase of the different slot/pole combinations in the presence of DE. It may be appreciated that the relative cogging torque increase effectively depends on the difference between the slot count and the pole count, as indicated in the spatial field harmonic analysis. Cogging torque of modular and monolithic machines have a similar response to eccentricity, although some slot/pole combinations have mild differences due to the break of stator/rotor periodicity, as indicated in [18].

Table 11. Relative cogging torque increase of different PMSM and MPMSM slot/pole combinations in the presence of DE.

ECC $Q_s/2p$	$\Delta(Q_s, 2p)$	**0.25 mm**		**0.50 mm**		**0.75 mm**		**1.00 mm**	
		Mod [%]	Mon [%]	Mod [%]	Mon [%]	Mod [%]	Mon [%]	Mod [%]	Mon [%]
18S 12P	6	0.19	0.22	0.53	0.65	1.15	1.30	2.07	2.18
18S 20P	2	27.23	26.21	102.72	105.80	238.69	236.47	422.04	424.21
24S 20P	4	0.29	0.69	1.33	3.05	4.42	7.62	11.00	17.45
24S 22P	2	12.58	16.57	72.73	89.18	180.61	215.49	374.00	435.19
24S 28P	4	0.41	0.11	1.62	2.12	4.64	8.61	10.33	26.39

5.3. SE: Evaluation on 24-Slot, 22-Pole PMSM and MPMSM

In Figure 7, the cogging torque outcomes of the FE evaluation of a 24-slot, 22-pole PMSM and a 24-slot, 22-pole MPMSM are presented for SE. Similar to DE results, SE results were extracted considering the rotor structure completes one full turn to correctly obtain the harmonic content of the cogging torque signal. However, only the main period (when eccentricity is present) is presented in order to provide a clearer visualization. In Figure 7a,c, the cogging torque waveform is shown for a 24-slot, 22-pole MPMSM and PMSM, respectively. In turn, Figure 7b,d present the harmonic spectrum of the cogging torque waveform for both machines, modular and conventional, when SE is present.

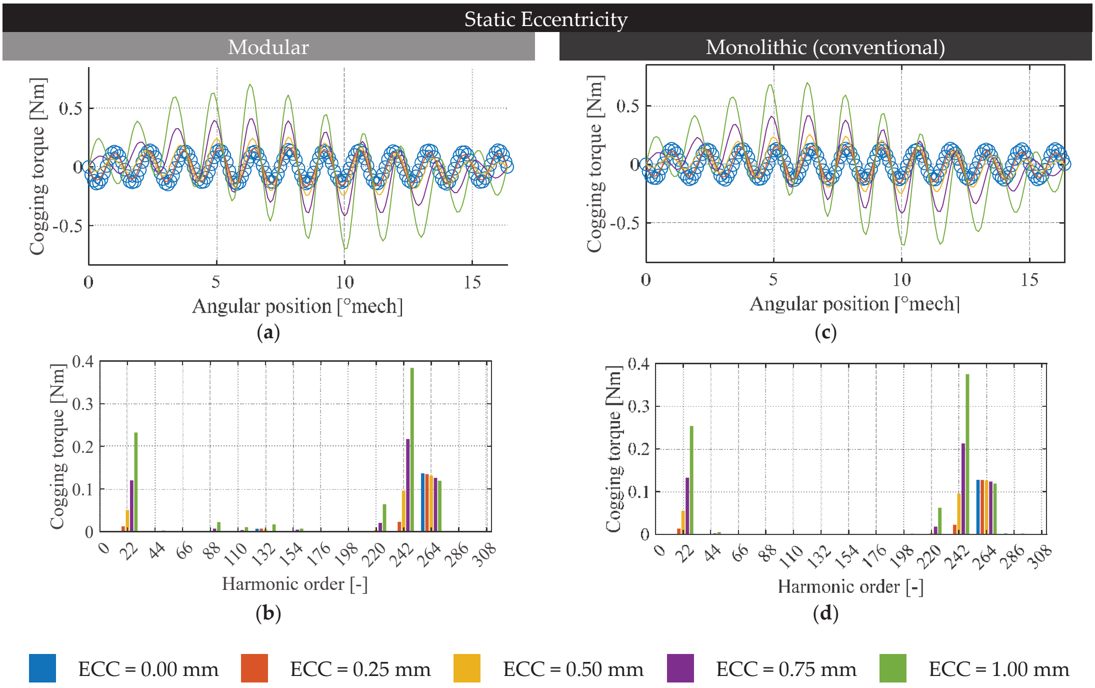

Figure 7. FE evaluation of cogging torque in the presence of SE for 24-slot, 22-pole PMSM and MPMSM: (**a**) cogging torque waveform for the modular machine, (**b**) cogging torque spectrum for the modular machine, (**c**) cogging torque waveform for the monolithic machine, (**d**) cogging torque spectrum for the monolithic machine.

When SE is present, the main period of the cogging torque changes from 1.36 to 16.36 mechanical degrees, which corresponds to the pole pitch. From (2), it may be noted that the cogging torque main period is defined by the periodicities of the stator and rotor structures when no eccentricity is present, but eccentricity breaks the stator/rotor periodicity. For the case of SE, the minimum airgap is stationary, and the relative position between the magnet symmetry axis and teeth symmetry axis depends exclusively on the movement of the poles, which is periodical and repeats each $360/2p$ mechanical degrees. Therefore, the main cogging torque period should change to the additional harmonic components generated, given by:

$$T_{T\ \mathrm{AHC\ SE}} = \frac{360}{2p}, \tag{8}$$

From Figure 7, it can be noted that significant cogging torque components with HO = 22 and its multiples are generated with SE, which results in a peak-to-peak value increase of up to 400%. Nevertheless, this does not hold true for all evaluated slot/pole combinations.

5.4. SE: Comparison of Slot/Pole Combinations for PMSMs and MPMSMs

In Table 12, the natural harmonic component of cogging torque for different SE magnitudes is presented. Both the modular and monolithic machines are evaluated considering different slot/pole combinations. From Table 12, it can be seen that the NHC of the cogging torque is barely affected by SE and, therefore, the natural cogging torque HO ($T_{T\ NHC}$) can be used as a comparative indicator for cogging torque magnitude. Similar to the results obtained for SE, from Table 12, it can be noted that HO_{NHC} is able to compare slot/pole combinations regardless of the eccentricity magnitude.

Table 12. Cogging torque NHC of different PMSM and MPMSM slot/pole combinations in the presence of SE.

ECC / $Q_s/2p$	HO_{NHC}	**0 mm (Faultless)**		**0.25 mm**		**0.50 mm**		**0.75 mm**		**1.00 mm**	
		Mod [Nm]	Mon [Nm]	Mod [Nm]	Mon [Nm]	Mod [Nm]	Mon [Nm]	Mod [Nm]	Mon [Nm]	Mod [Nm]	Mon [Nm]
18S 12P	72	19.10	22.42	19.13	22.44	19.16	22.46	19.20	22.49	19.24	22.54
18S 20P	180	0.63	0.66	0.62	0.66	0.60	0.63	0.57	0.59	0.52	0.54
24S 20P	120	3.90	2.66	3.90	2.68	3.87	2.74	3.83	2.82	3.82	2.96
24S 22P	264	0.27	0.25	0.27	0.25	0.26	0.25	0.25	0.25	0.24	0.24
24S 28P	168	2.28	0.72	2.28	0.73	2.30	0.75	2.34	0.78	2.40	0.81

In Table 13, the relative cogging increase of the cogging torque for different SE magnitudes is summarized, which is calculated as the ratio between the peak-to-peak value of the AHC and the NHC. Both the modular and monolithic machines are evaluated considering different slot/pole combinations. From Table 13, it is clear that the generated AHC of cogging torque is very different from a slot/pole combination to another. It may be appreciated that the relative cogging torque increase depends on $\Delta(Q_s, 2p)$ in a similar manner to what was observed for DE (see Table 11). This tendency is defined by the spatial field harmonics that interact to generate cogging torque for each machine as per (5) to (7). Furthermore, the cogging torque of modular and monolithic machines have a similar response to eccentricity.

Table 13. Relative cogging torque increase of different PMSM and MPMSM slot/pole combinations in the presence of SE.

ECC $Q_s/2p$	HO_{NHC}	$\Delta(Q_s, 2p)$	**0.25 mm**		**0.50 mm**		**0.75 mm**		**1.00 mm**	
			Mod [%]	Mon [%]	Mod [%]	Mon [%]	Mod [%]	Mon [%]	Mod [%]	Mon [%]
18S 12P	72	6	0.19	0.22	0.54	0.66	1.17	1.31	2.05	2.19
18S 20P	180	2	28.92	24.87	117.38	107.98	260.77	244.69	462.91	439.94
24S 20P	120	4	0.41	0.83	1.52	2.89	4.63	7.72	11.22	17.86
24S 22P	264	2	12.31	16.10	67.51	87.25	178.98	210.45	373.15	417.45
24S 28P	168	4	0.55	0.59	1.46	2.72	4.37	9.48	10.14	25.80

5.5. Summary: SE and DE on Cogging Torque of PMSMs and MPMSMs

In summary, it was found that the cogging torque can be separated into two components: NHC, which are originally present in the faultless machine, and AHC, which appears due to eccentricity. In this regard:

- NHC is not affected by eccentricity, and its magnitude can be related to the slot/pole combination by means of the main harmonic order of the cogging torque, which can be determined as the least common multiple of slot and pole number.
- AHC is affected by eccentricity and can translate into severe peak-to-peak increases of the cogging torque. Machines that have a slot number close to their pole number are very sensitive to eccentricity and develop a higher cogging torque increase. In terms of magnitude, there are no significant differences between DE and SE. However, the order of the AHC generated by DE are multiples of the slot number, and the order of the AHC generated by SE are multiples of the pole number.
- Modular machines may have different native harmonic components when compared to their monolithic counterparts due to the stator/rotor periodicity break when adopting a modular stator core. Nevertheless, AHC is generated to a similar extent in both modular and monolithic machines.

These findings can be used for diagnosis ends: in machines with their slot number close to their pole number, anomalous cogging torque increases with certain harmonic orders can indicate the presence of SE or DE.

6. Results and Discussion: Back-Emf

6.1. DE: Evaluation on a 24-Slot, 22-Pole PMSM and MPMSM

In Figure 8, the back-emf outcomes of the FE evaluation of a 24-slot, 22-pole PMSM and a 24-slot, 22-pole MPMSM are presented for DE. The results were extracted considering the rotor structure completes one full turn to correctly obtain the harmonic content of the back-emf signal, which is depicted in the figures. In Figure 8a,c, the three-phase back-emf waveforms are presented for a 24-slot, 22-pole MPMSM and PMSM, respectively. In turn, Figure 8b,d show the harmonic spectrum of the back-emf for both machines, modular and conventional, when DE is present.

From Figure 8, it can be noted that the back-emf waveform is composed of a high magnitude fundamental component and a third-order harmonic component of low magnitude. In addition, it is evident that eccentricity does not have a significant impact on the back-emf magnitude, and no significant unbalance between phases is observed either, contrary to what was suggested in [30].

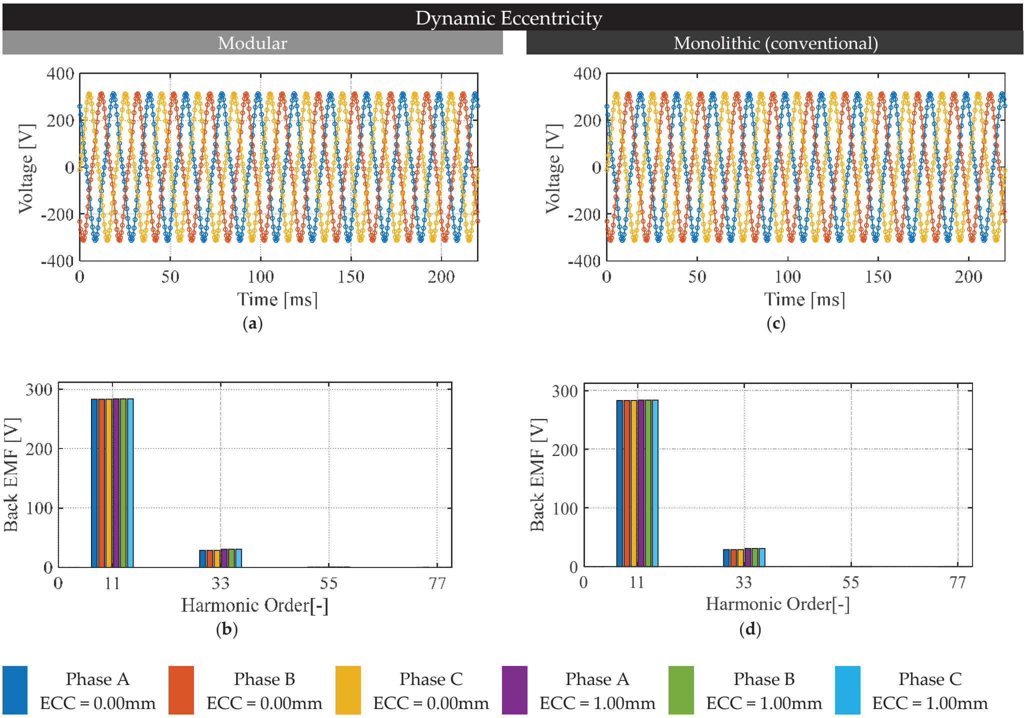

Figure 8. FE evaluation of the back-emf in the presence of DE for a 24-slot, 22-pole PMSM and MPMSM: (**a**) back-emf waveform for the modular machine, (**b**) back-emf spectrum for the modular machine, (**c**) back-emf waveform for the monolithic machine, (**d**) back-emf spectrum for the monolithic machine.

A significant back-emf unbalance was observed in [30] when evaluating eccentricity on a 9-slot, 8-pole PMSM with conventional stator core. This can be explained by analyzing the spatial distribution of phases of that 9-slot, 8-pole machine when compared to an 8-slot, 12-pole PMSM, which are represented in Figure 9a,b, respectively.

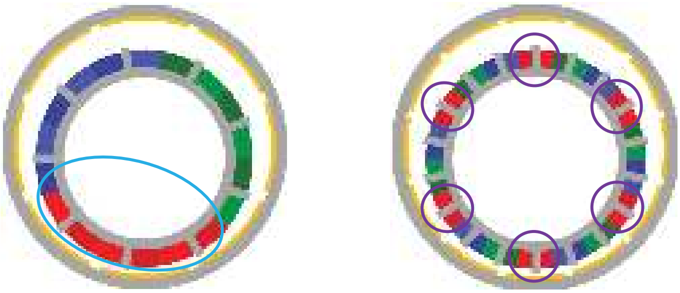
(**a**) (**b**)

Figure 9. Schematics of (**a**) a 9-slot, 8-pole PMSM with conventional stator core subject to eccentricity. In this case, the phase windings form a single group of conductors (light blue oval) distributed in a specific part of the stator circumference and (**b**) an 18-slot, 12-pole PMSM with conventional stator core subject to eccentricity. In this case, the phase windings form six group of conductors (light blue oval) evenly distributed in the stator circumference, damping the potential back-emf unbalance.

For the case of the 9-slot, 8-pole PMSM, when eccentricity is applied, the minimum airgap position can increase or decrease the back-emf magnitude of a phase depending on how close it is to the phase windings, since it can strengthen or weaken the linked flux. As can be seen from the schematics of Figure 9a, phase A is strengthened as the airgap in front of phase A is smaller, and the back-emf of phase B and C should be lower since the equivalent airgap is larger than the original. In that case, the phase windings are not evenly distributed in the stator circumference, which translates into an unbalanced back-emf waveform when eccentricity is present. By the contrary, in the case of the 18-slot, 12-pole machine shown in Figure 9b, the phase windings are forming six groups of conductors evenly distributed in the stator circumference. Even when the rotor and stator are misaligned, the flux linked by a phase is strengthened on one side of the machine but weakened on the other side of the machine, which results into a low-to-null variation of the back-emf. The number of evenly distributed phase groups will be denoted by N_{pg} from now on.

In summary, relevant features of the back-emf results can be summarized by the following indicators, useful to evaluate and compare the different slot/pole combinations of Table 2.

- Fundamental component of the back-emf, measured in V;
- Third-order harmonic of the back-emf, measured in V;
- Maximum unbalance between phases, measured in V.

6.2. DE: Comparison of Slot/Pole Combinations for PMSMs and MPMSMs

In Table 14, the fundamental component of back-emf in the presence of the maximum DE magnitude (1.00 mm) is presented for both the modular and monolithic machines considering different slot/pole combinations. As in the case of the 24-slot, 22-pole machine, no significant effect is observed in the back-emf fundamental and third-order harmonics caused by eccentricity.

Table 14. Fundamental component and third-order harmonic of back-emf for different PMSM and MPMSM slot/pole combinations in the presence of DE.

ECC / $Q_s/2p$		**0 mm (Faultless)**						**1.00 mm**					
		Modular [V]			Monolithic [V]			Modular [V]			Monolithic [V]		
	HO	A	B	C	A	B	C	A	B	C	A	B	C
18S 12P	1st	247.5	247.5	247.5	263.7	263.8	263.7	247.6	247.7	247.6	263.7	263.9	263.7
	3rd	21.9	21.9	21.9	24.6	24.0	24.6	22.0	22.0	22.0	24.8	24.4	24.9
18S 20P	1st	281.0	281.1	281.0	275.4	275.5	275.4	281.7	281.7	281.6	276.2	276.2	276.2
	3rd	31.6	31.6	31.6	35.9	36.0	36.0	33.3	33.3	33.3	37.8	37.8	37.8
24S 20P	1st	276.7	276.7	276.6	275.9	275.9	275.8	277.5	277.5	277.5	276.7	276.6	276.6
	3rd	37.9	37.9	37.9	37.8	37.8	37.9	40.5	40.6	40.6	39.7	39.7	39.7
24S 22P	1st	283.4	283.4	283.3	283.2	283.2	283.2	284.1	284.1	284.1	283.9	283.9	283.9
	3rd	28.7	28.7	28.7	29.0	28.9	29.0	30.7	30.7	30.7	30.8	30.8	30.9
24S 28P	1st	300.9	300.9	300.9	292.5	292.5	292.5	303.4	303.4	303.4	294.8	294.8	294.8
	3rd	9.5	9.5	9.7	18.9	18.9	19.1	9.6	9.6	9.8	19.8	19.8	19.8

In Table 15, the maximum unbalance between phases in the presence of the maximum DE magnitude (1.00 mm) is presented for both the modular and monolithic machines considering different slot/pole combinations. It can be noted that the number of phase groups evenly distributed in the stator circumference is a strong indicator of the magnitude of back-emf unbalance for a given slot/pole combination. No significant differences were found by comparing the results of modular and monolithic machines.

Table 15. Maximum back-emf unbalance for different PMSM and MPMSM slot/pole combinations in the presence of DE.

ECC	Modular [V]	Monolithic [V]	N_{pg}
18S 12P	0.526	0.657	6
18S 20P	10.386	9.091	2
24S 20P	1.331	1.312	4
24S 22P	6.660	6.286	2
24S 28P	1.065	1.301	4

6.3. SE: Evaluation on a 24-Slot, 22-Pole PMSM and MPMSM

In Figure 10, the back-emf outcomes of the FE evaluation of a 24-slot, 22-pole PMSM and a 24-slot, 22-pole MPMSM are presented for SE. The results were extracted considering the rotor structure completes one full turn to correctly obtain the harmonic content of the back-emf signal, which is depicted in the figures. In Figure 10a,c, the three-phase back-emf waveforms are presented for a 24-slot, 22-pole MPMSM and PMSM, respectively. In turn, Figure 10b,d show the harmonic spectrum of the back-emf for both machines, modular and conventional, when SE is present.

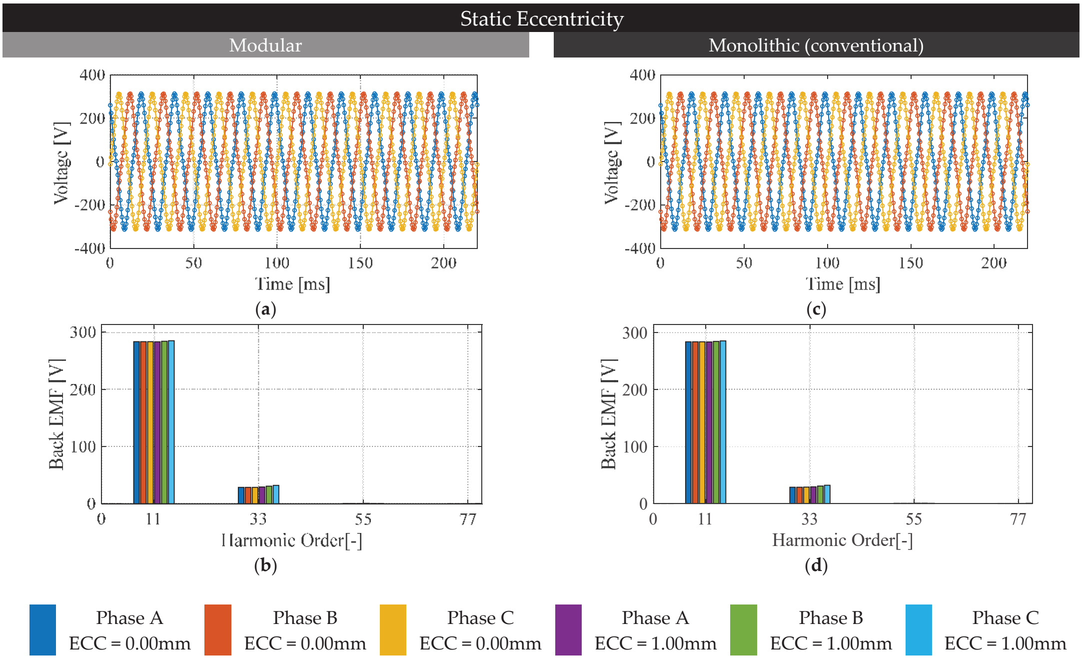

Figure 10. FE evaluation of the back-emf in the presence of SE for a 24-slot, 22-pole PMSM and MPMSM: (**a**) back-emf waveform for the modular machine, (**b**) back-emf spectrum for the modular machine, (**c**) back-emf waveform for the monolithic machine, (**d**) back-emf spectrum for the monolithic machine.

From Figure 10, and similar to what was observed in Figure 8, eccentricity does not have a significant impact on the back-emf magnitude, and no significant unbalance between phases is observed either.

6.4. SE: Comparison of Slot/Pole Combinations for PMSMs and MPMSMs

In Table 16, the fundamental component of back-emf in the presence of the maximum SE magnitude (1.00 mm) is presented for both the modular and monolithic machines considering different slot/pole combinations. As in the case of the 24-slot, 22-pole machine, no significant effect is observed in the back-emf fundamental and third-order harmonics caused by eccentricity.

Table 16. Fundamental component and third-order harmonic of back-emf for different PMSM and MPMSM slot/pole combinations in the presence of SE.

ECC / $Q_s/2p$		**0 mm (Faultless)**						**1.00 mm**					
		Modular [V]			Monolithic [V]			Modular [V]			Monolithic [V]		
	HO	A	B	C	A	B	C	A	B	C	A	B	C
18S 12P	1st	247.2	247.3	247.2	263.5	263.7	263.5	247.5	247.6	247.4	263.7	263.8	263.7
	3rd	21.9	21.9	21.9	24.5	24.1	24.5	21.9	22.0	22.1	24.6	24.6	24.6
18S 20P	1st	280.7	280.8	280.7	275.1	275.2	275.1	281.2	280.6	283.0	275.3	275.4	277.5
	3rd	31.7	31.7	31.7	36.0	36.1	36.1	30.5	32.9	36.97	36.2	36.2	41.3
24S 20P	1st	276.7	276.8	276.7	281.7	281.7	281.7	277.4	277.4	277.3	282.3	282.3	282.2
	3rd	37.9	37.8	37.9	38.6	38.6	38.6	40.3	40.4	40.4	40.4	40.4	40.5
24S 22P	1st	283.4	283.4	283.3	283.2	283.2	283.2	283.1	284.0	285.0	282.9	283.9	284.9
	3rd	28.7	28.7	28.7	29.0	29.0	29.0	29.3	30.8	32.2	29.6	31.0	32.2
24S 28P	1st	300.9	301.0	300.9	292.5	292.5	292.5	303.2	303.2	303.1	294.6	294.6	294.5
	3rd	9.5	9.5	9.6	19.0	19.0	19.1	9.7	9.7	9.7	19.8	19.8	19.8

In Table 17, the maximum unbalance between phases in the presence of the maximum SE magnitude (1.00 mm) is presented for both the modular and monolithic machines considering different slot/pole combinations. As in the case of DE, it is clear that the number of phase groups evenly distributed in the stator circumference is a strong indicator of the magnitude of back-emf unbalance for a given slot/pole combination. However, in the case of SE, this unbalance is static, which depends on the position of the minimum airgap, and it does not change from one phase to another. Notwithstanding, no significant differences were found by comparing the results of modular and monolithic machines.

Table 17. Maximum back-emf unbalance for different PMSM and MPMSM slot/pole combinations in the presence of SE.

ECC	**Modular [V]**	**Monolithic [V]**	N_{pg}
18S 12P	0.453	0.527	6
18S 20P	7.134	7.284	2
24S 20P	0.391	0.367	4
24S 22P	4.012	3.934	2
24S 28P	0.397	0.539	4

6.5. Summary: SE and DE on Back-Emf of PMSMs and MPMSMs

In summary, it was found that eccentricity has a low impact on the back-emf of the evaluated slot/pole combinations. In this regard:

- Back-emf magnitude is not affected by eccentricity, which was observed for all the evaluated slot/pole combinations and can translate into a low impact of eccentricity on the mean torque;
- Slot/pole combinations having a high number of evenly distributed phase groups (see Figure 9) are less likely to develop back-emf unbalance. That is the case for the 18- slot, 12-pole, 24-slot, 20-pole, and 24-slot, 28-pole machines.

7. Results and Discussion: Mean Torque

7.1. DE: Comparison of Slot/Pole Combinations for PMSMs and MPMSMs

In Table 18, the mean torque for different DE magnitudes is presented. Both the modular and monolithic machines are evaluated considering different slot/pole combinations. From Table 18, it can be seen that the mean torque is not affected by DE regardless of the slot/pole combination, which was expected from the back-emf results: since the flux linkage is not considerably penalized by eccentricity, the mean torque should not be decreased either.

Table 18. Mean torque of different PMSM and MPMSM slot/pole combinations in the presence of DE.

ECC $Q_s/2p$	0 mm (Faultless)		0.25 mm		0.50 mm		0.75 mm		1.00 mm	
	Mod [Nm]	Mon [Nm]	Mod [Nm]	Mon [Nm]	Mod [Nm]	Mon [Nm]	Mod [Nm]	Mon [Nm]	Mod [Nm]	Mon [Nm]
18S 12P	147.8	171.8	148.0	172.0	147.8	171.8	147.9	171.8	148.0	171.9
18S 20P	218.9	226.1	218.7	225.8	218.9	226.0	218.9	226.0	219.0	226.2
24S 20P	208.4	215.4	207.6	214.6	207.6	214.6	208.1	215.1	208.3	215.3
24S 22P	216.2	218.4	216.2	218.4	216.3	218.5	216.4	218.6	216.6	218.8
24S 28P	207.4	232.4	207.2	232.2	207.4	232.4	207.8	232.7	208.5	233.4

It could be noted that the 18-slot, 12-pole modular machine develops significantly lower mean torque than the monolithic counterpart. This can be explained by the same analysis carried out for the radial forces in Section 4.2 (see Figure 5): the absence of ferromagnetic material between stator modules penalizes the flux linkage in machines having a high value of q.

7.2. SE: Comparison of Slot/Pole Combinations for PMSMs and MPMSMs

In Table 19, the mean torque developed by the machines for different SE magnitudes is summarized, considering different slot/pole combinations. From Table 19, and complementing the findings of Table 18, it is apparent that the mean torque is not affected by DE either. The mean torque difference between machines with eccentricity and faultless machines is always lower than 0.5%.

Table 19. Mean torque of different PMSM and MPMSM slot/pole combinations in the presence of SE.

ECC $Q_s/2p$	0 mm (Faultless)		0.25 mm		0.50 mm		0.75 mm		1.00 mm	
	Mod [Nm]	Mon [Nm]	Mod [Nm]	Mon [Nm]	Mod [Nm]	Mon [Nm]	Mod [Nm]	Mon [Nm]	Mod [Nm]	Mon [Nm]
18S 12P	147.7	171.7	147.7	171.8	147.7	171.7	147.7	171.8	147.8	171.8
18S 20P	218.2	225.3	218.4	225.5	218.4	225.5	218.6	225.7	218.7	225.9
24S 20P	207.9	214.9	208.0	215.0	208.0	215.0	208.3	215.3	208.4	215.3
24S 22P	216.2	218.4	216.2	218.4	216.3	218.5	216.4	218.6	216.6	218.8
24S 28P	207.3	232.2	207.2	232.2	207.4	232.4	207.8	232.7	208.1	232.9

7.3. Summary: SE and DE on the Mean Torque of PMSMs and MPMSMs

In summary, it was found that eccentricity has a negligible impact on the mean torque of the evaluated slot/pole combinations. Modular machines may develop a lower mean torque than monolithic machines depending on the number of slots per pole per phase.

8. Conclusions

In this paper, the impact of eccentric tolerances on relevant performance indices of MPMSMs was identified and described for different slot/pole combinations, as well as compared with equivalent machines with conventional monolithic stator. Both static and dynamic eccentricity were assessed for five slot/pole combinations, and the radial forces, cogging torque, back-EMF, and mean torque were analyzed. It was found that:

- Radial forces on machines with SE and DE scale with the slot number and pole number, and that the severity of these forces is lower in the case of modular machines with a high value of slots per pole per phase. In addition, a high-frequency force ripple of significant magnitude is present in machines with a slot number and pole number close to each other.
- When assessing the cogging torque, additional harmonic components (AHC) of severe magnitude are generated due to eccentricity. In this regard, machines which slot number is close to its pole number are very sensitive to eccentricity and develop a substantial cogging torque increase of up to 400%. There are no significant differences between DE and SE in terms of the cogging torque increase magnitude. Nevertheless, the harmonic order of the AHC generated by DE corresponds to the slot number and multiples, while the order of the AHC generated by SE is equivalent to pole number and its multiples.
- Back-emf magnitude and mean torque are not affected by eccentricity, indistinctly for DE or SE. This was observed for all the evaluated slot/pole combinations. However, slot/pole combinations with a low number of evenly distributed phase groups can develop a mild back-emf unbalance.

The findings of this analysis can be used in the design stage of a MPMSM and aim to enable the inclusion of the sensitiveness of each performance indicator to quickly compare the performance between slot/pole combinations. Furthermore, the observed results for the cogging torque and radial forces can be used for diagnosis ends: in MPMSMs with a slot number close to their pole number, anomalous cogging torque increases can indicate the presence of SE or DE, which can be distinguished by the harmonic order of the cogging torque signal.

Author Contributions: Conceptualization, D.R., C.M., and W.J.; methodology, D.R., W.J., and G.B.; software, D.R. and C.M.; validation, D.R. and C.M.; formal analysis, D.R. and W.J.; investigation, D.R.; resources, W.J., J.R., J.A.T., and G.B.; data curation, D.R. and C.M.; writing—original draft preparation, D.R., C.M., W.J., G.B., and J.R.; writing—review and editing, D.R., W.J., G.B., and J.A.T.; visualization, D.R.; supervision, W.J., J.A.T., and G.B.; project administration, W.J.; funding acquisition, W.J., J.R., and G.B. All authors have read and agreed to the published version of the manuscript.

Funding: This work is supported in part by the Agencia Nacional de Investigación y Desarrollo (ANID), Chile through grant ANID-PFCHA/Doctorado Nacional/2020-21200350, project FONDECYT REGULAR #1201667, and project FONDEF ID21I10099.

Institutional Review Board Statement: Not applicable.

Informed Consent Statement: Not applicable.

Data Availability Statement: Data are contained within the article.

Conflicts of Interest: The authors declare no conflict of interest.

References

1. Ullah, S.; McDonald, S.P.; Martin, R.; Benarous, M.; Atkinson, G.J. A Permanent Magnet Assist, Segmented Rotor, Switched Reluctance Drive for Fault Tolerant Aerospace Applications. *IEEE Trans. Ind. Appl.* **2019**, *55*, 298–305. [CrossRef]
2. Kang, H.; Zhou, L.; Wang, J.; Peng, X. Investigation of multiphase modular stator SPM with fault tolerance. In Proceedings of the 2014 17th International Conference on Electrical Machines and Systems (ICEMS), Hangzhou, China, 22–25 October 2014; pp. 1572–1575. [CrossRef]
3. Zhao, W.; Xu, L.; Liu, G. Overview of permanent-magnet fault-tolerant machines: Topology and design. *CES Trans. Electr. Mach. Syst.* **2018**, *2*, 51–64. [CrossRef]

4. Zheng, P.; Sui, Y.; Zhao, J.; Tong, C.; Lipo, T.A.; Wang, A. Investigation of a Novel Five-Phase Modular Permanent-Magnet In-Wheel Motor. *IEEE Trans. Magn.* **2011**, *47*, 4084–4087. [CrossRef]
5. Liu, G.; Chen, M.; Zhao, W.; Chen, Q.; Zhao, W. Design and Analysis of Five-Phase Fault-Tolerant Interior Permanent-Magnet Vernier Machine. *IEEE Trans. Appl. Supercond.* **2016**, *26*, 1–5. [CrossRef]
6. Dusek, J.; Arumugam, P.; Brunson, C.; Amankwah, E.K.; Hamiti, T.; Gerada, C. Impact of Slot/Pole Combination on Inter-Turn Short-Circuit Current in Fault-Tolerant Permanent Magnet Machines. *IEEE Trans. Magn.* **2016**, *52*, 1–9. [CrossRef]
7. Jiang, X.; Xu, D.; Gu, L.; Li, Q.; Xu, B.; Li, Y. Short-Circuit Fault-Tolerant Operation of Dual-Winding Permanent-Magnet Motor Under the Four-Quadrant Condition. *IEEE Trans. Ind. Electron.* **2019**, *66*, 6789–6798. [CrossRef]
8. Bianchini, C.; Torreggiani, A.; David, D.; Davoli, M.; Bellini, A. Fault Tolerance Analysis of a Ironless PM Machine for Energy Storage. In Proceedings of the 2020 IEEE Energy Conversion Congress and Exposition (ECCE), Detroit, MI, USA, 11–15 October 2020; pp. 4499–4504. [CrossRef]
9. Deng, W.; Zuo, S. Electromagnetic Vibration and Noise of the Permanent-Magnet Synchronous Motors for Electric Vehicles: An Overview. *IEEE Trans. Transp. Electrif.* **2019**, *5*, 59–70. [CrossRef]
10. Tahanian, H.; Aliahmadi, M.; Faiz, J. Ferrite Permanent Magnets in Electrical Machines: Opportunities and Challenges of a Non-Rare-Earth Alternative. *IEEE Trans. Magn.* **2020**, *56*, 1–20. [CrossRef]
11. Bird, J.Z. A Review of Electric Aircraft Drivetrain Motor Technology. *IEEE Trans. Magn.* **2022**, *58*, 1–8. [CrossRef]
12. Gan, C.; Chen, Y.; Qu, R.; Yu, Z.; Kong, W.; Hu, Y. An Overview of Fault-Diagnosis and Fault-Tolerance Techniques for Switched Reluctance Machine Systems. *IEEE Access* **2019**, *7*, 174822–174838. [CrossRef]
13. Sarigiannidis, A.G.; Beniakar, M.E.; Kakosimos, P.E.; Kladas, A.G.; Papini, L.; Gerada, C. Fault Tolerant Design of Fractional Slot Winding Permanent Magnet Aerospace Actuator. *IEEE Trans. Transp. Electrif.* **2016**, *2*, 380–390. [CrossRef]
14. Chen, H.; Liu, X.; Zhao, J.; Demerdash, N.A.O. Magnetic-Coupling Characteristics Investigation of a Dual-Rotor Fault-Tolerant PMSM. *IEEE Trans. Energy Convers.* **2018**, *33*, 362–372. [CrossRef]
15. Petrov, I.; Di, C.; Lindh, P.; Niemelä, M.; Repo, A.; Pyrhönen, J. Fault-tolerant modular stator concentrated winding permanent magnet machine. *IEEE Access* **2020**, *8*, 7806–7816. [CrossRef]
16. Jara, W.; Petrov, I.; Tapia, J.; Lindh, P.; Pyrhönen, J. Analytical model of tooth-coil winding permanent magnet synchronous machines with modular U-Shape stator. In Proceedings of the 2016 XXII International Conference on Electrical Machines (ICEM), Lausanne, Switzerland, 4–7 September 2016; pp. 145–151.
17. Madariaga, C.; Jara, W.; Tapia, J.; Riedemann, J.; Bramerdorfer, G.; Castro, P.; Sarlioglu, B. Analytical model and sensitivity analysis of tooth-coil-winding permanent magnet synchronous machine with modular U-shape stator. In Proceedings of the 2019 IEEE Energy Conversion Congress and Exposition (ECCE), Baltimore, MD, USA, 29 September–3 October 2019; pp. 1761–1768.
18. Madariaga, C.; Jara, W.; Riquelme, D.; Bramerdorfer, G.; Tapia, J.; Riedemann, J. Impact of tolerances on the cogging torque of tooth-coil-winding PMSMs with modular stator core by means of efficient superposition technique. *Electronics* **2020**, *9*, 1594. [CrossRef]
19. Li, G.J.; Zhu, Z.Q.; Chu, W.Q.; Foster, M.P.; Stone, D.A. Influence of flux gaps on electromagnetic performance of novel modular PM machines. *IEEE Trans. Energy Convers.* **2014**, *29*, 716–726. [CrossRef]
20. Wang, H.; Zhu, H.; Ding, S.; Dai, Y.; He, C.; Wang, X. A New Partitioned Stator Field Modulation Machine With H-Shape Permanent Magnet Excitation. *IEEE Trans. Magn.* **2022**, *58*, 1–6. [CrossRef]
21. Perez, E.; Jara, W.; Madariaga, C.; Tapia, J.; Bramerdorfer, G.; Riedemann, J.; Pyrhönen, J. Comparison of Optimized Fault-Tolerant Modular Stator Machines with U-shape and H-shape Core Structure. In Proceedings of the Comparison of Optimized Fault-Tolerant Modular Stator Machines with U-shape and H-shape Core Structure, Vancouver, BC, Canada, 10–14 October 2021; pp. 4254–4259.
22. Khan, S.; Pasund, A.; Ahmad, N.; Ahmed, S.; Khan, H.A.; Cheema, K.M.; Milyani, A.H. Performance Investigation and Cogging Torque Reduction in a Novel Modular Stator PM Flux Reversal Machine. *Energies* **2022**, *15*, 2261. [CrossRef]
23. Wang, A.; Li, S. Investigation of E-Core Modular Permanent Magnet Wind Turbine. *Energies* **2020**, *13*, 1751. [CrossRef]
24. Riquelme, D.; Jara, W.; Madariaga, C.; Tapia, J.; Bramerdorfer, G.; Riedemann, J. Impact of Static and Dynamic Eccentricity on the Performance of Permanent Magnet Synchronous Machines with Modular Stator Core. In Proceedings of the 2021 IEEE Energy Conversion Congress and Exposition (ECCE), Vancouver, BC, Canada, 10–14 October 2021; pp. 3775–3780. [CrossRef]
25. Ebrahimi, B.M.; Faiz, J.; Roshtkhari, M.J. Static-, Dynamic-, and Mixed-Eccentricity Fault Diagnoses in Permanent-Magnet Synchronous Motors. *IEEE Trans. Ind. Electron.* **2009**, *56*, 4727–4739. [CrossRef]
26. Wang, Y.; Liu, K.; Hua, W.; Zhang, C.; Wu, Z.; Zhang, H. Analysis and Detection of Rotor Eccentricity in Permanent Magnet Synchronous Machines Based on Linear Hall Sensors. *IEEE Trans. Power Electron.* **2022**, *37*, 4719–4729. [CrossRef]
27. Zhang, A.; Bai, Y.; Yang, B.; Li, H. Analysis of Nonlinear Vibration in Permanent Magnet Synchronous Motors under Unbalanced Magnetic Pull. *Appl. Sci.* **2018**, *8*, 113. [CrossRef]
28. Bessous, N.; Chemsa, A.; Sbaa, S. New Vision about the Mixed Eccentricity Fault Causes in Induction Motors and its relationship with the Rolling Element Bearing Faults: Analytical model dedicated to the REB faults. In Proceedings of the 2018 International Conference on Communications and Electrical Engineering (ICCEE), El Oued, Algeria, 17–18 December 2018; pp. 1–11. [CrossRef]
29. Zhu, Z.Q.; Jamil, M.L.M.; Wu, L.J. Influence of slot and pole number combinations on unbalanced magnetic force in permanent magnet machines. In Proceedings of the 2011 IEEE Energy Conversion Congress and Exposition, Phoenix, AZ, USA, 17–22 September 2011; pp. 3291–3298. [CrossRef]

30. Park, J.-C.; Park, S.-H.; Kim, J.-H.; Lee, S.-G.; Lee, G.-H.; Lim, M.-S. Diagnosis and Robust Design Optimization of SPMSM Considering Back EMF and Cogging Torque due to Static Eccentricity. *Energies* **2021**, *14*, 2900. [CrossRef]
31. Lee, H.K.; Bang, T.K.; Woo, J.H.; Shin, H.S.; Choi, J.Y. Electromagnetic Characteristic Analysis of Permanent Magnet Synchronous Machine Considering Current Waveform According to Static Rotor Eccentricity. *Appl. Sci.* **2020**, *10*, 8453. [CrossRef]
32. Madariaga, C.; Jara, W.; Tapia, J.A.; Pyrhönen, J.; Lindh, P.; Riedemann, J.A. Closed-Form Solution for the Slot Leakage Inductance of Tooth-Coil-Winding Permanent Magnet Machines. *IEEE Trans. Energy Convers.* **2019**, *34*, 1572–1580. [CrossRef]
33. Zhu, Z.Q.; Wu, L.J.; Jamil, M.L.M. Influence of Pole and Slot Number Combinations on Cogging Torque in Permanent-Magnet Machines With Static and Rotating Eccentricities. *IEEE Trans. Ind. Appl.* **2014**, *50*, 3265–3277. [CrossRef]
34. Gašparin, L.; Fišer, R. Intensity of the native and additional harmonic components in cogging torque due to design parameters of permanent-magnet motors. In Proceedings of the 2009 International Conference on Power Electronics and Drive Systems (PEDS), Taipei, Taiwan, 2–5 November 2009; pp. 1062–1067. [CrossRef]
35. Guo, L.; Wang, H. Research on Stator Slot and Rotor Pole Combination and Pole Arc Coefficient in a Surface-Mounted Permanent Magnet Machine by the Finite Element Method. *World Electr. Veh. J.* **2021**, *12*, 26. [CrossRef]

electronics

MDPI

Article

Transmission Performance of Halbach Array Cylindrical Permanent Magnet Governor

Yonglong Zhu [1,2,†], Hai Wang [1,2,*,†], Henian Li [1,2], Chunlai Yang [1,2] and Jingsong Gui [3]

[1] School of Mechanical Engineering, Anhui Polytechnic University, Wuhu 241000, China
[2] Anhui Key Laboratory of Advanced Numerical Control & Servo Technology, Wuhu 241000, China
[3] Wuhu Ruilong Robot Technology Co., Ltd., Wuhu 241000, China
* Correspondence: wanghai@ahpu.edu.cn; Tel.: +86-0135-1553-3761
† These authors contributed equally to this work.

Abstract: A novel cylinder permanent magnet governor (CPMG) with Halbach segmentation is proposed in this paper. In order to improve the transmission performance of the CPMG, different permanent magnet (PM) arrangement methods are adopted. To achieve a fair comparison result, all the PMs are of the same size. The main magnetic fluxes are considered to obtain a comprehensive equivalent magnetic circuit model of the CPMG with Halbach array and analytical output torque that is calculated. The analytical method of transmitted torque for CPMG is then presented. Additionally, the effect of the average output torque of CPMG under parameters of the thickness of the copper rings, the slip rate and the effective coupling of the copper rings are investigated. Finally, the prototype platform is ready for testing on the field. The results were consistent with the results of the simulation, and the error was kept within the range of 5%. This research can provide a theoretical and practical reference for the optimal design of the transmission characteristic of CPMG.

Keywords: permanent magnet governor; Halbach array; magnetic field characteristics; output torque

Citation: Zhu, Y.; Wang, H.; Li, H.; Yang, C.; Gui, J. Transmission Performance of Halbach Array Cylindrical Permanent Magnet Governor. *Electronics* **2023**, *12*, 1161. https://doi.org/10.3390/electronics12051161

Academic Editor: Ahmed Abu-Siada

Received: 4 January 2023
Revised: 24 February 2023
Accepted: 24 February 2023
Published: 27 February 2023

1. Introduction

As a new type of transmission equipment, cylindrical permanent magnet governor (CPMG) has attracted much attention in recent years and is widely used in fan and pump systems [1,2]. Compared to traditional mechanical connections, cylindrical permanent magnet governor (CPMG) uses magnetic field coupling between a motor and a load shaft to transfer torque in the transmission system without any direct mechanical connections, which can produce less mechanical friction with over-torque protection ability as well as soft start through adjusting the coupling ratio between the conductor and magnet [3–5]. Unlike an axial permanent magnet governor, CPMG is a simple structure with fewer axial forces during operation. The permanent magnet governor operates in noncontact mode, which avoids vibration operation.

In recent years, many researchers have carried out a series of studies on permanent magnet governors. A large number of researchers are dedicated to the analysis and design optimization of the PMG with 2D and 3D FEA [6–11]. These works provide ideas on how to select meshing for FEA models, reduce numerical errors, selection of design parameters and constraints for the optimization process. Taqavi Omolbanin has calculated flux densities in different parts of the axial-flux permanent magnet machines combining the solution of Maxwell's equations and the magnetic equivalent circuit (MEC), taking into account the effects of permanent magnet (PM) reluctance, leakage flux between PM-to-PM, PM-to-rotor leakage flux at different PM edges, and the fringing flux effect. By considering these leakage fluxes as a factor called variation function in the design procedure of the machine, the analysis time is dramatically reduced compared to numerical methods while maintaining high reliability [12,13]. These works provide ideas on how to analyze the modeling of CPMG. Similarly, CPMG can also be called transmitted torque calculation considering theoretical and FEA models [12] and detailed theoretical and experimental analysis of CPMG under steady-state and transient operation [14]. In-cheol Kim designed a magnetic coupling that improves the water tightness of a marine current turbine (MCT). The results show that the new design is watertight and has lower mechanical losses [15]. Tian Mengmeng and others designed a novel flux-adjustable permanent magnet coupler (PMC) with a double-layer permanent magnet rotor (PMR) and used a two-layer arrangement of permanent magnets N-S to achieve optimum control of the speed of the torque [15–17]. Lu designed a general 3D analytical method for calculating the magnetic field distributions and eddy currents [18]. These researches are mainly focused on improving output torque through structural design for high torque applications. Furthermore, by focusing on the recent trends in electromagnetic devices, the design of magnetic gear could be mentioned here. Magnetic gears also have a similar structure to that of the CPMG, and the only difference is the inclusion of an extra component called modulation pieces between the two rotors [18–24].

From the research mentioned above, the methods are large-costly and time-consuming. This paper aims to improve the output Torque performance of the CPMG drives for different operating conditions. A comparative analysis of different magnets arrangement to ensure a torque production capability higher than traditional arrangement and the analysis is performed considering the same number of magnets. The traditional design of permanent magnet governor is mainly focused on magnetic fields and transmission properties with typical N- and S-arrangement magnetization. Halbach magnet array can generate the strongest magnetic field with the least amount of magnets, which is proposed by Klaus Halbach [24]. Halbach's permanent magnet array has a unidirectional magnetic field, which improves the air gap magnetic flux density, increases the sinusoidal magnetic field of the air gap and enhances transmission stability [20–27]. A cylindrical permanent magnet governor with a Halbach magnet array is proposed in this paper. The main magnetic fluxes are considered to obtain a comprehensive magnetic circuit model. The analytical method of transmitted torque for CPMG is then presented. Based on the comparative analysis, the CPMG model with the best performance is prototyped and tested on the inductor motor dynamometer testbed. The following sections provide a detailed description of the proposed work.

2. Materials and Methods

2.1. Cylindrical Permanent Magnet Governor with Halbach Magnet Array

CPMG is composed of the conductor rotor, which is mainly composed of a conductor barrel, a copper ring and the permanent magnet rotor. The permanent magnet rotor contains a permanent magnet tray and PMs, where the PMs are embedded in the permanent magnet tray. As shown in Figure 1, the conductor rotor is connected to the motor shaft, and the output axis is connected to the permanent magnet rotor. There is no contact between the conductor and the permanent magnet rotor, which allows a certain alignment error during installation.

When the motor is in operation, the conductor barrel connected to the motor shaft is rotating, which cuts the magnetic field generated by the permanent magnet array. An induced current is generated in the copper ring. A Lorentz force is applied to the copper ring, which generates a torque to drive the permanent magnet array. There is always a rotation speed difference between the conductor and permanent magnet array in order to ensure the presence of output torque. The rotation speed of the output shaft and output torque can be adjusted by regulation of the effective coupling area between the conductor and the permanent magnet array.

The schematic diagram of the specific speed regulation principle is shown in Figure 2. The output torque and rotation speed can be tuned through the adjustment of the effective coupling ratio (the ratio of the actual coincidence area between the conductor and the permanent magnet to the full coincidence area). The maximum output torque can be realized when the permanent rotor is fully coupled to the rotor of conductors (100% effective coupling ratio).

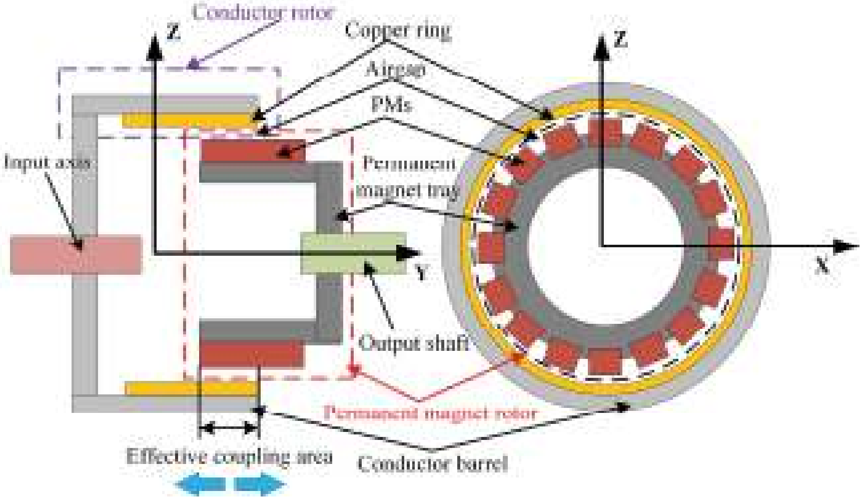

Figure 1. Structure of CPMG.

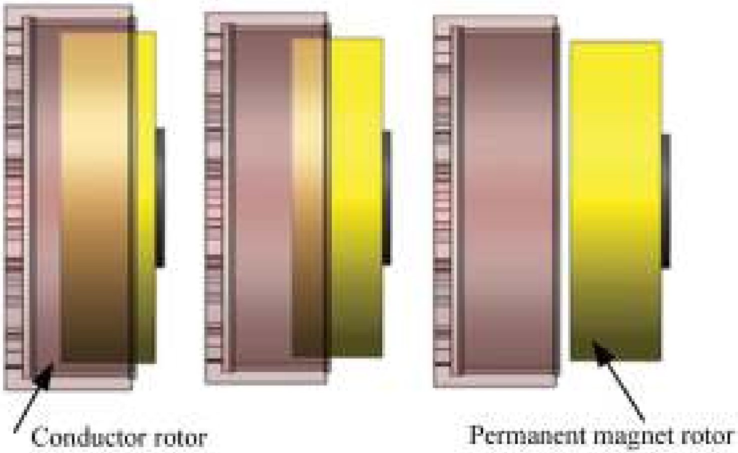

Figure 2. Speed regulation principle of CPMG.

2.2. Equivalent Magnetic Circuit of Halbach Permanent Magnet Cell and Simulation Model

In order to simplify the process for analysis, the main components of CPMG were unfolded radially into a 2D model. The magnetic field distribution was assumed to be linear in CPMG without consideration of leakage. The equivalent model of a Halbach cell is shown in Figure 3. The permanent magnet's geometry was considered to be rectangular shaped, which can be equalized to the magnetomotive. The main flux paths (solid line) were where it passes through PMs, airgap, copper ring, conductor barrel and permanent magnet tray. The leakage flux paths (dashed line) were mainly generated between adjacent permanent magnets.

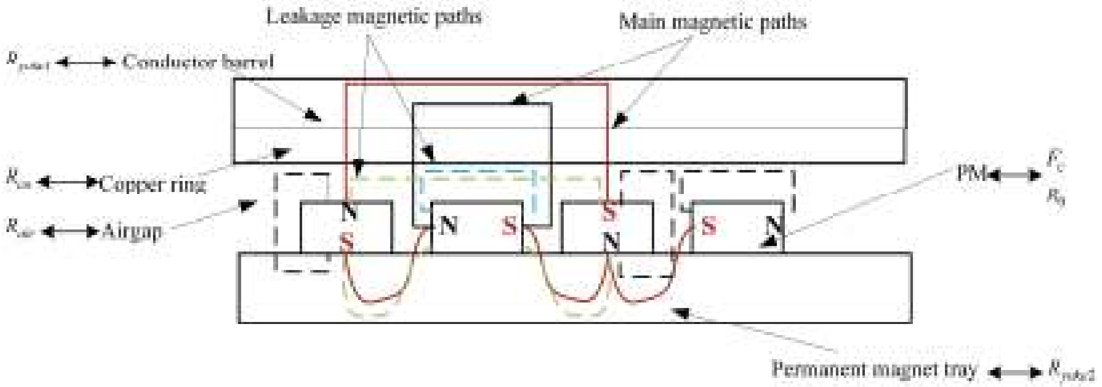

Figure 3. Equivalent magnetic model of a Halbach permanent magnet cell.

On the basic, before-mentioned Equivalent magnetic model of a Halbach permanent magnet cell analysis, the permanent magnet's geometry is considered to be rectangular shaped, which is equalized to be magnetomotive. The Conductor barrel is regarded as R_{yoke2}, the permanent magnet tray is regarded as R_{yoke1}, the copper ring is regarded as R_{cu}, and the space in between the adjacent permanent magnets is regarded as R_L. Therefore, the magnetic reluctance circuit of the Halbach permanent magnet cell is presented in Figure 4, where only a pair of Halbach array magnets is considered on account of the symmetry of the magnetic circuit.

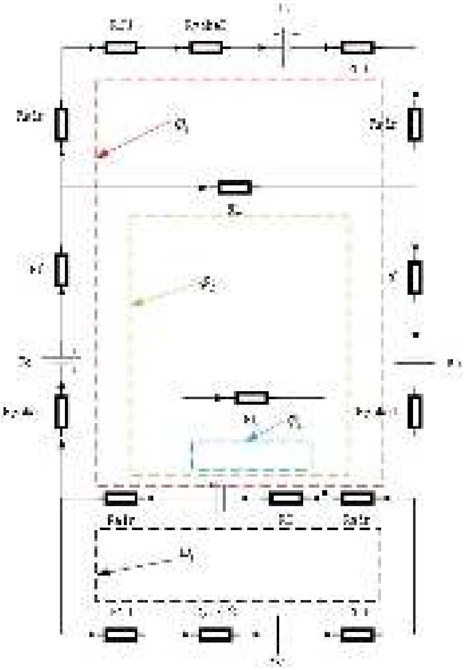

Figure 4. Magnetic reluctance circuit of Halbach permanent magnet cell.

According to the principles of equal magnetic circuits, a magnetic circuit was studied under a pair of magnetic poles, and a permanent magnet was regarded as the magnetomotive force F_c, in series with the internal reluctance r_0 of the permanent magnet, to form the magnetomotive force source.

$$F_c = H_c h_{mp} \tag{1}$$

where H_c is the coercive force of the permanent magnet, and h_{mp} is the magnetization direction length of the permanent magnet. When the permanent magnet governor is operating, the induced electromotive force in the copper ring during the cutting of the magnetic field generated by the permanent magnet array is created by the eddy current, which increases the armature magnetomotive force F_a.

The magnetic reluctance in the circuit is calculated below:

$$R = \frac{L}{\mu S} \tag{2}$$

where L represents the length and S represents the cross-section of the magnet circuit, and μ represents the magnetic permeability.

According to the current KCL law, the magnetic circuit equations of the Halbach magnet cell are built as below:

$$\begin{cases} \left(3\mathrm{R}_0 + 2R_{\mathrm{Yoke1}} + 4R_{air} + 2R_{Cu} + R_{\mathrm{yoke2}}\right)\varphi_1 + (3R_0 + 2R_{Yoke1} + 2R_{air})\varphi_2 \\ +R_0\varphi_3 + (2R_{air} + R_0)\varphi_4 = 3F_m - F_a \\ (3R_0 + 2R_{Yoke1} + 2R_{air})\varphi_1 + (2R_0 + 2R_{Yoke1} + 2R_{air} + R_L)\varphi_2 + R_0\varphi_3 \\ +(2R_{air} + R_0)\varphi_4 = 3F_m \\ R_0\varphi_1 + R_0\varphi_2 + (R_0 + R_L)\varphi_3 + R_0\varphi_4 = F_m \\ (2R_{air} + R_0)\varphi_1 + (2R_{air} + R_0)\varphi_2 + R_0\varphi_3 + (2R_{air} + 2R_{Cu} + R_{Yoke2} + R_0) \\ = F_m - F_a \end{cases} \tag{3}$$

In Equation (3), φ_1, φ_2, φ_3 and φ_4 represent the flux of air between the four magnets. Magnetic induction strength in the air gap

$$B = \frac{\phi}{A_0} \tag{4}$$

where ϕ is the average magnetic flux of the pair of polar poles and A_0 is a cross-sectional area that corresponds with the air gap.

The average electromotive force is calculated as follows:

$$\overline{F} = \frac{\pi}{2\sqrt{2}} B \omega_s N_p A_0 \tag{5}$$

The induced current inhibits the penetration of magnetic fields in the ring of copper, and it only allows magnetic fields to penetrate at a specific depth, which is called the skin effect. Due to the skin effect, the inducing currents are concentrated at the surface of the copper ring. The current decays rapidly beyond the depth of penetration. The penetration is decreased with the rotation frequency. The penetration depth expression is as follows

$$\delta = \sqrt{\frac{2}{\omega \sigma \mu}} \tag{6}$$

$$\omega = \frac{\pi \omega_s N_P}{30} \tag{7}$$

In Equation (6), ω is a radial frequency, σ is copper conductivity, and μ represents the relative permeability of copper rings. In Equation (7), ω_s is the speed difference and N_P is the number of pole pairs.

The induced eddy current region is generated by a single permanent magnet on the copper ring, which is equivalent to a circular region with a diameter of d. Therefore, the reluctance of the ring of the eddy current is shown below:

$$dR = \rho \frac{2\pi \mathrm{r}}{\delta dr} \tag{8}$$

The area of the eddy current region is as follows:

$$A_m = \pi \left(\frac{d}{2}\right)^2 \tag{9}$$

The instantaneous eddy current obtained from the above equation is:

$$i = \int_0^{\frac{d}{2}} di = \int_0^{\frac{d}{2}} \frac{\varepsilon}{dR} \tag{10}$$

The eddy current loss generated by the permanent magnet corresponding to the copper ring is

$$P_{Cu} = \frac{n \cdot A_m^2 \cdot B^2 \cdot \omega^2 \cdot \delta}{16 \cdot \pi \cdot \rho \cdot \sin(\omega^2 t)} \tag{11}$$

where n is the number of permanent magnet blocks.

Since the permanent magnet governor is connected to a constant torque load, according to the energy conservation law, which can be obtained:

$$T_1\omega_1 = T_2\omega_2 + P_{Cu} \tag{12}$$

Simulation Model

The simulation model of the CPMG is built by using Maxwell Software, as shown in Figure 5. It is mainly composed of a conductor rotor and a permanent magnet rotor, and a band motion domain. The conductor rotor contains a conductor barrel and a copper ring, where the copper ring is welded to the inner wall of the conductor barrel. The permanent magnet rotor contains a permanent magnet tray and PMs (NdFeB), where the permanent magnets are embedded in the permanent magnet array tray by means of a Halbach array. The number of PMs is 36. In addition, The band motion domain is a finite element mesh restriction and not an actual structure.

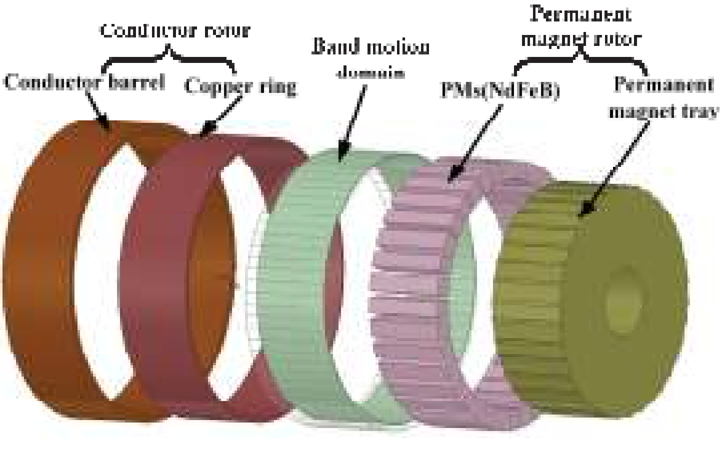

Figure 5. Simulation model of CPMG.

The material of the CPMG parts is given, of which the material of the conductor rotor and the permanent magnet rotor is Steel_1008, and the permanent magnet is selected N48H.

Due to the components of the copper ring, the induced currents in the copper ring are crucial for the transfer of the output torque to the CPMG. Therefore, it is particularly important to pay attention to the meshing subdivision of permanent magnets and the copper ring in the 3D FEM, as shown in Figure 6. In order for the higher precision results to be obtained, the quality of meshing of CPMG should be above 0.3. Moreover, it should be noted that 3D FEM results with stabilization and convergence are taken as valid data, the residual error of which is less than the set value ($\varepsilon < 0.003$).

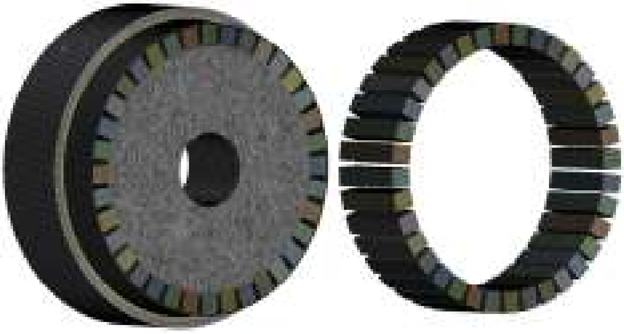

Figure 6. Meshing of CPMG.

3. Analysis of Results

3.1. Magnetic Field Distribution

The output torque of CPMG is determined by the magnet field in the air gap between the conductor and the permanent magnet. As shown in Figure 7, there are three types of permanent magnet arrangements in Figure 7.

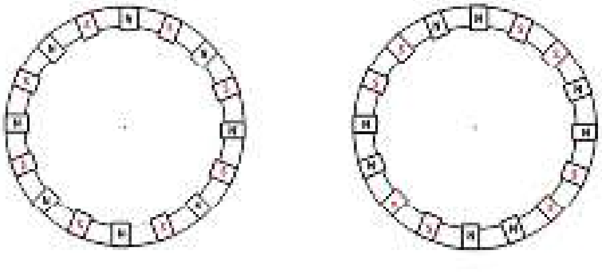

(a) Conventional Arrangement (b) Concentrate Arrangement

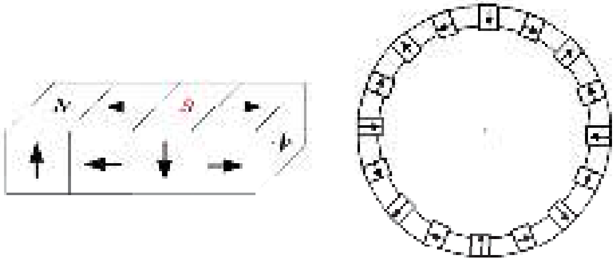

(c) Halbach Arrangement

Figure 7. Permanent magnet arrangement. (The direction of the arrow represents the direction of the magnetic poles).

The air gap flux in the above three arrangements is compared and analyzed. The distribution of magnetic field lines is studied under static magnetic field conditions, and the boundary condition is 0 vector boundary. In Figure 8, the magnetic flux density distributions are shown, and the magnetic field is more dense in the Halbach arrangement CPMG than in the conventional and concentrated arrangement. However, a small part of the magnetic field lines directly returns to the adjacent S pole through the air gap, which causes a few flux leakage. Most of the magnetic flux lines are concentrated in the air gap and the conductor side, which realizes the effect of unilateral magnetic concentration.

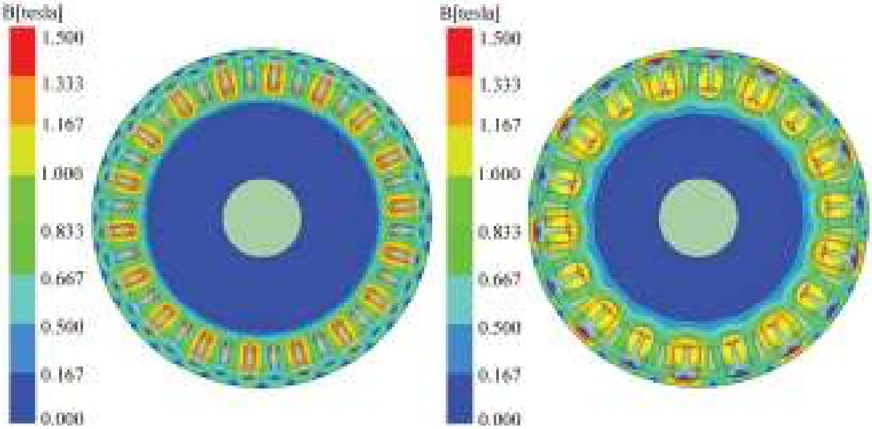

(a) Conventional Magnet Arrangement (b) Concentrate Magnet Arrangement

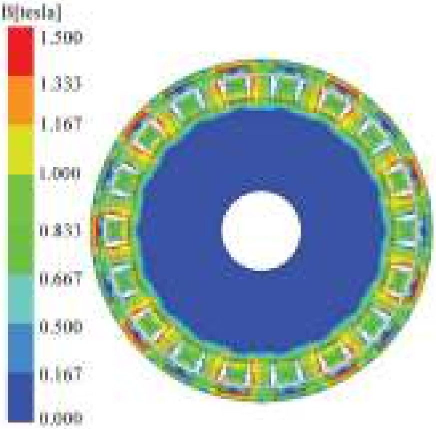

(c) Halbach Magnet Arrangement

Figure 8. Magnetic flux density distribution in CPMG.

The magnetic flux density of CPMG under the different PMs arrangements was quantitively compared. According to Figure 9, the density of magnetic flux density in the air gap is different under different magnet arrangements. It is clear that the flux density in the airgap of the Halbach arrangement is more than that of the conventional arrangement and concentrate arrangement under the same number of magnets. Because of the symmetries of a permanent magnet, the magnetic flux density curve shows the sine-variations under the Halbach arrangement, which can improve transmission stability. The magnetic characteristics in the air gap with different arrangements are listed in Table 1.

The average magnet density in air gaps with the Halbach arrangement is 13% and 6.2% higher than the other two arrangements, respectively.

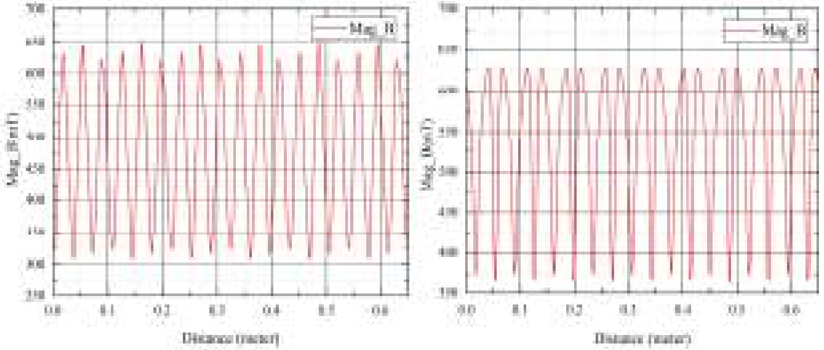

(a)Conventional Magnet Arrangement (b)Concentrate Magnet Arrangement

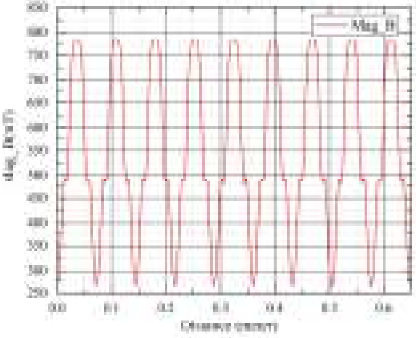

(c)Halbach Magnet Arrangement

Figure 9. Magnetic flux density in the air gap along the tangential direction.

Table 1. Comparison of the performance between different magnet arrangements.

Type of Permanent Magnet Arrangement	Conventional Arrangement	Concentrate Arrangement	Halbach Arrangement
peak magnetic induction line (Wb/m)	0.012	0.013	0.015
average magnetic flux density (mT)	497.98	511.30	545.15
Peak magnetic flux density (mT)	653.59	610.65	785.88
Average output torque (N·m)	269.40	287.26	320.30

At the beginning of the simulation, the input rotation speed was maintained at 1000 rpm, and the output rotation speed was maintained at 900 rpm. The transient output torque of CPMG under different magnets arrangements are shown in Figure 10. It is clear that the Halbach arrangement has the highest output torque. The detailed comparison is listed in Table 1. As shown in Table 1, The average output torque of the Halbach arrangement is increased by 15.89% and 10.31%, which is compared to the conventional arrangement and concentrate arrangement.

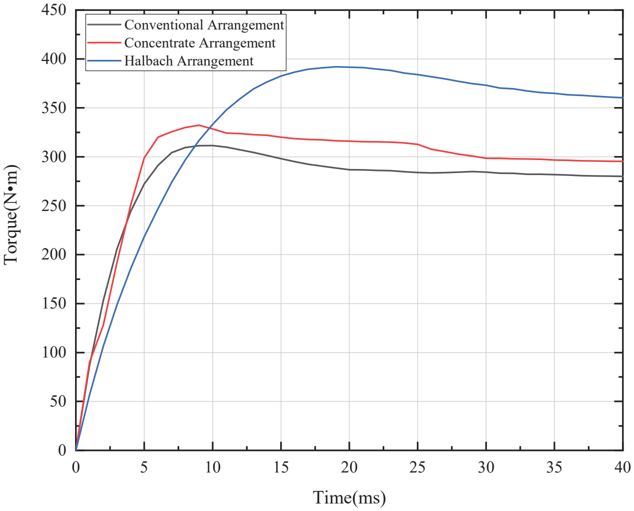

Figure 10. Output torque of CPMG under different magnets arrangements.

3.2. Eddy Current Density Distribution in the Copper Rings

When the slip rate is 0.01, and the effective coupling ratio between the conductor and permanent magnet is 100%, the distribution of the eddy current density in the copper ring is illustrated in Figure 11. As we can see in Figure 11, the eddy current density of the permanent magnet in the copper ring is the largest area mapped to the area of the copper ring. At a maximum density of 2.52×10^7 Am^{-2}, the eddy current density between adjacent permanent magnet mapping areas dropped sharply and reduced to 3.20×10^6 Am^{-2}. The center of the loop formed by the induced eddy current in the copper ring is located in the center between the two mapping regions of permanent magnets. The induced magnetic field generated by the circular eddy current interacts with the permanent magnetic field, thereby providing torque for CPMG.

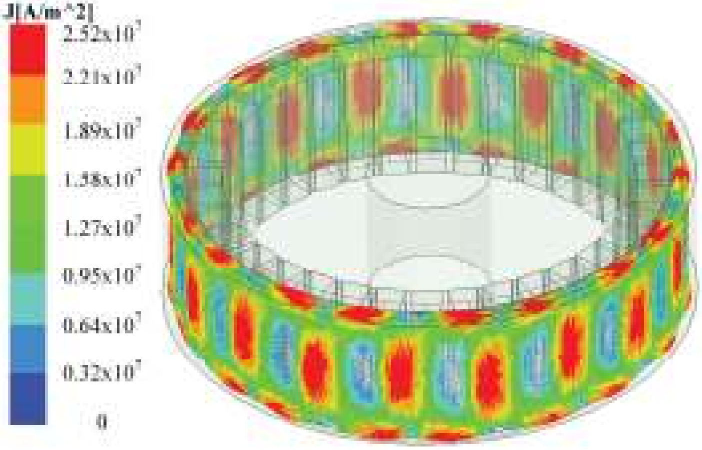

Figure 11. Eddy current distribution across copper rings.

3.3. Ohmic Loss in the Copper Ring

The induced current generated in the copper coil of the permanent magnet regulator produces Ohmic loss due to the existence of the coil reluctance. The Ohmic loss distribution of the copper ring under 0.1 slip rate and 100% effective coupling ratio is shown in Figure 12. The maximum Ohmic loss is concentrated in the center of the copper ring. Moreover, the Ohmic loss is increased with the effective coupling ratio between the conductor and permanent magnet.

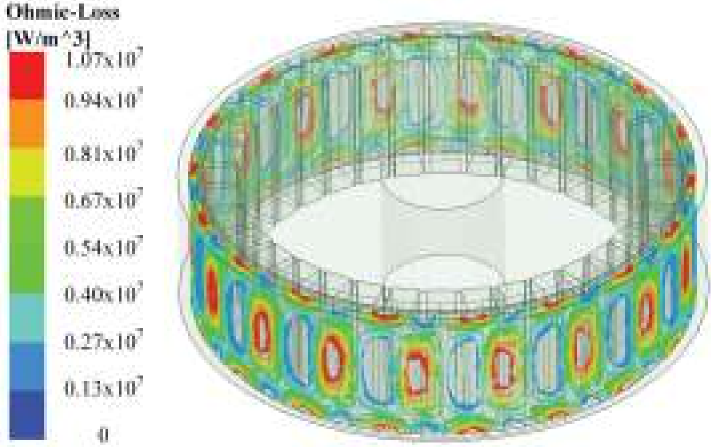

Figure 12. Ohmic loss distribution in the copper rings.

3.4. Output Torque of CPMG

During the simulation, the input rotation speed is maintained at 1000 rpm, and the output rotation speed is adjusted from 600 to 950 rpm, which means the slip rate range from 0.05 to 0.4. The thickness of the copper ring is 6 mm. The output torque of CPMG under the different slip rates and effective coupling ratio is listed in Table 2 and shown in Figure 13. The output torque is increased with the effective coupling ratio at a constant slip rate. The output torque is increased first, then decrease the slip with a constant effective coupling ratio, whose peak value is 74.56 N·m at 230 rpm output rotation speed (slip rate = 0.23) with a 25% effective coupling rate. The peak output torque is 185.20 N·m, 316.01 N·m and 390.28 N·m at 180 rpm (slip rate = 0.18) with 50%, 75% and 100% effective coupling rates, respectively.

Table 2. Average output torque at different coupling ratio(N·m).

Slip Rate	25%	50%	75%	100%
0.05	30.10	89.83	149.51	179.49
0.1	53.75	153.95	258.58	320.30
0.15	67.42	179.15	307.52	384.38
0.16	67.84	184.23	314.96	388.46
0.17	68.12	185.04	315.95	390.26
0.18	69.48	185.20	316.01	390.28
0.19	70.12	184.74	313.28	388.82
0.2	72.64	180.70	307.63	386.12
0.25	73.13	172.62	289.09	364.51
0.3	71.31	162.94	267.45	340.86
0.35	68.54	152.96	250.59	317.23
0.4	65.08	141.98	230.19	291.81

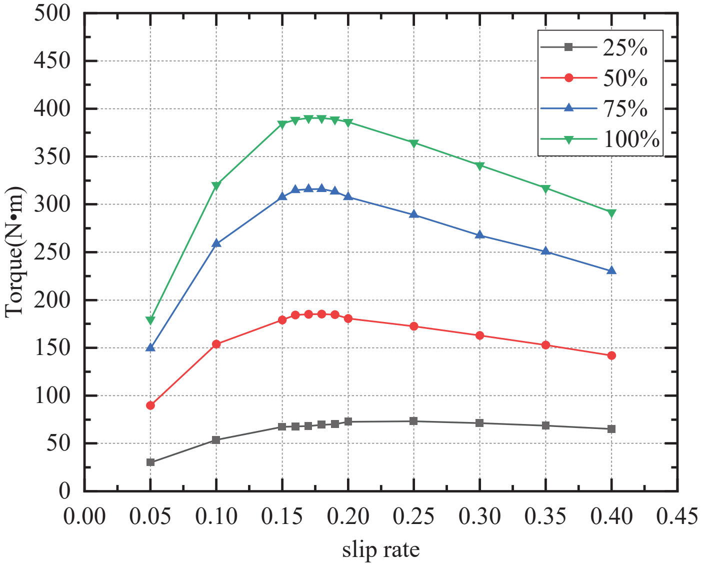

Figure 13. Average output torque at different effective coupling ratio.

3.5. Influence of Copper Ring Thickness on Transmission Performance

In the transmission process of the CPMG, the main function of the copper ring is to be cut to magnetic wire induced by the permanent magnets, generating eddy currents. However, the changes in the thickness of the copper ring cause a change in resistance to copper; thus, the thickness of the copper ring has an important effect on transmission performance.

At the beginning of the simulation, the input rotation speed was maintained at 1000 rpm, and the output rotation speed was maintained at 900 rpm. The transient output torque of CPMG 25%, 50%, 75% and 100% effective coupling ratio under difference copper ring thickness is shown in Figure 14.

As shown in Figure 14, the transient output torque of CPMG has an overshoot at the beginning due to a small damping ratio of the system. The output torque reached a stable value after dozens of ms. The transient output torque of CPMG with different copper ring thicknesses is shown in Figure 13. The transient output torque increases with the copper ring thickness.

The stable output torque for a different copper ring thickness under a constant effective coupling ratio and slip rate is listed in Table 3. The table shows the output torque peak value at 6 mm thickness and 100% effective coupling ratio, which is 340.05 N·m. The output torque increases with the copper ring thickness. However, the minimum value of the air gap must be greater than 5 mm taking into account the assembly problems and costs in the actual production process, which is limited to the copper ring thickness. Here, we take the maximum copper ring thickness as 6 mm.

Table 3. Output torque at different copper ring thicknesses.

Copper Ring Thickness (mm)	**Effective Coupling Ratio (%)**			
	25	**50**	**75**	**100**
6	57.75	163.33	275.57	340.05
5	50.40	147.72	247.39	304.18
4	42.49	128.97	214.60	261.73
3	33.95	104.95	175.63	212.46

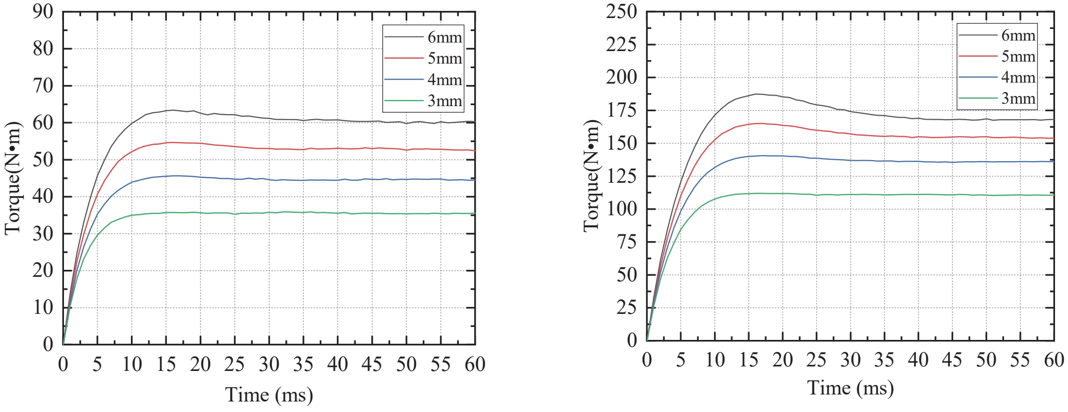

(**a**) 25% effective coupling ratio (**b**) 50% effective coupling ratio

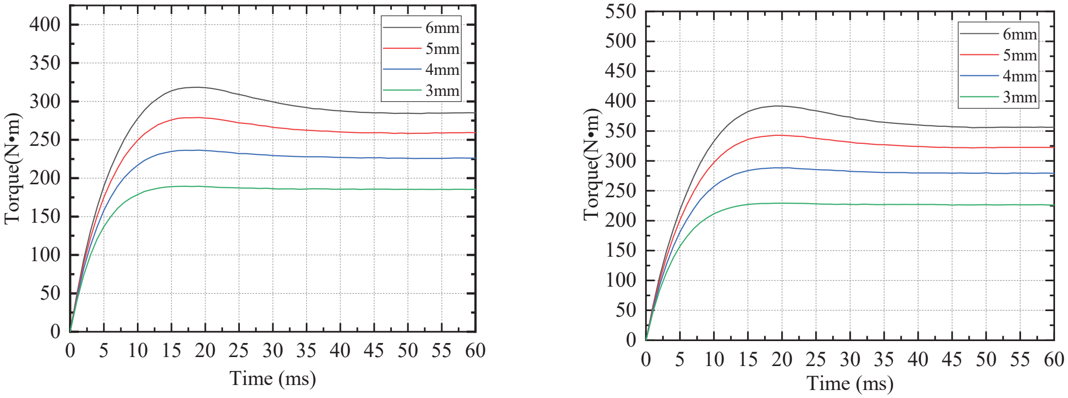

(**c**) 75% effective coupling ratio (**d**) 100% effective coupling ratio

Figure 14. Output torque of CPMG under different copper ring thicknesses.

4. Experimental Analysis

4.1. Setup of Experimental Platform

To verify the correctness of the transmission characteristic model and the accuracy of the calculation results. An experimental platform was constructed, as shown in Figure 15, including an eddy current dynamometer providing the required output load, which can change the load by adjusting its control current. A torque sensor measures the output torque; the CPMG can be tested; and the YE2-200L-4 three-phase asynchronous motor is an electromotor providing the driving torque, where the rated output power of the motor is 30 kW, the rated rotation speed is 1470 rpm, and the rated current is 56.8 A. Two frequency converters control the rotating speed of the electromotor and eddy current dynamometer, and the testing instrument displays the output torque. An IKTM1000 electric actuator is connected to the rotor of the conductor to realize the adjustment of the effective coupling ratio. All these components were installed on the test platform, as shown in Figure 16.

The thickness of the copper ring is measured in advance of the test, and the copper ring is assembled in the inner wall of the conductor barrel. The Gaussian meter was used to measure the air gap magnetic field after assembly. Finally, the CPMG was started, and the torque data were sampled by the test equipment.

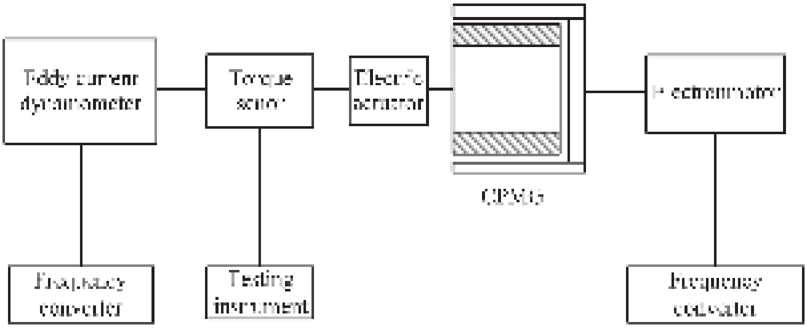

Figure 15. Basic structure diagram of test platform.

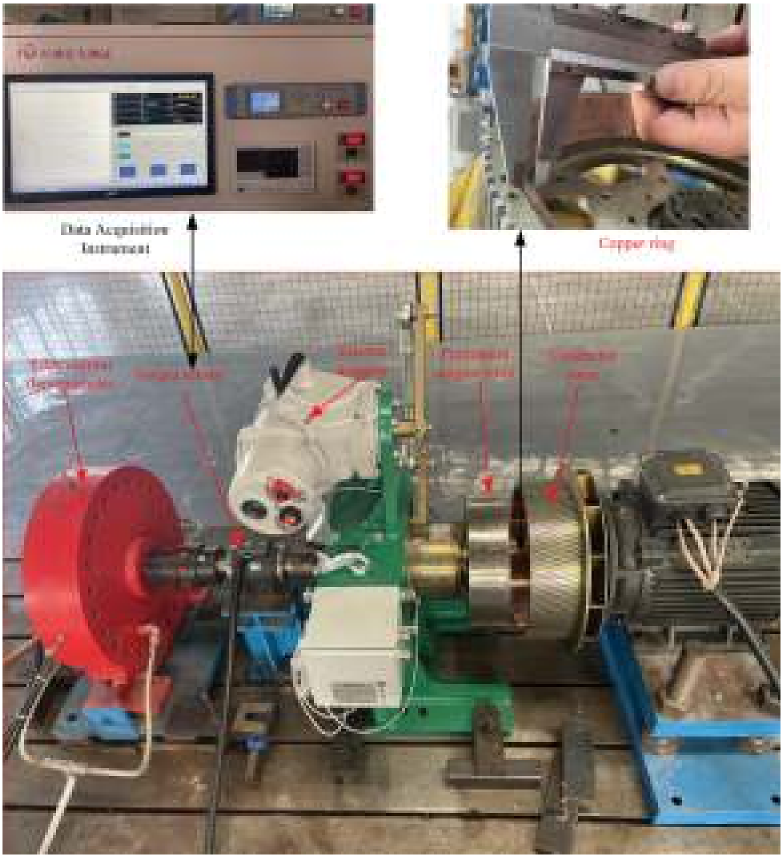

Figure 16. Test prototype construction.

4.2. Output Torque Test

The CPMG 100% effective coupling ratio, 6 mm thickness of the copper ring for testing, and start motor were selected. The CPMG input speed (speed of the conductor motor) was maintained at 1000 rpm; the output torque of the Permanent Magnet Rotor was tested at 950 rpm, 900 rpm, 850 rpm, 800 rpm,750 rpm, 700 rpm, 650 rpm, 600 rpm (slip rate range from 0.05 to 0.4), respectively; and the average air gap flux measured by the Gauss meter was substituted into the torque equation derived in Section 2.2 through MATlab software to be calculated, which is the analytical torque. The output torque test was carried out on the experimental platform. The experimental data, which are T_{test1}, were obtained with the slip rate range from 0.05 to 0.4 and compared with the theoretical calculation data and simulation results, as shown in Figure 17. The experimental results show that the variation trend of the output torque is consistent with numerical simulation. The maximum output torque is reached when the slip rate is 0.2. The error of experimental results of output torque compared with analytical and numerical counterparts are less than 5%, under 100% effective coupling ratio and 6 mm copper ring thickness. The output torque of CPMG does not always increase with the increased slip rate. This is due to the adverse effects of the inductive magnetic field of permanent magnets. In addition, the slip rate increases the skin effect, which reduces the equivalent permeability in the copper ring, thereby reducing the intensity of the induced current in the copper ring, leading to the transfer of torque that is gradually reduced.

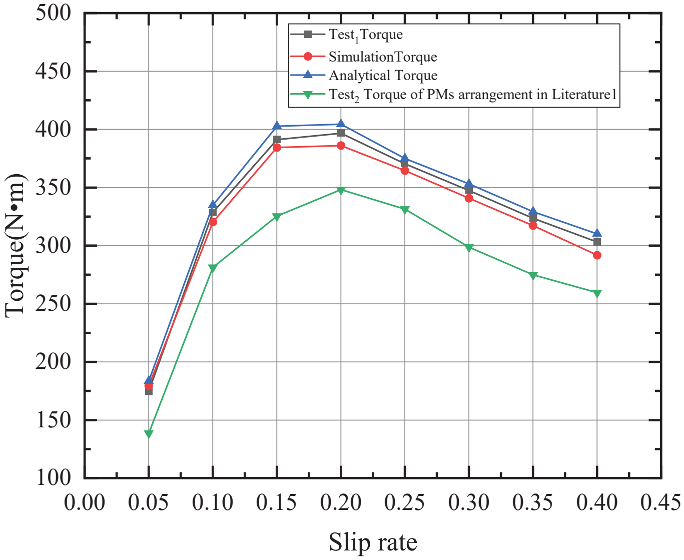

Figure 17. Comparison of average output torque under different slip rates.

According to the magnet arrangement in Ref. [1], the same size and quantity of PMs were installed in the CPMG for testing. Additionally, the CPMG was operated, and the torque data were sampled by the test equipment. The detailed comparison is listed in Table 4. During the test, the output torque of the Halbach array was higher than the magnets' arrangement in Ref. [1]. Furthermore, the peak torque of the Halbach array was increased by 12.21% when compared to the magnet arrangement in Ref. [1].

Table 4. Comparison of output torque under different speed differences.

Slip Rate	T_{test1}	T_{test2}	T_{sim}	T_{ana}	err_{sim}	err_{ana}
0.05	174.89	138.75	179.49	183.62	2.63%	4.99%
0.1	328.62	281.41	320.30	334.82	2.53%	1.89%
0.15	391.25	325.48	384.38	402.77	1.75%	2.94%
0.2	396.73	348.25	386.12	404.42	2.67%	1.94%
0.25	370.43	331.38	364.51	375	1.74%	1.23%
0.3	347.52	298.82	340.86	353.13	1.92%	1.61%
0.35	323.56	274.89	317.23	329.35	1.96%	1.79%
0.4	303.21	259.63	291.81	310.23	3.75%	2.31%

In Table 4, T_{test1} represents the test measurements of the Halbach array, T_{sim} is simulated stable torque, T_{test2} represents the test measurements of PMs arrangement in Ref. [1]. T_{ana} is the theoretical torque of the theoretical analysis of the principle of the equivalent magnetic circuit. err_{sim} is the error between the simulation and the experimentation. err_{ana} is the error between the theoretical analysis and the experimentation.

In order to test the effect of the thickness of the copper ring on the output torque of the CPMG, a series of copper ring thicknesses of 6, 5, 4 and 3 mm, respectively, were installed in the inner walls of the conductor barrel and the tested output torque in the different effects of the coupling. During the test procedure, the speed of the input CPMG was maintained at 1000 rpm, and then the speed of the permanent magnet rotor was adjusted at 900 rpm (the slip rate was 0.1) to test the output torque of the CPMG. The test results were obtained and compared with the numerical simulation results, as shown in Figure 18. The torque measured by the sensor and obtained by a finite element is shown below in Table 5. When the effectiveness of the coupling is constant, the torque of the output increases with the increasing thickness of the ring of copper. The errors of experimental results of output torque compared with the numerical counterpart are less than 5%.

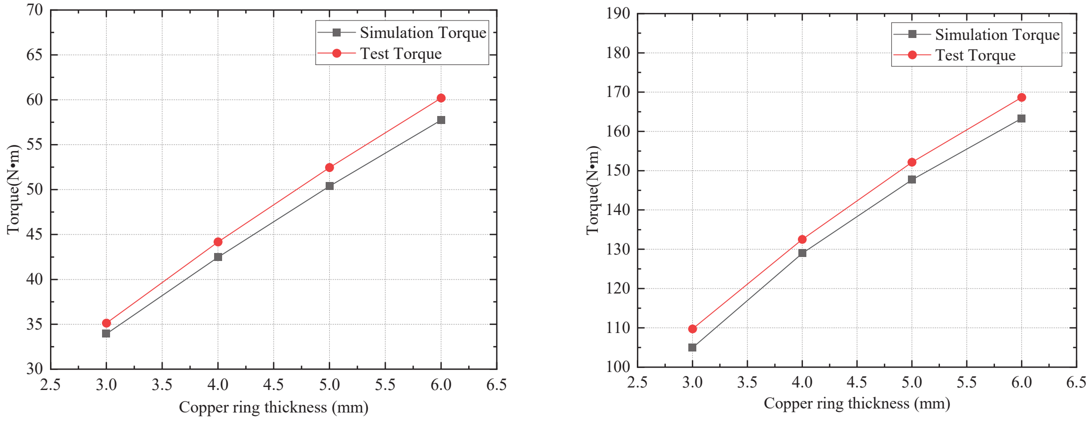

(**a**) 25% effective coupling ratio

(**b**) 50% effective coupling ratio

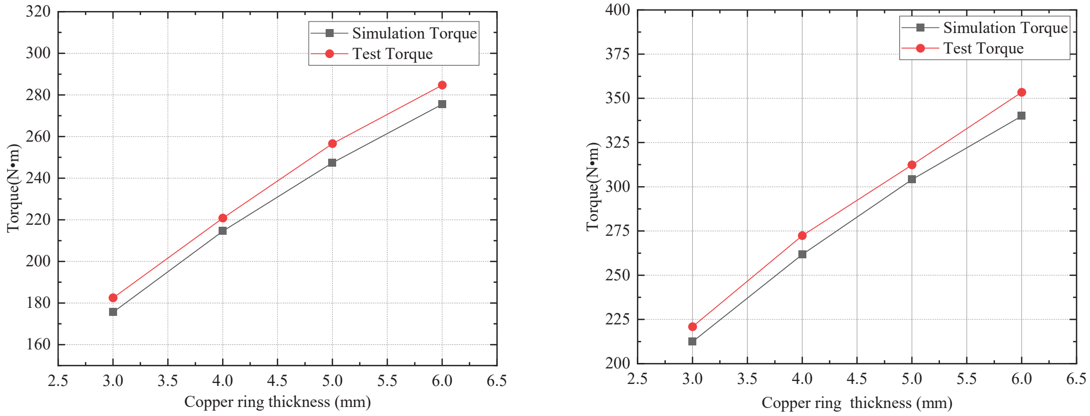

(**c**) 75% effective coupling ratio

(**d**) 100% effective coupling ratio

Figure 18. Output torque simulation and test comparison under different thicknesses.

Table 5. Comparison of experimental and simulation results of output torque under different copper ring thicknesses.

Effective Coupling Ratio (%)	h_{copper} (mm)	T_{sim} (N·m)	T_{test} (N·m)	Error (%)
25	3	33.95	35.14	3.86
	4	42.49	44.18	3.82
	5	50.40	52.47	3.94
	6	57.75	60.21	4.08
50	3	104.95	109.72	4.34
	4	128.97	132.51	2.67
	5	147.72	152.18	2.93
	6	163.33	168.69	3.18
75	3	175.63	182.56	3.79
	4	214.60	220.87	2.84
	5	247.39	256.64	3.6
	6	275.57	284.73	3.21
100	3	212.46	220.94	3.84
	4	261.73	272.42	3.93
	5	304.18	312.46	2.65
	6	340.05	353.48	3.78

5. Conclusions

This paper shows a comparative analysis of the performance of the CPMG under the three different types of PM arrangements. Considering the same number of PMs and the cost, the Halbach array is suitable for high-torque appliances, such as high-power fans. The main magnetic fluxes are considered to obtain a comprehensive equivalent magnetic circuit model of the CPMG with Halbach array, and analytical output torque is calculated. Moreover, the transmission properties of the CPMG under the Halbach array were studied, taking into account the effects of slip rate, effective coupling ratio and thickness of the copper ring on the torque output of the CPMG under the Halbach array. By comparing the simulation results with the field-test data of the CPMG, it was found that the simulation results match well with the measured data, which validates the effectiveness of the proposed model and calculation method. The main conclusion of this paper is summarized as follows:

1. The air gap flux density under the Halbach arrangement is 13% and 6.2% higher than the other two arrangements, respectively. The average output torque of the Halbach arrangement is increased by 15.89% and 10.31%, which is compared with the conventional arrangement and concentrate arrangement.
2. When the effective coupling ratio and the thickness of the copper ring are constant, the output torque increases first and then drops with the slip rate increasing, which reaches the maximum torque of around 0.2. The results were consistent with the results of the simulation, and the error was kept within the range of 5%. The output torque of the Halbach array is higher than the magnets' arrangement in Ref [1]. The peak torque of the Halbach array is 12.21% higher when compared to the magnets' arrangement in Ref. [1].
3. When the slip rate is constant, the output torque increases with the increase in the effective coupling ratio (between conductor and magnet), and the thickness of the copper ring increases.

Author Contributions: Conceptualization, H.W. and C.Y.; methodology, H.W., Y.Z. and C.Y.; software, J.G.; validation, C.Y.; formal analysis, C.Y. and Y.Z.; investigation, H.W.; resources, C.Y.; data curation, H.W. and H.L.; writing—original draft preparation, H.W.; writing—review and editing, Y.Z.; visualization, H.W. and C.Y.; supervision, C.Y.; project administration, H.W. and C.Y.; funding acquisition, J.G. All authors have read and agreed to the published version of the manuscript.

Funding: This research was funded by "The overseas study visit and training program for outstanding young backbone talents of Anhui Province, grant number gxgwfx2021035", "Graduate Student Innovation Project of Anhui Province, grant number 2022xscx097 ", "The Innovation team of Anhui Polytechnic University, Special display and Imaging Technology Anhui Technology Innovation Center open project, grant number 2020AJ06001 " and "Anhui Polytechnic University-Jiujiang District Industrial Collaborative Innovation Special Fund Project, grant number 2022cyxtb4".

Conflicts of Interest: The authors declare no conflict of interest.

Sample Availability: Samples of the compounds are available from the authors.

Abbreviations

The following abbreviations are used in this manuscript:

DPMG	disk permanent magnet governor;
CPMG	cylindrical permanent magnet governor;
MEC	magnetic equivalent circuit;
MCT	marine current turbine;
PM	permanent magnet;
PMR	permanent magnet rotor;
KCL	Kirchhoff current law.

References

1. Cheng, X.; Liu, W.; Zhang, Y.; Liu, S.; Luo, W. A Concise Transmitted Torque Calculation Method for Pre-design of Axial Permanent Magnetic Coupler. *IEEE Trans. Energy Convers.* **2020**, *35*, 938–947.
2. Seo, S.W.; Kim, Y.H.; Lee, J.H.; Choi, J.Y. Analytical torque calculation and experimental verification of synchronous permanent magnet couplings with Halbach arrays. *AIP Adv.* **2020**, *8*, 056609. [CrossRef]
3. Wang, L.; Jia, Z.Y.; Zhang, L. Investigation on the accurate calculation of the temperature field of permanent magnet governor and the optimization method of heat conduction. *Case Stud. Therm. Eng.* **2019**, *13*, 100360. [CrossRef]
4. Guo, B.; Li, D.; Shi, J.; Gao, Z. A Performance Prediction Model for Permanent Magnet Eddy-Current Couplings Based on the Air-Gap Magnetic Field Distribution. *IEEE Trans. Magn.* **2022**, *58*, 1–9. [CrossRef]
5. Dolisy, B.; Mezani, S.; Lubin, T.; Levrque, J. A new analytical torque formula for axial field permanent magnets coupling. *IEEE Trans. Energy Convers.* **2015**, *30*, 892–899. [CrossRef]
6. Yang, X.; Liu, Y.; Wang, L. An Improved Analytical Model of Permanent Magnet Eddy Current Magnetic Coupler Based on Electromagnetic-Thermal Coupling. *IEEE Access* **2020**, *8*, 95235–95250. [CrossRef]
7. Shi, J.; Suo, S.; Meng, G. The theoretical calculation model of torque transmission in permanent-magnet couplers. *AIP Adv.* **2021**, *11*, 025303. [CrossRef]
8. Orlova, S.; Konuhova, M.; Kamolins, E.; Otankis, R. Design of magnetic couplings for bioreactors: Analytical treatment and optimization. In Proceedings of the 2018 20th European Conference on Power Electronics and Applications (EPE'18 ECCE Europe), Riga, Latvia, 17–21 September 2018.
9. Sun, K.; Shi, J.; Cui, W.; Meng, G. Theoretical Computational Model for Cylindrical Permanent Magnet Coupling. *Electronics* **2021**, *10*, 2026. [CrossRef]
10. Deshan, K.; Dazhi, W.; Wenhui, L.; Sihan, W.; Zhong, H. Analysis of a novel flux adjustable axial flux permanent magnet eddy current coupler. *IET Electr. Power Appl.* **2023**, *17*, 181–194. [CrossRef]
11. Park, J.; Paul, S.; Chang, J.; Hwang, T.; Yoon, J. Design and comparative survey of high torque coaxial permanent magnet coupling for tidal current generator. *Electr. Power Energy Syst.* **2020**, *120*, 105966. [CrossRef]
12. Taqavi, O.; Taghavi, N. Development of a Mixed Solution of Maxwell's Equations and Magnetic Equivalent Circuit for Double-Sided Axial-Flux Permanent Magnet Machines. *IEEE Trans. Magn.* **2021**, *57*, 1–11. [CrossRef]
13. Yang, C.; Peng, Z.; Tai, J.; Zhu, L.; Telezing, B.J.K. Torque characteristics analysis of slotted-type eddy-current couplings using a new magnetic equivalent circuit model. *IEEE Trans. Magn.* **2020**, *56*, 1–8. [CrossRef]
14. Lubin, T.; Mezani, S.; Rezzoug, A. Experiment and analytical analyses of axial magnetic coupling under steady-state and transient operations. *IEEE Trans. Ind. Electron.* **2014**, *61*, 4356–4365. [CrossRef]
15. Kim, I.C.; Wata, J.; Tongphong, W.; Yoon, J.S.; Lee, Y.H. Magnetic Coupling for a 10 kW Tidal Current Turbine: Design and Small Scale Experiments. *Energies* **2020**, *13*, 5725. [CrossRef]
16. Lukočius, R.; Vilkauskas, A.; Marčiulionis, P.; Grigaliūnas, V.; Nakutis, Ž.; Deltuva, R. An Analysis of Axial Magnetic Coupling Force and Torque Dependencies on Its Structure Parameters Using a 3D FEM. *Appl. Sci.* **2022**, *12*, 6546. [CrossRef]

17. Tian, M.; Zhao, W.; Wang, X.; Wang, D.; Yang, Y.; Diao, J.; Ma, X. Analysis on a Novel Flux Adjustable Permanent Magnet Coupler With a Double-Layer Permanent Magnet Rotor. *IEEE Trans. Magn.* **2018**, *54*, 1–5. [CrossRef]
18. Lu, X.; He, X.; Jin, P.; Huang, Q.; Yang, Y.; Diao, J.; Ma, X. General 3D Analytical Method for Eddy-Current Coupling with Halbach Magnet Arrays Based on Magnetic Scalar Potential and H-Functions. *IEEE Trans Magn.* **2021**, *14*, 8458. [CrossRef]
19. Lee, H.J.; Joung, H.K.; Kim, C.H. Optimal Design of the Halbach Array of the Halbach Array of Magnetic Coupling. In Proceedings of the 2022 25th International Conference on Electrical Machines and Systems(ICEMS), Shanghai, China, 29 November–2 December 2022; pp. 1–5.
20. Li, Y.; Hu, Y.; Guo, Y.; Song, B.; Mao, Z. Analytical Modeling and Design of Novel Conical Halbach Permanent Magnet Couplings for Underwater Propulsion. *J. Mar. Sci. Eng.* **2021**, *9*, 290. [CrossRef]
21. Li, Z.; Zhang, L.; Qu, B.; Wang, D. Evaluation and analysis of novel flux-adjustable permanent magnet eddy current couplings with multiple rotors. *IET Electr. Power Appl.* **2021**, *15*, 754–768. [CrossRef]
22. McGilton, B.; Crozier, R.; McDonald, A.; Mueller, M. Review of magnetic gear technologies and their applicants in marine energy. *IET Reneaable Power Gener.* **2018**, *12*, 174–181. [CrossRef]
23. Mateev, V.; Marinova, I. Loss estimation of magnetic gears. *Electr. Eng.* **2020**, *102*, 387–399. [CrossRef]
24. Zhao, X.; Niu, S. Design and optimization of a new magnetic-geared pole-changing hybrid excitation machine. *IEEE Trans. Ind. Electron.* **2017**, *12*, 9943–9952. [CrossRef]
25. Huang, J.; Fu, W.; Niu, S.; Zhao, X. Comparative Analysis of Different Permanent Magnet Arrangements in a Novel Flux Modulated Electric Machine. *IEEE Access* **2021**, *1*, 14437–14445. [CrossRef]
26. Yang, K.; Zhao, F.; Wang, Y. Analysis of Double Layer Permanent Magnet Flux Reversal Machines with Different Permanent Magnet Arrangements in Stator. *IEEE Trans. Magn.* **2021**, *57*, 1–5. [CrossRef]
27. Li, B.; Yang, B.; Xiang, F.; Guo, J. Optimal Design of a New Rotating Magnetic Beacon Structure Based on Halbach Array. *Appl. Sci.* **2022**, *12*, 10506. [CrossRef]

machines

MDPI

Article

Design and Verification of Adaptive Adjustable Output Control on Micro Spray Gun †

Jiun-Hung Lin [1], Chih-Hong Chen [2] and Shih-Tsang Tang [3],*

[1] College of Electrical Engineering and Computer Science, National Kaohsiung University of Science and Technology, Kaohsiung 824005, Taiwan
[2] Department of Electronic Engineering, Kun Shan University, Tainan 710303, Taiwan
[3] Department of Biomedical Engineering, Ming Chuan University, Taoyuan 333321, Taiwan
* Correspondence: sttang@mail.mcu.edu.tw

† This paper is an extended version of our paper published in 2022 International Conference on Fuzzy Theory and Its Applications (iFUZZY), Kaohsiung, Taiwan, 3–5 November 2022; Available online: https://doi.org/10.1109/iFUZZY55320.2022.9985228.

Abstract: The general spray gun is used for industrial large-area spraying, and there is less demand for different pressures and the accuracy of spraying pressure, so mechanical pressure regulators are mostly used. However, as the demand for artistic innovation continues to grow, it promotes the advent of the micro spray gun. The micro spray gun is currently commonly known as an airbrush. The micro spray gun is mainly used for fine drawing, so it must provide different pressures with high precision pressures, but the existing mechanical regulators cannot meet this requirement. For these unmet requirements, this study proposed a solution for PID (proportional-integral-derivative) control micro spray gun system. The results showed that the PID control could effectively provide various stable output pressures of the micro spray gun. The pressure-varying range of 30 kPa could rapidly return to the target value in 10 s (the usual spraying time). The proposed solution then presents better spraying effects.

Keywords: micro air pump; micro spray gun; pressure control; pulse width modulation

Citation: Lin, J.-H.; Chen, C.-H.; Tang, S.-T. Design and Verification of Adaptive Adjustable Output Control on Micro Spray Gun. *Machines* **2023**, *11*, 354. https://doi.org/10.3390/machines11030354

Academic Editors: Kan Liu and Wei Hu

Received: 5 February 2023
Revised: 3 March 2023
Accepted: 3 March 2023
Published: 4 March 2023

1. Introduction

A compressor is a mechanical device used for increasing distinct compressible fluid or air pressure, whereas an air compressor is the commonest one using air output technology. An air compressor is an inevitable and important piece of equipment in various industries converting the mechanical energy of a motor into air pressure energy. Compressed air is used as the power source for industrial pneumatic tools, paint-spraying machines, and sand-blast equipment. Many air compressors are applied to paint spraying with spray guns [1,2]. Such a traditional sprayer is generally equipped with a mechanical air pressure regulator to adjust the pressure output with manual mode, and a pneumatic throttle valve is used for tuning the pressure for paint output. An air compressor running with an electric motor, rather than a mechanical principle, is called an air pump. The principle of the air pump is to exhaust from an enclosed space or to generate air from an enclosed space. When it is used for small-size vacuum pumping, it is also called a micro air pump, or a micro air compressor.

With either mechanical or electric air compressors, the paint going through the spray gun might be interfered by air pressure or the external environment. It would result in the change of air current in the spray gun to cause unstable working of the spray gun or affect the spraying efficiency and effectiveness [3]. The control valve of current spray gun systems generally balances the air manually, without the function to regulate signal feedback. It is rather difficult to regulate air output along with experience or condition during the work, and air pressure might not be stabilized. Due to the rapid development of microcontrollers in past years, there are many studies on the application of control technology to medium sprayers, in which variable control technique is added to largely reduce unstable output, e.g., intermittent and continuous variable rate spraying based on pulse width modulation [4–7]. Pulse width modulation (PWM) changes the winding driving module through impulse signals to achieve the variable spray coating through the duty ratio of pulse-width signals. Researchers also control the spraying amount by flow control with pressure monitoring and pulse width modulation [8–11]. Such variable pressure control is limited the regulation range and appears unstable atomization characteristics, but the principle is simple and the cost of constructing control circuits is lower. The technology of adaptive air compressors, therefore, is a long-term development direction.

A pressure-monitoring output control technology is proposed for micro spray guns in art drawing, body painting, and cosmetic fields [12–14]. Such micro air pumps cannot use mechanical air pressure modulators and air receivers due to the cost and size limit that the pressure output is modulated with simple power control. A proportional-integral-derivative (PID) control algorithm with pressure feedback is therefore developed to provide stable air output for the micro air compressor in the sprayer as well as modulate the air output. The motor valve in the air pump is modulated by pulse width modulation, according to the algorithm calculation result, so that the spray gun presents pressure feedback and adaptability to achieve the variable spraying effect. We implemented an adaptive micro spray gun simulation platform in 2022 [15]. The simulation results show that the PID algorithm is feasible in the control of the micro-spray gun device. Therefore, in this study, we applied the method on the real device, and further determined the ranges of the algorithm parameters and convergence conditions. We applied the pulse-like driving waves to observe the influences of the algorithm parameters. At the same time, the performances of algorithm convergence are analyzed. All considerations are for determining the operation optimization.

2. Materials and Methods

The basic components for this system contain a micro air pump, DC motor drive module, and PID control unit.

2.1. DC Motor Drive Module

The micro air pump used in this study is a kind of electric diaphragm pump with an intake and exhaust structure, Figure 1. During the compression, the air intake is closed, while the exhaust port is open to form the positive pressure; during the stretch, the exhaust port is closed, and the air intake is open to form negative pressure. The pressure difference appears on the air intake of the air pump and the ambient pressure, and under the pressure difference, the air is sucked into the pump chamber. It is the entire exhaust motion of the micro air pump. Unlike a large air pump requiring lubricating oil and vacuum pump oil, a micro air pump would not pollute the working medium and shows the advantages of small size, low noise, maintenance-free, and continuous running [16].

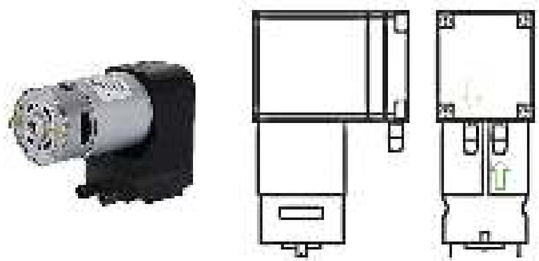

Figure 1. Picture and side shot of a micro electric air pump.

The DC motor revolution basically presents analog modulation and pulse-width modulation. Analog modulation linearly modulates the input voltage or current of a motor; since the signals show linear changes, they are more easily interfered with by ambient electric noise and affected stability. Furthermore, control signals would easily drift with time and appear large power dissipation and worse energy efficiency. Moreover, the motor torque depends on the current going through the motor winding; when the voltage on the motor winding is changed, the current going through the motor winding would be unstable and the motor torque is also unstable. Unlike the instability of analog modulation, pulse width modulation is often used for DC motor drives as well as power conversion of DC/DC converters and AC/DC converters [17]. PWM, in principle, outputs the required power through switching impulse, and pulse amplitude and cycle are constant. The output power is controlled with conducting pulse width. The voltage output, therefore, is the average of the ratio of the corresponding conducting and pulse cycle time, called duty ratio or duty cycle which the unit is a percentage (%). Since the motor torque depends on the current going through motor winding, the increase in duty ratio also increases power output, and the motor speed would be relatively faster. With PWM control, the impulse voltage is comparatively constant, and the current stability is influenced that the motor torque output being relatively stable.

2.2. PID Control Unit

Stable air output is required in this study and the adaptive control presents is important. In industrial control, PID control is a mature control system with broad applications [18–20]. It is often used for control feedback to stabilize output signals. PID control technology is suitable for a system and a controlled object not being completed understood or the system parameters not being acquired through effective measurement. A PID controller is composed of a proportional unit (*P*), integral unit (*I*), and derivative unit (*D*), whose parameters of proportional gain, integral gain, and differential gain could be used for modulating the system output characteristics. Figure 2 shows the basic architecture of the PID control module.

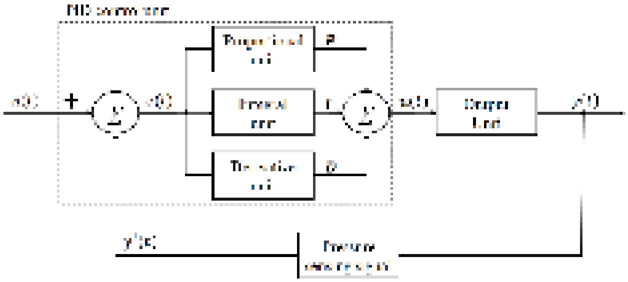

Figure 2. The basic architecture of the PID control unit.

PID control is a linear control method, which subtracts the desired target value $n(t)$ and $y'(t)$ to obtain the deviation $e(t)$, where $y'(t)$ is the digitalized version of the actual output air pressure signal $y(t)$. The deviation $e(t)$ is further operated in the proportional control, integral control, and derivative control equations and then combined with the output $u(t)$ to control the output object. The PID algorithm is denoted with the following equations.

$$u(t) = P + I + D \tag{1}$$

$$P = K_p \times e(t) \tag{2}$$

$$I = K_i \times \int_0^t e(\tau)d\tau \tag{3}$$

$$D = K_d \times \frac{d}{dt}e(t) \tag{4}$$

where

K_p: proportional gain adjustable parameter,
K_i: integral gain adjustable parameter,
K_d: differential gain adjustable parameter,
t: current time,
τ: variable of integration, with the number from 0 to current time t.

When the system is continuously operated, the PID control unit must constantly modulate proportional gain, integral gain, and differential gain parameters according to the feedback of the barometric pressure sensing signal to have the system achieve optimal control, i.e., achieving system stability without divergence or excessive oscillation of output signals. When PID is applied to the micro spray gun (airbrush) system that can switch the spray on and off, its robustness can make the spray gun maintain a constant output speed and allow the spray gun to maintain the required output speed under different working conditions. Through the feedback control, the motor can reduce the jitter when starting and stopping, reducing the wear or damage of the motor.

2.3. Experimental Design

2.3.1. System Architecture

Figure 3 depicts the PID control process, mainly containing two dotted square boxes of software function and hardware function. The software box includes a PID control algorithm and outputs pulse width modulation through programming. NI LabVIEW (National Instruments Co., Austin, TX, USA), the graphic high-level programming language, is used for software development. The hardware box covers a multifunction I/O card (NI USB-6211, National Instruments Co., Austin, TX, USA), a DC motor drive module, and a pressure sensor module. The $u(t)$ in the PID control block is eventually driven for the output unit, which contains a pulse width modulation converting module and DC motor drive module to drive the micro air pump. In order to acquire the feedback signal output for the parameter modulation in the PID control module, a barometric pressure sensor is selected for capturing the pressure change in the pipe, Figure 3.

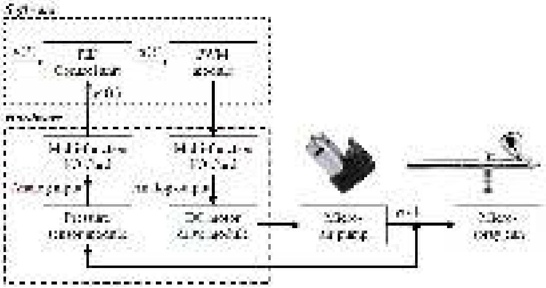

Figure 3. PID control test architecture of micro air pump.

NI USB-6211 isolated multifunction I/O card, with digital and analog output/input function and the highest digital-analog resolution and sampling rate of up to 16 bits and 250 k samples per second, is utilized as the digital-analog interface card. The hardware interface card reads analog signals from the pressure sensor module as real-time feedback data for the PID control module, and the analog output refresh rate is 250 k samples per second, of the interface card, which could generate high-frequency impulse shape to modulate accurate duty ratio for controlling the micro air pump.

The small air pump, Airpon D2028 (Ningbo Forever Electronic Appliance Co., Ltd., Ningbo, Zhejiang, China) with a working pressure from −70 to +250 kPa, is used as the micro air pump in this study. DC motor drive module with dull-channel full-bridge motor driver chip produced by STMicroelectronics company (Geneva, Switzerland) is used for driving the micro air pump. The driver module with the features of high operating voltage, large output current, strong driving capability, low calorific power, and strong anti-jamming capability is often used for driving relay, solenoid, solenoid valve, DC motor, and stepping motor. To reduce shock at the beginning of the air pump start, the micro air pump is directly fixed on the plastic mat with plastic ties, Figure 4a. Two control signal wires of the air pump are connected to the DC motor drive module so that the exhaust would first pass a unidirectional valve to prevent airflow from backflow and affecting motor operation. The exhaust pipe of the micro air pump, through a three-way pipe, as the dotted square in Figure 4a, is connected to the micro spray gun and a pressure sensor module.

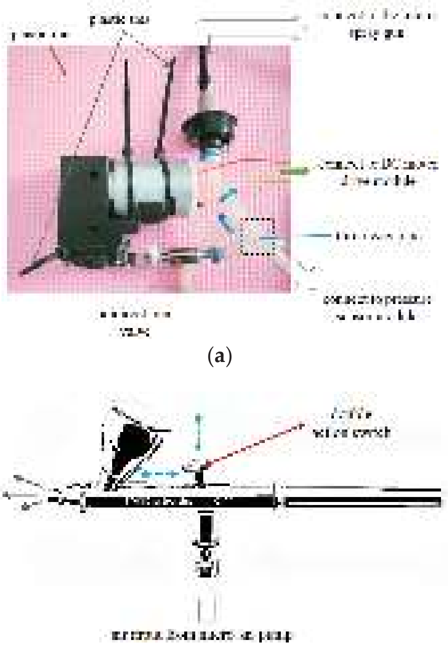

(**a**)

(**b**)

Figure 4. Micro air pump and micro spray gun configuration. (**a**) Picture of micro air pump fixed on the plastic mat material and the I/O contact layout. (**b**) Picture of micro spray gun and the schematic diagram of exhaust switch start. The green arrow stands for pressing down the switch, and the blue arrow reveals pressing the switch to the back of the spray gun.

To test the control effect of the sprayer of the air pump, an airbrush is added to the back of the micro air pump. The system is called a micro spray gun. The professional spray gun (Iwata NEO N4500 Airbrush, Anest Iwata Co., Nishio-shi, Aichi, Japan) is adopted; it is the spray gun suitable for dealing with details or large areas. Figure 4b shows the picture of the spray gun. The micro spray gun sprays paint through air pressure, and the spray gun is generally equipped with an air exhaust switch. The spray gun applies dual action function, as green and blue arrows in Figure 4b. The exhaust volume is controlled by pressing the button or pressing the back of the spray gun. The air input source comes from the micro air pump shown in Figure 4a. The connection point can be seen from the plastic hose above the picture.

To observe the pressure change in the system operating process, another side of the three-way pipe is connected to a pressure sensor module, which integrates a Wheatstone bridge sensor and signals processing chip and covers circuits of a differential amplifier, automated calibration, and temperature compensation. The pressure sensor module could transmit the pressure in the pipe, through the analog-digital conversion of a multifunction I/O card, to the software box for algorithm operation.

2.3.2. Characteristics of the Micro Air Pump

To test the air pressure changes after the multifunction I/O card driving the micro air pump, the PID control algorithm is not utilized, but simply using the multifunction I/O card to output the PWM signals to the DC motor drive module for the micro air pump exhaust. A program is planned with software to change the duty ratio of PWM signal output from 0% to 100% in 20 s, meaning that the duty ratio would increase by 1% per 200 ms. Finally, the multifunction I/O card would read and record the pressure in the pipe.

After the 20 s experimental recording, Figure 5a shows the air pressure change without pressing the micro spray gun switch, as a black solid line, and the air pressure change when pressing the micro spray gun switch, as a gray solid line. The left vertical axis is the pressure change. From the data in Figure 5a,b, the micro air pump appears slow pressure rise on PWM being 55% in both experiments, i.e., the motor smoothly runs at about 11 s, and the initial running of the motor appears on the PWM duty ratio about 55–65%. As shown in the red square in Figure 5b, there is a comparatively large pressure fluctuation. The pressure fluctuation is considered as the micro air pump exhaust not being stable yet, and the pressure signal change would also affect the algorithm in successive PID control experiments. In this case, the duty ratio of the PWM output is controlled at >70% in the successive PID experiment, as to set the micro air pump pressure above 40 kPa, to stabilize the system. It is also discovered in Figure 5b that a large amount of exhaust appears when the micro spray gun switch is pressed, and the maximal pressure difference, under the same PWM output control, is about 30 kPa; it could be understood from the green area in the figure. From Figure 5b, it can be found that when the PWM output is in the range of 70% to 100%, the pressure fluctuation does not exceed 10 kPa. Therefore, assumed that the $e(t)$ of pressure should be controlled below 10 kPa when the algorithm could stabilize the convergence.

The relationship between the driving motor speed and the current of the micro air compressor is quite complicated, and it will vary due to factors such as structure, power supply, and load. This study used a 12 V micro air compressor. When the PWM duty ratio reaches the maximum percentage rate (100%), the motor will also reach the highest speed. When the motor starts from the static, the speed of the motor is not a linear relationship with the driving current, and it must be known according to the actual experiment. Therefore, to understand the relationship between the speed and current of the driving motor, the current corresponding to different PWM duty ratios must be measured. The correlation characteristic curve of the two is shown in Figure 5c. There are five slope lines in Figure 5b that indicate the pressure delta to PWM duty ratio. The slope is in order p3 > p2 > p5 > p4 > p1, and the unit is kPa/%. The driving current of the corresponding PWM duty ratio is shown in Figure 5c. Compared with Figure 5b,c, which would present the driving currents at each stage. The Area-A area of Figure 5c are the currents when the PWM duty ratio is below 55%. Due to insufficient driving current, the motor is almost un-rotated. Area-B was just starting, so the pressure shown in Figure 5b has not yet stabilized. When the micro spray gun is not started, it can be seen from Figure 5b,c that the current value of the Area-C is large, the current delta is relatively large, and the pressure slope is largest. Currently, the PWM duty ratio is about 69–77%. The current in Area-D is relatively stable. So, when the PWM duty ratio is more than 77%, it can reach stability. When the micro spray gun starts to spray, the p4 slope line in Figure 5b corresponds to the Area-C, D, and E in Figure 5c, the PWM duty ratio is more than 69%, and the current is relatively stable. This should be because the gas starts to discharge, lifting the previous closed chamber effect, so that pump can operate stably; improve efficiency.

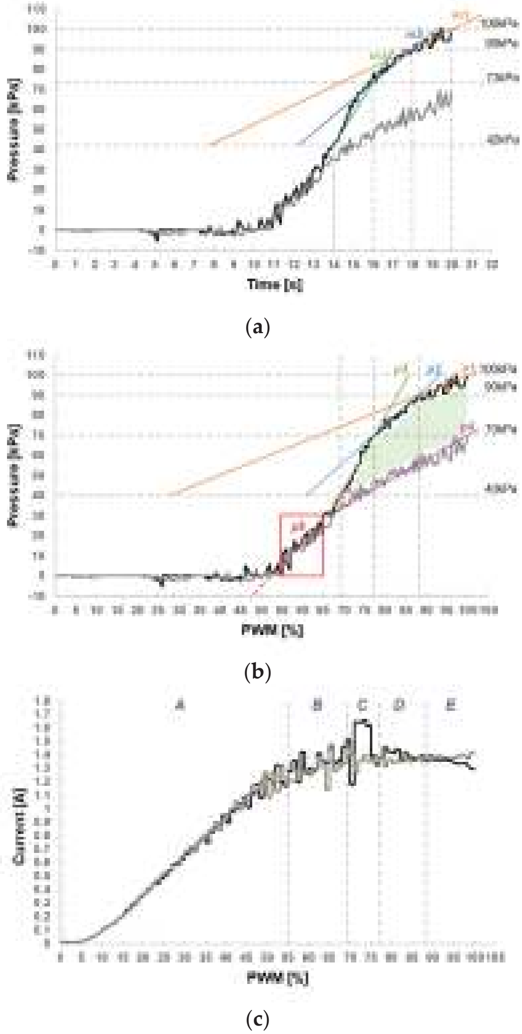

(**a**)

(**b**)

(**c**)

Figure 5. Numerical change of pressure sensor in the micro air pump operating process without PID control algorithm. (**a**) The cross plot of time and pressure sensor value, PWM duty ratio, (**b**) The cross plot of PWM duty ratio and pressure sensor value. (**c**) The cross plot of PWM duty ratio and current value.

2.3.3. Convergence Condition

The algorithm convergence condition is further defined in the section. In the PID control experiment, the $e(t)$ is generally observed by modulating the parameters to analyze the most suitable parameters for the expected target value n(t). m_1, m_2, and m_3 in Figure 5a are used for denoting the pressure above 40 kPa changing with time. For instance, m_3 shows a 15.5 kPa rise per second, m_2 reveals a 8.5 kPa rise per second, and m_1 appears at a 5 kPa rise per second. It also reveals that the PWM output could have the pressure rise 10 kPa within 2 s when the PID parameter is modulated to a stable stage. From another point of view, when the parameter could have the algorithm converge, the $e(t)$ in this system could control it under 10 kPa within 2 s.

Aiming at the monitoring time interval of the $e(t)$ getting into the convergence state at least higher than 2 s, the monitoring time interval is set to 5 s in our experiment. That is, when the $e(t)$ could be inhibited in the minimal convergence error amount of 10 kPa in 5 s intervals, the experiment achieves the convergence condition. It would be easier to comprehend from the curve in Figure 6. When the pressure of $e(t)$ starts to drop below the convergence critical threshold (10 kPa), the change maintaining below 10 kPa in 5 s is observed. When it conforms to the condition within 5 s, the time point dropping down to 10 kPa is called the convergence time (T_c), also the convergence starting point.

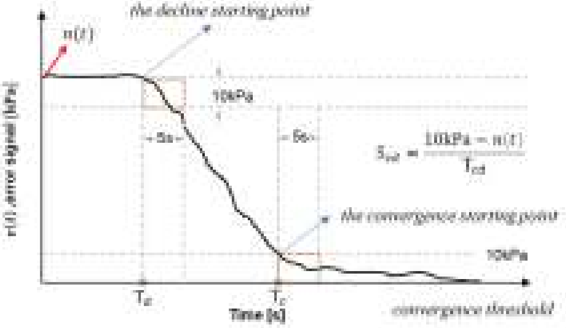

Figure 6. Definition points of convergence condition aiming at PID control algorithm observing error amount.

When the PID algorithm is executed, it would appear distinct fall trend due to different target values $n(t)$. In this case, the convergence condition in the previous paragraph is defined; that is, when the $e(t)$ starts to be lower than the $n(t)$, the observation would be continued for 5 s. When $e(t)$ is lower than $n(t)$ in the 5 s, it is called the decline time (T_d), i.e., the decline starting point. To compare the convergence condition under different parameters, the convergence and decline intervals (T_{cd}) of $e(t)$ is defined as the time difference between T_c and T_d. The convergence and decline slope (S_{cd}) is subtracting the target value $n(t)$ from the minimal convergence error amount (10 kPa) and then divided by T_{cd}, as the equation in Figure 6. Incidentally, the $e(t)$ convergence change curve presented in Figure 6 is the data collected continuously for 0.1 s, and then reproduced with the data of 1 s after averaging 10 points.

3. Results

3.1. Effects under Different Target Values

To verify the effect of the PID control algorithm on the micro air pump, the experimental design and software planning are preceded according to the system architecture in Figure 3. A micro spray gun is added on the back of the micro air pump but exhausted by not pressing the switch of the micro-spray gun. According to the data explanation in Section 2.3.2, the micro spray gun is suitable for the application to exhaust volume above 40 kPa. $n(t)$ is therefore set to 40, 50, 60, 70, 80, 90, and 100 kPa as the target value for the algorithm.

The PID controller could generally acquire the close parameters through trial and error. First, according to the experience, merely K_p is added to the system. K_p is set as the minimum to observe the convergent tendency of $e(t)$. If the system response is slow, increase the K_p value, otherwise decrease the K_p value to obtain the range suitable for the experimental parameters. So, with these rules of thumb, we finally set the differential gain adjustable parameter K_d to 0, the integral gain adjustable parameter K_i is set to 0.1, and the proportional gain adjustable parameter K_p is modulated to 0.1, 0.05, 0.01, and 0.005 to observe the convergence condition.

Figure 7 shows the condition of $e(t)$ being continuously monitored for 100 s when the target value $n(t)$ is set to 60 kPa, and the PID parameters are set with four K_p values. The smaller $e(t)$ reveals the closer $y'(t)$ from the pressure sensor to the target value $n(t)$.

According to the convergence condition described in Section 2.3.3, the PID algorithm monitors the stability when $e(t)$ gets in the minimal convergence error amount (10 kPa). From Figure 7, it is discovered that the decline point T_d could be achieved in about 2–3 s when the K_p is set to 0.1. However, the $e(t)$ is hard to achieve the convergence condition in a short period; it takes about 96 s to drop down to the convergence critical threshold (10 kPa). Strictly speaking, the parameter has the system approach the divergence. The other three K_p values reach the convergence condition; when K_p is 0.05, 0.01, and 0.005, the T_c appears at 9 s, 27 s, and 52 s, respectively. Such a result reveals that the fastest speed to achieve the convergence critical threshold appears when K_p is set to 0.05.

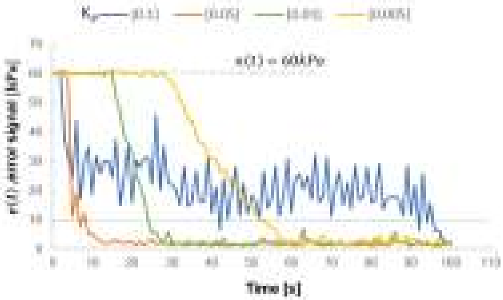

Figure 7. The changing trend of each error amount $e(t)$, when target value $n(t)$ is set to 60 kPa, and set PID parameter K_p = 0.1, 0.05, 0.01, and 0.005.

The experimental data are organized in Figure 8. The x-coordinate in Figure 8a is the target value $n(t)$ with the PID algorithm. In this case, the selection of K_p indeed presents distinct effects on T_c, under the same target value. K_p being 0.005, compared with 0.05 and 0.01, appears longer convergence time; when K_p is 0.1, signal oscillation appears at 60 kPa and 70 kPa, without being stably adapted. Furthermore, the convergence time T_c, relative to the target pressure, is out of proportion, and, even when $n(t)$ is 60 kPa, T_c is longer than K_p being set to 0.005. In this case, when K_p is set to 0.1, $n(t)$ should be above 80 kPa to really conform to the convergence condition; it could be viewed from the blue round in Figure 8a. In Figure 8b, convergence decline slope S_{cd} is applied to present the difference under a different target value. It is discovered that the S_{cd} change to the convergence situation of each target value is not big, when K_p is 0.005 and 0.01, maximally dropping the $e(t)$ amount about 7.8 kPa per second. When K_p is 0.05, as shown in Figure 8b, the slope of S_{cd} increases with the increase of $n(t)$, which means that the algorithm can achieve a convergence effect at a similar time when $n(t)$ is between 40 and 100 kPa. As shown in the orange triangle in Figure 8a, the overall T_c are very close.

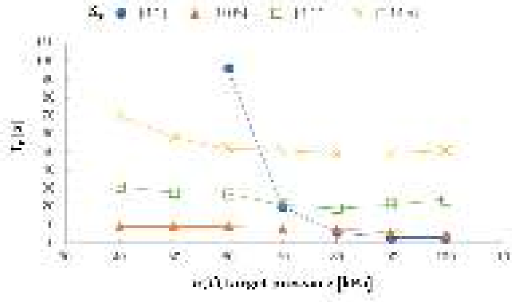

(**a**)

Figure 8. *Cont.*

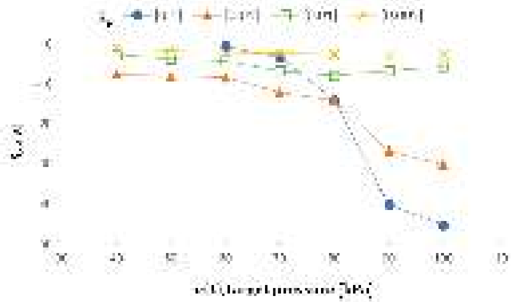

(**b**)

Figure 8. When K_p = 0.1, 0.05, 0.01, and 0.005, (**a**) The different $n(t)$ values and the corresponding convergence time T_c and (**b**) The different $n(t)$ values and the corresponding convergence decline slope S_{cd}.

3.2. Effects under Pulse-like Variables

When using a micro spray gun, pressing down the switch for spraying paint results in dropping pressure in the pipe, with a change of about 30 kPa. In this case, a pulse-like sequence variable, target value $n(t)$, is regarded as the target to understand the adaption of PID parameters to different pressure changes. It simulates two target amounts, 65 kPa, and 95 kPa, in the time interval as the alternate output. The sequence data, according to the software planning, would change the $n(t)$ of the system at 20, 40, and 60 s, as the switch between 65 kPa and 95 kPa of the grey curve in Figure 9.

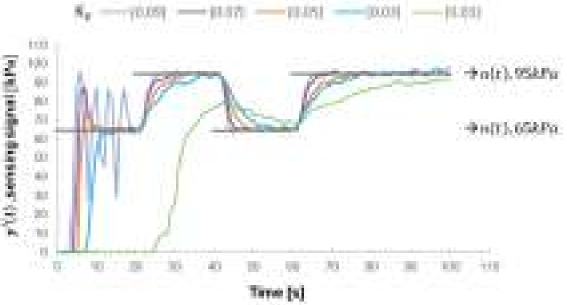

Figure 9. The grey line indicates a pulse-like curve simulating the target value $n(t)$ in 65 kPa and 95 kPa, and converged at 20, 40, and 60 s. Output pressure $y'(t)$ under PID parameter K_p = 0.1, 0.05, 0.01, and 0.005.

Since better convergence appears on K_p being 0.05, the intervals ±0.02 and ±0.04 are selected for observing the effect of such K_p on pulse-like sequence data, while K_i remains 0.1 and K_d remains 0. From Figure 9, five curves show the results of tracing the target value with the PID control technology, when K_p is 0.01, 0.03, 0.05, 0.07, and 0.09.

In the first 20 s, $n(t)$ as 65 kPa is the target of PID when the micro air pump is just started; it is discovered that the system appears to overshoot when K_p is 0.09. The result is similar to Figure 8a in that oscillation is more easily appear when K_p is 0.1 and $n(t)$ is under 70, it is hard to get into the region of convergence. When K_p is 0.01, it is difficult to catch the target value of 65 kPa in the first 20 s, due to the relatively smaller value. The convergence effect could be achieved at about 10 s with the other three parameters of K_p being 0.03, 0.05, and 0.07; that is, the rising speed and the effect of overshoot, when K_p appears 0.05 ± 0.02, are more acceptable. Overall, the overshoot and time for rising to the target value under K_p being 0.05 show better adaptability on 20 s after the system startup.

After 20 s, the target value $n(t)$ is programmed to 95 kPa and the standard of convergence is soon achieved when K_p is 0.09, as it is close to 0.1. According to the observation of Figure 8a, it would get into the region of convergence soon when K_p is 0.1 and $n(t)$ is above 90. The experimental result with the parameters is therefore reasonable. When K_p is 0.09 and the system is modulated to a steady state, it would not appear unstable error variation as in the starting, even when the target value is changed to 65 kPa after 40 s. When K_p is 0.01, although it takes a long time to keep up with the target value $n(t)$, it has begun to catch up gradually, but $e(t)$ is still much larger than other parameters. With the rest three parameters, e.g., $K_p = 0.03$, 0.05, and 0.07, the change is stable along with the target value and the convergence is achieved within a short period. Furthermore, after 20 s and the overshoot phenomenon as in the system starting does not appear when K_p are 0.05 and 0.07.

3.3. Effects of PID Convergence

As the system architecture in Figure 3, when pressing down the switch on the spray gun, the spray nozzle starts to spray air and immediately reduces the air pressure in the pipe. To have the air maintain certain output, the system would enhance the exhaust volume of the micro air pump through the PID algorithm, i.e., enhancing the percentage of PWM.

Figure 10a shows the pressure change $y'(t)$ before/after pressing the switch of the micro spray gun. The experimental parameters selected K_p to be 0.05, K_i remained at 0.1, and K_d is 0. The grey line in Figure 10a shows the system locking the target value $n(t)$ on 65 kPa. In this case, the system, after starting, would catch up with the set target value $n(t)$ according to the parameters set by PID. The result reveals to catch up to the target value at about 10 s. When the time achieves 20 s, the switch of the micro spray gun, as the green arrow indicated in Figure 4b, is pressed. It is discovered that the pressure, after pressing the switch, immediately drops about 25 kPa, and PID would control output after the system detects the pressure change. As a result, when the pressure is reduced, PID would increase the percentage of PWM to enhance the exhaust output volume to maintain the pressure at the target value of 65 kPa. Figure 10a shows that it takes about 10 s, after pressing down the switch, to have the pressure return the target value. The process could be viewed through the change in PWM modulation. Figure 10b displays the PWM change after pressing down the switch of the micro spray gun. When the system achieves stability, the PWM modulation value does not appear to large changes, e.g., PWM stably maintains 70% after starting for 10–20 s, as the red dotted double arrows in Figure 10b. When the spray gun switch is pressed at 20 s, PWM starts to increase the output percentage; after 30 s, PWM almost remains at 95%, without much modulation, as the black dotted arrow in Figure 10b.

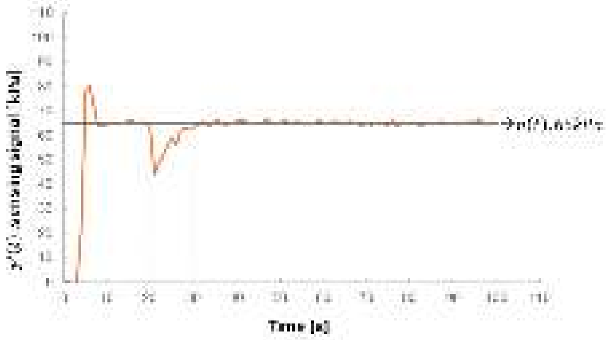

(**a**)

Figure 10. *Cont.*

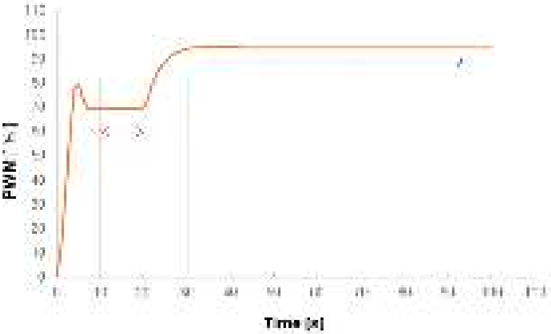

(**b**)

Figure 10. When the PID parameter is set $K_p = 0.05$, $K_i = 0.1$, $K_d = 0$, (**a**) The sensed pressure change, and (**b**) The change in PID modulating PWM output, before and after pressing down the micro spray gun.

4. Discussions

Aiming at the experiment results, three points are discussed.

1. The experimental data reveal that the internal structure of the micro air pump presents certain effects on the control response, rather than simply a linear state. Consequently, the experiment results shown in Figure 5a could verify the better pressure output range of the micro air pump above 40 kPa. The exhaust, when the spray gun is pressed, results in dropping pressure in the pipe to influence the overall pressure output. In this case, the maximal pressure sensed is about 70 kPa when PWM is modulated to the maximal 100%, with the difference of about 30 kPa from the spray gun not being pressed. In the experiment in Section 3.3, the preset target value of 65 kPa would drop down to 40 kPa after pressing the spray gun. The low pressure during paint spray would affect the spray quality and result in the irregular operation of the motor, due to the unstable air pump, damaging the life. Automatic control technology could effectively change the exhaust output volume and stabilize the operation of the air pump. This study verifies the driving module and algorithm control technology of the automatic system. The experiment results after pressing the spray gun proves that proper parameter modulation allows the system design to return the target pressure within a specified period.
2. The proportional gain adjustable parameter K_p determines the ratio of the output response to the error signal. In general, increasing K_p will increase the responsiveness of the control system, but if the proportional gain is too large, the process variable will start to oscillate. If K_p is increased further, the vibration will become larger and larger, and the system will become unstable, and even uncontrollable vibration may occur. As the result in Figure 7, $K_p = 0.1$ is obviously a larger value in this experiment; under the same target value $n(t)$, the error is comparatively difficulty to be controlled in the convergence range. Perhaps, K_p appears faster convergence time and convergence speed when $n(t)$ is above 80 kPa with several larger target values $n(t)$, as in Figure 8a. Nevertheless, the higher instability results in $n(t)$ being 60 and 70 kPa, the convergence time being largely prolonged, and the convergence time, with $n(t)$ being 60 kPa, is even longer than it when K_p is 0.005. Particularly, it could not get into the convergence condition when $n(t)$ is 40 kPa and 50 kPa. Such applications would cause several unpredictable errors and even non-practical ones. When smaller K_p is selected, the error signal is less sensitive and the response to the target signal being suddenly interfered with or appearing larger variable would be too slow and the output control signal is not large enough to catch up with the variable quantity. As in Figure 9, the target value $n(t)$ in the moment of conversion at 65 kPa and 95 kPa, when K_p is 0.01, does not cause system instability or divergence, but the speed to catch up with the

target value is indeed slower. In real applications, it is difficult to predict or limit users to stably press the spray gun so that the pressure variable would happen at any time. The pulse-like target variable experiment planned in Section 3.2 is used for coping with such pressure variables with proper parameter settings so that the micro spray gun system could be normally operated.

3. After pressing the micro spray gun, the pressure of the feedback signal immediately drops to have the PID system make larger output modulation. It reveals the same operation idea of pulse-like variable target value; but the pressure disturbance in the pipe, after pressing the spray gun, cannot be predicted. Figure 10a shows that $y'(t)$, after returning the target value, still appears slight fluctuation. However, the PID output control could have the PWM stably increase, without overshoot of the system, Figure 10b. It is therefore considered that K_p being set to 0.05 could effectively catch up with the target within a short period, and selecting proper K_i could accelerate the system approaching the target and eliminate the steady state error on K_p.

5. Conclusions

The micro spray gun (airbrush) is primarily used for fine art drawing, and the quality of the spraying depends on the accuracy and stability of the air pressure. However, traditional mechanical regulation may not always meet the necessary requirements. Our study introduces the PID method for the first time to improve the spray quality, even without an air receiver. The experiment results show that, under a proper selection of K_p and K_i, the target pressure changes within 30 kPa could achieve the convergence condition in 10 s. The results as well show that the instant pressure difference of 25 kPa after spraying could be increased to the target pressure in 10 s.

Consequently, the entire system architecture design could realize the adaptive micro sprayer, effectively reduces wear, and enhances the service life. The system architecture designed in this study would provide the reference for the realization of miniaturized micro-controller in the future to achieve the goal of adaptive portable micro spray gun equipment.

Author Contributions: Conceptualization, J.-H.L. and C.-H.C.; methodology, C.-H.C.; software, J.-H.L.; validation, S.-T.T.; formal analysis, S.-T.T.; investigation, C.-H.C.; resources, J.-H.L.; data curation, S.-T.T.; writing—original draft preparation, C.-H.C.; writing—review and editing, J.-H.L. and S.-T.T.; visualization, J.-H.L.; supervision, S.-T.T.; project administration, S.-T.T.; funding acquisition, J.-H.L. All authors have read and agreed to the published version of the manuscript.

Funding: This research received no external funding.

Conflicts of Interest: The authors declare no conflict of interest.

References

1. Sudduth, K.A.; Borgelt, S.C.; Hou, J. Performance of a chemical injection sprayer system. *Appl. Eng. Agric.* **1995**, *11*, 343–348. [CrossRef]
2. Erkan, U.; Huseyin, G.; First, K. A review of electrostatic spraying for agricultural applications. *J. Agric. Mach. Sci.* **2016**, *12*, 229–233.
3. Liu, Z.B. High-Precision Spray Gun Spraying Control System Based on Linear Regulation. China Patent CN113019732A, 2021.
4. Giles, D.K.; Bensalem, E. Spray droplet velocity and energy in intermittent flow from hydraulic nozzles. *J. Agric. Eng. Res.* **1992**, *51*, 101–112. [CrossRef]
5. Deng, W.; Zhao, C.; Chen, L.; Wang, X. Comparison of spray characteristics for three types of variable spray. *J. Agric. Eng. Res.* **2016**, *XLVII 512*, 148–156. [CrossRef]
6. Grella, M.; Gioelli, F.; Marucco, P.; Zwertvaegher, I.; Mozzanini, E.; Mylonas, N.; Nuyttens, D.; Balsari, P. Field assessment of a pulse width modulation (PWM) spray system applying different spray volumes: Duty cycle and forward speed effects on vines spray coverage. *Precis. Agric.* **2022**, *23*, 219–252. [CrossRef]
7. Orti, E.; Cuenca, A.; Perez, M.; Torregrosa, A.; Ortiz, C.; Rovira-Mas, F. Preliminary evaluation of a blast sprayer controlled by pulse-width-modulated nozzles. *Sensors* **2022**, *22*, 4924. [CrossRef] [PubMed]
8. Maski, D.; Durairaj, D. Effects of electrode voltage, liquid flow rate, and liquid properties on spray chargeability of an air-assisted electrostatic-induction spray-charging system. *J. Electrost.* **2010**, *68*, 152–158. [CrossRef]

9. Chen, S.; Yin, D.; Wei, X.; Pei, W. Design and simulation of variable weed spraying controller based on adaptive neural fuzzy inference system. *J. Drain. Irrig. Mach. Eng.* **2011**, *29*, 272–276.
10. Patel, M.K.; Ghanshyam, C.; Kapur, P. Characterization of electrode material for electrostatic spray charging: Theoretical and engineering practices. *J. Electrost.* **2013**, *71*, 55–60. [CrossRef]
11. Sasaki, R.S.; Teixeira, M.M.; Fernandes, H.C.; Paulo, M.; Denílson, E.R.; Cleyton, B. Parameters of electrostatic spraying and its influence on the application efficiency. *Rev. Ceres* **2013**, *60*, 474–479. [CrossRef]
12. Shilkrot, R.; Maes, P.; Paradiso, J.A.; Zoran, A. Augmented airbrush for computer aided painting. *ACM Trans. Graph.* **2015**, *34*, 1–11. [CrossRef]
13. Mohamed, A.A.S. An Investigation into the History of the Airbrush and the Impact of the Conservation Treatment of Airbrushed Canvas Paintings. Ph.D. Thesis, Northumbria University, Newcastle upon Tyne, UK, 2016.
14. Chen, Y.C. Study on the Airbrush Makeup Applied to the Whole Fashion Design Combining with the Concept of Multi-Media. Master's Thesis, Department of Cosmetics Science, Vanung University, Taoyuan, Taiwan, 2022.
15. Lin, J.H.; Tang, S.T.; Chen, C.H.; Cheng, Y.T.; Tai, C.C.; Lin, M.H. The Prototype Design and Verification of Intelligent Variable Output Control Apply on Micro-spray Gun Simulation Platform. In Proceedings of the 2022 International Conference on Fuzzy Theory and Its Applications (iFUZZY), Garden Villa, Kaohsiung, Taiwan, 3–5 November 2022.
16. Yan, H. Diaphragm Air Pump. China Patent CN201714643U, 2011.
17. Jalnekar, R.M.; Jog, K.S. Pulse-width-modulation techniques: A review. *IETE J. Res.* **2020**, *46*, 175–183. [CrossRef]
18. Li, Y.; Ang, K.H.; Chong, G.C.Y. Patents, software and hardware for PID control—An overview and analysis of the current art. *IEEE Control Syst. Mag.* **2006**, *26*, 42–54.
19. Lopez-Gomez, J.; Vargas-Trevino, M.A.D.; Vergara-Limon, S.; Vargas-Trevino, M.; Gutierrez-Gutierrez, J.; Palomino-Merino, A.D.; Martinez-Solis, F.; Felix-Beltran, O. Influence of PWM torque control frequency in DC motors by means of an optimum design method. *IEEE Access* **2020**, *8*, 80691–80706. [CrossRef]
20. Zhang, R.; Gao, L.X. Research on motor control and simulation based on PID and internet of things system. *Microprocess. Microsyst.* **2021**, *80*, 103602. [CrossRef]

applied sciences

MDPI

Article

Analysis of Explicit Model Predictive Control for Track-Following Servo Control of Lunar Gravity Compensation Facility

Yonggui Zheng [†], Meng Liu [†], Hao Wu * and Jun Wang

School of Aeronautic Science and Engineering, Beihang University, Beijing 100191, China;
zhengyonggui@buaa.edu.cn (Y.Z.)
* Correspondence: haowu@buaa.edu.cn
† These authors contributed equally to this work.

Abstract: The Lunar Gravity Compensation Facility (LGCF) is a critical component in ground tests for a crewed lunar roving vehicle (CLRV). The track-following servo subsystem's performance is of critical importance in the LGCF, as it needs to achieve high-precision tracking of the CLRV's fast, wide range of motion in the horizontal direction. The subsystem must also operate within various constraints, including those related to speed, acceleration, and position. These requirements introduce new challenges to both the design and control of the subsystem. To tackle these challenges, this paper employs a Permanent-Magnet Synchronous Motor (PMSM) vector control method based on Space Vector Pulse Width Modulation (SVPWM) to achieve accurate speed tracking. Additionally, this paper presents an Explicit Model Predictive Control (EMPC) strategy for precise position servo control of the track-following system under multi-parameter constraints. The simulation model of the track-following servo subsystem is established based on the above methods. The simulation results demonstrate that the position tracking error of the gravity compensation system, constructed using the above method combined with EMPC control, is less than 0.2 m. The control performance of the EMPC is significantly better than those of the PI and LQI controllers. The influence of errors on the drawbar pull is within 12.5%, and its effect on the compensation force is negligible. These results provide theoretical support for the design of a track-following servo subsystem.

Keywords: lunar gravity compensation facility; track-following servo subsystem; PMSM; explicit MPC

Citation: Zheng, Y.; Liu, M.; Wu, H.; Wang, J. Analysis of Explicit Model Predictive Control for Track-Following Servo Control of Lunar Gravity Compensation Facility. *Appl. Sci.* **2023**, *13*, 4411. https://doi.org/10.3390/app13074411

Academic Editors: Kan Liu and Wei Hu

Received: 11 March 2023
Revised: 29 March 2023
Accepted: 29 March 2023
Published: 30 March 2023

1. Introduction

The crewed lunar roving vehicle (CLRV) is essential in Chinese plans to build a lunar base. The CLRV is an essential and indispensable exploration tool that not only transports astronauts to great distances from the lunar module but also ensures their safety as they move on the lunar surface [1]. To mitigate the potential issues of the CLRV, it is imperative to conduct a comprehensive ground test of the full rover before launch. Furthermore, the differences in gravity between the Moon and Earth give rise to distinct steering properties and driving sensations for the astronauts using the CLRV. Therefore, it is essential to construct a ground test facility on Earth that accurately simulates lunar gravity to facilitate astronaut training and evaluate the CLRV's performance.

A problem common to the ground test facility is simulating a low-gravity environment similar to the spacecraft's natural working environment [2]. Simulating a low-gravity field is an essential issue in the motion performance experiment of the planetary rover. The simulation method of offsetting part of the lunar rover's gravity by an external force is called gravity compensation. The primary ways to achieve artificial micro-gravity include free-fall testing [3], the air-bearing table [4], neutral buoyance [5,6], and the suspension system [7,8]. Among the available methods, the suspension system [9,10] is widely adopted because of its relatively simple structure, easy construction, and 3-D simulation with unlimited time.

The track-following servo subsystem is a critical component of the suspension gravity compensation system, which is used to precisely track the movement of the test object in the horizontal direction. In the suspension gravity compensation system of the CLRV, due to the large motion velocity, acceleration, and range of the CLRV, the track-following servo subsystem also requires a corresponding motion capability and a large scale. In this context, the crane as the servo motion mechanism exhibits significant inertial characteristics [11]. At the same time, the subsystem is also faced with various constraints such as speed, acceleration, and position. These characteristics often result in significant tracking errors and even control failure.

Currently, research on the effectiveness of the track-following servo subsystem in the suspension gravity compensation system of the CLRV remains unexplored. The active response gravity offload system (ARGOS) at NASA's Johnson Space Center is a typical suspension system [12]. However, the track-following servo subsystem of this system is only applicable for walking tests of astronauts with low velocity in a single direction. The Harbin Institute of Technology built a suspension lunar gravity compensation system, which was only suitable for slow-moving unmanned lunar rovers [2]. The max speed of the Yutu lunar rover is about 200 m/h, while the theoretical maximum speed of the CLRV in pre-research is about 4 m/s. The Soviet Union's planetary rover ground test used an active tracking constant tension suspension scheme [13], which generated a constant vertical pulling force using a parallelogram with a spring. However, this solution is only suitable for ground tests on Mars rovers and may not work well for driving a large vehicle on simulated soft lunar soil. NASA proposed a suspension system scheme suitable for CLRV ground tests in the last century, but the track-following servo control in the program lacks simulation validation and practical implementation [14]. The suspended gravity compensation system is more commonly used in slow-motion microgravity experiments, such as deployable antennas [7] and satellites [8], and its tracking servo subsystem is not suitable for the CLRV.

To meet the CLRV's test requirements, this paper conducts research on the system design and control scheme of the track-following servo subsystem in an overhead-crane-like Lunar Gravity Compensation facility (LGCF) based on a single-cable gravity compensation system. As shown in Figure 1, the system compensates 5/6 of the CLRV's weight over a square test field of 80 × 20 square meters. As shown in Figure 1, the primary research of this paper is the track-following servo subsystem in the LGCF, consisting of an overhead moving crane and a trolley. The crane moves on the bridge, tracking the real-time position of the CLRV in the X direction, and the trolley moves along the crane girder to follow the real-time Y position of the CLRV. The servo motors drive the crane and trolley.

The paper introduces the vector control of the PMSM to the track-following servo subsystem, enabling high-precision and rapid tracking control. In servo motors, the permanent-magnet synchronous motor (PMSM) has many outstanding advantages compared with other motors. The PMSM vector control system can achieve high precision, high dynamic performance, and an extensive range of speed regulation, tracking, and control, attracting wide attention and research from scholars worldwide [15–17].

This track-following servo subsystem includes the position servo closed-loop and closed-loop control of the motor speed and current. In the simulation model of the speed and current closed-loop control, the surface-mounted PMSM (SPMSM) vector control system based on the Space Vector Pulse Width Modulation (SVPWM) method was used in the paper [18], which highly simulated the actual system. The PI method was used for the PMSM vector control system.

In the position servo closed-loop, there are constraints on the movement speed and acceleration of the crane and trolley to avoid motor idling [19] or over-speed. Moreover, the motion ranges of the crane and trolley are also constrained by the size of the facility. The traditional PID control cannot meet the control requirements, due to multi-variable constraints in the position servo closed-loop. In particular, this paper employs the explicit model predictive controller (EMPC) [20] in the position servo closed-loop so that the overhead moving crane and the trolley follow the motion of the CLRV in the X and Y directions, respectively. The MPC is a new computer optimization control algorithm that can effectively deal with multi-variable constraint systems [21]. It has become a standard optimization method for complex constraint systems. In recent years, the MPC has received significant attention in path tracking and fast tracking [22,23]. The main reason is that the MPC can better handle the constraints of concern to physical and safety systems, which benefits system control performance and component protection. Despite the advantages of the MPC mentioned above, its substantial computational complexity resulting from online optimization at each sampling time poses a significant drawback and limits its applicability to relatively small and slow systems. To address this challenge, Bemporad and Alberto et al. proposed a novel approach based on an MPC scheme that moves all computational efforts offline, enabling the scheme to overcome the aforementioned limitation [24,25], and the method is the EMPC.

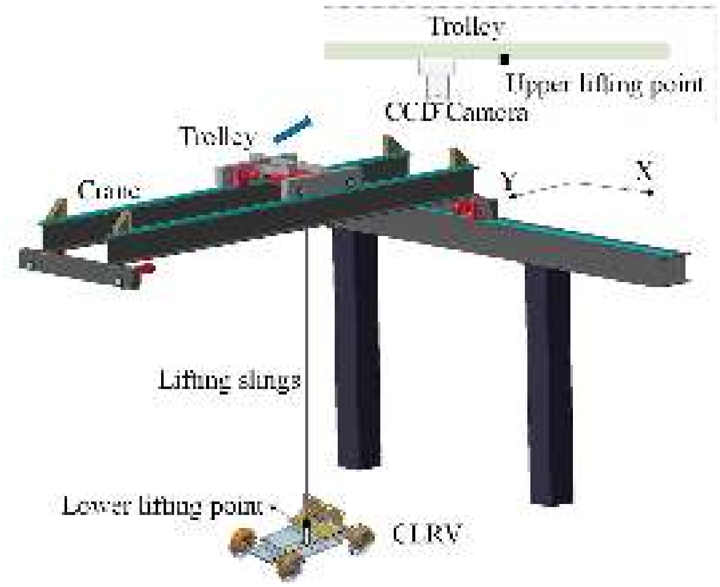

Figure 1. The structure diagram of LGCF.

Overall, this study provides an innovative and promising design proposal for a track-following servo subsystem of an LGCS suitable for the CLRV ground test. The vector control of the PMSM based on SVPWM is used in this paper to achieve a fast response of the track-following servo control. Notably, this paper adopts an EMPC in the position servo closed-loop to obtain good control performance. The EMPC controller can be applied to multi-constrained systems, ensuring a fast response while reducing overshoot. Finally, simulation models of the subsystem are built, and the simulation results are presented and discussed to evaluate the proposed system design and control scheme. The study provides a significant contribution to the field of the LGCS and serves as a valuable reference for future research.

The paper is organized as follows. Section 2 presents the design scheme of the tracking servo subsystem and establishes the system's three-loop servo control model of the current loop, speed loop, and position loop. Section 3 introduces the implementation process of the EMPC control strategy. In Section 4, the desired trajectory of the system, EMPC, and LQI position loop control model parameters are presented. Section 5 discusses and presents the simulation results to evaluate the system performance. Finally, Section 6 concludes the paper.

2. Methodology

In this section, we present the mechanical design of the track-following servo subsystem. The subsystem comprises a moving crane system, a moving trolley system, and multiple motors that enable the track-following servo in both the X and Y directions, as illustrated in Figure 2. The crane is driven by four motors, and the trolley is driven by two motors. The motors power the steel wheels of the crane and trolley to move on the rail. The servo motors transmit power to the system, which is then transmitted to the low-speed shaft end of the reducer via the coupling. The reducer’s low-speed shaft end outputs to the driving wheel shaft through another coupling, and the driving wheels propel the crane and trolley to follow the CLRV with high precision.

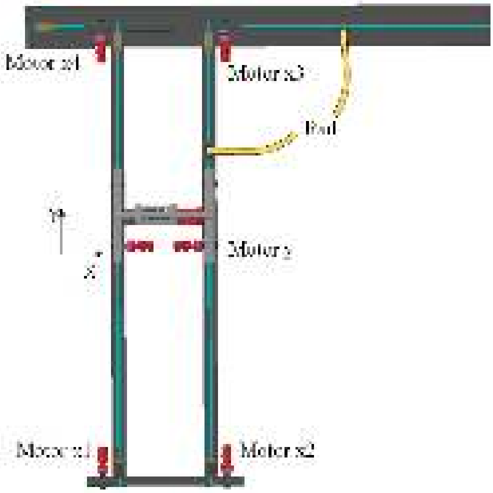

Figure 2. Schematic diagram of the subsystem movement.

Then, based on the mechanical design of the subsystem, suitable equipment is selected, and a simulation model of the track-following servo subsystem is established. In this paper, the servo motors used are PMSMs. The track-following servo subsystem comprises a position servo closed-loop and closed-loop control of the motor speed and current; the crane control model is illustrated in Figure 3. The position control loop is situated on the outer layer of the double closed-loop, which includes the speed and current loops of the servo motor. The position control loop receives a reference signal and subsystem state variables and calculates the expected velocity increment of the crane or trolley in a given unit of time. This value is then passed to the motor’s speed loop controller. The speed loop controller calculates the expected current output by comparing the expected speed with the actual speed. The motor’s current loop controller then calculates the expected voltage input based on the expected current and the actual current. Together, these three loops form the track-following servo subsystem.

To achieve high-precision control of the crane and trolley, the PMSM vector control method based on SVPWM is adopted for fast response in speed control. The PI control method, with its advantages of being a simple algorithm, having good stability, and having high reliability in the motor speed control system, is widely used for controlling motor speed and current. Therefore, the PI method is applied to the PMSM vector control system, as depicted in Figure 3.

The performance of the outermost position servo loop plays a crucial role in the track-following servo subsystem’s tracking performance. However, the position loop’s control is limited by the electromechanical system’s kinematics and dynamics. To overcome this multi-parameter constraint, the present paper proposes utilizing the EMPC controller within the position servo closed-loop.

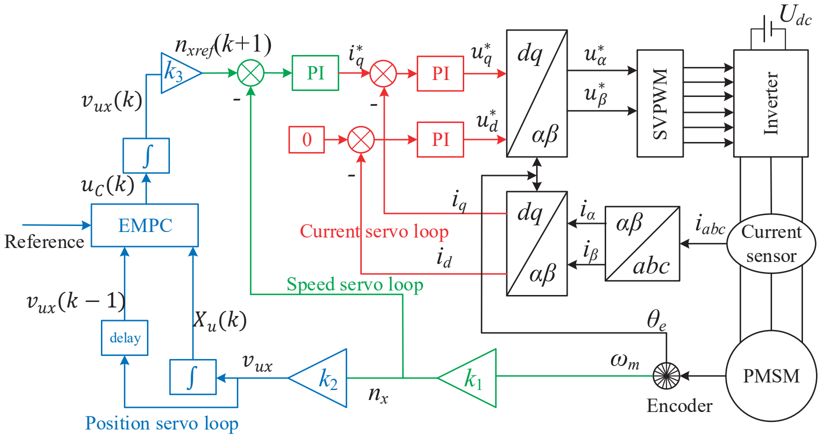

Figure 3. Three-loop control of the crane in track-following servo subsystem.

This section mainly describes the establishment of the mathematical model for the three-loop control system, including the mathematical model and model parameters of the PMSM, as well as the mathematical model of the position loop.

2.1. Mathematical Model of PMSM

As shown in Figure 3, this paper adopts vector control technology based on SVPWM to realize the decoupling control of torque and excitation components. Following the stator flux linkage orientation control rules, the d-axis of the reference coordinate is aligned with the motor flux direction, where $i_d = 0$. The stator flux linkage component on the d-axis is represented as $\psi_f = \psi_d$. The voltage equation of the PMSM is formulated in the two-phase synchronous rotating reference frame.

$$\begin{cases} \frac{di_d}{dt} = \frac{1}{L_d}\left(-Ri_d + P_n\omega_m L_q i_q + u_d\right) \\ \frac{di_q}{dt} = \frac{1}{L_q}\left(-Ri_q - P_n\omega_m L_d i_d + u_q - P_n\omega_m\psi_f\right) \\ \frac{d\omega_m}{dt} = \frac{1}{J}\left(T_e - T_L - B_u\omega_m\right) \end{cases} \tag{1}$$

The torque reference (electromagnetic torque) T_e in the following equation is used:

$$T_e = 1.5P_n\left[\psi_f i_q + \left(L_d - L_q\right)i_d i_q\right] \tag{2}$$

where R is the stator resistance (Ω); L_d and L_q are the inductances (H) of the stator on the d and q axes, respectively; i_d and i_q are the current (A) of the stator on the d and q axes, respectively; u_d and u_q are the voltage (V) of the stator on the d and q axes, respectively; P_n is the number of pole pairs of the rotor; J is the inertia; ω_m is the angular velocity measured from the motor; T_L is a constant load torque; B_u is the mechanical damping constant.

Suppose that the load torque of the four motors in the X direction is equal, the output torque and speed are equal, the load torque of the two motors in the Y direction is equal, and the output torque and speed are equal. In order to build the mathematical model of the motor, it is necessary to select the specific motor first according to the required motor torque and speed.

The motor torque T_{out} is divided into load torque T_u for overcoming rolling friction and accelerating torque T_a for maximum acceleration.

$$T_{out} = q_{motor}\left(T_u + T_a\right) = q_{motor}\left(\mu mgr_w + mar_w\right) \tag{3}$$

where the gross load hauled by the crane is about $m_x = 12,000$ kg, and the gross load hauled by the trolley is about $m_y = 2000$ kg. The number of motors for the moving crane system and the moving trolley system are $q^X_{motor} = 4$ and $q^Y_{motor} = 2$, respectively. The coefficient of rolling friction with railroad steel wheels on steel rails is $\mu = 0.05$, and the radius of the steel wheel is $r_w = 0.2$ m.

The design speed of the crane is larger than the maximum speed (v_{rmax}) of the CLRV, so $v^{max}_{ux} = 5$ m/s is set. Additionally, the VLRV moves in a small range in the Y direction, so $v^{max}_{uy} = 3.5$ m/s is set. The v_{ux} and v_{ux} are the actual speeds of the crane and trolley, respectively.

According to Equation (4), the max speeds of motors n^{max}_x and n^{max}_y can be calculated:

$$n = \frac{60r_g}{2\pi r_w} v_u \tag{4}$$

where the gear ratio of the crane motors is $r^X_g = 10$ and the gear ratio of the trolley motors is $r^Y_g = 10$.

According to the calculation, the motors are selected. The parameters of the motors are shown in the following Table 1.

Table 1. Permanent-magnet synchronous motors parameters table.

Parameters	Motors x (1, 2, 3, 4)	Motors y (1, 2)
bus voltage U_{dc}	380 V	380 V
stator rated current I_N	63 A	20 A
stator inductance $L_d = L_d$	0.0083 H	0.0024 H
stator resistance R	0.376 Ω	0.369 Ω
permanent magnet flux ψ_f	0.9720 Wb	0.8815 Wb
the rotor moment of inertia J	0.2026 kg·m^2	0.0182 kg·m^2
the number of pole pairs P_n	1	1
viscous damping B_u	0.00464 N·m·(s·rad^{-1})	0.003 N·m·(s·rad^{-1})
the rated speed n	2500 rpm	2500 rpm
The rated torque T_e	123 N·m	37.4 N·m

In the system, the motors' speeds are n_x and n_y, and the actual angular velocities of the motors are ω_{mx} and ω_{my}, respectively.

$$v_{ux} = \frac{2\pi r_w n_x}{60 r^X_g} = \frac{r_w \omega^X_m}{r^X_g} \tag{5}$$

$$v_{uy} = \frac{2\pi r_w n_y}{60 r^Y_g} = \frac{r_w \omega^Y_m}{r^Y_g} \tag{6}$$

In this paper, the PI control is adopted in the motor's current loop and speed loop control. The primary constraints during the controller design are the voltage and current constraints on the quadrature axis and direct axis. The constraints are as follows:

$$\begin{aligned} \sqrt{\left(i_d^2 + i_q^2\right)} &\le \sqrt{2} I_N \\ \sqrt{\left(u_d^2 + u_q^2\right)} &\le \tfrac{U_{dc}}{\sqrt{3}} \end{aligned} \tag{7}$$

As this is a real physical system, constraints on the states and inputs have to be considered during the controller design given. In the wheel/rail transmission, the premise for obtaining different traction forces is not to destroy the adhesion moment between the wheel/rail. In this paper, the calculation formula of the train wheel/rail adhesion coefficient

u_j is used to calculate the maximum traction torque. When the train speed $v < 50$ km/h, the u_j is as follows [26]:

$$\mu_j = 0.24 + \frac{12}{100 + 8v_{max}} \tag{8}$$

Then, the maximum traction torque is

$$T_j = \frac{\mu_j m g r_w}{r_g q_{motor}} \tag{9}$$

The maximum accelerations a_{ux}^{max} and a_{uy}^{max} can be calculated from the maximum output torque T_{out}^{max}:

$$T_{out}^{max} = min\{\text{rated torque } T_e,\ \text{maximum traction torque } T_j\} \tag{10}$$

The maximum accelerations of the crane and trolley are $a_{ux}^{max} = 1.558\ \text{m/s}^2$ and $a_{uy}^{max} = 2.608\ \text{m/s}^2$, respectively.

Additionally, this system adopts 17-bit incremental rotary encoders to measure the angular velocity and rotor-position of the motors. The measurement error of the motor rotor-position is ±0.001°, and the measurement error of the motor angular velocity is ±0.2 rad/s. Rotor-position measurement noise adds Gaussian white noise to the θ_e, the amplitude is 0.001°, and the sampling period is 1/10,000 s. Angular velocity measurement noise adds Gaussian white noise to the angular velocity feedback ω_m, the amplitude is 0.2 rad/s, and the sampling period is 1/10,000 s. The current measurement noise also adds Gaussian white noise to the feedback loop of i_d and i_q, the noise amplitude is 0.2 A, and the sampling period is 1/10,000 s. The discrete signals θ_e, i_d, and i_q are delayed by one sampling period. Then, the signals are passed to the PI controllers or $dq/\alpha\beta$ converters.

2.2. Position Servo Loop Model

In this paper, the position servo loop receives the lifting points' information from the position and orientation measurement system. The EMPC controller outputs the desired movement increment Δv_{ux} of the crane in the X direction and the desired movement increment Δv_{uy} of the trolley in the Y direction. In this section, the subscript C denotes the crane and the subscript T denotes the trolley.

Under the fixed coordinates OXY on the ground, the kinematic equation of the trolley and crane in X and Y directions is as follows:

$$u(k) = \begin{pmatrix} \dot{X}_u(k) \\ \dot{Y}_u(k) \end{pmatrix} = \begin{pmatrix} v_{ux}(k) \\ v_{uy}(k) \end{pmatrix} \tag{11}$$

where X_u and Y_u are the position of the crane and trolley in the coordinate system OXY, respectively.

In Figure 3, n_{xref} (rpm) is the reference speed of the motor that drives the crane to move in the X direction, and n_{yref} (rpm) is the reference speed of the motor that drives the trolley to move in the Y direction. The relationship between n_{ref} and $u(k)$ is as follows:

$$n_{ref}(k+1) = \begin{pmatrix} n_{xref}(k+1) \\ n_{yref}(k+1) \end{pmatrix} = \begin{pmatrix} \frac{60 r_{gx}}{2\pi r_w} v_{ux}(k) \\ \frac{60 r_{gy}}{2\pi r_w} v_{uy}(k) \end{pmatrix} \tag{12}$$

When designing the position loop servo controller, the position servos of the X and Y directions are designed independently. In engineering, the system control generally adopts the incremental control method, and the incremental control is to output the increment Δv of the control variable v every period:

$$v_{ux}(k) = v_{ux}(k-1) + \Delta v_{ux}(k) = v_{ux}(k-1) + u_C(k)T_s \tag{13}$$

$$v_{uy}(k) = v_{uy}(k-1) + \Delta v_{uy}(k) = v_{ux}(k-1) + u_T(k)T_s \tag{14}$$

The reference signal can be regarded as a state variable:

$$X_u(k+1) = X_u(k) + v_{ux}(k)T_s \tag{15}$$

$$Y_u(k+1) = Y_u(k) + v_{uy}(k)T_s \tag{16}$$

The state-space models for the moving crane system and the moving trolley system are as follows:

$$\begin{array}{c} x_C(k+1) = A_C x_C(k) + B_C u_C(k) \\ y_C(k) = C x_C(k) \end{array} \tag{17}$$

$$\begin{array}{c} x_T(k+1) = A x_T(k) + B u_T(k) \\ y_T(k) = C_T x_T(k) \end{array} \tag{18}$$

where

$$\begin{array}{c} \begin{bmatrix} -40 \\ -5 \end{bmatrix} \le x_C(k) = \begin{bmatrix} X_u(k) \\ v_{ux}(k-1) \end{bmatrix} \le \begin{bmatrix} 40 \\ 5 \end{bmatrix} \\ \begin{bmatrix} -10 \\ -3.5 \end{bmatrix} \le x_T(k) = \begin{bmatrix} Y_u(k) \\ v_{uy}(k-1) \end{bmatrix} \le \begin{bmatrix} 10 \\ 3.5 \end{bmatrix} \\ \begin{bmatrix} -1.558 \\ -2.608 \end{bmatrix} \le \begin{pmatrix} u_C(k) \\ u_T(k) \end{pmatrix} \le \begin{bmatrix} 1.558 \\ 2.608 \end{bmatrix} \\ A_C = A_T = \begin{bmatrix} 1 & T_s \\ 0 & 1 \end{bmatrix},\ B_C = B_T = \begin{bmatrix} {T_s}^2 \\ T_s \end{bmatrix}, \\ C_C = C_T = \begin{bmatrix} 1 & 0 \end{bmatrix}. \end{array}$$

The deviation in the crane and trolley's position in the X and Y directions from the desired trajectory converges to zero through the proposed control scheme. To implement Equations (17) and (18) in an explicit MPC scheme, a zero-order hold method with a sampling time of 0.005 s is utilized in this paper.

3. Explicit Model Predictive Control

To ensure robustness and meet complex constraints, this study employs MPC [27,28] as a crucial optimal control scheme. At each sampling time k, the optimal control law of the inner loop is solved by formulating and solving a control problem that is then transformed into an online quadratic programming (QP) problem. The cost function used in this control problem is defined as follows:

$$
\begin{gathered}
\min_{\Delta u}\left\{\begin{aligned} J(U,x(k)) = {} & x_{k+N_p|k}^{T} P x_{k+N_p|k} \\ & + \sum_{i=0}^{N_p-1}\left[(y_{k+i|k}-y_{k+i|k}^{ref})^{T} Q_y\left(y_{k+i|k}-y_{k+i|k}^{ref}\right)+x_{k+i|k}^{T} Q x_{k+i|k}\right. \\ & \left. + u_{k+i|k}^{T} R u_{k+i|k}\right] \end{aligned}\right\} \\
s.t.\ \ x_{k|k} = x(k) \\
x_{k+i+1|k} = A_d x_{k+i|k} + B_d u_{k+i|k} \\
y_{k+i|k} = C_d x_{k+i|k} \\
u_{min} \le u_{k+i|k} \le u_{max}, i = 0, 1, \cdots, N_c \\
x_{min} \le x_{k+i|k} \le x_{max}, i = 0, 1, \ldots, N_p \\
u_{k+i|k} = K x_{k+i|k},\ N_c < i \le N_p
\end{gathered}
\tag{19}
$$

where A_d, B_d, and C_d are the discrete-time versions of the system, input, and output matrices, respectively. N_p is the prediction horizon and N_c is the control horizon. The notation $x_{k+i|k}$ represents the predicted value of x at i steps ahead of k. Here, Q, R, and P are the weighting matrices for the state, input, and terminal state, respectively. Q_y is the output weighting matrix used to measure tracking error.

In addition, the output can be obtained with corresponding dimensions K and P by solving the discrete-time algebraic Riccati equation [29], given by

$$
\begin{gathered}
P = A_d^T P A_d - \left(A_d^T P B_d\right)\left(R + B_d^T P B_d\right)^{-1}\left(B_d^T P A_d\right) + Q \\
K = \left(R + B_d^T P B_d\right)^{-1} B_d^T P A_d
\end{gathered}
\tag{20}
$$

Using these weighting matrices, the MPC controller computes a sequence of optimal vectors U that minimize the cost function J.

Although MPC offers several advantages, such as optimal control and handling of constraints, the online optimization process can lead to a significant computational burden, which is a major drawback. To address this issue, Alberto proposed a new MPC scheme that can reduce the computational load [30].

The equations for predicting the state vector $X(k)$ can be obtained through the following derivation:

$$X(k) = \Theta x(k) + \Lambda U(k) \tag{21}$$

where

$$
X(k) = \begin{bmatrix} x(k+1|k) \\ \vdots \\ x\left(k+N_p|k\right) \end{bmatrix}, U(k) = \begin{bmatrix} u(k|k) \\ \vdots \\ u\left(k+N_p-1|k\right) \end{bmatrix},
$$

$$
\Theta = \begin{bmatrix} A_d \\ {A_d}^2 \\ \vdots \\ {A_d}^{N_p} \end{bmatrix},\ \Lambda = \begin{bmatrix} B_d & 0 & 0 & \cdots & 0 \\ A_d B_d & B_d & 0 & \cdots & 0 \\ {A_d}^2 B_d & A_d B_d & B_d & \cdots & 0 \\ \vdots & \vdots & \vdots & & \vdots \\ {A_d}^{N_p-1} B_d & {A_d}^{N_p-2} B & {A_d}^{N_p-3} B_d & \cdots & B_d \end{bmatrix}.
$$

Equations (19) and (21) can be reformulated as follows:

$$
\begin{gathered}
V(x(k)) = U(k)^T\left(\Lambda^T Q_{N_p} \Lambda + R_{N_c}\right)U(k) + 2x(k)^T \Theta^T Q_{N_p} \Lambda U(k) \\
+ x(k)^T\left(\Theta^T Q_{N_p} \Theta + Q\right)x(k)
\end{gathered}
\tag{22}
$$

where

$$\hat{Q} = \begin{bmatrix} Q & & & \\ & \ddots & & \\ & & Q & \\ & & & P \end{bmatrix},\ \hat{R} = \begin{bmatrix} R & & \\ & \ddots & \\ & & R \end{bmatrix}.$$

By defining $H = \left(\Lambda^T \hat{Q} \Lambda + \hat{R}\right)$, $F = \Theta^T \hat{Q} \Lambda$, and $G = \Theta^T Q_{N_p} \Theta + Q$, Equation (22) can be formulated as the following equivalent form:

$$\begin{gathered} V(x(k)) = \tfrac{1}{2} U(k)^T H U(k) + x(k)^T F U(k) \\ s.t.\ \hat{A} U(k) \leq W + E x(k) \end{gathered} \tag{23}$$

where

$$\hat{A} = \begin{bmatrix} \Lambda_i \\ -\Lambda_i \end{bmatrix},\ i = 1, \cdots, N_p\ ,\ W = \begin{bmatrix} x_{max} \\ -x_{min} \end{bmatrix},\ E = \begin{bmatrix} -A_d^i \\ A_d^i \end{bmatrix},\ i = 1, \cdots, N_p.$$

In Equation (23), Λ_i indicates the ith row of Λ.

By defining $z \triangleq U(k) + H^{-1} F^T x(k)$, the reformulated optimization problem presented in Equation (23) can be expressed as a mixed-integer quadratic programming (mp-QP) problem, as shown below [24]:

$$\begin{gathered} V_z(x) = \min_z \tfrac{1}{2} z^T H z \\ s.t.\ \hat{A} z \leq W + S x(k) \end{gathered} \tag{24}$$

where $S \triangleq E + \hat{A} H^{-1} F^T$ and $V_z(x) = V(x(k)) - \frac{1}{2} x(k)^T \left(G - F H^{-1} F^T\right) x(k)$.

The Karush–Kuhn–Tucker (KKT) optimization conditions are used for the above problem [30]:

$$\begin{gathered} Hz + \hat{A}^T \lambda = 0, \lambda \in \mathbb{R}^q \\ \lambda^i \left(\hat{A}^i z - W^i - S^i x\right) = 0, i = 1, \ldots, q \\ \lambda \geq 0 \\ \hat{A} z \leq W + S x \end{gathered} \tag{25}$$

Solving the above equations:

$$\lambda_a = -\left(\hat{A}_a H^{-1} \hat{A}_a^T\right)^{-1} (W_a + S_a x) \tag{26}$$

$$z = H^{-1} \hat{A}_a^T \left(\hat{A}_a H^{-1} \hat{A}_a^T\right)^{-1} (W_a + S_a x) \tag{27}$$

Based on the above equation, it can be observed that Equations (26) and (27) are linear affine functions of the state $x(k)$. Furthermore, it is apparent that the control variable U is also a linear affine function of the state $x(k)$ when considered in conjunction with equation $z = U + H^{-1} F^T x(0)$. The subscript a indicates the active constraint, and the subscript i indicates the inactive constraint.

Based on the KKT condition, it is evident that the validity of the above equation is contingent on satisfying the inequality constraints:

$$-\left(\hat{A}_a H^{-1} \hat{A}_a^T\right)^{-1} (W_a + S_a x(0)) \geq 0 \tag{28}$$

$$\hat{A} H^{-1} \hat{A}_a^T \left(\hat{A}_a H^{-1} \hat{A}_a^T\right)^{-1} (W_a + S_a x(0)) \leq W + S x(0) \tag{29}$$

The polyhedral set (critical region) CR_0 can be formed:

$$CR_0 = \left\{ x \in \mathbb{R}^n \middle| \lambda_a \geq 0,\ \hat{A}_i z \leq W_i + S_i x \right\} \tag{30}$$

By applying different constraints, more critical regions are formed for different groups of states. Therefore, a map of states to optimal control inputs is eventually created.

4. Controller Design

4.1. Desired Path

First, the reference signal needs to be determined. In this system, the input signal should be given according to the driving characteristics of the CLRV. The performance test of the LVR should include the ability to accelerate, decelerate, drive at a uniform speed, move forward, reverse, turn, and climb over slopes of about 20°. Suppose the maximum speed of the pre-researched CLRV is $v_{rmax} = 4\ \mathrm{m/s}$ with $a_{rmax} = 1\ \mathrm{m/s^2}$.

Additionally, the signal-to-noise ratio of a_{rx} and a_{ry} is 20 dB. After integrating the accelerations a_{rx} and a_{ry}, the speeds v_{rx} and v_{ry} can be obtained. Then, integrating the speeds v_{rx} and v_{ry}, the position information X_r and Y_r of the CLRV can be obtained, respectively. Figure 4 illustrates the position X_r as well as the speed v_{rx} of path one of the CLRV in the X direction. When the CLRV is going uphill or downhill, its speed in the X direction quickly decreases before stabilizing as it ascends, and quickly increases before stabilizing as it descends.

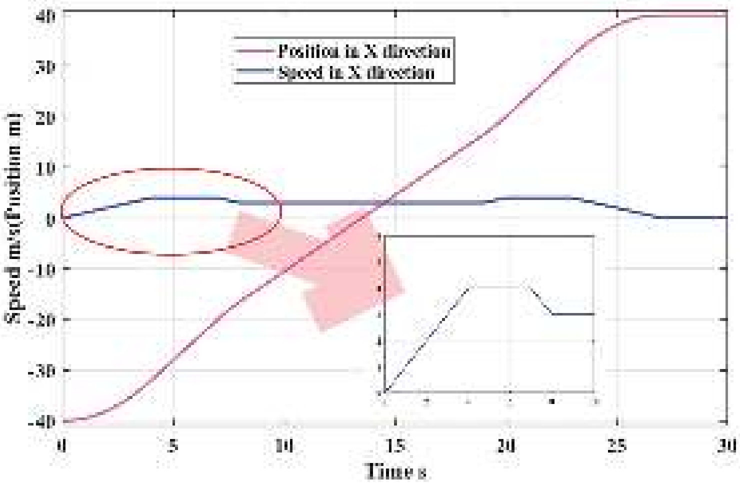

Figure 4. Desired path one for track-following servo control is plotted in this figure. The initial position of the CLRV is (−40, 0). Path one is the trajectory of the CLRV moving in the X-direction. The trajectory consists of uniform acceleration, uniform deceleration, uniform motion, and changes in X-directional speed due to uphill and downhill slopes.

Path two is the trajectory of the CLRV moving forward and backward in the Y-direction. The speed v_{ry} and position Y_r changes in the Y direction of path two are shown in Figure 5.

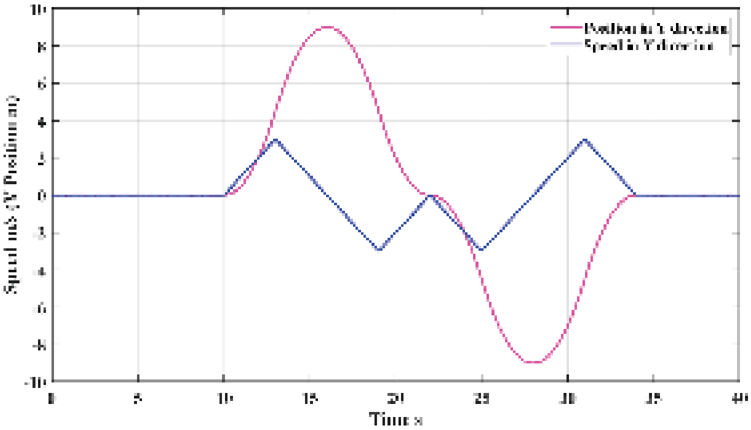

Figure 5. Desired path two for track-following servo control is plotted in this figure. The initial position of the CLRV is (−40, 0).

Path three represents the trajectory of the CLRV as it makes a turn with a radius of 10 m and a velocity of 3 m/s. Path four is the trajectory of the CLRV navigating a turn while avoiding obstacles. The speeds of the CLRV in the *X* and *Y* directions for paths three and four are also displayed in Figures 6 and 7, respectively.

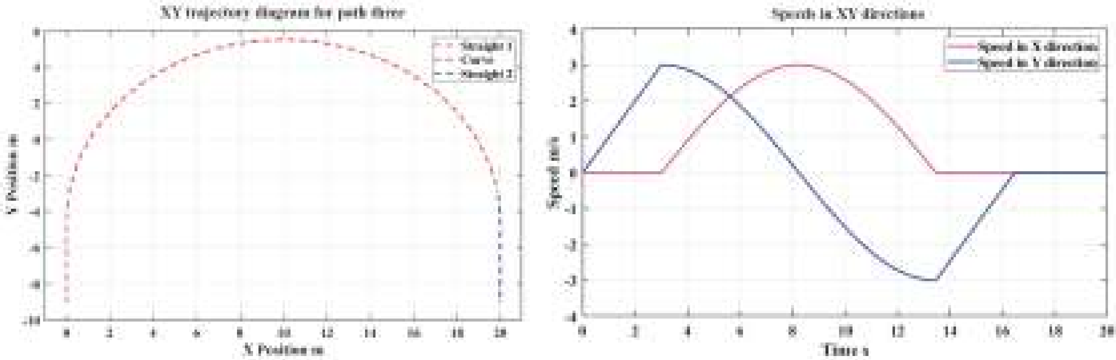

Figure 6. CLRV's motion trajectory and speeds in the *XY* directions for desired path three. The initial position of the CLRV is (0, −9). This path mainly consists of three parts: a section of straight motion with uniform acceleration, a turning curve with a radius of 10 m, and a section of straight motion with uniform deceleration.

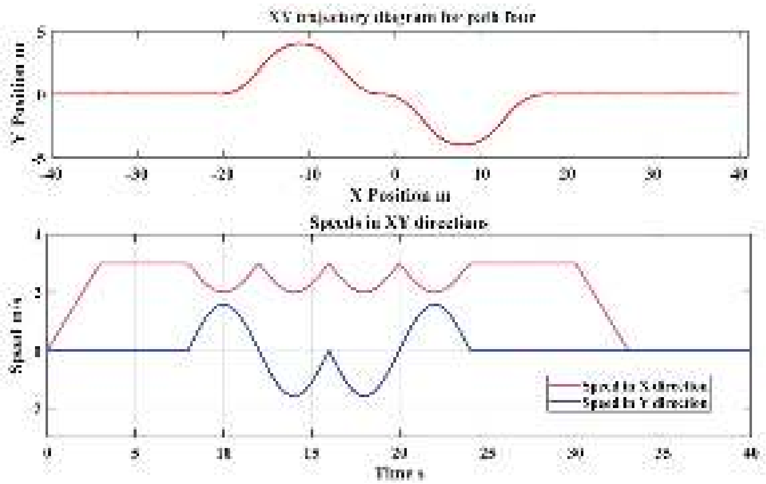

Figure 7. CLRV's motion trajectory and speeds in the *XY* directions for desired path four. The initial position of the CLRV is (−40, 0). This path mainly comprises five parts: a uniformly accelerated straight motion part, two turning curves, uniform straight motions, and a uniformly decelerated straight motion part.

In order to accurately control the crane, the controller must handle digital values obtained from sensors rather than continuous values of the states. Therefore, it is necessary to convert the desired path signal from continuous time to discrete time for more accurate representation. This system uses a monocular vision system to measure the position and orientation of lifting points, with a range of $-40 \leq X \leq 40$ m (or $-10 \leq Y \leq 10$ m) and positioning accuracy of ±10 mm. The processing frequency of the visual system is 20 Hz. The present positions of the crane and the trolley in the X and Y directions are measured by the high-precision magnetic scale, the response time is 1 ms, and the measurement error is better than ±10 µm.

The position measurement noise is added to the output of the desired path with Gaussian white noise. The Gaussian noise amplitude is 0.01 m and the sampling time is 0.05 s. The sampling period of the desired path is 0.05 s, the discrete signal is delayed by one sampling period, and then the signal is passed to the position servo loop controller.

4.2. Design of Explicit MPC Controllers

This section elaborates on the design of the explicit model predictive controller, including the controller structure and the process of determining the weighting matrices Q, R, and Q_y, are shown in the following Table 2. In this section and the next section, the superscript C refers to the crane and the superscript T refers to the trolley.

Table 2. EMPC Controller design parameters.

Parameters	Value
Predicted horizon N_p	$N_p^C = 12, N_p^T = 6$
Control horizon N_c	$N_c^C = N_c^T$=2
State weighting matrix Q	$Q^C = Q^T = \begin{bmatrix} 0.00001 & 0 \\ 0 & 0.00001 \end{bmatrix}$
Output weighting matrix Q_y	$Q_y^C = Q_y^C = 10,000$
Input weighting matrix R	$R^C = R^T = 0.08$
Sampling time T_s	5 ms

In this paper, the EMPC controller, designed using the MPT toolbox 3.0 [31], generates an optimal input while satisfying the system's constraints. The performance of the EMPC scheme can be tuned by appropriately adjusting the weighting matrices Q, R, and Q_y, and by a suitable choice of the prediction horizon N_p and N_c. The EMPC controller for the crane moving system has 993 critical regions, whereas the EMPC controller for the trolley moving system has 685 critical regions. Figure 8 shows the feasible critical regions of the trolley moving system's controller.

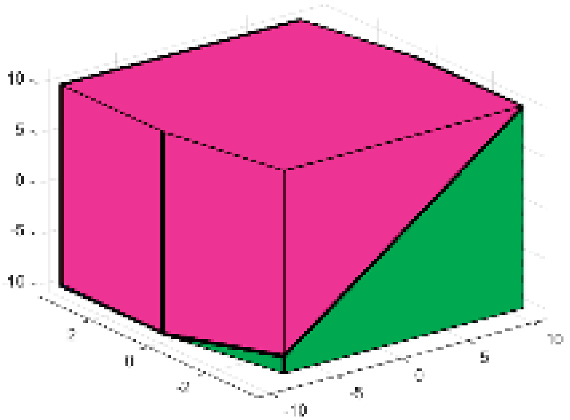

Figure 8. Critical regions. The figure illustrates the critical regions generated by the EMPC controller for the moving trolley system.

4.3. Linear-Quadratic-Integral Controller Design

In this paper, the LQI controller [32] is also employed for the position-loop servo control and is compared with the performance of the EMPC controller. Taking crane control as an example, in the design of the LQI controller, the ultimate goal is to track the position reference of the lunar rover. Therefore, in practice, the optimal control scheme should be applied as follows:

$$u_c^{LQI} = -K_{LQI}^{C}\begin{bmatrix} x \\ x_i \end{bmatrix} = -K_{LQI}^{C}\begin{bmatrix} e_X(k) \\ v_{ux}(k-1) \\ \int e_X(k) \end{bmatrix} \tag{31}$$

where $e_X(k) = X_r(k) - X_u(k)$ is the tracking error. Assuming that the reference signal is constant in the future, the state equation for the reference signal is:

$$X_r(k+1) = X_r(k) \tag{32}$$

Combining Equations (31), (32), and (17) results in the following equation:

$$\begin{bmatrix} e_X(k+1) \\ v_{ux}(k) \\ \int e_X(k+1) \end{bmatrix} = \begin{bmatrix} 1 & -T_s & 0 \\ 0 & 1 & 0 \\ 1 & -T_s & 1 \end{bmatrix}\begin{bmatrix} e_X(k) \\ v_{ux}(k-1) \\ \int e_X(k) \end{bmatrix} + \begin{bmatrix} -T_s{}^2 \\ T_s \\ -T_s{}^2 \end{bmatrix} u_C(k) \tag{33}$$

Similarly, we can obtain the spatial state equation for position tracking control of the trolley by following the same procedure as we did for the crane moving system. In both the crane and trolley moving systems for position servo control, the weighting matrices used in the LQI controllers are as follows:

$$Q_{LQI}^{C} = \begin{bmatrix} 40{,}000 & & \\ & 0.00001 & \\ & & 1 \end{bmatrix},\ Q_{LQI}^{T} = \begin{bmatrix} 10{,}000 & & \\ & 0.00001 & \\ & & 1 \end{bmatrix}, \\ R_{LQI}^{C} = R_{LQI}^{T} = 0.1, \tag{34}$$

During the parameter selection process of the weight matrix, special consideration is given to prioritize accurate tracking. As a result, the error state is given a high penalty. Additionally, the integral error state is also assigned a high penalty to minimize the deviation from the steady state as much as possible. Furthermore, the plant input weight is chosen relatively high to prevent any significant changes in the system. Then, the state feedback gain K_{LQI} for the LQI controllers can be determined by solving the algebraic Riccati equation, as illustrated in Equation (20).

5. Results and Discussion

In this system, the impact of the tracking error of the track-following system mainly includes the impact on the drawbar pull force F_{DP} [33] and gravity compensation force F_C of the CLRV.

Supposing that the upper lifting point is positioned 10 m above the CLRV, the drawbar pull force error in the horizontal direction caused by the tracking error denoted as ΔF_h can be expressed as:

$$\frac{\Delta F_h}{\frac{5}{6}G_c} = \frac{\delta P}{10} \tag{35}$$

where G_c is the weight of the CLRV and δP is the tracking error.

The gravity compensation force error ΔF_v in the vertical direction caused by the position tracking error is:

$$\Delta F_v = F_C\left[1 - cos\left(arctan\frac{\delta P}{10}\right)\right] \tag{36}$$

Supposing that the drawbar pull factor of the CLRV's wheel with a radius of 0.4 m on loose soil is $u_{DP} = 0.8$, the maximum drawbar pull force and gravity compensation force can be roughly expressed as:

$$F_{DP} = u_{DP}W_N \tag{37}$$

$$F_C = \frac{5G_c}{6} \tag{38}$$

where W_N is the wheel vertical load. Hence, the maximum drawbar pull of the entire rover can be estimated by setting W_N as $1/6G_c$.

Combining Equations (35)–(38) gives:

$$\varepsilon_h = \frac{\Delta F_h}{F_{DP}} \tag{39}$$

$$\varepsilon_v = \frac{\Delta F_v}{F_C} \tag{40}$$

where ε_h and ε_v are the error impact factors to measure the influence of tracking errors.

This section presents and discusses the simulation results of the track-following servo control for paths one, two, three, and four using the PI, LQI, and EMPC controllers.

Figure 9 presents a comparison of simulation results for track-following servo control along path one, using three different controllers: PI, LQI, and EMPC. The "Reference" curve shows the real-time position of the CLRV. The figure displays the tracking results, tracking errors, and the crane speed of the track-following servo for each controller.

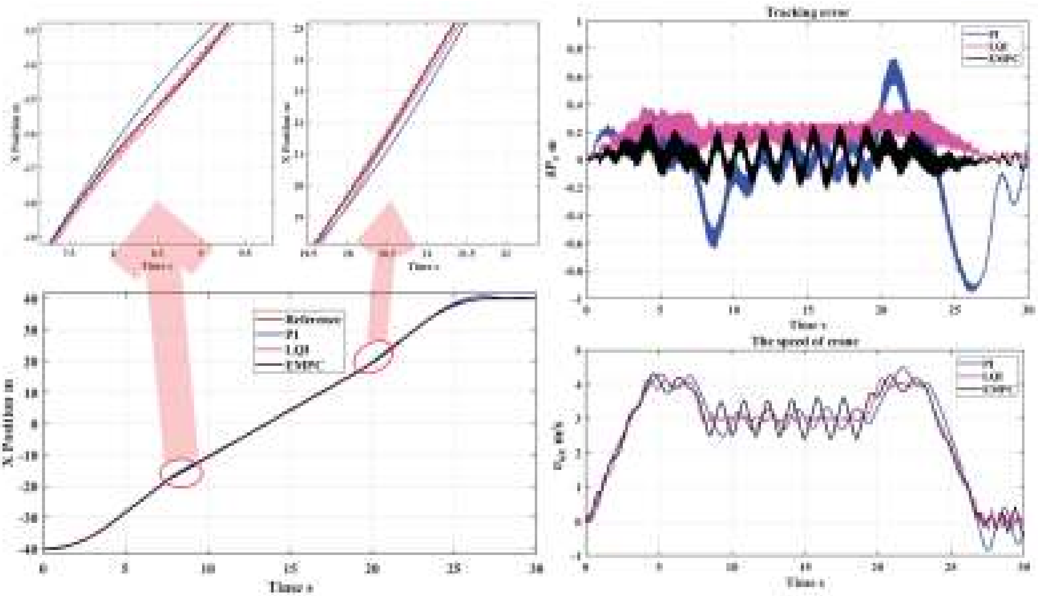

Figure 9. The simulation results' comparison of tracking path one used the PI, LQI, and EMPC controllers. The figures present the following results: the results of the crane tracking desired path one in the *X* direction; tracking errors δP_x between the crane's position and the desired position along path one in the *X* direction; the crane speed v_{ux} of tracking path one.

It can be observed from Figure 9 that the EMPC controller has the best performance and the smallest tracking error against the disturbance caused by the rapid change in the *X*-direction speed of the CLRV, followed by the LQI and PI controllers. Moreover, by examining the motion speed diagram of the crane, it can be inferred that the tracking stability of LQI is highest.

As shown in Figure 9, the positional deviation resulting from the track-following servo of the PI controller is significantly greater than those of the EMPC and LQI controllers. This is primarily due to the high inertia of the crane, which poses challenges in tracking the desired path. To overcome this, a simple PI controller with higher proportional coefficients is employed, leading to improved response speed but degraded steady-state performance. Interestingly, LQI has a lower settling time than PI and EMPC, and its stability is best. This can be attributed to its very high weight in the state of the tracking error, which helps it reach the steady state earlier. However, LQI suffers from delay errors between the desired path and the crane position, resulting from its reliance on the output value of the error integrator.

In contrast, the EMPC controller enhances control performance by generating optimal inputs while satisfying constraints. The model predictive control algorithms used in EMPC are more complex, taking into account various parameters and predicting the most optimal path for possible trajectories. As a result, the EMPC controller performs better at minimizing errors compared to controllers that use a simple cost function or a set of gains to correct deviations.

Figure 9 shows the tracking error of tracking desired path one using the EMPC controller. P_x refers to the real-time error of the crane and lunar rover in the *X* direction, while P_y refers to the real-time error of the trolley and lunar rover in the *Y* direction. In the tracking servo of path one, there is only an error in the *X* direction. The tracking error $\delta P = \delta P_x$ and the tracking error of the EMPC controller for path one is within 0.2 m.

Figure 10 depicts the simulation results of the trolley tracking path two, which involves frequent acceleration, deceleration, and forward and reverse movements in the *Y* direction.

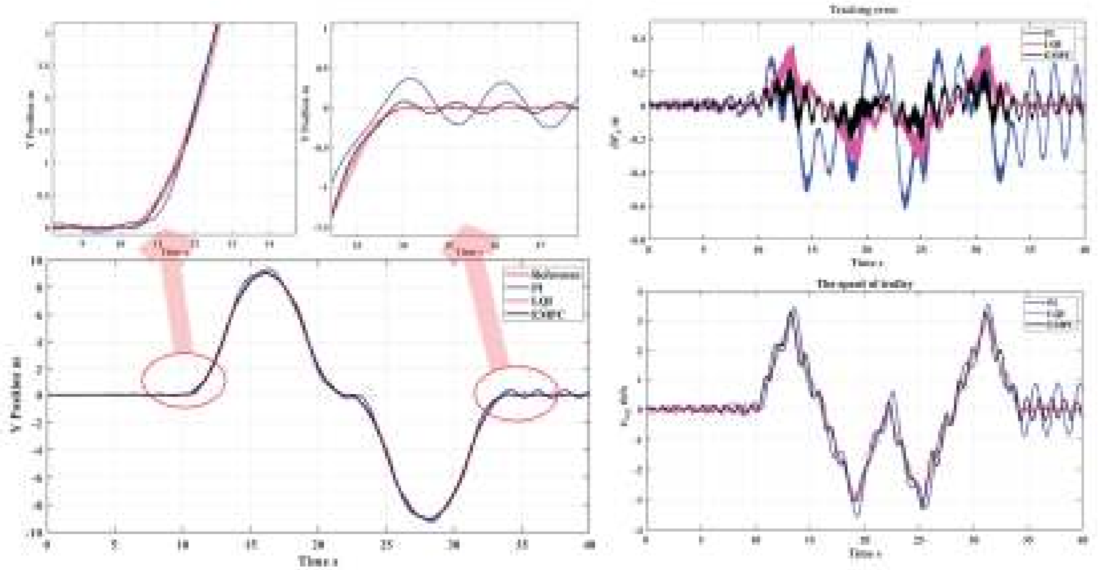

Figure 10. Results of the trolley tracking desired path two. The figures present the following results: the results of trolley tracking desired path one in the *Y* direction; tracking errors δP_y between the trolley's position and the desired position along path two in the *Y* direction; the trolley speed v_{uy} of tracking path two.

Figure 10 shows the simulation results of the trolley tracking path two in the *Y* direction. The tracking error is mainly caused by the trolley's inertia. Comparing it with Figure 9, it can be observed that as the crane's inertia is much greater than that of the trolley, the error will be even greater when the crane tracks the expected path with rapid changes in the *X*-directional speed. The results shown in Figure 10 show the trolley's speed $\mathrm{v_{uy}}$ of tracking path two. From the tracking error plot and trolley speed plot, it can be seen that large errors usually occur during the time periods when the trolley undergoes acceleration and deceleration switching. To minimize the impact of the crane's large inertia on tracking performance, it is recommended to avoid frequent acceleration and deceleration of the lunar rover in the *X* direction. Instead, it is advisable to conduct forward and reverse movement performance testing solely in the *Y* direction to achieve optimal results.

In the tracking servo of path two, there is only an error in the *Y* direction. The tracking error $\delta P = \delta P_y$ and the tracking error of the EMPC controller for path two is within 0.2 m.

Figure 11 depicts the simulation results of the crane and trolley tracking desired path three, which follows a turning motion trajectory of the CLRV with a radius of 10 m, and operates at a speed of 3 m/s. On the other hand, Figure 12 illustrates the crane and trolley tracking path four, which represents the driving trajectory of the CLRV when encountering continuous turns during obstacle avoidance. The CLRV operates at a speed of around 3 m/s while following this path.

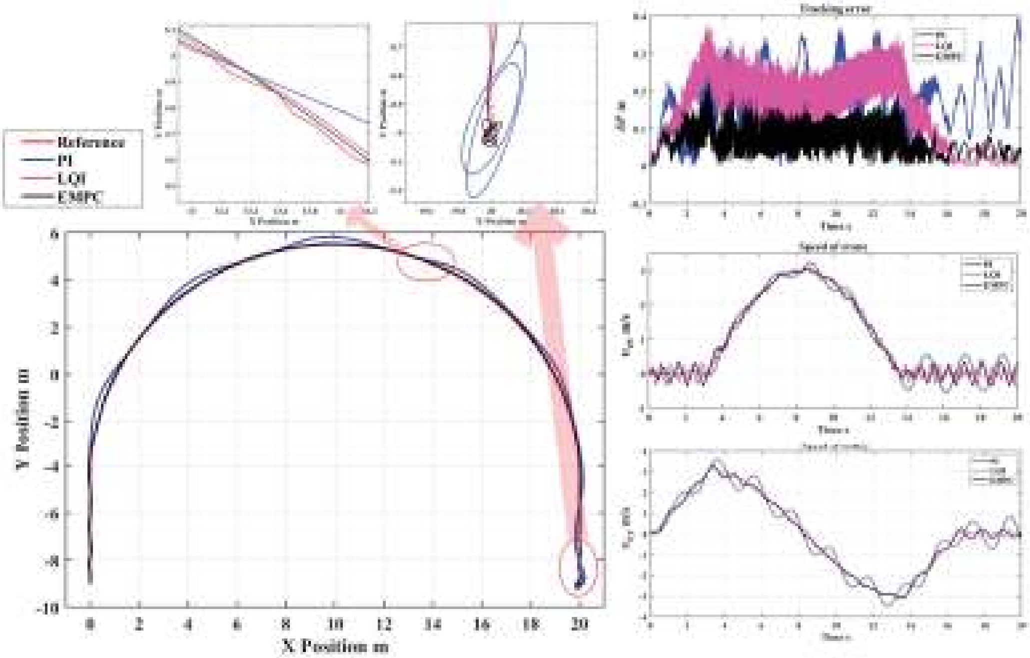

Figure 11. The results of tracking desired path three by the crane and trolley are presented. The figures illustrate the following outcomes: a comparison between the trajectory of the upper lifting point and the expected trajectory under three different controllers, the tracking error $\delta P = \sqrt{\delta P_x^2 + \delta P_y^2}$ of the track-following servo subsystem, and the movement speed of both the crane and trolley.

Figures 11 and 12 illustrate that the EMPC controller results in the smallest tracking error, followed by LQI and PI controllers. Furthermore, the results suggest that the LQI controller exhibits excellent stability, as the movement speed of the crane and trolley remains relatively stable in response to dynamic disturbances. On the other hand, when using a PI controller for a large inertia system, the overshoot can be relatively large, and it can be challenging to balance the response speed and stability.

Figures 11 and 12 displays the simulation results of crane and trolley tracking for desired paths three and four, utilizing the EMPC controller. The tracking error $\delta P = \sqrt{\delta P_x^2 + \delta P_y^2}$ is basically less than 0.2 m.

The simulation results show that the maximum tracking errors δP of the track-following servo subsystem using EMPC controllers are almost less than 0.2 m. According to Equations (39) and (40), it can obtain the influence factor of the tracking error on the CLRV motion in the horizontal direction:

$$\varepsilon_h < 0.125 \tag{41}$$

In addition, the error impact factor in the vertical direction is as follows:

$$\varepsilon_v < 0.00045 \tag{42}$$

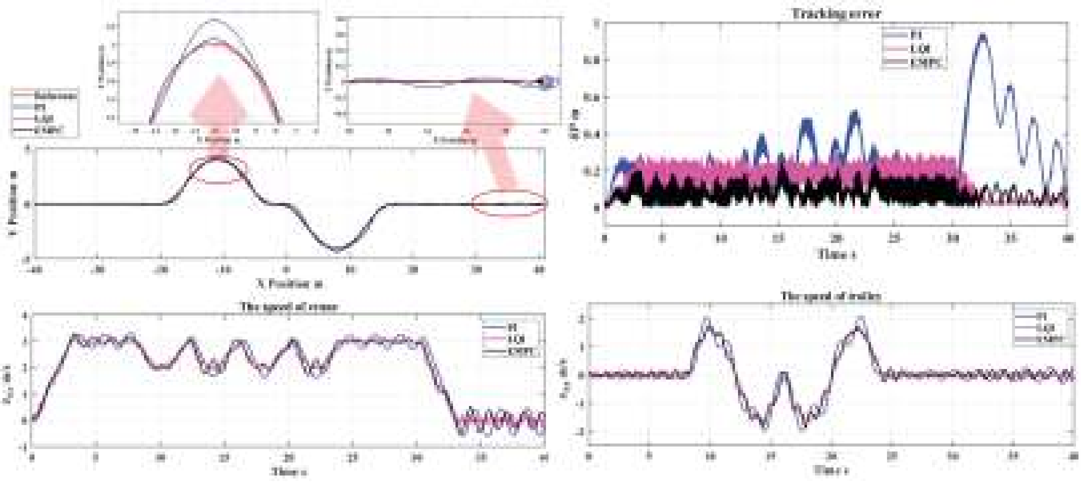

Figure 12. The results of tracking desired path four by the crane and trolley are presented. The figures illustrate the following outcomes: a comparison between the trajectory of the upper lifting point and the expected trajectory under three different controllers, the tracking error $\delta P = \sqrt{\delta P_x^2 + \delta P_y^2}$ of the track-following servo subsystem, and the movement speed of both the crane and trolley.

The simulations yield some key findings: the EMPC demonstrates a notably impressive performance for the system, with explicit MPC delivering the objectively best results. While the PI and LQI controllers show comparatively inferior results, they remain reliable options with their own strengths. The PI controller is easy to apply, while the LQI controller exhibits excellent robustness and stability. However, their application is limited for multi-constraint control systems. Although the EMPC shows good performance under different expected trajectories, it also has some limitations in terms of stability, especially in dealing with large disturbances in the X direction (i.e., when the CLRV speed changes rapidly). In such cases, the crane may lose control. To address this issue, future work will focus on conducting relevant methods to further analyze the stability of the proposed EMPC controller.

In conclusion, EMPC is a controller that can provide the smallest possible dynamic tracking error and steady-state error under the condition of dealing with multiple constraints, and it has better control performance. Moreover, frequent acceleration and deceleration should be avoided in the X direction when driving the CLRV, to reduce the impact of the large inertia of the crane on the controller's tracking performance.

Based on the simulation results, we compare the tracking performance of the track-following servo subsystem of the suspension gravity compensation system to that of the system designed by Liu et al. [2]. Although the maximum tracking error of Liu et al.'s system is approximately 0.1 m, its crane employs open-loop control, making it only suitable for tracking a slow-moving unmanned lunar rover. In contrast, the research presented in this paper provides a solution to the theoretical research gap of the track-following servo subsystem suitable for CLRV experiments.

6. Conclusions

This paper proposes a design and control scheme for a track-following servo subsystem of a LGCS suitable for CLRV ground testing:

1. The track-following servo subsystem consists of a crane, trolley, and servo motors. The crane moves along the bridge, tracking the real-time position of the CLRV, while the trolley moves along the crane girder to follow the real-time position of the CLRV. Three-loop control models are established for both the crane and trolley, including the position loop, motor speed loop, and current loop.

2. The driving force of the track-following servo subsystem is provided by a PMSM. Specific parameters for the motor and transmission mechanism are determined based on the subsystem's motion capability. PMSM vector control based on the SVPWM is adopted to achieve fast response and precise control of the motor speed. PI controllers are employed in both the current and speed loops of the motors.
3. In the position loop control of the track-following servo subsystem, explicit MPC control is introduced for multi-parameter constraint control. This paper presents an EMPC controller suitable for the track-following servo subsystem, including the cost function design and offline calculation process. The weighting matrices, prediction horizon, and control horizon are also determined.

Especially, the effectiveness of the proposed EMPC controller is demonstrated through a comparison with PI and LQI controllers. The simulation results show that the maximum tracking error δP of the track-following servo subsystem is consistently below 0.2 m. The impact of the errors on the drawbar pull is within 12.5%, and their effect on the compensation force is negligible. The simulation results also suggest that, due to the large inertia of the crane, the CLRV should avoid frequent forward, backward, acceleration, and deceleration in the X direction to reduce the influence of the crane's large inertia on tracking performance. These simulation results provide valuable theoretical support for designing a track-following servo subsystem that is suitable for CLRV ground testing.

In our future work, our objective is to develop a track-following servo subsystem that is suitable for ground testing of the CLRV. The primary contribution of this paper is the development of an EMPC controller for the position control loop, along with PMSM vector control, which has demonstrated excellent tracking performance for the subsystem. However, implementing the EMPC controller in engineering settings may pose significant challenges. In our upcoming research, we plan to refine our work further, including addressing potential deviations in motor load torque, exploring cooperative control of multiple motors, and enhancing the robustness of the EMPC controller. These are essential considerations that must be addressed to fully realize the potential of the proposed approach in practical applications.

Author Contributions: Conceptualization, M.L. and J.W.; methodology, Y.Z.; software, Y.Z.; validation, Y.Z., H.W. and M.L.; formal analysis, H.W.; investigation, H.W.; resources, Y.Z.; data curation, Y.Z.; writing—original draft preparation, Y.Z.; writing—review and editing, Y.Z.; visualization, Y.Z.; supervision, H.W.; project administration, H.W. All authors have read and agreed to the published version of the manuscript.

Funding: This research received no external funding.

Institutional Review Board Statement: Not applicable.

Informed Consent Statement: Not applicable.

Data Availability Statement: The data presented in this study are available on request from the corresponding author. All data are calculated by the author and have been included in this paper.

Acknowledgments: In addition, we would like to express our appreciation to all the individuals who provided administrative and technical support throughout this research.

Conflicts of Interest: We declare that there is no conflict of interest regarding the submission of this manuscript, and that all authors have provided their approval for publication. We confirm that this work represents original research that has not been previously published, nor is it currently being considered for publication elsewhere, in its entirety or in part. We can also confirm that all listed authors have reviewed and approved the final version of the manuscript.

References

1. Liang, Z.; Gao, H.; Ding, L.; Deng, Z. Approach to imitate maneuvering of Manned lunar roving vehicle under lunar gravity using a terrestrial vehicle. *Mechatronics* **2015**, *30*, 383–398. [CrossRef]
2. Liu, Z.; Gao, H.B.; Deng, Z.Q. Design and Implementation of a Large-Scale Gravity Compensation System for Lunar Rover. *Appl. Mech. Mater.* **2013**, *385–386*, 759–767. [CrossRef]

3. Callens, N.; Ventura-Traveset, J.; De Lophem, T.-L.; De Echazarreta, C.L.; Pletser, V.; Van Loon, J.J.W.A. ESA Parabolic Flights, Drop Tower and Centrifuge Opportunities for University Students. *Microgravity Sci. Technol.* **2010**, *23*, 181–189. [CrossRef]
4. Kwok-Choon, S.; Buchala, K.; Blackwell, B.; Lopresti, S.; Wilde, M.; Go, T. Design, fabrication, and preliminary testing of air-bearing test vehicles for the study of autonomous satellite maneuvers. In Proceedings of the 31st Florida Conference on Recent Advances in Robotics, Orlando, FL, USA, 10–11 May 2018.
5. Alves, F.; Park, J.; McCarty, L.; Rabelo, R.; Karunasiri, G. MEMS Underwater Directional Acoustic Sensor in Near Neutral Buoyancy Configuration. *Sensors* **2022**, *22*, 1337. [CrossRef]
6. Davis, K.; Meginnis, I. Testing of the NASA Exploration Extravehicular Mobility Unit Demonstration (xEMU Demo) Architecture at the Neutral Buoyancy Laboratory. In Proceedings of the 49th International Conference on Environmental Systems, Boston, MA, USA, 7–11 July 2019.
7. Zhao, Z.; Fu, K.; Li, M.; Li, J.; Xiao, Y. Gravity compensation system of mesh antennas for in-orbit prediction of deployment dynamics. *Acta Astronaut.* **2020**, *167*, 1–13. [CrossRef]
8. Jia, J.; Jia, Y.; Sun, S. Preliminary design and development of an active suspension gravity compensation system for ground verification. *Mech. Mach. Theory* **2018**, *128*, 492–507. [CrossRef]
9. Jin, Y.; Wu, R.; Liu, W.; Tang, X. Visual servo for gravity compensation system. *Neurocomputing* **2017**, *269*, 256–260. [CrossRef]
10. Liu, Z.; Niu, F.; Gao, H.; Yu, H.; Ding, L.; Li, N.; Deng, Z. Design, analysis, and experimental validation of an active constant-force system based on a low-stiffness mechanism. *Mech. Mach. Theory* **2018**, *130*, 1–26. [CrossRef]
11. Hičár, M.; Ritók, J. Robust crane control. *Acta Polytech. Hung.* **2006**, *3*, 91–101.
12. Cunningham, T. *System Requirements Document for the Active Response Gravity Offload System (Argos)*; NASA Engineering Directorate document AR&SD-08007; NASA: Washington, DC, USA, 2010.
13. Kemurdjian, A.; Khakhanov, U.A. Development of Simulation Means for a Gravity Forces. In *Robotics 2000*; American Society of Civil Engineers: Reston, VA, USA, 2000. [CrossRef]
14. Preliminary Design Study of a Lunar Gravity Simulator Interim Report [EB/OL]. Available online: https://ntrs.nasa.gov/search.jsp?R=19670022528 (accessed on 1 January 2023).
15. Zwerger, T.; Mercorelli, P. Using a Bivariate Polynomial in an EKF for State and Inductance Estimations in the Presence of Saturation Effects to Adaptively Control a PMSM. *IEEE Access* **2022**, *10*, 111545–111553. [CrossRef]
16. Ullah, K.; Guzinski, J.; Mirza, A.F. Critical Review on Robust Speed Control Techniques for Permanent Magnet Synchronous Motor (PMSM) Speed Regulation. *Energies* **2022**, *15*, 1235. [CrossRef]
17. Bida, V.M.; Samokhvalov, D.V.; Al-Mahturi, F.S. PMSM vector control techniques—A survey. In Proceedings of the 2018 IEEE Conference of Russian Young Researchers in Electrical and Electronic Engineering (EIConRus), Moscow, Russia, 29 January–1 February 2018; IEEE: Piscataway, NJ, USA, 2018.
18. Kaiqi, Z. The study of improved PI method for PMSM vector control system based on SVPWM. In Proceedings of the 2011 IEEE Industry Applications Society Annual Meeting, Orlando, FL, USA, 9–13 October 2011; IEEE: Piscataway, NJ, USA, 2011. [CrossRef]
19. Xu, Z.; Tao, N.; Du, M.; Liang, T.; Xia, X. Damage Prediction for the Starter Motor of the Idling Start-Stop System Based on the Thermal Field. *SAE Int. J. Commer. Veh.* **2017**, *10*, 443–453. [CrossRef]
20. Barata, B.; Lundgre, K. Methods for Servo Position Control. Master's Thesis, Chalmers University of Technology, Gothenburg, Sweden, 2019.
21. Brandão, A.S.M.; Lima, D.M.; Filho, M.V.A.D.C.; Normey-Rico, J.E. A Comparative Study on Embedded MPC for Industrial Processes. In Proceedings of the Congresso Brasileiro de Automatica—CBA, João Pessoa, Brazil, 8–12 September 2018; Volume 1. No. 1.
22. Wang, H.; Liu, B.; Ping, X.; An, Q. Path Tracking Control for Autonomous Vehicles Based on an Improved MPC. *IEEE Access* **2019**, *7*, 161064–161073. [CrossRef]
23. Nubert, J.; Koehler, J.; Berenz, V.; Allgower, F.; Trimpe, S. Safe and Fast Tracking on a Robot Manipulator: Robust MPC and Neural Network Control. *IEEE Robot. Autom. Lett.* **2020**, *5*, 3050–3057. [CrossRef]
24. Bemporad, A.; Morari, M.; Dua, V.; Pistikopoulos, E.N. The explicit linear quadratic regulator for constrained systems. *Automatica* **2002**, *38*, 3–20. [CrossRef]
25. Oravec, J.; Klaučo, M. Real-time tunable approximated explicit MPC. *Automatica* **2022**, *142*, 110315. [CrossRef]
26. Zhang, W.; Chen, J.; Wu, X.; Jin, X. Wheel/rail adhesion and analysis by using full scale roller rig. *Wear* **2002**, *253*, 82–88. [CrossRef]
27. Hewing, L.; Wabersich, K.P.; Menner, M.; Zeilinger, M.N. Learning-Based Model Predictive Control: Toward Safe Learning in Control. *Annu. Rev. Control Robot. Auton. Syst.* **2020**, *3*, 269–296. [CrossRef]
28. Berberich, J.; Kohler, J.; Muller, M.A.; Allgower, F. Data-Driven Model Predictive Control With Stability and Robustness Guarantees. *IEEE Trans. Autom. Control* **2021**, *66*, 1702–1717. [CrossRef]
29. Wang, L. Numerical Algorithms of the Discrete Coupled Algebraic Riccati Equation Arising in Optimal Control Systems. *Math. Probl. Eng.* **2020**, *2020*, 1841582. [CrossRef]
30. Bemporad, A. Explicit Model-Predictive Control. In *Encyclopedia of Systems and Control*; Springer: Berlin, Germany, 2014.
31. Herceg, M.; Kvasnica, M.; Jones, C.N.; Morari, M. Multi-parametric toolbox 3.0. In Proceedings of the 2013 European Control Conference (ECC), Zurich, Switzerland, 17–19 July 2013; IEEE: Piscataway, NJ, USA, 2013.

32. Ahmadi, A.; Mohammadi-Ivatloo, B.; Anvari-Moghaddam, A.; Marzband, M. Optimal Robust LQI Controller Design for Z-Source Inverters. *Appl. Sci.* **2020**, *10*, 7260. [CrossRef]
33. Shibly, H.; Iagnemma, K.; Dubowsky, S. An equivalent soil mechanics formulation for rigid wheels in deformable terrain, with application to planetary exploration rovers. *J. Terramech.* **2005**, *42*, 1–13. [CrossRef]

energies

Article

Super-Twisting Sliding Mode Control to Improve Performances and Robustness of a Switched Reluctance Machine for an Electric Vehicle Drivetrain Application †

Rabia Sehab [1,*], Ahmad Akrad [1] and Yakoub Saadi [2]

[1] ESTACA'Lab—ESTACA, Ecole Supérieure des Techniques Aéronautiques et de Construction Automobile, 53000 Laval, France
[2] ICube, CNRS (UMR 7357) INSA Strasbourg, University of Strasbourg, 67000 Strasbourg, France
* Correspondence: rabia.sehab@estaca.fr

† This paper is an extended version of our paper published in 2017 IEEE Vehicle Power and Propulsion Conference (VPPC), Belfort, France, 11–14 December 2017; Performance Comparison between Conventional and Robust Control for the Powertrain of an Electric Vehicle Propelled by a Switched Reluctance Machine.

Abstract: In electric vehicles, performances of electric vehicle drivetrains depend on the electric machine and the control. Switched Reluctance Machines (SRMs) are today an alternative to rare earth magnets machines such as Permanent Magnet Synchronous Machine (PMSM), which is used in the vehicle drivetrain. Because of its high nonlinear behavior, the classical control designed for SRMs is not sufficient to obtain good performances. The objective of this paper is to make performance and robustness comparisons of the designed robust controllers considering the high nonlinear behavior of SRMs. Sliding Mode Control (SMC) and Super-Twisting Sliding Mode Control (STSMC) are developed and validated by simulation for the velocity control loop and the current control loops of the control strategy. However, an evaluation of their performances compared to classical control based on PI controllers is carried out. For a robustness comparison, a variation of SRM parameters is carried out by simulation using the three controllers. Finally, an experimental validation on a developed test bench using the three controllers is conducted to show that Super-Twisting Sliding Mode Control (STSMC) is the best in terms of performances and robustness for an electric vehicle application.

Keywords: electric vehicle; switched reluctance machine; PI control; sliding mode control; super-twisting sliding mode control; performance; robustness

Citation: Sehab, R.; Akrad, A.; Saadi, Y. Super-Twisting Sliding Mode Control to Improve Performances and Robustness of a Switched Reluctance Machine for an Electric Vehicle Drivetrain Application. *Energies* **2023**, *16*, 3212. https://doi.org/10.3390/en16073212

Academic Editors: Kan Liu and Wei Hu

Received: 21 February 2023
Revised: 17 March 2023
Accepted: 21 March 2023
Published: 2 April 2023

1. Introduction

Nowadays, electric vehicles (EVs) are gaining increased attention due to environmental and energy concerns. EVs can limit environmental impacts and reduce greenhouse gases. In the vehicle drivetrain, the main component is the electric machine. In such an application, high power density, high torque density, wide speed range, and efficiency are of primary importance [1]. To meet these demands, Rare Earth Magnetic Material (REMM) has been widely used in different types of electric machines dedicated to the EV applications such as the sintered Neodymium Iron Boron and Samarium Cobalt [2]. However, the cost of REMM-based machines has increased over several years. Moreover, due to the limited resources, the use of REMM-based machines in EVs applications is now being challenged. In fact, many researchers and industrials are working on other machines that can be competitive in terms of size, efficiency, and torque density. This is the case of the Wound-Rotor Synchronous Machine (WRSM), which is designed and manufactured by Renault for the first urban electric vehicle; Renault Zoe and the Switched Reluctance Machine (SRM) is used today by Land Rover in the electric vehicle Land Rover'110 defender.

Considering the requirements, Switched Reluctance Machines (SRMs) represent an alternative. They not only feature a salient pole stator with concentrated coils, which provides earlier winding and shorter end turn than other types of electric machines, but also feature a salient pole rotor, which has neither conductors nor magnets. Simplicity in its construction makes the SRM manufacturing and its maintenance inexpensive. Its high reliability and performance at high-speed range with a constant power, fault-tolerant operation capability, and the simplicity of the power converter [3,4] make it a very interesting candidate for electric vehicles propulsion. However, the SRM exhibits high torque ripples and acoustic noises [5]. However, these drawbacks can be significantly reduced with an optimal SRM mechanical design [6] and a good control strategy [7–10]. In [10], for example, the dynamic performance of direct torque control (DTC) method is improved by replacing the PI controller of the SRM velocity loop by a sliding mode controller associated with a disturbance observer.

Unlike most of the other types of electric machines, the SRM is highly nonlinear and operates in saturation to maximize the output torque. Moreover, the torque, the current, and the position are strongly coupled through nonlinear characteristics. Consequently, the design of the controllers is tedious [11]. Because of the high requirements of drivability for electric vehicles, the control of speed and torque is an important issue [12].

In the literature, there is a huge number of control techniques for speed and/or current control of SRM. Each one has its own advantages and disadvantages. For example, we can mention direct torque control [10], the variable gains proportional-integral (PI) controller [13], LPV adaptive controllers [14], fuzzy logic, and artificial neural network controllers [15,16]. The Variable Structure Control (VSC) with a sliding mode control has also been applied in several works to the speed control of SRM [17,18]. Despite its good performances, the chattering is a serious drawback for EV because it excites non-modeled dynamics that may cause unexpected problems and instability [19]. A robust controller based on H-infinity approaches has been proposed in [20]. Moreover, Pulse Width Modulation (PWM), hysteresis current regulation [21], and model predictive controllers (MPC) [22] are commonly used to drive the SRM. Unfortunately, they are not suited to eliminate the chattering phenomenon of SRM. In this paper, PI control, Sliding Mode Control, and higher-order sliding mode control based on Super-Twisting Algorithm are simultaneously proposed for currents and velocity loops of the suggested control strategy. Even they are robust, Super-Twisting Sliding Mode Control remains the best way to eliminate the phenomenon of chattering, particularly for electric vehicle applications. Indeed, with the improvement of vehicle drivetrain performances using SRM and STSM control, other applications can be improved since they depend on the dynamic behavior of the vehicle where the model of vehicle drivetrain is considered. In vision-aided intelligent vehicle sideslip, angle estimation is based on a dynamic model [23]. Similarly, automated vehicle sideslip angle estimation considers signal measurement characteristics [24].

The main contributions of this paper are focused on the following:

- Performance comparison of the designed Sliding Mode Control (SMC) and the Super-Twisting Sliding Mode Control (STSMC) for the current and the velocity control loops of SRM control strategy with the designed classical control. These controllers are developed and validated by simulation in [12];
- Robustness Comparison of the designed Sliding Mode Control (SMC) and Super-Twisting Sliding Mode Control (STSMC) for the current and the velocity control loops of SRM control strategy with the classical control by varying SRM physical parameters;
- Implementation and validation of the three designed controllers [12] on a developed test bench using a multicore dSpace 1005 with a SRM and a DC machine to create a load torque;
- Finally, performances comparison is carried with the collected experimental data showing that the Super-Twisting Sliding Mode Control is the best algorithm to select for the improvement of electric vehicle drivetrain performance.

This paper is organized as follows: The model of the SRM and SRM power stage converter are presented in Sections 2 and 3, respectively. A short description of PI, SMC, and STSMC control design is proposed in Section 4. Section 5 is devoted to the validation of the designed controllers by simulation and the comparison with the PI controllers' results. Section 6 gives the description of the developed test bench, and the experimental validation of the designed controllers. Conclusion and perspectives are drawn in Section 7.

2. SRM Modeling

The SRM has a simple construction, but the solution of its mathematical model is relatively difficult due to its dominant nonlinear behavior [25] related to the flux linkage and the torque, which both depend on the current phase and the rotor position.

The electromagnetic model of the equivalent circuit of one phase is [3] the following:

$$V_j = R_j.I_j + \frac{\partial \psi_j(\theta, I)}{\partial t} \tag{1}$$

with j = 1, 2, 3, 4.

The flux linkage ψ_j of Equation (1) is a nonlinear characteristic depending on two variables: the phase current I (0 to 80A) and the rotor position θ (0 to 60°). In this study, Figure 1 shows the flux linkage characteristics of the used SRM with the topology 8S/6R given in the Appendix A.

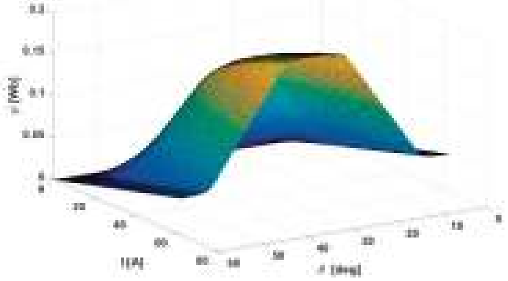

Figure 1. Flux in terms of position and phase current.

The electromechanical model of the SRM associated with a load and viscous friction torques can be expressed as follows [3]:

$$\frac{d\Omega}{dt} = \frac{1}{J}(T_e(\theta, I) - f_r\Omega - T_L) \tag{2}$$

The torque T_e of Equation (2) is, according to Figure 2, a nonlinear characteristic which depends on the phase current I (0 to 80A) and the rotor position θ (0 to 60°).

The torque T_e (Equation (3)) given by Figure 2 is computed from the sum of the instantaneous torque (Equation (4)) developed by phase j according to [3]:

$$T_e = \sum_{1}^{j=4} T_{phase_j} \tag{3}$$

where:

$$T_{phase_j} = \frac{1}{2}\frac{dL(\theta)}{d\theta}{I_j}^2 \tag{4}$$

All the variables of the model are given by the following: θ: Rotor position, Ω: Angular velocity of rotor, J: Moment of inertia (rotor), T_e: Total electromagnetic torque, f_r: Friction Coefficient, T_L: Load torque, I_j: Current in the jth phase, ψ_j: Flux linkages in jth phase, V_j: Voltages of jth phase, R_j: Resistance of the jth phase, L: Instantaneous inductance.

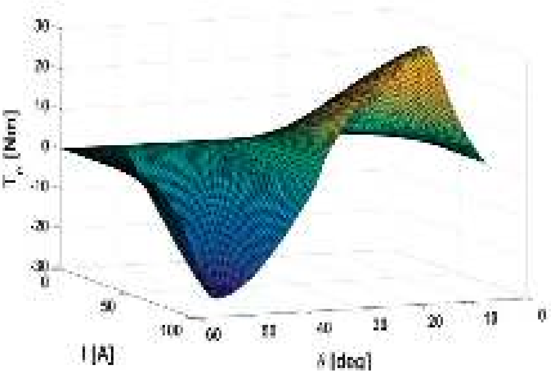

Figure 2. Torque in terms of position and phase current.

3. SRM Power Stage Converter

As the SRM is four phases, four asymmetric H-bridges are selected to supply the stator windings because of the simple design, control, and low cost. Indeed, different types of converters are listed in the literature to supply the SRM [26]. Figure 3 gives a view of the selected converter supplying each phase of the SRM. The DC link voltage Vdc to supply the converter is fixed according to the SRM specification at 250 V/61 A. The supply of each phase is carried out by each asymmetric H-bridge. On the other hand, PWM signals for supplying the drivers of the transistors are provided by the current loops of the implemented control strategy, which is given in Section 4. Using MATLAB/Simscape, the power stage to supply the SRM is modelized by four asymmetric H-bridges.

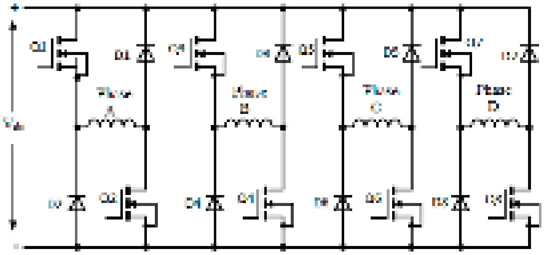

Figure 3. SRM four asymmetric H-bridges.

4. SRM Control Strategy

For velocity or torque control, different control strategies are suggested [12]. Direct and indirect torque control are among the control strategies. The control strategy selected for the velocity control is based on two cascade control loops: velocity and current loops [12]. Figure 4 shows the block diagram of this control strategy. The velocity control loop provides, according to the velocity point (*) the total torque setpoint (*) of SRM to a torque sharing function in charge of generating torque setpoint (*) for each phase. From each phase torque setpoint (*), a phase current setpoint (*) is deduced using the reverse of the nonlinear torque characteristics given by Figure 2. The deduced current sept points (*) are finally provided to the four current control loops to generate PWM signals of the converter.

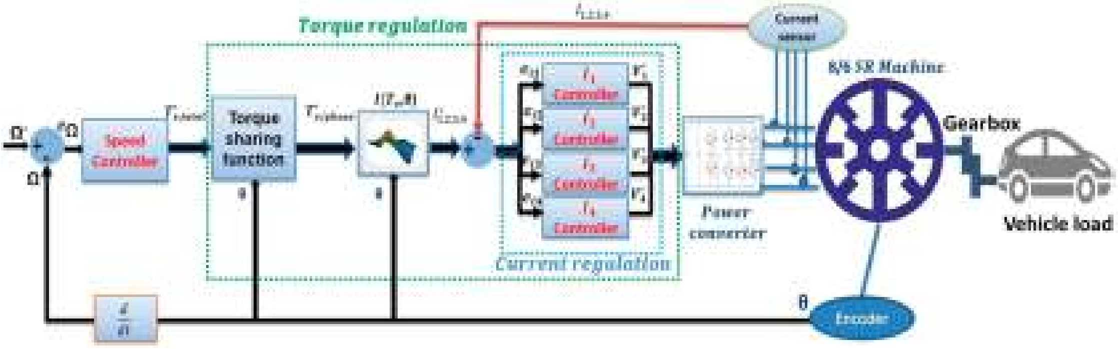

Figure 4. Block diagram of the control strategy.

Based on the control strategy given by Figure 4, PI, SMC, and STSMC controllers are designed for velocity and current control loops. SMC and STSM are developed separately for current and velocity control loops in [12] using the nonlinear model of the SRM given in Section 2.

4.1. PI Controllers

PI controllers are widely used in industries due to their simplicity and low cost. Moreover, their implementation in analog or digital hardware is simple and easy. Under limited operating conditions, they perform well and their steady state performance is good. For any PI controller, the control design is defined by the following:

$$u(t) = K_p e(t) + K_i \int_0^t e(\Gamma) d\Gamma \tag{5}$$

where $e(t)$ is the error defined as the difference between the desired set point and the measured variable. K_p and K_i are the proportional and integral gains.

For the velocity control loop, $e(t)$ is defined by the following:

$$e_\Omega(t) = \Omega^*(t) - \Omega(t) \tag{6}$$

Ω^* and Ω are the velocity set point and the measured velocity, respectively.

For the current loop, $e(t)$ is given by the following:

$$e_i(t) = i^*(t) - i(t) \tag{7}$$

i^* and i are the current set point and the measured current, respectively.

The PI parameters K_p and K_i are designed for current and velocity loops using the classical methods of control.

4.2. Sliding Mode Control (SMC)

The design of SMC can be achieved in two steps. In the first step, we define the sliding mode, which is a surface (switching function) that is invariant to the controlled dynamics, where the controlled dynamics are exponentially stable and where the system tracks the desired set point. In the second step, the control law is designed in such a way that it should guarantee steering the system trajectories towards the sliding surface [27].

4.2.1. SMC Controller for Velocity Loop

The switching function is defined as follows:

$$S_1(t) = e_\Omega(t) + \lambda_1 \int_{-\infty}^t e_\Omega(\Gamma) d\Gamma \tag{8}$$

where λ_1 is a positive constant.

The aim is that the error will converge to zero exponentially (if $S_1(t) = 0$ then $e_\Omega = 0$). The state space variables are defined as the following:

$$\begin{cases} x_1(t) = \int_0^t e_\Omega(\Gamma)d\Gamma \\ x_2(t) = e_\Omega(t) \end{cases} \dot{x_1}(t) = x_2(t) \tag{9}$$

Using (8) and (9), we can write the following:

$$S_1(t) = x_2(t) + \lambda_1 x_1(t) \tag{10}$$

According to (9), the dynamical model of SRM, (2) can be rewritten as follows:

$$\dot{x_2} = \frac{1}{J}T_e - \frac{1}{J}f_r\Omega^* - \frac{1}{J}f_r x_2 - \Omega^* - \frac{1}{J}T_{\ L} \tag{11}$$

In a state space representation, (11) becomes the following:

$$\begin{cases} \dot{x_1} = x_2 \\ \dot{x_2} = f(t) + g.u + d \end{cases} \tag{12}$$

with $f(t) = -\frac{1}{J}f_r\Omega^*(t) - \frac{1}{J}f_r e_\Omega(t) - \Omega^*(t)$, $g = \frac{1}{J}$, $d = -\frac{1}{J}T_{\ L}$, and $u = T_e$.

The equivalent SMC law (u_{eq}) that ensures the asymptotic convergence of the velocity error towards zero verifies the following equality [27]:

$$S_1(t) = \dot{S_1}(t) = 0 \tag{13}$$

From (10) and (12), we deduce the equivalent control input as follows:

$$u_{eq} = g^{-1}(-f(x) - d - \lambda_1 x_2) \tag{14}$$

u_{eq} represents the total reference torque ($T^*_{e,total}$).

Additionally, the discrete SMC law (u_d) that guarantees the reachability of SMC in finite time is warranted if the following is the case [27]:

$$S_1\dot{S_1} < 0 \tag{15}$$

From (10), (15) can be rewritten as the following:

$$S_1\dot{S_1} = S_1(f(x) + g.u + d + \lambda_1 x_2) \tag{16}$$

if we set the following:

$$u_d{}' = g.u = g.u_d \tag{17}$$

and

$$u_d{}' = -(f(x) + d + \lambda_1 x_2) - C_1\, sign(S_1) \tag{18}$$

where C_1 is a positive constant. Therefore, the SMC law that ensures the asymptotic convergence of the velocity towards zero in finite time is given by the following:

$$u = u_{eq} + u_d \tag{19}$$

4.2.2. SMC Controller for Current Loop

For the current SMC controller, the sliding surface is defined as the following:

$$S_2(t) = \mathrm{K}_1 e_i(t) + \mathrm{K}_2\int_{-\infty}^{t} e_i(\Gamma)d\Gamma \tag{20}$$

where K_1 and K_2 are two positive coefficients.

The reason for this choice is obvious. If $S(t) = 0$, then $\dot{e}{=}-\frac{K_2}{K_1}e$, so the current error will converge to zero exponentially.

Equation (1) can be written as follows:

$$V_j = R_j.I_j + \frac{\partial\psi_j(\theta, I_j)}{\partial\theta}\frac{d\theta}{dt} + \frac{\partial\psi_j(\theta, I_j)}{\partial I_j}\frac{dI_j}{dt} \tag{21}$$

in which $\frac{d\theta}{dt} = \Omega$, where $\frac{\partial\psi_j(\theta,I_j)}{\partial I_j}$ represents the self-inductance of the phase and $\frac{\partial\psi_j(\theta,I_j)}{\partial\theta}\Omega$ is the back counter-electromotive force (EMF) produced in the *j*th phase. From (21), we can write the following:

$$\frac{dI_j}{dt} {=} (V_j - R_j.I_j).\frac{\partial I_j}{\partial\psi_j(\theta, I_j)} - \frac{\partial I_j}{\partial\theta}\Omega \tag{22}$$

The equivalent voltage (V_{eq}) obtained by the following:

$$S_2(t) = \dot{S_2}(t) = 0 \tag{23}$$

From (22) and (23), the equivalent voltage (V_{eq}) for each current regulation is written as the following:

$$V_{eq}{=}\ R_j I_j{}^* + \frac{\partial\psi_j(\theta, I_j)}{\partial\theta}\Omega + \frac{\partial\psi_j(\theta, I_j)}{\partial I}\frac{dI_j{}^*}{dt} + (R_j - \frac{\partial\psi_j(\theta, I_j)}{\partial I}\frac{K_2}{K_1})e_i(t) \tag{24}$$

Finally, the current SMC controller law is defined as the following:

$$V_{SMC} = V_{eq} - C_2 sign(S_2) \tag{25}$$

with C_2 is a positive constant.

4.3. Super Twisting Sliding Mode Control (STSMC)

The implementation of sliding mode control presents an undesirable phenomenon of oscillation, which is known as "chattering". The Super-Twisting Sliding Mode control (STSMC) has been developed to avoid chattering in variable structure control (VSC) for the case of systems that have a relative degree equal to one [27].

Consider sliding variable dynamics given by a system with a relative degree of two, the following is the case:

$$\dot{y_1}(t) = \varphi_{ST}(y_1, t) + Y_{ST}(y_1, t)u_{ST}(t) \tag{26}$$

where $y_1(t)$ is the sliding function S, in which φ_{ST} and Y_{ST} are uncertain functions with the upper and lower bounds of (27) and (28), respectively, and $u_{ST}(t)$ is the scalar control input.

$$|\varphi_{ST}(y_1, t)| \leq \phi_{ST} \tag{27}$$

$$0 < Y_{mST} \leq Y_{ST}(y_1, t) \leq Y_{MST} \tag{28}$$

The control signal $u_{ST}(t)$ can be given as the sum of two terms [27]:

$$u = u_1(t) + u_2(t) \tag{29}$$

$$\dot{u_1}(t){=}\begin{cases} u(t)_{ST} if |u(t)_{ST}| > U \\ -W sign(y_1(t)) else \end{cases} \tag{30}$$

$$u_2(t) = \begin{cases} -\lambda|S_0|^{\rho} sign(y_1(t)) if |y_1(t)| > S_0 \\ -\lambda|y_1(t)|^{\rho} sign(y_1(t)) else \end{cases} \tag{31}$$

where U is the control value boundary and S_0 is a boundary layer around the sliding surface S. The sufficient condition of limited time convergence is the following:

$$\begin{cases} W > \frac{\phi_{ST}}{Y_{mST}} \\ \lambda^2 > \frac{4\phi_{ST}}{{Y_{mST}}^2} \frac{Y_{MST}(W+\phi_{ST})}{Y_{mST}(W-\phi_{ST})} \\ 0 < \rho \leq 0.5 \end{cases} \tag{32}$$

4.3.1. STSMC Controller for Velocity Loop

To compare the SMC and STSMC, we use the same switching function expression used in SMC controller design:

$$S_3(t) = y_1(t) = e_\Omega(t) + c\int_{-\infty}^{t} e_\Omega(\Gamma) d\Gamma, c > 0 \tag{33}$$

The aim of this mathematical development is to write the systems having a relative degree equal to one and to compare it with (26) to find the sufficient conditions and to use the control law defined in (29).

From (2), (33) can be rewritten as the following:

$$\dot{y_1} = \dot{\Omega}^* + \frac{1}{J}T_L + \frac{1}{J}f_r\Omega^* + \left(-\frac{f_r}{J} + c\right)e_\Omega - \frac{1}{J}T_e \tag{34}$$

Defining the variable as the following:

$$\varphi_{ST} = \dot{\Omega}^* + \frac{1}{J}T_L + \frac{1}{J}f_r\Omega^* + \left(-\frac{f_r}{J} + c\right)e_\Omega \tag{35}$$

$$Y_{ST} = 1 \tag{36}$$

$$u_{ST} = -\frac{1}{J}T_e \tag{37}$$

Equation (34) becomes the following:

$$\dot{y_1} = \varphi_{ST} + Y_{ST}u_{ST} \tag{38}$$

If we set the following:

$$\begin{cases} 0 < Y_{mST} = 0.5 \leq Y_{ST} = 1 \leq Y_{MST} = 2 \\ u_{ST} = -\frac{1}{J}T_e < U = \frac{1}{J}T_{Max} \\ \phi_{ST} = \left|\dot{\Omega}^* + \frac{T_L}{J} + \frac{f_r\Omega^*}{J} + \left(-\frac{f_r}{J} + c\right)e_\Omega\right| + \left|\frac{T_e}{J}\right| \end{cases} \tag{39}$$

where T_{Max} is the maximum torque of the SRM. Conditions in (27) and (28) are satisfied.

To design the control law defined in (29), it is necessary to choose the controller parameters that verify (32).

4.3.2. STSMC Controller for Current Loop

In the same way as in the previous paragraph, for the STSMC current controller, the switching surface is defined as the following:

$$S_4(t) = y_2(t) = \mathrm{K}_3 e_i(t) + \mathrm{K}_4\int_{-\infty}^{t} e_i(\Gamma) d\Gamma \tag{40}$$

Putting $e_i(t)$ with its expression (21) in (38), we can write the following:

$$\dot{y_2} = \mathrm{K}_3 {e_i}^* + \mathrm{K}_4 e_i + \mathrm{K}_3 R_j.I_j \frac{\partial I_j}{\partial \psi_j(\theta, I_j)} - \mathrm{K}_3 \frac{\partial I_j}{\partial \theta} \Omega + - \frac{\partial I_j}{\partial \psi_j(\theta, I_j)} V_j \tag{41}$$

where K_3 and K_4 are two positive numbers.

Defining the variable as the following:

$$\varphi_{ST}{}' = \mathrm{K}_3 {e_i}^* + \mathrm{K}_4 e_i + \mathrm{K}_3 R_j.I_j \frac{\partial I_j}{\partial \psi_j(\theta, I_j)} - \mathrm{K}_3 \frac{\partial I_j}{\partial \theta} \Omega \tag{42}$$

$$Y_{ST}{}' = \frac{\partial I_j}{\partial \psi_j(\theta, I_j)} \tag{43}$$

$$u_{ST\prime} = -V_j \tag{44}$$

Equation (41) is expressed as the following:

$$\dot{y_2} = \varphi_{ST}{}' + Y_{ST}{}' u_{ST}{}' \tag{45}$$

where

$$\begin{cases} 0 < Y'_{mST} = 0.5 \frac{\partial I_j}{\partial \psi_j(\theta, I_j)} \leq Y'_{ST} = \frac{\partial I_j}{\partial \psi_j(\theta, I_j)} \leq Y'_{MST} = 2 \frac{\partial I_j}{\partial \psi_j(\theta, I_j)} \\ u'_{ST} = \left| -V_j \right| < U' = V \\ \phi'_{ST} = \left| \mathrm{K}_3 {e_i}^* + \mathrm{K}_4 e_i + \mathrm{K}_3 R_j.I_j \frac{\partial I_j}{\partial \psi_j(\theta, I_j)} \right| + \left| \mathrm{K}_3 \frac{\partial \mathrm{I_j}}{\partial \theta} \Omega \right| \end{cases} \tag{46}$$

It satisfies the conditions in (27) and (28).

5. Performances of the Designed Controllers

For the velocity and current loops, controllers are designed for both using PI Controllers, Sliding Mode Controller (SMC), and Super-Twisting Sliding Mode Controller (STSMC). Simulations are performed at a reduced scale for a vehicle drivetrain (Figure 4) using Matlab/Simulink to evaluate the proposed controllers [12]. The objectives are to minimize the velocity error and to ensure a smooth total torque waveform of the SRM. A velocity profile from zero to SRM maximum velocity (10,000 rpm) is chosen (Figure 5) with a load torque $T_L = 8$ Nm applied, in steady state, at *t* = 1.5 s, for a duration of 2 s. In addition, SRM torque viscous friction defined by fr*Ω where fr is the viscous friction coefficient (see Appendix A) is considered for all the simulation. The velocity profile tracking of the PI, SMC, and STSMC controllers and torques responses are presented in Figures 5 and 6, respectively. Indeed, Figure 5 shows that the velocity profile is well followed using the three controllers except the PI controller. Indeed, with the zooms displayed in Figure 5, STSM control is the best in terms of tracking. In Figure 6, the torque responses confirm on the one hand that the STSM control is the best, in terms of response time, to follow the torque profile, and on the other hand, as shown in the zoom of Figure 6, the torque ripple is considerably reduced in steady state compared to the SMC. In addition, the motor torque (current) at standstill is not zero because of the applied load torque of 8Nm for a duration of 3 s. However, viscous friction torque is zero because it depends on the motor velocity.

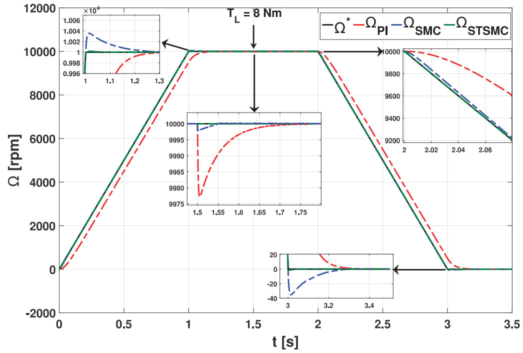

Figure 5. Velocity responses for the designed controllers.

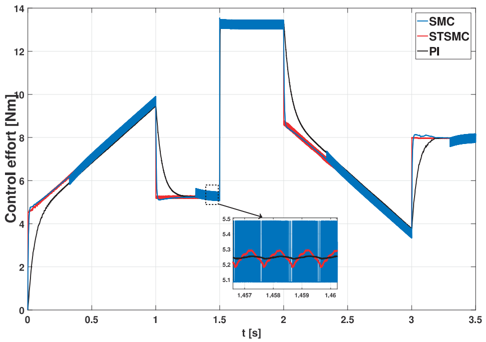

Figure 6. Torque responses for the designed controllers.

Based on these simulation results, Table 1 summarizes performances of the three controllers, namely rise time, maximum steady state error, maximum overshoot of velocity responses given by Figure 5, and torque ripples computed from torques responses given by Figure 6. Finally, performances comparison is carried out to show that Super-Twisting Sliding Mode Control is the best algorithm to provide the best performances for an electric vehicle drivetrain using a Switched Reluctance Machine.

Table 1. Performances comparison of the designed controllers.

Performances	PI	SMC	STSMC
Rise time	0.105 s	0.08 s	0.01 s
Max of steady state error	6%	0.3%	0.1%
Max of overshoot	27‰	23‰	8‰
Torque ripple at maximum velocity	14.5%	13.9%	12%

6. Robustness of the Designed Controllers

In the context of an electric vehicle application, the study of the robustness of the proposed controllers is necessary to check the limits of performances degradation with respect to the variations of the SRM physical parameters. The parameters to be varied are the resistance of the stator windings of a phase, the moment of inertia, the viscous friction coefficient, and the vehicle load torque whose variations are due to driving conditions (acceleration/deceleration), road slope, and state of the road (speed bumps, presence of obstacles, etc.). Based on the designed controllers where performances are evaluated by simulation in [12], a second simulation creating the variation of physical parameters of the vehicle drivetrain is carried with the designed controllers PI, SMC, and STSMC.

6.1. Stator Resistance Windings Variation

As the stator resistance windings varies because of temperature and ageing of the SRM, two values are chosen with −50% and +100% of the nominal value. Using the same simulator with the three controllers, namely PI, SMC and STSMC, response velocities and stator currents responses are collected. Figure 7a (with PI control), Figure 7b (with SMC), and Figure 7c (with STSMC) show the effect of these variations. Indeed, if the stator resistance of a phase decreases, an overshoot occurs; if the stator resistance of a phase increases, dynamic responses are slow. In addition, the zooms associated with these figures for the current and velocity responses show the interest to use the STSMC for the resistance varyies.

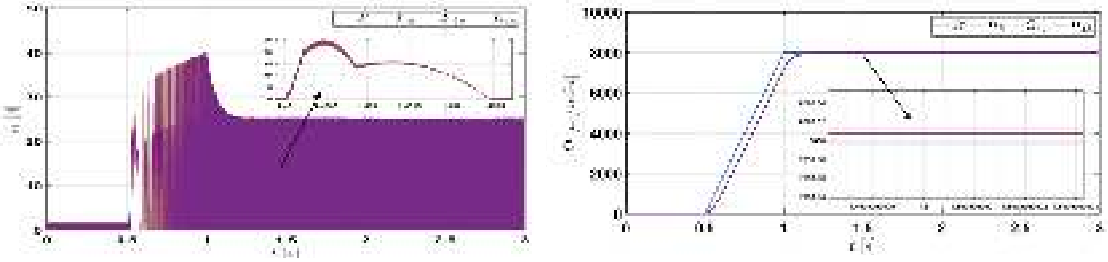

(**a1**) Current response with PI Controllers (**a2**) Velocity response with PI controllers

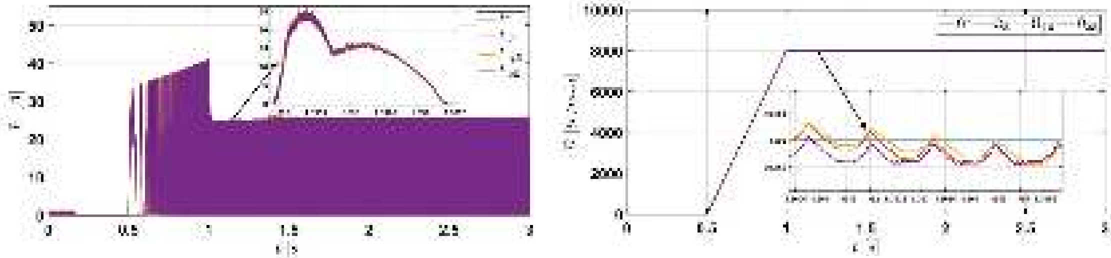

(**b1**) Current response with SMC (**b2**) Velocity response with SMC

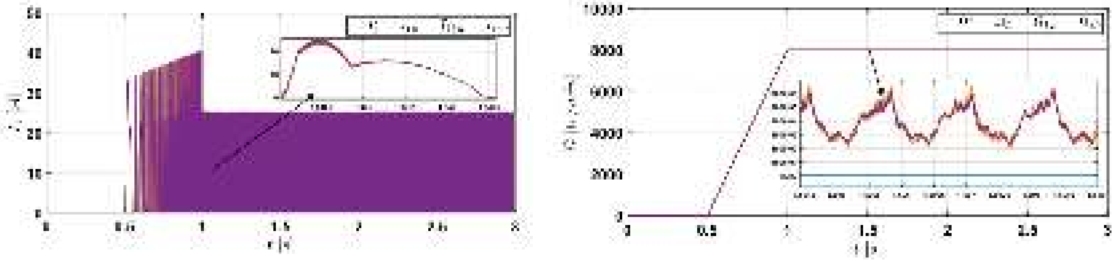

(**c1**) Current response with STSMC (**c2**) Velocity response with STSMC

Figure 7. Velocity and current responses with the three controllers.

6.2. Load Inertia Variation

As the vehicle inertia varies because of the vehicle load inertia, two values are chosen with −50% and +100% from the SRM inertia nominal value. Velocity responses show the effect of these variation on the velocity responses with the PI controller (Figure 8a), SMC (Figure 8b), and STSM (Figure 8c).

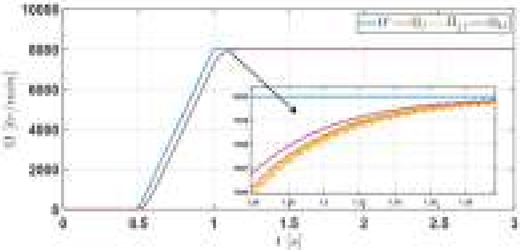

(**a**) Velocity responses with PI controllers

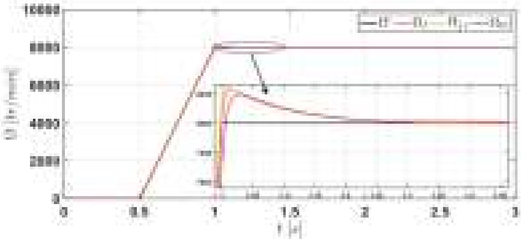

(**b**) Velocity responses with SMC

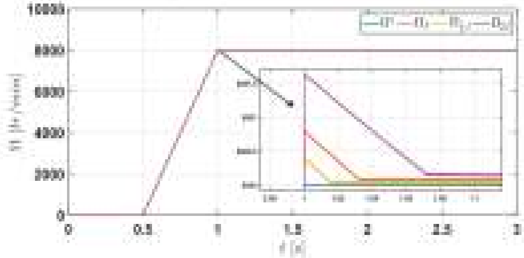

(**c**) Velocity responses with STSMC

Figure 8. Velocity responses with the three controllers.

6.3. Viscous Friction Coefficient Variation

For the viscous friction coefficient, a variation of 1/2 f_r and 2 f_r of the friction coefficient is carried out by simulation using the three controllers. Figure 9a–c show the velocity and torque responses. Indeed, STSMC is more robust compared to the other controllers. The zooms show that the errors are neglected when the viscous friction coefficient varies.

6.4. Load Torque Variation

For load torque variation, a first step load torque of 12 Nm is applied at t = 1.5 s and a second step of 16 Nm is applied at t = 2 s. Figure 10a–c show torque and velocity responses using the three controllers. Indeed, the load torque change is well compensated by the motor torque. In addition, as shown in the zoom of velocity responses, the overshoot error is neglected.

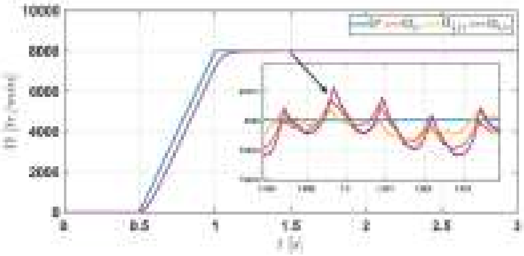

(**a**) Velocity responses with PI controllers

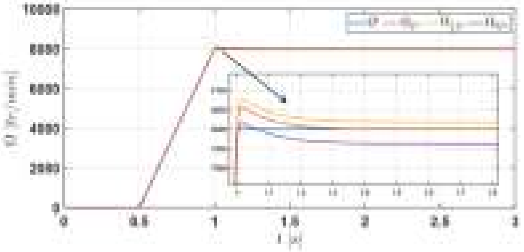

(**b**) Velocity responses with SMC

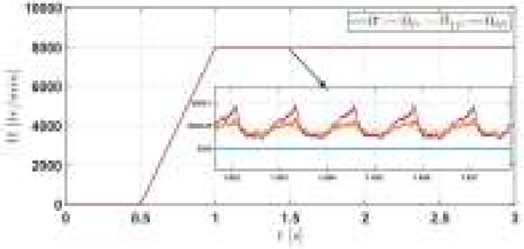

(**c**) Velocity responses with STSMC

Figure 9. Velocity responses with the three controllers.

Based on the responses of Figures 7–10, a quantification of the maximum error in steady state is carried out for current and velocity responses, while from torque responses, torque error is quantified in % using the following formula:

$$\Delta T_e(\%) = \frac{T_{emax} - T_{emin}}{T_{eaverage}}$$

Table 2 summarizes the computed values of the maximum errors at the maximum velocity using PI control, SMC, and STSMC.

Table 2. Evaluation of the robustness of the three controllers.

Physical Parameter Variation	PI	SMC	STSMC
Resistance R	Velocity emax = 2 rpm	Velocity emax = 0.8 rpm	Velocity emax = 0.5 rpm
	Current emax = 1.3 A	Current emax = 0.97 A	Current emax = 0.3 A
Moment of inertia J	Velocity emax = 5 rpm	Velocity emax = 5 rpm	Velocity emax = 1.5 rpm
Friction Coefficient f_r	Velocity emax = 3 rpm	Velocity emax = 40 rpm	Velocity emax = 0.5 rpm
load torque T_L	Velocity emax = 48 rpm	Velocity emax = 8 rpm	Velocity emax = 5 rpm
	Torque emax in % = 0.6	Torque emax in % = 0.1	Torque emax in % = 0.06

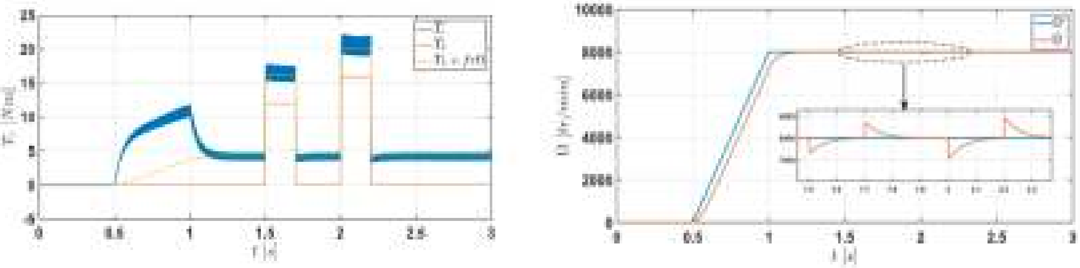

(**a1**) Torque responses with PI controllers (**a2**) Velocity responses with PI controllers

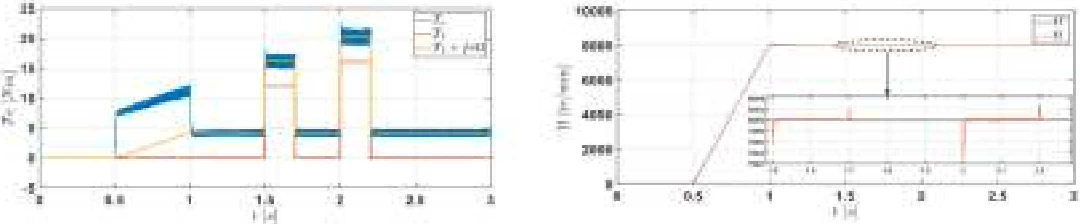

(**b1**) Torque responses with SMC (**b2**) Velocity responses with SMC

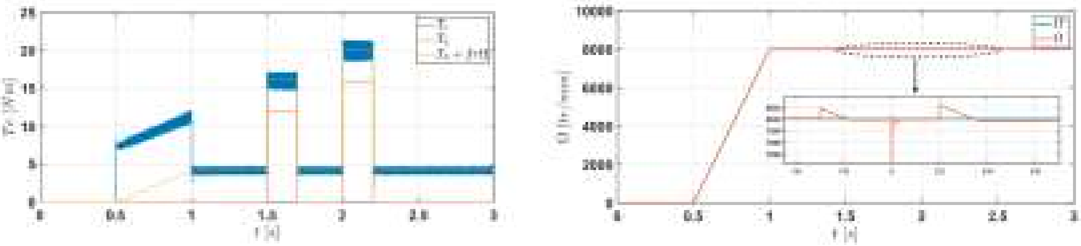

(**c1**) Torque responses with STSMC (**c2**) Velocity responses with STSMC

Figure 10. Velocity and torque responses with the three controllers.

In comparing the maximum errors of the three controllers, STSMC also shows its added value in robustness. Indeed, for all physical parameter variations, the maximum errors are the smallest ones for velocity, current, and torque responses. However, STSMC remains the best controller in terms of performance and robustness for electric vehicle applications. Finally, in Table 3, performance and robustness of the three controllers shows that Super-Twisting Sliding Mode Control is the best comparing to the PI and sliding mode controllers.

Table 3. Performances and robustness evaluation of the three controllers.

		Controller		
		PI	**SMC**	**STSMC**
Performances	Tracking	-	++	++
	Rapidity	+	++	++
	Precision	+	++	++
	Torque ripple	+	-	++
Robustness	R	+	+	++
	f_r	+	+	++
	J	+	++	++
	T_L	+	++	++

++: Very good, +: Good, -: Poor.

7. Experimental Validation

For the experimental validation, an emulation of the electric vehicle drivetrain is carried out at a reduced scale. As shown in Figure 11, a test bench is set up using a Switched Reluctance Machine of 8.3 kW (1) and a DC machine (2) with a resistive load (3) to emulate the vehicle load torque. The power supply of SRM is provided by four asymmetric half-bridges (4) supplied by a DC link of 250 V (7). In addition, the PWM signals to provide to the drivers of the IGBTs of each half-bridge converter are computed from the control strategies implemented on a multicore dSpace 1005 platform (5). The provided PWM signals are amplified from 5 V to 15 V using an electronic stage (8). For all the implemented control strategies, four current sensors (6) are used to provide, in real time, the stator currents through A/D inputs of the dSpace panel.

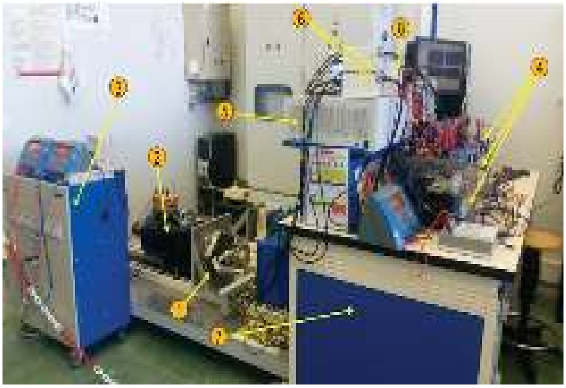

Figure 11. Test bench SRM-DC machine.

The real-time interface RTI of the implemented control strategies is mainly composed of four blocks. Figure 12 gives the general block scheme of the implemented control strategies, namely PI, SMC, and STSMC with a sample time of 10^{-5} s and a PWM frequency of 18 kHz.

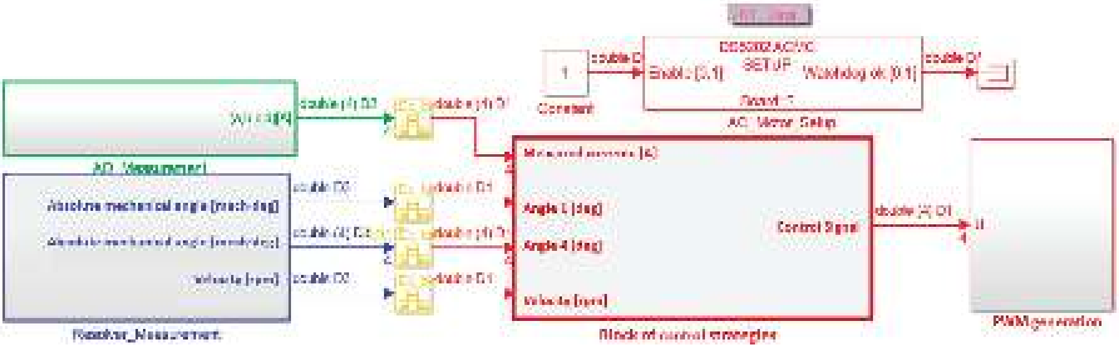

Figure 12. RTI block scheme of the implemented control strategies. 1—block of the four measured currents i_a, i_b, i_c, and i_d. 2—block of the measured position and velocity with a resolver mounted on the shaft of the SRM. 3—block of the control strategies with the designed robust controllers; PI, SMC, and STSM implemented separately. 4—block of PWM signal generation.

For the experimental validation, a velocity profile (*) of 3000 rpm max is chosen with acceleration, steady state, and deceleration phases for a duration of 180 s. Based on the velocity responses of Figure 13, responses errors are plotted in Figure 14a–c showing, respectively, a zoom of the reached velocity in steady state errors with PI, SMC, and STSMC.

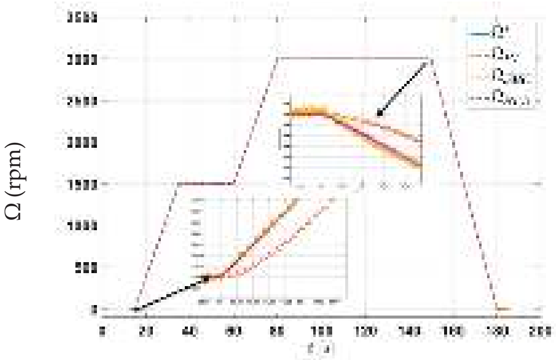

Figure 13. Velocity responses of the implemented robust controllers.

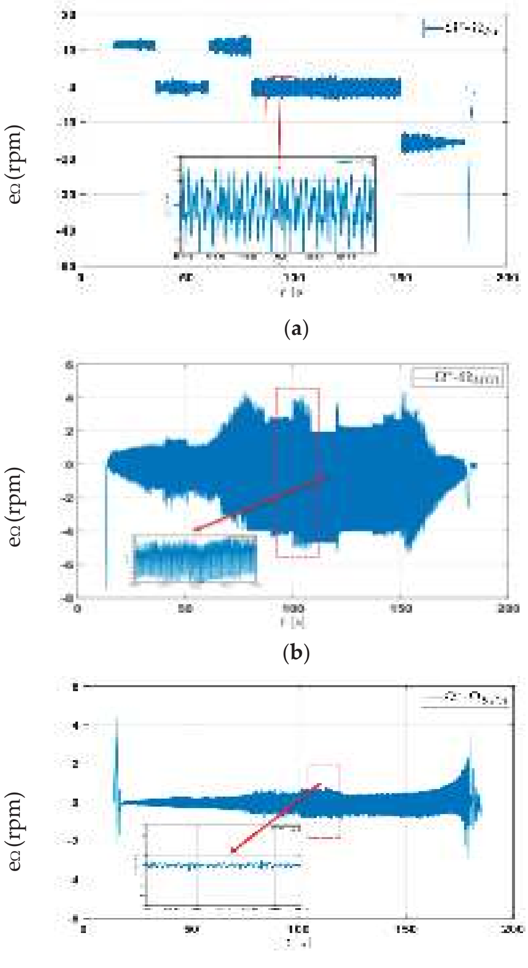

(**a**)

(**b**)

(**c**)

Figure 14. Zoom on the velocity responses in steady state.

Indeed, the best robust control given the minimum of oscillations around the steady state value is STSMC and, consequently, the minimum error in a steady state compared to other controllers. Moreover, when comparing the response of SMC and STA, the velocity response ripples, as shown in the zooms of Figure 13, are significantly improved due to the elimination of the chattering phenomenon.

Finally, simulation and experimental results confirm that, according to the performance comparison, STSMC is the best algorithm to be selected for an electric vehicle drivetrain with a Switched Reluctance Machine.

For the same controllers, current responses for a current set point (*) are collected from the test bench and plotted to make a performance comparison. Figures 15–17 show the current responses of phase 1 using PI, SMC, and STSMC, while Figures 18–20 show the corresponding current error responses.

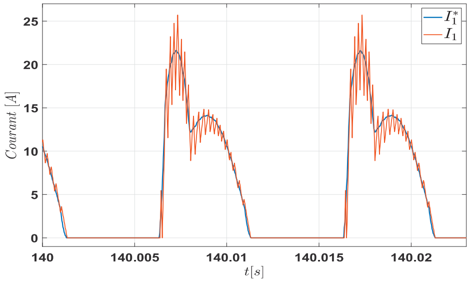

Figure 15. Current response of phase 1 using PI control.

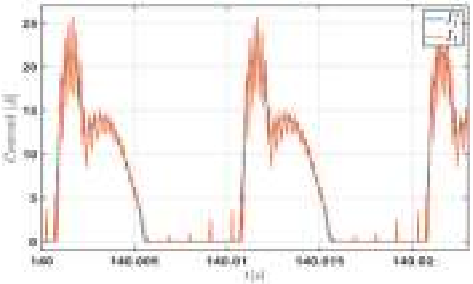

Figure 16. Current response of phase 1 using SMC.

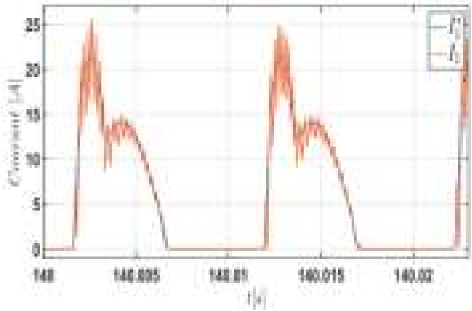

Figure 17. Current response of phase 1 using STSMC.

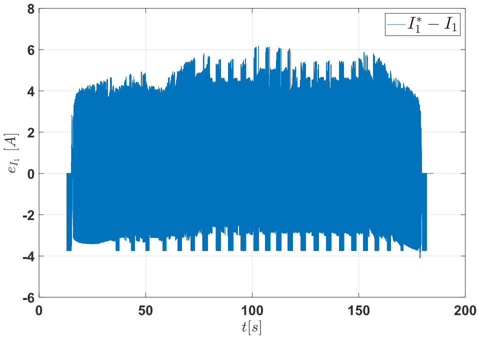

Figure 18. Current error response of phase 1 using PI control.

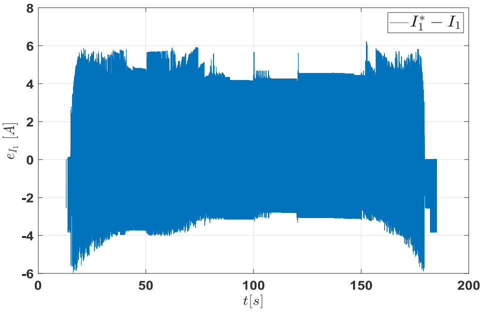

Figure 19. Current error response of phase 1 using SM.

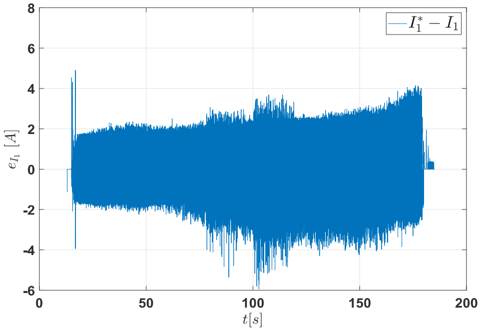

Figure 20. Current error response of phase 1 using STSMC.

According to the experimental current responses, it is shown that STSMC implemented in the current loop is the best algorithm to obtain minimum oscillations around the steady state value and, consequently, minimum torque ripple. Finally, the three robust controllers implemented simultaneously in the velocity loop and in the four current loops of the SRM control strategy confirm that STSMC performances are better compared to the other robust controls, namely PI and SM controllers.

8. Conclusions

In this paper, STSMC, SMC, and PI controllers are successfully validated and implemented to deal simultaneously with the velocity and current tracking problem of a Switched Reluctance Machine for electric vehicle applications. A cascade control strategy is adopted to control separately the SRM velocity and each phase current.

- The simulation and the experimental results show and confirm the benefits of using STSMC in terms of tracking performances and torque ripple minimization, thanks to the significant reduction in the chattering.
- The performances of electric vehicle drivetrain are improved using a Switched Reluctance Machine and STSMC. Both could be a new solution for future electric vehicles drivetrains: SRM as a fault-tolerant design component without rare earth material and STSMC as a robust control to obtain better performances and comfort in the electric vehicle.
- Improvement of performances and robustness of electric vehicle drivetrain using switched reluctance machine can improve performances of other functions of safety in electric vehicle applications and/or in autonomous vehicles where the dynamic behavior of the vehicle on the road depends on the dynamic behavior of the vehicle drivetrain in closed loop.
- This work can be extended to deal with electric and mechanical faults of the electric vehicle drivetrain to show the added value of SRM as a fault tolerant design machine.
- Finally, this study can be extended to Four-Wheel Independent Control Electric Vehicles (FWIC-EV) using Switched Reluctance Machines and STSMC.

Author Contributions: Validation, Y.S.; Writing—original draft, R.S.; Writing—review & editing, A.A. All authors have read and agreed to the published version of the manuscript.

Funding: This research received no external funding.

Data Availability Statement: Not applicable.

Conflicts of Interest: The authors declare no conflict of interest.

Appendix A

Parameter	Value
Topology	8 S/6 R
Phase number	4
Power supply (DC)	250 V
Maximum current	61 A
Nominal Power	8 kW
Maximum torque T_{Max}	20 Nm
Maximum speed	10,000 rpm
Phase resistance R	0.0404 Ohm
Moment of inertia J	0.0043 Kg/m^2
Viscous friction coefficient fr	0.005 Nm/s

References

1. Husain, I. *Electric and Hybrid Vehicles: Design Fundamentals*; CRC Press: Boca Raton, FL, USA, 2003.
2. Widmer, J.D.; Martin, R.; Kimiabeigi, M. Electric vehicle traction motors without rare earth magnets. *Sustain. Mater. Technol.* **2015**, *3*, 7–13. [CrossRef]
3. Krishnan, R. *Switched Reluctance Motor Drives: Modeling, Simulation, Analysis, Design, and Applications*; CRC Press: Boca Raton, FL, USA, 2001.
4. Biczyski, M.; Sehab, R.; Whidborne, J.; Krebs, G.; Luk, P. Fault-tolerant Switched Reluctance Motor Propulsion System for eVTOLs. In Proceedings of the 12th EASN International Conference on "Innovation in Aviation & Space for opening New Horizons, Barcelona, Spain, 18–21 October 2022.
5. Colby, R.S.; Mottier, F.M.; Miller, T.J.E. Vibration modes and acoustic noise in a four-phase switched reluctance motor. *IEEE Trans. Ind. Appl.* **1996**, *32*, 1357–1364. [CrossRef]
6. Chiba, A.; Kiyota, K.; Hoshi, N.; Takemoto, M.; Ogasawara, S. Development of a Rare-Earth-Free SR Motor With High Torque Density for Hybrid Vehicles. *IEEE Trans. Energy Convers.* **2015**, *30*, 175–182. [CrossRef]

7. Takiguchi, M.; Sugimoto, H.; Kurihara, N. Acoustic Noise and Vibration Reduction of SRM by Elimination of Third Harmonic Component in Sum of Radial Forces. *IEEE Trans. Energy Convers.* **2015**, *30*, 883–891. [CrossRef]
8. Rana, A.K.; Raviteja, A. A mathematical torque ripple minimization technique based on nonlinear modulating factor for switched reluctance motor drives. *IEEE Trans. Ind. Electron.* **2022**, *69*, 1356–1366. [CrossRef]
9. Ding, W.; Liu, G.; Li, P. A hybrid control strategy of hybridexcitation switched reluctance motor for torque ripple reduction and constant power extension. *IEEE Trans. Ind. Electron.* **2020**, *67*, 38–48. [CrossRef]
10. Sun, X.; Wu, J.; Lei, G.; Guo, Y.; Zhu, J. Torque ripple reduction of srm drive using improved direct torque control with sliding mode controller and observer. *IEEE Trans. Ind. Electron.* **2021**, *68*, 9334–9345. [CrossRef]
11. Kelly, L.; Cossar, C.; Miller, T. *Electronic Control of Switched Reluctance Machines*; Newnes Power Engineering Series; Newnes: Oxford, UK, 2001.
12. Saadi, Y.; Sehab, R.; Chaibet, A.; Boukhnifer, M.; Diallo, D. Performance comparison between conventional and robust control for the powertrain of an Electric Vehicle propelled by a Switched Reluctance Machine. In Proceedings of the IEEE Vehicle Power and Propulsion Conference (VPPC), Arlington, TX, USA, 9–12 September 2007; pp. 1–6.
13. Hannoun, H.; Hilairet, M.; Marchand, C. Gain-scheduling pi current controller for a switched reluctance motor. In Proceedings of the IEEE International Symposium on Industrial Electronics, Vigo, Spain, 4–7 June 2007; pp. 1177–1182.
14. Ouddah, N.; Boukhnifer, M.; Chaïbet, A.; Monmasson, E. Robust LPV current control of switched reluctance motor. In Proceedings of the 22nd Mediterranean Conference on Control and Automation, Palermo, Italy, 16–19 June 2014.
15. Ghani, M.; Frah, N.; Tamjis, M. Vector Control of Switched Reluctance Motor Using Fuzzy Logic and Artificial Neutral Network. In Proceedings of the International Conference on Electrical, Electronics, and Optimization Techniques (ICEEOT), Chennai, India, 3–5 March 2016; pp. 4412–4417.
16. Ling, F.; Ma, M.; Yang, Q.; Li, F. Torque Ripple Reduction of Switched Reluctance Motor by Segmented Harmonic Currents Injection Based on Adaptive Fuzzy Logic Control. In Proceedings of the 14th IEEE Conference on Industrial Electronics and Applications (ICIEA), Xi'an, China, 19–21 June 2019.
17. John, G.; Eastham, A. Speed control of switched reluctance motor using sliding mode control strategy. In Proceedings of the IAS '95. Conference Record of the 1995 IEEE Industry Applications Conference Thirtieth IAS Annual Meeting, Orlando, FL, USA, 8–12 October 1995; Volume 1, pp. 263–270.
18. Ruiwei, Z.; Xisen, Q.; Liping, J.; Yingch, Z.; Jintong, N. An adaptive sliding mode current control for switched reluctance motor. In Proceedings of the IEEE Conference and Expo Transportation Electrification Asia-Pacific (ITEC Asia-Pacific), Beijing, China, 31 August–3 September 2014.
19. Canale, M.; Fagiano, L.; Ferrara, A.; Vecchio, C. Comparing Internal Model Control and Sliding-Mode Approaches for Vehicle Yaw Control. *IEEE Trans. Intell. Transp. Syst.* **2009**, *10*, 31–41. [CrossRef]
20. Ouddah, N.; Boukhnifer, M.; Chaibet, A.; Monmasson, E. Robust controller designs of switched reluctance motor for electrical vehicle. In Proceedings of the 22nd Mediterranean Conference on Control and Automation, Palermo, Italy, 16–19 June 2014.
21. Peng, F.; Emadi, A. A digital PWM current controller for switched reluctance motor drives. In Proceedings of the IEEE Transportation Electrification Conference and Expo (ITEC), Dearborn, MI, USA, 15–18 June 2014; pp. 1–6.
22. Li, X.; Shamsi, P. Model Predictive Current Control of Switched Reluctance Motors with Inductance Auto-Calibration. *IEEE Trans. Ind. Electron.* **2016**, *63*, 3934–3941. [CrossRef]
23. Liu, W.; Xiong, L.; Xia, X.; Lu, Y.; Gao, L.; Song, S. Vision-aided intelligent vehicle sideslip angle estimation based on a dynamic model. *IET Intell. Transp. Syst.* **2020**, *14*, 1183–1189. [CrossRef]
24. Liu, W.; Xiong, L.; Xia, X.; Yu, Z. Intelligent vehicle sideslip angle estimation considering measurement signals delay. In Proceedings of the IEEE Intelligent Vehicles Symposium (IV), Changshu, China, 26–30 June 2018; pp. 1584–1589.
25. Husain, I.; Hossain, S. Modeling, Simulation, and Control of Switched Reluctance Motor Drives. *IEEE Trans. Ind. Electron.* **2005**, *52*, 1625–1634. [CrossRef]
26. Pollock, C.; Williams, B. A unipolar converter for a Switched Reluctance Motor. *IEEE Trans. Ind. Appl.* **1990**, *26*, 222–228. [CrossRef]
27. Bartolini, G.; Ferrara, A.; Usai, E. Chattering avoidance by second order sliding mode control. *IEEE Trans. Autom. Control* **1998**, *43*, 241–246. [CrossRef]

applied sciences

Article

Structure Optimization and Control Design of Electronic Oxygen Regulator

Dongsheng Jiang *, Yue Liu, Haowen Yang, Xingxing Fang, Binbin Qian and Hui Li

School of Mechanical and Electrical Engineering, Anhui Jianzhu University, Heifei 230009, China;
liuyue566@stu.ahjzu.edu.cn (Y.L.)
* Correspondence: jiangds922@163.com

Abstract: The oxygen regulator is the core component of the aircraft life support system, which adjusts the flow and pressure of the breathing gas according to the pilot's breathing needs. In response to the problem that structural parameters are difficult to adjust and prone to jitter when the indirect oxygen regulator system is stable, a direct oxygen regulator is designed using a stepper motor to drive a lung-type flapper, replacing the diaphragm lever-type structure of the indirect oxygen regulator. Due to the nonlinearity and time-varying nature of the dynamic characteristics of oxygen regulators, a single-neuron PID control strategy based on online identification of RBF neural networks is proposed to improve the PID control performance. The RBF neural network is used to identify the Jacobian information of the controlled object, and the single-neuron PID controller completes the online adjustment of the controller parameters to realize the intelligent control of the system. Simulation experimental studies are conducted to verify the performance of the direct oxygen regulator. The result analysis verifies the excellence of the single-neuron PID control strategy based on online recognition of the RBF neural network to improve the system performance.

Keywords: electronic oxygen regulator; structural optimization; RBF neural network; single neuron; life support system

Citation: Jiang, D.; Liu, Y.; Yang, H.; Fang, X.; Qian, B.; Li, H. Structure Optimization and Control Design of Electronic Oxygen Regulator. *Appl. Sci.* **2023**, *13*, 5431. https://doi.org/10.3390/app13095431

Academic Editors: Kan Liu and Wei Hu

Received: 31 March 2023
Revised: 21 April 2023
Accepted: 23 April 2023
Published: 27 April 2023

1. Introduction

With the development of onboard electronics, electronic oxygen supply regulators using electronic technology and sensor technology for control began to appear [1,2]. It is mainly through the pressure sensor that one can feel the small pressure difference, with the use of the solenoid valve to control the opening of the valve, or using the micro-motor-driven diaphragm to indirectly drive the opening of the oxygen supply valve to achieve oxygen supply regulation [3]. The performance of the electronic oxygen supply regulator has greatly improved, and it can adapt to the low outlet pressure of molecular sieve oxygen system and has the advantages of small size, light weight, high flow rate, low suction resistance, and fast dynamic response, which is the future development direction of airborne oxygen supply regulators [4–6].

At present, the actuator of the electronic oxygen regulator is mainly mechanical, and the control part adopts the electronic auxiliary regulation [7]. The system is dominated by mechanical actuator regulation and is supplemented by electronic regulation control to improve the comprehensive performance of the system, where the oxygen supply regulator and anti-charge regulator are integrated into a system, which compared to the mechanical control system performance makes it a great improvement [8]. This indirect oxygen regulator indirectly controls the opening and closing of the pulmonary oxygen supply valve by controlling the residual pressure valve with a motor. However, there are still disadvantages in that the mechanical oxygen regulator mechanism parameters are difficult to adjust, and the pressure is easy to fluctuate.

In the research on oxygen regulator structures, Wan et al. studied the calculation of the structural parameters of an indirect oxygen regulator [9]. The performance parameters of the indirect oxygen regulator were analyzed by Zou et al. [10]. Concerning the electronic control of oxygen regulators, Yu et al. used switching control [11] and Sun et al. applied fuzzy control to design a control law for an electronic oxygen regulator [12]. Li et al. used expert control to automatically adjust the PID parameters, which solved the deficiency of fixed control parameters [5]. Jiang et al. pointed out that disturbance suppression is a key issue in the control of oxygen regulators. Generalized predictive control (GPC) [13], automatic disturbance rejection control (ADRC) [14], and the adaptability has been applied to controllers to improve performance [15].

In the control application of an oxygen regulator, there are unknown perturbations acting on the system such as gas source pressure changes and suction flow changes in the oxygen regulator, and it is difficult to achieve the desired control effect with a fixed parameter PID regulator. Therefore, the control method of a single-neuron PID is adopted, and an RBF neural network is introduced for online identification of system output to provide system dynamic information for the learning process of single-neuron PID.

Through the study and analysis of an indirect oxygen regulator, it is found that the parameters of the indirect oxygen regulator are not easily adjustable, and they jointly affect the overall performance. It is necessary to optimize the structure of the indirect oxygen regulator by changing the parameters and proposing a direct oxygen regulator to solve the jitter problem caused by the diaphragm lever mechanism. An intelligent control method is applied to improve the breathing resistance and pressure fluctuation of the oxygen regulator. This paper designs a direct oxygen regulator structure based on the indirect oxygen regulator by merging the lung type valve mechanism and the electronically controlled residual pressure valve mechanism of the indirect electronic oxygen regulator, and optimizing it to a direct motor-driven valve mechanism to close or open the valve for oxygen supply and establish a mathematical model of respiratory pressure control. In this control system structure, the RBF neural network is used to identify the Jacobian information of the controlled object and the online adjustment of the controller parameters is completed by the single-neuron PID controller to realize the intelligent control of the system. The control performance of the structure's design and control method on pressure fluctuation and breathing resistance is verified through a simulation and experiment.

2. Oxygen Regulator Principle Analysis

2.1. Indirect Oxygen Regulator Principle

Combined with the structure principle of indirect oxygen regulator in Figure 1, when the pilot inhales, the P2 pressure measurement point detects the negative pressure generated by the pilot's inhalation, and the electronic control device controls the electronically controlled residual pressure valve to move forward to establish the residual pressure chamber pressure (P2 pressure measurement point); the residual pressure chamber pressure acts on the main lung valve diaphragm, which deforms the main lung valve diaphragm to open the main valve to supply air to the pilot. When the pilot exhales, P1 detects the exhalation action, and the electronic control device controls the electronically controlled residual pressure valve to move backward and remove the residual pressure chamber pressure, and the main lung valve diaphragm returns to its initial state to close the main valve and stop supplying air to the pilot. When the height rises, the electronic control device controls the electronically controlled residual pressure valve to move forward and establish the safety residual pressure (P2 pressure measurement point). The breathing chamber pressure is controlled by the residual pressure chamber pressure through the main lung type valve diaphragm 8 and the main valve to establish the safety residual pressure.

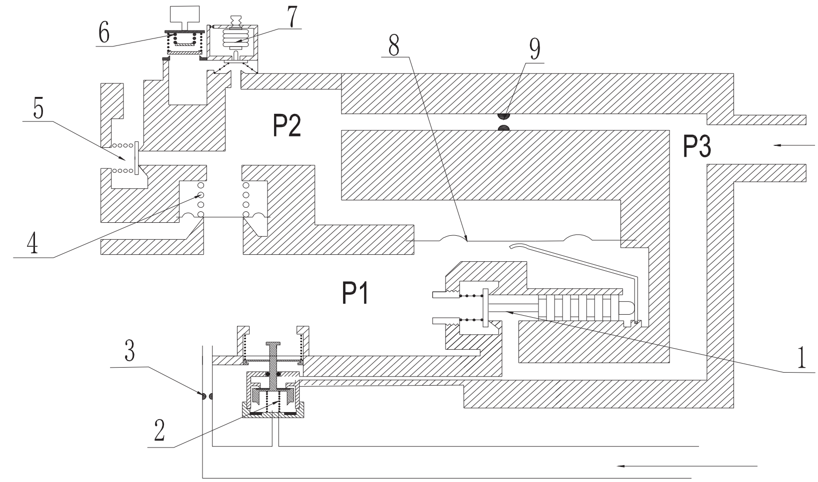

Figure 1. Indirect oxygen regulator structure schematic. P1: breathing chamber pressure measuring point; P2: residual pressure chamber pressure measuring point; P3: inlet pressure measuring point; 1: pulmonary valve; 2: air valve; 3: limiting hole; 4: ventilation valve; 5: safety valve; 6: residual pressure valve; 7: high residual pressure valve; 8: membrane; 9: sizing hole.

2.2. Optimized Design

The literature [15] proposes that the phenomenon of positive pressure fluctuations is caused by a combination of inlet pressure fluctuations and diaphragm deformation. At low lung flux, the effects of both causes are similar. At high lung flux, diaphragm deformation becomes the main cause of significant positive pressure fluctuations.

To address this one drawback of the indirect oxygen regulator, a structural solution design was focused on the oxygen supply assembly. The lung-type flapper mechanism and the electronically controlled residual pressure flapper mechanism of the indirect electronic oxygen supply anti-charge regulator are combined and optimized to close or open the flapper for oxygen supply by direct motor drive. The design of removing the diaphragm can fundamentally improve the system performance of the oxygen regulator.

The stepper motor is driven to open or close the oxygen supply door of the lung mechanism according to the parameters of cockpit height, acceleration, and product input and output pressure collected by the sensor set. The opening and closing of the oxygen supply door of the lung mechanism is realized by the electronic control device. The schematic sketch of the pulmonary mechanism is shown in Figure 2. The flow restrictor provides a continuous flow of oxygen supply. When the control or power failure occurs in the electronically controlled oxygen supply, and normal oxygen supply cannot be carried out, oxygen regulation must be implemented to downgrade the oxygen supply. When a power failure occurs or the electronic control device monitors the abnormal output of the subsystem, the electronic control device drives the normally open solenoid valve down to turn on the continuous flow and implement the downgraded oxygen supply. The oxygen supply assembly mainly consists of a shell assembly, a linear stepping motor, a normally open solenoid valve, a lung mechanism, a flow limiter, a time delay mechanism, a safety valve mechanism, an anti-asphyxiation mechanism, and a pressure limiting mechanism. The structure's schematic diagrams are shown in Figures 2 and 3, respectively.

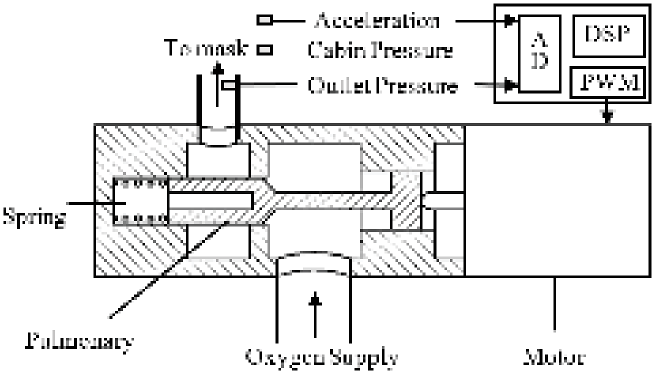

Figure 2. Electronic oxygen regulator working principle diagram.

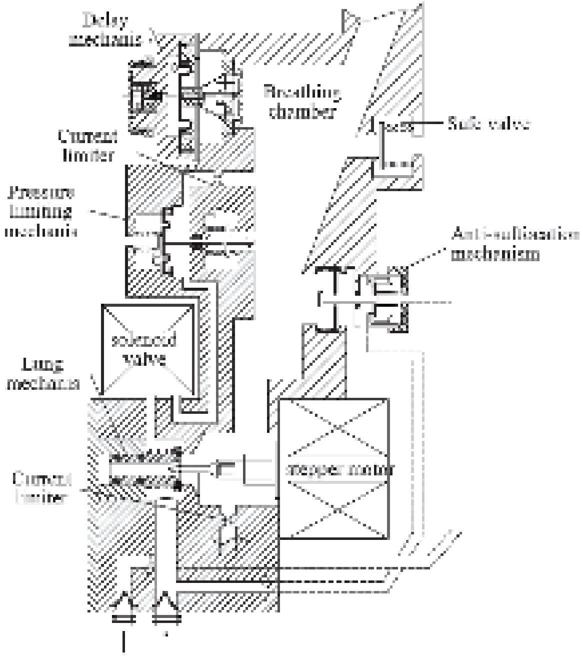

Figure 3. Direct oxygen regulator structure schematic.

3. Control Method Design

3.1. Mathematical Modeling

The mathematical model of the oxygen regulator consists of two parts: the pulmonary valve and the stepper motor. Due to the complex structure of the entire oxygen regulator, model identification using system identification techniques is very difficult. Combining the advantages of identification techniques and mechanistic analysis, both the lung valve and stepper motor models are based on mechanistic analysis.

Before building the mathematical model, it can be assumed that the gas is regarded as an ideal gas and satisfies the ideal gas equation [16]. The process of gas flow through the positive pressure chamber and the valve is very short, so the heat exchange can be neglected and the gas flow state is regarded as an isentropic process [15]. Considering the gas in the suction chamber as a control body, the dynamic equations of the gas pressure and flow in the suction chamber are as follows:

$$\frac{dp}{dt} = \frac{\mathrm{K} \cdot R_g \cdot T \cdot \delta_m}{V} \tag{1}$$

$$\delta_m = G_{in} - G_{out} \tag{2}$$

where p is the gas pressure in the suction chamber, T is the gas temperature, K is the gas adiabatic index, R_g is the gas constant, V is the volume of the suction chamber, δ_m is the mass change, G_{in} is the gas mass flow rate into the suction chamber, and G_{out} is the gas mass flow rate out of the suction chamber.

The gas flow area of the valve is calculated as follows:

$$A = \pi \cdot (d - x \sin\theta \cos\theta) x \cdot \sin\theta \tag{3}$$

where d is the diameter of the valve hole, θ is the valve half taper, and x is the valve opening.

The gas flow in the suction chamber can be considered an isentropic flow [16]. When expressing the gas mass flow equation, there are two cases.

In the first case, when $p/p_{in} > \varepsilon$

$$G_{in} = \frac{C_d \cdot A \cdot p_{in}}{\sqrt{R_g \cdot T_{in}}} \sqrt{\frac{2\kappa}{K-1} \left(\frac{p}{p_{in}}\right)^{\frac{2}{\kappa}} \left(1 - \left(\frac{p}{p_{in}}\right)^{\frac{\kappa}{\kappa-1}}\right)} \tag{4}$$

In the second case, when $p/p_{in} \leq \varepsilon$

$$G_{in} = \frac{C_d \cdot A \cdot p_{in} \cdot B}{\sqrt{R_g \cdot T_{in}}} \sqrt{\frac{2\kappa}{\kappa+1} \left(\frac{2}{\kappa+1}\right)^{\frac{2}{\kappa-1}}} \tag{5}$$

where C_d is the flow coefficient of the flapper, A is the flow area of the flapper, $\varepsilon = \left(\frac{2}{\kappa+1}\right)^{\frac{\kappa}{\kappa-1}}$ is the critical pressure ratio, p_{in} is the inlet gas pressure, and T_{in} is the inlet gas temperature.

The following force balance equation is satisfied during the motion of the stepper motor:

$$m\frac{d^2x}{dt} = F_m - c\frac{dx}{dt} - kx + F_d \tag{6}$$

$$F_m = k_m \cdot i \tag{7}$$

where m is the mass of the moving part, F_m is the electromagnetic force, c is the viscous damping factor, k is the spring stiffness, and F_d is the disturbance force, i is the coil current, and k_m is the electromagnetic force coefficient.

The mathematical model can be synthesized as follows:

$$\begin{cases} \dot{p} = f_1(p, w_1) + b_1 x \\ \ddot{x} = f_2(x, \dot{x}, w_2) + b_2 u \\ y = p \end{cases} \tag{8}$$

where w_1 and w_2 are unknown perturbations.

$$f_1(p, w_1) = \frac{\kappa \cdot R_g \cdot T}{V}(k_1 p - G_{out}) \tag{9}$$

$$f_2(x, \dot{x}, w_2) = -\left(\frac{c}{m} + \frac{k_m k_E}{mR}\right)\dot{x} - \frac{k}{m}x + \frac{F_d}{m} \tag{10}$$

$$b_1 = \frac{\kappa \cdot R_g \cdot T}{V} k_2 \tag{11}$$

$$b_2 = \frac{k_m}{mR} \tag{12}$$

In the simulation calculation, G_{out} is calculated by the human lung capacity model. The variation of human lung capacity can be regarded as a sinusoidal law variation.

3.2. Controller Design

According to the oxygen regulation principle of the direct oxygen regulator, the electronic control device drives the stepper motor to open or close the oxygen supply valve of the pulmonary mechanism according to parameters such as cockpit height, acceleration, and product input and output pressure collected by the sensor group. The goal of the controller design is, on the one hand, to regulate u to keep the output pressure y close to a given reference input; on the other hand, to regulate u to counteract the effects of various disturbances w. In both cases, the smaller the control error $e = r - y$, the smaller the suction resistance and pressure fluctuations. During the operation of the oxygen regulator, the output gas pressure was affected by various disturbances such as pilot suction flow, change in gas source pressure, a disturbance force acting on the flapper, change in motor parameters, etc. The structural parameters of the whole control system are time-varying and non-linear, and the PID regulator with fixed parameters cannot get the ideal control quality. A single-neuron PID control method is used, and an RBF neural network is introduced for online identification of the system output to provide system dynamic information for the learning process of the single-neuron PID [17]. The control system structure is shown in Figure 4. In Figure 4, SNPID is the single-neuron PID controller and RBFNNI is the RBF neural network discriminator.

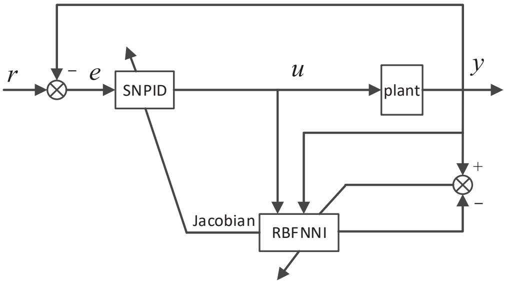

Figure 4. Structure of a single-neuron PID control system based on RBF identification.

An adaptive single-neuron PID control method based on dynamic RBF neural network identification is proposed in the reference paper [18], where a dynamic neural network identifier identifies the system model online, obtains online tuning information of the PID parameters, and the single-neuron controller realizes the self-tuning of the controller parameters. The system has the advantages of high adaptability and robustness compared with the traditional RBF neural network-based PID control method. The single-neuron PID controller based on RBF neural network recognition consists of a single-neuron PID controller and a dynamic RBF neural network recognizer. The dynamic RBF neural network is used to model the system, obtain a predictive mathematical model of the system, replace the actual output of the object with the predicted output of the model, and then design the single-neuron PID controller. The network recognition structure adopts a series-parallel structure to ensure the stability of the system.

The single-neuron PID controller is a controller that combines PID control laws and neural networks [19], and the implicit layer contains three units that are proportional (P), integral (I), and differential (D), and the structure of this controller is shown in Figure 5. Adaptivity is achieved through the adjustment of single-neuron weighting coefficients and the commonly used learning rules are the unsupervised Hebb learning rule, supervised Delta learning rule, and supervised Hebb learning rule [19]. In this paper, the controller performs online rectification of the weights based on the gradient descent method and the Jacobian information provided by the RBFNNI. The control and learning algorithms are as follows:

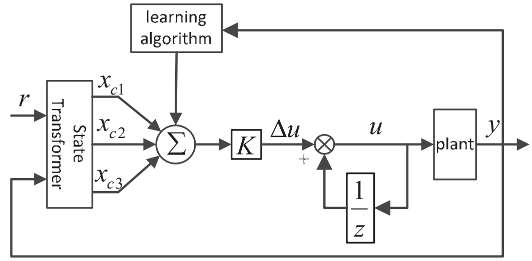

Figure 5. Single-neuron controller structure.

Let the system control error be *e(k)* = *r(k)* − *y(k)*. Take the neuron input as:

$$\begin{cases} x_{c1}(k) = e(k) - e(k-1) \\ x_{c2}(k) = e(k) \\ x_{c3}(k) = e(k) - 2e(k-1) + e(k-2) \end{cases} \tag{13}$$

Neuronal outputs are:

$$u(k) = u(k-1) + K\sum_{i=1}^{3} v_i(k)x_{ci}(k) \tag{14}$$

where $v_i(k)$ is the weight coefficient of a single-neuron network, and $K > 0$ is the scale factor of single neuron. The performance index function of the controller was taken as:

$$J_c = \frac{1}{2}e^2(k) \tag{15}$$

According to the gradient descent method, the adjustment of the single-neuron weighting coefficient is:

$$\Delta v_i(k+1) = -\eta_i \frac{\partial J_c}{\partial v_i(k)} = -\eta_i \frac{\partial J_c}{\partial y}\frac{\partial y}{\partial u}\frac{\partial u}{\partial v_i(k)} = \eta_i e(k)\frac{\partial y}{\partial u}Kx_{ci}(k) \tag{16}$$

where n is the learning rate and y can be replaced by the RBFNN discrimination information u. From this, the adjusted weighting coefficient was obtained as:

$$v_i(k+1) = v_i(k) + v_i(k+1) \tag{17}$$

To ensure the convergence and robustness of the control algorithm Equations (16) and (17), the learning algorithm was normalized [20] to obtain:

$$\begin{cases} u(k) = u(k-1) + K\sum\limits_{i=1}^{3} v_i(k)x_{ci}(k) \\ v'_i(k) = v_i(k) / \sum\limits_{i=1}^{3} |v_i(k)| \end{cases} \tag{18}$$

3.3. Simulation Results

For the structural characteristics of the direct oxygen regulator, the performance of the direct oxygen regulator is analyzed by a simulation focusing on the pulmonary mechanism and pressure limiting mechanism, and the simulation structure is represented in Figure 6. The respiratory flow rate of the user varies approximately according to the sinusoidal law. A joint simulation of the model was implemented using amsim and simulink. The sampling time is 0.001 s. The parameters used in the simulation and their values are listed in Table 1.

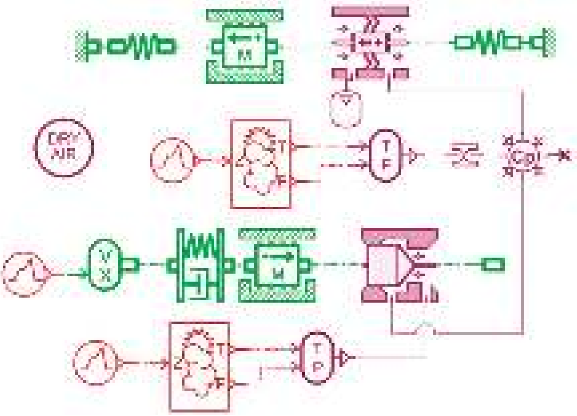

Figure 6. Oxygen regulator simulation structure.

Table 1. Structural parameters.

Parameter	Value
Spring stiffness (N/m)	470
Volume of chamber (cm^3)	13
Diameter of hole (mm)	10
Diameter of poppet (mm)	15
Orifice area (mm^2)	0.1

Oxygen supply is mainly achieved by stepper motors opening or closing the oxygen supply valve of the pulmonary mechanism. The simulation structure includes only the motor and its driven lung mechanism, the pressure limiting mechanism, and the breathing chamber. The principle of the pulmonary mechanism is mainly a motor pushing the pulmonary valve, and the simplified simulation mechanism is represented in Figure 6. The pressure profile of the output respiratory chamber fluctuates after a given respiratory pressure profile.

It can be seen in Figure 7 that the pressure in the breathing chamber is essentially consistent with the reference pressure and that it follows this well.

Combined with the single-neuron PID control strategy based on online identification of the RBF neural network, the sampling time in the simulation is 0.001 s and the main parameters are shown in Table 2. The network structure of the RBFNNI is 3-6-1, and the network input is $x = [u(k)\ y(k)\ y(k-1)]$, $\eta = 0.2$, $\alpha = 0.05$. SNPID in taking $K = 6$, $\eta_1 = 0.2$, $\eta_2 = 0.001$, and $\eta_3 = 0.1$.

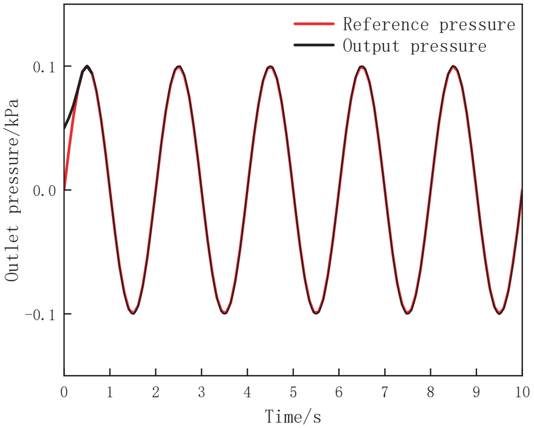

Figure 7. Respiratory chamber outlet pressure curve.

Table 2. Main parameters in the simulation.

Parameter (Unit)	Value
m (kg)	0.037
K (N/m)	700
d (m)	0.07
Θ (°)	11
R (Ω)	15
K_m (N/A)	23
K_E (V/(m/s))	23
V (m^3)	0.0005
κ	1.4
R_g ($m^2/(s^2 \cdot K)$)	260
Cd	0.8

At a lung ventilation rate of 44 L/min and inlet gas pressures of 40 kPa, 70 kPa, 150 kPa, and 300 kPa, the oxygen regulator outlet pressure curve is shown in Figure 8.

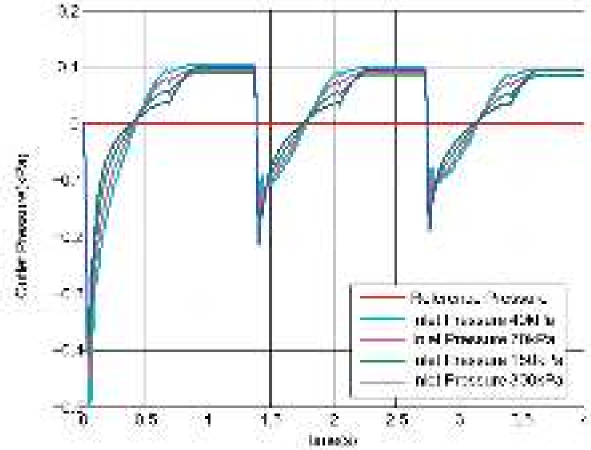

Figure 8. Outlet pressure curve of the regulator with 44L/min ventilation.

The reference pressure is used as both the regulation target value and the dividing line of respiratory resistance. An outlet pressure value above the reference pressure indicates expiratory resistance and an outlet pressure value below the reference pressure indicates inspiratory resistance. After entering the respiratory cycle, the desired outlet pressure should converge to the reference pressure. The peak pressure fluctuations in Figure 8 are between 0.1 kPa and −0.2 kPa. Near the positive and negative peak pressures, the outlet pressure is essentially the same; at the respiratory pressure transition, with an inlet pressure of 300 kPa, the regulator output pressure converges more closely to the reference pressure. Changes in the regulator′s inlet gas pressure have little effect on the output pressure, and the oxygen regulator is able to output a stable pressure. When the inlet gas pressure is higher, the regulator output pressure is closer to the reference pressure.

4. Experimental Analysis

The electronic oxygen regulator designed in this paper was tested under ground test chamber conditions using mechanical lungs for pressurization, with industrial oxygen as the gas source and a pressurized oxygen supply mask for simulation experiments.

4.1. Experimental Projects

The indirect oxygen regulator was compared with the designed direct oxygen regulator for the experiment.

1. Breathing resistance test

The flow characteristics of the oxygen regulator are mainly ensured by the pulmonary mechanism, and the suction resistance is the main characteristic of this mechanism. To verify the flow characteristics of the direct oxygen regulator, a breathing resistance experiment was designed. Respiratory resistance tests were performed on mechanical lungs with lung ventilation volumes of 20 L/min, 30 L/min, and 44 L/min at an inlet gas pressure setting of 150 kPa, and the pressure fluctuations in the mask chamber were measured. As shown in Figure 9, piece 4 should be connected to piece 5; piece 12 should be opened, the breathing gas resistance test mode should be selected; switch 1 should be turned on, the pressure reducer 2 should be turned on; the pressure reducer 2 should be turned on according to the pressure gauge 3 to establish the pressure of 150 kPa; the dummy lung 9 should open in order to establish a 20 L/min, a 30 L/min, and a 44 L/min lung gas exchange volume; the value of the pressure gauge 11 should be recorded.

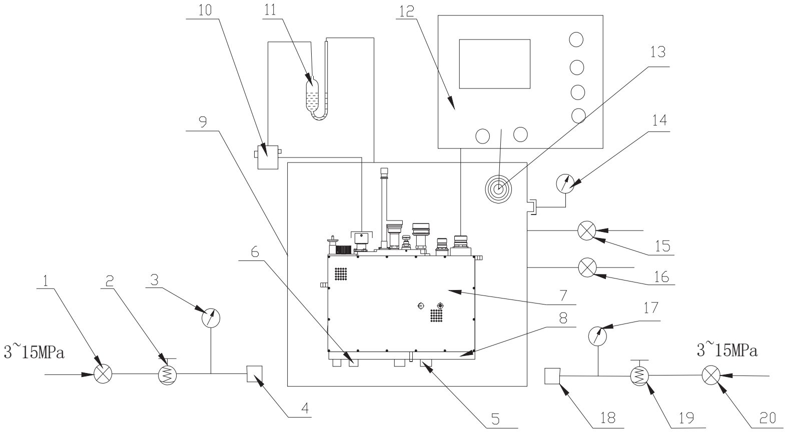

Figure 9. Experimental equipment connection diagram. 1: high pressure switch; 2: reducer adjustable; 3: pressure gauge; 4: connector; 5: anti-load inlet; 6: main oxygen inlet; 7: regulator; 8: tooling for simulating gas source distributor; 9: vacuum box; 10: mask model; 11: oil pressure gauge; 12: exciter; 13: height sensor; 14: altimeter; 15: vacuum switch; 16: deflation switch; 17: pressure gauge; 18: connector; 19: reducer adjustable; 20: high pressure switch.

2. Pressurization test

In high-altitude and overload situations, a certain amount of positive pressure needs to be established in the oxygen supply mask through active control based on the altitude and overload values to achieve pressurized respiratory protection and to improve the pilot's tolerance in high-altitude and overload environments. Calculate the target pressure according to the cockpit height and control and adjust the target pressure of the oxygen supply. The cockpit height is expressed by atmospheric pressure, and the relationship between the oxygen supply target pressure and the cockpit height is shown in Figure 10 [21]. When the cockpit altitude $PH < 16.5$ kPa, the target pressure value of the oxygen supply is shown in the equation.

$$PB = -0.756PH + 14.14 \tag{19}$$

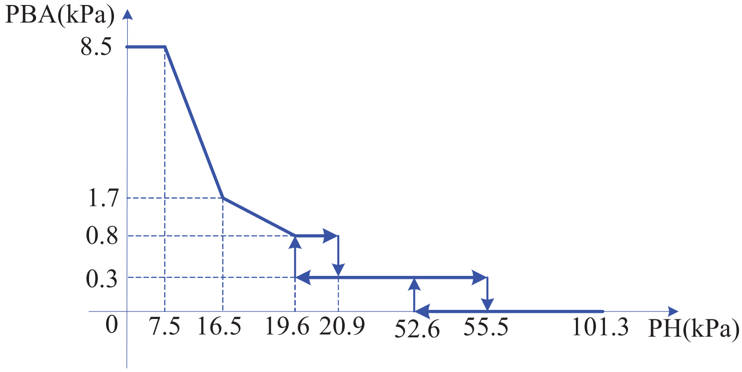

Figure 10. Relationship between cockpit height and oxygen supply target pressure curve.

When the oxygen supply regulator works in pressurized breathing regulation, it needs to pressurize the mask chamber at 2.0 kPa, 5.0 kPa, 7.5 kPa, and 8.5 kPa, as well as measure the pressure value of the mask chamber. It should connect according to Figure 10; connect piece 4 to piece 6, turn on switch 1, turn on pressure reducer 2 to establish a pressure of 2 kPa according to the pressure gauge 3; turn on switch 1, turn on pressure reducer 2 to establish a pressure of 0.2 MPa according to the pressure gauge 3; turn on switch 15 and slowly rise to 16 kPa according to the pressure gauge 14; record the residual pressure establishment height and residual pressure value.

4.2. Analysis of Experimental Results

The pressure profiles of the mask chamber at different lung fluxes at an inlet gas pressure of 150 kPa are shown in Figure 11. The positive peak of the waveform indicates the maximum expiratory pressure, and the negative peak indicates the inspiratory pressure [17]. At a lung ventilation volume of 20 L/min, the maximum inspiratory resistance was 0.25 kPa and the maximum expiratory resistance was 0.1 kPa. At a lung ventilation rate of 30 L/min, the maximum inspiratory resistance was 0.27 kPa and the maximum expiratory resistance was 0.13 kPa. At a lung ventilation rate of 44 L/min, the maximum inspiratory resistance was 0.4 kPa and the maximum expiratory resistance was 0.25 kPa. Comparing the appeal data with the ideal boundary values of respiratory resistance in Table 3, the peak resistance was all within the ideal boundary and much smaller than the boundary of respiratory resistance [22].

Table 3. Ideal boundary of respiratory resistance.

Ventilation Volume (L/min)	Expiratory Resistance (kPa)	Inspiratory Resistance (kPa)
20	≤0.29	≤0.49
30	≤0.49	≤0.59
44	≤1.08	≤0.88

The experimental data on the respiratory resistance of the indirect electronic oxygen supply anti-charge regulator are shown in Table 4. In comparison with the indirect oxygen regulator, it can be seen that the output of the direct oxygen regulator has less breathing resistance, which greatly enhances the comfort of the pilot when in use.

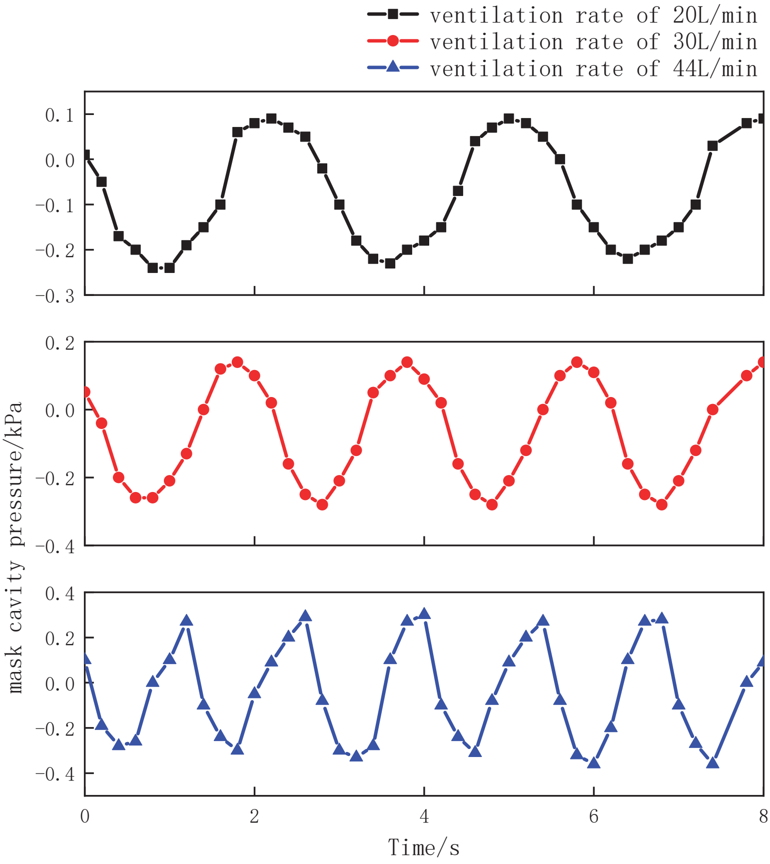

Figure 11. Mask pressure curves under different lung fluxes.

Table 4. Suction resistance of indirect oxygen regulator.

Lung Ventilation (L/min)	Peak Inspiratory Resistance (kPa)
20	0.49
30	0.59
44	0.88

When the oxygen supply regulator was used for pressurized breathing, the target pressure values of the pressurization test were 2.0 kPa, 5.0 kPa, 7.5 kPa, and 8.5 kPa, respectively. The pressure curves of the mask cavity are shown in Figure 12a,b.

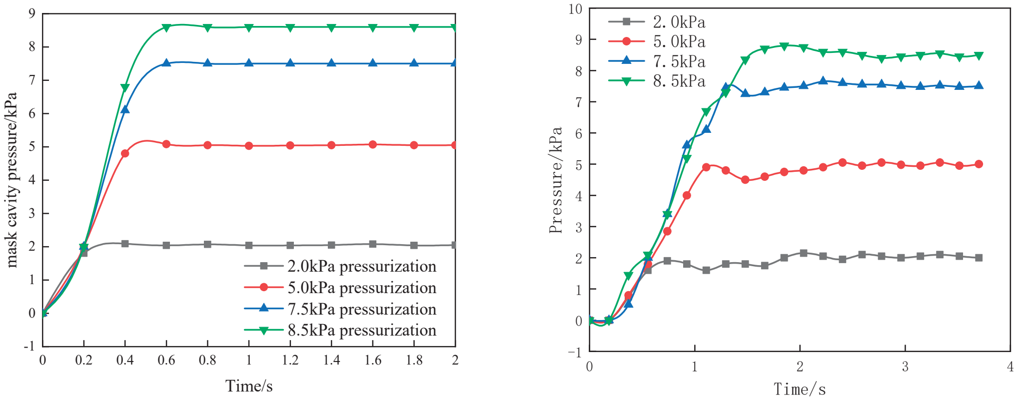

(**a**)

(**b**)

Figure 12. (**a**) Pressure curve of the mask chamber during pressurization; (**b**) indirect oxygen regulator mask chamber pressure.

During pressurization at 2.0 kPa, the pressure values can reached the target values at 0.4 s. When the pressurization value was at 8.5 kPa, the pressure value reached the stable target value at 0.6 s. The pressurization test process of the electronic oxygen regulator builds pressure quickly at different pressure targets. The speed of pressure building was within 0.8 s for all the different pressure tests. The smaller the target pressure of the pressurization test, the faster the pressure-building speed. For example, during the pressurization process at 2.0 kPa, the pressure value can reach the target value in 0.4 s. After the indirect oxygen regulator reaches the regulated pressure, there is a significant pressure fluctuation. However, indirect oxygen regulators have a longer pressure build-up time and exhibit significant pressure fluctuations.

The direct oxygen regulator solves the problem of pressure fluctuation of the indirect oxygen regulator, and the single-neuron PID control strategy based on online recognition of the RBF neural network improves the system performance, resulting in less breathing resistance and faster pressure building during pressurized breathing with the direct oxygen regulator.

5. Conclusions

In this paper, a direct oxygen regulator is designed for the problems of jittering output pressure and the difficult adjustment of structural parameters of an indirect oxygen regulator, and a stepper motor was used to drive the lung type valve, replacing the diaphragm lever-type structure of traditional indirect oxygen regulator.

A direct oxygen regulator with a single-neuron PID control strategy based on online recognition of the RBF neural network is designed by combining the current advanced intelligent control theory. The simulation results show that the control strategy makes the oxygen regulator have better control accuracy and system response speed.

The control performance of the oxygen regulator was verified experimentally. This control method reduces respiratory resistance by 50% and improves respiratory comfort compared to indirect oxygen regulators at different lung fluxes. In pressurized breathing, the output pressure fluctuation does not exceed 0.1kPa and the pressure build-up time is within 0.6 s, both of which show better performance than the indirect oxygenator regulator.

Author Contributions: Conceptualization, D.J. and Y.L.; methodology, D.J.; software, Y.L. and H.Y.; validation, Y.L., X.F. and B.Q.; investigation, H.L.; resources, D.J.; writing—original draft preparation, Y.L.; writing—review and editing, D.J.; All authors have read and agreed to the published version of the manuscript.

Funding: This research was funded by the Anhui Provincial University Natural Science Research Project (K2210033) and the Provincial Natural Science Research Projects of Anhui Provincial Universities (KJ2021A0635).

Institutional Review Board Statement: Not applicable.

Informed Consent Statement: Not applicable.

Data Availability Statement: The data is available from the corresponding author upon reasonable request.

Conflicts of Interest: The authors declare no conflict of interest.

References

1. Fan, Y.; Sun, Q.; Dong, F.; Chen, Q. An adaptive oxygen regulator control system based on particle swarm optimization and back propagation neural network. *Control Theory Appl.* **2020**, *3*, 687–695.
2. Siska, W.D., Jr.; Robert, C. Electromechanical Oxygen Valve and Regulator. U.S. Patent No. 7,677,529, 16 March 2021.
3. Yan, S.H.I.; Yixuan, W.A.N.G.; Maolin, C.A.I.; Zhang, B.; Jian, Z.H.U. An aviation oxygen supply system based on a mechanical ventilation model. *Chin. J. Aeronaut.* **2018**, *31*, 197–204.
4. Jiang, D.; Bu, X.; Lin, G.; Sun, B.; Huang, J.; Fang, L.; Zhao, H. Control design and experimental verification of three-bed airborne oxygen generation system. *J. Beijing Univ. Aeronaut. Astronaut.* **2018**, *44*, 6.
5. Li, X.; Lin, G.; Zeng, Y.; Wu, F. Design of electronic oxygen regulator PID control system based on LabVIEW. *Comput. Meas. Control* **2016**, *3*, 80–83.
6. Jiang, Y.; Sun, Q.; Tan, P.; Chen, Z. Modeling and Simulation of an Electronic Oxygen Regulator Based on All-Coefficient Adaptive Control. *J. Dyn. Syst. Meas. Control* **2016**, *138*, 081010. [CrossRef]
7. Yuxin, J.; Qinglin, S.; Zengqiang, C.; Sanpeng, D. Modeling and simulation of an electronic oxygen regulator based on generalized predictive control algorithm. In Proceedings of the 2015 34th Chinese Control Conference (CCC), Hangzhou, China, 28–30July 2015; IEEE: Piscataway, NJ, USA, 2015; pp. 4067–4072.
8. Jiang, D.; Jin, H.; Sun, B.; Lin, G.; Bu, X.; Zhao, H. Design and experiment research of pressure control cavity on electronic oxygen regulator. In Proceedings of the 2017 8th International Conference on Mechanical and Aerospace Engineering (ICMAE), Prague, Czech Republic, 22–25 July 2017; IEEE: Piscataway, NJ, USA, 2017; pp. 656–660.
9. Wan, Y.; Zhao, J.; Zeng, Y. Design and calculation of structural parameters of aviation oxygen regulator. *J. Beijing Univ. Aeronaut. Astronaut.* **2011**, *37*, 351–354.
10. Zou, N.; Zhang, B.; Wang, D.; Xiao, H.; Liu, X.; Zang, B. Performance parameter adjustment analysis and experimental verification of YTQ-7 oxygen regulator. *Aerosp. Sci. Technol.* **2011**, *5*, 45–48.
11. Yu, X.; Sun, B.; Lin, G.; Wang, H. The application of ATmega128 single chip microcomputer in electronic oxygen regulator. *Microcomput. Appl.* **2009**, *12*, 50–56.
12. Sun, C.; Cai, Y.; Long, H. Research on stepping motor fuzzy control technology application in the aircraft electronic oxygen regulator. *Meas. Control Technol.* **2013**, *32*, 78–81.
13. Jiang, Y.; Sun, Q.; Zhang, X.; Chen, Z. Pressure regulation for oxygen mask based on active disturbance rejection control. *IEEE Trans. Ind. Electron.* **2017**, *64*, 6402–6411. [CrossRef]
14. Morris-ward, M. Modification of Oxygen Regulator Functionality Tester for X-59 Regulator Testing. In *Student Poster Day*; NTRS—NASA Technical Reports Server: Washington, DC, USA, 2020.
15. Pan, R.; Lin, G.; Shi, Z.; Zeng, Y.; Yang, X. Analysis and control optimization of positive pressure fluctuation in electromechanical oxygen regulator. *Chin. J. Aeronaut.* **2021**, *34*, 205–213. [CrossRef]
16. Saha, B.K.; Songjing, L.I.; Xinbei, L.V. Analysis of pressure characteristics under laminar and turbulent flow states inside the pilot stage of a deflection flapper servo-valve: Mathematical modeling with CFD study and experimental validation. *Chin. J. Aeronaut.* **2020**, *33*, 1107–1118. [CrossRef]
17. Pan, R.; Lin, G.; Shi, Z.; Zeng, Y.; Yang, X. The application of disturbance-observer-based control in breath pressure control of aviation electronic oxygen regulator. *Energies* **2021**, *14*, 5189. [CrossRef]
18. Yinhu, L.; Shaoming, L. Single neuron PID control based on dynamic RBF neural network on-line identification. *J. Syst. Simul.* **2006**, *18* (Suppl. 2), 804–807.
19. Zhang, S.T.; Yang, F.; Hao, Q. Research and simulation of single neuron PID controller. *Mech. Eng. Autom.* **2009**, *39*, 69–70.
20. Wang, N.; Tu, J.; Chen, J. Intelligent control using a single adaptive neuron. In Proceedings of the Third Congress of Chinese Association of Automation, Beijing, China; 1991; pp. 173–177.

21. Liu, X.; Xiao, H.; Shi, Q. Evaluation of hypobaric chamber physiological test of YX-11 oxygen supply system. *Chin. J. Aerosp. Med.* **2007**, *18*, 20–25.
22. Xiao, H. Review and Prospect of Physiological Research on Aviation Oxygen Supply Equipment. In Proceedings of the Academic Conference on Environmental Control and Ergonomics of Chinese Aviation Society, Beijing, China; 2000.

energies

Article

Research on the Modulation and Control Strategy for a Novel Single-Phase Current Source Inverter

Yi Zhang [1,*], **Tao Yang** [2,3] **and Yiru Miao** [3]

[1] School of Vehicle Engineering, Chongqing University of Technology, Chongqing 400054, China
[2] School of Rail Transit and Aviation Service, Chongqing Industry Polytechnic College, Chongqing 401120, China; justmuch@163.com
[3] State Key Laboratory of Power Transmission Equipment & System Security and New Technology, Chongqing University, Chongqing 400044, China; miaoyiru@cqu.edu.cn
* Correspondence: zagyi81@cqut.edu.cn

Abstract: Compared to the voltage source inverter, the current source inverter (CSI) can boost voltage and improve filtering performance. However, the DC side of CSI is not a real current source, and the DC input current comprises a DC power supply and an inductor. In the switching process, the DC-link inductor is charged or discharged and is in an uncontrollable state. This paper proposes a novel CSI topology containing five switching tubes and a modulation strategy based on the hysteresis control strategy of the DC-link current. Due to the conduction and switching loss being positive to the DC-link current, the calculation method for the least reference value of the DC-link current is derived to meet power requirements. By constructing a virtual axis, we then present the control strategy of the output voltage in a two-phase rotating reference frame. Finally, we carry out the simulation and experiment are to validate the proposed topology, modulation, and control strategy.

Keywords: current source inverter; DC-link current; modulation; control strategy

Citation: Zhang, Y.; Yang, T.; Miao, Y. Research on the Modulation and Control Strategy for a Novel Single-Phase Current Source Inverter. *Energies* **2023**, *16*, 6729. https://doi.org/10.3390/en16186729

Academic Editors: Kan Liu and Wei Hu

Received: 3 September 2023
Revised: 17 September 2023
Accepted: 19 September 2023
Published: 20 September 2023

1. Introduction

Inverters can be categorized as voltage source inverters (VSI) [1] and current source inverters (CSI) [2] according to the characteristics of input power supplies. Some unique advantages of CSIs have been discovered [3], such as their boost capacity, inherent short-circuit protection capacity, and AC filtering structure. CSI, therefore, has potential applications [4] in the solar photovoltaic industry, wind energy power generation, motor drive systems, and HVDC transmission systems.

In recent years, various control and modulation strategies for CSI have been proposed [5], such as decoupling methods, low common voltage modulation, and digital vector control strategy. However, the DC-link current is considered a constant value in the above studies in which the charging or discharging process of the DC-link inductor has been ignored, leading to the DC-link current being discontinuous or continuously increasing.

Unlike VSI, the DC-link current of CSI is formed by the DC input voltage DC-link inductor, and constant DC-link current output is a necessary condition for high performance operation of CSI [6]. In [7–11], several novel CSI topologies are proposed to achieve control of the DC-link current. In [7], a three-phase current source rectifier (CSR) is introduced to adjust the DC-link current, but this topology is very complex and only suitable for AC-DC-AC applications. A buck converter is added to the DC side to regulate the DC-link current in [8]. In [6], the buck converter is replaced with a bi-directional converter that can control the current, and the buck operation can also be realized. However, the switching and conduction losses increase as the converter is introduced. In [9], a buck-boost CSI is proposed, which has the advantages of a simple structure and large voltage output range, but the control strategy is difficult to implement. The current-fed quasi-Z-source inverter is proposed in [10]. However, with the addition of many passive components, both efficiency and power density are greatly reduced.

In [11], an additional switching tube and diode are connected in parallel with the DC-side inductor of the three-phase CSI. The DC-side inductor can self-continuate when the switch is turned on. During the zero vector period, the continuous current mode is used to replace the traditional magnetizing mode, which can prevent the increase of the DC-link current. On this basis, a novel single-phase five-switch CSI topology is proposed in this paper. The modulation and control strategies are studied to obtain the constant DC-link current and high-quality AC voltage output. Finally, the simulation and experimental verification are carried out.

2. Topology and Operating Modes of the Proposed Single-Phase CSI

2.1. Analysis of the Proposed Single-Phase CSI's Operating Modes

The topology of the proposed single-phase CSI is shown in Figure 1. The DC side is composed of a DC voltage source and DC-link inductance L_{dc}. The inverter part is composed of switching tubes (S_1, S_2, S_3, S_4) and diodes (D_1, D_2, D_3, D_4). The AC side contains the filter capacitor C and the resistive load R. The switching tube S_0 and diode D_0 are parallel with L_{dc}.

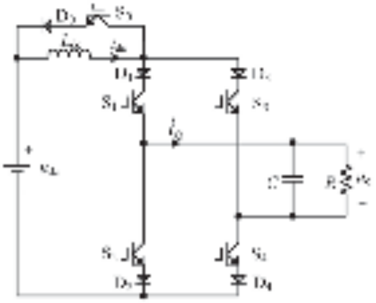

Figure 1. The topology of the proposed single-phase CSI.

There are four operating modes of the proposed single-phase CSI. The corresponding switching states are shown in Table 1.

Table 1. The operating modes, switching state, and switching function.

Operating Modes	Switching State	Switching Function p and q
magnetizing mode	S_1 and S_2 ON, S_0, S_3, and S_4 OFF	$p = 0$, $q = 1$
energy-supplying mode I	S_1 and S_4 ON, S_0, S_2, and S_3 OFF	$p = 1$, $q = 0$
energy-supplying mode II	S_2 and S_3 ON, S_0, S_1, and S_4 OFF	$p = -1$, $q = 0$
freewheeling model	S_0 ON, S_1, S_2, S_3, and S_4 OFF	$p = 0$, $q = 0$

(1) Magnetizing mode: S_1 and S_2 are turned on, and the equivalent circuit under magnetizing mode is shown in Figure 2a. At this moment, i_o is equal to 0 A, the u_{dc} is charging to L_{dc}, and C provides energy for the load separately.

(2) Energy-supplying mode I: S_1 and S_4 are turned on, and the equivalent circuit under this operating mode is shown in Figure 2b. At this moment, i_o is equal to i_{dc}, and the u_{dc} and L_{dc} provide energy to the AC load together.

(3) Energy-supplying mode II: S_2 and S_3 are turned on, and the equivalent circuit under this operating mode is shown in Figure 2c. Different from energy-supplying mode I, the polarity of the output current is negative; i_o is equal to $-i_{dc}$.

(4) Freewheeling model: Only S_0 is turned on, and the equivalent circuit under the freewheeling model is shown in Figure 2d. The i_{dc} freewheels through S_0, and C provides energy for the load separately.

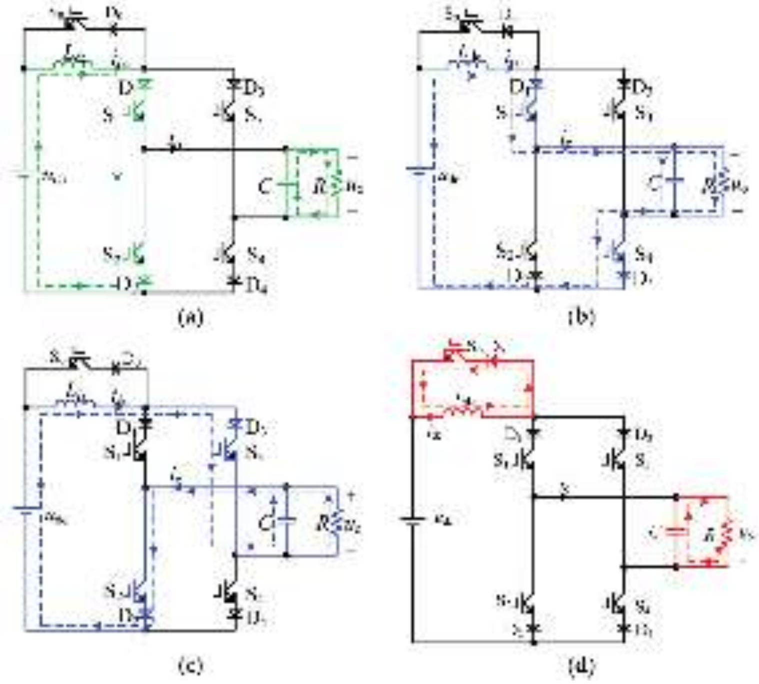

Figure 2. The operating modes of the proposed single-phase CSI: (**a**) magnetizing mode; (**b**) energy-supplying mode I; (**c**) energy-supplying mode II; (**d**) freewheeling model.

Two switching functions (p and q) are defined and shown in Table 1. The p is used to indicate whether the CSI is operating in energy-supplying mode, and the math relationship between i_{dc} and i_{o} can be expressed as

$$i_{\mathrm{o}} = i_{\mathrm{dc}} p \tag{1}$$

The state equation of u_{o} follows:

$$C\frac{\mathrm{d}u_{\mathrm{o}}}{\mathrm{d}t} = p i_{\mathrm{dc}} - \frac{u_{\mathrm{o}}}{R} \tag{2}$$

q is used to indicate whether the CSI is operating in magnetizing mode. The state equation of i_{o} follows:

$$L_{\mathrm{dc}}\frac{\mathrm{d}i_{\mathrm{dc}}}{\mathrm{d}t} = q u_{\mathrm{dc}} - p u_{\mathrm{o}} \tag{3}$$

Since the conduction current of all switching tubes is i_{dc}, the current stresses of all switching tubes are equal to the DC-link current. The voltage stresses can be derived according to Figure 2, and the voltage stresses of all switching tubes under different operating modes are summarized in Table 2.

Table 2. Voltage stresses of all switching tubes under different operating modes.

Operating Mode	**Withstand Voltage S_0**	**Withstand Voltage S_1**	**Withstand Voltage S_2**	**Withstand Voltage S_3**	**Withstand Voltage S_4**
Magnetizing mode	u_{dc}	0	0	$-u_{\mathrm{o}}$	u_{o}
Energy-supplying mode	$u_{\mathrm{dc}} - u_{\mathrm{o}}$	0	$-u_{\mathrm{o}}$	$-u_{\mathrm{o}}$	0
Freewheeling model	0	u_{o}	$-u_{\mathrm{dc}} - u_{\mathrm{o}}$	0	$-u_{\mathrm{dc}}$

2.2. Comparison of Different CSI Topologies

The recent literature presents many CSI structures comprising distinct tradeoffs among different topologies, as shown in Figure 3. According to [12,13], a cost function (*CF*) is established in (4) to carry out a fair comparison of different CSI topologies:

$$CF = N_V(N_{\text{US}} + 2N_{\text{BS}} + N_D + N_C + N_{\text{drv}} + N_T)/N_l \tag{4}$$

where N_V is the number of DC voltages, N_{US} is the number of unidirectional switches, N_{BS} is the number of bidirectional switches, N_D is the number of diodes, N_C is the number of capacitors, N_{drv} is the number of individual drivers, N_T is the number of transformers, and N_l is the number of output current levels.

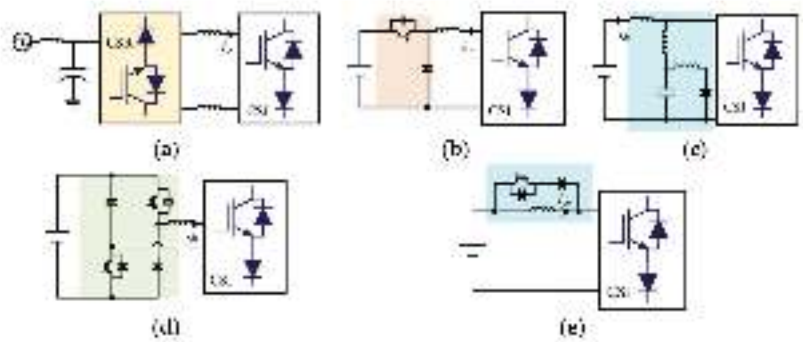

Figure 3. The topologies of different CSI: (**a**) current source rectifier; (**b**) buck converter; (**c**) quasi-Z source network; (**d**) bidirectional DC chopper; (**e**) proposed single-phase CSI.

The comparison result is presented in Table 3. Although the quasi-Z source network receives the lowest *CF*, it contains numerous passive components, and its control system is too complex. The proposed single-phase CSI and the buck converter have the same CF. However, the buck converter contains more switches than the proposed single-phase CSI. The bidirectional DC chopper's *CF* is slightly higher than the proposed one because of the additional two diodes and switching tubes. The current source rectifier rates the worst *CF* because it includes too many components.

Table 3. Comparison of different CSI topologies.

Parameter	**Current Source Rectifier**	**Buck Converter**	**Quasi-Z Source Network**	**Bidirectional DC Chopper**	**Proposed Single-Phase CSI**
N_V	1	1	1	1	1
N_{US}	0	0	0	0	0
N_{BS}	8	5	4	6	5
N_D	8	5	5	6	5
N_C	2	1	2	1	1
N_{drv}	8	5	4	6	5
N_T	0	0	1	0	0
N_l	3	3	3	3	3
CF	11.33	7	6.67	8.33	7
Input H Bridge	Yes	No	No	Yes	No
Modulation	PWM	PWM	PWM	PWM	PWM

3. Modulation Strategy Based on DC-Link Current Control

Unlike VSI, switching signals cannot be directly generated by comparing modulated signals with carrier waves [14]. In [15], a logic conversion circuit is adopted to convert the switching signals, which will delay them. In this section, a novel modulation strategy is presented which can be implemented by the DSP without a logic conversion circuit. Three logic signals (p_1, p_2, and p_3) are set, where p_1 represents the comparison result between the modulation wave and carrier wave, as shown in Figure 4, and where d is the duty cycle and is defined as

$$d = \frac{|i_\mathrm{o}|}{i_\mathrm{dc}} \tag{5}$$

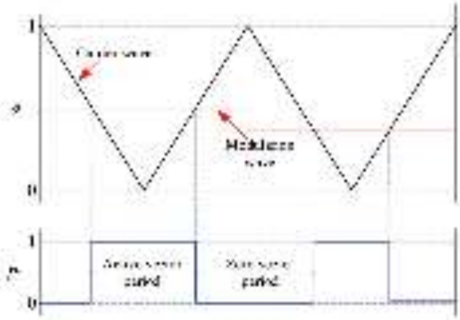

Figure 4. The diagram of p_1, carrier wave, and modulation wave.

p_1 = 1 represents the active vector period, and the CSI operates at energy-supplying mode I or II, which is determined by the polarity of i_o. p_2 represents the polarity of i_o. If $i_\mathrm{o} > 0$, p_2 = 1; otherwise, p_2 = 0.

p_1 = 0 represents the zero vector period, and the CSI operates on either the magnetizing mode or freewheeling model, which is determined by i_dc. If i_dc > the reference value i^*_dc, the freewheeling model will be selected to prevent i_dc from increasing in the zero vector period. Otherwise, the magnetizing mode will be implemented to charge L_dc in the zero vector period. p_3 is defined to represent the math relationship between i_dc and i^*_dc. If $i_\mathrm{dc} > i^*_\mathrm{dc}$, p_3 = 1; else, p_3 = 0. The changing process of i_dc and p_3 is described in Figure 5. i_dc can be adjusted according to p_3. This approach belongs to a hysteresis control method [16].

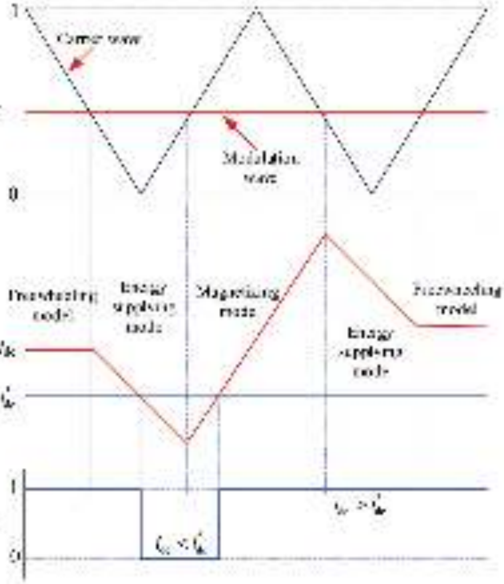

Figure 5. The changing process of i_dc and p_3.

Based on the above settings and analysis, the production logic of the five switching signals is shown in Figure 6. The specific logic expression for each switching is described as follows:

$$\begin{cases} p_{S1} = \overline{p}_1 \& \overline{p}_3 \big| p_2 \\ p_{S2} = \overline{p}_1 \& \overline{p}_3 \big| \overline{p}_2 \\ p_{S3} = p_1 \& \overline{p}_2 \\ p_{S4} = p_1 \& p_2 \\ p_{S0} = \overline{p}_2 \& p_3 \end{cases} \tag{6}$$

where p_{S1}, p_{S2}, p_{S3}, p_{S4}, and p_{S5} represent the driving logic of switch S_1, S_2, S_3, S_4, and S_5, respectively.

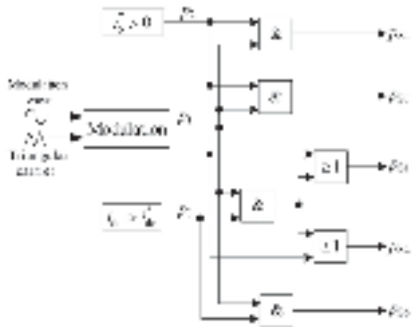

Figure 6. Logical conversion for the proposed single-phase CSI.

4. Calculation for the Optimal Reference of DC-Link Current

In Section 3, a DC-link current hysteresis control is introduced into the modulation scheme. However, the reference of the DC-link current must be determined for the following reasons [17]. If i_{dc}^* is set too small, the DC-link current is unable to provide sufficient power to the AC load. If i_{dc}^* is set too great, the conduction loss, switching loss, and harmonic distortion will increase. Thus, the DC-link current should be reduced to satisfy the current requirements. The calculation method for the optimal reference of the DC-link current is derived in this section.

It is assumed that u_o remains in a constant state in a switching period. Under energy-supplying mode, the reduction Δi_{dc_down} of i_{dc} can be expressed as follows:

$$\Delta i_{dc\_down} = \frac{T_s}{L_{dc}} d(t)[u_o(t) - u_{dc}] \tag{7}$$

The increment of Δi_{dc_up} under magnetizing mode can be expressed as

$$\Delta i_{dc\_up} = \frac{u_{dc} T_s}{L_{dc}} [1 - d(t)] \tag{8}$$

According to (7) and (8), the total reduction Δi_{dc} of i_{dc} in a switching period can be expressed as

$$\Delta i_{dc} = \Delta i_{dc\_down} - \Delta i_{dc\_up} = \frac{T_s}{L_{dc}} [u_o(t) d(t) - u_{dc}] \tag{9}$$

By substituting (5) with (9), Δi_{dc} can be rewritten as

$$\Delta i_{dc} = \frac{T_s}{L_{dc}} \left[\frac{u_o(t) i_o(t)}{i_{dc}(t)} - u_{dc} \right] \tag{10}$$

Ignoring the harmonic component and initial phase, u_o is expressed as

$$u_\mathrm{o}(t) = U \sin \omega t \tag{11}$$

where U represents the fundamental amplitude of u_o, and ω represents the fundamental frequency. i_o is expressed as

$$i_\mathrm{o}(t) = I \sin(\omega t + \theta) \tag{12}$$

where I represents the amplitude of i_o, and θ represents the initial phase of i_o. Due to the load of the inverter consisting of the resistance and the capacitance paralleling with the load, the following relations are satisfied:

$$\begin{cases} I = U\sqrt{1 + (\omega CR)^2}/R \\ \theta = \arctan(\omega CR) \end{cases} \tag{13}$$

Substituting (11) and (12) with (10), the following can be obtained:

$$\Delta i_\mathrm{dc} = \frac{T_\mathrm{s}}{L}\left[\frac{UI\sin(\omega t)\sin(\omega t + \theta)}{i_\mathrm{dc}(t)} - u_\mathrm{dc}\right] \tag{14}$$

Formula (14) is simplified as follows:

$$\Delta i_\mathrm{dc} = \frac{T_\mathrm{s}}{2L}\left\{\frac{UI[\cos\theta - \cos(2\omega t + \theta)]}{i_\mathrm{dc}(t)} - 2u_\mathrm{dc}\right\} \tag{15}$$

The maximum reduction Δi_dcmax of i_dc in a switching period is shown as follows:

$$\Delta i_{dc\mathrm{max}} = \frac{T_\mathrm{s}}{2L}\left[\frac{UI(\cos\theta + 1)}{i_\mathrm{dc}(t)} - 2u_\mathrm{dc}\right] \tag{16}$$

If $\Delta i_\mathrm{dcmax} < 0$, i_dc can continue increasing in any switching period, which consists of magnetizing mode and energy-supplying mode. Thus, i_dc needs to be satisfied as follows:

$$i_\mathrm{dc} > \frac{UI(\cos\theta + 1)}{2u_\mathrm{dc}} \tag{17}$$

Substituting (13) with (17), and replacing i_dc with i^*_dc, Formula (17) can be rewritten as follows:

$$i^*_\mathrm{dc} > \frac{U^2\left[1 + \sqrt{1 + (\omega CR)^2}\right]}{2u_\mathrm{dc}R} \tag{18}$$

The theoretical waveforms in a fundamental period, including i_dc, u_o, and switching signals are presented in Figure 7. Based on the operation mode, switching signals, DC-link current optimal reference, and control strategy, the theoretical waveform is divided into eight stages:

(1) Stage 1 ($t_0 - t_1$): $0 < u_\mathrm{o} < u_\mathrm{dc}$, L_dc is charged in energy-supplying mode I; S_1 remains on-state; S_0 is turned on in the zero vector period to prevent i_dc from continuously increasing.

(2) Stage 2 ($t_1 - t_2$): $-u_\mathrm{dc} < u_\mathrm{o} < 0$, L_dc is charged in energy-supplying mode II; S_3 remains on-state; S_0 is turned on in the zero vector period to prevent i_dc from continuously increasing.

(3) Stage 3 ($t_2 - t_3$): $u_\mathrm{o} < -u_\mathrm{dc}$; L_dc discharges in energy-supplying mode II due to i_dc being still greater than i^*_dc; S0 is also turned on in the zero vector period; i_dc begins to decrease.

(4) Stage 4 ($t_3 - t_4$): $u_\mathrm{o} < -u_\mathrm{dc}$ and $i_\mathrm{dc} < i^*_\mathrm{dc}$; to prevent i_dc further decrease, S4 is turned on in the zero vector period, since i^*_dc is the optimal reference of the DC-link current; i_dc will be clamped near i^*_dc.

(5) Stage 5 ($t_4 - t_5$), Stage 6 ($t_5 - t_6$), Stage 7 ($t_6 - t_7$), and Stage 8 ($t_7 - t_8$) are similar to Stage 1 ($t_0 - t_1$), Stage 2 ($t_1 - t_2$), Stage 3 ($t_2 - t_3$), and Stage 4 ($t_3 - t_4$), respectively.

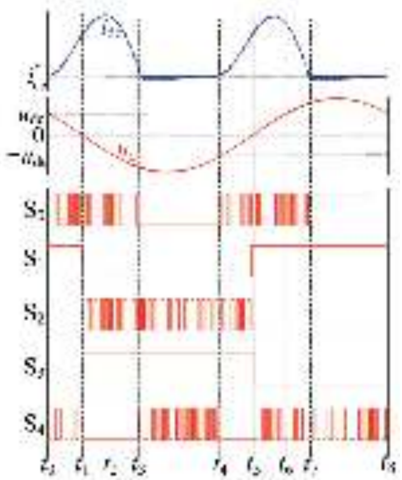

Figure 7. The theoretical waveforms in a fundamental period.

5. Control Strategy of the Output Voltage

Since the PI controller is not suitable for AC models, the math model of the singe phase CSI is established in d-q frame. The fundamental component of u_{o} is represented as follows:

$$u_{\text{o}}(t) = u_{\text{od}} \sin(\omega t) + u_{\text{oq}} \cos(\omega t) \tag{19}$$

where u_{od} = U, and u_{oq} = 0. The quadrature virtual component of u_{o} is introduced, which is shown as follows:

$$u'_{\text{o}}(t) = -U_{\text{o}} \sin(\omega t - \frac{\pi}{2}) \tag{20}$$

The d-q frame components u_{od} and u_{oq} can be obtained as follows:

$$\begin{cases} u_{\text{od}}(t) = u_{\text{o}}(t)\sin(\omega t) + u'_{\text{o}}(t)\cos(\omega t) \\ u_{\text{oq}}(t) = u_{\text{o}}(t)\cos(\omega t) - u'_{\text{o}}(t)\sin(\omega t) \end{cases} \tag{21}$$

The same representation for i_{o} is shown as follows:

$$i_{\text{o}}(t) = i_{\text{od}} \sin(\omega t) + i_{\text{oq}} \cos(\omega t) \tag{22}$$

where i_{od} and i_{oq} are the DC component. Substituting Equations (21) and (22) with (2), it yields the following:

$$\begin{cases} C\frac{du_{\text{od}}}{dt} + \frac{u_{\text{od}}}{R} = \omega C u_{\text{oq}} + i_{\text{od}} \\ C\frac{du_{\text{oq}}}{dt} + \frac{u_{\text{oq}}}{R} = -\omega C u_{\text{od}} + i_{\text{oq}} \end{cases} \tag{23}$$

u_{od} and u_{oq} are adjusted by the PI controller, and feedback decoupling is adopted to cancel out the coupling terms $\omega C u_{\text{od}}$ and $\omega C u_{\text{oq}}$. The control strategy of u_{o} is shown in Figure 8, where u^*_{od} and u^*_{oq} are the reference of u_{od} and u_{oq}, and i^*_{od} and i^*_{oq} are the reference of i_{od} and i_{oq}, respectively. i^*_{od} and i^*_{oq} are expressed as follows:

$$\begin{cases} i^*_{\text{od}} = \frac{k_{\text{p}}s + k_{\text{i}}}{s}(u^*_{\text{od}} - u_{\text{od}}) - \omega C u_{\text{oq}} \\ i^*_{\text{oq}} = \frac{k_{\text{p}}s + k_{\text{i}}}{s}(u^*_{\text{oq}} - u_{\text{oq}}) + \omega C u_{\text{od}} \end{cases} \tag{24}$$

where k_{p} and k_{i} are the proportional coefficient and integral coefficient, respectively.

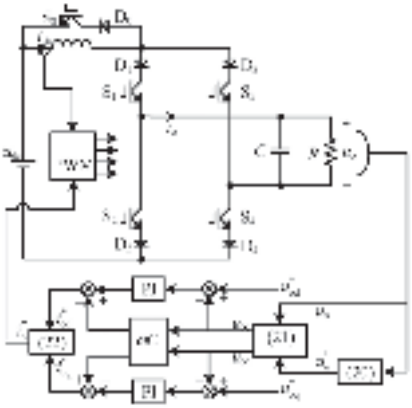

Figure 8. Control strategy diagram of output voltage.

Considering the digital delay, the open-loop transfer function $G_{\mathrm{open}}(s)$ can be derived as follows:

$$G_{\mathrm{open}}(s) = \frac{k_{\mathrm{p}}s + k_{\mathrm{i}}}{s(1 + T_{\mathrm{s}}s)(1 + RCs)} \tag{25}$$

where T_{s} is the switching period and is equal to 100 µs. Zero point is set to offset the pole, and the cutoff frequency is set at 1 kHz. k_{p} and k_{i} are set as $2000\pi RC$ and 2000π. The Bode plot of $G_{\mathrm{open}}(s)$ is shown in Figure 9a, and the Bode plot of the closed-loop transfer function $G_{\mathrm{close}}(s)$ is shown in Figure 9b. Good track performance and fast dynamic response can thus be achieved.

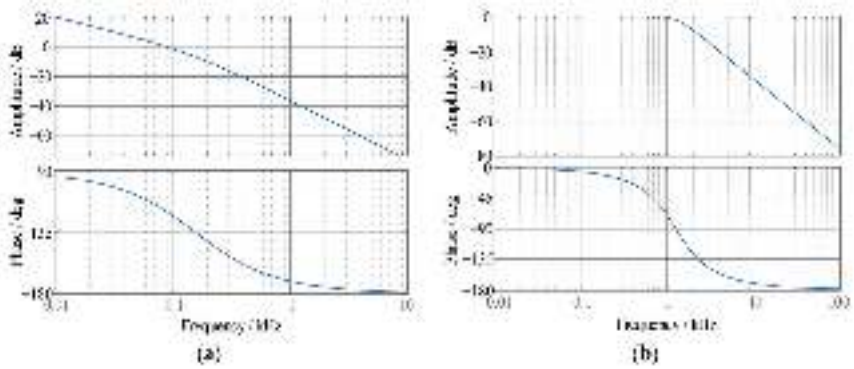

Figure 9. The Bode-plots of the output voltage control: (**a**) $G_{\mathrm{open}}(s)$, (**b**) $G_{\mathrm{close}}(s)$.

6. Experimental Results

An experimental prototype of a single-phase CSI is established and shown in Figure 10. The corresponding soft simulation is presented in the Supplementary Material. The algorithm of modulation and control are implemented by TMS320F28335, and the IGBT and diode are PM400HSA120 and RM300HA-24F, respectively. u_{dc} is supplied by a DC power supply. The parameters of the passive components are consistent with Table 4.

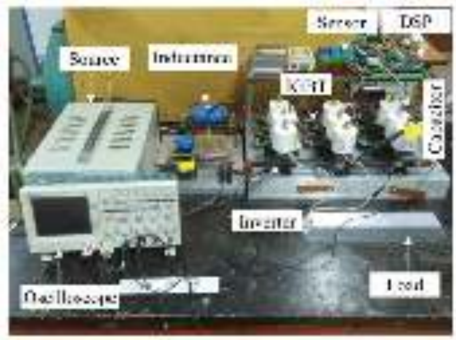

Figure 10. Experimental prototype of proposed single-phase CSI.

Table 4. Parameters of experiment.

Name	Value
DC input voltage (V)	25
AC output voltage (V)	30~150
Load power (W)	$\leq 10^3$
Output frequency (Hz)	$\leq$500 Hz
Switching frequency (Hz)	10 k
Sampling frequency (Hz)	10 k
L_{dc} (mH)	4
C (μF)	265
R (Ω)	25

6.1. Experimental Results of Steady-State

The amplitude and frequency of the reference of u_o are 50 V and 50 Hz. i^*_{dc} is set to 13.5 A. The experimental waveforms of i_{dc} and u_o are shown in Figure 11a, where the amplitude and frequency of u_o are consistent with the reference, and i_{dc} is maintained in the range of 13.5 A to 15 A. Figure 11b shows that u_o's THD is only 0.61%, and its harmonics are limited.

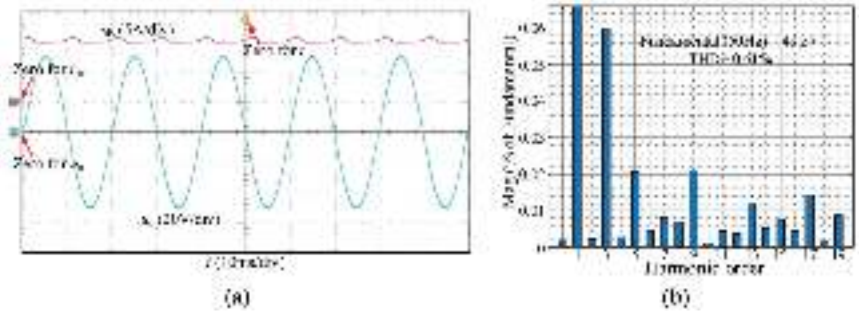

(a) (b)

Figure 11. Experimental results under i^*_{dc} = 13.5 A: (**a**) experimental waveforms of i_{dc} and u_o; (**b**) FFT results.

In order to verify that i^*_{dc} = 13.5 A is the optimal reference of the DC-link current, a steady-state experiment is carried out in Figure 12, where i^*_{dc} is set to 11.5 A. A large fluctuation occurs in i_{dc}, which cannot maintain above 11.5 A. In some switching periods, i_{dc} cannot meet the requirement of current for the AC load. Therefore, significant low-order harmonic distortion occurs in u_o, whose THD is 23.88%, and fundamental amplitude is 38.5 V, lower than the reference 50 V.

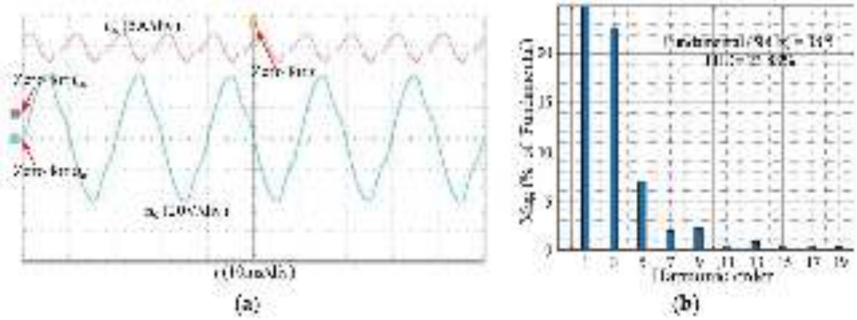

Figure 12. Experimental results under i_{dc}^{*} = 11.5 A: (**a**) experimental waveforms of i_{dc} and u_o; (**b**) FFT results.

In Figure 13, i_{dc}^{*} is set to 20 A, and i_{dc} maintains above 20 A with small fluctuation. Since i_{dc} is higher than the amplitude of i_o, u_o can track the reference. u_o's THD is 1.38%, greater than the one when i_{dc}^{*} = 13.5 A. Meanwhile, the switching loss and conduction loss of IGBT and diode are positively related to i_{dc}. The above experimental results show that the calculation method for the optimal reference of DC-link current is correct and feasible.

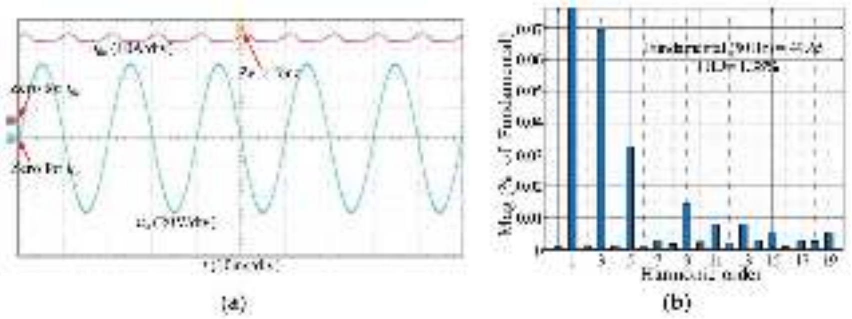

Figure 13. Experimental results under i_{dc}^{*} = 20 A: (**a**) Experimental waveforms of i_{dc} and u_o; (**b**) FFT results.

6.2. Experimental Results of Dynamic-State

The dynamic performance of the output voltage control strategy will be verified in this section. The frequency remains 50 Hz, and the amplitude of the reference voltage is adjusted from 40 V to 60 V. According to Formula (18), i_{dc}^{*} is set to 9 A and 17.5 A, respectively. The experimental waveforms of i_{dc} and u_o are shown in Figure 14. i_{dc} reaches the steady state again after 2 ms and remains above 17.5 A. In Figure 14, the u_o's amplitude is adjusted to 60 V with smooth changing.

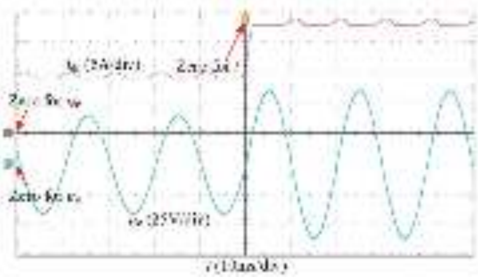

Figure 14. The dynamic-state experimental waveforms under amplitude changing.

Figure 15 shows the experimental waveforms when the amplitude is set to 50 V, and the frequency ω changes from 50 Hz to 100 Hz. According to (18), i_{dc}^{*} is related to ω, so it should be adjusted from 13.5 A to 16.5 A. In Figure 15, i_{dc} and u_{o} can track the reference quickly. In conclusion, the superior steady-state and dynamic-state performance of the output voltage control strategy can be fully proved, and the DC-link current reference from the proposed calculation method is the minimum value that can meet the power demand.

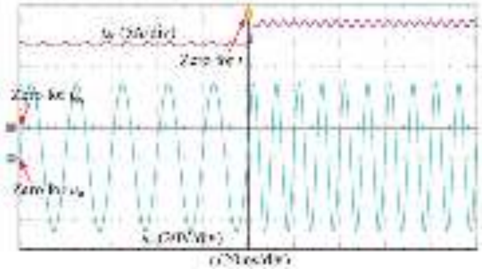

Figure 15. The dynamic-state experimental waveforms under frequency changing.

Finally, the CSI's efficiency has been tested under different load powers from 100 W to 500 W. A curve map of the CSI's efficiency is illustrated in Figure 16. When the load power increases, the power loss in the conduction and switching increases relatively more slowly than the load power, so the CSI's efficiency rises with the increased load power.

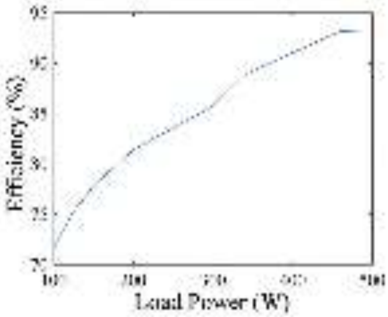

Figure 16. The efficiency map of the proposed single-phase CSI.

7. Conclusions

This paper proposes a novel PWM modulation method to control DC-link current for the improved topology of single-phase CSI; the corresponding operating modes and modulation strategy with DC-link current hysteresis control are also introduced in detail. The relationship between the optimal reference of DC-link current and output voltage is derived. A voltage control strategy based on d-q frame components is discussed. A series of simulations and experiments is set up to demonstrate the feasibility of the proposed method. The conclusions are summarized as follows:

(1) DC-link current can remain in the expected range by adopting the improved PWM modulation, and the number of switching activities is the same as the traditional modulation.

(2) The calculation method of optimal reference for DC-link current can meet the AC side load demand, improving current utilization and reducing loss.

(3) The control of DC-link current is implemented by switching magnetizing mode and freewheeling mode, which is separated from output voltage control. Thus, the DC-side model can be considered a controlled current source.

Supplementary Materials: The following supporting information can be downloaded at: https://www.mdpi.com/article/10.3390/en16186729/s1. Figure S1. Simulation waveforms in steady state: (a) DC-link current; (b) AC output volt-age. Figure S2. Simulation waveforms on the traditional single-phase CSI when the initial DC-link current is 0A: (a) DC-link current; (b) AC output voltage. Figure S3. Simulation waveforms on the traditional single-phase CSI when the initial DC-link current is 16A: (a) DC-link current; (b) AC output voltage.

Author Contributions: Methodology, Y.Z. and T.Y.; Software, T.Y.; Writing—original draft, Y.Z.; Writing—review and editing, Y.M. All authors have read and agreed to the published version of the manuscript.

Funding: This work is supported by the Youth project of science and technology research program of Chongqing Education Commission of China (No. KJQN202001105).

Data Availability Statement: The data presented in this study are available on request from the corresponding author. The data are not publicly available due to the funder's requirement.

Conflicts of Interest: The authors declare no conflict of interest.

Nomenclature

VSI	Voltage Source Inverter
CSI	Current Source Inverter
HVDC	High Voltage Direct Current
L_{dc}	DC-link inductance (mH)
C	AC side's filter capacitor (μF)
R	AC side's resistive load (Ω)
i_{dc}	DC side's current (A)
i_{o}	Output current on the resistive load R (A)
u_{dc}	DC side's voltage (V)
u_{o}	Output voltage on the resistive load R (A)
p/q	Switching functions for S_0, S_1, S_2, S_3, and S_4 (-)
d	Duty cycle (%)
i_{o}^*	Reference of the output current i_{o} (A)
i_{dc}^*	Reference of the DC side's current i_{dc} (A)
$\Delta i_{\mathrm{dc\_down}}$	Decrement of i_{dc} when discharging (A)
$\Delta i_{\mathrm{dc\_up}}$	Increment of i_{dc} when charging (A)
T_{s}	Switching period (s)
U	Fundamental amplitude of u_{o} (V)
I	Fundamental amplitude of i_{o} (A)
θ	Initial phase of i_{o} (rad)
ω	Fundamental frequency of i_{o} (Hz)
$\Delta i_{\mathrm{dcmax}}$	Maximum reduction of i_{dc} (A)
u_{od}/u_{od}	d-q frame components of u_{o}
$u_{\mathrm{od}}^*/u_{\mathrm{oq}}^*$	Reference of u_{od}/u_{od}
i_{od}/i_{od}	d-q frame components of i_{o}
$i_{\mathrm{od}}^*/i_{\mathrm{oq}}^*$	Reference of i_{od}/i_{od}

References

1. Chakrabarti, A.; Sarkar, K.; Kasari, P.R.; Das, B.; Biswas, S.K. A CB-PWM Technique for Eliminating CMV in Multilevel Multiphase VSI. *IEEE Trans. Ind. Electron.* **2022**, *70*, 8666–8675. [CrossRef]
2. He, J.; Zhang, C.; Lei, M.; Han, J.; Guo, P.; Li, Y. An Active Bypass Pulse Injection-Based Low Switching Frequency PWM Approach for Harmonic Compensation of Current-Source Converters. *IEEE Trans. Power Electron.* **2021**, *36*, 1614–1625. [CrossRef]
3. Rajeev, M.; Agarwal, V. Single phase current source inverter with multiloop control for transformerless grid–PV interface. *IEEE Trans. Ind. Appl.* **2018**, *54*, 2416–2424. [CrossRef]
4. Titus, J.; Harikrishnan, P.; Hatua, K. An SCR-Based CSI-Fed Induction Motor Drive for High Power Medium Voltage Applications. *IEEE Trans. Ind. Electron.* **2020**, *68*, 4657–4666. [CrossRef]
5. Guo, X.-Q.; Sui, S.; Wang, B.; Zhang, W. A Current-Based Approach for Short-Circuit Fault Diagnosis in Closed-Loop Current Source Inverter. *IEEE Trans. Ind. Electron.* **2019**, *67*, 7941–7950. [CrossRef]

6. Miao, Y.; Liao, W.; Huang, S.; Liu, P.; Wu, X.; Song, P.; Li, G. DC-Link Current Minimization Scheme for IM Drive System Fed by Bidirectional DC Chopper-Based CSI. *IEEE Trans. Transp. Electrif.* **2023**, *9*, 2839–2850. [CrossRef]
7. Li, Y.W.; Pande, M.; Zargari, N.R.; Wu, B. DC-link current minimization for high-power current-source motor drives. *IEEE Trans. Power Electron.* **2008**, *24*, 232–240.
8. Geng, Y.; Yang, K.; Lai, Z.; Zheng, P.; Liu, H.; Deng, R. A Novel Low Voltage Ride Through Control Method for Current Source Grid-Connected Photovoltaic Inverters. *IEEE Access* **2019**, *7*, 51735–51748. [CrossRef]
9. Wang, W.; Gao, F.; Yang, Y.; Blaabjerg, F. Operation and modulation of H7 current-source inverter with hybrid SiC and Si semiconductor switches. *IEEE J. Emerg. Sel. Top. Power Electron.* **2017**, *6*, 387–399. [CrossRef]
10. Yang, S.; Peng, F.Z.; Lei, Q.; Inoshita, R.; Qian, Z. Current-fed quasi-Z-source inverter with voltage Buck–Boost and regeneration capability. *IEEE Trans. Ind. Appl.* **2010**, *47*, 882–892. [CrossRef]
11. Guo, X.; Wang, N.; Zhang, J.; Wang, B.; Nguyen, M.-K. A Novel Transformerless Current Source Inverter for Leakage Current Reduction. *IEEE Access* **2019**, *7*, 50681–50690. [CrossRef]
12. Nascimento, A.J.P.; de Menezes, B.F.; de Mesquita, S.J.; Costa, K.R.; Tofoli, F.L.; Daher, S.; Antunes, F.L.M. Bidirectional Isolated Asymmetrical Multilevel Inverter. *IEEE Trans. Circuits Syst. II Express Briefs* **2022**, *70*, 151–155. [CrossRef]
13. Sun, R.; Wang, X.; Ye, Y. Seventeen-Level Inverter Based on Switched-Capacitor and Flying-Capacitor-Fed T-type Unit. *IEEE Access* **2022**, *10*, 33561–33570. [CrossRef]
14. Ding, L.; Li, Y.W. Simultaneous DC current balance and common-mode voltage control with multilevel current source inverters. *IEEE Trans. Power Electron.* **2018**, *33*, 9188–9197. [CrossRef]
15. Guo, Q.; Zhou, C.; Li, S. A Multiple Loops Control Strategy Based on DC Link Voltage of Current Source PWM Rectifiers. *Trans. China Electrotech. Soc.* **2022**, *37*, 2051–2063.
16. Wu, F.; Feng, F.; Luo, L.; Duan, J.; Sun, L. Sampling period online adjusting-based hysteresis current control without band with constant switching frequency. *IEEE Trans. Ind. Electron.* **2014**, *62*, 270–277. [CrossRef]
17. Wang, Z.; Wu, B.; Xu, D.; Cheng, M.; Xu, L. DC-link current ripple mitigation for current-source grid-connected converters under unbalanced grid conditions. *IEEE Trans. Ind. Electron.* **2016**, *63*, 4967–4977. [CrossRef]

applied sciences

MDPI

Article

Clustering Optimization of IPMSM for Electric Vehicles: Considering Inverter Control Strategy

Jiabao Bu, Shangbin Yuan † and Jinhua Du *

The State Key Laboratory of Electrical Insulation and Power Equipment, Xi'an Jiaotong University,
Xi'an 710049, China; 3122104026@stu.xjtu.edu.cn (J.B.); yuanshangbin000@163.com (S.Y.)
* Correspondence: jinhuadu@mail.xjtu.edu.cn
† Current address: Power Dispatch and Control Center of Guangxi Power Grid, Nanning 530023, China.

Abstract: The actual performance of driving motors in the electric vehicle (EV) powertrain depends not only on the electromagnetic design of the motor itself but also on the driving condition of the vehicle. The traditional motor optimization method at the rated point is difficult to deal with because of the mismatch between its high-efficiency area and the actual operation area. This paper systematically proposes an optimal design method for driving motors for EVs, considering the driving conditions and control strategy to improve motor efficiency and passengers' riding comfort. It uses cluster analysis to identify representative points and related energy weights to consider motors' comprehensive performance in different driving cycles. Three typical operation conditions are selected to implement the proposed optimization process. In the design process, by using the sensitivity analysis method, the significance of the structural parameters is effectively evaluated. Moreover, the semianalytical efficiency model and torque model of permanent magnet driving motors based on finite element analysis results are deduced to consider the influence of magnetic saturation, space harmonics, and cross-coupling between d-axis and q-axis magnetic fields. Based on the driving system demands of an A0 class pure EV, the whole optimization design is divided into four steps and three scales, including the motor scale, control scale, and system scale. By using the multi-objective optimization method, Pareto optimality of motor efficiency and torque ripple is achieved under the city driving cycle and highway driving cycle. Compared to the optimization only at the rated condition, the proportion of motor sweet region increased about 1.25 times and 3.5 times by the proposed system-scale optimization under two driving cycles, respectively. Finally, the effectiveness of the proposed optimization method is verified by the prototype experiments.

Keywords: multi-objective optimization; control strategy; driving cycle; electric vehicle

Citation: Bu, J.; Yuan, S.; Du, J. Clustering Optimization of IPMSM for Electric Vehicles: Considering Inverter Control Strategy. *Appl. Sci.* **2023**, *13*, 10792. https://doi.org/10.3390/app131910792

Academic Editors: Kan Liu and Wei Hu

Received: 15 August 2023
Revised: 25 September 2023
Accepted: 26 September 2023
Published: 28 September 2023

1. Introduction

With the deepening of vehicle electrification in the global market, the driving motor as the main power of the electrical vehicle (EV) drive system holds promising growth potential and attracts extensive attention [1,2]. At present, more than 80% of driving motors in the electrical drive system of pure and hybrid EVs on the market adopt permanent magnet synchronous motors (PMSM) for wider speed regulation range, higher efficiency, and power density [3–5], such as Toyota Prius, Chevrolet Bolt, BMW i3, BYD E6, and so on. To obtain a better driving experience and a longer driving range, it is of great significance to improve PMSM performances through optimization design technologies [6,7].

Generally, the optimization design of PMSM for an EV can be based on a single operation condition, such as the rated operation point of the torque-speed curve, which could ensure satisfactory working performance at this specific point. Yet, once the condition changes, the PMSM performance will deteriorate and even result in undesired reliability in the power train. The operating conditions of EVs are very complex and involve frequent starting and braking, frequent accelerating and decelerating, cruising, and climbing.

Therefore, the optimized PMSM at the rated operation point could not guarantee the whole operation requirements within the considered driving cycle of an EV, which puts forward inevitable demands for the PMSM design considering the driving cycle [8–11]. Different from the PMSM that operated at the rated operation point, the actual performance of the PMSM at each operating point in different driving cycles is closely related to the control strategy and control parameters. To achieve high system-level performance, the perfect cooperation of the motor and its control systems, considering the driving cycle, must be investigated synchronously.

Although both motor and control are important to the system's performance, not much work has been reported in the literature. The design and optimization are mostly at the component level of motors [10,11], which can be classified into two types of single-objective and multi-objective optimization. For single-objective optimization, any one of efficiency, torque ripple, cost, or weight can be used as the optimization objective. In [12,13], by using the finite element method (FEM)-based model and the exact subdomain model with intelligent optimization algorithms, the torque ripple and cogging torque are respectively obtained minimally in the PMSM. For multi-objective optimization, two or more design objectives are selected simultaneously [14,15]. Efficiency and cogging torque are selected as the two design objectives for optimization of a PMSM in [16], where two-stage design optimization using the Taguchi method and response surface model are used to identify the three design variables. In [17], the multi-objective genetic algorithm is adopted to achieve low cost and low torque ripple for a PMSM optimization, and the resulting motor performances meet all the given design demands. The above optimization on the component level of motors is generally conducted under the rated operation point.

When component-level-based optimization involves more operation points in the driving cycle, the simple way is to repeat the performance calculation process in rated point optimization at all operation points and then use the optimization algorithm to select the optimal scheme [18,19]. However, the optimizations with a precise model that includes all operating points will be very time-consuming, with a significant increase in computational cost and complexity. There are two main solutions to this problem. One is using approximate models for as many operating points as possible to obtain the global optimal design. The approximate models for the former solution could be the Kriging model, equivalent circuit model, and response surface model [20–22], which are generally used to replace the finite element precise model and reduce the computer cost. However, the inclusion of more points will still make the calculation more complicated. The other solution is choosing representative points (RPs) to represent the driving cycle and the application torque-speed profile [23,24]. The accuracy of this solution depends on the number and values of the RPs and the corresponding current calculation under different RPs. At present, motor optimizations using RPs to consider driving cycles mainly use the ideal current value, which ignores the influence of controllers [25,26]. However, individually optimizing motor structure parameters cannot ensure optimal performance for the entire drive system, especially when the difference in the impact of the PWM carrier harmonic on the loss is significant under different control strategies and control parameters [27,28].

On the other hand, for the control part, although there is much literature related to control strategies focusing on torque ripple reduction or motor efficiency improvements, such as advanced angle field weakening control, loss minimization direct torque control, and robust adaptive current control with disturbance observer [29–31], they usually consider the influence of harmonics or control parameters on the performance of the motor after the motor geometry structure is determined. It means that the proposed control strategies are generally designed and optimized at the control level and have not been combined with the motor design. As previously discussed, it can hardly achieve optimal system performance with this component-level-based optimization based only on motor or control. Therefore, to meet the challenging requirements and satisfy the wide operating range of EVs, it is necessary to optimize the driving motor, considering the inverter control strategy throughout the whole driving cycle in the product design phase.

To deal with the aforementioned issue, this paper presents an effort to develop a system-scale multi-objective optimization procedure for driving motors based on the clustering technique under different operating conditions. And a full-speed domain vector controller with maximum torque per current (MTPA) and flux weakening control strategies [32–34] is adopted to meet the requirements of EVs. The main contributions of this paper are shown as follows:

- The K-means clustering analysis is proposed as a preprocessing step to obtain insight into the distribution of operation points in two typical driving cycles, and the RPs of the torque-speed profile with their energy weights are identified.
- The semianalytical efficiency model and torque model of an interior PMSM (IPMSM) based on FEM results are deduced to consider the influence of magnetic saturation, space harmonics, and cross coupling between d-axis and q-axis magnetic fields.
- An optimal method to tune the motor and control parameters based on the multi-objective particle swarm optimization (MOPSO) algorithm is proposed, where the control model is added to consider the performance of IPMSMs under different control strategies in the whole driving cycle.

This paper is organized as follows: Section 2 describes the clustering optimization design procedure for the IPMSM driving motor. Section 3 presents the motor-scale, control-scale, and system-scale optimization models. Based on these models, a comparative study has been carried out under three working condition requirements: one is under the rated operation point, and the other two are under driving cycles. And the optimization results are discussed and verified by experiments in Section 4, followed by the Section 5.

2. Clustering Optimization Design Procedure

The target driving system that powers an A0 class pure EV [34] consists of a 48-slot 8-pole IPMSM and a full-speed domain vector controller with MTPA and flux weakening control strategies, whose design requirements are shown in Table 1.

Table 1. Specification of the investigated EV.

Parameter	Value	Parameter	Value
Vehicle mass	1100 kg	Radius of wheels	0.308 m
Maximum gradeability	20%	Maximum climbing speed	20 km/h
Motor rated speed	3000 rpm	Motor maximum speed	8000 rpm
Acceleration time	<10 s for 0~50 km/h, <15 s for 50~100 km/h		

2.1. Design Framework

The overall optimization procedure is represented in Figure 1, which includes the following four steps.

Step 1: Analyze the driving conditions of EVs and make a preliminary design for the motor. The K-means clustering algorithm is used to identify the RPs of the motor for evaluating the performance of the motor in the whole driving cycle of EVs.

Step 2: Establish the semianalytical models and evaluate the steady performance of the motor on the motor scale. The optimal parameters of the motor are selected by sensitivity analysis.

Step 3: Evaluate the dynamic performance of the motor on the control scale with respect to the nonlinear factors given by the motor characteristic parameters. The full-speed domain control strategy is considered to meet the requirements of low-speed starting and high-speed cruising for the proposed IPMSM driving motor.

Step 4: Performance evaluation of the system scale based on the fitness function and obtaining the optimal design with MOPSO. When the result satisfies the iterative stop condition, the Pareto solution is output. Otherwise, the motor parameters are updated based on the MOPSO and then returned to Step 2.

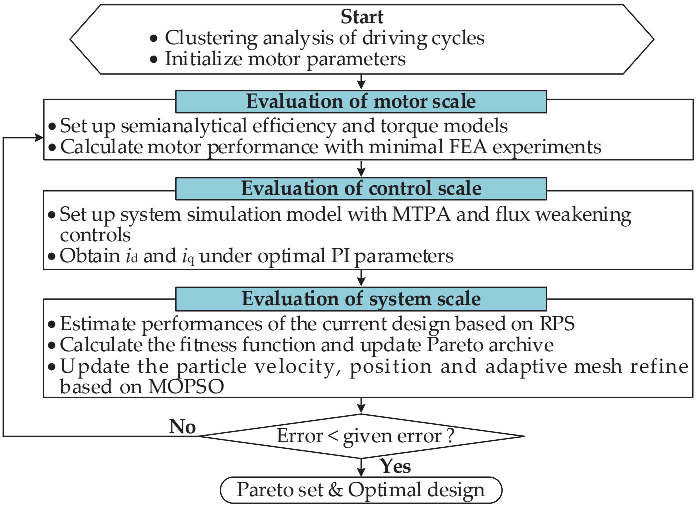

Figure 1. Framework of the proposed system-scale optimization for driving motors targeting driving cycles.

2.2. Clustering Analysis of Driving Cycles

There are three case studies proposed in this paper, which are optimizations at the rated operation point, under the urban dynamometer driving schedule (UDDS), and the highway fuel economy test (HWFET). To improve the optimization efficiency, the K-means clustering method is used to analyze driving cycles [24,26], which splits the torque-speed profile obtained from the driving cycle data into different groups considering the position and density of the operating points on the plane. Euclidean distance is used to determine the similarity between samples; therefore, the cluster S_i and its centroid l_i can be determined iteratively as follows:

$$S_i^{(t)} = \left\{ z_j : \left\| z_j - l_i^{(t)} \right\|^2 \le \left\| z_j - l_i^{(t)} \right\|^2 \forall i, i = 1,2,3\ldots k \right\} \tag{1}$$

$$l_i^{(t+1)} = \frac{1}{\left| S_i^t \right|} \sum_{x_j \in S_i^t} x_j \tag{2}$$

The iteration repeats until the centroid of each cluster no longer changes. The cluster number k is determined based on the sum of the distances of the load points to their corresponding cluster centroid, and the cluster centroid is selected as the RP of motor optimization. In this way, the two specific driving cycles shown in Figure 2a,c can be partitioned into several clusters, as shown in Figure 2b,d. Moreover, the RPs and their energy weights are listed in Table 2. It can be found that the motor operating conditions are mostly located in the low-speed or low-torque region in UDDS, and the motor runs less in the conditions of high speed or heavy load. Meanwhile, the motor operating conditions are mostly located in the high-speed and low-torque regions of HFET. Therefore, the clusters and the number of RPs determined by the proposed clustering analysis are different for the two driving cycles, which will be used for the subsequent optimization design.

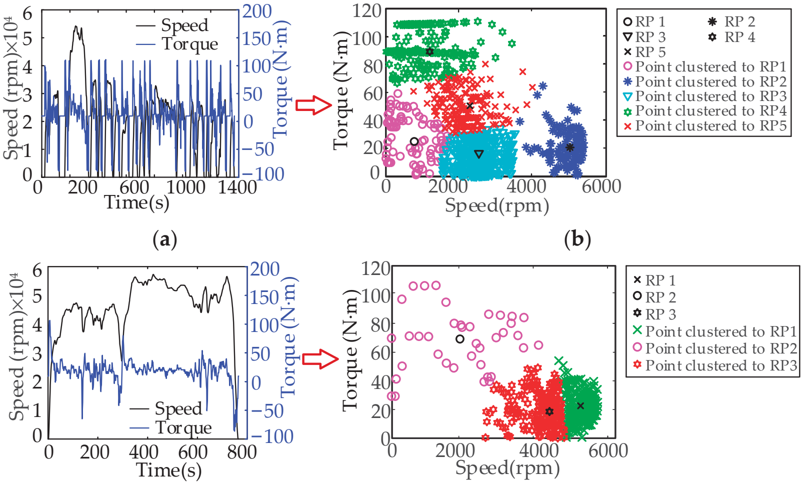

(**a**) (**b**)

(**c**) (**d**)

Figure 2. Driving cycle clustering results. (**a**) Speed curve of UDDS. (**b**) Torque-speed curve of UDDS. (**c**) Speed curve of HWFET. (**d**) Torque-speed curve of HWFET.

Table 2. Specification of RPs in two driving cycles.

	RPs	Speed (rpm)	Torque (N·m)	*w* (%)
UDDS	1	738	27	7.8
	2	4934	21.66	9.9
	3	2546	14	46.26
	4	1126	91	18.63
	5	2157	50	17.37
HWFET	1	5308	21	47
	2	2051	68	5
	3	4269	20	48

2.3. Optimization Algorithm and Fitness Function

The multi-objective PSO algorithm is utilized to obtain the optimal design, which includes adaptive mesh generation based on the roulette algorithm and global best updating as presented in [34].

In order to improve the vehicle range and driving comfort, two objectives are considered: maximize the driving cycle efficiency and minimize the torque ripple. Efficiency is the most important target for EV motors, which has a great influence on vehicle range and comfort, especially considering the current constraints of battery technology faced by vehicles. Maximum driving cycle efficiency can ensure the maximum efficiency of the drive system in the driving cycle. Likewise, the torque ripple is another key factor influencing the performance of the EV motor, which can lead to electromagnetic noise and vibration, affect vehicle comfort, and shorten the service life of the power train. Accordingly, the design objectives could be written as

$$\min f_1(x) = 1 - \frac{\sum_{j=1}^{m}(w_j T_j \Omega_j)}{\sum_{j=1}^{m}(w_j(T_j\Omega_j + P_{\text{loss},j}))} \times 100\%, \tag{3}$$

$$\min f_2(x) = \sum_{j=1}^{m}(\frac{T_{\text{r}j} w_j}{T_j}) \times 100\%, \tag{4}$$

where $\boldsymbol{x}$ is the optimization variable, the subscript j represents the RP j, and m is the total RP number.

Furthermore, the fitness function can be defined as

$$\begin{array}{c} \min F(\boldsymbol{x}) = \min(f_1(\boldsymbol{x}), f_2(\boldsymbol{x})) \\ s.t.\ g_1(\boldsymbol{x}) = 30000 - P_{\text{out}}|_{n_{\max}} \le 0 \\ g_2(\boldsymbol{x}) = 2 - n_{\max}/n_{\text{N}} \le 0 \\ g_3(\boldsymbol{x}) = k_{\text{s}} - 0.8 \le 0 \end{array}. \tag{5}$$

3. System-Scale Optimization of Drive Systems

For system-scale optimization, it is crucial to investigate the perfect cooperation of the motor and its controller synchronously. A design example with the semianalytical efficiency model and torque model of IPMSMs and a full-speed domain vector controller is investigated in this section.

3.1. Optimization Model for Motor Level

The investigated motor is parameterized as shown in Figure 3, where five independent design variables x_1, x_2, x_3, x_4, and x_5 are selected and are listed in Table 3. They are the air gap, tooth width, slot width, permanent magnet width, and yoke thickness, respectively. Therefore, $\boldsymbol{x} = [x_1, x_2, x_3, x_4]^T$. It should be noted that the outer and inner diameters and the stack length are fixed [34] throughout the optimization process to meet the maximum installation space shown in Table 3.

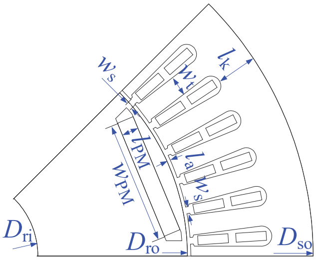

Figure 3. Parameterized model of the investigated IPMSM.

Table 3. Design parameters of the investigated IPMSM.

Parameter	Value	Parameter	Value	Parameter	Value
D_{so} (mm)	210	l_{e} (mm)	153	w_{PM} (mm)	x_4
l_{PM} (mm)	5	l_{a} (mm)	x_1	l_k (mm)	x_5
D_{ri} (mm)	48	w_{t} (mm)	x_2	α	x_6
D_{ro} (mm)	136	w_{s} (mm)	x_3	β	x_7

3.1.1. Semianalytical Torque Model and Efficacy Model of IPMSMs

For each RP with a specific torque and speed, motor performance is evaluated by semianalytical models based on FEA results to balance accuracy and computation cost. Considering the saturation, cross coupling, and spatial harmonics of IPMSMs, the torque T is derived through the co-energy method [26] as follows:

$$\begin{aligned} T &= \frac{\partial W'_{\text{m}}(i_{\text{d}},i_{\text{q}},\theta)}{\partial\theta} = i_{\text{s}}\frac{\partial\lambda(i_{\text{d}},i_{\text{q}},\theta)}{\partial\theta} - \frac{\partial W_{\text{m}}(i_{\text{d}},i_{\text{q}},\theta)}{\partial\theta} \\ &= \frac{\frac{3p}{2}(\lambda_{\text{d}}i_{\text{q}} - \lambda_{\text{q}}i_{\text{d}}) + \frac{3}{2}(i_{\text{q}}\frac{\partial\lambda_{\text{d}}}{\partial\theta} + i_{\text{d}}\frac{\partial\lambda_{\text{q}}}{\partial\theta}) - \frac{\partial W_{\text{m}}(i_{\text{d}},i_{\text{q}},\theta)}{\partial\theta}}{T_1 \qquad\qquad T_2 \qquad\qquad T_3} \end{aligned}, \tag{6}$$

where the subscribed d and q represent variables under the d-axis and q-axis.

It can be noted that there are three torque components in (6), which take torque ripple components T_2 and T_3 into consideration compared with the traditional torque equation, which only considers the average torque T_1.

Moreover, the magnetic density inside the driving motor core is usually non-sinusoidal and rich in harmonics. Additionally, the two magnetization modes, alternating and rotating, will make the variation trends of the magnetic density trajectory completely different. In order to consider the effects of alternating magnetization, rotating magnetization, and magnetic field harmonics, the iron losses P_{Fe} of each RP are calculated by the magnetic density orthogonal decomposition model [21] as follows:

$$P_{\mathrm{Fe}} = K_{\mathrm{y}}(fh)\sum_{h=1}^{h_{\mathrm{m}}}\left(B_{\mathrm{r}h}^2 + B_{\mathrm{t}h}^2\right) + K_{\mathrm{c}}(fh)^2\sum_{h=1}^{h_{\mathrm{m}}}\left(B_{\mathrm{r}h}^2 + B_{\mathrm{t}h}^2\right) + K_{\mathrm{e}}(fh)^{1.5}\sum_{h=1}^{h_{\mathrm{m}}}\left(B_{\mathrm{r}h}^2 + B_{\mathrm{t}h}^2\right). \quad (7)$$

where h, or the subscript h, represents the number of magnetic density harmonics, and h_{m} is the total harmonic number.

The λ_{d}, λ_{q}, B_{r}, and B_{t} in analytical expressions (6) and (7) are calculated using computationally efficient FEA [26], which is the so-called semianalytical model. According to the magnetic and electric symmetry and periodicity of the considered IPMSM, when n position samples are selected and flux linkage of winding and flux density of iron core are calculated by n magnetostatics FEA of 1/8 model, there will be another $5n$ samples reconstructing by post-processing techniques, which is much more time-saving than FEA. Figure 4 shows the reconstructed results of λ_{d}, λ_{q}, B_{r}, and B_{t}, which are used to set up the efficiency model and torque model of IPMSMs. Figure 4a,b presents the variation of λ_{d} and λ_{q} with stator phase current amplitude I_{s} and rotor angle θ, where the rainbow color maps the flux linkage value. Figure 4c,d present the variation of B_{r} and B_{t} with stator current and rotor angle in the stator teeth, where the rainbow color maps the flux density value.

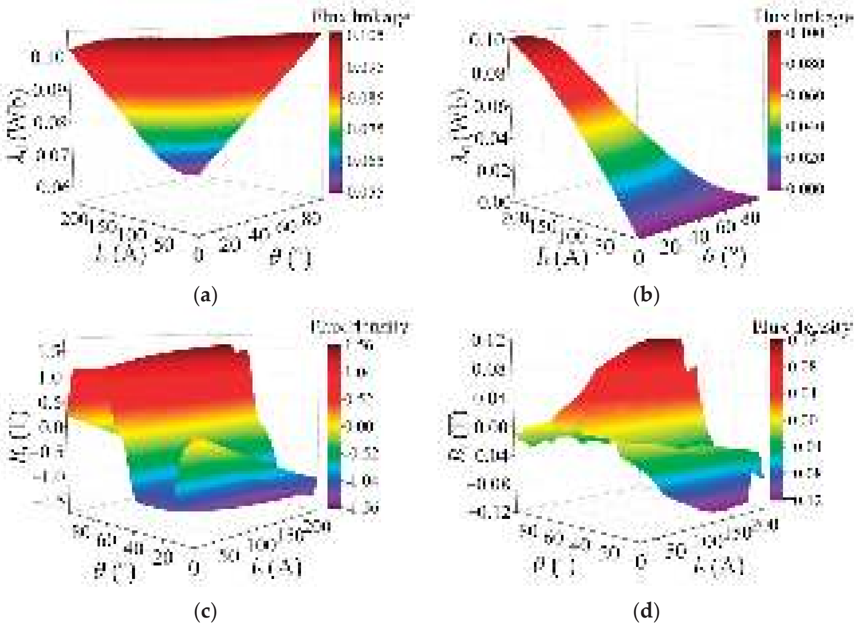

(**a**) (**b**)

(**c**) (**d**)

Figure 4. Computationally efficient FEA results for semianalytical models. (**a**) λ_{d}. (**b**) λ_{q}. (**c**) B_{r} in stator teeth. (**d**) B_{t} in stator teeth.

3.1.2. Sensitivity Analysis of Optimization Parameters

In this paper, the Taguchi method [35] is adopted to analyze the parameter sensitivity to save computation costs for the following global optimization. The orthogonal table selects four horizontal values for each factor as shown in Table 4, which include row number 16, factor number 5, and level number 4, and can be expressed as $L_{16}(4^5)$. Considering the geometric constraints of the motor structure, the range of values for each parameter above is specified.

Table 4. Orthogonal table of motor factors.

Number	x_1	x_2	x_3	x_4	x_5
1	0.93	5.59	1.87	32.4	11.2
2	1.2	5.59	2.13	35.87	9.6
3	1.07	5.83	2.13	34.13	14.4
4	1.07	5.83	2.13	32.4	12.8
5	0.8	5.36	1.6	32.4	9.6
6	1.2	5.36	1.87	37.6	12.8
7	0.8	5.83	1.87	35.87	14.4
8	1.07	5.36	2.4	35.87	11.2
9	1.07	6.06	1.87	34.13	9.6
10	1.07	5.59	1.6	37.6	14.4
11	1.2	5.83	1.6	34.13	11.2
12	0.8	5.59	2.4	34.13	12.8
13	0.8	6.06	2.13	37.6	11.2
14	0.93	5.83	2.4	37.6	9.6
15	1.2	6.06	2.4	32.4	14.4
16	0.93	6.06	1.87	35.87	12.8

The sensitivity analysis method [35] is considered an effective approach to analyzing the significance of design variables. And the sensitivity calculation model $S(O)$ in this paper can be expressed as

$$S(O) = \frac{\sum_{i=1}^{d} \left(p_{\mathrm{O}(i)} - p_{\mathrm{t}}\right)^2}{d}. \tag{8}$$

Based on (8), the effects of the selected five variables on the optimization objectives can be evaluated effectively. Figure 5 shows the sensitivity results. It can be seen that the factors x_4 and x_5 have great impacts on efficiency, and the factors x_3 and x_4 have great influences on torque ripple. Consequently, x_3, x_4, and x_5 are comprehensively considered as optimization variables for the following optimization design.

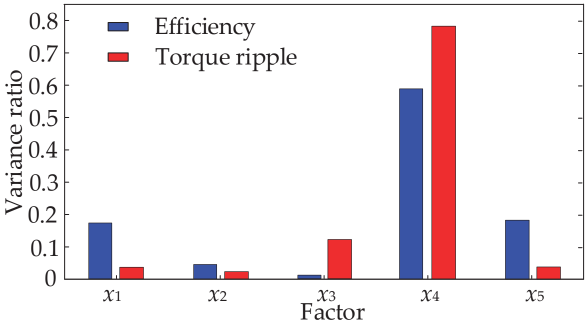

Figure 5. Variance ratio of motor parameters.

3.2. Optimization Model for Control Level

The response current of the motor under different operating conditions is related to the control strategy and the limits of the inverter bus voltage. A full-speed domain vector controller is adapted to meet the requirements of low-speed starting and high-speed cruising for the proposed IPMSM driving motor. In order to optimize the performance of the motor under different operating conditions, MTPA and flux-weakening control are used in this paper to meet the requirements of EVs. The control block is shown in Figure 6.

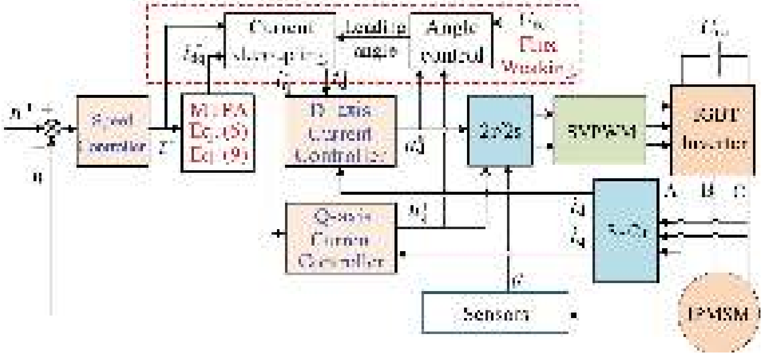

Figure 6. Control block diagram of the full-speed domain vector controller.

When the load is given and the motor terminal voltage does not reach the limit with the speed below base speed, the IPMSM adopts the MTPA control strategy and runs at the MTPA trajectory. As shown in Figure 6, in this MTPA mode, by comparing the real speed *n* with the speed demand *n**, the torque demand *T** could be obtained from the speed controller and input into the MTPA control part. And then, the current demand i_{dq}* can be solved from torque Equations (6) and (9). If the motor operates in MTPA mode, d-axis and q-axis current demand i_{d}*, i_{q}* are decoupled from i_{dq}* and sent directly to the d-axis current controller and the q-axis current controller, respectively. Subsequently, the voltage demands u_{d}*, u_{q}* are obtained, and through the 2r/2s transformation and SVPWM module, they are finally turned into the switching signal to control the IGBT inverter.

$$\frac{\partial(T/i_{\mathrm{s}})}{\partial i_{\mathrm{d}}} = \frac{\partial(T/i_{\mathrm{s}})}{\partial i_{\mathrm{q}}} = 0. \tag{9}$$

When the speed demand is higher, the motor provides more torque to accelerate the rotor. At the early stage of speed regulation, the motor does not reach the base speed. However, as the motor voltage reaches its limit shown in (10), the motor speed approaches the base speed, and the speed loop saturates with the maximum given current. Therefore, the flux-weakening control strategy is adopted to redistribute the current in the dq axis through the leading angle so that the speed loop exits the saturation state and the motor torque meets the load. As shown in Figure 6, in this flux weakening mode, the leading angle δ is calculated from the angle controller by comparing the bus voltage U_{dc} with the motor voltage. And the d-axis and q-axis current demand i_{d}*, i_{q}* are redistributed by the current decoupling module according to δ as (11). It can be found that the flux-weakening control can increase the motor torque and expand the operating range in comparison with the MTPA control at the same motor speed.

$$u_{\mathrm{s}}^2 = p\Omega\sqrt{(L_{\mathrm{q}} i_{\mathrm{q}})^2 + (L_{\mathrm{d}} i_{\mathrm{d}} + \lambda_{\mathrm{pm}})} \le u_{\mathrm{lim}}^2, \tag{10}$$

where the motor stator resistance is neglected, and u_{lim} is the limited value of motor phase voltage.

$$\begin{cases} i_{\mathrm{d}}^{*} = i_{\mathrm{s}}\cos(\delta+\Delta\delta) \\ i_{\mathrm{q}}^{*} = i_{\mathrm{s}}\sin(\delta+\Delta\delta) \end{cases}. \tag{11}$$

As described above, the speed demand is converted into torque demand by the speed controller, and the current demand is converted into voltage demand by two current controllers. In the implementation, the three PI controllers shown in Figure 6 have the form

$$\begin{cases} K_{\mathrm{sp}} = \frac{\alpha+1}{\alpha}\frac{\pi J}{360 T_{\mathrm{s}} p \lambda_{\mathrm{pm}}}; K_{\mathrm{si}} = \frac{1}{\alpha}\frac{K_{\mathrm{sp}}}{4T_{\mathrm{s}}} \\ K_{\mathrm{ip\_d}} = \beta L_{\mathrm{d}}; K_{\mathrm{ip\_q}} = \beta L_{\mathrm{q}}; K_{\mathrm{ii\_d}} = K_{\mathrm{ii\_q}} = \beta R_{\mathrm{s}} \end{cases}. \tag{12}$$

In the whole optimization process, motor parameters and operating points change frequently, which means the fixed PI controller based on classical control theory could not satisfy the optimization demand. Therefore, to ensure that the performance evaluation of each motor scheme is carried out under the same optimal control level, two parameters α and β are optimized in the control level with the minimum control error as follows:

$$\min f(\alpha,\beta) = \int_{0}^{\infty} t|e(t)|\mathrm{d}t. \tag{13}$$

where t is the calculation time, and $e(t)$ is the instantaneous response error [36].

4. Discussion and Optimization Results

4.1. Optimization Results

According to the optimization procedure shown in Figure 1, after determining the value of representative currents of RPs under different operating conditions, the system's performance could be evaluated based on the fitness function, and MOPSO is used to obtain the optimal design. To illustrate the optimistic effect, the optimized motor scheme designed by the proposed optimization method will be compared with that designed by the single operation point optimization method in this section. The results of multi-objective optimization are shown in Figure 7. Figure 7a–c shows the Pareto solution set optimized by the rated operation point optimization method and the proposed optimization method under UDDS and HWFET, respectively. The black curves in these three figures are the Pareto optimal fronts for each optimization design. Each solution in the Pareto front solution set is optimal. Hence, the optimal motor scheme could be selected from this Pareto front solution set by the decision maker. Based on the VIKOR model [37], which is a multi-attribute decision-making method, the optimal solution could be selected according to (14).

$$\max f(\boldsymbol{x}) = v_1\frac{\eta-\eta_{\min}}{\eta_{\max}-\eta_{\min}} + v_2\frac{T_{\mathrm{r\,max}}-T_{\mathrm{r}}}{T_{\mathrm{r\,max}}-T_{\mathrm{r\,min}}}, \tag{14}$$

where η and T_{r} are the efficiency and torque ripple corresponding to the current scheme, and the subscript max and min represent the maximum and minimum values of the corresponding variables. v_1 and v_2 are weight coefficients of two objectives, which depend on the will and preference of decision-makers, and are 0.55 and 0.45, respectively, in this paper.

In this way, three optimal motor schemes are selected and marked as red points in Figure 7. The motor scheme designed by the rated operation point optimization method is termed L1. The motor scheme designed by the proposed optimization method under UDDS is termed L2, and that optimized under HWFET is termed L3.

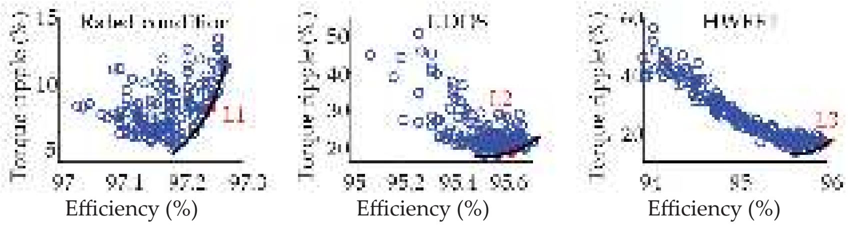

(**a**) (**b**) (**c**)

Figure 7. Motor optimization results under different working conditions. (**a**) Underrated condition. (**b**) Under UDDS. (**c**) Under HWFET. The blue dots are optimization solutions and black curves are Pareto optimal fronts.

The values of the optimal variables and objective performance of the three motor schemes are listed in Table 5. Furthermore, their performances under different driving cycles are shown in Figure 8. The area in the red dotted box in Figure 8 is defined as the sweet region with high efficiency and low torque ripple, where 92% < T_r < 98% and 5% < η < 30%. Figure 8a shows the performance evaluation of L1 and L2 under UDDS. It can be observed that the motor optimized at the rated point (L1) has about 40% of the operation points falling into the sweet region, and this ratio is about 90% for the motor optimized under UDDS (L2). Figure 8b shows the performance evaluation of L1 and L3 under HWFET. It can be seen that L1 has about 20% of the operation points falling into the sweet region, and this ratio is over 90% for the motor optimized under HWFET (L3). Therefore, it can be concluded that the sweet region can be expanded by the proposed system-scale optimization, considering driving cycles.

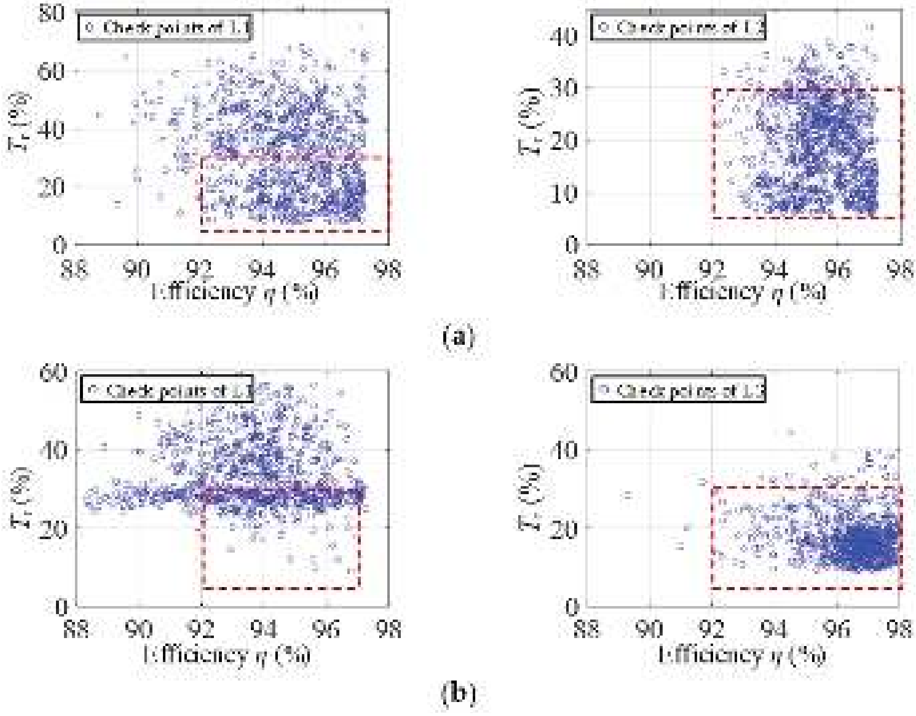

(**a**)

(**b**)

Figure 8. Performance evaluations of three motor schemes under different working conditions. (**a**) UDDS. (**b**) HWFET. The area in the red-dotted box is the sweet region.

Table 5. Objective performances and optimal variables.

		L1	**L2**	**L3**
	RPs	**I_P (A), P_{Fe} (W), P_{Cu} (W), T_r (%)**		
UDDS	1	29.8, 39.35, 53.25, 21	31.56, 34.24, 59.76, 14	none
	2	66.8, 355.11, 268, 35	53.37, 324.2, 171.24, 21	
	3	15.26, 178.09, 14, 42	16.32, 155.81, 16, 25	
	4	92.74, 80.5, 515.9, 10	96.55, 76.14, 559.18, 8	
	5	52.6, 154.5, 165.8, 15	55.18, 140.78, 182.7, 11	
HWFET	1	82.8, 381, 411.25, 38	none	82.75, 59.48, 325, 15
	2	71, 153.22, 303.4, 14		71.11, 76.4, 135.76, 10
	3	34.39, 327, 71.27, 28		34.39, 21.14, 296.67, 17
Rated		97.3, 284, 567.9, 7.91	100.75, 274, 608.92, 6.1	103, 268.32, 638, 9.26
Optimal results		$x_1, x_2, x_3, x_4, x_5, x_6, x_7$		
		0.8, 5.5, 1.5, 36, 14, 8750, 6500	0.8, 5.5, 1.7, 33.5, 14.5, 7854, 6280	0.8, 5.5, 1.7, 32.5, 14.5, 7525, 7500

4.2. Performance Evaluation by Experiments

To further prove the effectiveness of the optimization method described above, an IPMSM prototype is tested on the experimental platform shown in Figure 9, which is based on the dSPACE controller. The magnetic powder brake is used to provide various load torques, and a dynamic torque sensor is used to measure dynamic torque and speed. The target motor is used to power an A0 class pure EV, which adopts UDDS as the main test specification for emissions certification and fuel economy performance testing. Therefore, L2 shown in Table 5 is chosen to be tested as the prototype, which is optimized under UDDS. Meanwhile, the UDDS driving cycle is carried out to conduct the motor performance evaluation.

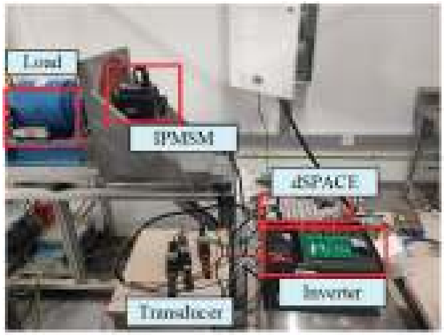

Figure 9. Experimentation platform of the IPMSM prototype.

Firstly, the no-load performance of the proposed IPMSM is tested, and the results are shown in Figure 10. In Figure 10a, it can be observed that the IPMSM can quickly follow the given speed during the starting or speed switching process. And Figure 10b shows the torque ripple at no load is less than ±0.2 N·m, which demonstrates the good design of cogging torque. From Figure 10c, it can be seen that its three-phase back EMFs are sinusoidal and symmetric. Moreover, the no-load current is smaller than 1A to provide no-load loss, as shown in Figure 10d. The changes in the above curves are consistent with the changes in motor working conditions, and the motor speed regulation effect shows the feasibility of the proposed control system.

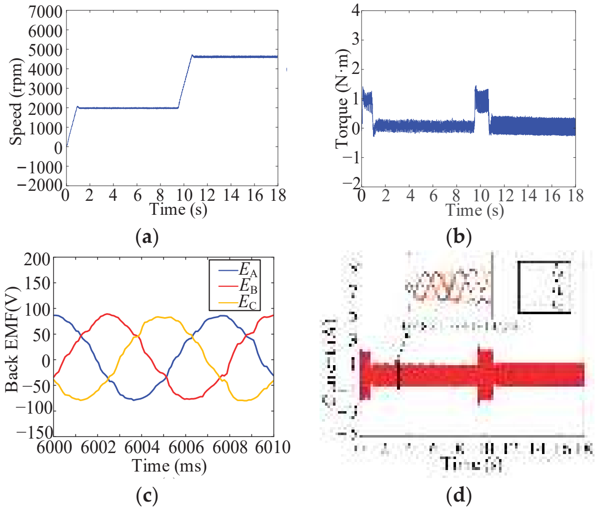

(**a**) (**b**)

(**c**) (**d**)

Figure 10. Experimental results at no load. (**a**) Speed. (**b**) Torque. (**c**) Back EMF. (**d**) Current.

Moreover, the loaded performance of the proposed IPMSM under MTPA and flux weakening control is tested, and the results are shown in Figure 11. It can be seen from Figure 11a,b that the motor driving modes can be switched from MTPA mode to flux weakening mode at about 5 s to expand its high-speed carrying capacity. With the flux weakening control under constant power operation, more negative i_d is applied to the IPMSM to achieve the same torque requirements as the MTPA shown in Figure 11c. In Figure 11a, it can be seen that the IPMSM can quickly follow the given speed at starting, speed switching, or load-changing working conditions. Moreover, the torque ripple at 2000 rpm with 5 N·m is about ±1 N·m; it is similar at 3500 rpm with 5 N·m; and it is about ±3 N·m at 3500 rpm with 15 N·m, which is shown in Figure 11b. Generally, torque ripples in the two modes are about 20%, which agrees with the results in Table 5. Furthermore, the three-phase currents shown in Figure 11c are sinusoidal and symmetric, which also shows the effectiveness of the proposed control system.

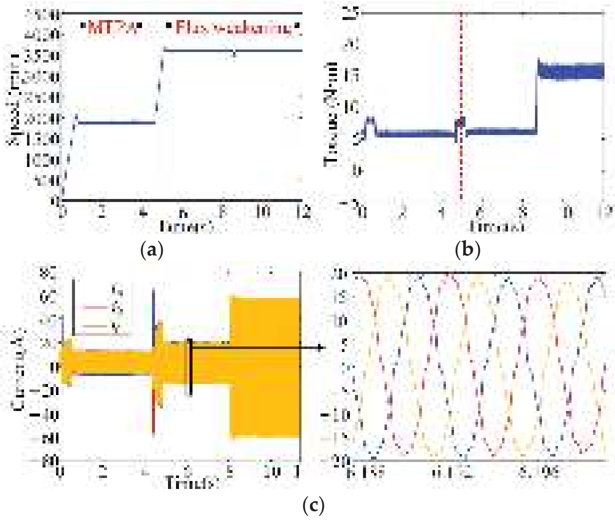

(**a**) (**b**)

(**c**)

Figure 11. Experimental results are loaded. (**a**) Speed. (**b**) Torque. (**c**) Current.

In order to further verify the effectiveness of the proposed optimization method, the prototype is tested under the five RPs of UDDS. The measured efficiency and torque ripple of the prototype with the proposed control system are compared with the calculated results from the optimization process, which are listed in Table 6. The calculated results of efficiency shown in Table 6 are obtained according to the data in Tables 2 and 5, where the input power is calculated by $2\pi nT/60$ from Table 2 and the output power is approximately equal to the sum of the input power, P_{Fe}, and P_{Cu} in Table 5. Meanwhile, the calculated results of torque ripple shown in Table 6 are the same as T_{r} in Table 5. It can be observed that the measured results are almost in accordance with the optimized results. The error of efficiency is within 8%, and the maximum error of torque ripple is 20%. These errors are mainly due to the inaccurate estimation of losses and vibrations caused by mechanical factors such as wind wear and bearing in simulations. In spite of this, it can still greatly reflect the effectiveness of the proposed system-scale optimization design method, considering driving cycles.

Table 6. Optimization parameters of the investigated IPMSM.

L2	RPs	Efficiency (%)			Torque Ripple (%)		
		Calculated Result	Experimental Result	Error *	Calculated Result	Experimental Result	Error *
UDDS	1	95.7	91	5.15	14	15	6.67
	2	95.7	89	7.59	21	20	−5
	3	95.6	89	7.41	25	23	−8.7
	4	94.4	89	6.07	8	10	20
	5	97.2	91	6.83	11	13	15

* Error = (Calculated result-Experimental result)/Experimental result.

5. Conclusions

In this paper, a system-scale multi-objective optimization methodology for driving motors based on the clustering technique under different operating conditions is proposed for electric vehicle applications. The clustering approach has been introduced to identify energy weights and RPs in the torque-speed profile for two vehicle driving cycles. To evaluate the effectiveness of the system-scale optimization design of the driving motor, a comparative study has been carried out based on the semianalytical efficiency model and torque model of IPMSMs, where the motor was optimized for UDDS, HWFET, and the rated operating point. Finally, a prototype of IPMSM with an MPTA-flux weakening controller was investigated to verify the proposed method. From the discussion, the following conclusions could be drawn:

First, compared with the optimization design under the rated operation point, the solution from the proposed optimization considering driving cycles has a larger sweet region with higher efficiency and lower torque ripple.

Second, the control parameters are considered in the proposed system-scale optimization as well as the motor parameters, which can ensure the system's dynamic performances and are valuable for engineering batch production. Third, the proposed clustering optimization of driving motors considering inverter control strategy could well be applied for the rapid development of serialized motors in other applications, e.g., ship propulsion motors and robot motors.

The future work will be extended to more structural forms of motors with more diverse control strategies, e.g., axial-flux PMSM with direct torque control. Moreover, the multidisciplinary approach for system-scale optimization will be investigated in the following, which will consider the effects of thermal and mechanical factors from the perspective of practical engineering applications.

Author Contributions: Resources, S.Y.; Writing—original draft, J.B.; Writing—review & editing, J.D. All authors have read and agreed to the published version of the manuscript.

Funding: This research was funded by the Natural Science Foundation of China, grant number 52277065, and the National Key R&D Program of China, grant number 2020YFA0710500.

Institutional Review Board Statement: Not applicable.

Informed Consent Statement: Not applicable.

Data Availability Statement: Not applicable.

Conflicts of Interest: The authors declare no conflict of interest.

Nomenclature

B_{r}	Radial magnetic density component	P_{loss}	Motor power loss
B_{t}	Tangential magnetic density component	P_{out}	Motor output power
d	Total level number	P_{Fe}	Iron loss
f	Magnetic field alternates frequency	P_{Cu}	Copper loss
i_s	Stator phase current	R_{s}	Phase resistance
J	Moment of inertia	T_{s}	Sampling period
k_{s}	Fill factor of winding	T_{r}	Motor torque ripple
K_{c}	Eddy current loss coefficient	u_{lim}	Motor phase voltage limitation
K_{e}	Additional loss coefficient	w	Energy weights
K_{y}	Hysteresis loss coefficient	W'_{m}	Co-energy
K_{sp}	Proportion coefficient of speed controller	W_{m}	Stored energy
K_{si}	Integration coefficient of speed controller	z_i	Data point of sample i
$K_{\mathrm{ip\_d}}$	Proportion coefficient of d-axis current controller	$l_i^{(t)}$	Centroid of sample i in the t^{th} iteration
$K_{\mathrm{ii\_d}}$	Integration coefficient of d-axis current controller	$S_i^{(t)}$	Cluster of sample i in the t^{th} iteration
$K_{\mathrm{ip\_q}}$	Proportion coefficient of q-axis current controller	$p_{\mathrm{O}(i)}$	Average motor performance of factor O at level i
$K_{\mathrm{ii\_q}}$	Integration coefficient of q-axis current controller	δ	Angle between the current vector and the d-axis
n_{max}	Motor maximum speed	θ	Rotor position
n_{N}	Motor rated speed	λ	Flux linkage
p	Pole pair number	λ_{pm}	Permanent magnet flux linkage
p_{t}	Overall mean of motor performance data	Ω	Rotor mechanical angular velocity

References

1. Cui, W.; Ren, L.; Zhou, J.; Zhang, Q. A new IPMSM with Hybrid rotor structure for electrical vehicle with reduced magnet loss. *IEEE Trans. Magn.* **2022**, *58*, 1. [CrossRef]
2. Geethanjali, S.; Vijayakumar, K. Testing and implementation of dual way DC-DC converter for electric vehicle power train system. *IEICE Electron. Express* **2022**, *19*, 20220343. [CrossRef]
3. Zhao, X.; Kou, B.; Huang, C.; Zhang, L. A reverse-salient permanent magnet synchronous motor for electric vehicles considering operating conditions. *IEEE Trans. Energy Convers.* **2023**, *38*, 262–272. [CrossRef]
4. Xu, Y.; Ai, M.; Xu, Z.; Liu, W.; Wang, Y. Research on interior permanent magnet synchronous motor based on performance matching of electric bus. *IEEE Trans. Appl. Supercond.* **2021**, *31*, 8. [CrossRef]
5. Liu, J.; Liang, Y.; Yang, P. Research on novel flat wire transposed winding of pmsm for electric vehicle. *IEEE Trans. Transp. Electrif.* **2023**, *9*, 771–781. [CrossRef]
6. Sun, X.; Shi, Z.; Cai, Y.; Lei, G.; Guo, Y.; Zhu, J. Driving-Cycle-oriented design optimization of a permanent magnet hub motor drive system for a Four-Wheel-Drive electric vehicle. *IEEE Trans. Transp. Electrif.* **2020**, *6*, 1115. [CrossRef]
7. Sun, X.; Hu, C.; Zhu, J.; Wang, S.; Zhou, W.; Yang, Z.; Lei, G.; Li, K.; Zhu, B.; Guo, Y. MPTC for PMSMs of EVs with multi-motor driven system considering optimal energy allocation. *IEEE Trans. Magn.* **2019**, *55*, 6. [CrossRef]
8. Chen, Q.; Fan, X.; Liu, G.; Xu, L.; Xu, M. Regulation of high-efficiency region in permanent magnet machines according to a given driving cycle. *IEEE Trans. Magn.* **2017**, *53*, 1. [CrossRef]
9. Tian, L.; Wu, L.; Huang, X.; Fang, Y. Driving range parametric analysis of electric vehicles driven by interior permanent magnet motors considering driving cycles. *CES Trans. Electr. Mach. Syst.* **2019**, *3*, 377–381. [CrossRef]
10. Fatemi, A.; Demerdash, N.A.O.; Nehl, T.W.; Ionel, D.M. Large-scale design optimization of PM machines over a target operating cycle. *IEEE Trans. Ind. Appl.* **2016**, *52*, 3772–3782. [CrossRef]
11. Sarigiannidis, A.G.; Beniakar, M.E.; Kladas, A.G. Fast adaptive evolutionary PM traction motor optimization based on electric vehicle drive cycle. *IEEE Trans. Veh. Technol.* **2017**, *66*, 5762–5774. [CrossRef]
12. Polat, M.; Yildiz, A.; Akinci, R. Performance analysis and reduction of torque ripple of axial flux permanent magnet synchronous motor manufactured for electric vehicles. *IEEE Trans. Magn.* **2021**, *57*, 1. [CrossRef]

13. Xue, Z.; Li, H.; Zhou, Y.; Ren, N.; Wen, W. Analytical prediction and optimization of cogging torque in surface-mounted permanent magnet machines with modified particle swarm optimization. *IEEE Trans. Ind. Electron.* **2017**, *64*, 9795–9805. [CrossRef]
14. Jung, S.-W.; Yoon, J.; Choi, K.; Bang, J.; Bong, U.; Hahn, S. Comparative design study of HTS synchronous motor with inner and outer rotor type based on multi-objective optimization. *IEEE Trans. Appl. Supercond.* **2022**, *32*, 6. [CrossRef]
15. Liu, X.; Hu, C.; Li, X.; Gao, J.; Huang, S. An Online data-driven multi-objective optimization of a permanent magnet linear synchronous motor. *IEEE Trans. Magn.* **2021**, *57*, 7. [CrossRef]
16. Cho, S.-K.; Jung, K.-H.; Choi, J.-Y. Design optimization of interior permanent magnet synchronous motor for electric compressors of air-conditioning systems mounted on EVs and HEVs. *IEEE Trans. Magn.* **2018**, *54*, 1–5. [CrossRef]
17. Zhao, W.; Yang, Z.; Liu, Y.; Wang, X. Analysis of a Novel surface-mounted permanent magnet motor with hybrid magnets for low cost and low torque pulsation. *IEEE Trans. Magn.* **2021**, *57*, 1. [CrossRef]
18. Diao, K.; Sun, X.; Lei, G.; Bramerdorfer, G.; Guo, Y.; Zhu, J. System-level robust design optimization of a switched reluctance motor drive system considering multiple driving cycles. *IEEE Trans. Energy Convers.* **2021**, *36*, 348–357. [CrossRef]
19. Carraro, E.; Morandin, M.; Bianchi, N. Traction PMASR motor optimization according to a given driving cycle. *IEEE Trans. Ind. Appl.* **2016**, *52*, 209. [CrossRef]
20. Bernard, N.; Dang, L.; Moreau, L.; Bourguet, S. A Pre-sizing method for salient pole synchronous reluctance machines with loss minimization control for a small urban electrical vehicle considering the driving cycle. *Energies* **2022**, *15*, 9110. [CrossRef]
21. Yamazaki, K.; Seto, Y. Iron loss analysis of interior permanent-magnet synchronous motors-variation of main loss factors due to driving condition. *IEEE Trans. Ind. Appl.* **2016**, *42*, 1045. [CrossRef]
22. Lei, G.; Wang, T.; Zhu, J.; Guo, Y.; Wang, S. System-level design optimization method for electrical drive systems—Robust approach. *IEEE Trans. Ind. Electron.* **2015**, *62*, 4702–4713. [CrossRef]
23. Zhou, X.; Zhu, X.; Wu, W.; Xiang, Z.; Liu, Y.; Quan, L. Multi-objective optimization design of variable-saliency-ratio PM motor considering driving cycles. *IEEE Trans. Ind. Electron.* **2021**, *68*, 6516. [CrossRef]
24. Qiu, H.; Cui, S.; Wang, S.; Wang, Y.; Feng, M. A Clustering-Based optimization method for the driving cycle construction: A case study in fuzhou and Putian, China. *IEEE Trans. Intell. Transp. Syst.* **2022**, *23*, 18681. [CrossRef]
25. Salameh, M.; Brown, I.P.; Krishnamurthy, M. Fundamental evaluation of data clustering approaches for driving Cycle-Based machine design optimization. *IEEE Trans. Transp. Electrif.* **2019**, *5*, 1395. [CrossRef]
26. Chen, H.; Liu, X.; Demerdash, N.A.; El-Refaie, A.M.; Chen, Z.; He, J. Computationally efficient optimization of a Five-Phase Flux-Switching PM machine under different operating conditions. *IEEE Trans. Veh. Technol.* **2019**, *68*, 6495. [CrossRef]
27. Lai, C.; Feng, G.; Iyer, K.L.V.; Mukherjee, K.; Kar, N.C. Genetic Algorithm-Based current optimization for torque ripple reduction of interior PMSMs. *IEEE Trans. Ind. Appl.* **2017**, *53*, 4493–4503. [CrossRef]
28. Jia, H.; Cheng, M.; Hua, W.; Zhao, W.; Li, W. Torque ripple suppression in flux-switching PM motor by harmonic current injection based on voltage Space-Vector modulation. *IEEE Trans. Magn.* **2020**, *46*, 1527–1530. [CrossRef]
29. Zhang, R.; Yin, Z.; Du, N.; Liu, J.; Tong, X. Robust Adaptive current control of a 1.2-MW Direct-Drive PMSM for traction drives based on internal model control with disturbance observer. *IEEE Trans. Transp. Electrif.* **2021**, *7*, 1466–1481. [CrossRef]
30. De Klerk, M.L.; Saha, A.K. A Comprehensive Review of advanced traction motor control techniques suitable for electric vehicle applications. *IEEE Access* **2021**, *9*, 125080–125108. [CrossRef]
31. Deng, T.; Su, Z.; Lin, J.; Tang, P.; Chen, X.; Liu, P. Advanced angle field weakening control strategy of permanent magnet synchronous motor. *IEEE Trans. Veh. Technol.* **2019**, *68*, 3424–3435. [CrossRef]
32. Alzayed, M.; Chaoui, H.; Farajpour, Y. Dynamic direct voltage MTPA current sensorless drives for interior PMSM-Based electric vehicles. *IEEE Trans. Veh. Technol.* **2023**, *72*, 3175–3185. [CrossRef]
33. Song, C.-H.; Song, I.-S.; Shin, H.-S.; Lee, C.-H.; Kim, K.-C. A Design of IPMSM for High-Power electric vehicles with wide-field-weakening control region. *IEEE Trans. Magn.* **2022**, *58*, 2. [CrossRef]
34. Yuan, S.; Du, J.; Wei, Y. Optimization of Permanent Magnet Machine for Electric Vehicles Considering the Control Strategy and Inverter. In Proceedings of the 2020 23rd International Conference on Electrical Machines and Systems (ICEMS), Melaka, Malaysia, 24–27 November 2020. [CrossRef]
35. He, J.; Li, G.; Zhou, R.; Wang, Q. Optimization of Permanent-Magnet spherical motor based on taguchi method. *IEEE Trans. Magn.* **2020**, *56*, 2. [CrossRef]
36. Abdo, Q.M.; Ewad, H.; Mohamed, K.A. Optimized PID Controller for Single Area Thermal Power System Based on Time Varying Acceleration Coefficients Particle Swarm optimization. In Proceedings of the 2020 International Conference on Computer, Control, Electrical, and Electronics Engineering, Khartoum, Sudan, 26 February–1 March 2021; pp. 1–5. [CrossRef]
37. Falch, L.; de Silva, C.W. Improvement of VIKOR method with application to Multi-Objective design problems. *Int. J. Inf. Technol. Decis. Mak.* **2023**, *22*, 777–802. [CrossRef]

machines

MDPI

Article

Increased Dynamic Drivetrain Performance by Implementing a Modular Design with Decentralized Control Architecture

Niels Divens [1,*], Théo Tuerlinckx [1], Bernhard Westerhof [1], Kurt Stockman [2,3], David van Os [2,3] and Koen Laurijssen [1]

[1] MotionS Core Lab, Flanders Make vzw, 3001 Leuven, Belgium; theo.tuerlinckx@flandersmake.be (T.T.); bernhard.westerhof@flandersmake.be (B.W.); koen.laurijssen@flandersmake.be (K.L.)
[2] Department of Electromechanical, Systems and Metal Engineering, Ghent University, 9052 Gent, Belgium; kurt.stockman@ugent.be (K.S.); david.vanos@ugent.be (D.v.O.)
[3] MIRO Core Lab, Flanders Make vzw, 9052 Gent, Belgium
* Correspondence: niels.divens@flandersmake.be

Abstract: This paper assesses the energy consumption, control performance, and application-specific functional requirements of a modular drivetrain in comparison to a benchmark drivetrain. A decentralised control architecture has been developed and validated using mechanical plant models. Simscape models have been validated with data from an experimental setup including an equivalent modular and benchmark drivetrain. In addition, the control strategy has been implemented and validated on the experimental setup. The results prove the ability of the control strategy to synchronize the motion of the different sliders, resulting in crank position tracking errors below 0.032 radians on the setup. The model and experimental data show an increased performance of the modular drivetrain compared to the benchmark drivetrain in terms of energy consumption, control performance, and functional requirements. The modular drivetrain is especially advantageous for machines running highly dynamic motion profiles due to the reduced inertia. For such motion profiles, an increased position tracking of up to 84% has been measured. In addition, it is shown that the modular drivetrain root mean square (RMS) torque is reduced with 32% compared to the benchmark drivetrain. However, these mechanical energy savings are partly counteracted by the higher motor losses seen in the modular drivetrain, resulting in potential electrical energy savings of around 29%.

Keywords: modular drivetrain; drivetrain performance; energy consumption

Citation: Divens, N.; Tuerlinckx, T.; Westerhof, B.; Stockman, K.; van Os, D.; Laurijssen, K. Increased Dynamic Drivetrain Performance by Implementing a Modular Design with Decentralized Control Architecture. *Machines* **2023**, *11*, 1036. https://doi.org/10.3390/machines11111036

Academic Editors: Kan Liu and Wei Hu

Received: 2 October 2023
Revised: 14 November 2023
Accepted: 17 November 2023
Published: 20 November 2023

1. Introduction

In the manufacturing industry, more stringent requirements are continuously set on operating machines and systems as a way to leverage manufacturers' competitive advantages. Productivity, reliability, energy consumption, and flexibility are frequently recurring key performance indicators (KPI) for designing, developing, and selecting machines. The concept of modularity has been proposed [1–3] as a potential method to design and build machines with increased operational performance and customisation potential. The demand for easy customisation requires more flexibility in machine configuration. The literature has shown that modularity has benefits when it comes to developing more flexible machines [4,5]. A module-based approach can further reduce engineering and time costs [6], as scaling the system does not require a detailed redesign, instead relying on the addition or removal of modules built from standardized components. This paper adheres to the following definition of modularity [7]: the degree to which a system's components may be separated and recombined, often enhancing the system's scalability, flexibility, and variety of use cases. The unique set of separated and recombined components is called a module.

In [2], the authors showed that for direct drive systems a modular approach can result in increased operational efficiency. Furthermore, controller reference tracking outperformed the benchmark case, indicating the potential to push machines to higher operating speeds and thereby obtain an increased production rate. The benefits of introducing modularity have been illustrated for other applications as well, such as cranes [8], wind turbines [9], and electric vehicles [10,11]. For crane applications, ref. [8] showed that load-sharing electrical drive configurations result in a more uniform load distribution between motors and have the ability to eliminate crane skew. The grid connection of large wind turbines [9] can benefit from reduced capacitor voltage ripple when connected to a hybrid modular multilevel converter. For electric vehicle applications, ref. [11] demonstrated low harmonic distortion and high efficiency when implementing a modular multilevel topology using power electronics transformers.

This research paper aims to assess the performance of application cases for modular drivetrains typically used in tufting, weaving, and stamping machines. These machines often rely on the conversion of rotational motion to translational motion by means of bar and/or slider–crank mechanisms, which typically introduce a variable inertia. In [12], the authors demonstrated the robust performance of a slider–crank mechanism driven by a permanent magnet synchronous machine (PMSM) with an adaptive controller. However, this paper is limited to the motion control of a single slider–crank mechanism. Therefore, a modular drivetrain concept with six motors and slider-crank mechanisms (modules) is used as a test case to evaluate the performance of a decentralized control architecture for a modular drivetrain. Each independent drivetrain module executes a local control strategy without any information on the neighbouring modules. In addition, a benchmark (non-modular) drivetrain is developed in detail as a reference for a performance comparison. An experimental setup including the modular and benchmark drivetrain was designed and built, allowing the operational performance of the modular drivetrain system to be experimentally compared with the benchmark system.

Industrial weaving machines typically contain different functional components operating at high speeds, and each of their respective motion patterns must be synchronized to meet the machines' functional requirements. Traditionally, these machines have a single motor that is mechanically linked to the machine load through bar linkages, cams, etc. This is equivalent to the benchmark drivetrain presented in this paper. The sliders of this benchmark drivetrain are inherently synchronized (neglecting the non-rigidity of crankshaft) by the mechanical design; ref. [13] already showed that the application of programmable controllers and electronic drive regulators can improve the operational efficiency and reliability of multi-motor machines in the textile industry. Modularity in drivetrain systems furthermore implies modifications in the control architecture. The motions of each individual module need to be electronically synchronized with each other in order to achieve the required motion of the load without causing unnecessary internal stresses or damage to the system. This topic has been discussed elaborately in previous research [14–19] for different kind of applications. In [16], for example, the authors applied the total sliding mode control method in order to synchronize multiple asynchronous machines. However, the above research focuses on centralized control architectures for synchronizing the modules, introducing the disadvantage of a single point of failure; if the controller fails, the entire drivetrain system fails to operate. For example, ref. [19] presented a speed control method for a dual PMSM connected in parallel and regulated with a single inverter. In [20], the author investigated a decentralised control strategy for synchronized control of multi-motor drive systems; however, his research was limited to a simulation environment and was not experimentally validated. Furthermore, the case of mechanically coupled motor loads, which are often present in textile machines, was not investigated. In contrast, the contributions of the present research include a performance analysis of a drivetrain system with mechanically linked loads. In practice, the six sliders are connected with an aluminum bar as the load. With respect to drivetrain modularization, this poses more stringent requirements on drivetrain control performance in order to avoid mechanical failures during drivetrain operation. Assuming a rigid system, multiple actuators provide control with a single degree of freedom. Along with implementing a modular mechanical design of the drivetrain system, this research further aims to implement a modular and scalable masterless control architecture. This paper describes a decentralised control architecture, aiming to avoid a single point of failure and allow continuous drivetrain operation in the event that the controller of a single module fails. The local module control strategy consists of cascaded proportional–integral (PI) loops and a feed-forward term. The dynamic drivetrain model in Matlab Simscape [21] allows this control strategy to be safely validated in a virtual environment before implementing and testing it on the experimental setup. To the best of our knowledge, introducing modularity in terms of both mechanical design and control architecture on a slider–crank drivetrain system with coupled loads represents a novel research approach.

The remainder of this paper is organised as follows. Section 2 introduces the theory, models, and methods used to design, develop, and implement the modular slider–crank drivetrain on both the system and component levels. Section 2.5 elaborates the design of the experimental setup and planned experiments used to assess the drivetrain performance. The model validation and drivetrain performance assessment are then discussed in Section 3, while Section 4 provides a final summary.

2. Materials and Methods

This section first elaborates on the methodology used to compare and assess the different drivetrain architectures. Second, the the concepts underlying the two drivetrain architectures under investigation are described. Third, the modelling of the drivetrain architectures and the control architecture and strategy are explained. Lastly, the design of the experimental setup is described in detail and the drivetrain KPIs are defined.

2.1. Assessment Methodology

The comparison of the drivetrains was executed following the principles illustrated in Figure 1. In [22], this methodology was explained and applied for the assessment of modular drivetrains in a simulation environment. Multiple drivetrain architectures have been conceptually designed and modelled. An architecture can consist of Z physical models, representing, for example, a slider–crank mechanism. The detailed simulation parameters are implemented in the simulation model. These may include physical component parameters, controller parameters, environmental conditions, etc. The simulation models are run with a certain load profile that defines the motion and external forces applied to the system. Furthermore, a set of key performance indicators are defined; using the output of the simulation models, the KPI values are calculated for the different drivetrain architectures, allowing a performance assessment and comparison to be carried out. Figure 1 focuses on a model-based performance assessment approach. This paper applies a similar methodology, using data from experimental setups instead of simulation models.

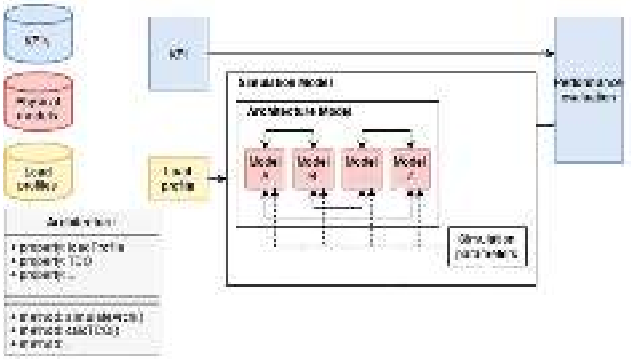

Figure 1. Assessment methodology.

2.2. Drivetrain Architectures

The definition of the modular drivetrain concept is based on the application of an industrial weaving (tufting) machine [1]. These machines make use of multiple slider–crank and/or multi-link bar mechanisms in parallel to convert rotational motion to translational motion on the load. In this case, the load is a uniformly-distributed mass connecting all of the sliders. Traditionally, these slider–crank mechanisms are connected by a crankshaft and driven by a single rotational power source, e.g., an electric motor. Figure 2 illustrates a simplified system architecture of this benchmark drivetrain with six slider–crank mechanisms. In [1], a novel modular alternative to this benchmark drivetrain was introduced, as shown schematically in Figure 2. This modular drivetrain architecture contains six slider–crank mechanisms, with the sliders all connected to a single load. This load is identical to the one in the benchmark drivetrain; however, each slider–crank mechanism is driven by a separate electric motor. Hence, the modular drivetrain system has six independently powered and controlled modules moving the load. This paper evaluates and compares the performance of both the benchmark and modular drivetrains by means of a dynamic mechanical model developed in Mathworks Simscape and an experimental test setup.

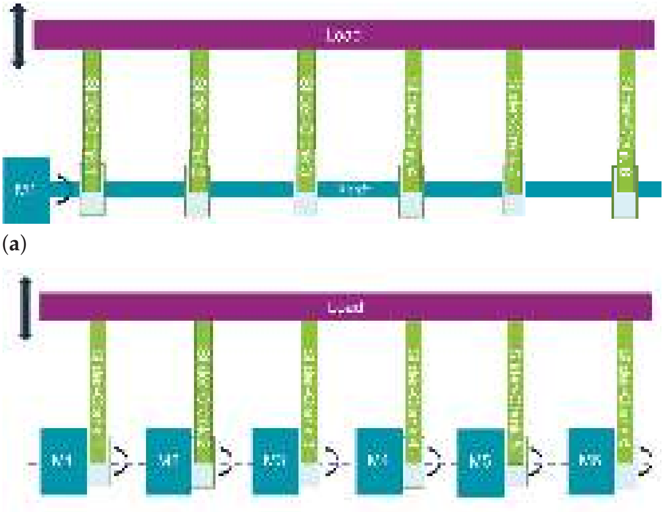

(**a**)

(**b**)

Figure 2. Drivetrain architectures: (**a**) benchmark and (**b**) modular.

2.3. Drivetrain Models

The two system architectures depicted in Figure 2 were both modelled in the Matlab Simscape (R2019a) environment. Blocks from the Simscape foundation library were used, and custom Simscape blocks were developed as well. In order to build the models of the above-mentioned drivetrain systems, component models of the electric motor, slider–crank mechanism, and inertial load are required. The benchmark system architecture additionally requires modelling of the crankshaft. The different component models are described in more detail below.

The permanent magnet synchronous machine (PMSM) and its drive were simplified as a first-order system with rotational inertia and output torque saturated at the motor peak torque curve. In order to add a minimum of motor dynamics, a discrete low-pass filter was implemented. The transfer function for this filter allows the electromagnetic dynamic performance of the modelled motor to be limited by filtering the motor torque target T_{Tgt} generated by the controller:

$$G = \frac{T_{Act}}{T_{Tgt}} = \frac{(t_s/\tau)z^{-1}}{1 + (t_s/\tau - 1)z^{-1}} \tag{1}$$

where T_{Act} is the actual torque generated by the electric motor. The time constant τ is chosen such that the filter cutoff frequency (-6 dB) equals 800 Hz. Furthermore, the motor resolver data is modelled to include a communication delay and measurement noise. The delay is simple signal time delay between the resolver and the motor controller feedback loop (Section 2.4). White noise with a constant power spectral density (PSD) was superimposed on the crank resolver signal. The delay and noise values were fitted using experimental data of the setup, and are listed in Table 1.

A separate Matlab script based on the power loss model of the PMSM, inverter, and cables was used to estimate the consumed electrical energy from the grid based on the measured (or simulated) motor speed and torque. The power loss model of the PMSM was defined by first establishing the current and voltage equations of a PMSM depending on the torque and speed setpoint [23], allowing efficiency maps to be computed by taking into account iron loss, copper loss, and mechanical loss [24] and validation to be carried out based on the efficiency maps provided by the the supplier. The motor performance characteristics were obtained from the datasheets of the PMSM motors used in the physical setup; more details can be found in Section 2.5. The cable Joule losses were directly computed from the motor currents and cable resistance. The inverter model was simplified through a load-dependent efficiency curve that was tuned to match the nominal loss from the suppliers' datasheets.

In the benchmark drivetrain, the PMSM is connected to a crankshaft, as depicted in Figure 2. The crankshaft is driven by the electric motor, and connects the cranks of the six slider–crank mechanisms. The shaft was modelled based on the rotational stiffness, damping, and inertia.

While the Simscape foundation library already collects a large set of component models, a detailed model for the slider–crank mechanism was lacking. First, the default Simscape slider–crank block does not include friction. Second, it does not include the effect of the position of the centre of gravity (Cog) of the crank and rod on the dynamic behavior. Third, gravity itself is unmodelled behaviour in the default Simscape block. Thus, the slider–crank mechanism [25] was analytically modelled and implemented in a custom Simscape block. The analytical equations included the kinematic and dynamic relationships between the rotational motion of the crank and the translational motion of the end of the rod (i.e., the slider) while taking into account the variable inertia effects. Second, the vertical and horizontal forces at the crankshaft, crank rod, and rod–load connections were calculated while taking into account the gravitational effects. All equations were derived based on the slider–crank free-body diagram depicted in Figure 3, and can be found in Appendix A.

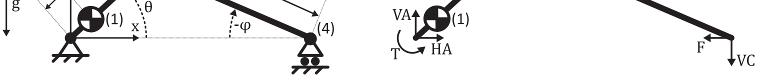

Figure 3. Slider–crank free-body diagram.

Table 1. Component properties.

Component	Parameter	Value	Units
AM8063L motor	Nominal power	4.97	kW
	Nominal torque	33.9	Nm
	Peak torque	111	Nm
	Torque constant	3.33	Nm/A
	Rotor inertia	29.0	$kg \times cm^2$
AM8051F motors	Nominal power	1.52	kW
	Nominal torque	5.8	Nm
	Peak torque	17.7	Nm
	Torque constant	1.77	Nm/A
	Rotor inertia	2.24	$kg \times cm^2$
Motor resolver	delay	1.1	ms
	Noise sample time	10^{-5}	s
	Noise PSD	10^{-20}	Mag^2/Hz
Crankshaft	Inertia	1.208×10^{-3}	$kg \times m^2$
	Length	1.96	m
	Torsional stiffness	3.4×10^3	Nm/rad
	Torsional damping	0.02	$Nm \times s/rad$
Slider-crank	Crank length	20	mm
	Rod length	95	mm
	Crank inertia	12	$kg \times cm^2$
	Rod inertia	28	$kg \times cm^2$
	Crank mass	1.04	kg
	Rod mass	0.77	kg
	Slider friction coefficient	0.45	/
	Crank Coulomb friction	0.77	Nm
	Crank viscous friction	0.03	$Nm \times s/rad$
Load	Mass	4.42	kg
	Length	1.8	m
	Segment stiffness	9.55×10^5	N/m
	Segment damping	8.29	$N \times s/m$

The load consisted of an aluminium bar connecting the six sliders of the slider–crank mechanisms. For modelling purposes, the load was divided into five segments, with each located in between two slider–cranks. The segments were modelled using the lateral bending stiffness and damping along with the translational mass between the different sliders. The load's total mass was determined on the basis of the mechanical CAD model and the lateral moment of inertia ($I_y = 51,739\ mm^4$), which is necessary in order to calculate the load segment stiffness. For each segment, the stiffness was separately calculated using the following equation:

$$K = \frac{1}{2} \times \frac{48 \times E \times Iy}{2 \times L_{segment}^3} \tag{2}$$

where E is the Young's modulus, I_y is the moment of inertia, and $L_{segment}$ is the length of the segment. The parameter values of the load are summarized in Table 1.

Additionally, static and kinetic frictions were taken into account in the model using a Simscape rotational friction element for the crank bearings and the translational friction for the slider carriage. The slider carriage friction model additionally took into account the total normal force acting on the slider carriage, including the gravitational force and the dynamic vertical force on the rod–load connection computed by the model of the slider–crank mechanism. The friction coefficients were determined by parameter optimization using experimental data from the setup (see Section 2.5), and are summarized in Table 1.

Figure 4 schematically shows how the modular drivetrain system model was built using the component models. The figure only shows two of the six modules. The benchmark drivetrain system model was built up equivalently, with the additional inclusion of a crankshaft model connecting all six cranks.

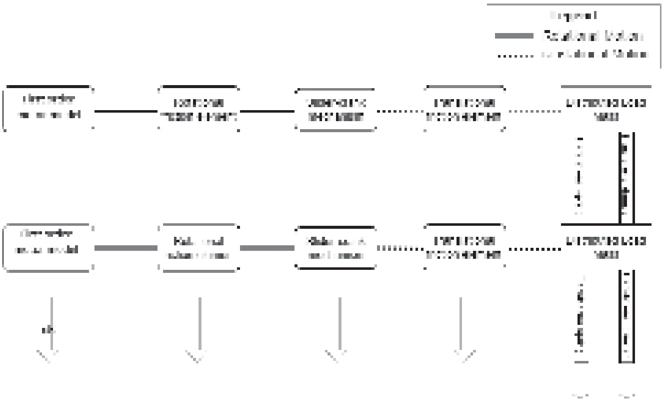

Figure 4. Modular drivetrain mechanical system model.

The main model parameters were defined from the component datasheets, and the friction parameters were tuned and validated by comparison with measurements taken on the physical setup. Table 1 provides the parameters values.

The mechanical system plant models of the benchmark and modular drivetrain were utilized to develop and validate the drivetrain control strategy, which is discussed in Section 2.4 below.

2.4. Control Architecture and Strategy

The sliders of the benchmark drivetrain are inherently synchronized by the presence of the crankshaft, which mechanically connects all six cranks. However, the modular drivetrain does not have mechanically linked slider–crank mechanisms, and as such the sliders have to be electronically synchronized through adequate control of all six motors.

Previous research on control methods has shown good performance for multi-drive systems; however, the control architectures were largely implemented in a centralized manner [8,14–18], limiting the modularity to the mechanical design of the system. In this research, a decentralised control architecture for the modular drivetrain has been developed, with each motor being controlled locally. In this way, the concept of drivetrain modularity is further extended to the drivetrain control. In addition, removing the master controller scheme eliminates it as a potential single point of failure. A schematic of this control architecture is visualized in Figure 5. Each motor is controlled by a local controller with a sample time of 4 kHz. All local controllers act towards the same reference position and speed. This decentralised control architecture allows for increased system reliability and fault tolerance while maintaining synchronization of the six sliders.

Both the benchmark and modular drivetrains were implemented with an identical local control strategy, which is visualized in Figure 6. While in the benchmark drivetrain only a single motor needs to be controlled, the modular drivetrain requires synchronized control of six independent motors. The applied control strategy is composed of the two main components depicted in Figure 6. First, a cascaded proportional integrator (PI) loop contains two PI feedback loops. This includes a positional PI controller which aims to track a rotational reference position for the motor. The output of this position controller is an input for the second PI loop, which aims to track a reference velocity. The proportional term of this velocity feedback loop is equivalent to the derivative term of a traditional PID feeback loop. Both PI loops include an anti-windup mechanism. The cascaded PI loop (position + velocity) was chosen over a traditional PID position controller because it enables sharing of the control parameter tuning between continuous and reciprocating motion (see Section 2.6 for definitions of continuous and reciprocating motion). For both drivetrains, the control parameters of the cascaded PI loop were optimized using the model-based PI tuning method. The control performance for each setup was numerically optimized for position and velocity tracking during high-speed operation.

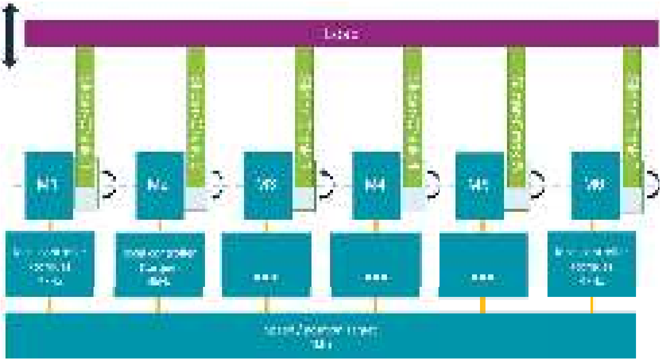

Figure 5. Modular control architecture.

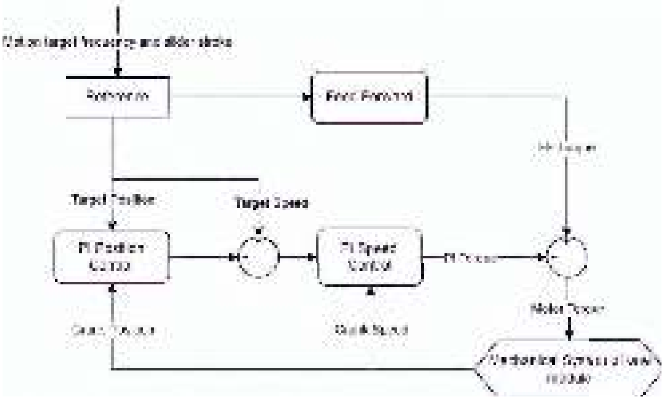

Figure 6. Local control strategy.

Second, a feed-forward controller based on the analytic equations of the slider–crank mechanism (see Appendix A) was implemented. This block outputs an estimation of the required motor torque for a certain reference crank position, velocity, acceleration, and slider–crank properties. The slider–crank properties include the dimensions, weight, inertia, and frictional characteristics of the mechanism. The exact properties and their values are listed in Table 1. The frictional characteristics were empirically defined using the experimental data from the setup, which is described below and is equivalent to the inverse of the slider–crank model described in Section 2.3.

The target motion time series is defined by a motion profile type, target slider frequency (number of slider cycles/second), and target stroke length (only applicable for the reciprocating motion type). Using the above two inputs, the reference block in Figure 6 computes the target crank position, velocity, and acceleration time traces for the different motion profile types under investigation. More information on these time-dependent motion profiles can be found in Section 2.6.

It is important to note that for the modular drivetrain, this control strategy needs to be applied in a decentralized manner; hence, each motor has its own local independent controller acting towards the same reference, resulting in a total of six active controllers. Such a decentralized control architecture eliminates the single point of failure and allows the system to remain functional (potentially with limited performance) in the event that a motor or its respective controller fails.

The combination of the mechanical plant models and control algorithm in the Matlab Simscape environment allows the performance of both the modular and non-modular (benchmark) system architectures to be virtually evaluated. Next, we aimed to further validate these findings with experimental results. Therefore, an experimental setup was developed and built, which is described in the next section.

2.5. Design of Experimental Setup

A mechanical design and component selection process was executed based on the conceptual diagrams of the system architectures visualized in Figure 2.

The setup is visualized in Figure 7 and its operation is demonstrated in the video provided in [26]. Both the modular and benchmark drivetrain were installed on the same Welda test bed table and rotated in opposite directions, resulting in the inertial forces of both setups being counterbalanced, thereby reducing the vibrations and swinging of the table. However, this has the negative consequence that a single drivetrain cannot be operated individually at high speeds, inhibiting the experimental evaluation of the maximum operating speed of the fastest drivetrain. The Welda table was installed with multiple T-slot plates, allowing for easy and flexible mounting of all components on the table. This mounting flexibility and freedom is particularly important for the modular drivetrain, as the mechanical alignment of the six modules is both challenging and critical for proper operation. For the benchmark drivetrain, the six slider–crank mechanisms were inherently aligned (within design tolerances) by the presence of the crankshaft.

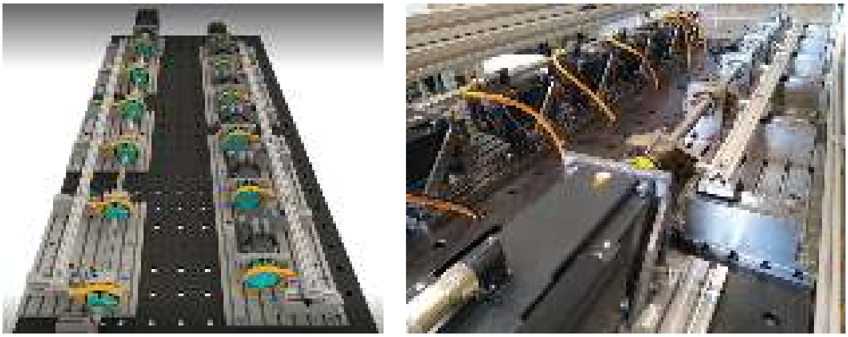

(**a**) (**b**)

Figure 7. Experimental setup: (**a**) CAD design and (**b**) setup in the lab.

To keep the research industrially relevant, component sizing and selection focused primarily on off-the-shelf components. The modular drivetrain used six AM8051F motors, while the benchmark drivetrain used a single AM8063L motor. Table 1 lists several basic properties of these motors. The motors' front faces were bolted onto a steel frame. This steel frame had slots in the bottom to affix the frame to the test bed using the T-slots, allowing for a range of movement when positioning the motors. This range of movement is particularly important for the modular drivetrain, as it has no crankshaft connecting all modules, meaning that the six slider–crank mechanisms are not inherently mechanically aligned. Custom alignment tools were developed together with a specific alignment procedure to achieve mechanical alignment within tolerances. The slider carriage was a caged ball linear guide of THK (SSR 15 X W 1 SS QZ + 160 L), and is shown in Figure 8. The load bar connecting all six slider carriages was a standard aluminum item profile with a total weight of 4.42 kg. All electronic components, such as the motor drives, IPC, IO cards, and low-voltage power supply, were stock components. A total of four type AX5000 Beckhoff drives were installed in the electrical cabinet: a single drive for the benchmark drivetrain, and three dual-channel drives for the modular drivetrain. For the latter dual-channel drives, the two channels were separated, allowing independent control of the six motors of the modular drivetrain. Each drive was operated at a switching frequency of 8 kHz. The IPC implemented and ran the control algorithm, as discussed in Section 2.4, at a sample frequency of 4 kHz. The IPC then sent the individual torque targets to each drive over an EtherCAT communication network.

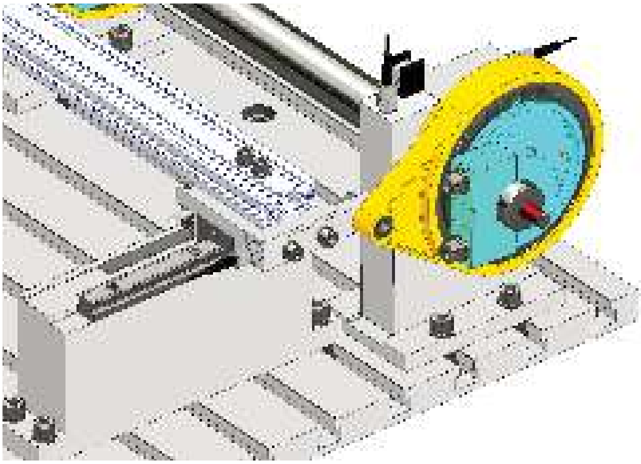

Figure 8. Slider carriage and eccentric bearing.

The main custom components of the setup were the crankshaft and the slider–crank mechanism. The crankshaft was a custom machined steel rod connecting the motor to the six slider–crank mechanisms of the benchmark drivetrain. The modular drivetrain did not have this crankshaft. All slider–crank mechanisms were identical by design. The mechanism was composed of an eccentric bearing converting the rotational motion to translational motion. The eccentricity of the bearing was obtained by offsetting the bearing's centre axis with respect to the rotational axis. The eccentric bearing is visualized in more detail in Figure 8. The slider–crank mechanism had a crank length of 20 mm, allowing a maximum full slider stroke of 40 mm to be achieved. The dimensions and properties of the main off-the-shelf and custom components are listed in Table 1.

2.6. Performance KPIs

The availability of a simulation environment and experimental environment allowed an accurate performance assessment of the benchmark and modular drivetrains to be carried out.

The following KPIs were defined for evaluating the performance of both drivetrain systems following the approach described in Section 2.1.

The maximum torque required for a certain operating condition is an indicator of the peak load of a drivetrain system. A lower peak load results in higher system reliability and lifetime. The crank torque is calculated on the basis of the motor currents reported by the respective drive. The following equation was applied for field-oriented controlled (FOC) PMSM:

$$T(t) = k_t * i_q(t) \tag{3}$$

where k_t and $i_q(t)$ are the motor torque constant and the motor q-axis current, respectively. Next, the maximum torque for a time series torque signal is calculated as follows:

$$T_{max} = \max(\|T(t)\|) \tag{4}$$

For the modular drivetrain, $T(t)$ is the total drivetrain torque, which is equal to the sum of the torques of the six independent motors.

RMS torque allows the mechanical energy consumption of the system drivetrains to be compared for a given motion profile.

$$T_{rms} = \sqrt{mean(T(t)^2)} \tag{5}$$

The crank position control error defines the control accuracy of the system drivetrain. The crank position is measured by the motor resolvers and read out from the drives. Based on these resolver signals, the KPI is calculated as follows.

$$e_{\theta}^{max} = \max\{\left\|\left(\theta_{act}(t) - \theta_{ref}(t)\right)\right\|\} \tag{6}$$

The slider error defines how accurately the slider positions are aligned and synchronized with each other during motion. For an ideal drivetrain (meaning one without disturbances such as misalignment and other design tolerances), this largely correlates with the above-mentioned crank position control error; however, for a non-ideal system such as the experimental setup, this is not necessarily the case. In practice, design tolerances, mounting misalignments, etc., are inherently present. The slider positions are measured using linear encoders (RLS LA11) attached to the slider carriage. Based on these measurements, the maximum slider error is calculated as follows:

$$e_{sliderPos}^{max} = \max_{t\epsilon[t_0,t_{end}]}\{\| \max_{i\epsilon[1,6]}\{PS_{i,t}\} - \min_{i\epsilon[1,6]}\{PS_{i,t}\}\|\} \tag{7}$$

where $PS_{i,t}$ is the position of slider number i at instant t, t_0 is the start time of the experiment with the machine at steady speed, and t_{end} is the end of the experiment.

The RMS electrical power defines the average power drawn from the electrical grid for a certain motion profile. The instantaneous electrical power $P^{elec}(t)$ is estimated using the motor, inverter, and cable loss models, which require the motor speed and torque as inputs. For accurate estimation of the electrical energy consumption, the measured speed and estimated torque signals of the setup experiments are used as inputs to the loss models. The RMS electrical power consumption for a certain motion profile is calculated as follows.

$$P_{rms}^{elec} = \sqrt{mean\left(P^{elec}(t)^2\right)} \tag{8}$$

The performance comparison using the above KPIs of the benchmark and modular system drivetrain was performed for an equal load profile (see Figure 1). The performance was investigated for three different motion profiles: continuous motion, reciprocating motion, and start/stop motion. In the continuous motion profile, the crankshaft continuously rotates in one direction at a constant speed. The start/stop motion rotates the crankshaft in one direction as well, except that the shaft stops rotating every full cycle with a duty cycle of 50%. This motion profile is typical for pick-and-place applications. In reciprocating motion, the crankshaft smoothly oscillates in two directions, which means that the motor operates in both positive and negative speed ranges. Examples of these different motion profiles are visualised in Figure 9 for the crank. It is clear that both the reciprocating and start/stop motion profiles are far more dynamic and introduce higher acceleration than the more stationary continuous motion profile. Both the continuous motion and start/stop motion profiles have a fixed stroke length, i.e., the maximum stroke is defined by the mechanical design. The reciprocating motion profile has the additional benefit of providing an electronically controllable stroke length, meaning that the stroke length is determined by the amplitude of the sinusoidal crank position time signal.

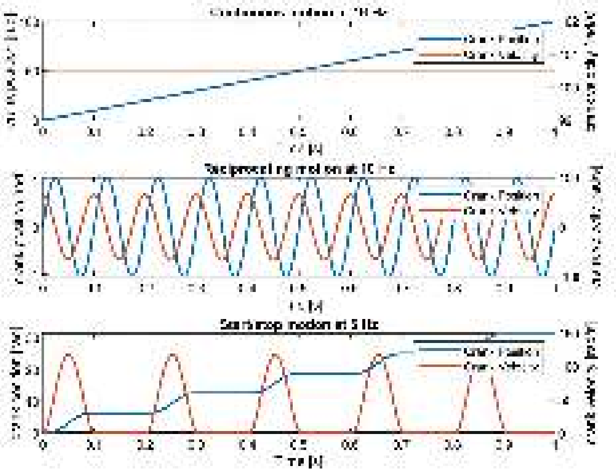

Figure 9. Crank motion profiles.

3. Results and Discussion

3.1. Simulation Versus Experimental Results

A first analysis was carried out to compare the simulation results with the experimental results for both the modular and benchmark drivetrains. For the continuous, reciprocating, and start/stop motion profiles, the above mentioned KPIs were compared using a fixed slider motion frequency of 16 Hz, 10 Hz, and 5 Hz, respectively. These operational frequencies are close to the maximum obtainable operational frequencies of the experimental benchmark drivetrain for the continuous, reciprocating and start/stop motion profiles, respectively. Figure 10 shows a comparison of the results for the modular drivetrain running the start/stop motion profile. The accuracy of the simulation estimation for each KPI is calculated as follows:

$$accuracy_{pct} = (1 + (KPI_{sim} - KPI_{exp})/KPI_{exp}) * 100 \tag{9}$$

The resulting accuracy is a percentage value, where 100 percent indicates a perfect match between simulation and experiment.

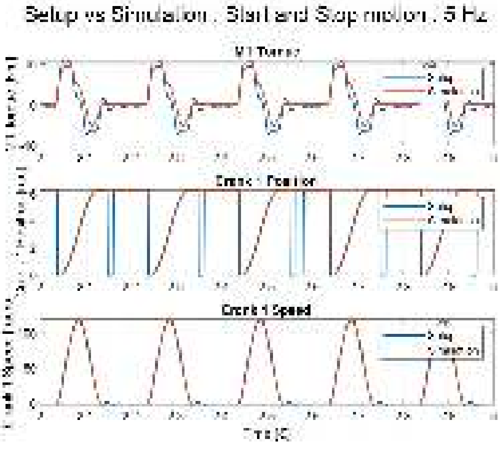

Figure 10. Modular drivetrain and start/stop motion profile: simulation versus experiment.

All analysis results are summarized in Tables 2 and 3.

Table 2. Modular drivetrain: simulation versus experiment.

KPI		**Reciprocating 10 Hz**	**Continuous 16 Hz**	**Start/Stop 5 Hz**
RMS torque	simulation	32 Nm	27 Nm	28 Nm
	experiment	38 Nm	13 Nm	28 Nm
	accuracy	83%	202%	98%
Max torque	simulation	51 Nm	42 Nm	67 Nm
	experiment	57 Nm	23 Nm	64 Nm
	accuracy	90%	183%	105%
Max crank error	simulation	0.018 rad	0.025 rad	0.026 rad
	experiment	0.032 rad	0.019 rad	0.022 rad
	accuracy	56%	132%	122%

Table 3. Benchmark drivetrain: simulation versus experiment.

KPI		**Reciprocating 10 Hz**	**Continuous 16 Hz**	**Start/Stop 5 Hz**
RMS torque	simulation	42 Nm	32 Nm	32 Nm
	experiment	57 Nm	13 Nm	41 Nm
	accuracy	74%	235%	76%
Max torque	simulation	59 Nm	40 Nm	85 Nm
	experiment	98 Nm	28 Nm	108 Nm
	accuracy	60%	145%	79%
Max crank error	simulation	0.071 rad	0.067 rad	0.111 rad
	experiment	0.160 rad	0.023 rad	0.135 rad
	accuracy	45%	286%	82%

The slider error is not analysed in the tables, as the simulation was assumed to be ideal in the sense that mechanical misalignment or design tolerances were not included in the model. The electrical power consumption is not included either, as the sensors required for electrical measurements were not installed in the experimental setup.

The results show accurate torque estimation of the models for both the start/stop motion and reciprocating motion profiles. This can be clearly seen in Figure 10 for the modular drivetrain running the start/stop motion profile, and is reflected in the comparison of RMS and maximum torque as well. For example, in Table 2, a 98% fit for the RMS torque of the modular drivetrain running the start/stop motion profile can be observed. A less accurate fit is observed for the continuous motion profile, with an accuracy of only about 200% when estimating the RMS and maximum torque. This can be explained by the need to analyse the different terms of the total required torque for the three motion profiles. The total torque amount consists of the inertial torque, gravity torque, and friction torque. The model relies on accurate analytic, kinematic, and dynamic equations for estimating the inertial and gravity torque based on known design parameters such as the geometry, mass, and inertia. These parameters are easily measured and/or calculated with a high degree of confidence. However, the friction torque is far more difficult to predict, and is a source of uncertainty. Although the friction parameters were fitted using measured data, the friction model can be further improved. For example, a large temperature dependency of the friction torque on the setup was observed. The current model does not include a thermal domain, which would help to estimate component temperatures. As our model does not include temperature-dependent friction, its estimation of the friction torque is far less accurate than that of the inertial and gravity torque. Start/stop and reciprocating motion are highly dynamic motion profiles causing high inertial torque values. As a result, the total required torque for these motion profiles is dominated by the inertial torque, meaning that the ratio of the accurately estimated inertial torque over the less accurately estimated friction torque is fairly high. This explains the better torque estimation results for the more dynamic start/stop and reciprocating motion profiles.

The same reasoning applies when comparing the torque estimation accuracy of the modular and benchmark drivetrains. The results in Tables 2 and 3 generally show a better model fit for the modular drivetrain. The benchmark drivetrain design includes a crankshaft and supporting bearings, while the modular drivetrain does not have these components. Our experimental observations using the testing setup show a significant amount of friction in these grease-lubricated supporting bearings of the crankshaft on the benchmark drivetrain. Accordingly, the frictional torque is higher for the benchmark, resulting in lower model accuracy for this drivetrain.

3.2. Performance Comparison of the Benchmark and Modular Drivetrains

This subsection focuses on a technical performance comparison between the modular and benchmark drivetrains. Similar to the previous subsection, the performance of both drivetrains was analyzed for the three different motion profiles with the modular and benchmark drivetrains running simultaneously at the same speed. Table 4 shows the resulting KPI values of both drivetrains for each motion profile and the KPI differences between the modular drivetrain and the benchmark drivetrain in percentages. All KPI values shown in the table were directly derived from experimental data except for the RMS electrical power.

Table 4. Performance comparison.

KPI		**Reciprocating 10 Hz**	**Continuous 16 Hz**	**Start/Stop 5 Hz**
RMS torque	Benchmark	57 Nm	13 Nm	41 Nm
	Modular	38 Nm	13 Nm	28 Nm
	Delta	−33%	−2%	−32%
Max torque	Benchmark	98 Nm	28 Nm	108 Nm
	Modular	57 Nm	23 Nm	64 Nm
	Delta	−42%	−18%	−41%
Max crank error	Benchmark	0.160 rad	0.023 rad	0.135 rad
	Modular	0.032 rad	0.019 rad	0.022
	Delta	−80%	−9%	−84%
Max slider error	Benchmark	0.43 mm	0.95 mm	0.46 mm
	Modular	0.39 mm	0.83 mm	0.41 mm
	Delta	−9%	−13%	−11%
RMS electrical power	Benchmark	3.58	2.01	5.17
	Modular	3.1	2.2	3.68
	Delta	−13%	+9%	−29%

For the continuous motion profile, the measurements show only a minor reduction of 2% in the RMS torque required to run the motion cycle. The maximum observed torque is reduced by about 18%. Hence, while the peak load of the modular drivetrain is clearly reduced, the average mechanical power delivered by the motors in the continuous motion profile is not significantly altered. Unfortunately, the electrical power consumption of the modular drivetrain is 9% higher than the benchmark drivetrain. Figure 11 shows that this can be explained by the increased overall motor losses of the six smaller motors compared to the motor loss of the single motor in the benchmark drivetrain. Furthermore, the experimental results shows a 19% increase in the position tracking performance of the modular drivetrain compared with the benchmark. As a result, the maximum slider error is reduced by 13%.

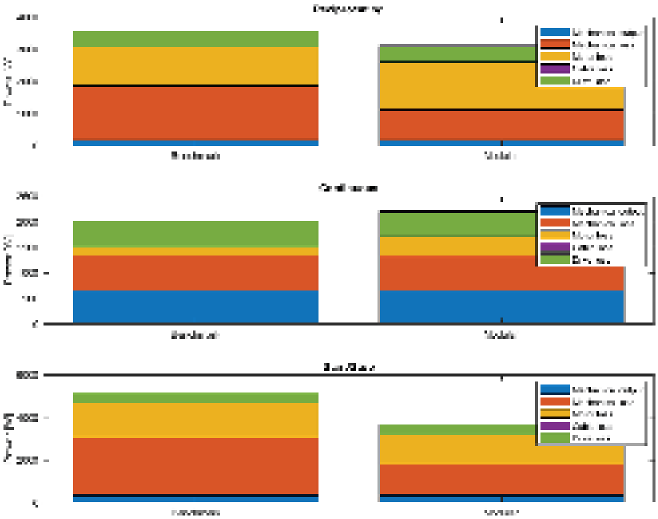

Figure 11. Electrical power consumption.

More significant performance improvements are experimentally observed for the reciprocating and start/stop motions. The total RMS torque delivered by the six modular motors is up to 33% lower compared to the RMS torque delivered by the single motor of the benchmark drivetrain. The maximum torque is decreased by up to 42%, resulting in lower fatigue stress on the modular drivetrain. As a result, for these more dynamic (high-acceleration) motion profiles, significantly less average mechanical power is required to drive the modular system compared to the benchmark system. In addition, a reduction in electrical energy consumption of up to 29% is estimated, and an 84% reduction in the tracking error is observed. Having the system load distributed over the six actuators helps to achieve better control performance. As a consequence, the slider error is reduced due to mechanical play in the pin connection between the slider and the rod, albeit less drastically, up to 11%.

These experimental results demonstrate that a modular drivetrain can result in better tracking performance, lower peak system loads, and reduced average mechanical and electrical power consumption with respect to the standard non-modular drivetrains currently used by industry. This is especially true for highly dynamic motion profiles with large acceleration values, which can benefit from a mechanical system with reduced inertia.

3.3. Outlook

Improvements could be made to both the testing setup and the model. The accuracy of the friction model could be increased by including the thermal domain. For validation of thermal behavior, temperature sensors would need to be added to the setup. In order to analyse the high-frequency system dynamics (>1 kHz), the simulation environment could benefit from a detailed model of the motor drive that includes current control.

Interesting future work could include the application of novel robust control techniques for uncertain nonlinear systems on the modular drivetrain discussed in this research. For example, a sliding mode controller such as the one described in [27] could be implemented and tested using the experimental setup described in this paper.

Future research should examine additional functionalities that modular drivetrains could potentially generate for applications in tufting, weaving, and stamping machines. We have already begun research on the potential of active damping of vibrations in the modular system. Because the modular drivetrain has six independently acting motors at different locations, there is the possibility of correcting any crank and/or slider errors. An active damping method based on a dynamic average consensus algorithm [28] has been developed and integrated in the current decentralized control architecture. Experimental validation is ongoing, and simulations already show promising results [29].

Furthermore, the impact of modular drivetrains on system reliability is being investigated. Future work could include researching safe and robust methods for handling failure. As the modular drivetrain has built-in actuator redundancy, the system can operate in the event of a single motor failure. How to implement and execute this failure handling method and what performance can be expected after such a failure are among the questions that we plan to answer in our future research.

Other future work could focus on the economics of modular drivetrains through a comparison of the total cost of ownership (TCO), including the purchase cost, cost of usage (energy), and maintenance and repair costs. Such an analysis should further build on the performance and reliability conclusions of existing research to support industrial machine manufacturers in quantifying the economical impact of modular drivetrains and making informed design decisions.

4. Conclusions

Machine manufacturers continuously aim to increase their market competitiveness by designing machines with improved productivity, reliability, energy consumption, and flexibility. The concept of drivetrain modularity was proposed in [1,2] as a method to enhance the operational performance of industrial machines. In this paper, we have introduced the concept and detailed design of a modular drivetrain architecture that implements a decentralized control architecture. A simulation plant model was set up to support the development and validation of the control strategy. The modular drivetrain performance was assessed and compared with a benchmark drivetrain using the above-mentioned simulation model as well as an experimental setup. Both drivetrains were subjected to the same load profiles, and a performance evaluation was conducted based on a set of key performance indicators: maximum torque, RMS torque, crank position tracking error, slider error, and electrical energy consumption. In addition, three different load profiles (motion cycles) were defined: continuous, reciprocation, and start/stop motion.

Comparison of the simulation KPI results with the experimental KPI results showed a good match for the more dynamic motion cycles (reciprocating and start/stop motion). For the modular drivetrain, a simulation accuracy of 98% was observed for the RMS torque KPI. The continuous motion profile, on the other hand, showed a slightly less accurate fit between the results of the simulation model and those of the experimental setup, which was due to unmodelled thermal characteristics in the friction model. The same reasoning applies to the observed discrepancies between the simulation and testing setup results for the benchmark drivetrain. As the benchmark drivetrain has more bearings, the (less accurately known) frictional force are more dominant.

Our experiments on the test setup showed significant performance improvements for the modular drivetrain as compared to the benchmark drivetrain for the highly dynamic motion profiles (reciprocating and start/stop motion). A 42% reduction in peak torque was observed and the position tracking performance was increased up to 84%, resulting in an 11% reduction in the slider error. The electrical power consumption could be reduced by up to 29%. Unfortunately, the performance increase was less pronounced for motion cycles with lower accelerations, such as the continuous motion cycle, which is largely due to the increased electrical motor losses. In closing, it can be concluded that the operating load profiles of industrial machines with high acceleration rates could benefit from a more modular drivetrain architecture.

Author Contributions: Conceptualization, N.D., T.T., B.W., K.S., D.v.O. and K.L.; methodology, N.D., T.T., B.W. and K.L.; software, N.D., T.T. and B.W.; validation, N.D. and T.T.; formal analysis, N.D., T.T. and B.W.; investigation, N.D., T.T. and B.W.; resources, K.L. and K.S.; writing—original draft preparation, N.D.; writing—review and editing, N.D., T.T., B.W., KS, D.v.O. and K.L.; visualization, N.D. and T.T.; supervision, K.L. and K.S.; project administration, K.L. and K.S.; funding acquisition, K.L. and K.S. All authors have read and agreed to the published version of the manuscript.

Funding: This research is part of the ModulAr SBO project funded and supported by Flanders Make vzw, the strategic research center for the manufacturing industry.

Data Availability Statement: The data presented in this study are available on request from the corresponding author. The data are not publicly available due to privacy restrictions.

Conflicts of Interest: The authors declare no conflict of interest.

Abbreviations

The following abbreviations are used in this manuscript:

MDPI	Multidisciplinary Digital Publishing Institute
TLA	Three-Letter Acronym
KPI	Key Performance Indicator
PI	Proportional Integrator
RMS	Root Mean Square
PMSM	Permanent Magnet Synchronous Machine
CAD	Computer-Aided Design
CoG	Center of Gravity

Appendix A. Slider–Crank Mechanism Equations

In Figure 3, (1) is the CoG of the crank, (3) is the CoG of the rod, and (4) is the slider position. The angular position of te crank is defined by θ, while the angular position of the rod is defined by ϕ; ϕ is indicated as a negative angle in order to maintain right-hand sign conventions. The respective centers of gravity (CoG) in (1) and (3) have the inertial properties $m_{1,2}$ and $I_{1,2}$, respectively, while gravity is indicated by g.

The kinematic relationships are as follows.

$$x_1 = l_{1,c}\cos(\theta) \tag{A1}$$

$$y_1 = l_{1,c}\sin(\theta) \tag{A2}$$

$$x_2 = l_1\cos(\theta) \tag{A3}$$

$$y_2 = l_1\sin(\theta) \tag{A4}$$

$$x_3 = x_2 + (l_2 - l_{2,c})\cos(-\phi) \tag{A5}$$

$$y_3 = l_{2,c}\sin(-\phi) \tag{A6}$$

$$x_4 = x_2 + l_2\cos(-\phi) \tag{A7}$$

$$\phi = -\arcsin\left(\frac{l_1}{l_2}\sin(\theta)\right) \tag{A8}$$

The equations of motion are as follows.

$$\ddot{x}_1 = \frac{HA - HB}{m_1} \tag{A9}$$

$$\ddot{y}_1 = \frac{VA - VB}{m_1} - g \tag{A10}$$

$$\ddot{x}_3 = \frac{HB - F}{m_2} \tag{A11}$$

$$\ddot{y}_3 = \frac{VB - VC}{m_2} - g \tag{A12}$$

$$\begin{aligned}\ddot{\theta} &= \frac{T + (l_{1,c}HA + (l_1 - l_{1,c})HB)\sin(\theta)}{I1} \\ &\quad + \frac{(-l_{1,c}VA - (l_1 - l_{1,c})VB)\cos(\theta)}{I1}\end{aligned} \tag{A13}$$

$$\ddot{\phi} = \frac{(-l_{2,c}F - (l_2 - l_{2,c})HB)\sin(-\phi)}{I2}$$

$$+\frac{(-l_{2,c}VC-(l_2-l_{2,c})VB)\cos(-\phi)}{I2} \tag{A14}$$

Using the the MATLAB symbolic toolbox and differentiating (A1)–(A8) except for x_2, y_2, and θ provides the following.

$$\ddot{x}_1=-l_{1,c}\sin(\theta)\ddot{\theta}-l_{1,c}\cos(\theta)\dot{\theta}^2 \tag{A15}$$

$$\ddot{y}_1=l_{1,c}\cos(\theta)\ddot{\theta}-l_{1,c}\sin(\theta)\dot{\theta}^2 \tag{A16}$$

$$\begin{aligned}\ddot{x}_3=&\frac{l_1^2\sin(\theta)^2(l_2-l_{2,c})\dot{\theta}^2}{l_2^2\sqrt{1-\frac{l_1^2\sin(\theta)^2}{l_2^2}}}-l_1\sin(\theta)\ddot{\theta}\\&-\frac{l_1^2\cos(\theta)^2(l_2-l_{2,c})\dot{\theta}^2}{l_2^2\sqrt{1-\frac{l_1^2\sin(\theta)^2}{l_2^2}}}-l_1\cos(\theta)\dot{\theta}^2\\&-\frac{l_1^4\cos(\theta)^2\sin(\theta)^2(l_2-l_{2,c})\dot{\theta}^2}{l_2^4\left(1-\frac{l_1^2\sin(\theta)^2}{l_2^2}\right)^{3/2}}\\&-\frac{l_1^2\cos(\theta)\sin(\theta)(l_2-l_{2,c})\ddot{\theta}}{l_2^2\sqrt{1-\frac{l_1^2\sin(\theta)^2}{l_2^2}}}\end{aligned} \tag{A17}$$

$$\ddot{y}_3=\frac{(l_1l_{2,c}\cos(\theta)\ddot{\theta})-(l_1l_{2,c}\sin(\theta)\dot{\theta}^2)}{l_2} \tag{A18}$$

$$\begin{aligned}\ddot{\phi}=&\frac{l_1\sin(\theta)\dot{\theta}^2}{l_2\sqrt{1-\frac{l_1^2\sin(\theta)^2}{l_2^2}}}-\frac{l_1\cos(\theta)\ddot{\theta}}{l_2\sqrt{1-\frac{l_1^2\sin(\theta)^2}{l_2^2}}}\\&-\frac{l_1^3\cos(\theta)^2\sin(\theta)\dot{\theta}^2}{l_2^3\left(1-\frac{l_1^2\sin(\theta)^2}{l_2^2}\right)^{3/2}}\end{aligned} \tag{A19}$$

References

1. Vandenhove, T.; Diltoer, R.; Lenaerts, B.; van Os, D.; Stockman, K.; Schlimpert, S. Modular Drivetrains for Increased Performance and Reliability. In Proceedings of the 2021 IEEE International Conference on Mechatronics (ICM), Kashiwa, Japan, 7–9 March 2021; pp. 1–8. [CrossRef]
2. Lemmens, J.; Driesen, J. Synchronization and efficiency analysis of a direct-drive multi-motor application. In Proceedings of the 6th IET International Conference on Power Electronics, Machines and Drives (PEMD 2012), Bristol, UK, 27–29 March 2012; pp. 1–6. [CrossRef]
3. Otto, K.; Hölttä-Otto, K.; Simpson, T.W.; Krause, D.; Ripperda, S.; Ki Moon, S. Global Views on Modular Design Research: Linking Alternative Methods to Support Modular Product Family Concept Development. *J. Mech. Des.* **2016**, *138*, 071101. [CrossRef]
4. Schuh, G.; Dölle, C.; Barg, S.; Kuhn, M.; Breunig, S. Efficient Modular Product Platform Design of Mechatronic Systems. In Proceedings of the 2018 IEEE International Conference on Industrial Engineering and Engineering Management (IEEM), Bangkok, Thailand, 16–19 December 2018; pp. 1391–1395. [CrossRef].
5. Xu, Z.; Xi, F.; Liu, L.; Chen, L. A Method for Design of Modular Reconfigurable Machine Tools. *Machines* **2017**, *5*, 5. [CrossRef]
6. Leandro Gauss, D.P.L.; Miguel, P.A.C. Module-based product family design: Systematic literature review and meta-synthesis. *J. Intell. Manuf.* **2021**, *32*, 265–312. [CrossRef]
7. Definition of Modularity. Available online: https://www.merriam-webster.com/dictionary/modularity (accessed on 8 August 2023).
8. Mitrovic, N.; Petronijevic, M.; Kostic, V.; Jeftenic, B. Electrical Drives for Crane Application. In *Mechanical Engineering*; IntechOpen: London, UK, 2012. [CrossRef]
9. Debnath, S.; Saeedifard, M. A New Hybrid Modular Multilevel Converter for Grid Connection of Large Wind Turbines. *IEEE Trans. Sustain. Energy* **2013**, *4*, 1051–1064. [CrossRef]
10. Nemeth, T.; Bubert, A.; Becker, J.N.; De Doncker, R.W.; Sauer, D.U. A Simulation Platform for Optimization of Electric Vehicles With Modular Drivetrain Topologies. *IEEE Trans. Transp. Electrif.* **2018**, *4*, 888–900. [CrossRef]

11. Chang, F.; Lienkamp, M. A modular multilevel topology using power electronic transformers for the modular drivetrains of electric vehicles. In Proceedings of the 2016 18th European Conference on Power Electronics and Applications (EPE'16 ECCE Europe), Karlsruhe, Germany, 5–9 September 2016; pp. 1–9. [CrossRef]
12. Lin, F.J.; Fung, R.F.; Lin, Y.S. Adaptive control of slider-crank mechanism motion: Simulations and experiments. *Int. J. Syst. Sci.* **1997**, *28*, 1227–1238. [CrossRef]
13. Grumelart, A.; McKinnon, W.L. Application of Sectional Drives and PLC's to Textile Ranges. *IEEE Trans. Ind. Appl.* **1983**, *2*, 145–147. [CrossRef]
14. Perez-Pinal.; Nuñez, C.; Alvarez, R.; Cervantes, I. Comparison of multi-motor synchronization techniques. In Proceedings of the 30th Annual Conference of IEEE Industrial Electronics Society, 2004 IECON, Busan, Republic of Korea, 2–6 November 2004; Volume 2, pp. 1670–1675.
15. Zhao, D.; Li, C.; Ren, J. Speed synchronization of multiple induction motors with adjacent cross coupling control. In Proceedings of the 48h IEEE Conference on Decision and Control (CDC) held jointly with 2009 28th Chinese Control Conference, Shanghai, China, 15–18 December 2009; pp. 6805–6810. [CrossRef]
16. Peng, W.; Zhao, D. Speed Synchronization of Multi Induction Motors with Total Sliding Mode Control. In Proceedings of the 2010 Asia-Pacific Power and Energy Engineering Conference, Chengdu, China, 28–31 March 2010; pp. 1–9. [CrossRef]
17. Kong, W.; Wang, J.; Kong, D.; Cong, Y.; Feng, S. Motor shifting and torque distribution control of a multi-motor driving system in electric construction vehicles. *Adv. Mech. Eng.* **2021**, *13*, 16878140211028446. [CrossRef]
18. Xu, X.; Su, P.; Wang, F.; Chen, L.; Xie, J.; Atindana, V.A. Coordinated Control of Dual-Motor Using the Interval Type-2 Fuzzy Logic in Autonomous Steering System of AGV. *Int. J. Fuzzy Syst.* **2021**, *23*, 1070–1086. [CrossRef]
19. Asri Abd Samat, A.; Ishak, D.; Saedin, P.; Iqbal, S. Speed- Sensorless Control of Parallel- Connected PMSM fed by A Single Inverter Using MRAS. In Proceedings of the 2012 IEEE International Power Engineering and Optimization Conference (PEOCO2012), Melaka, Malaysia, 6–7 June 2012. [CrossRef]
20. Mikhov, M. An Algorithm for Synchronized Control of Multi-Motor Drive Systems. In Proceedings of the International Scientific Conference on Information, Communication and Energy Systems and Technologies, Sofia, Bulgaria, 16–18 October 2003.
21. Simscape r2019b. Available online: https://nl.mathworks.com/help/simscape/index.html (accessed on 14 July 2023).
22. Van Os, D.; Laurijssen, K.; Vansompel, H.; Sergeant, P.; Divens, N.; Stockman, K. Evaluation Framework for the Comparison of Modular Drivetrain Architectures. In Proceedings of the 2023 IEEE International Conference on Mechatronics (ICM), Loughborough, UK, 15–17 March 2023; pp. 1–6. [CrossRef]
23. MathWorks: Permanent Magnet Synchronous Motor with Sinusoidal Flux Distribution. Available online: https://nl.mathworks.com/help/sps/ref/pmsm.html (accessed on 14 July 2023).
24. Novak, M.; Novak, J.; Novak, Z. Efficiency Mapping of a Small Permanent Magnet Synchronous Motor. In *Mechatronics 2017: Recent Technological and Scientific Advances*; Březina, T., Jabłoński, R., Eds.; Springer: Cham, Switzerland, 2018; pp. 185–193.
25. Ha, J.L.; Fung, R.F.; Chen, K.Y.; Hsien, S.C. Dynamic modeling and identification of a slider-crank mechanism. *J. Sound Vib.* **2006**, *289*, 1019–1044. [CrossRef]
26. Youtube, Modular Motion System. Available online: https://www.youtube.com/watch?v=rURG46nZq28 (accessed on 14 November 2023).
27. Shao, K.; Zheng, J.; Tang, R.; Li, X.; Man, Z.; Liang, B. Barrier Function Based Adaptive Sliding Mode Control for Uncertain Systems With Input Saturation. *IEEE/ASME Trans. Mechatron.* **2022**, *27*, 4258–4268. [CrossRef]
28. Kia, S.S.; Van Scoy, B.; Cortes, J.; Freeman, R.A.; Lynch, K.M.; Martinez, S. Tutorial on Dynamic Average Consensus: The Problem, Its Applications, and the Algorithms. *IEEE Control. Syst. Mag.* **2019**, *39*, 40–72. [CrossRef]
29. Tuerlinckx, T.; Divens, N.; Laurijssen, K. Modular Drivetrain Active Damping based on Dynamic Average Consensus Algorithm in Continuous Motion. In Proceedings of the 2023 3rd International Conference on Electrical, Computer, Communications and Mechatronics Engineering (ICECCME), Tenerife, Spain, 19–21 July 2023; pp. 1–10. [CrossRef]

machines

MDPI

Article

Thermal Model and Thermal Analysis of the Dual Drive Sliding Feed System

Hui Li [1,2], Haiyang Liu [1,2,*], Xianying Feng [1,2], Yandong Liu [1,2], Ming Yao [1,2] and Anning Wang [1,2]

[1] School of Mechanical Engineering, Shandong University, Jinan 250061, China; lihuifs@sdu.edu.cn (H.L.); fxying@sdu.edu.cn (X.F.); liuyandong@mail.sdu.edu.cn (Y.L.); 202014301@mail.sdu.edu.cn (M.Y.); 202014288@mail.sdu.edu.cn (A.W.)

[2] Key Laboratory of High Efficiency and Clean Mechanical Manufacture of Ministry of Education, Shandong University, Jinan 250061, China

* Correspondence: haiyangliu@mail.sdu.edu.cn

Abstract: The dual drive sliding feed system can obtain a uniform and stable resolution at extremely low speeds and significantly reduce the system's nonlinear friction. However, the numerous thermal sources within the system and the multipoint sliding contact during transmission result in a significant temperature rise, leading to considerable thermal deformation and errors. Moreover, the responsive mechanism of the thermal characteristics needs to be clarified. Therefore, firstly, a frictional torque model of the engagement of the screw and nut is established, and the heat generation, heat transfer, and thermal contact resistance (TCR) are solved. Then, based on the solution, a finite element thermal simulation model of the dual drive sliding feed system is established, and experiments are performed for validation. The results show that the error in temperature at the measuring point is less than 2.1 °C, and the axial thermal elongation of the screw is less than 6.2 μm. Finally, the thermal characteristics of the feeding system under various operating conditions are analyzed. The results show that the established thermal simulated model can effectively describe the dynamic thermal characteristics of the dual drive sliding feed system during operation. The effects of the rotational speed and ambient temperature on the dynamic thermal characteristics of the dual drive sliding feed system are investigated separately. The temperature increase in each part of the screw during the operation is characterized.

Keywords: sliding screw; friction torque; feed system; thermal characteristic

Citation: Li, H.; Liu, H.; Feng, X.; Liu, Y.; Yao, M.; Wang, A. Thermal Model and Thermal Analysis of the Dual Drive Sliding Feed System. *Machines* **2023**, *11*, 1084. https://doi.org/10.3390/machines11121084

Academic Editors: Kan Liu and Wei Hu

Received: 13 November 2023
Revised: 8 December 2023
Accepted: 11 December 2023
Published: 13 December 2023

1. Introduction

Due to the rising demand for diversity and quality products in recent years, many high-end parts now need their surface form and precision to reach the micron or even nano-scale levels. As an important part of the machining process, the feed system's positional accuracy directly affects the part's final forming accuracy. However, a large amount of heat will be generated during the operation of the feed system [1,2]. Numerous studies have shown that thermal errors are difficult to control in machining due to their nonlinear and random characteristics. Thermal errors have become the most important factor affecting positioning errors [3,4]. Studying the thermal characteristics of a feed system under complex working conditions is essential for improving the forming accuracy.

Most existing feed systems use mechanical feed mechanisms; however, they are difficult to use in ultra-precision machining due to their disadvantages: mechanical clearance, friction and wear, and crawling. Therefore, Feng et al. proposed a dual drive feed system [5], which utilizes two motors rotating at approximately equal speeds in the same direction at high speeds. The worktable may get an exact micro-feed by the difference between the two speeds. The system can also adjust the worktable's speed from extremely low to very high by switching the two motors from opposite to reverse spin. The system becomes a traditional ball screw drive system when just the screw motor is powered. This type of drive significantly reduces the impact of nonlinear friction on the feed system [6]. However, because the actuator employed in the existing dual drive feed system is a ball screw pair, when the system enters nano-scale control, the unevenness of the ball and the multibody dynamic coupling characteristics have a significant impact on motion control at very low speeds, which leads to difficulties in achieving accurate and uniform displacement under nano-scale conditions. Therefore, based on previous research [7], this paper presents a novel dual drive sliding feed system that replaces the ball screw in the conventional dual drive feed system with a low-cost sliding screw pair, aiming to achieve uniform and stable displacement resolution under extremely low-speed conditions. However, due to the addition of the nut motor and the nut bearing and the multipoint contact inside the sliding screw pair, more frictional heat will be generated during operation. Therefore, the thermal field of the dual drive sliding feed system is extremely complex for obtaining accurate and uniform feed displacement and improving the forming accuracy. Clearly, it is necessary to establish a thermal estimation model of the dual drive sliding feed system and analyze the thermal characteristics of the system.

Due to its high frictional resistance and severe wear, the standard sliding screw feed system has been restricted in its application for ultra-precision machining. Therefore, studies on the frictional properties and heat generation mechanism of sliding screws are rare. However, research on planetary roller screws, ball screws, rolling bearings, and other related transmission parts is highly developed [8,9]. Zhao et al. [10] analyzed the relationship between the friction coefficient and torque balance equation of angular contact bearing between a rolling body and a raceway. They clarified the change law of the friction coefficient under changes in external factors. Helmig et al. [11] realized the dynamic calculation of the heat transfer coefficient during bearing operation using infrared thermal imaging. Ba et al. [12] established a friction model of the ball screw feed system and designed a corresponding feed-forward compensation controller. Min et al. [13] established a finite element model of a ball screw feed system and analyzed the temperature characteristics of the system during operation. Ma et al. [14] established the motion model of a planetary roller screw, analyzed the relative motion speed of the internal contact interface, and solved the distribution of the friction forces inside it. Du et al. [15] established a finite element model of a planetary roller screw and analyzed the temperature characteristics of the system at different times and positions by considering the moving heat source during operation.

In conclusion, although research on the friction characteristics, heat generation mechanism, and thermal field characteristics of rolling ball screws and other transmission components has reached a high level of maturity, the working mode of the dual drive sliding feed system still differs significantly from that of traditional transmission components. A thermal model for a dual drive sliding feed system based on existing calculation methods cannot be established. Moreover, there is no existing research on the thermal characteristics analysis of the dual drive sliding feed system. This paper establishes a thermal model of the feed system by analyzing the friction at the engagement of the screw and nut. The influence of feed speed and ambient temperature on the dynamic thermal field characteristics of the dual drive sliding feed system are explored. The framework of this paper is organized as follows. In Section 2, the thermal boundary conditions of the dual drive sliding feed system, including the heat generation, the thermal contact resistance (TCR) between components and the convective heat transfer coefficient (CHTC) are solved separately. On this basis, a finite element simulation model of the dual drive sliding feed system is established in Section 3 to analyze the thermal characteristics of the dual drive sliding feed system. The accuracy of the established thermal estimation model in terms of temperature rise characteristics and axial deformation is also verified through experiments in Section 4. Conclusions are provided in Section 5.

2. Friction Torque Modeling of the Sliding Screw

2.1. Dual Drive Sliding Feed System

The dual drive sliding feed system is illustrated in Figure 1. The main difference between this system and the traditional feed system is the addition of a motor to drive the nut. During operation, the screw and the nut rotate simultaneously, and the worktable obtains displacement through the velocity difference between the two. The distinction between the dual drive sliding feed system and the existing dual drive feed system lies in the replacement of the ball screw with a sliding screw.

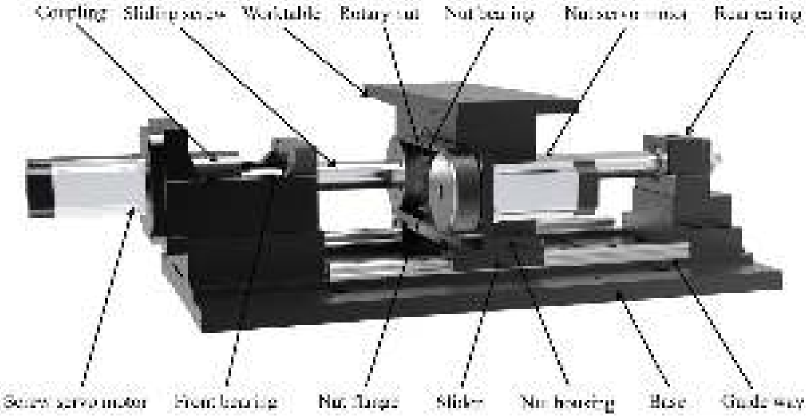

Figure 1. Structure of the dual drive sliding feed system.

The friction between components is the source of heat generation within the dual drive sliding feed system, and the friction torque is an important parameter for measuring the friction effect. Therefore, the thermal estimation model of the dual drive sliding feed system is accurately established, and the internal heat generation mechanism of the system is explored. Modeling and analyzing the frictional torque of the sliding screw are necessary. The frictional torque of a dual drive sliding feed system is affected by many factors, such as lubrication, material, and usage environment. The main reason for the frictional torque is the sliding frictional resistance that is generated by the threaded tooth contact when the relative rotation of the screw and nut occurs. Sliding friction comes from the differential sliding, elastic hysteresis, and lubrication viscosity between the screw and nut raceways. Therefore, the total friction torque of the sliding screw M_T can be expressed as:

$$M_T = \sum (M_d + M_f + M_l) \tag{1}$$

where M_d is the friction torque caused by differential sliding, M_f is the friction torque caused by elastic hysteresis, and M_l is the friction torque caused by the lubrication viscosity.

In the following, the details of each friction torque will be provided in Sections 2.2–2.4, respectively.

2.2. Friction Torque Caused by Differential Sliding

The contact part of the screw and nut is obtained as the dual drive sliding feed system is not rigid. According to the Hertz contact law, the contact surface of the screw and nut will produce a small contact area under the normal driving force, and its shape is an ellipse, as shown in Figure 2. The red area in the figure indicates the contact area between the screw and the nut, and the circumferential speed of the screw surface v_s is proportional to the distance to its axis. Similarly, the circumferential speed of the nut surface v_n is proportional to the distance to its axis. Pure rolling occurs only on two lines in the contact area. Therefore, relative sliding in opposite directions, called differential sliding, occurs at the remaining positions. The frictional moment caused by differential sliding is due to the local shear stress in the contact area. Therefore, the differential sliding friction torque M_d can be expressed as [16]:

$$M_d = \int \tau \cdot z \cdot dA = \int \mu \cdot P \cdot z \cdot dA \tag{2}$$

where z is the distance between the pure rolling line in the contact area and the local shear stress location, mm, μ is the differential sliding friction coefficient, P is the normal pressure in the contact area, MPa, and A is the area of contact, mm^2.

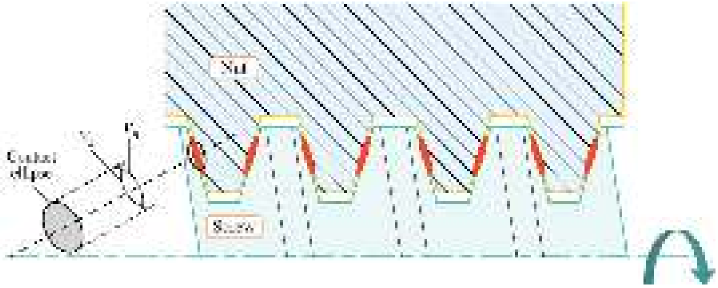

Figure 2. Schematic of differential sliding of dual drive sliding feed system.

Essentially, the actuator of the dual drive sliding feed system is similar to the driving mechanism of the planetary roller screw. Therefore, the differential sliding friction torque of the dual drive sliding screw pair is modeled and analyzed utilizing the friction torque modeling method of the planetary roller screw [17]. Taking the j contact area of the screw and nut as an example, the differential sliding friction of the contact area is integrated, and the differential sliding friction moment of the j contact area M_{dj} can be obtained as follows:

$$M_{dj} = 0.1\mu Q_j \frac{a^2}{2R}\left(\int_{-1}^{1}\left(X^2 - X^4\right)dX - 2\int_{X_1}^{X_2}\left(X^2 - X^4\right)dX\right) \tag{3}$$

where Q_j is the normal load of the j contact area, N, a is the semi-major axis of the contact ellipse, mm, R is the radius of the effective ball for Hertzian deformation (mm), and X_1 and X_2 are dimensionless parameters specified as:

$$\begin{gathered} X = \frac{x}{a} \\ X_1 = \frac{a_1}{a} \\ X_2 = \frac{a_2}{a} \end{gathered} \tag{4}$$

where a_1 and a_2 are the distances between the centerline of the contact ellipse and the pure rolling line on both sides (mm).

Due to the direction of the differential sliding friction torque being along the long axis of the contact ellipse, there exists an angle between it and the centerline of the screw. Consequently, in the process of engagement between the screw and the nut, the resulting differential sliding friction torque can be expressed as:

$$M_d = \sum_{j=1}^{\sigma} M_{dj} \cos\alpha \tag{5}$$

where σ is the number of engaged thread teeth.

2.3. Frictional Moment Caused by Elastic Hysteresis

During the meshing and transmission process of double-drive sliding screw pairs, elastic deformation occurs at some positions on the thread teeth. Consequently, the strain lags behind the stress during loading and unloading, resulting in unbalanced elastic contact forces on both sides of the meshing surface. This imbalance leads to resistive torque during operation, referred to as frictional torque caused by elastic hysteresis. According to the Hertz contact law, the work done by the compressive stress when moving forward one unit distance is:

$$W = \frac{3bBP}{32} \tag{6}$$

where b is the short axis of the contact ellipse (mm), B is the effective axial distance of the engaging contact between balls $B = 2R$ (mm).

During the rotation of the screw and the nut, the system loses energy due to the elastic hysteresis phenomenon. Therefore, the friction torque can be expressed as:

$$M_e = \eta W \tag{7}$$

where η is the energy loss coefficient.

Since the rotation of the dual drive sliding screw is driven through the threaded teeth, the frictional moment caused by elastic hysteresis occurs between all the engaged threaded teeth. The total elastic hysteresis frictional moment is evenly distributed among the engaged parts and can therefore be expressed as [18]:

$$M_f = \sum_{i=1}^{\sigma} \frac{3}{32}\eta B\gamma \sqrt[3]{\frac{3E}{2\sum\rho}} P_i^{\frac{4}{3}} \tag{8}$$

where γ is the dimensionless coefficient of the semi-short axis of the contact ellipse, E is the Young's modulus, MPa, and $\sum\rho$ is the sum of the curvatures on the contact side.

2.4. Friction Torque Caused by Lubrication Viscosity

To enhance the transmission efficiency and minimize friction, lubricating grease must be injected at the meshing point of the screw and nut. Therefore, when the screw and the nut are driven by differential rotation, the system needs to overcome the friction caused by the shearing effect of the grease. Concerning the rolling bearing calculation method, the frictional characteristics at the engagement are analyzed by the elastic dynamics lubrication effect. The resistance caused by the viscosity of the lubrication F_l can be solved as follows [19]:

$$F_l = 2.86E' f_t {R_x}^2 k^{0.348} G^{0.022} U^{0.66} W^{0.47} \tag{9}$$

where f_t is the thermal influence coefficient, R_x is the equivalent radius of curvature of the contact ellipse in the semi-major axis direction (mm), k is the equivalent radius of curvature ratio, G is the dimensionless material coefficient, U is the dimensionless velocity coefficient, W is the dimensionless load coefficient, and E' is the equivalent modulus of elasticity of the screw and nut (Mpa), and can be expressed as:

$$E' = \left(\frac{1-\mu_{\mathrm{I}}^2}{E_{\mathrm{I}}} + \frac{1-\mu_{\Pi}^2}{E_{\mathrm{II}}} \right)^{-1} \tag{10}$$

where μ_{I} and μ_{Π} are the Poisson's ratios of the screw and nut, respectively, E_{I} and E_{Π} are the Young's modulus of the screw and nut, respectively (Mpa).

The j contact area between the screw and the nut is taken as an example. The frictional moment caused by the lubricating viscosity of the j contact area can be obtained as:

$$M_{lj} = F_{lj} R_s \tag{11}$$

where R_s is the nominal radius of the screw (mm). Therefore, the friction torque caused by the lubrication viscosity is as follows:

$$M_l = \sum_{j=1}^{\sigma} M_{lj} \tag{12}$$

3. Thermal Boundary Conditions of the Dual Drive Sliding Feed System

In the case of the feed system, a significant basis when performing a simulation of thermal characteristics is to establish accurate thermal boundary conditions. The heat transfer coefficient includes heat generation, the TCR between components, and the convective heat transfer coefficient. Existing studies have revealed that the thermal error of a feed system is influenced by external and internal heat sources. External heat sources mainly include space temperature and previous environmental memory. It is difficult to carry out a quantitative analysis. Precision machining processes mostly occur in a constant temperature and humidity environment, so such heat sources are not considered in this paper. The internal heat sources mainly include motors, bearings, screw nut, and guideways. To accurately establish the thermal behavior model of the system, it is necessary to clarify the heat generation and heat transfer mechanism. The heat generation and heat transfer mechanism of the dual drive sliding feed system are shown in Figure 3.

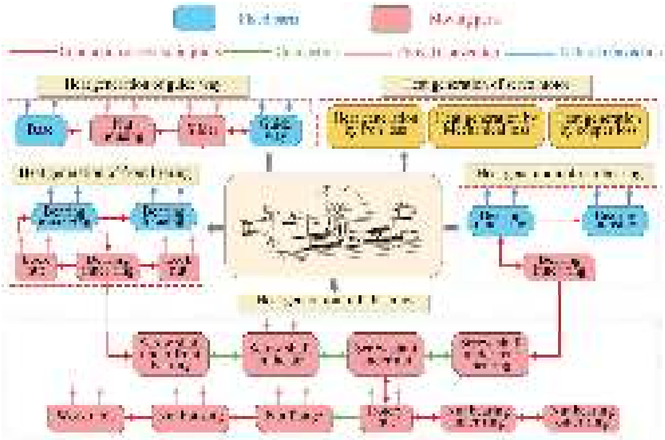

Figure 3. Heat generation and heat transfer mechanism.

3.1. Analysis of Heat Generation

The dual drive feed system has 4 major heat sources: (1) heat generation of the guideways, (2) heat generation of the servo motors, (3) heat generation of the bearings, and (4) heat generation of the sliding screw. The sliders move continuously on the guideways; the friction caused by the rotating motion of the ball between the sliders and guideways is the main reason for the heat generation of the guideway. The heat generated by the guideways H_g can be expressed as:

$$H_g = \lambda f_g F_g v_g \tag{13}$$

where f_g is the friction coefficient of the guideways, F_g is the vertical load carried by the guideways, N; and v_g is the moving speed of the sliders relative to the guideways (m/s).

The dual drive sliding feed system has two servo motors, which drive the screw shaft and the nut. The motor heat generation can be calculated by [20]:

$$H_m = \frac{M_m n_m}{9550}(1 - \delta) \tag{14}$$

where M_m is the output torque of the motor (N.mm), n_m is the rotation speed of the motor (rpm), and δ is the mechanical efficiency of the motor.

When bearing as a rotating part, friction is the main source of heat. The heat generation of bearings can be calculated by [21]:

$$H_b = 1.047 \times 10^{-4} n_b (M_s + M_v) \tag{15}$$

where n_b is the rotation speed of the bearing (rpm), M_s is the load friction torque caused by the elastic lag of the material and the local differential friction, (N·mm), and M_v is the viscous friction torque generated by the bearing and the lubricant (N·mm). The load friction torque can be calculated by:

$$M_s = f_1 p_1 d_b \tag{16}$$

where f_1 is the coefficient related to the type and load of the bearing, p_1 is the preload of the bearing (N), and d_b is the mean diameter of the bearing (mm).

For the front bearing and nut bearing [22]:

$$f_{1a} = 10^{-3} (P_0/C_0)^{0.33} \tag{17}$$

$$p_{1a} = 1.4Fa - 0.1Fr \tag{18}$$

where P_0, C_0, Fa, and Fr are the equivalent static load (N), the rated static load (N), axial load (N), and a radial load of the bearing (N), respectively.

For the rear bearing:

$$f_{1b} = 9 \times 10^{-4} (P_0/C_0)^{0.55} \tag{19}$$

$$p_{1b} = 3Fa - 0.1Fr \tag{20}$$

The viscous friction torque generated by the bearing and the lubricant can be calculated by [21]:

$$M_v = 10^{-7} f_0 (v_0 n_b)^{2/3} d_b.\ \ v_0 n_b \geq 2000 \tag{21}$$

$$M_v = 160 \times f_0 {d_b}^3.\ \ v_0 n_b < 2000 \tag{22}$$

where f_0 is the coefficient related to the bearing type and lubrication, and v_0 is the kinematic viscosity of the lubricant inside the bearing. In this study, Equation (21) is used for the calculation.

The friction of the dual drive sliding screw is the cause of its heat generation, which is related to the total friction torque and the speed of the sliding screw. The heat generation can be expressed as [8]:

$$H_T = \frac{M_T n_T}{9550} \tag{23}$$

where n_T is the relative speed of the screw and the nut (rpm).

3.2. Analysis of Heat Transfer

The heat transfer process of the dual drive sliding feed system can be divided into two types. One is the natural convective heat transfer between the fixed surface and the surrounding air. The other is the forced convective heat transfer due to the relative motion of the parts and the air. The CHTCs of both can be expressed as [23]:

$$h = \frac{Nu \cdot \lambda}{L_s} \tag{24}$$

where Nu is the Nusselt number, λ is the fluid thermal conductivity (W/m·K), and L_s is the component feature size (mm).

Natural convection heat transfer occurs on the surfaces of fixed components such as the bearing housing and base. The Nusselt number Nu_n can be calculated by:

$$Nu_n = C(Gr \cdot Pr)_{\varepsilon}^{\partial} \tag{25}$$

where C and ∂ are the constants determined by the shape of the heat source and fluid conditions, Gr is the Grashof number, Pr is the Prandtl number, and ε is the qualitative temperature. Gr can be calculated by:

$$Gr = \frac{g\beta {L_s}^3 (T_s - T_a)}{{v_a}^2} \tag{26}$$

where g is the acceleration of gravity (m/s^2), β is the volume expansion coefficient of air, T_s is the surface temperature of the part (°C), T_a is the ambient temperature (°C), and v_a is the kinematic viscosity of the air (mm^2/s).

Forced convection heat transfer occurs on the surface of the moving components, mainly including the screw shaft, worktable, nut servo motor, and other parts. The screw shaft rotates and has a spiral groove on its surface, and its Nusselt number can be calculated as:

$$Nu_s = 0.133 Re^{2/3} Pr^{1/3} \tag{27}$$

where Re is the Reynolds number. For the top and lateral surfaces of the remaining parts, the Nusselt constant Nu_p can be calculated by:

$$Nu_p = 0.332 Re^{1/2} Pr^{1/3} \tag{28}$$

For the front surface perpendicular to the direction of motion, the Nusselt constant Nu_v can be calculated by:

$$Nu_\mathrm{v} = 0.228 Re^{0.731} Pr^{1/3} \tag{29}$$

The motion of the worktable of the dual drive sliding feed system is the combined motion of the screw motor and the nut motor. To analyze the thermal field characteristics of the dual drive sliding feed system, the heat generation and key heat transfer coefficients of each part of the system were calculated based on Equations (13)–(29) at an ambient temperature of 20 °C for a synthesis speed of 0.18 m/min, as shown in Tables 1 and 2.

Table 1. Partial heat production of the dual drive sliding feed system.

Speed of Synthesis (m/Min)	Speed of Screw (Rpm)	Speed of Nut (Rpm)	Heat Production (W)					
			Guideways	Screw Servo Motor	Nut Servo Motor	Front Bearing	Nut Bearing	Rear Bearing
0.18	396	360	0.39	1.87	1.70	4.95	5.31	4.36

Table 2. Partial CHTCS of the dual drive sliding feed system.

Speed of Synthesis (m/Min)	Speed of Screw (Rpm)	Speed of Nut (Rpm)	CHTCS (W/m^2·K)					
			Screw Pair	Screw Shaft	Nut Servo Motor	Nut Housing	Slider	Worktable
0.18	396	360	9.17	56.3	15.52	31.26	14.53	16.23

3.3. TCRs between Rough Contact Surfaces

The surface of the internal joint of the feed system is particularly rough at the micro level due to the processing level constraint, resulting in the so-called rough joint. When heat flows through a rough joint, it differs from heat conduction in a solid, which is hampered, and a portion of the heat is lost. The temperature will drop on both contact surfaces.

Therefore, to improve the simulation accuracy of the thermal model of the dual drive sliding feed system, it is necessary to accurately describe the TCR between the rough contact surfaces inside the system. According to the previous analysis of the TCR solution by this group, the TCRs of some key bond surfaces of the dual drive sliding feed system are shown in Table 3.

Table 3. The TCRs of the dual drive sliding feed system at key joints.

Joint Component	TCR ($m^2 \cdot K/W$)
Bearing outer ring-bearing housing	1.25×10^{-3}
Bearing inner ring-screw shaft	1.48×10^{-4}
Nut-screw	1.65×10^{-4}
Guideway-slider	6.89×10^{-4}
Nut servo motor-nut	3.68×10^{-3}

4. Establishment and Verification of the Thermal Model for Dual Drive Sliding Feed System

To accurately describe the thermal characteristics of the dual drive sliding feed system and compensate for the thermal error generated by the system, it is necessary to establish a simulation model of the thermal characteristics of the feed system. The finite element method is used to simulate the system, and an experiment is carried out to verify the comparative analysis.

4.1. Finite Element Simulation Model of Dual Drive Sliding Feed System

A finite element simulation model of the dual drive feed system was created based on the TCR, heat generation, and heat transfer coefficient calculated above to analyze the thermal characteristics of the dual drive sliding feed system. To increase the solving efficiency, the following appropriate simplifications and assumptions were made:

(1) The chamfers and some tiny parts inside the system were ignored;
(2) The screw shaft ignores the grooves on its surface and treats it as a cylinder;
(3) The parameters of heat generation and CHTCs obtained from the previous calculation do not vary with the movement or temperature rise of the components.

The hexahedral and tetrahedral meshes were used to mesh the model once it was imported into ANSYS. The heat sources, such as the screw and bearing, were coarsely meshed to reduce simulation error. The mesh created 152,924 nodes and 282,832 elements. The dual drive sliding feed system was subjected to the same thermal boundary conditions and material attributes as in the preceding section. Table 4 shows the material qualities of several of the system's essential components.

Table 4. Material properties of the dual drive sliding feed system.

Application Components	Material	Density (kg/m^3)	Modulus of Elasticity (GPa)	Poisson's Ratio	Linear Expansion Coefficient (10^{-5}/K)	Thermal Conductivity (W/m·K)	Specific Heat Capacity (J/kg·K)
Nut	Copper alloy	8400	110	0.34	1.7	115	387
Screw/bearing	GCr15	7800	200	0.28	1.2	48	729
Base/bearing housing	Q345B	7850	206	0.3	1.2	46	460
Guideways/slider	40Cr	7850	200	0.3	1.13	51	477

4.2. Experimental Verification Device and Scheme

To verify the accuracy of the solution of the simulation model, an experimental study on the temperature rise and deformation of the dual drive sliding feed system is necessary. Figure 4 depicts the experimental device. Concerning current studies, the temperature measurement locations that have a substantial impact on the total thermal field of the feed system were chosen [22–24]. The temperatures of the front bearing (T1), the rear bearing (T2), the nut flange (T3), the screw shaft (T4), the worktable (T5), the environment (T6), and the axial elongation of the screw shaft (*D*) were measured separately. The temperature data were acquired at T1-T3, T5, and T6 by five temperature sensors (PT100, KAIPUSEN, Xinghua, China) with a resolution of 0.1 °C. The NI PXIe-1082 was used to acquire and process the temperature data. The temperature at T4 was measured by a thermal infrared imager (E86, FLIR, Oregon, United States) with a resolution of 0.1 °C. Axial elongation (*D*) was measured using the laser displacement sensor (CL-3000, KEYENCE, Osaka, Japan). When the temperature rise reached 95% of the maximum temperature rise and the stable fluctuation of the value of the multiple temperature measurement points was less than 0.5 °C. The system can be considered to have reached thermal equilibrium. To minimize the influence of experimental errors on the analysis results, the values of each temperature measurement point were taken as the result of this experiment when the system reached thermal equilibrium.

Figure 4. Temperature rise and deformation experimental device.

To clarify the thermal characteristics of the dual drive sliding feed system, the operating conditions shown in Table 5 are used for exploratory tests. The thermal characteristics of the dual drive sliding feed system at different operating speeds and different ambient temperatures are analyzed separately. Since the working temperature of the machine tool is generally 15–25 °C, the working conditions in this paper are set the ambient temperature to 15, 20, and 25 °C.

Table 5. Operating conditions of the experiments.

Operating Condition	Speed of Synthesis (m/Min)	Speed of Screw (Rpm)	Speed of Nut (Rpm)	Ambient Temperature (°C)
I	0.18	396	360	20
II	0.36	1116	1080	20
III	0.54	2214	2160	20
IV	0.36	1116	1080	15
V	0.36	1116	1080	25

4.3. Comparison of the Simulation and Experimental Results

In the simulation platform, the nut was defined to reciprocate relative to the screw, and the worktable was moved periodically throughout the entire stroke. The transient thermal analysis end time was set to 10,800 s. The corresponding simulation parameters were set according to the five operating conditions in Table 6. The temperature field and the axial deformation of the screw after the stabilization of the dual drive sliding feed system are shown in Figures 5–9.

Table 6. Comparison of the measured and simulated temperatures.

Operation Condition	Measured Position	Simulated Value (°C)	Measured Value (°C)	Deviation (°C)
I	T1	28.1	27.1	1.0
	T2	25.7	24.5	1.2
	T3	35.9	34.5	1.4
	T4	33.9	33.2	0.7
	T5	33.7	31.9	1.8
II	T1	30.8	29.6	1.2
	T2	27.4	26.2	1.2
	T3	38.5	37.1	1.4
	T4	36.4	35.8	0.6
	T5	36.2	34.2	2.0
III	T1	31.1	30.1	1.0
	T2	28.3	27.3	1.0
	T3	42.1	40.1	2.0
	T4	39.2	38.2	1.0
	T5	38.7	36.6	2.1
IV	T1	24.7	23.6	1.1
	T2	21.9	20.9	1.0
	T3	33.4	31.8	1.6
	T4	30.2	29.5	0.7
	T5	30.0	28.5	1.5
V	T1	34.5	33.2	1.3
	T2	31.7	30.5	1.2
	T3	42.4	40.8	1.6
	T4	39.9	38.8	1.1
	T5	40.0	37.9	2.1

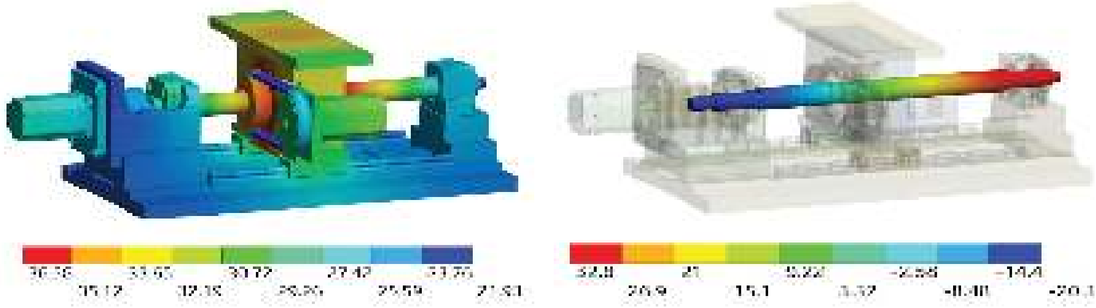

(**a**) (**b**)

Figure 5. Temperature field and axial deformation under the operating condition I. (**a**) Temperature field distribution. (**b**) Axial deformation distribution of the screw shaft.

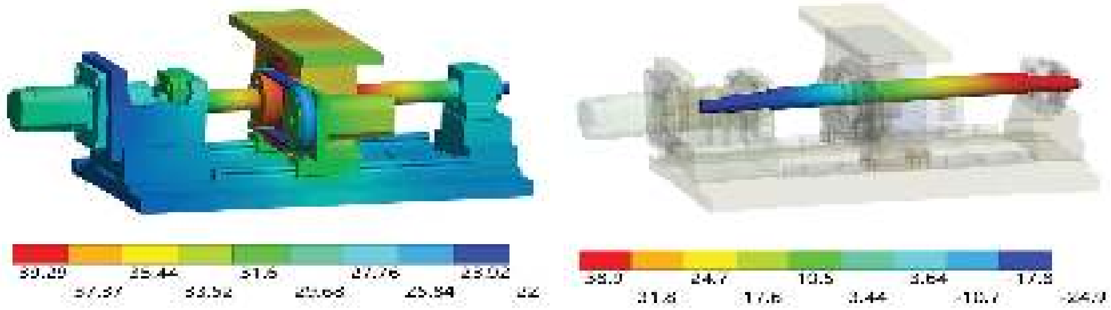

(**a**) (**b**)

Figure 6. Temperature field and axial deformation under the operating condition II. (**a**) Temperature field distribution. (**b**) Axial deformation distribution of the screw shaft.

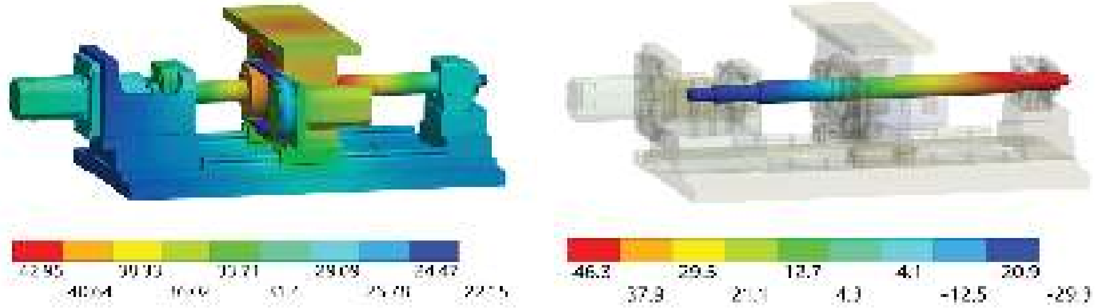

(**a**) (**b**)

Figure 7. Temperature field and axial deformation under the operating condition III. (**a**) Temperature field distribution. (**b**) Axial deformation distribution of the screw shaft.

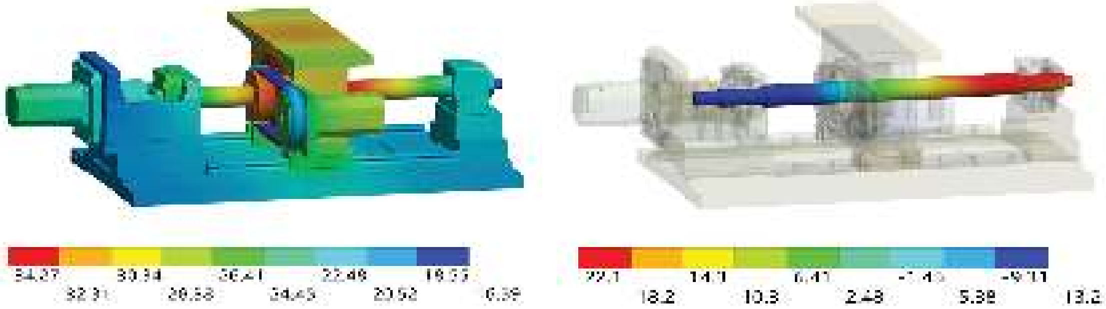

(**a**) (**b**)

Figure 8. Temperature field and axial deformation under the operating condition IV. (**a**) Temperature field distribution. (**b**) Axial deformation distribution of the screw shaft.

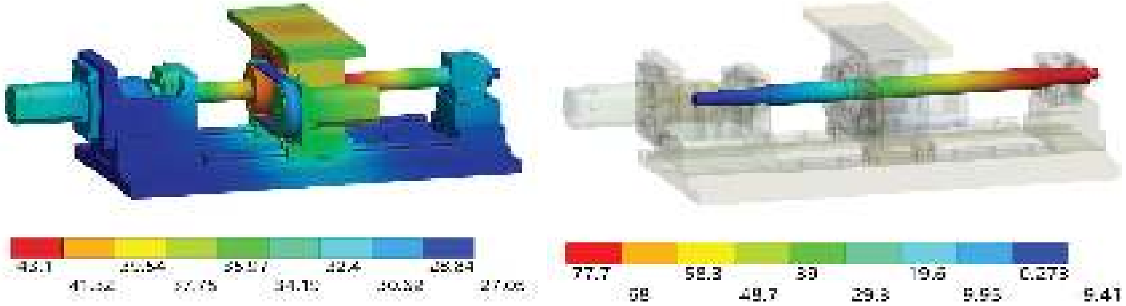

(**a**) (**b**)

Figure 9. Temperature field and axial deformation under the operating condition V. (**a**) Temperature field distribution. (**b**) Axial deformation distribution of the screw shaft.

The solved thermal field distribution shows that the dual drive sliding feed system generates heat through the friction of the contact area, which leads to thermal deformation and thermal error. Among them, the sliding friction at the engagement of the nut and screw produces the most heat and is also affected by the heat generated by the nut bearing. Moreover, because the bearing is inside the nut housing, convective heat transfer with the surrounding air does not occur. This results in heat accumulation and local high temperatures. Therefore, the highest temperature occurs at the nut. The lowest temperature appears at the synchronous belt, which is due to the material of the synchronous belt being rubber and its low heat transfer rate. The synchronous belt experiences forced convective heat transfer with the surrounding air during operation, resulting in a lower temperature than that of the other components.

From the solved axial deformation of the screw, it can be seen that the screw generates thermal elongation in the axial direction under the action of a temperature load. The deformation of the screw is affected by multiple thermal loads, such as the nut, front bearing, and rear bearing. Thermal deformation occurs in both the forward and reverse directions of the screw axis. The axial deformation at the connection between the screw shaft and the front bearing is small. The axial deformation at the connection between the screw shaft and the rear bearing is the largest. The reason is that the rear bearing is supporting and cannot limit the axial displacement of the screw at all. Given the numerous internal heat sources and the substantial heat generation of the sliding screw in the dual drive sliding feed system, the axial deformation of the system under identical operating conditions is greater than that of the conventional feed system [6].

The minimum and maximum temperatures of the thermal field of the entire dual drive sliding feed system increased with increasing rotational speed. The thermal elongation at the rear bearing also increased. Moreover, Figures 8 and 9 show that the thermal field distribution, as well as the axial elongation, significantly changes after the ambient temperature changes. Therefore, the dynamic thermal characteristics of the dual drive sliding feed system are analyzed. The transient thermal field and axial elongation of the screw are analyzed for the dual drive sliding feed system. According to the preliminary experiment, the temperature increased rapidly during the initial period. Therefore, every 120 s was taken as a measurement cycle before 600 s, and every 600 s was taken as a measurement cycle after 600 s. All rotating axes operated at specified speeds during the experiment, and the worktable moved periodically throughout its entire stroke. The comparative analysis results are shown in Figure 10, the temperature deviation after the system reaches the thermal equilibrium state is shown in Table 6, and the axial thermal elongation deviation is shown in Table 7.

Table 7. Comparison of the measured and simulated elongations.

Operation Condition	Simulated Value (μm)	Measured Value (μm)	Deviation (μm)
I	32.8	29.9	2.9
II	38.9	35.5	3.4
III	46.3	42.5	3.8
IV	22.1	20.3	1.8
V	77.7	71.5	6.2

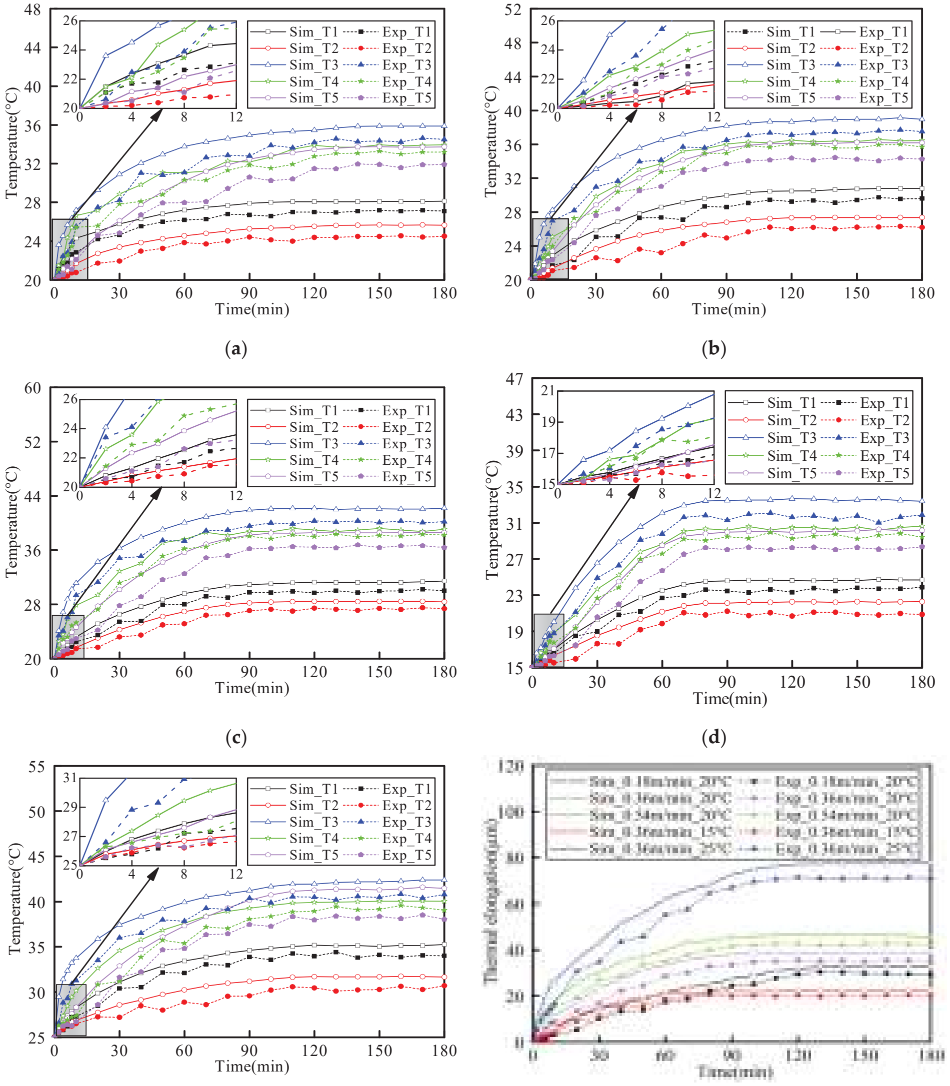

(**a**) (**b**)

(**c**) (**d**)

(**e**) (**f**)

Figure 10. Comparative analysis results. (**a**) Temperature field under operating condition I. (**b**) Temperature field under operating condition II. (**c**) Temperature field under operating condition III. (**d**) Temperature field under operating condition IV. (**e**) Temperature field under operating condition V. (**f**) Axial thermal elongation under the screw.

As shown in Figure 10, along with the increase in the system running time, the temperature of each part, as well as the axial thermal elongation, will increase. Moreover, the temperature difference at T3 is large relative to the other temperature measurement points. The reason is that T3 is the result of the superposition of two major heat sources, and the sliding screw produces more heat. As shown from the experimental and simulated comparison data for each temperature measurement point in Figure 10, the values measured in the experiment are lower than the simulation values. The reason is that the temperature sensor is attached to the component surface. There is a large thermal contact resistance, which affects the accuracy of the temperature measurements. In contrast, the deviation in the temperature measured at T4 is smaller because the temperature at T4 was measured by an infrared thermometer. There was no thermal contact resistance between the sensor and the component. In addition, this experiment used air conditioning for temperature control. Moreover, the experimental environment space is small, and the airflow was disrupted during the experiment. As a result, the accuracy of temperature collection was compromised, causing fluctuations in the experimental temperature measurement data. Comparing the characteristics of the temperature rise for each operating condition in Figure 10. It can be seen that the location with a higher temperature at the end has a faster temperature rise at the beginning due to its higher heat generation. However, the temperature rise at T5 was slower than at T3 and T4. The reason was that the T5 was not a heat source, and temperature rise could only be realized through heat transfer between components. Therefore, the temperature at T5 was also easily affected by the environment and other heat sources. So, the error between the experiment and simulation was more significant.

A comparison of Figure 10a–c reveals that the temperature increase rate at each temperature measurement point increases with increasing rotational speed. The temperature at which thermal equilibrium was reached also increased, and the thermal equilibrium time gradually decreased. The system reached a thermal equilibrium state at 120, 100, and 90 min. The heat generation and heat transfer of the system reached a dynamic equilibrium state. However, the increase in each part is different. Because the temperature at the engagement point between the screw and the nut was the highest, the temperature increase in the surrounding parts was greater. The temperature increase in the regions away from the meshing was low, as shown in T1 and T2 in the figure.

Comparing Figure 10b,d,e, it can be seen that the influence of ambient temperature on the temperature characteristics of the feed system was significant. When the ambient temperature was high, the heat generated by the system was more difficult to dissipate, resulting in a faster temperature rise. On the contrary, when the ambient temperature was low, the system can more easily dissipate heat, resulting in a slower rate of temperature rise. The ambient temperature will affect the time for the feed system to reach thermal equilibrium. At an ambient temperature of 25 °C, the dual drive sliding feed system reached thermal equilibrium at 110 min. At an ambient temperature of 15 °C, the dual drive sliding feed system reached thermal equilibrium at 70 min. It can be seen that at a higher ambient temperature, the feed system needs longer to achieve thermal equilibrium due to the difficulty of heat dissipation. The feed system can achieve heat equilibrium with the environment at a lower ambient temperature more quickly.

Comparing Figure 10c,e,f, the temperature field of condition III was similar to that of condition V when the thermal equilibrium state is reached. However, due to the difference in ambient temperature, the final axial thermal elongation of the screw was 29 μm. This once again shows that the ambient temperature has an essential influence on the thermal elongation of the feed system. Therefore, the feed system's regular operation and precision stability must be ensured. Not only can the internal heat generation be controlled, but the ambient temperature should also be controlled within the appropriate range.

Tables 6 and 7 show the key temperature measurement points of the dual drive sliding feed system. The deviation in the temperature simulation of the thermal model was less than 2.1 °C, and the error in the axial elongation of the screw was less than 6.2 μm, which proves the effectiveness of the built thermal simulation model. It is shown that the developed thermal simulation model can more accurately describe the thermal characteristics of the dual drive sliding feed system. The error in the axial thermal elongation of the screw will be slightly greater than the error at each temperature measurement point. The reason is that the axial elongation of the screw is the result of the combined action of all the heat sources in the feed system and the environmental conditions. The deviation results at several key temperature measurement points do not fully represent the final axial deformation deviation of the screw. Therefore, a more accurate simulation solution model was established, laying the foundation for thermal error modeling. The key temperature measurement points of the dual drive feed system should be further optimized, and the thermal boundary conditions of the system should be optimized.

Thermal simulation can obtain more operational process data than experiments can, thus providing insight into the thermal characteristics of the feed system. Operation condition I is taken as an example based on the transient thermal analysis of the feed system. The temperature field of the screw shaft with respect to time and position changes is determined. This is shown in Figure 11.

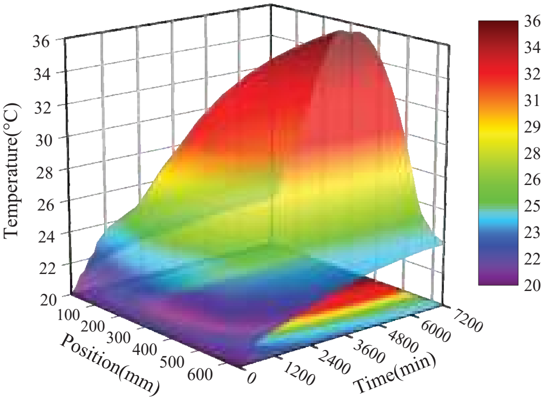

Figure 11. The overall temperature rise of the screw.

As shown in Figure 11, over time, all the parts of the screw have different degrees of temperature rise. The temperature in the middle of the screw is the highest, and the temperature at both ends is the lowest. The axial variation along the screw is from low to high and back again. The temperature at both ends is approximately symmetrical relative to the middle. The conventional screw axial temperature distribution is the opposite of the dual drive sliding feed system. The axial temperature distribution of the conventional screw is low in the middle and high at both ends [25]. The reason for this difference is that the dual drive sliding feed system utilizes a sliding screw, which results in greater heat generation. In addition, a bearing is added inside the nut, and the nut motor affects the distribution of the temperature field during operation. Therefore, the temperature rise of the screw should be controlled, and the axial deformation should be reduced. Subsequently, the structure of the dual drive sliding feed system should be further optimized to improve the temperature field distribution.

5. Conclusions

To accurately depict the thermal field characteristics of a dual drive sliding feed system under complex heat source effects and to elucidate the response mechanism of temperature rise and thermal deformation. In this study, the dynamic thermal characteristics of the system are explored by establishing a thermal simulation model and verifying the analysis with the experimental results. Based on the results and analysis, the following conclusions can be drawn:

1. The established thermal simulation model can effectively describe the dynamic thermal characteristics of the dual drive sliding feed system. By comparing the temperature rise and thermal elongation under simulation and experimental conditions, it can be concluded that the temperature rise deviation under five operating conditions is less than 2.1 °C, and the error in the axial thermal deformation of the screw is less than 6.2 μm. The established thermal characteristic simulation model can effectively describe the thermal dynamic response characteristics of the dual drive sliding feed system during operation.
2. The thermal field distribution and axial deformation of the dual drive sliding feed system differ from those of conventional feed systems. Due to the difficulty of heat dissipation and the combined effect of the screw and nut bearings, the main heat distribution region of the dual drive feed system is at the nut. Given the numerous heat sources in the system and the significant temperature increase in the sliding screw, the axial deformation of the screw in the dual drive sliding feed system is greater than that in the conventional feed system under the same operating conditions.
3. The thermal characteristics of a dual drive sliding system are significantly influenced by both rotational speed and ambient temperature. An increase in rotational speed results in a faster rate of temperature rise and a shorter time to reach thermal equilibrium. Conversely, higher ambient temperatures lead to a quicker temperature rise and a longer time to achieve thermal equilibrium. The ambient temperature also has a significant impact on the axial deformation of the screw. Even when the temperature field is similar, substantial differences in the axial thermal elongation of the screw can occur due to varying ambient temperatures.

This study investigates the temperature and deformation field distributions of a dual drive sliding system under various operating conditions and describes the dynamic thermal characteristics of the system. This research provides a foundation for temperature rise and deformation control and guidance for structural optimization and installing cooling systems. This work also lays the foundation for developing data-driven models to realize dynamic thermal error compensation. However, due to the use of empirical formulas in establishing thermal models, there are deviations in the simulation results. Future work should consider optimizing the system's thermal boundary conditions to further improve the thermal model's accuracy.

Author Contributions: H.L. (Hui Li): investigation, software, writing—original draft. H.L. (Haiyang Liu): conceptualization, data curation, formal analysis, writing—review and editing, supervision. X.F.: funding acquisition, writing—review and editing. Y.L.: methodology. M.Y.: validation. A.W.: validation. All authors have read and agreed to the published version of the manuscript.

Funding: This work was supported by the Shandong Provincial Natural Science Foundation (grant number ZR2019MEE003).

Data Availability Statement: Data supporting this study are included within the article.

Conflicts of Interest: The authors declare that they have no known competing financial interest or personal relationships that could have appeared to influence the work reported in this paper.

References

1. Li, Z.-J.; Tan, Z.; Chen, Y.; Lu, Z.-C.; Fan, Y.-C. Thermal error prediction of ball screw feed system based on inverse heat transfer analysis. *Int. J. Adv. Manuf. Technol.* **2022**, *122*, 2607–2624. [CrossRef]
2. Li, Y.; Wei, W.; Su, D.; Wu, W.; Zhang, J.; Zhao, W. Thermal characteristic analysis of ball screw feed drive system based on finite difference method considering the moving heat source. *Int. J. Adv. Manuf. Technol.* **2020**, *106*, 4533–4545. [CrossRef]
3. Lei, M.; Yang, J.; Wang, S.; Zhao, L.; Xia, P.; Jiang, G.; Mei, X. Semi-supervised modeling and compensation for the thermal error of precision feed axes. *Int. J. Adv. Manuf. Technol.* **2019**, *104*, 4629–4640. [CrossRef]
4. Liu, J.; Ma, C.; Wang, S.; Wang, S.; Yang, B.; Shi, H. Thermal boundary condition optimization of ball screw feed drive system based on response surface analysis. *Mech. Syst. Signal Process.* **2019**, *121*, 471–495. [CrossRef]
5. Du, F.; Zhang, M.; Wang, Z.; Chen, Y.; Feng, X.; Li, P. Identification and compensation of friction for a novel two-axis differential micro-feed system. *Mech. Syst. Signal Process.* **2018**, *106*, 453–465. [CrossRef]

6. Yang, H.; Xing, R.; Du, F. Thermal error modelling for a high-precision feed system in varying conditions based on an improved Elman network. *Int. J. Adv. Manuf. Technol.* **2020**, *106*, 279–288. [CrossRef]
7. Lu, Z.; Feng, X.; Su, Z.; Liu, Y.; Yao, M. Friction Parameters Dynamic Change and Compensation for a Novel Dual-Drive Micro-Feeding System. *Actuators* **2022**, *11*, 236. [CrossRef]
8. Xu, Z.Z.; Liu, X.J.; Kim, H.K.; Shin, J.H.; Lyu, S.K. Thermal error forecast and performance evaluation for an air-cooling ball screw system. *Int. J. Mach. Tools Manuf.* **2011**, *51*, 605–611. [CrossRef]
9. Qiao, G.; Liu, G.; Ma, S.; Wang, Y.; Li, P.; Lim, T.C. Thermal characteristics analysis and experimental study of the planetary roller screw mechanism. *Appl. Therm. Eng.* **2019**, *149*, 1345–1358. [CrossRef]
10. Zhao, C.J.; Yu, X.K.; Huang, Q.K.; Ge, S.D.; Gao, X. Analysis on the load characteristics and coefficient of friction of angular contact ball bearing at high speed. *Tribol. Int.* **2015**, *87*, 50–56. [CrossRef]
11. Helmig, T.; Kneer, R. A novel transient infrared-thermography based experimental method for the inverse estimation of heat transfer coefficients in rotating bearings. *Int. J. Therm. Sci.* **2021**, *167*, 107000. [CrossRef]
12. Bui, B.D.; Uchiyama, N.; Simba, K.R. Contouring control for three-axis machine tools based on nonlinear friction compensation for lead screws. *Int. J. Mach. Tools Manuf.* **2016**, *108*, 95–105. [CrossRef]
13. Min, X.; Jiang, S. A thermal model of a ball screw feed drive system for a machine tool. *Proc. Inst. Mech. Eng. Part C J. Mech. Eng. Sci.* **2011**, *225*, 186–193. [CrossRef]
14. Ma, S.; Wu, L.; Liu, G.; Fu, X. Local contact characteristics of threaded surfaces in a planetary roller screw mechanism. *J. Struct. Mech.* **2020**, *48*, 1–26. [CrossRef]
15. Du, C.; Liu, G.; Qiao, G.; Ma, S.; Cai, W. Transient thermal analysis of standard planetary roller screw mechanism based on finite element method. *Adv. Mech. Eng.* **2018**, *10*, 1687814018812305. [CrossRef]
16. Houpert, L. Numerical and analytical calculation in ball bearings. *Proc. Congr. Roulements Toulouse Toulouse* **1999**, *5–7*, 1–15.
17. Qiao, G.; Liu, G.; Ma, S.; Shi, Z.; Wang, Y.; Lim, T.C. An improved thermal estimation model of the inverted planetary roller screw mechanism. *Proc. Inst. Mech. Eng. Part C J. Mech. Eng. Sci.* **2018**, *232*, 4430–4446. [CrossRef]
18. Yang, J.J. Effect of Preload on Axial Deformation and Friction of Planetary Roller Screw. *J. Mech. Transm.* **2011**, *35*, 16–22.
19. Olaru, D.; Puiu, G.C.; Balan, L.C.; Puiu, V. A New Model to Estimate Friction Torque in a Ball Screw System. *Prod. Eng. Eco-Des. Technol. Green Energy* **2005**, 333–346. Available online: https://link.springer.com/chapter/10.1007/1-4020-2933-0_20 (accessed on 12 November 2023).
20. Kim, J.-J.; Jeong, Y.H.; Cho, D.-W. Thermal behavior of a machine tool equipped with linear motors. *Int. J. Mach. Tools Manuf.* **2004**, *44*, 749–758. [CrossRef]
21. Su, D.; Li, Y.; Zhao, W.; Zhang, H. Transient thermal error modeling of a ball screw feed system. *Int. J. Adv. Manuf. Technol.* **2023**, *124*, 2095–2107. [CrossRef]
22. Li, D.; Feng, P.; Zhang, J.; Wu, Z.; Yu, D. Method for modifying convective heat transfer coefficients used in the thermal simulation of a feed drive system based on the response surface methodology. *Numer. Heat Transf. Part A Appl.* **2015**, *69*, 51–66. [CrossRef]
23. Oyanguren, A.; Larraaga, J.; Ulacia, I. Thermo-mechanical modelling of ball screw preload force variation in different working conditions. *Int. J. Adv. Manuf. Technol.* **2018**, *97*, 723–739. [CrossRef]
24. Mao, X.; Mao, K.; Wang, F.; Yan, B.; Lei, S. A convective heat transfer coefficient algorithm for thermal analysis of machine tools considering a temperature change. *Int. J. Adv. Manuf. Technol.* **2018**, *99*, 1877–1889. [CrossRef]
25. Wu, H.; Guan, Q.; Xi, C.; Zuo, D. Construction of dynamic temperature field model of ball screw based on superposition of positive and negative temperature fields. *Numer. Heat Transf. Part A Appl. Int. J. Comput. Methodol.* **2023**, *83*, 343–360. [CrossRef]

MDPI
St. Alban-Anlage 66
4052 Basel
Switzerland
www.mdpi.com

MDPI Books Editorial Office
E-mail: books@mdpi.com
www.mdpi.com/books

Academic Open
Access Publishing

mdpi.com

ISBN 978-3-7258-1074-1